C.1

SANDIA REPORT

SAND87—2290 • UC—235
Unlimited Release
Printed May 1992

A Final Report on the Phase I Testing of a Molten-Salt Cavity Receiver

Volume II – The Main Report

David C. Smith, James M. Chavez, Editor

Prepared by
Sandia National Laboratories
Albuquerque, New Mexico 87185 and Livermore, California 94550
for the United States Department of Energy
under Contract DE-AC04-76DP00789

468p.

Issued by Sandia National Laboratories, operated for the United States Department of Energy by Sandia Corporation.

Available to DOE and DOE contractors from
Office of Scientific and Technical Information
PO Box 62
Oak Ridge, TN 37831

Prices available from (615) 576-8401, FTS 626-8401

Available to the public from
National Technical Information Service
US Department of Commerce
5285 Port Royal Rd
Springfield, VA 22161

NTIS price codes
Printed copy: A09
Microfiche copy: A01

SAND87-2290
Unlimited Release
Printed May 1992

Distribution
Category UC-235

A FINAL REPORT ON THE PHASE I TESTING OF A MOLTEN-SALT CAVITY RECEIVER

VOLUME II - THE MAIN REPORT

COORDINATING AUTHOR
David C. Smith*
Nuclear Equipment Division
The Babcock & Wilcox Company
Barberton, Ohio

EDITOR
James M. Chavez
Central Receiver Technology Branch
Sandia National Laboratories
Albuquerque, New Mexico

ABSTRACT

This report describes the design, construction, and testing of a solar central receiver using molten nitrate salt as a heat exchange fluid. Design studies for large commercial plants (30-100 MWe) have shown molten salt to be an excellent fluid for solar thermal plants as it allows for efficient thermal storage. Plant design studies concluded that an advanced receiver test was required to address uncertainties not covered in prior receiver tests. This recommendation led to the current test program managed by Sandia National Laboratories for the U.S. Department of Energy. The 4.5 MWt receiver is installed at Sandia National Laboratories' Central Receiver Test Facility in Albuquerque, New Mexico. The receiver incorporates features of large commercial receiver designs. This report describes the receiver's configuration, heat absorption surface (design and sizing), the structure and supporting systems, and the methods for control. The receiver was solar tested during a six-month period at the Central Receiver Test Facility in Albuquerque, NM. The purpose of the testing was to characterize the operational capabilities of the receiver under a number of solar operating and stand-by conditions. This testing consisted of initial check-out of the systems, followed by steady-state performance, transient receiver operation, receiver operation in clouds, receiver thermal loss testing, receiver start-up operation, and overnight thermal conditioning tests. This report describes the design, fabrication, and results of testing of the receiver.

*Currently with Science Applications International Corp., Albuquerque, NM

ACKNOWLEDGMENTS

We would like to acknowledge and express our appreciation to all those who contributed to the program. They include the other authors of this Appendix: Patricia Bator and Phil Reed of the Babcock & Wilcox Company; Stan Saloff, Mark (Buzz) Lanning, and Gene Riley of the McDonnell Douglas Company; Bob Boehm of the University of Utah; Russ Skocypec of Sandia National Labs; and Gio Carli of Foster Wheeler. In addition, we would like to acknowledge the following personnel whose contributions made the program successful.

SANDIA NATIONAL LABORATORIES

Nina Bergan	Marty Hall	Hal Norris
Ken Bolt	John Holmes	John Otts
Bob Bradshaw	Joy Holton	Anne Poore
Nova Carter	Jim Grossman	Vince Romero
Bill Couch	Jim Imboden	Al Skinrood
Bill Delameter	Sam Jenkins	Milt Stomp
Sam Dunkan	Roy Johnton	Jack Swearengen
Bob Edgar	J. J. Kelton	Kathy Tate
Boe Ellis	Rod Mahoney	Arleen Vance
Lindsey Evans	Matt Matthews	Craig Tyner
Paul Flora	Clay Mavis	Bill Wilson

BABCOCK & WILCOX

Wes Allman	George Grant	Joe Stadelman
Gene Campbell	Vic Leahock	John Swank
Jim Clevenger	Earl Livingston	Candy Woodruff
Arlis Cooper	Earl Martin	Dan Young
Ralph Dowling	Byron Pritchard	Tom Fewell
Karen Sluka	Curt Flora	Mark Smith
Chuck Getz	Charlie Somers	

McDONNELL DOUGLAS

Bob Gervais	Chick Finch	Tom McKowen
Dave Carey	Matt Russell	
Gerry Coleman	John Navickus	

FOSTER WHEELER

Rich McMillan	Tom Staed

ARIZONA PUBLIC SERVICE

Dale Thornburg	Eric Weber

SOUTHERN CALIFORNIA EDISON

Paul Skavarna	Charles Trilling	Chuck Lopez

BLACK & VEATCH

John Harder	Larry Dubal

CONTRACTORS

George Mulhuland	Tom Tracy

FOREWORD

This report is of work funded by the U.S. Department of Energy under Contract DE-AC04-76DP00789. The report is published in three volumes:

Volume I -- A Summary Report

Volume II -- Appendix I - The Main Report

Volume III -- Appendices A - J

The research and development described in this report was conducted within the U. S. Department of Energy's (DOE) Solar Thermal Technology Program. The goal of the Solar Thermal Technology Program is to advance the engineering and scientific understanding of solar thermal technology, and to establish the technology base from which private industry can develop solar thermal power production options for introduction into the competitive market.

In a solar thermal system, mirrors or lenses focus sunlight onto a receiver where a working fluid absorbs the solar energy as heat. The system then converts the energy into electricity or uses it as process heat. There are two kinds of solar thermal systems: central receiver systems and distributed receiver systems. A central receiver system uses a field of heliostats (two-axis tracking mirrors) to focus the sun's radiant energy onto a receiver mounted on a tower. A distributed receiver system uses three types of optical arrangement--parabolic troughs, parabolic dishes, and hemispherical bowls--to focus sunlight onto either a line or point receiver.

This report describes the design, construction, testing, and evaluation of a solar central receiver that uses molten nitrate salt as a heat transport fluid. The receiver is a 4.5 MWt salt-in-tube cavity receiver that is a scaled down version of a commercial receiver design. This development and test program was carried out by a team of companies on a cost-shared basis with the DOE. The receiver was tested at Sandia National Laboratories' Central Receiver Test Facility in Albuquerque, New Mexico.

VOLUME II MSS/CTE RECEIVER FINAL REPORT
TABLE OF CONTENTS

LIST OF FIGURES

LIST OF TABLES

INTRODUCTION

D. Smith
Babcock & Wilcox Corp.

A 4.5-MWt salt-in-tube cavity receiver was designed, built, and tested as part of the U.S. Department of Energy (DOE) solar thermal research program. A preliminary design study was performed by Arizona Public Service (APS) Company in 1983 recommended a development plan to reduce the technical risk of building a central receiver power plant. The APS study recommended the fabrication and testing of a scaled-down salt-in-tube receiver. Responding to this recommendation, DOE authorized the Molten-Salt Subsystem/Component Test Experiment (MSS/CTE) Program (also called the Repowering Category B Program) with contracting and technical management by Sandia National Laboratories. The MSS/CTE program consists of three experiments:

- A 4.5-MWt Receiver Test
- A Valve Seal Bench Test
- A Pump and Valve Test

This report presents the 4.5-MWt Receiver Test, including the design, fabrication, erection, testing, and test results. Separate reports will be prepared for the other tests. The MSS/CTE program was carried out by a team of companies on a cost shared basis with the DOE. Babcock & Wilcox acted as prime contractor for the program with the following subcontractors:

- Arizona Public Service
- McDonnell Douglas
- Black & Veatch
- Foster Wheeler
- Southern California Edison

The receiver was designed for and tested at Sandia Laboratories Central Receiver Test Facility (CRTF) in Albuquerque, New Mexico.

1.1 Background

The development of the solar thermal central receiver (SCR) began in the early 1970s. The first central receiver systems used water as a working fluid, converting it to steam to drive a turbine generator directly. This system is typified by the Solar 1 plant in Barstow, California. The disadvantages of such a system (i.e., sensitivity to clouds, two-phase-flow problems, etc.) led to a study of other fluids, including molten-salt, sodium, and air. It was found that there were economic advantages to systems using low pressure non-phase change liquids for electric power generation [1]. These systems could employ on-line storage systems to store solar energy for peak power generation and buffer the electric power generation system from cloud transients experienced by the receiver. Molten nitrate salt was found to have a number of advantages, which led to its selection as the thermal transport fluid for numerous solar power plant

A schematic of a typical molten nitrate salt solar central receiver plant is shown in Figure 1.1.1. The salt has the advantages of being chemically stable at temperatures up to 1100°F allowing generation of high temperature steam for an efficient Rankine cycle and a high heat capacity per unit volume for efficient storage of energy as sensible heat. The salt is also relatively inexpensive, allowing for large storage systems. The principal disadvantages of the fluid are its relatively high freezing point (430-470°F), its corrosive nature, and its low conductivity. These difficulties are addressed in the design of the receiver and balance of plant.

The test receiver was incorporated into the existing system at the Central Receiver Test Facility (CRTF). In this test system, heat collected by the salt in the receiver is used to generate steam, which is condensed in a heat rejection system and its heat transferred to a water/glycol mixture. No electricity is generated. This mixture is pumped to air-cooled heat exchangers, where the heat is rejected to the atmosphere.

FIGURE 1.1.1
CONCEPT OF THE MOLTEN-SALT CENTRAL RECEIVER SYSTEM

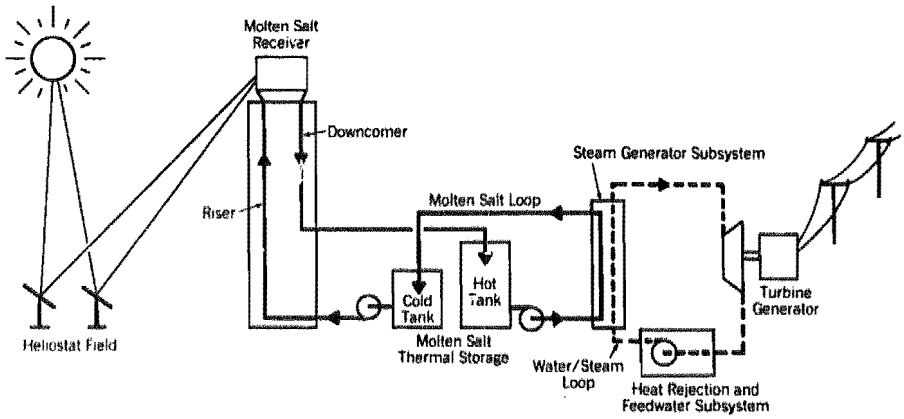

1.2 Synopsis of Research and Development on the Solar Central Receiver

Since 1978, several studies have addressed the design of commercial-scale molten-salt central receivers and power plants [2,3,4,5,6,7]. In addition to the design studies, several test programs were carried out to develop and demonstrate molten-salt technology. In 1981, a first-generation molten-salt receiver test was performed on a receiver designed and built by Martin Marietta Corp. [8]. The test of this receiver and supporting laboratory testing formed the basis for the current receiver designs. In 1983 through 1985, the Molten-Salt Electri Experiment (MSEE) was conducted at the CRTF reusing the Martin Mariett receiver [9].

With this work serving as background, recommendations were made to fabricate and test a new molten-salt receiver incorporating features of the more current design studies. The Solar 100 Conceptual Study [7] by Southern California Edison Company identified a number of areas of technical risk associated with a molten-salt receiver. The Saguaro Repowering Study [6] also identified the receiver as a component with high technical risk. The Saguaro report included a recommendation to make and test a scaled down receiver with features typical of the commercial design.

Since the Saguaro and Solar 100 receiver designs were similar, the Molten-Salt Subsystem/Component Test Experiment (MSS/CTE) was proposed by a team of companies representing both studies to address common issues. This experiment included the design, fabrication, and testing of a new scaled-down receiver incorporating features of both the Saguaro and Solar 100 designs. This proposal was presented to the Department of Energy, and funding for the project was allocated through Sandia National Laboratories (SNL), which was charged with technical management of the project. The cost of the program was divided between the DOE and the industry participants according to a cost-sharing agreement.

1.2.1 Description of the Saguaro Repowering Study

The Saguaro Repowering Study [7] was performed under contract to DOE by a team of companies including Martin Marietta, Black and Veatch, Babcock and Wilcox, and Olin under contract to Arizona Public Service (APS). The study prepared a preliminary design to repower the existing Saguaro power plant north of Tucson, Arizona, with steam generated by a solar receiver and steam generator combination. The receiver designed for the study was a north-facing C-shaped cavity receiver. An illustration of this receiver is presented in Figure 1.1.2. The receiver employs a heat-absorption surface made of vertical tubes painted black for maximum solar heat absorption. The absorbed power rating is 190 MW_{th}. The receiver heat absorption panels are of tangent tube construction, with tubes attached to horizontal buckstays for support. The tubes are divided at the receiver vertical centerline into two separate control zones, each with its own inlet control valve. Each control zone is split into 12 passes connected with headers at the top and bottom. Flow in the receiver followed a serpentine path up one pass and down the adjacent pass. The tube panels are hung from above, allowing gravity to act in the direction of thermal expansion. The buckstays move with the panel using a roller arrangement. The receiver aperture is surrounded by passive insulation board.

FIGURE 1.1.2
SAGUARO C-SHAPED CAVITY RECEIVER

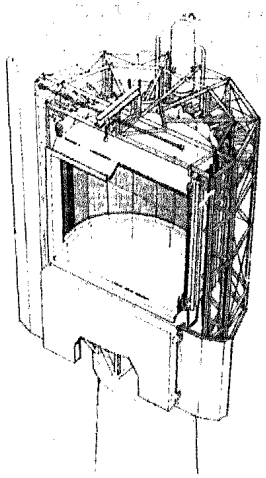

1.2.2 Solar 100 Conceptual Study Description

The Solar 100 plant design was prepared in response to an opportunity notice distributed by Southern California Edison (SCE) presenting its desire to install a large solar plant on its grid. McDonnell Douglas Corp. responded to this solicitation with a proposal prepared by a team of companies including Bechtel and Foster Wheeler. The receiver designed for this study was also a north-facing cavity receiver, but with a power rating of 312 MW_{th}. The receiver employed a heat-absorption panel made up of vertical tubes painted black for high solar absorptivity. The cavity was tilted downward toward the field as shown in Figure 1.1.3. Panel construction employed tangent tubes held in place from behind by horizontal buckstays.

The tube panel was divided into multiple passes, with flow passing upward through each pass to an upper header. Flow collected in the upper header of the pass was then piped to the lower header of the next pass to preserve upflow in each pass and avoid concerns about flow stability resulting from heated downflow in parallel channels. The panels were hung from above, and

FIGURE 1.1.3
SOLAR 100 RECEIVER CONCEPT

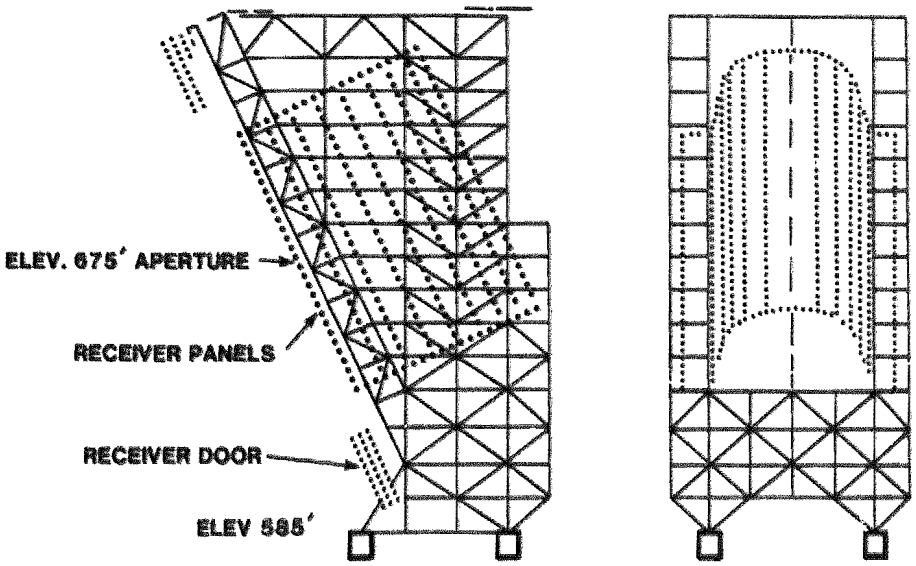

the lateral buckstay supports were connected to the receiver structure through a system of pivoting links, allowing for the thermal growth. In the aperture plane, the receiver employed "wing panels" on both sides of the opening to absorb flux spillage. First, salt entered the wing panels at 550°F then proceeded to the cavity panels to be heated to an outlet temperature of 1050°F.

1.2.3 Description of the Molten-Salt Electric Experiment

The Molten-Salt Electric Experiment (MSEE) was conducted at the CRTF between 1983 and 1985 [10,11]. The molten-salt receiver, previously tested by Martin Marietta Corp., was refurbished and returned to the CRTF tower. Piping was installed in the tower to connect the system to a storage experiment on the ground [12].

A steam generation subsystem was installed [13] to cool the salt from the storage subsystem and produce steam to drive a turbine generator. The MSEE

was a full-system demonstration capable of generating 750 kW of electric power. Much was learned about molten-salt receivers during its testing, and a list of recommendations for future receivers was developed.

1.3 Objectives of this Receiver Test Program

The overall objective of the MSS/CTE receiver test program was to design, fabricate, and test a molten-salt solar receiver typical of the commercial-sized power plant designs and to demonstrate to the industry/utility/financial community the feasibility and efficiency of a molter-salt solar receiver. The MSS/CTE receiver incorporates features of new plant designs and benefits from the lessons learned on the MSFE and previous test programs. The objective of the test program for the MSS/CTE receiver was to demonstrate the features of a commercial-scale receiver, and further, to define the operating range, flexibility, and limitations of current molten-salt receiver technology.

Specific objectives were to:

- Provide a sound technological base for development of the molten-salt solar industry.
- Provide data to support future design and construction plans for commercial-sized plants.
- Demonstrate to the utilities and investment community that the major technical issues perceived as risks can be resolved.
- Demonstrate receiver performance and operation under steady-state, transient, and emergency conditions.
- Define the operating range, flexibility, and limitations of the receiver design.

- Obtain, evaluate, and document receiver efficiency to verify design methods, and identify uncertainties.

- Verify receiver thermal-hydraulic characteristics.

- Develop efficient operational methods and control systems to maximize receiver output.

- Demonstrate the operation, performance, and reliability of critical receiver components, overnight thermal conditioning operations, cavity doors, and door seals.

- Investigate the effectiveness of the emergency cooling system design.

- Investigate the durability of the panel absorber surface coating.

- Demonstrate panel tube wall conditions compatible with a 30-year life.

- Verify the ability of the receiver thermal expansion system design to allow panel growth.

- Improve manufacturers' warranty position on receiver performance and life.

- Continue reduction in plant capital costs by improved fabrication methods, reduction of design conservatisms, and improved designs.

To accomplish these objectives, the receiver was designed using features and methods that would be employed in a commercial-scale design. The receiver was built using materials and methods also typical of those used for commercial receivers. A test program was then conducted to 1) confirm that the design was operating as intended, 2) measure the thermal

performance of the receiver, and 3) define the operating range, flexibility, and limitations of the design. Results from the test were analyzed and are presented in this report.

1.4 Program Team Organization

The MSS/CTE receiver was designed, built, and tested by a team of companies led by Babcock & Wilcox (B&W). The contract for the test program was managed by Sandia Laboratories, and the test was conducted at Sandia Laboratories' CRTF facility in Albuquerque, New Mexico.

The team of companies consisted of McDonnell Douglas Astronautics Company (MDAC), Black and Veatch Consulting Engineers, and Arizona Public Service (APS), subcontracting to Babcock & Wilcox. McDonnell Douglas also had subcontracts with Foster Wheeler (FW) and Southern California Edison (SCE). The role of Sandia Laboratories and each of the team members is described in more detail below.

Sandia National Laboratories-Livermore

As program manager, Sandia-Livermore entered into contractual arrangements with the project team and managed the project funding. It also provided the overall technical direction for the project and reported to the Department of Energy. Late in the program, these functions were transferred to Sandia-Albuquerque, as the Livermore office ended its involvement with solar energy.

Sandia National Laboratories - Albuquerque

The site for the test was the Central Receiver Test Facility (CRTF) at Sandia National Laboratories in Albuquerque. Sandia Albuquerque made the test site available and provided personnel to erect the receiver test, maintain the test equipment, operate the test, and collect the test data.

Babcock & Wilcox

Babcock & Wilcox was prime contractor for the project and entered into an agreement with Sandia Livermore to construct the receiver and

perform the test. Subcontracts were written to McDonnell Douglas, Black & Veatch, and Arizona Public Service to provide support. B&W provided overall design of the test receiver, design of a majority of the absorber panels, the complete receiver structure, and the balance of the detailed design. B&W fabricated and assembled the test receiver and managed its erection at the CRTF, and provided technical support for the testing and reduction of the data. It also made progress reports to Sandia, and prepared this final report, which includs contributions from the subcontractors.

McDonnell Douglas

McDonnell Douglas was responsible for the collector field interface with the receiver design, including mapping the heat flux, aiming the heliostats, and sizing the receiver aperture. They also designed the receiver control system, planned the tests, and conducted the testing and participated in the data evaluation. Subcontracts were written by McDonnell Douglas to Foster Wheeler and Southern California Edison.

Foster Wheeler

Foster Wheeler designed and made one backwall heat-absorption panel and the wing panels for installation in the receiver. With them, they provided test support and evaluation of data related to their panels.

Arizona Public Service and Southern California Edison

The utility subcontractors provided technical overview of the program from the standpoint of an eventual end user of the technology.

Black & Veatch

Black & Veatch assisted with the safety analysis for the test and provided consulting services.

This team represents a combination of government, industrial, and public utility organizations currently involved in pursuing development of solar energy.

SECTION 2

DESCRIPTION OF THE RECEIVER AND TEST FACILITY

D. Smith - Babcock & Wilcox Corp.
G. Carli - Foster Wheeler Corp.
S. Saloff - McDonnell Douglas Astronautics Corp.
G. Riley - McDonnell Douglas Astronautics Corp.

The MSS/CTE receiver was designed to demonstrate key features for a commercial central receiver design. It converts solar energy to thermal energy using molten salt as the working medium. The receiver, located at the top of the CRTF tower, receives concentrated solar energy from the collector field. Molten salt from the "cold" (550°F) storage tank, located at ground level, is pumped up the tower piping and through the receiver where it is heated to 1050°F. The salt then flows through a downcomer into the hot-salt storage tank. The test receiver was incorporated into the existing system at the CRTF. Heat collected in the salt is used to generate steam. This steam is condensed in a heat rejection system and its heat transferred to a water/glycol mixture. This mixture is pumped to air cooled heat exchangers where the heat is rejected to the atmosphere.

A complete, detailed description of the MSS/CTE receiver and test facility is contained in the following subsections.

2.1 Receiver Subsystem

The receiver is located at the top of the CRTF tower as shown in Figure 2.1.1. The concentrated insolation redirected from the heliostat field impinges on the absorber panels through which molten-salt flow absorbs the thermal energy. The design specifications for the receiver are shown in Table 2-I, and equations defining the properties of the molten salt are given in Table 2-II. The receiver subsystem consists of the receiver absorber panels, cavity enclosure with a two-piece aperture door,

insulation, heat tracing, cold surge tank, hot surge tank, instrumentation, and valves. The general configuration of the receiver is illustrated in the artist's concept shown in Figure 2.1.2. Each of the main features of the design is discussed below.

Cavity Enclosure

The receiver employs a C-shaped cavity configuration, as shown in Figure 2.1.3, similar to both the Saguaro and Solar 100 designs. The back wall of the cavity is composed of heat-absorption panels, and the sidewalls, floor and ceiling are composed of insulation. At either side of the aperture are "wing panels," which collect the portion of the reflected solar beam that is too wide to enter the aperture. They also preheat the molten salt before it enters the main absorption panel. The frame above and below the aperture and to either side of the wing panels is constructed of passively cooled insulation board.

FIGURE 2.1.1
CRTF AERIAL VIEW

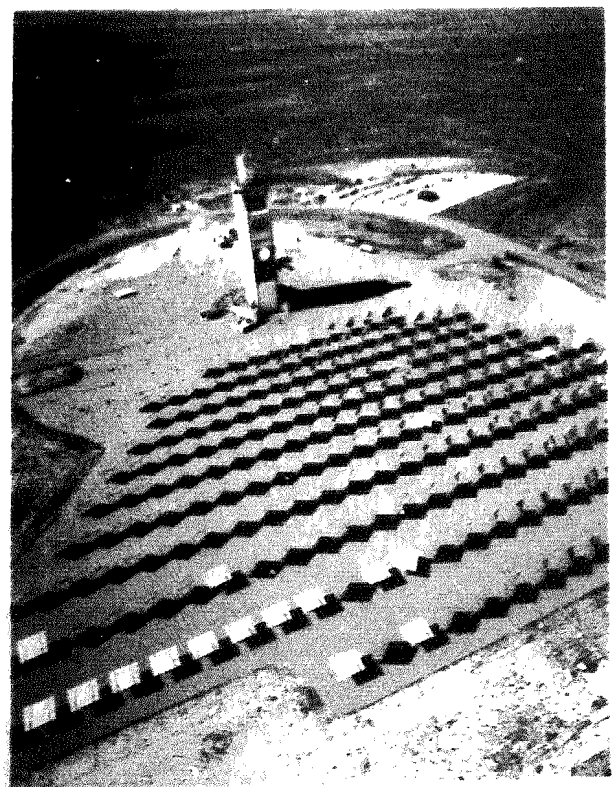

TABLE 2-I

DESIGN CONDITIONS

Full Load Absorbed Power	4.5 MW_{th}
Salt Inlet Temperature	550°F
Salt Outlet Temperature	1050°F
Full Load Salt Flow	94,800 lb/h

FIGURE 2.1.2

5-MW MODEL RECEIVER SUBSYSTEM EXPERIMENT

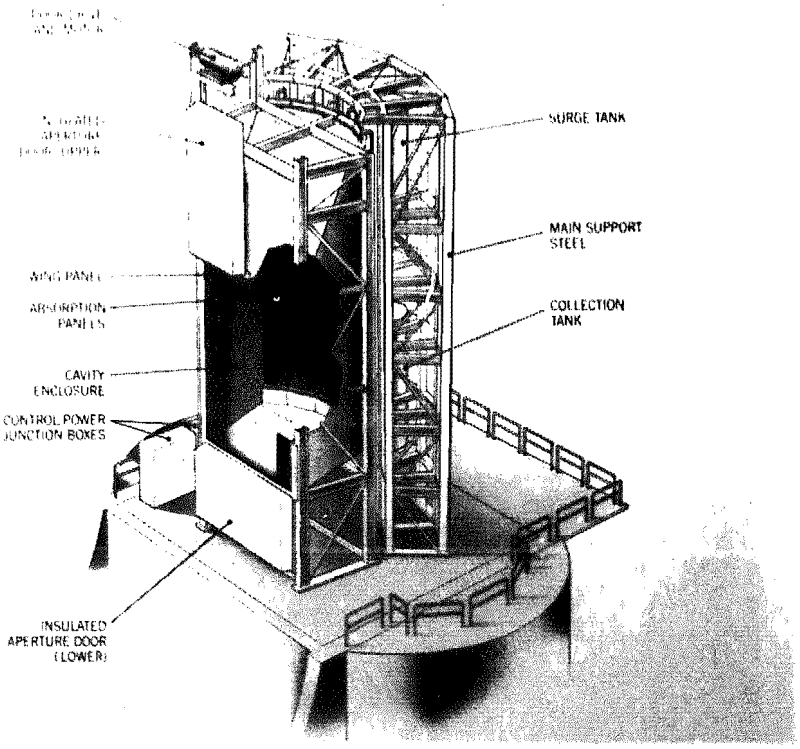

TABLE 2-II

Molten Nitrate Salt Properties (4)
60% $NaNO_3$, 40% KNO_3

T values in °C

Specific Heat, J/kg-C	1447.5 + 0.1718*T
Density, kg/m³	2090. - 0.636*T
Viscosity, mPa-sec	22.714 - 0.120*T
	$+2.281 \times 10^{-4} * T^2$
	$-1.474 \times 10^{-7} * T^3$
Thermal Conductivity W/m-C	$0.442 + 1.954 \times 10^{-4} * T$
Melting-freezing Temperature, °C	221 to 245

FIGURE 2.1.3
LAYOUT OF THE TEST RECEIVER CAVITY

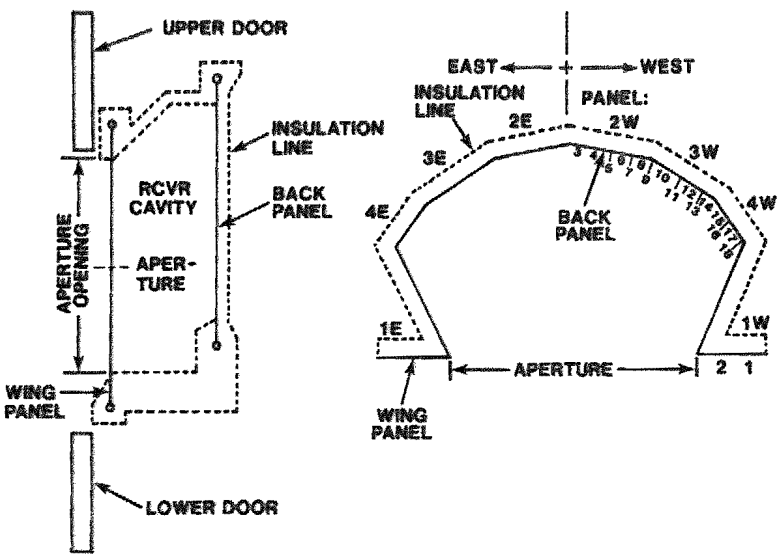

Absorber Panels

The heat-absorption panel is divided symmetrically into an east and a west zone. Each zone is composed of 18 passes connected in a series arrangement. Each pass consists of six tubes through which the total flow for the zone passes, either up or down. Passes 1 and 2 are in the wing panels and the remaining panels are in the back wall, as shown in Figure 2.1.3 To facilitate manufacture and assembly, the absorption surface was arranged in eight individual panels consisting of a number of passes. These panels are designated 1 through 4 east and 1 through 4 west. Panel 1-east and panel 1-west are the wing panels; panels 2 through 4 (east and west) are back panels. Panels 2 and 3 (east and west) have six passes each, and panels 4-east and 4-west have four passes each.

The heat-absorption panels were supplied by two fabricators; Babcock & Wilcox and Foster Wheeler. Foster Wheeler supplied both wing panels and one back panel (panel 3 west), and Babcock & Wilcox supplied the balance of five back panels.

The surface of all panels exposed to solar radiation are painted with black Pyromark 2500 paint, which has demonstrated an absorptivity of 97 percent for the solar spectrum. A more detailed description of the panels is provided in Sections 2.1.1 and 2.1.2.

Aperture Door

The receiver aperture door is a two-piece door operated by an electric motor and chain drive. The door is fabricated of structural steel with insulation applied to its inner surface. The door also has a seal, which compresses against the aperture frame insulation board when the door closes, sealing the cavity from the outside atmosphere. The arrangement of the insulation on the inner surface of the door allows the cavity to be heated, without heating the door structure.

Surge Tanks and Piping

The cold and hot surge tanks are located in the inlet and outlet lines of the receiver, respectively. Salt is piped up the tower into the cold surge tank. In the cold surge tank a salt level is maintained with a cover gas of pressurized air above it. The tank serves to buffer the receiver flow control from the salt pump supply by allowing level fluctuations to accommodate flow surges. In addition, the tank serves as a reservoir of salt to maintain flow for a short time in the event of a pump trip. Salt exiting the receiver panels is piped into the hot surge tank. This tank mixes the streams from the two receiver control zones and is vented to atmosphere to provide a free level from which to control flow in the downcomer. The tank also provides a volume where salt can accumulate for a brief period in the event of a flow blockage in the downcomer.

Piping is used in the receiver to connect the passes of the absorber panels, and to provide lines for filling, draining, and venting the receiver.

An additional line is provided that allows distribution of flow from the riser to the upper header of all passes so that salt may be circulated downward in all receiver panels in a standby mode.

Control and Drain/Vent Valves

Two types of valves are employed in the receiver: 1) the main control valves, and 2) the smaller drain and vent valves. The control valves selected for the receiver were manufactured by Valtek Inc. The valves are 1-inch offset-globe-type valves, allowing for drainability of the salt. A nested bellows seal, shown in Figure 2.1.4, allowed for a compact bonnet arrangement.

FIGURE 2.1.4
RECEIVER FLOW VALVE

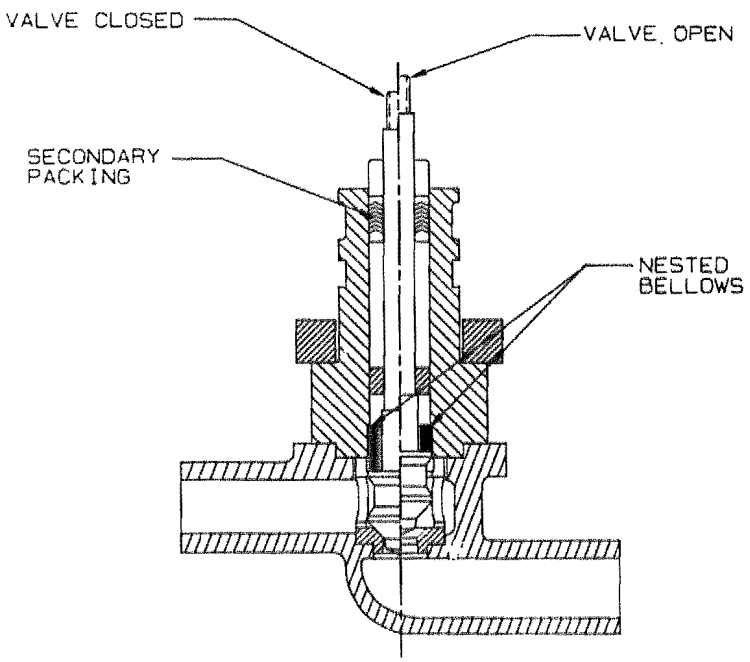

Drain/fill valves are located at the bottom of each pair of connected passes. Vent valves are located at alternate locations where passes connect at the top. Three-quarter inch valves manufactured by Nupro Company, illustrated in Figure 2.1.5, were used for this purpose.

Heat Trace and Insulation

Because the potassium-nitrate salt used in this receiver freezes between 430°and 460°F, the receiver piping must be heated above this temperature in order to allow it to be filled. To accomplish this, electric heat trace was applied to all pipes, headers, tanks, etc. that contain salt. Several types of heaters were used. On piping, mineral insulated cable was used. On the receiver control valves, fill and drain valves, and surge tanks, strip heaters were used, and on instrumentation, band heaters were used.

FIGURE 2.1.5
RECEIVER VENT AND DRAIN VALVE

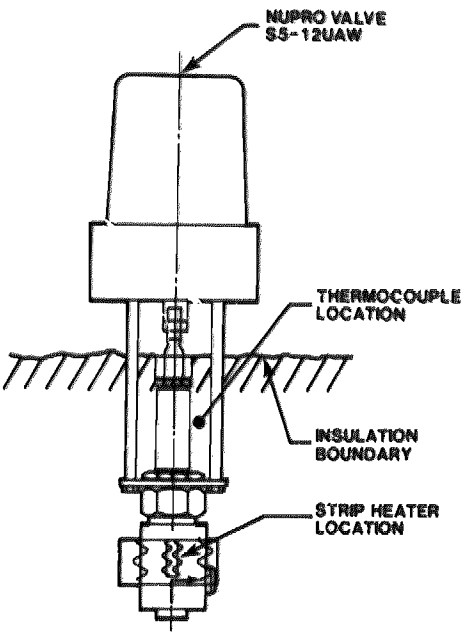

Figure 2.1.6 illustrates these heater types. Eight inches of blanket-type insulation was applied over the heaters, with the exception of the cold salt piping which has only six inches of insulation.

Inside the cavity, a radiant heater was installed under a floor grating. This consisted of six oven-type tubular heating elements.

FIGURE 2.1.6

HEAT TRACE HEATER TYPES

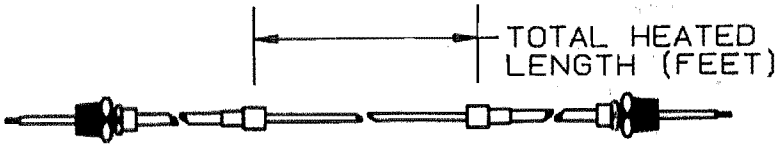

a) Mineral Insulated Cable

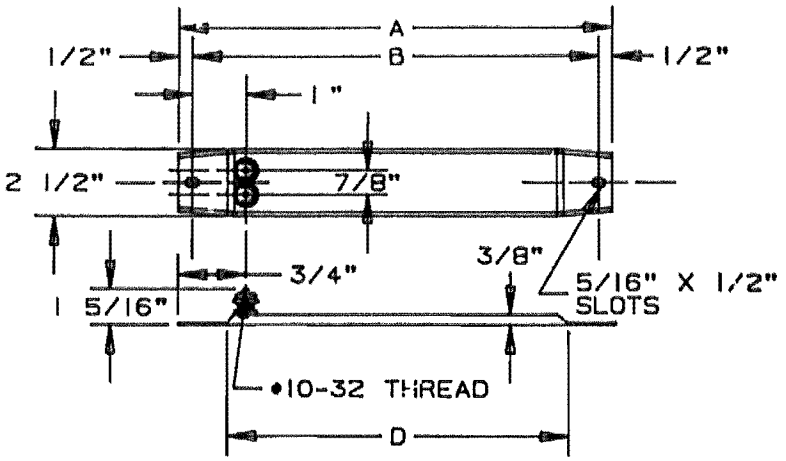

b) Strip Heater

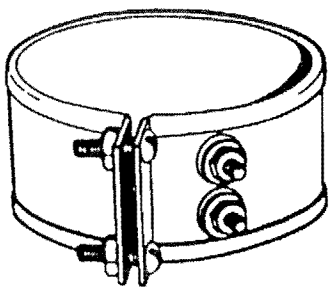

c) Band Heater

Salt Pumping System

Salt is pumped to the receiver by two vertical cantiliver pumps operating in series; a cold-salt pump and a boost pump. The pumps were the same as those used on as with the MSEE system [9]. Because the MSS/CTE test receiver had a higher pressure drop requirement than the MSEE receiver, the boost pump was modified to develop more head. The modifications included installing a higher horsepower motor and new pullies to spin the pump faster, and revising mechanical aspects of the pump to allow the higher power operation.

Instrumentation

The receiver was instrumented extensively. Figure 2.1.7 shows locations of the instrumentation, which included thermocouples, heat flux gages, displacement gages, strain gages, level gages, pressure gages and flow meters. Type-K thermocouples were used exclusively to measure temperature. Two types of flux gages were used to measure incident flux on the heat absorption panel, one air cooled, the other water cooled. Level in the vented hot surge tank was measured with a bubbler type instrument. Differential pressure transmitters were used to measure the level in the surge tanks, pressure drop across the Foster Wheeler back panel, and to measure pressure drop in venturis to obtain flow rate data. Absolute pressure transmitters were used to measure the total receiver pressure drop and cold surge tank ullage gas pressure. All pressure transmitters, except the one on the cold surge tank, employed isolation diaphragms and oil-filled capillaries to sense salt pressure.

FIGURE 2.1.7

SCHEMATIC OF THE RECEIVER SUBSYSTEM

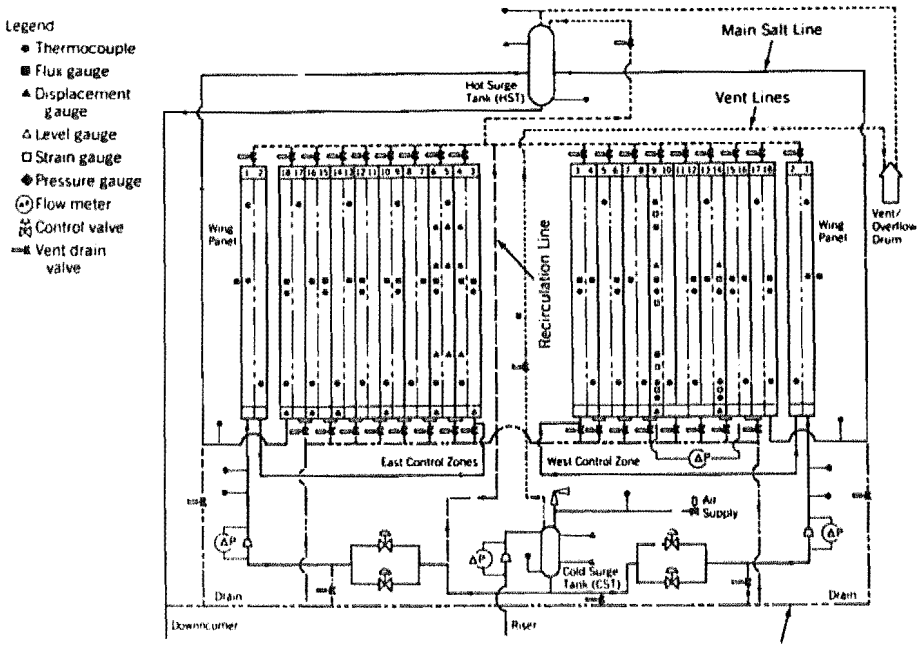

Structure

The structure of the receiver is a steel framework designed to carry the working loads as well as provide access to all parts of the receiver. Four levels are provided at the back of the receiver panel for access, these are connected by a caged ladder. For protection from the weather a steel-plate roof was installed on top of the structure, and corrugated siding was applied to enclose all of the working levels of the receiver. The CRTF articulating crane, which is normally installed at the top level of the tower, was installed on the roof of the receiver, along with an aircraft warning beacon.

2.1.1 Babcock & Wilcox Panel Description

The Babcock & Wilcox Company supplied five of the six back panels of the receiver heat-absorption panel. A typical panel is shown in Figure 2.1.8.

They are typical of those designed for the Saguaro Repowering receiver [6]. The main characteristics of the panel are listed in Table 2-III. The panels are fabricated of 3/4-inch tubes made of alloy 800 with a wall thickness of .065 inches. Panels 2-west, 2-east, and 3-east each have six passes of six tubes each. Panels 4-east and 4-west have four passes of six tubes. A thick-walled safe-end tube is welded to the end of each tube, which is in turn welded into the header. This safe-end provides a transition between the thin tube and thick walled header to reduce stresses induced by differential thermal expansion. The safe-ends are welded into the headers using a J-groove-type weld, as shown in Figure 2.1.9.

FIGURE 2.1.8
ABSORBER PANEL CONFIGURATION -- B&W PANEL

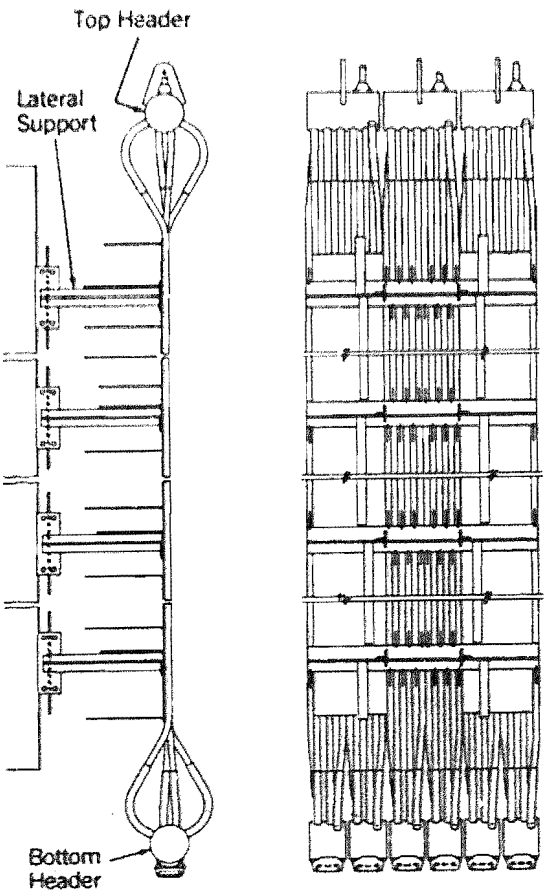

FIGURE 2.1.9

SAFE-END TO HEADER WELD -- B&W PANEL

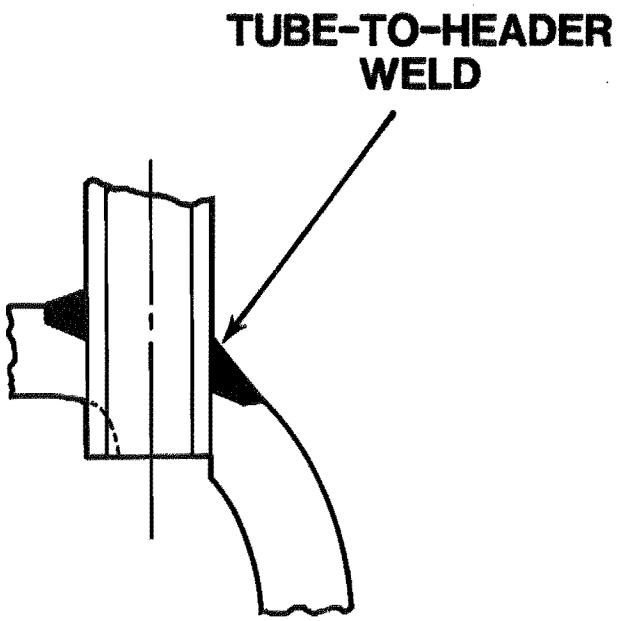

TABLE 2-III

BABCOCK & WILCOX PANEL CHARACTERISTICS

Description	Six Pass Cavity Panel	Four Pass Cavity Panel
Design Temperature, °C (°F)	649 (1200)	649 (1200)
Design Pressure, MPa (psig)	2.4 (350)	2.4 (350)
Tube Material	Alloy 800	Alloy 800
Safe-End Material	304 SS	304 SS
Header Material	304 SS	304 SS
Tube O.D./wall thickness (mm)	19/1.65	19/1.65
Number of Tubes	36	24
Number of Passes	6	4
Number of Tubes per Pass	6	6
Exposure Tube Length, m (ft)	3.7 (12)	3.7 (12)
Overall Width, m (inches)	0.7 (27)	.47 (18)

Each pair of adjacent panels shares a common upper header, which serves to conduct salt flow from one pass to the next. A lug is attached to each upper header from which the panel assembly is hung. Each pass has an individual lower header to allow for thermal expansion from pass to pass. The piping that connects adjacent lower passes is in the form of an expansion loop to allow each pass to grow downward individually.

The tube lateral support system is shown in Figure 2.1.10. It consists of a T-section buckstay to which the tubes are held by clips. The buckstay is supported off the structural steel by a standoff bracket and a series of rollers. The rollers hold the panel in plane as it grows downward due to thermal expansion. The clip arrangement allows individual tubes to expand at different rates by allowing tubes to move relative to the buckstay.

The panels were all shop fabricated and then assembled into a receiver module for shipment to the CRTF.

FIGURE 2.1.10

RECEIVER PANEL SUPPORT DETAILS -- B&W PANEL

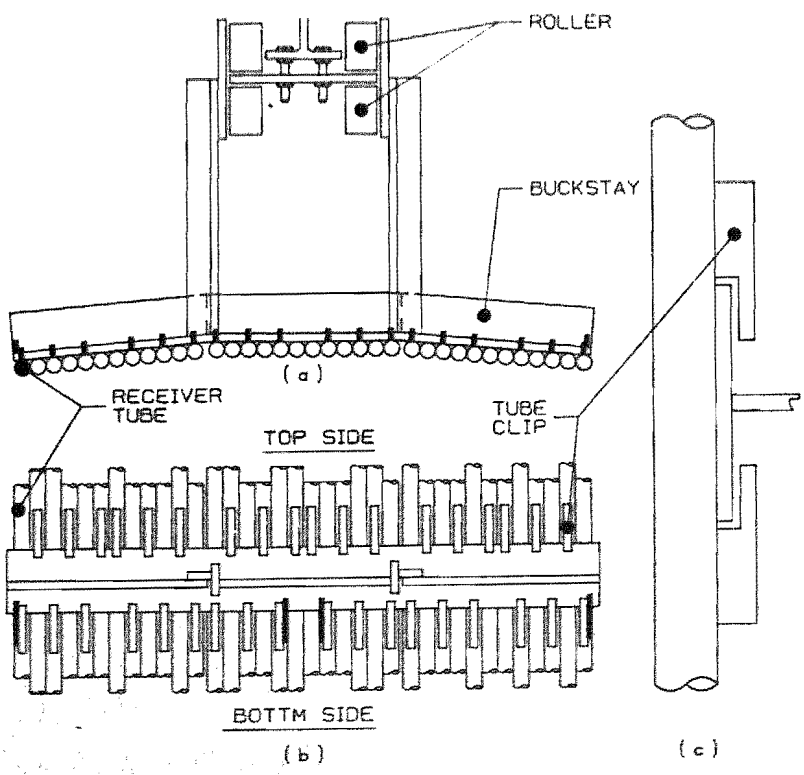

2.1.2 Description of the Foster Wheeler Panel

Foster Wheeler Company supplied the wing panels and panel 3W, which were fabricated in individual modules or subassemblies to facilitate handling, shipment, and installation. The panels (Figure 2.1.11) are representative of those selected in the design study of a commercial-sized receiver. In it, small-diameter, thin-walled tubes were chosen to minimize thermal stresses.

Tube size and number of tubes per pass were selected to duplicate the thermal/hydraulic characteristics of the commercial-sized receiver design [4,7]. Similarly, the materials for the test panels were selected to duplicate the materials for the commercial-sized unit. Thus the two low-temperature wing panels were made using 25.4-mm (1-inch) OD Type 304 SS tubes, and the six high-temperature cavity panels were made using 19-mm (0.75-inch) OD Incoloy 800 tubes. The main characteristics of the wing and cavity panels are summarized in Table 2-IV.

The panels were made of individual tubes welded to the top and bottom headers at either end of the panels. The headers, shown in Figure 2.1.12, were prefabricated sub-assemblies (made of 304 stainless steel) consisting of the header proper and a series of stub fittings. Stub fittings were welded to the headers using full penetration welds, then drilled through to create a high-integrity connection. The bottom header had two nozzle connections for the inlet and outlet piping. The headers were made with flat heads to reduce interference with adjacent panels.

FIGURE 2.1.11
PANEL CONFIGURATIONS

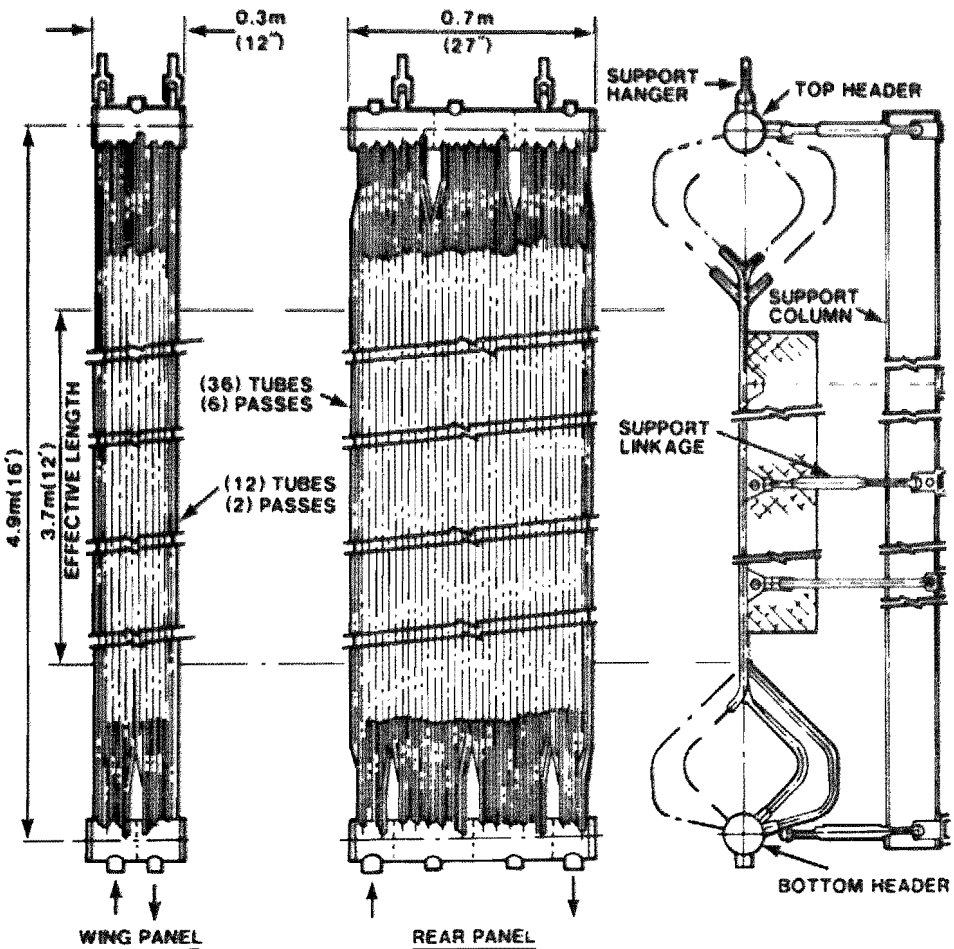

FIGURE 2.1.12

FOSTER WHEELER PANEL-HEADER DESIGN

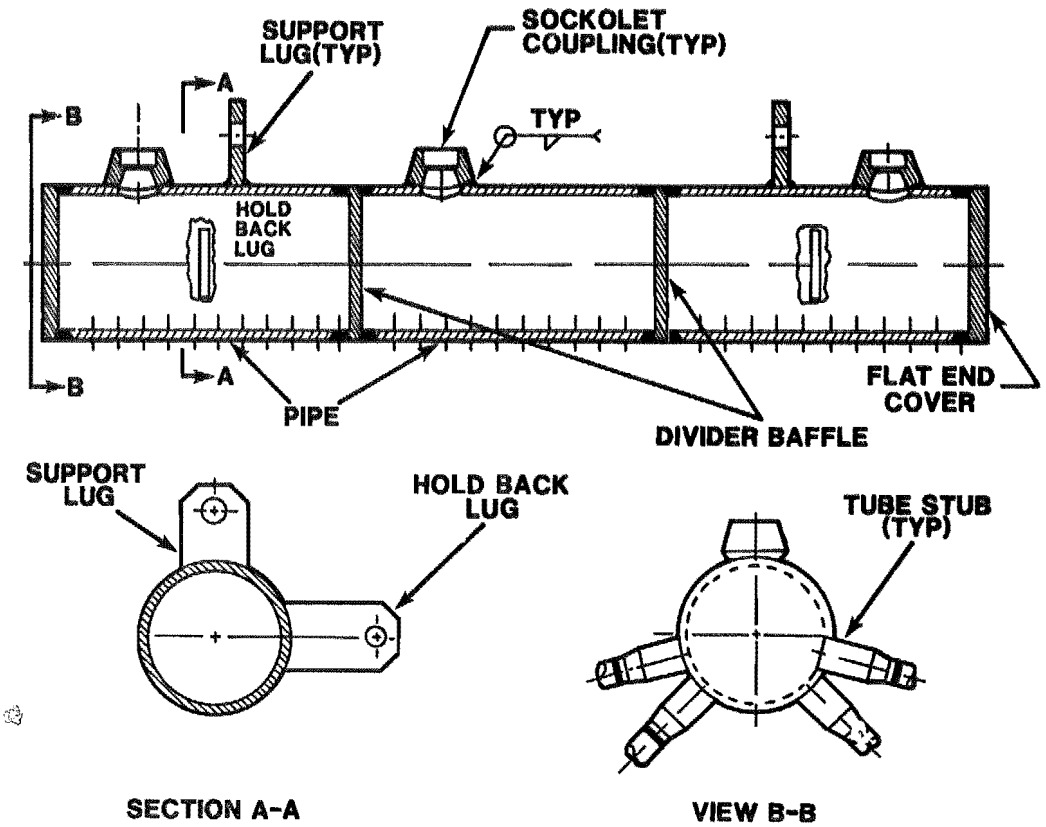

TABLE 2-IV
CHARACTERISTICS OF THE FOSTER WHEELER PANEL

Description	Wing Panel	Cavity Panel
Design temperature, °C (°F)	399 (750)	649 (1200)
Design pressure, MPa (psig)	2.4 (350)	2.4 (350)
Tube material	304 SS	Incoloy 800
Tube stub material	304 SS	304 SS
Header material	304 SS	304 SS
Tube O.D./wall thickness	25.4/1.65	19/1.65
mm (in.)	1.0/(0.065)	0.75/(0.065)
Number of tubes	12	36
Number of passes	2	6
Number of tubes per pass	6	6
Exposed tube length, m (ft)	3.7 (12)	3.7 (12)
Overall width, m (in.)	0.3 (12)	0.7 (27)

The panels are designed to be hung in position from the receiver support structure using hangers connected to the top headers (shown in Figure 2.1.11). The tubes are held in place by a tube support system designed to:

- Prevent lateral tube movement due to wind or seismic loads;
- Transmit the wind and seismic loads on the panel tubes to the supporting steel structure;
- Permit independent tube thermal expansion (vertical and lateral) within the plane of the panel; and
- Minimize longitudinal out-of-plane distortion (bowing).

When heated by the incident solar flux from cold (ambient) to hot (operating temperature), the panel tubes expand longitudinally in the vertical direction and horizontally across the panel width. Because of differences in salt flow and heat flux across the panel, some tubes will become hotter than others and expand more. Thus the tube support system is

a critical element of the panel design, which allows the tubes to expand independently.

The tube support method in the Foster Wheeler design (Figure 2.1.13) consists of a tiebar held in place by support lugs welded to the back of the tube (nonexposed side). Each lug has an elongated hole to allow for differences in thermal expansion of the tubes. To minimize movement of the tubes, cylindrical spacers made of steel tubing are inserted between the lugs. At three locations, the spacers are replaced by support collars attached to struts pinned at both ends. The loads exerted on the tubes are transmitted by these struts to the support structure.

FIGURE 2.1.13
TUBE SUPPORT SYSTEM - FOSTER WHEELER

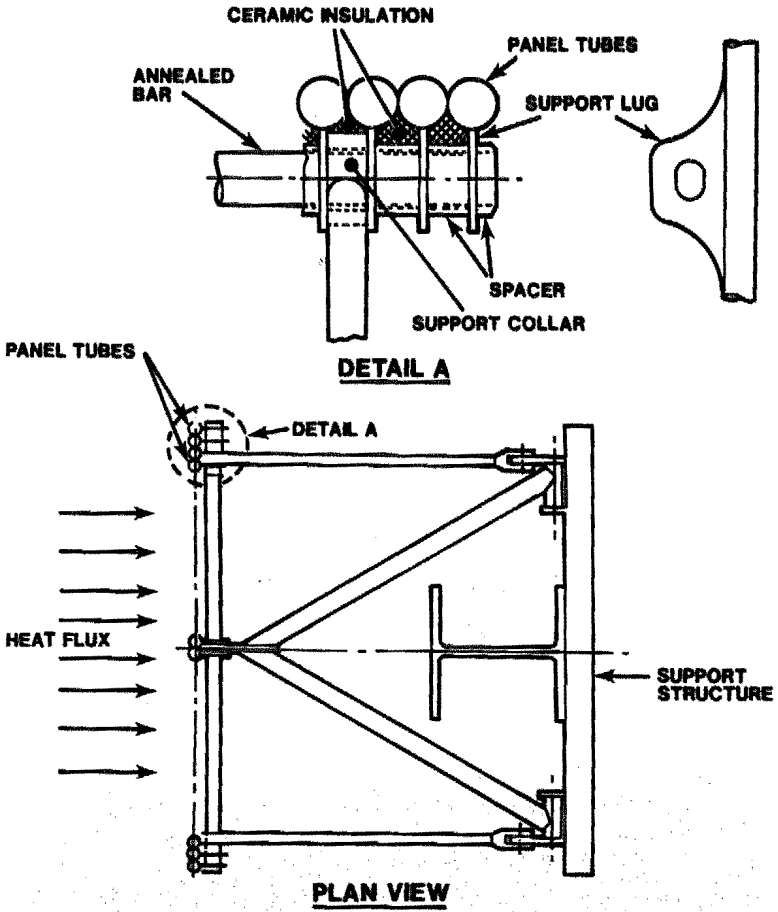

Each subassembly, consisting of the panel tubes, inlet and outlet headers, supporting links, and vertical support beams, was shop built and shipped as a unit. The insulation, sheathing, and instrumentation were added after installation.

2.2 Test Facility

The test facility, which was used in previous experiments was modified specifically to support this receiver test. It consists of a collector field subsystem (CS), heliostats, a salt loop thermal storage subsystem (TSS), and support systems to generate steam and reject heat. A brief description of the test facility is contained in the following subsections.

2.2.1 Collector Subsystem

The existing collector subsystem [10] at the CRTF consists of 221 two-axis tracking heliostats (192 used for MSS/CTE) and their control system. Under optimum insolation and heliostat conditions, the heliostats can concentrate approximately 5.5 MW_{th} onto the receiver.

Each heliostat has 37.2 m^2 (400 ft^2) of reflective surface, with a reflectivity of approximately 80 percent. The structure has motor-driven azimuth and elevation gimbals, which allow it to track the sun during the day.

The heliostats are operated remotely by the CRTF collector control system. Each heliostat receives azimuth and elevation pointing information once every second and responds with its own status. Commands and data transmitted to the individual heliostats are received and executed by the heliostat control electronics. The electronics compare commanded position to actual position and drive the heliostat via AC motors to the correct position.

2.2.2 Thermal Storage Subsystem

The thermal storage subsystem [10,12] supplies 550°F salt to the receiver and receives 1050°F salt for the steam generator. It can also furnish a source of thermal energy for overnight freeze protection of the receiver, steam generator, and salt piping and for early morning plant start-up. The subsystem includes the hot-salt and cold-salt storage tanks, propane-fired salt heater, two cold-salt pumps and one hot-salt pump, and cold-and hot-salt sumps.

The storage system is sized to hold approximately 6 MW_{th} of thermal energy. The hot-salt tank employs internal insulation and an Incoloy liner. This insulates the tank shell from the hot salt and allows the use of carbon steel for the shell. The tank is also insulated on the outside. The cold-salt tank is made of carbon steel and is similar in design to the hot tank except that it does not require the internal insulation and liner because of its lower operating temperature.

The salt pumps are a vertical cantilever design. The impeller and casing are suspended below the liquid level in a sump; however, the bearings are located above the salt level.

2.2.3 Steam Generation Subsystem

The steam generator is a forced circulation unit with three major components: an evaporator, a superheater, and a steam drum. Salt from the hot storage tank flows first through the superheater, where saturated steam at 567°F and 1200 psi from the steam drum is superheated to 1000°F. Salt leaving the superheater is mixed with cold salt before entering the evaporator. This allows the use of low-alloy, chrome-molybdenum steel in the evaporator, whereas the superheater requires more expensive 304 stainless steel to withstand salt corrosion at the elevated temperatures. In the evaporator, the salt is cooled to 570°F by heating saturated water. Salt leaving the evaporator returns to the cold-salt tank. Feedwater

enters the steam drum, where it mixes with saturated water in the downcomer line to the evaporator. Steam/water mixture generated in the evaporator returns to the steam drum. The evaporator has forced-circulation (driven by a pump) with a circulation ratio of 7:1 to avoid tube-wall dryout at the outlet. A separator in the steam drum allows only saturated steam into the superheater. Steam leaving the superheater is attemporated to achieve the design outlet temperature. Both heat exchangers are U-tube/U-shell designs to accommodate differential thermal expansion. The high-pressure water/steam is in the tubes, and the low-pressure molten-salt is in the shell. At design conditions, the steam generator produces 11,600 lbs per hour of steam at 950°F and 1100 psi and has a rating of 3.1 MW_{th}.

2.2.4 Heat Rejection and Feedwater Subsystem

The Heat Rejection and Feedwater Subsystem (HRFS) [10] rejects heat from the steam produced in the steam generator and provides preheated feedwater to the SGS. The subsystem includes the cooling towers, circulating water pump, deaerator, spray water heat exchanger, spray water pump, feedwater pump, feedwater heater, demineralizers, chemical feeders, condensate makeup pump, and chemical feed pump. The cooling towers consist of six forced-draft, finned-tube water-to-air heat exchangers designed to reject seven MW_{th}.

In this test, the deaerator is used to desuperheat and condense steam generated by the SGS. It is a horizontal, cylindrical pressure vessel designed to operate at 250 psia and 400°F. It includes a steam header with mixing spargers near the bottom of the tank, water spray nozzles across the top, and two immersion electric heaters, and is used as a direct-contact feedwater heater and deaerator. Steam is injected beneath the deaerator water level. Saturated water from the deaerator is circulated by a spray water pump at 400 gpm from the bottom of the deaerator to the spray water heat exchanger, where it is cooled. It returns to the deaerator through the spray nozzles in the vapor space at the top of the deaerator, where it condenses the steam.

The feedwater heater is a vertical, cylindrical pressure vessel with an internal steam condensing coil. Feedwater from the deaerator is pumped through the feedwater heater, where it is heated by steam from the SGS.

2.3 Master Control Subsystem

The master control subsystem provides for automatic computer measurement and control, operator monitoring and control, and test data recording. Master control of the MSS/CTE receiver and test facility is by digital computer systems. This subsystem comprises four independent systems: the Bailey Network 90 (NET-90) control system for process control of the thermal subsystems; the Acurex Control System for heat trace control of the thermal subsystems; the Heliostat Control System for control of the collector field subsystem; and the Data Acquisition System (DAS) for test data retrieval, storage, and evaluation. Each of these systems functions independently and each has an independent operator interface console, all of which are located in a centralized control room. The configuration of the master control subsystem is illustrated by Figure 2.3.1.

FIGURE 2.3.1
SCHEMATIC OF THE MSS/CTE CONTROL SYSTEM

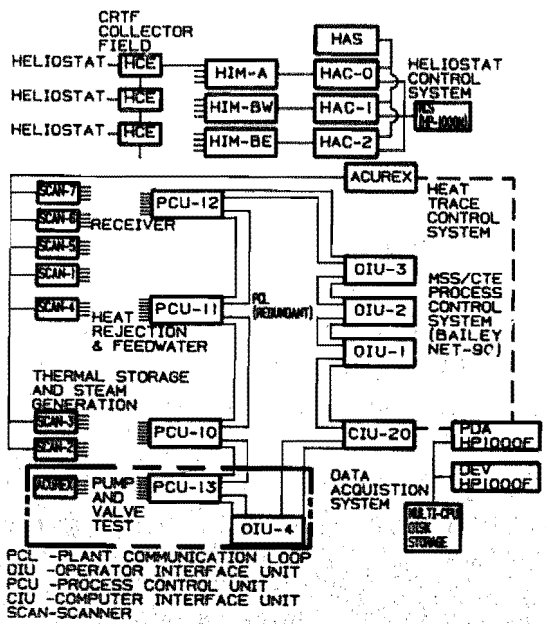

2.3.1 Bailey Network 90 Control System

The Bailey Network 90 control system (NET-90) is a state-of-the-art process control system used in many different industrial applications. As applied to the MSS/CTE receiver and test facility, the NET-90 performs three major functions for process control of the thermal subsystems (receiver, thermal storage, and support):

1) Automatic process control (relative to set points),
2) Safety interlocks/equipment protection, and
3) Operator control and monitoring.

The NET-90 is a distributed digital control system consisting of operator interface units (OIUs), computer interface units (CIUs), a plant communication loop (PCL), and process control units (PCUs). The MSS/CTE system uses three OIUs, one CIU, three PCUs, and the PCL. The three OIUs and CIU are located in the control room, whereas the PCUs are distributed among the subsystems for direct digital control of the equipment and processes. The PCL connects all of these units into a single network by providing complete communication capability between all points on the loop. All of these units are supported by uninteruptible power supplies, so safe shutdown is possible if commercial power is lost.

The OIUs are video consoles that provide access to the entire NET-90 system for MSS/CTE operation, control engineering, and system troubleshooting. Through an OIU, an operator monitors processes and takes control action anywhere in the system. An engineer configures and maintains control schemes within the three PCUs via an OIU In addition, custom graphics, trending, logging, and archival storage of data are provided by each OIU. Printers are connected to two of the OIUs to provide hard copies of any display, as well as automatic print-out of events as they occur. Three consoles are used to provide multioperator access, multisubsystem monitoring and control, and redundancy in case of an OIU failure.

In general, the CIU provides the capability to perform various input/output tasks for the NET-90 using an external computer. Specifically, the CIU

interfaces the NET-90 with the DAS to retrieve process data. As instructed by the DAS computer, the CIU retrieves up to 511 system data points per minute from the NET-90, then transfers the data to the DAS computer using the standard RS-232C communication protocol.

The PCL is a complete and flexible digital communication highway. Distributed multiplexing provides high-security data communications over a serial two-wire data loop. The loop is capable of supporting up to 50 active devices (i.e. PCUs, OIUs, CIUs). The MSS/CTE receiver and test facility requires only seven devices for successful operation: three OIUs, three PCUs, and one CIU. Redundant cables form the PCL and connect all seven devices into a single network. Complete communication among all points is provided on the PCL.

The PCUs are located in the field and are connected with the process equipment for distributed digital control. A PCU consists of three main elements: power system, control and process I/O modules, and termination units. Consequently, a PCU is fully self-contained so that a failure outside the PCU does not cause loss of process control. However, operator monitoring and commands through an OIU may be lost A PCU provides for instrumentation scanning (temperatures, flow rates, limit switches, etc.), data communication, control scheme execution, and actuation or regulation of field equipment (pumps, valves, motors, etc.) in order to achieve control over the performance of the subsystem processes, as well as relay data and commands for data acquisition and OIU monitoring and control via the PCL.

2.3.2 Acurex Control System

The Acurex Control System is actually a data logger with an expansion option that makes it capable of control. It performs two major functions for heat trace control of the thermal subsystem; they are:

1) Automatic heat trace control (relative to high/low set points), and
2) Operator control and monitoring.

The Acurex Control System is made up of a base unit (an Autodata 10/50) and remote scanners (Autodata 1016s). The stand-alone base unit is capable of 120 channels. However, with a capacity for ten remote scanners, an Acurex is capable of 1000 channels. The MSS/CTE system uses seven remote scanners, four of which are used for the receiver. The base unit and scanners are supported by uninterruptible power supplies, so that heat trace zone temperatures can be monitored when loss of commercial power occurs.

The base unit is an Autodata Ten/50, with an auxiliary 12-inch video monitor and local keyboard which resides in the CRTF control room. Also, a printer is connected to the Ten/50 so that system events and logs can be printed out. The Acurex operator control and monitoring capability is highly structured as compared to the NET-90s custom graphics capability.

The remote scanners are Autodata 1016s that simply read and convert thermocouple inputs and effect contact output commands for the Ten/50. The 1016s are essentially remote I/O racks with input and output cards, field wiring terminations, and digital data communication capability. The 1016s communicate with the Ten/50 in a star configuration in which each 1016 communicates separately with the Ten/50.

The Ten/50 contains the control logic to switch individual heat trace zones on and off. The high and low temperature control set points for each heat trace zone are compared to the actual zone temperature measurement to determine whether the zone is to be commanded on or off. The actual zone temperature is also compared to low and high alarm set points for annunciation at the operator console.

2.3.3 Heliostat Control System

The heliostats and associated control system were designed and built by Martin Marietta Corporation. Each heliostat pivots on two axes to provide both azimuth and elevation positioning. The Heliostat Control System (HCS) provides a means for real-time, high resolution, open-loop control of up to 512 individual heliostats. A network of five computers calculates the

sun's position, steering vector, and mode parameters for each of the 221 heliostats in the CRTF field. The position commands for azimuth and elevation are updated every second for each heliostat.

The main subsystems in the HCS are

1) Master control subsystem (MCS): an HP-1000M computer used primarily as the operator interface to the system. Through the use of operator commands or pre-programmed test files, the heliostat aim points are sent to the heliostat array controllers (HACs) on a 1-second update rate.
2) Heliostat Array Control Subsystem (HACS): four Modcomp computers. One of them serves as the Heliostat Array Subsystem (HAS) computer, takes the operating software from a disk, and downloads the programs to three HACs (one for each zone of the heliostat field). The communications protocol to the heliostats is supported by the heliostat interface modules (HIMs) of which there is one per HAC.
3) The CRTF field consists of 221 heliostats and heliostat control electronics (HCEs). There is one HCE per heliostat located on the yoke of the heliostat. The HCE supports the field communication protocol on the heliostat side.
4) The heliostat characterization system (HCS) is used to determine bias values for each heliostat using a back gazing video camera just below the receiver so that precise aiming can be achieved.

2.3.4 Data Acquisition System

The purpose of the data acquisition system (DAS) is to collect the MSS/CTE data for engineering analysis and evaluation. To accomplish this purpose, the DAS performs the following functions:

1) Data acquisition,
2) Data storage and archiving,
3) Data processing and reduction, and
4) Data display and print-out.

These functions are grouped and physically separated into two HP-1000 computers. The process data acquisition performs data acquisition, storage, and archival functions, whereas the posttest development computer performs the data reduction, display, and print-out functions. These two computers share a disc-drive so that a real-time data file is easily and quickly accessible by the posttest computer system. This structure facilitates efficient test data collection and engineering analysis and evaluation.

Process Data Acquisition Computer System

The Process Data Acquisition (PDA) computer system performs data acquisition, storage, and archival functions for the data acquisition system. The data acquired relates to plant operation and performance. Such data includes subsystem instrumentation and control, operator inputs, and environmental (weather) data. These acquired data were specifically tailored for receiver performance and design verification capability.

The PDA computer acquires data from a computer interface unit as described in subsection 2.3.1. Data are acquired through the use of tag identifiers, or tag IDs, which represent unique data points within the NET-90. A group of tag IDs to be acquired is called a scan list since the group represents a list of tag IDs to be scanned (acquired) at a specific frequency or time interval; a scan list may contain up to 511 tag IDs. The data are acquired either in a specified time interval of seconds or minutes or both. Data are routinely acquired in 1-minute intervals. Occasionally, it is necessary to acquire data as often as in 5-second intervals; usually for control-related evaluation. Only the first 100 tag IDs are acquired for the second intervals because of timing constraints. When both time intervals are requested, two different data files are created.

The data are acquired and time recorded in hours, minutes, and seconds, then stored on a removable disc cartridge for flexibility. Once a test is complete, or the data acquisition process has been terminated, the data are archived on magnetic tape for future use and distribution. Also, the data

can be copied to the shared disc for immediate use by the posttest computer system.

Posttest Development Computer System

The Posttest Development Computer System (DEV) performs data reduction, display, and print-out functions for the data acquisition system. There are essentially three methods to reduce data and output information:

1) Raw data print-out,
2) Plotting, and
3) Custom computer program.

These three methods provide the foundation for the MSS/CTE receiver performance and design verification capability.

A raw data print-out simply provides a hard copy of selected raw data in engineering units for hand analysis, quick look-up, and system troubleshooting.

Plotting provides the ability to plot up to four data points versus time on a single plot. The plot can be either output to the terminal screen for quick review or to the printer for a hard copy. The plotting program allows the time window and the low and high range values of the data points to be specified by the user. Also, multiple plots in time for the same data points can be generated by simply requesting plot continuation.

A custom computer program provides the user the ability to develop and execute custom programs for special computational analysis needs. For example, a statistical analysis program was generated to support measurement uncertainty analysis. The user specifies the data file, the data point, and time window to analyze, then the program searches the data file for the time window of data, performs the statistical analysis, and prints out the results. This type of programming alleviates tedious hand computations and usually renders quicker results when the particular analysis has to be done numerous times.

To facilitate the task of distributing test data to off-site personnel and to the solar community at large, convenient and compact floppy discs were used to transport and distribute test data. This was accomplished by transferring data from the posttest computer system to a personal computer work station via a high-speed serial communications link. The work station consisted of an IBM-personal computer (PC), which uses the DOS operating system to generate the diskettes.

SECTION 3

RECEIVER DESIGN

D. Smith - Babcock & Wilcox Corp.
G. Carli - Foster Wheeler Corp.
M. Lanning - McDonnell Douglas Astronautics Corp.
P. Reed - Babcock & Wilcox Corp.
P. Bator - Babcock & Wilcox Corp.
G. Riley - McDonnell Douglas Astronautics Corp.

One of the major objectives of the test program was to reduce the technical risks of building large-scale commercial receivers. To accomplish this, the design of the test receiver was made typical of large commercial designs. The most critical part of the receiver is the heat absorption panel. The panel must be designed to absorb the incident solar flux and to achieve a long lifetime. In addition to the panel, a large amount of hardware must be designed to support the overall function of the receiver. This hardware includes the cavity enclosure and receiver door, piping, surge tanks, valves, heat trace, insulation, structure, controls, and instrumentation. Most of this hardware can be designed using established engineering principles; however in many cases, unique aspects of molten-salt solar design were encountered. In these cases, methods developed for the commercial receiver designs were used, tempered by the experience gained in previous molten-salt testing at the CRTF.

3.1 Receiver Design Methodology

The configuration of the receiver is typical of the commercial Saguaro and Solar-100 receiver designs. The basic features of the configuration were established at the beginning of the design phase. The configuration was set as a cavity-type receiver employing wing panels, with a two-piece door to seal

the cavity. The heat-absorption panel employs vertically oriented tangent tubes in a multiple pass arrangement. These specifications set the basic characteristics of the design.

The design of the receiver had two basic steps that were performed to set the sizing and layout of the receiver before detailed design of the hardware began. These steps were:

1) Basic design of the heat absorption panel. This step set the tube size and number of tubes per pass, and selected a tube material. This basic design information was required in order to establish a heat flux limit for the panel, based on considerations of fatigue. Fatigue limits were based on ASME Code Case N-47 [14]. For the Saguaro receiver, an optimization was done trading off tube material and fabrication cost with panel size and pumping cost to arrive at the best design [6]. For the test receiver, the goal was to match the panel design to the Saguaro characteristics.

2) Once the panel flux limit was set, the second basic step was performed--sizing the cavity. The purpose of this exercise was to locate the heat absorption panel within a cavity, set its height and width, locate and size the aperture, and set up a collector field aiming strategy. The main goals were to meet the allowable flux limit on the panel, while minimizing the panel surface area.

In parallel with the design of the cavity geometry, details of the absorption panel were established, including details of panel supports, header design, and weld configurations.

Once both the panel design and cavity geometry were established, the receiver structure and piping were laid out, and major components such as the surge tanks were located. Then instrumentation was located and the heat trace system and insulation were designed. As the design progressed, fabrication drawings were prepared in sufficient detail to allow construction of the receiver.

3.2 Design of the Receiver Panel and Cavity Configuration

The receiver panel design must be set in order to allow flux limits to be established. These flux limits then can be used to lay out the receiver cavity geometry. The test receiver employs two types of receiver cavity panels; one designed by The Babcock & Wilcox Company, the other by Foster Wheeler Company. Because the panels would share a common cavity, they were designed with similar thermal/hydraulics. The following sections describe the design of both types of panels.

3.2.1 Babcock & Wilcox Panel Design and Cavity Configuration

The design of the Babcock & Wilcox panels is based on matching the thermal hydraulics and thermal structural aspects of the Saguaro commercial-design receiver. Once the panel design was set, heat flux limits for the panel were derived based on simplified creep fatigue analysis. The limits were typical of the Saguaro design and were based on 50,000 cycles of fatigue and 100,000 hours of creep damage at design conditions, which are based on a 30-year life. The cavity was then arranged to produce flux levels at the panels nearly equal to the limit. This would allow evaluation of the panels at fluxes higher than those used in the Saguaro design where a margin was applied. The receiver was not intended to serve as a lifetime test article, and designing without a margin would allow observations of effects somewhat more severe than might be expected in a commercial design.

Thermal/Hydraulics and Thermal Structural Parameters

The receiver panel was designed to match the characteristics of the Saguaro receiver panel design. For the design of the Saguaro receiver, these parameters were optimized to achieve a minimum cost receiver. For the test receiver, because of its small size, smaller diameter tubes were required. The key parameters that were matched were the panel temperatures and tube thermal stress. Tube temperatures could be matched by matching the thermal resistances of the Saguaro panel. This required maintaining the same tube wall thickness and matching the molten-salt heat-transfer coefficient. The tube stresses could be matched by matching the tube temperatures, and by

maintaining a tube large enough to be similar to the Saguaro tubes. The stresses in the Saguaro tubes result from through-thickness temperature gradients and front-to-back temperature differences. The stresses are characteristic of a thin-walled tube. It was found that thin-walled tube behavior held relatively well for tubes as small as 3/4 inch in diameter, while maintaining the .065-inch wall thickness. This set the lower bound on tube diameter for the test receiver.

The heat-transfer coefficient is a complex function of salt properties, tube size and the salt flow-rate in a tube. The design conditions of absorbed power and temperature rise set the salt flow rate for the test receiver design. Using this salt flow rate, the heat-transfer coefficient of the Saguaro design was matched within a few percent using six 3/4-inch tubes per pass in a two-zone design. The heat-transfer coefficients for the two designs are shown in Figure 3.2.1. Since salt properties vary with temperature, the heat-transfer coefficient is plotted as a function of salt temperature.

FIGURE 3.2.1
HEAT-TRANSFER COEFFICIENT -- SAGUARO DESIGN COMPARISON

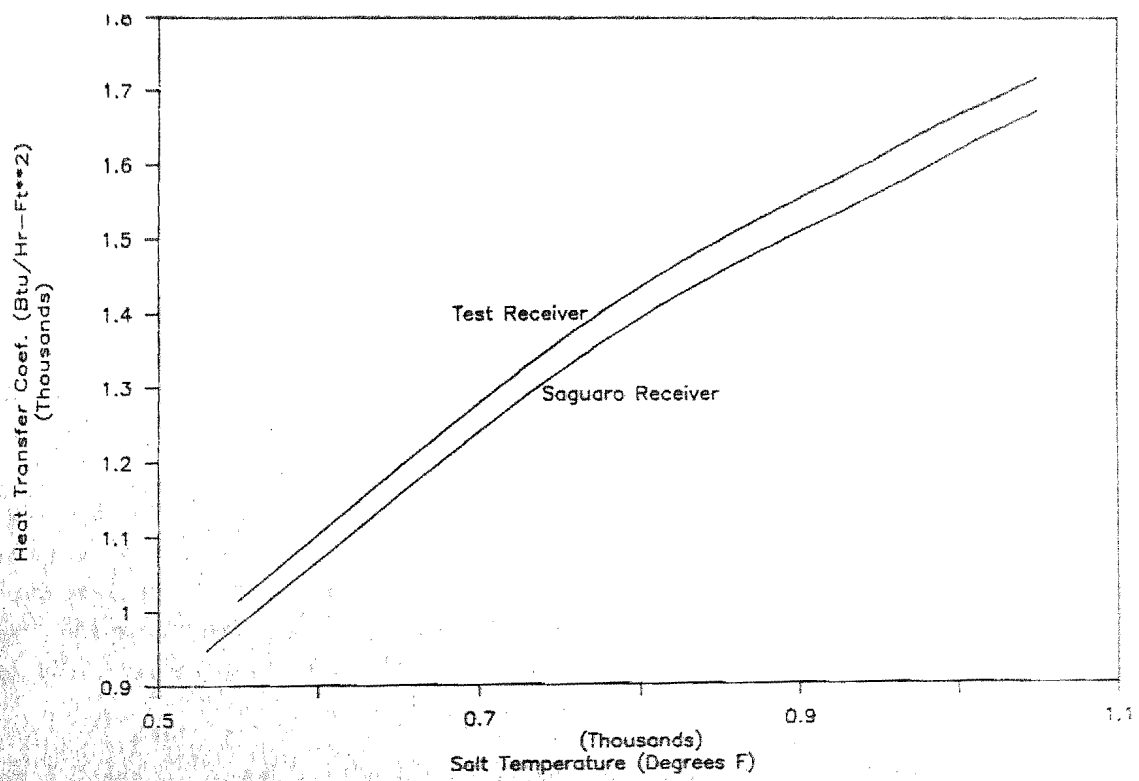

With the heat-transfer coefficients matched, the two dimensional temperature distribution and stress intensity distributions were predicted for both the Saguaro and test receiver tubes using the Babcock & Wilcox 157B tube analysis computer program. Figure 3.2.2 shows these distributions for a common heat transfer coefficient of 1000 btu/h-ft² and a heat flux of 100,000 btu/h-ft². The similarity in temperature and thermal stress profile is clear. The tube stresses presented in this figure are calculated assuming elastic behavior of the tube material. The tube stresses calculated using this method are proportional to the heat flux absorbed by the tube.

FIGURE 3.2.2
RECEIVER TUBE THERMAL STRESS -- SAGUARO DESIGN COMPARISON

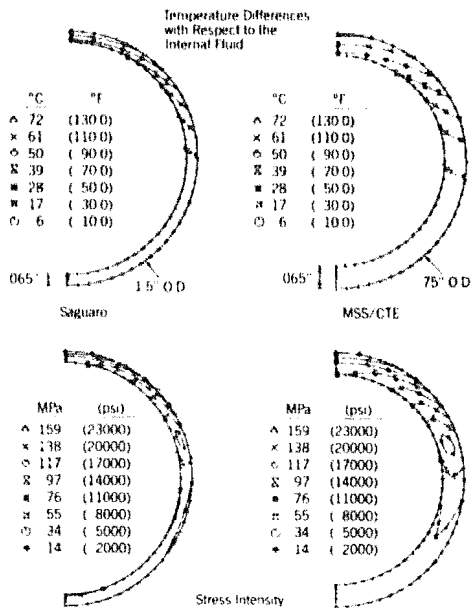

Structural Limits

The structural limits of the panel are set by the tube materials capability to withstand fatigue and, to some extent, creep. Thermal stress occurs in panels as a result of absorbed heat flux. This stress results in fatigue of the tubes because of the cyclic nature of daily operation and cloud passage. In addition, operation at high temperature causes damage due to the effects of

creep. The combined damage from these two effects was calculated by a simplified method based on ASME Code Case N-47 [14]. The panels are designed for a life of 30 years to be typical of a commercial design. During this time, a commercial receiver could experience 10,000 daily start-ups and an estimated 50,000 cycles due to cloud passage.

When high heat flux levels are initially applied, the front of a receiver tube experiences compression and yields, and upon removal of the flux, the tube crown goes into tension. Because the strain-hardened tensile yield stress is not exceeded in this design, the tube material will eventually cycle elastically. Compressive creep occurs at the tube crown as a result of operation at high temperature. With heat flux removed, the tube crown goes into tension as the tube temperature is reduced. Tensile creep does not occur, however, because the material is now at a low temperature. As a result, creep damage can be estimated by assuming normal stress relaxation in compression only. Elastic follow-up is possible in this situation because a significant portion of the tube cross section may experience creep. To allow for this, creep damage is conservatively increased by 50 percent. Subtracting the creep damage from unity gives the allowable damage due to fatigue. From this, the allowable fatigue strain range may be found using the data presented in ASME Code Case N-47, and since elastic behavior is assumed, the associated stress range can be found. Table 3-I presents the allowable stress range for alloy 800.

TABLE 3-I

ALLOWABLE STRESS RANGE FOR ALLOY 800

Temperature C	(F)	Creep Damage	Fatigue Damage	Allowable Stress Range MPa	(psi)
426	(800)	0.000	1.000	0.384	(55.7)
454	(850)	0.002	0.998	0.358	(51.9)
482	(900)	0.009	0.991	0.332	(48.1)
510	(950)	0.022	0.978	0.315	(45.6)
538	(1000)	0.009	0.991	0.300	(43.4)
565	(1050)	0.078	0.922	0.278	(40.4)
593	(1100)	0.162	0.838	0.257	(37.2)
621	(1150)	0.221	0.779	0.235	(34.0)
648	(1200)	0.352	0.648	0.210	(30.4)

Flux Limits

The thermal stress that occurs in a receiver tube is a function of the heat flux applied to it. This stress may be calculated in detail by using two-dimensional finite element stress analysis codes. However, for the elastic case, a simple formula based on temperature differences can be derived. Formulas for thermal stress may be written for through wall gradients, and for temperature difference between the front and back of the tube. Since both effects result in compression at the tube crown, the stresses may be superimposed. The temperature distribution in the tube may be calculated using simple one-dimensional conduction through the tube wall. For thin-wall tubes, this method has been shown to yield results in agreement with more detailed methods [3]. This simple formula can be employed to generate a flux limit for a tube by calculating the tube temperature and maximum stress as a

function of heat flux, for a given salt temperature. The flux that results in the allowable stress range is found using an iterative process. By repeating this for the range of salt temperatures, a flux limit can be established. In addition to the structural limit, a limit must be placed on the inside tube wall temperature to minimize corrosion by the molten-salt. A limit of 1100°F is indicated by corrosion data for the molten-salt [15,16]. This calculation is performed by the Babcock & Wilcox Computer Code SRPAN. The heat flux limit derived by this method is presented in Figure 3.2.3.

FIGURE 3.2.3
HEAT FLUX LIMIT FOR THE ABSORPTION PANEL

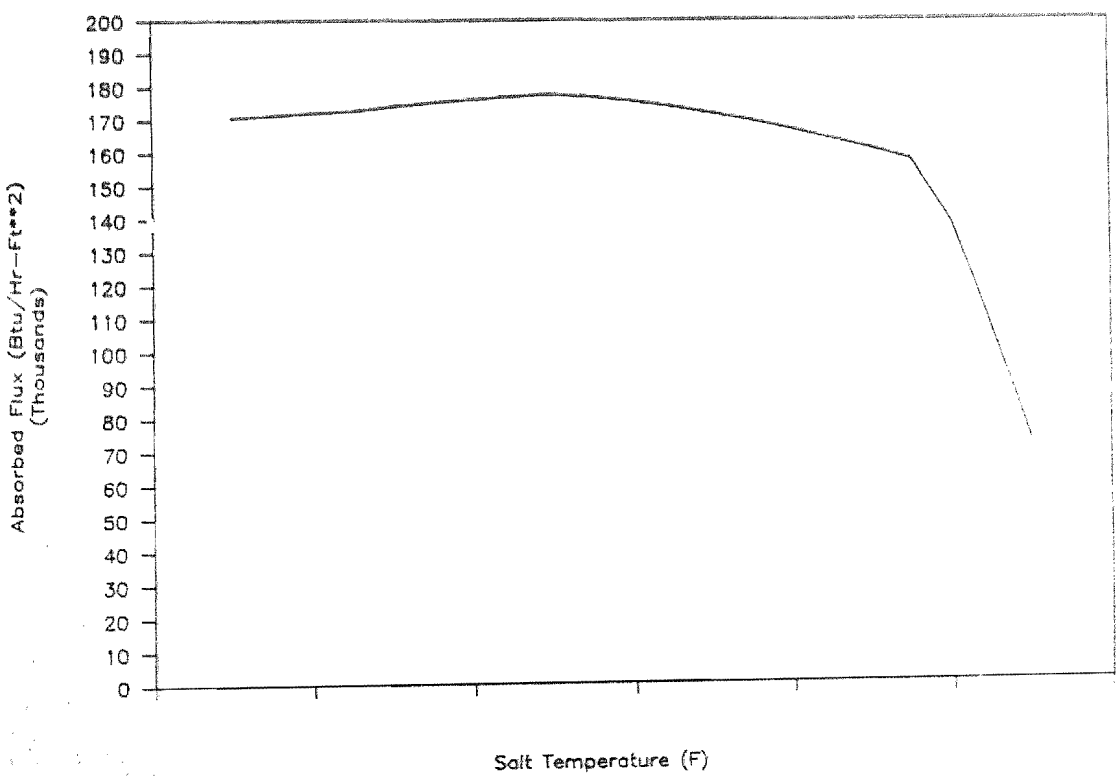

Cavity Layout

In a cavity receiver, the solar flux in the aperture is highly focused. Moving back from the aperture, the flux spreads out over a larger area. For the current test receiver, heat flux maps were produced by McDonnell Douglas Company using the CONCEN program for a range of cavity configurations. The parameters varied, included: the panel height, back wall radius, aperture width, number of passes, percentage of the heliostat field used, and the error parameters that characterize the CRTF heliostats. Table 3-II presents the different configurations for which calculations were made. For each configuration, the aperture height equaled the panel height, and a distributed aim-point strategy for the heliostat field was employed based on the aperture height. The configuration designated E.2.b was selected because the predicted heat flux closely matched the limit curve.

TABLE 3-II

RECEIVER ARRANGEMENT MATRIX

Designation	Height (ft)	Back Panel Radius (ft)	Wall Width (ft)	Aperture Aperture Passes	No. of % Field	Field Error
1) A.0.c.	14	7.2	6.0	20	100	Original
2) ----	10	7.2	6.0	20	100	Original
3) B.0.c.	11.8	7.2	6.0	20	100	Original
4) D.0.a.	12	6.6	6.0	20	90	Original
5) D.0.c.	12	6.6	6.0	20	100	Original
6) D 1.a.	12	6.6	7.0	20	90	Original
7) D.1.b.	12	6.6	7.0	20	90	Revised
8) D.1.c.	12	6.6	7.0	20	100	Original
9) D.1.d.	12	6.6	7.0	20	100	Revised
10) D.2.a.	12	6.6*	7.0	20	90	Original
11) D.2.b.	12	6.6*	7.0	20	90	Revised
12) E.1.b.	12	6.0	7.0	20	90	Revised
13) E.2.b.	12	6.0	7.0	18	90	Revised

*Radius Center 6" North of Aperture Plane

Figure 3.2.4 presents the estimated absorbed heat flux along with the flux limit. In all cases, the absorbed heat flux was assumed to be 90 percent of the incident flux.

FIGURE 3.2.4
HEAT FLUX PREDICTIONS

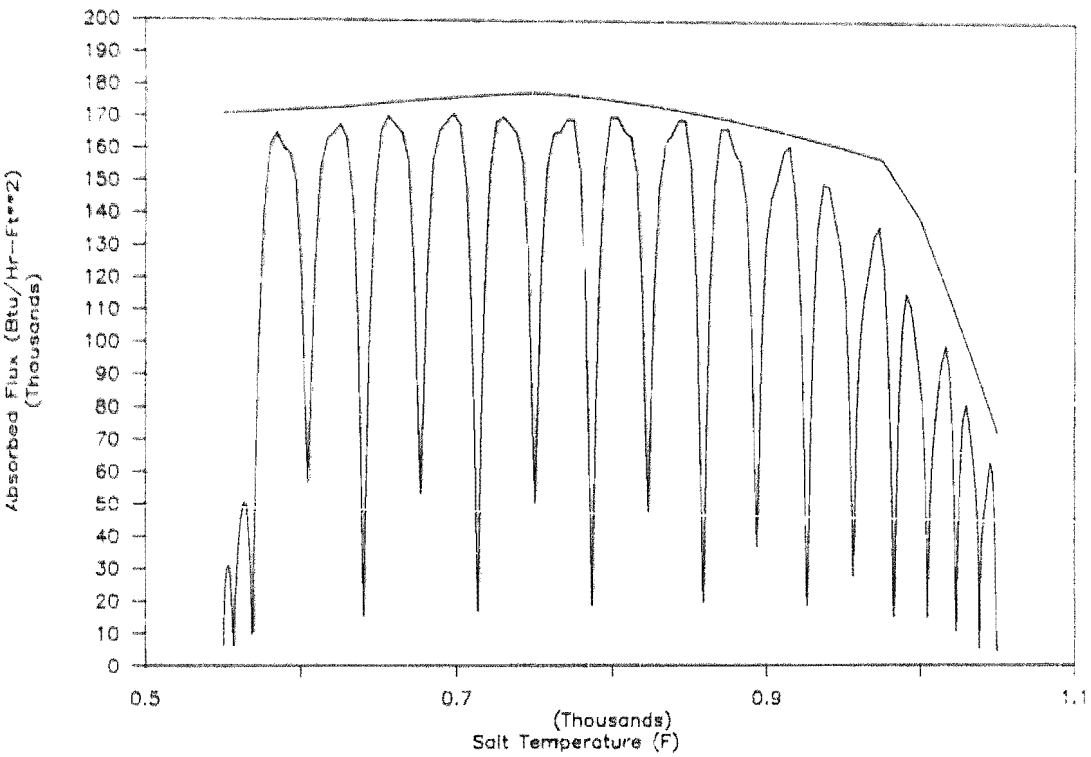

Recent Developments

Since the creation of the original design for the MSS/CTE receiver, several developments have been made for setting heat flux limits of receiver panels. A study of actual cloud cycles at Solar 1 by Kistler [17] showed that the equivalent number of cloud cycles experienced during a 30-year lifetime should be 20,000 and that start-up cycles could be insignificant. However, work done by Jones [18,19] indicates that thermal cycling of alloy 800 is more damaging than the isothermal data of Code Case N-47 indicates. In addition, the SRPAN computer code used by Babcock & Wilcox to calculate heat flux limits was

revised, and some errors in the code were corrected. A new allowable flux curve was generated taking these factors into account. Table 3-III presents the revised parameters employed in the evaluation, and Figure 3.2.5 presents the revised flux limit. The effects of these changes were, to some extent, offsetting but the net effect of the new developments is to increase the allowable flux by approximately 10 percent over the original limit employed in the test receiver design.

Material	Alloy 800	Alloy 1800
Cycles	50,000 Cloud	20,000 Equiv.
Start-up Cycles	10,000	0
Failure Mechanical	Creep/Fatigue	Creep Fatigue
Peak Flux Limit (btu/hrft^2)	177,000	190,000

FIGURE 3.2.5
REVISED FLUX LIMIT

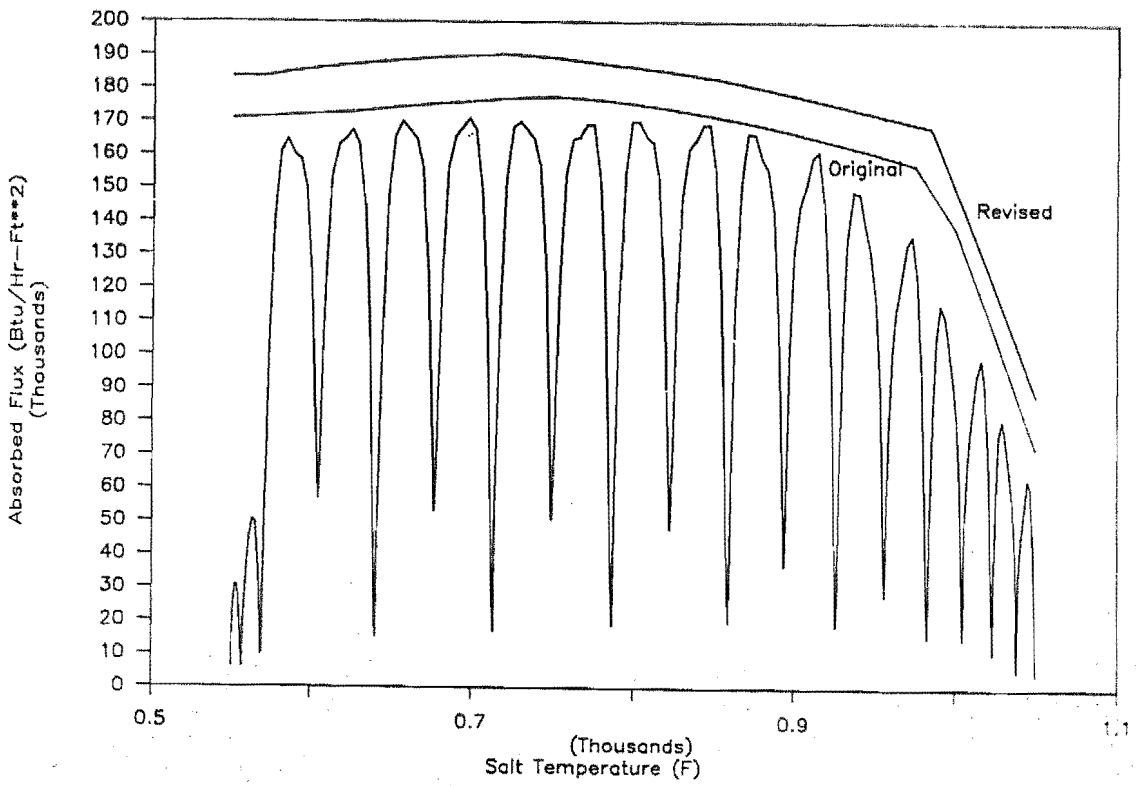

Mechanical Design of the Panel

The mechanical design of the 5 MW_{th} test receiver panels is based on the features of the commercial panel design of the Saguaro Study [5]. These features include a tangent tube-wall construction, lateral supports employing welded tube attachments and individual inlet/outlet headers. The B&W panel design is shown in Figure 3.2.6. Details of the design are provided in Appendix J.

FIGURE 3.2.6
BABCOCK & WILCOX PANEL DESIGN

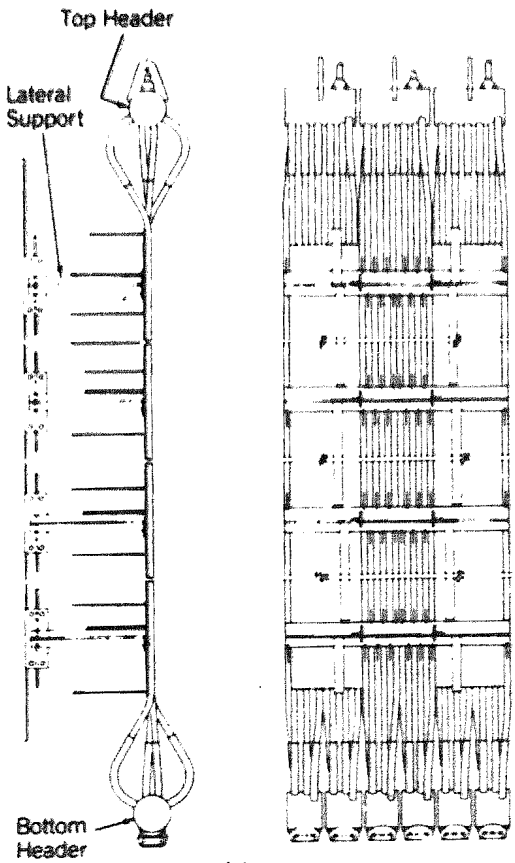

(a)

The receiver panels consist of combined four and six pass assemblies joined at various elevations by a common lateral support member (six tubes compose a pass). A configuration of tube clips embraces the lateral support (buckstay) with adequate clearance to permit differential thermal movement between adjacent tubes. The panels are hung from the top and grow downward when heated. Four lateral supports equally spaced guide the downward growth of the panel using a system of rollers and guide plates. The rollers track along either side of the guide plate, which is attached to a vertical steel member. Panel loads are absorbed by this member and are transferred to the main steel structure. A bolted connection between the guide plate and the vertical member permits adjustment to ensure proper alignment of the panels.

The lateral support system is an integral component of the receiver having specific functions. The lateral supports do the following:

- Maintain panel geometry
- Absorb lateral loads
- Guide thermal expansion
- Control panel deflections.

The lateral supports also serve a secondary function. Insulation is applied to the backside of the panels through connection to the buckstays. This approach is straightforward and poses no technical risk to receiver operation.

The pressure boundaries of the receiver panel were designed according to ASME Section I with supplementary requirements for cyclic-elevated temperature applied to establish the heat flux limits (receiver design limits are discussed in Section 3.2). The remainder of the panel assembly meets the requirements of the Uniform Building Code (UBC) and the Standards of the American Institute of Steel Construction (AISC). The design life of the receiver is 30 years with the exception of headers, which have a life span of three years (the design life of the receiver subsystem is three years with a total operating time of 16,000 hours). The panels are capable of surviving winds of 90 mph (144 km/h), which translates into a design pressure of 40 psf (1.92 KPa). This value was derived from the 1982 edition of UBC using a basic

wind speed of 75 mph (121 km/h). Seismic forces were calculated using a 0.1 g peak ground acceleration in accordance with UBC 1982--Zone 2. Details of the receiver panel's mechanical design are described in the following subsections.

Attachments: The attachments to the receiver panel include tube clip supports, flux gage and displacement gage connections.

Each receiver tube is supported at four locations using a welded tube clip. Details of the tube clip are shown in Figure 3.2.7. The tube clip absorbs lateral load and accommodates thermal displacements of the tube. The tube clip is therefore designed to transmit only mechanical loads to the buckstay with clearances specified to preclude binding. Because the mass of the tube clip lowers the overall mean tube temperature (thereby increasing peak thermal tube stress), the size of the tube clip is minimized. The tube clips were constructed of Alloy 800 to match the thermal expansion properties of the receiver tube.

FIGURE 3.2.7
WELDED TUBE CLIP

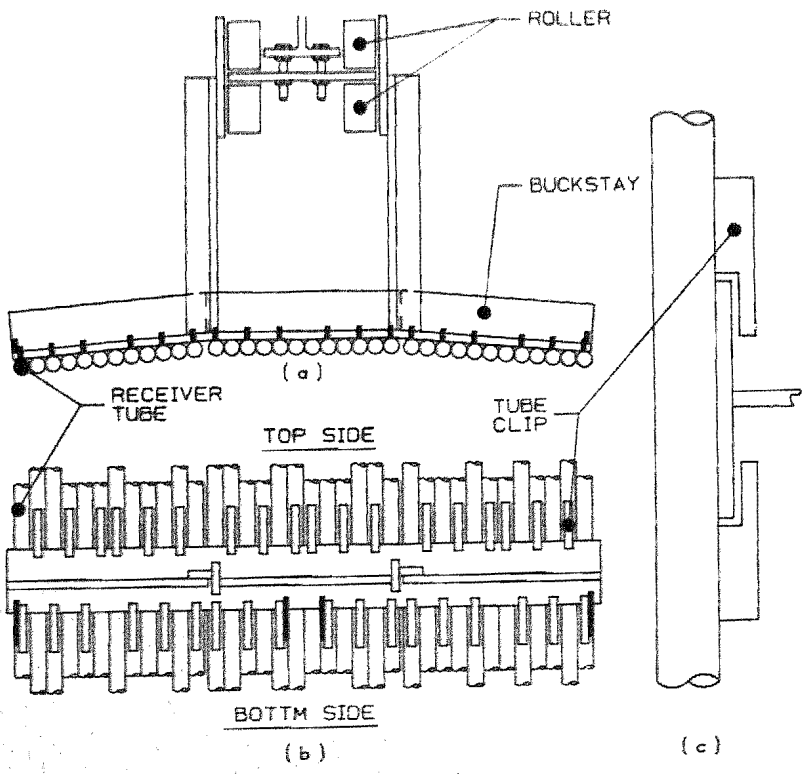

A commercial-scale receiver panel would employ this tube-clip design. Because the tube-wall thickness is also 0.065 inches for the commercial-scale receiver tube, weld size and tube-clip thickness would not change.

The heat flux gages are attached to the backside of the receiver using the mounting bracket shown in Figures 3.2.8 and 3.2.9. A 3/16-inch diameter hole, formed by indenting the sides of two adjacent tubes, accepts the 1/8-inch diameter sensor of the flux gage. A pair of U-shaped support lugs are welded to the receiver tubes above and below the cavity. The lugs prevent relative movement of the dented tubes, which is necessary to protect the delicate flux gage sensor. The connecting plate is bolted to the lugs to accommodate differential thermal expansion and minimize conduction of heat to the gage. Positioning and alignment of the flux gage are accomplished by a 1-3/16 inch diameter support tube bolted to the connecting plate. The tube was sized to accept the body of the air-cooled flux gage. The smaller water-cooled gage uses an additional support tube that is inserted into the larger tube. Adjustment screws are provided to maintain proper position of the gages. Insulation was installed between the connecting plates of the mounting bracket and surrounding the flux gage sensor to promote maximum cooling of the gages. A commercial pane would incorporate a similar design, although a larger receiver tube diameter would require some modification to the bracket configuration.

FIGURE 3.2.8

FLUX GAGE SUPPORT

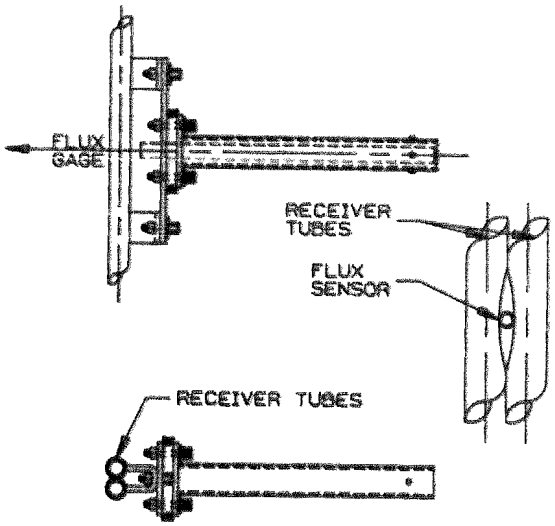

FLUX GAUGE SENSOR

FIGURE 3.2.9

FLUX GAGE MOUNTING BRACKET

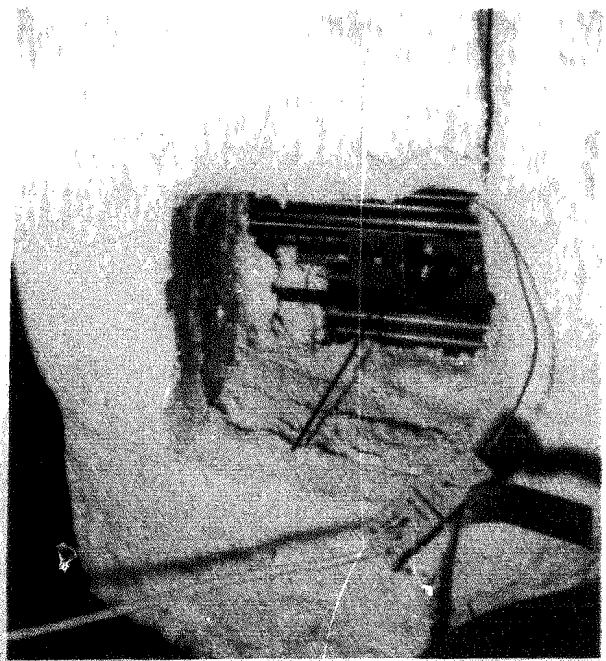

A welded tube attachment was also required to connect the wire cable of the displacement gages. This attachment experiences no significant mechanical loading; therefore, the design was straightforward. The displacement gages are described in the following section.

Buckstays and Spacing: The receiver panel's buckstay is shown in Figure 3.2.10. The buckstay consists of a T-shaped section that joins four or six receiver passes to form a panel (the four-pass panel design evolved during the receiver sizing process when the end passes were eliminated). Each buckstay has eight 1-inch diameter McGill Camrol Bearing (Model CF-1) rollers that are attached to a pair of horizontal members cantilevered from the T-section.

FIGURE 3.2.10
RECEIVER PANEL BUCKSTAY

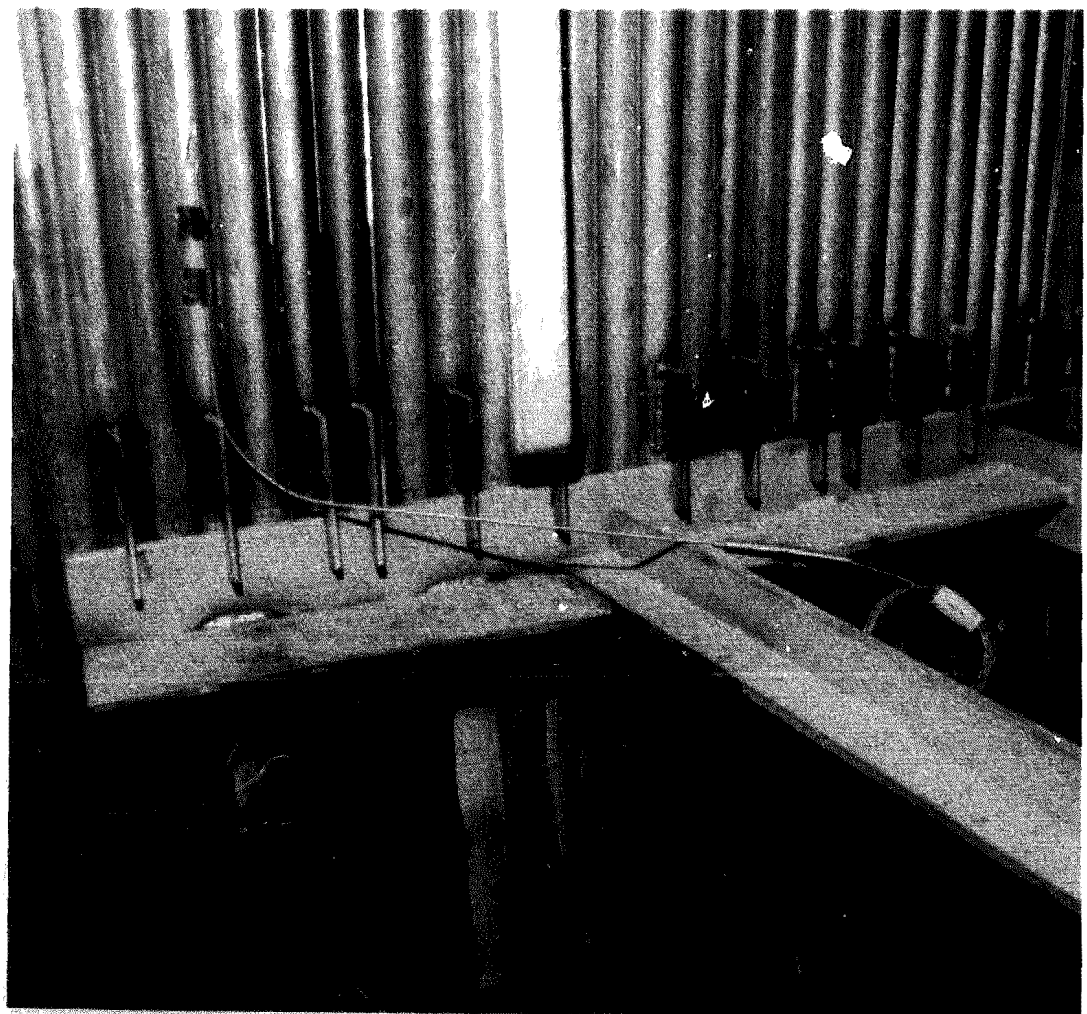

The basic functions of the buckstay are to preserve receiver geometry and transfer lateral loads to the main support structure. Conforming to the receiver curvature, the buckstay is angled outward at two locations. Clearances are maintained by the buckstay to allow the tubes to grow thermally. The buckstay arrangement, however, limits the maximum gap between tubes to 1/8 inch. (Refer to Section 4.2 for a discussion of tube gaps.)

The spacing of lateral supports, or buckstays, was established to limit tube deflections. Tube deflections can be either elastic or permanent. Elastic deflections occur during operation and result from a non-uniform heating of the receiver tube.

Elastic calculations, however, show this tube displacement to be minimal for laterally supported tubes. Permanent tube deformations were observed during the testing of the MSEE receiver (the majority ranging from 0.50 to 0.75 inch) and were considered in determining the support spacing at the MSS/CTE receiver. A nominal support spacing of 3' 10" was selected and was checked for the mechanical loads specified. Displacement gages were installed to monitor tube deformations of passes 4, 5 and 6 in the east zone.

The buckstay was sized based on mechanical loads (deadweight, wind and seismic) and in accordance with the AISC Code. Fabricability was an additional concern to the designers in specifying minimum weld configurations. The buckstay was constructed of 304 stainless steel.

The use of rollers in the lateral support system is a feature of the Saguaro receiver design. The rollers purchased for the receiver are the standard, economical bearing-type. Due to the high operating temperatures of the receiver, a high-temperature bearing grease was specified, although predicted roller temperatures were below 150°F. A typical connection is shown in Figure 3.2.11.

FIGURE 3.2.11

BABCOCK & WILCOX RECEIVER PANEL ROLLERS

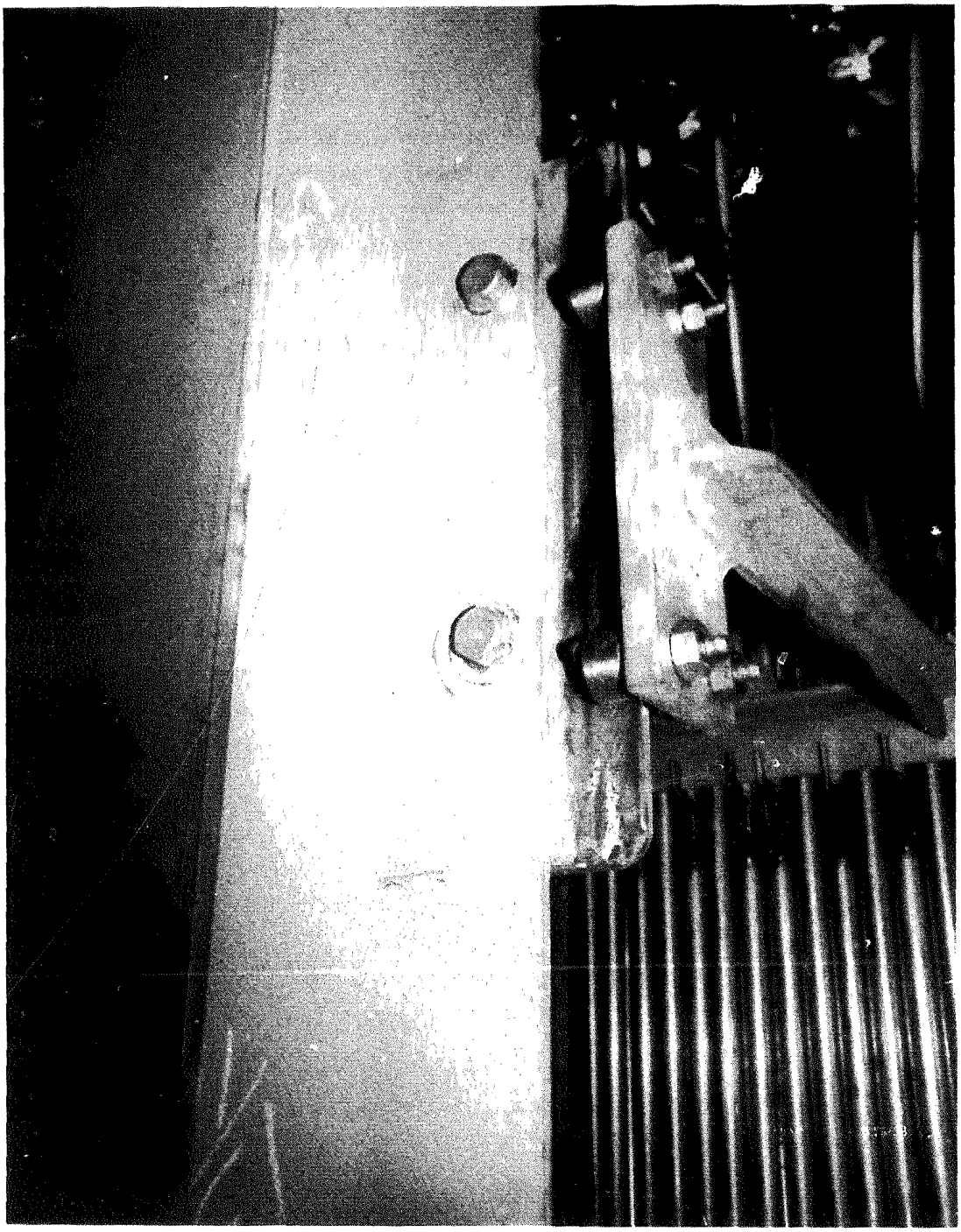

The panels are insulated on the back side with 8 inches of Kaowool 2600 fiber blanket. The insulation is attached to stainless steel straps suspended from each buckstay using standard pin stud connections. Therefore, the receiver panels support the weight of insulation. The insulation was applied in 2-inch thick layers with overlapping joints to minimize heat loss from the cavity.

The major difference between the test receiver panel and a commercial-scale panel is length. Maximum longitudinal thermal growth of the receiver panel is 38 mm (1 1/2 inches), whereas the maximum growth of a Saguaro panel would be approximately 190 mm (7 1/2 inches). The basic design characteristics of the panel lateral support system, however, apply to greater panel lengths also.

Headers and Safe Ends: The receiver panel design requires two header sizes. A single 114-mm (4.5-inch) diameter header joins two passes (subpanel). The header length is less than the width of the subpanel, 228 mm (9 inches), to avoid interference with adjacent headers. Connection of the receiver tubes to the header is accomplished using a 22-mm (7/8-inch) diameter transition piece called a jumper tube. The wall thickness of the jumper tube was established to reduce stresses at the tube-header junction induced by differential thermal expansion. The connection to the header is a J-groove welded joint. This type of connection permits the use of two joint configurations, the radial and non-radial tube entry shown in Figure 3.2.12.

FIGURE 3.2.12

BABCOCK & WILCOX HEADER ARRANGEMENT

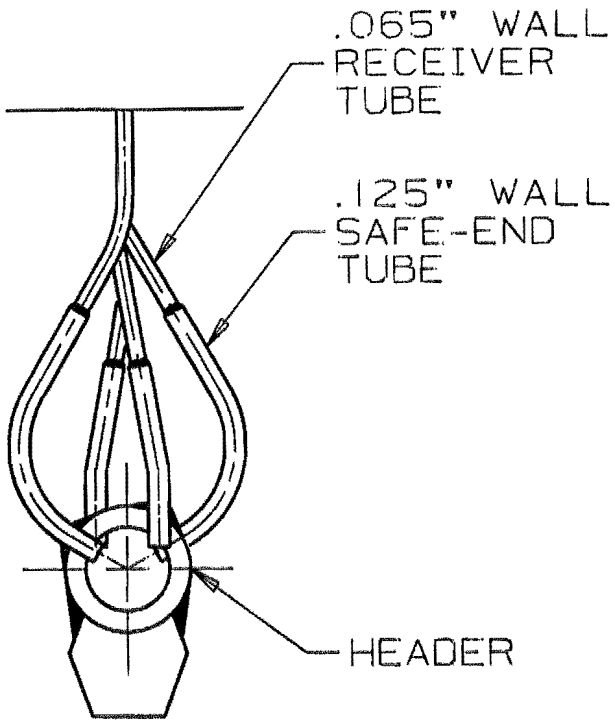

The majority of tube entries are the non-radial type, arranged in two rows equally offset from the panel centerline. This arrangement was selected to minimize eccentric loading to the tube-header connection to facilitate panel construction, and minimize the extent of tube ending, thereby reducing the overall size at the safe ends. The radial configuration was required for the header and tubes. This connection must clear the header and cap and maintain accessibility for welding. A tube-to-tube butt-welded joint connects the receiver tube to the jumper tube outside the heater length of panel.

Each pass has an individual lower header to accommodate the differential thermal expansion between passes. The safe-end configuration is similar to the upper safe end although two additional header tubes are required (per subpanel) because of the split header arrangement. The inter-pass connecting pipe contains an expansion loop that permits differential vertical movement of

adjacent passes. The piping loops extend radially inward and compose a large portion of the cavity floor. The inter-pass connecting pipe is suspended by the receiver panels and therefore will move relative to the panels. The headers, jumper tubes, and interconnecting pipe are constructed of 304 stainless steel.

The general header and safe-end arrangement is typical of the Saguaro panel design, although a future panel design would incorporate certain design improvements. During testing of the receiver, fluid-temperature ramp rates were found to be severe, imposing large stresses on the tube-header connection. An improved connection design would yield higher acceptable temperature ramp rates important to receiver control and operation. Such a connection would be a machined header stub offering one or more uniform transitions between the header and receiver tube. Similarly the header and cap would be designed to maximize the allowable fluid-temperature ramp rate.

3.2.2 Foster Wheeler Panel Design and Analyses

One of the major concerns in designing solar receivers is their structural integrity during a design life of up to 30 years (for a commercial plant). Receiver panels normally operate at elevated temperatures and are subjected to diurnal as well as cloud-cover cycles. The combination of elevated-temperature operation and cyclic behavior makes these components susceptible to creep-fatigue failure. Thus the panels are the most critical receiver components from thermal-stress and creep-fatigue points of view. They were analyzed extensively to determine the severity of the thermal gradients and their impact on the structural integrity and creep-fatigue life of the receiver.

Thermal/Hydraulic Analysis

The thermal/hydraulic analysis of the panels was made using a finite-element computer program/model that divides each tube into 15 nodal points (14 elements) along its length. Using the heat flux maps, inlet salt temperatures, flow rates, tube-wall and salt properties, and panel geometry, the program evaluates all six tubes in each pass. Tube-wall and salt

temperatures are calculated at each nodal point; absorbed power, salt temperature change, and frictional and gravitational pressure drops are calculated for each nodal element. The outlet salt conditions from the first element are used as the inlet conditions for the next element. The calculation continues through all nodes, finally giving the outlet salt temperature of each tube. The pass outlet salt temperature is the weighted average of the six tubes' salt temperatures. The program analyzes all passes using the outlet conditions of the previous pass as inlet conditions for the next pass.

Panel longitudinal thermal expansion was calculated using the average tube-wall temperature. The thermal expansion is less than 38 mm (1-1/2 inch) in the hottest tube. As a result of this longitudinal thermal growth, the bottom end of the panel moves in and out of its plane by less than 1.6 mm (1/16 inch) between the cold and hot positions (Figure 3.2.13). By comparison, in a 27.5-m (90-ft)-long commercial-sized panel, the maximum thermal growth is expected to be about 232 mm (9 inch), which results in a back-and-forth movement of the bottom end of the panel of less than 6.4 mm (.25 inch).

FIGURE 3.2.13
MOVEMENT OF LOWER HEADER IN A FULL-SIZED PANEL

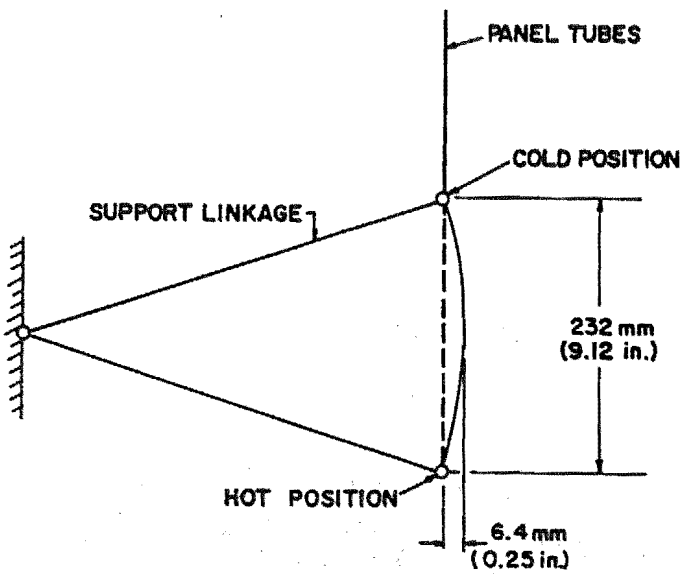

The program uses one of three correlations to calculate the molten-salt convective coefficient, depending upon the flow regime--Seider-Tate (laminar: Re>2100), Hauzen (transition: 2100>Re<10,000), or Dittus-Boelter (turbulent: Re>10,000) [20,21,22]. The salt Reynolds number and convective coefficient at the design flow increase from about 14,000 and 2843 W/m^2-°C (500 Btu/h-ft^2-°F) in the wing panel to about 58,000 and 8529 W/m^2-°C (1500 Btu/h-ft^2-°F) in the rear panels. Thus at design flow, the flow is turbulent in all panels. At minimum part load (25 percent of design flow), the wing panel flow is in the transition region.

To determine critical locations in the absorber panels for stress analysis and creep fatigue evaluation, the peak tube-wall temperatures and front-to-back temperature differences (which are proportional to thermal stresses) were calculated. The results show that a peak front-to-back tube temperature difference of 149°C (267°F) occurs in Pass 9 (See Figure 3.2.14) at the location of the peak absorbed heat flux [0.593 MW/m^2(188 x 10^{3}Btu/h-ft^2)]. The peak tube-wall temperature of 635°C (1175°F) occurs in Pass 14, where the absorbed heat flux is 0.487 MW/m^2 (143 x 10^3 Btu/h-ft^2). Metal and salt temperature profiles for the hottest tube are plotted in Figure 3.2.15.

FIGURE 3.2.14
SCHEMATIC OF THE SALT LOOP

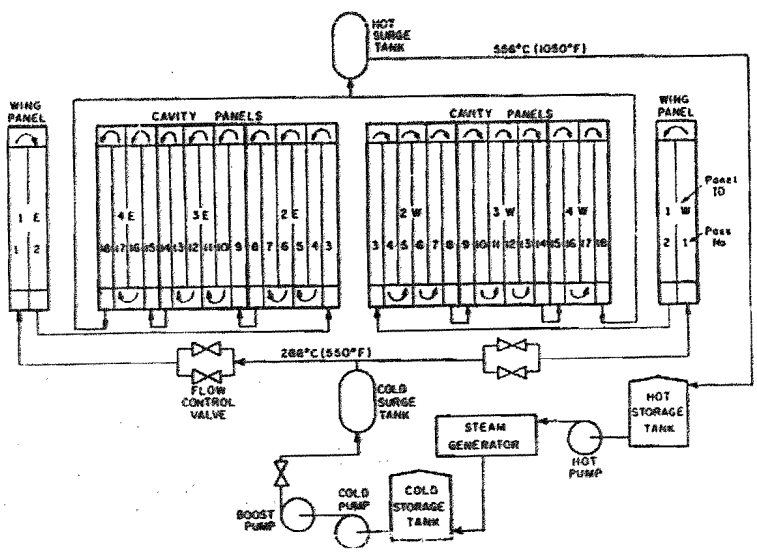

FIGURE 3.2.15
TEMPERATURE PROFILE OF HOTTEST TUBE

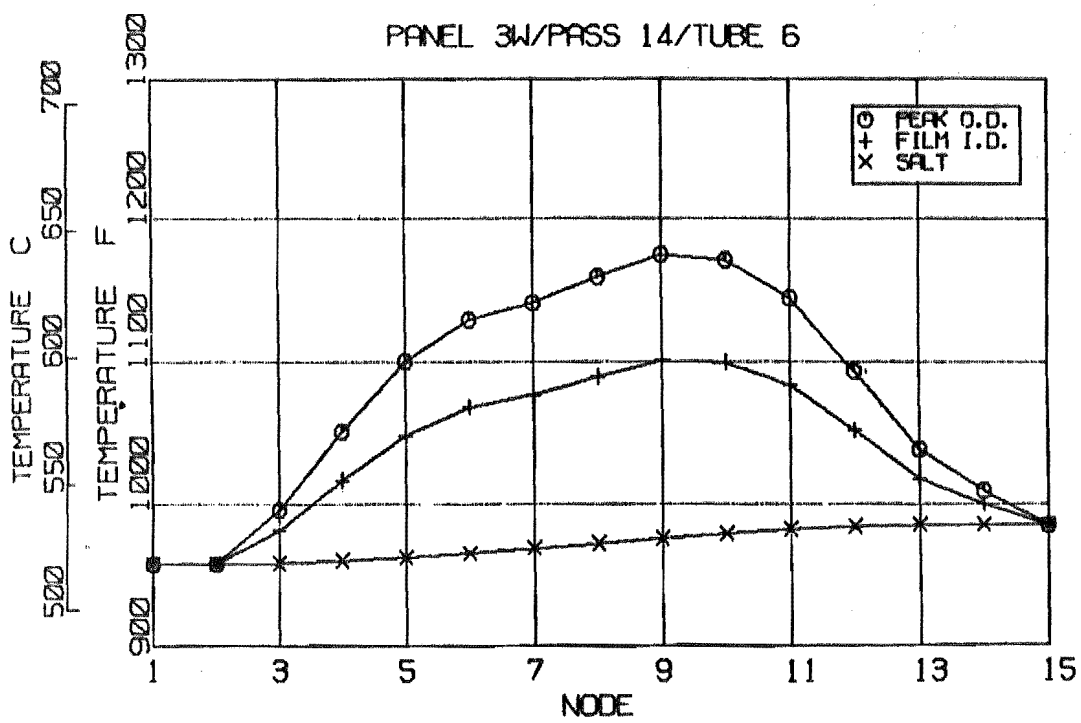

From these one-dimensional analyses, we determined that Pass 2 (Type 304 SS) and Passes 9 and 14 (Alloy 800) have the worst combinations of tubewall temperatures and temperature gradients and hence are the most critical. Therefore, these passes were chosen for detailed stress analysis and creep-fatigue evaluation. Results of the steady-state thermal/hydraulic analysis are summarized in Table 3-IV.

TABLE 3-IV
THERMAL/HYDRAULIC DATA SUMMARY

Salt flow rate,	10.7 kg/s (85,000 lb/h)
Peak absorbed heat flux, MW/m^2	0.593 MW/m^2 (188,000 btu/h ft^2)
Peak tubewall temperature	635 °C (1175 °F)
Peak front-to-back tube temp. diff.	149 °C (267 °F)
Salt Reynolds number	14,000 to 58,000
Salt velocity	1.2 to 2.6 m/s (4.0 to 8.6 ft/s)
Salt conductance	2843 to 8529 W/m-°C (500 to 1500 Btu/h-ft^2-°F)

Stress Analysis

In the design of the pressure boundary, all requirements of the American Society of Mechanical Engineers Boiler and Pressure Vessel Code, Section VIII-Division 1, were satisfied. In addition, because of the highly cyclic nature of receiver operations, the fatigue criteria of Section VIII-Division 2 for temperatures in the sub-creep regime were satisfied. For elevated-temperature design, there are no well-accepted criteria for creep-fatigue evaluation of solar plant components. (A Solar Energy Standards Committee appointed by the ASME is working on a Solar Code.)

The only widely accepted criteria for elevated-temperature creep-fatigue evaluation are those set forth in Section III and Code Case N-47 of the ASME Code [23]. Because they were written for nuclear components with their inherent higher risk level, the criteria are unnecessarily conservative for solar applications. Their use in solar receivers could lead to excessively conservative designs and may result in significant cost penalties. Hence the Code Case N-47 criteria were used with some modifications. They were deemed conservative enough to provide a reasonable level of safety and reliability. The inelastic fatigue curves (Figures T-1420-1C of Code Case N-47) were used in conjunction with inelastic strains approximated from an elastic analysis.

The rationale and justification for this approach were discussed by Narayanan, Rao, and Carli [24].

A two-dimensional steady-state thermal stress analysis was performed using the finite-element computer program NONAX [25] and a finite-element model of the tube cross section. The model (Figure 3.2.16) consisted of 114 isoparametric two-dimensional solid elements.

FIGURE 3.2.16
FINITE ELEMENT MODEL

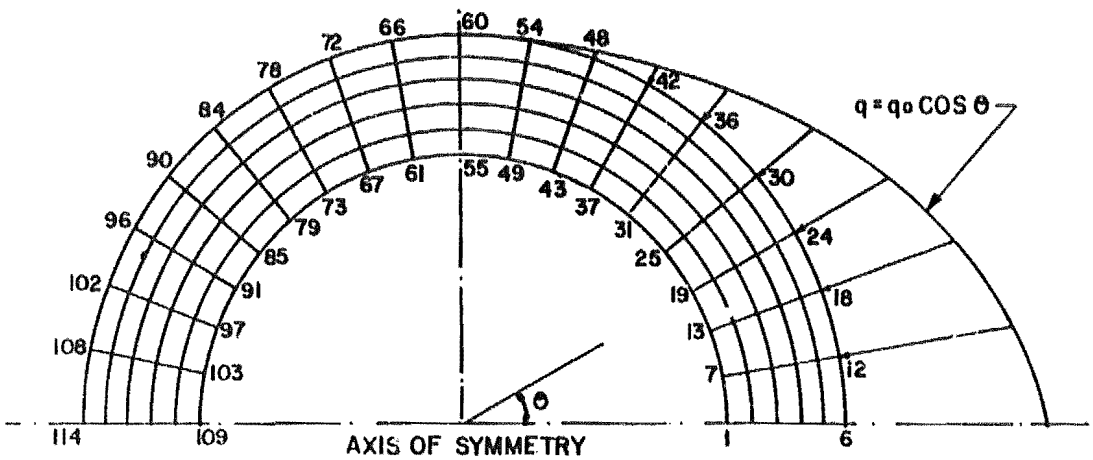

Because we assumed the flux to be symmetric, only one-half of the tube cross-section was considered in the analysis. The salt's bulk temperature and conductance from the thermal/hydraulic analyses as well as the absorbed heat flux were used as inputs in this analysis. The results of the analysis are listed in Table 3-V.

The maximum heat flux and front-to-back temperature gradients occurred in Pass 9, where the salt temperature was relatively low; the peak tube-wall temperature occurred in Pass 14, where the heat flux was relatively low. This combination of factors helped reduce tube-wall thermal stresses.

The prototype receiver was designed for three years' life. During its lifetime, the receiver is expected to encounter 1100 daily start-up/shutdown cycles and fewer than 5000 cloud cycles. The results of the analysis (Table 3-V) indicate that the creep and fatigue life for each of the test panels is more than adequate.

TABLE 3-V

CREEP-FATIGUE EVALUATION

Description	Pass 2	Pass 9	Pass 14
Tubewall material	Type 304SS	Incoloy 800H	Incoloy 800H
Absorbed heat flux, MW/m^2 ($Btu/h\text{-}ft^2$)	0.205 (65,000)	0.593 (188,000)	0.487 (154,000)
Salt conductance, $kW/m^2\text{-}°C$ ($Btu/h\text{-}ft^2\text{-}°F$)	2.95 (519)	7.50 (1321)	8.49 (1494)
Salt bulk temperature, °C, (°F)	297 (566)	432 (809)	524 (976)
Results of Analyses:			
Maximum front-to-back temperature difference, °C (°F)	98 (176)	149 (267)	111 (199)
Maximum metal temperature, °C (°F)	395 (742)	580 (1076)	635 (1175)
Maximum effective stress, MPa ($kip/in.^2$)	209.6 (30.4)	331.7 (48.1)	166.7 (24.2)
Elastic strain range	0.00117	0.0019	0.00097
Inelastic strain range	0.00129	0.0021	0.00107
Fatigue life (N_d), cycles	>1,000,000	15,000	>1,000,000
Creep-rupture time (T_d), hours			
based on S_y:	>500,000	>300,000	>45,000
based on pressure stress:	>1,000,000	>1,000,000	>500,000

3.3 Heliostat Aiming

The test receiver employs a distributed aiming strategy to even out the solar flux on the heat-absorption panel. This section describes the development of the aiming patterns for the CRTF that were employed during the test. Also described are the warm-up patterns used and special patterns developed for loss testing.

3.3.1 Normal Operational Pattern

The cavity and panel geometry for the Category B receiver were determined using the McDonnell Douglas CONCEN computer code. Total incident power, flux distributions, and spillage were predicted by CONCEN in order to determine the best receiver geometry and aim strategy to meet the design requirements. Several iterations were evaluated on the design day, February 21 at solar noon.

Results from CONCEN established a base-line heliostat-field configuration and aiming strategy consisting of aim points located along the receiver's vertical centerline in the cavity's aperture plane. The exact location of each aim point, shown in Table 3-VI, is based on the radial distance between each heliostat and the CRTF tower's vertical centerline. Assuming the CRTF heliostat field is symmetric, this resulted in 96 aim points, or one aim point for every two heliostats.

TABLE 3-VI

Heliostat Vertical Aim

Heliostat Radial Location (meters)	Vertical Aim Displacement* (meters)
30	-1.20
60	0.30
75	-1.10
90	-0.90
105	1.10
135	0.90
165	-0.40
190	-0.20
210	-0.20
240	0.10

* referenced from the aperture horizontal centerline

In order to simplify the job of setting up test files in the CRTF heliostat control system, the aiming strategy was simplified by breaking the heliostat field down into eight groups, each assigned a specific aim point. Aim points were still determined from Table 3-VI, although the exact locations were based on each group's average radial distance from the tower's vertical centerline.

Verification of this approach was accomplished with Sandia's HELIOS computer code. Flux distributions and incident power were computed and compared to predictions obtained from CONCEN. The results, shown in Figure 3.3.1, were consistent with the predicted uncertainties, approximately 10 percent estimated for the HELIOS and CONCEN computer codes.

FIGURE 3.3.1
RECEIVER FLUX DISTRIBUTIONS

Panel No. 2 West			Panel No. 3 West			Panel No. 4 West			Wing Panel West	
17.8 (20.1)	16.8 (18.9)	15.8 (17.6)	15.8 (17.0)	12.5 (13.1)	8.4 (8.8)	8.1 (6.3)	5.1 (3.6)	2.6 (1.3)		
									8.2 (2.8)	3.4 (1.6)
59.0 (58.4)	63.2 (59.7)	62.6 (59.3)	62.0 (59.3)	58.3 (57.3)	44.3 (46.4)	41.7 (38.9)	31.5 (29.5)	19.7 (19.8)		
									30.8 (17.6)	13.9 (10.7)
5.4 (5.7)	5.5 (6.7)	6.6 (7.0)	6.6 (6.9)	6.6 (6.8)	5.7 (5.5)	4.7 (5.0)	3.8 (4.4)	3.1 (2.9)		
									3.9 (2.2)	1.7 (1.3)

HELIOS predictions
(CONCEN) predictions

Note:

The base-line CRTF collector field configuration, shown in Figure 3.3.2, consists of 191 heliostats targeted at eight separate vertical aim points. Each heliostat is shown with its corresponding aim-point group number.

FIGURE 3.3.2
FIELD CONFIGURATION

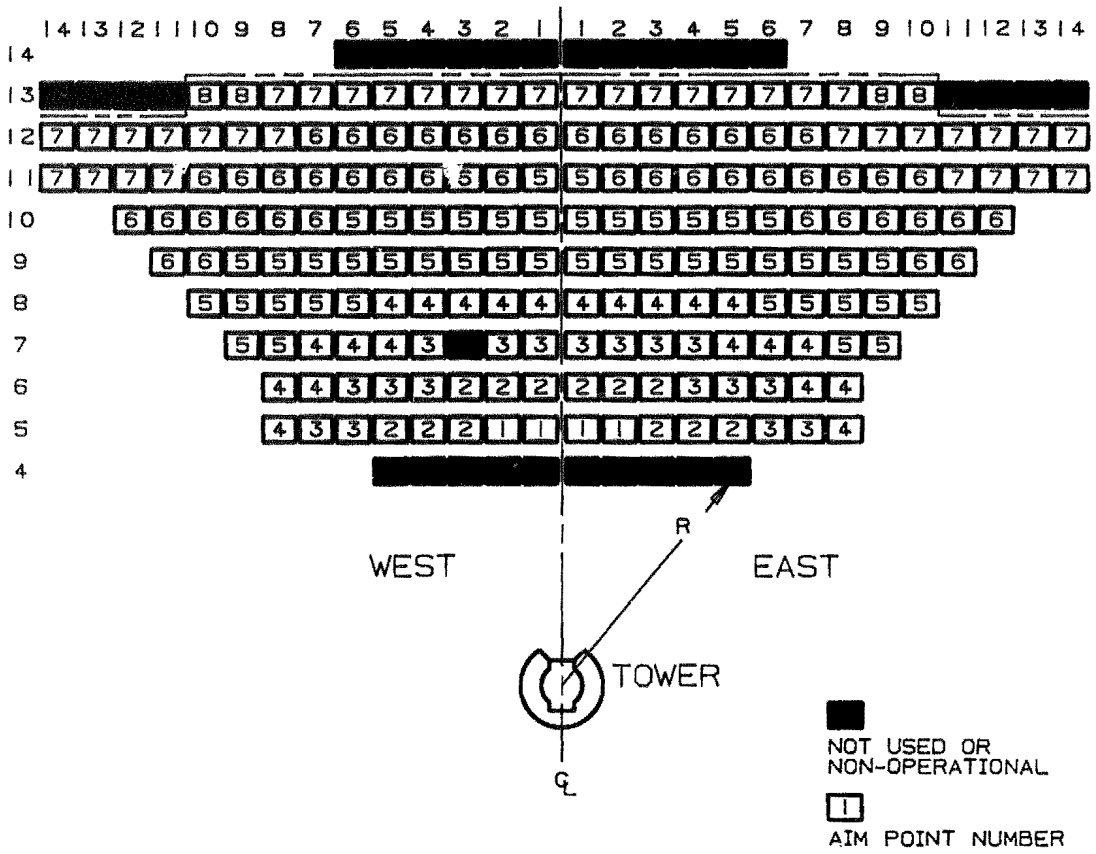

Figure 3.3.3 depicts the relative location of each target point positioned along the receiver's vertical centerline and Table 3-VII presents the location of the aim points.

FIGURE 3.3.3

NORMAL OPERATION -- AIM-POINT LOCATIONS

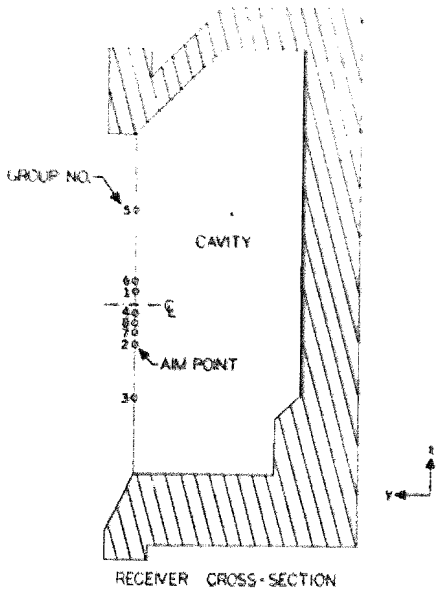

TABLE 3-VII

AIM-POINT LOCATIONS

Aim Point	Location (Ft.) (w.r.t. aperture center)
1	0.442913
2	-1.42716
3	-3.33005
4	-0.41010
5	3.297244
6	0.803805
7	-1.00065
8	-0.67257

3.3.2 Sunrise Warm-Up Pattern

Preliminary development of a sunrise warm-up pattern for the Category B receiver panels was accomplished by using the CONCEN computer code. The desired minimum panel temperature for warm-up was 550°F, with a maximum allowable panel temperature of 1050°F. Based on predictions using blackbody

radiation equilibrium temperatures, an incident flux of 5.6 to 32.0 kW/m² was required to obtain these panel temperatures.

A trial-and-error procedure was used to obtain these flux levels by selecting specific heliostats and aim-point coordinates. Based on CONCEN predictions using an insolation immediately after sunrise of 550 W/m² (estimated for 7:30 a.m. on February 21), a base-line configuration of 33 heliostats and several aim points, each located along the aperture's vertical centerline, was obtained.

Based on experience from the MSEE test program, 33 heliostats were considered insufficient for achieving this flux level and for warming the panels in a reasonable amount of time. This may be the result of incorrect calculation of shading and blocking in the CONCEN code; these effects are very important near sunrise. Therefore, a base-line configuration was developed for the warm pattern, shown in Figure 3.3.4, that included a much larger percentage of the field. the total number of heliostats targeted on the receiver was 144, or 68 percent (out of 212) of the available CRTF collector field. The aim-point group numbers are also shown for each heliostat.

FIGURE 3.3.4
FIELD CONFIGURATION FOR SUNRISE WARM-UP

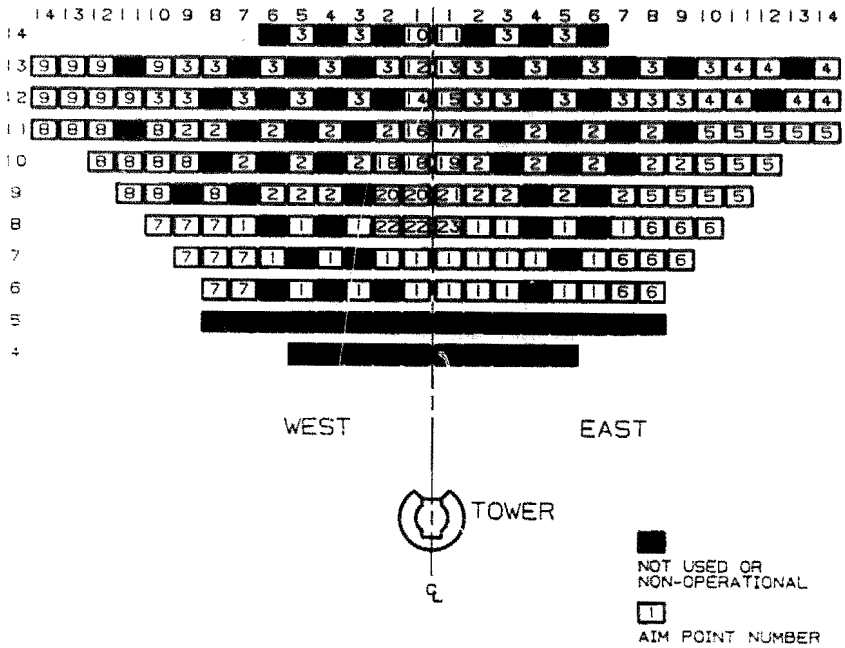

In addition to changing the heliostat configuration, the aim-point locations were also modified. Instead of locating the aim points along the centerline of the aperture, 23 target locations throughout the receiver were selected as shown in Figure 3.3.5. The coordinates of these aim points are given in Table 3-VIII. The objective was to evenly distribute the flux over 100 percent of the panel surfaces to prevent "cold" or "hot spots."

FIGURE 3.3.5
AIM-POINT LOCATIONS* FOR SUNRISE WARM-UP

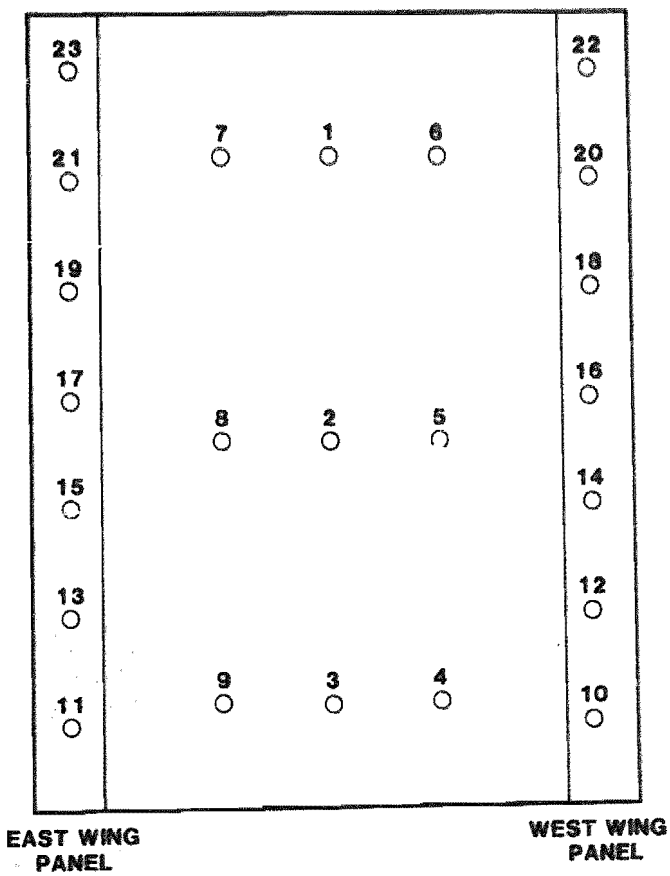

* All aim points are located in the aperture plane

TABLE 3-VIII

AIM POINT COORDINATES -- SUNRISE WARM-UP

Aim Point	Coordinates	
1	.27	67.50
2	.27	67.50
3	.27	65.40
4	-.23	65.00
5	-.23	66.20
6	-.23	67.50
7	.77	67.50
8	.77	66.20
9	.77	65.00
10	-.93	65.00
11	1.47	65.00
12	-.93	65.40
13	1.47	65.40
14	-.93	65.90
15	-.93	65.90
16	-.93	66.40
17	1.47	66.40
18	-.93	66.90
19	1.47	66.90
20	-.93	67.40
21	1.47	67.40
22	-.93	67.90
23	1.47	67.90

The aim points selected for specific heliostats were based on the heliostats' "line of sight" into the receiver cavity. For example, front row heliostats were designed to warm the top and upper corners of the cavity panels, back row heliostats the bottom and lower corners of the cavity panels, etc. Included were seven aim points located along the two "wing panels." Results from this configuration are discussed in detail in Section 5.2

3.3.3 Late Morning and Midday Warm-Up Pattern

Initially, several midday warm-up patterns for the Category B receiver were modeled using the DOMAIN computer code developed by the Solar Power Engineering Company (SPECO). The results from DOMAIN were based on achieving incident fluxes of 33 kW/m^2 during solar noon, at an insolation level of 950 W/m^2. The incident flux of 33 kW/m^2 was determined analytically by SPECO to generate panel temperatures of 1000°F.

Several configurations were tested at the CRTF to verify the prediction techniques used by DOMAIN. Test data generated from the aiming strategies developed by DOMAIN indicated the temperatures across the receiver panels were not uniformly distributed. Unfortunately, due to time constraints, the discrepancies between DOMAIN and the test data could not be resolved. Therefore, the heliostat pattern configuration obtained for late morning and midday warm-up was developed exclusively from actual test results.

The final late morning and midday warm-up pattern field configuration, shown in Figure 3.3.6, was determined using a trial-and-error procedure. Heliostats and aim points were selected and their effect on panel temperatures and ramp rates evaluated between 9:30 a.m. and solar noon. Modifications were made to eliminate any "cool" or "hot spots" by reselecting heliostats and adjusting the aim-point locations.

FIGURE 3.3.6
AIM-POINT LOCATIONS FOR LATE MORNING AND
MIDDAY WARM-UP

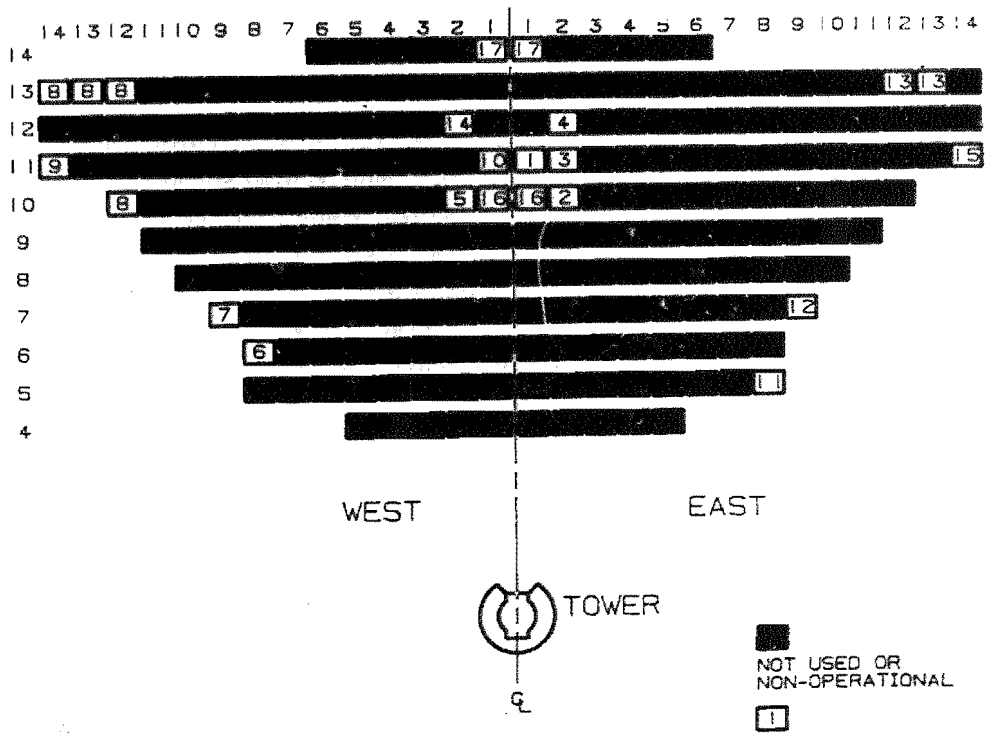

Shown in Figure 3.3.7 are the baseline aim-point locations obtained for the late morning and midday warm-up pattern. The coordinates of these aim points are given in Table 3-IX. The primary method for developing these specific aim points was based on each heliostat's "line of sight" into the receiver cavity. Front row heliostats were targeted at the upper sections of the cavity panels, outside heliostats targeted in the corners, etc. This was the same procedure used for determining the aim-point locations for the sunrise warm-up pattern.

FIGURE 3.3.7
LATE MORNING AND MIDDAY WARM-UP
AIM-POINT LOCATIONS*

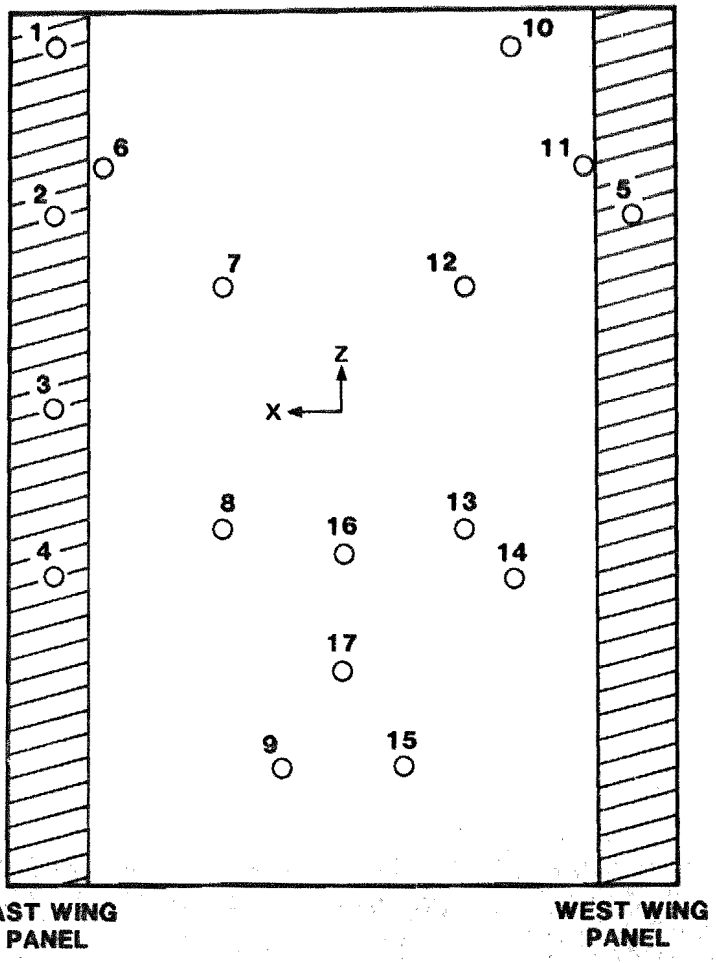

* All aim points are located in the aperture plane

TABLE 3-IX

AIM-POINT COORDINATES -- MIDDAY

Aim Point	Coordinates	
1	1.2	68.0
2	1.2	67.3
3	1.2	66.5
4	1.2	65.8
5	-1.2	67.3
6	1.0	67.5
7	0.5	67.2
8	0.5	66.0
9	0.25	65.3
10	-0.7	68.0
11	-1.0	67.5
12	-0.5	67.2
13	-0.5	66.0
14	-0.7	66.0
15	-0.25	65.3
16	0	66.1
17	0	65.4

3.3.4 Method of Barron - Transient Operation Test Patterns

Flux-on loss testing was conducted with the heliostat field divided into two 50 percent groups. This configuration was designed to reduce the incident power to the receiver by half in order to determine thermal losses at design conditions. These two groups were based on the normal operational pattern described in this section.

Also, the heliostat field was further divided into four 25 percent groups, including the two 50 percent groups. This configuration was designed to test the receiver algorithm under transient conditions. Incident power was varied in 25, 50, 75 and 100 percent increments based on the desired intensity of the transient. All of the groups use the normal operational aim-point locations. These patterns are described in more detail in Section 5.2.

3.4 Components and Interconnections

3.4.1 Surge Tanks

The pressure boundary of the receiver includes both a hot and cold surge tank. The general tank designs are shown in Figure 3.4.1. The tanks were sized in accordance with ASME Pressure Vessel Code, Section VIII, Division 1.

FIGURE 3.4.1
COLD AND HOT SURGE TANKS

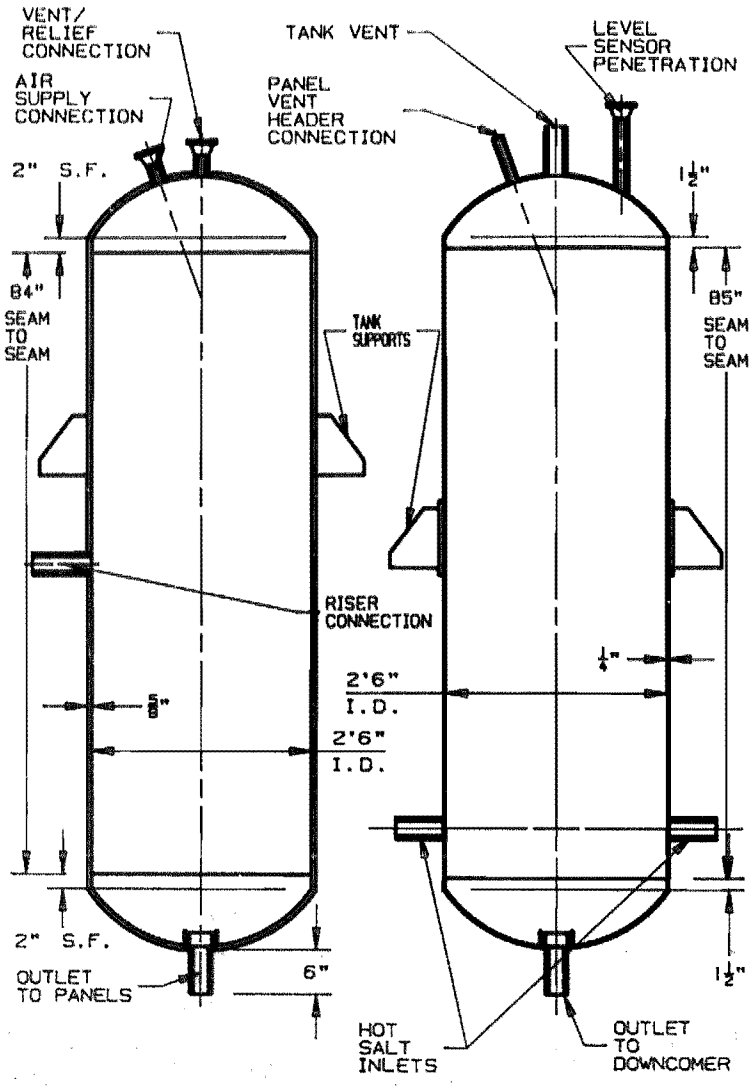

The tank volume of 40 cu ft was established based on the thermal hydraulic design (refer to Section 3.6).

The cold tank is constructed of 15.9-mm (5/8-inch) carbon steel plate rolled into a cylindrical shell 76.2 cm (30 inch^s) in diameter. Having 2:1 ellipsoidal heads and being oriented vertically, the overall height of the tank (excluding nozzles) is approximately 2.54 m (8.33 ft). Nozzles include a salt supply discharge, air supply, and vent. The tank was sized to withstand a design pressure of 3.69 Pa (535 psig) at a temperature of 343°C (650°F) and included a corrosion allowance of 0.38 mm (0.015 inches).

The hot tank is constructed of 0.64-cm (0.25-inch) stainless steel. The tank size is nearly identical to the cold tank, except for the wall thickness. Nozzles include two supplies, discharge, overflow, vent, and a level sensor. Although the tank is vented to the atmosphere when operating, thickness was established based on a design pressure of 0.552 Pa (80 psig) and a temperature of 579°C (1075°F), including a corrosion allowance of 0.38 mm (.015 inches).

A vortex inhibitor is installed at the discharge of each tank to ensure uniform flow through the tank. The tanks are supported by four support feet bolted to the main support structure.

3.4.2 Valves

The receiver subsystem-contains four flow-control valves and forty isolation valves. Two flow-control valves are arranged to operate in parallel in each of the two valve stations that control flow to each zone of the receiver. The isolation valves sere to vent and drain the receiver. All valves are air-operated and receive position signals from the process control unit. Design and fabrication are in accordance with ANSI B31.1.

The receiver flow-control valve is the 2.5-cm (1-inch) 300#-class valve shown in Figure 3.4.2. The valve type is a Valtek Mark Eleven with an offset in the body to permit self draining and a nested bellows seal arrangement. The bellows seal is a 316 stainless steel 2-ply construction housed mostly within the valve body.

The receiver flow-control valve is the 2.5-cm (1-inch) 300#-class valve shown in Figure 3.4.2. The valve type is a Valtek Mark Eleven with an offset in the body to permit self draining and a nested bellows seal arrangement. The bellows seal is a 316 stainless steel 2-ply construction housed mostly within the valve body.

FIGURE 3.4.2
RECEIVER FLOW-CONTROL VALVES

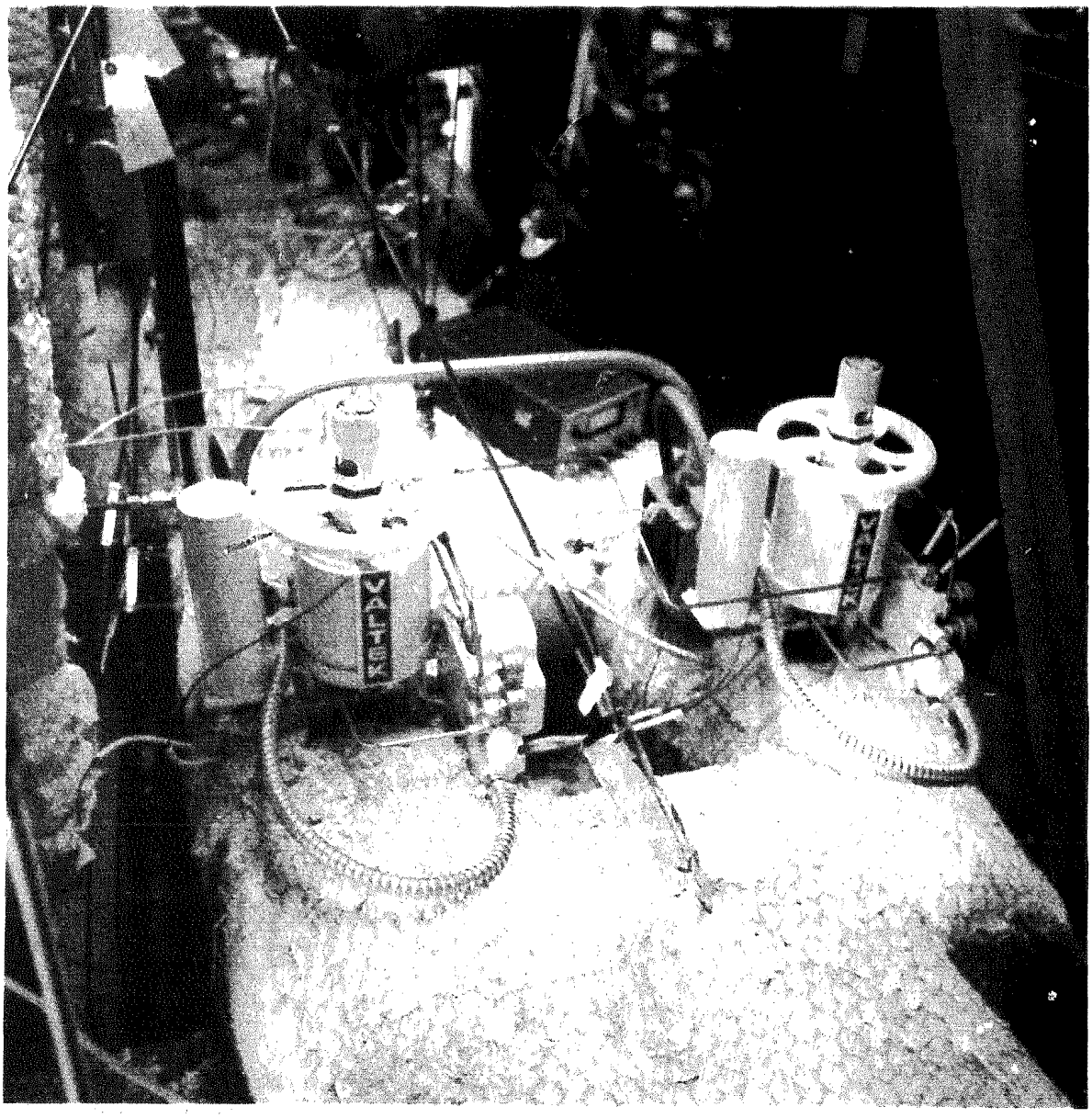

This compact bellows arrangement promotes better self-draining than a bellows above the bonnet in an isolated housing and inhibits salt freezing.

A typical receiver isolation valve is shown in Figure 3.4.3. The valve type selected for this service is the 2-cm (3/4-inch) "12U" Series Nupro Bellows valve. The general applications for this valve include toxic and corrosive fluids. The bellows is constructed of 316 stainless steel and is located near the valve body. The compact design (overall height is less than 451 cm (20 inches) makes this valve suitable for use in the receiver where space is at a premium. The use of the Nupro valve greatly simplified the piping arrangement and improved accessibility. The Nupro valve is fully drainable.

FIGURE 3.4.3
RECEIVER ISOLATION VALVES

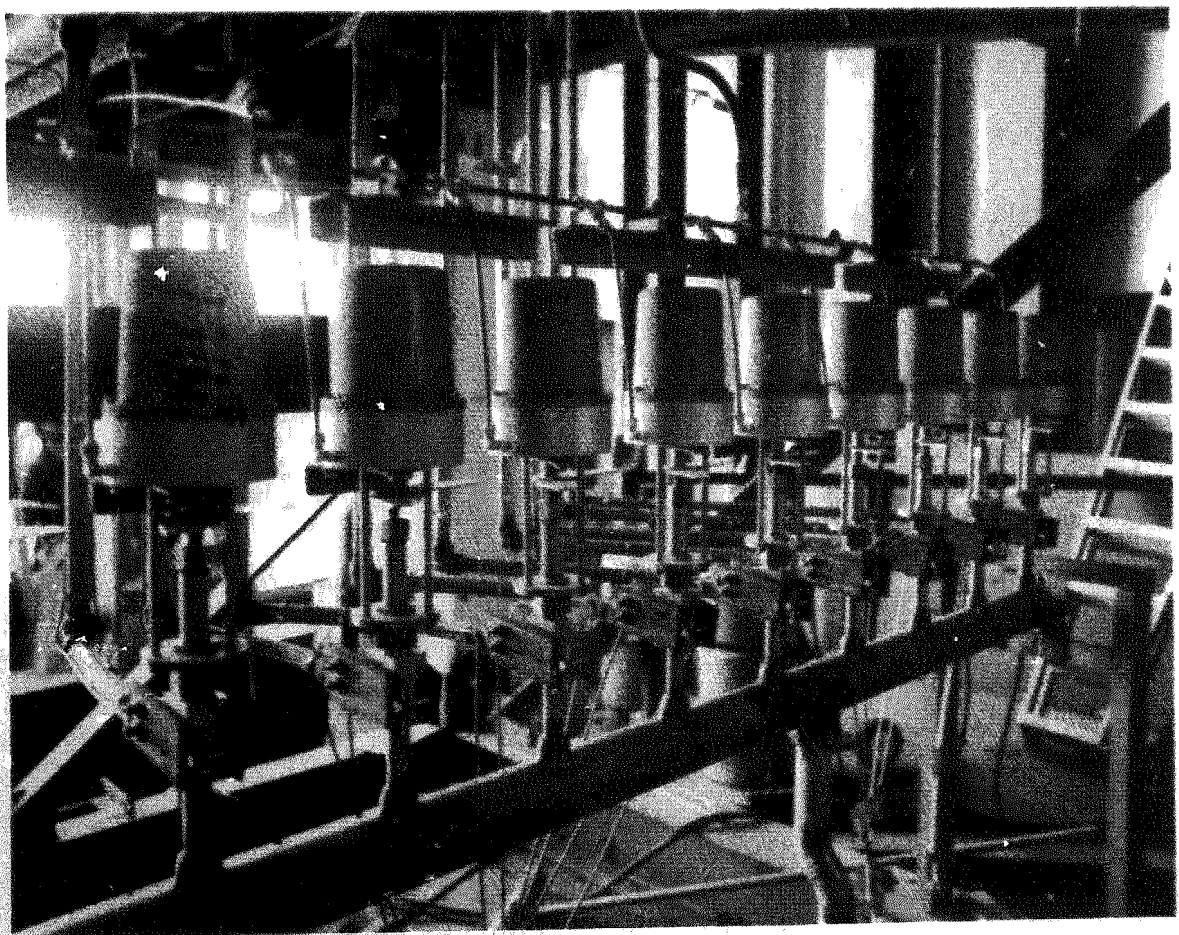

3.4.3 Piping

Receiver piping includes supply, return, recirculation, vent, and drain lines. Design and fabrication comply with the rules of the ANSI B31.1 "Power Piping Code." Design conditions for the major piping are presented in Table 3-X.

TABLE 3-X
DESIGN CONDITIONS

Piping Description	Pressure kPa (psig)	Temperature °C (°F)
Supply	3689 (535)	343 (650)
Return	552 (80)	579 (1075)
Recirculation	2344 (340)	343 (650)
Vent and Drain	2344 (340)	579 (1075)

Cold-salt piping (low temperature) is constructed of carbon steel and hot-salt piping (high-temperature) is constructed of stainless steel. Details of the receiver piping arrangement and specification are presented in the B&W drawings in Appendix J. The piping arrangement was established to preserve accessibility to the receiver hardware and to provide adequate space for the large amount of insulation to be installed. Additionally piping flexibility was checked to ensure that stresses did not exceed acceptable levels. Pipe hangers consist of rod, variable spring, and constant load hangers. Rigid calcium silicate insulation was used at each pipe support to minimize conductive heat loss.

Receiver panel vent and drain piping represents a significant portion of the piping system. These lines, including the vent/drain collection headers and valves, were included in the receiver module design as shop fabricated hardware. This approach had several advantages.

- The receiver panels (connected by the vent and drain piping) were hydrotested and inspected as a single unit.

- Panel vent and drain valves were checked out prior to erection.
- Shop fabrication was preferred over field installation minimizing cost and schedule impacts.

3.5 Hydraulic Design

The hydraulic analysis of the Category B receiver was performed in order to set specific characteristics and size components. The design of receiver hydraulics was done to set the design pressures of the system; specify pump capacities necessary to overcome losses and meet thermal requirements of the receiver; and size the hot and cold surge tanks.

In order to meet the requirements set for this test, the receiver was designed to match the thermal/hydraulic conditions of the Saguaro Solar Plant (Section 3.2). These conditions were matched through an iterative process using the SRPAN4A (Solar Receiver Parameter Analysis, Version 4A) design code. This code was used to calculate the pressure drop across each half of the receiver. The supply piping was analyzed for shock and functional losses and static head. The surge tanks (both hot and cold) were sized based on possible failure modes and control requirements. The control valves were sized and purchased in order to control flow through the receiver and maintain pressure in the cold surge tank. Analysis for all components was done for a range of operating conditions in order to cover worst cast operation of the receiver. These conditions include high and low power, a range of inlet temperatures and hot and cold flow.

3.5.1 Receiver Subsystem Pressures

The receiver subsystem pressures include receiver panel pressure drop, control valve pressure and system piping (receiver riser and downcomer). These system pressures are governed by friction and shock losses, static head and required valve pressure drop for control. The receiver subsystem is vented to atmosphere at the highest point in the hot surge tank. The following sections discuss the subsystem pressures.

Receiver Pressure Drops

The thermal/hydraulic analysis of the receiver panels was made using the computer code SRPAN4A that divides each pass into 12 elements and 13 nodes as shown in Figure 3.5.1. Each element represents 1 foot of heated tube length. Using heat flux maps, inlet and outlet salt temperatures, salt flow rate, tube-wall and salt properties and panel geometry, the temperatures (OD, ID, and salt), absorbed power, tube stresses, and pressure drop are calculated for each node.

FIGURE 3.5.1
SRPAN4A MODEL

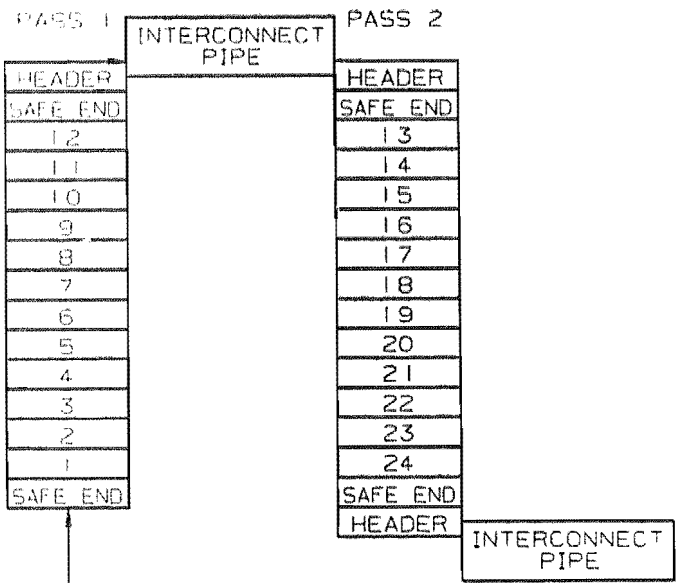

The pressure drop calculated for the receiver is calculated node by node for the heated sections of tubing, using the changing salt properties as it increases temperature while flowing through the receiver. The pressure drop is also calculated for each unheated section of the panels. These sections include the safe ends at the top and bottom of each tube, the headers and the inter-connecting pipe which connects one pass to the next. The properties of

the various receiver panel sections and receiver tubing is listed in Table 3-XI.

TABLE 3-XI

RECEIVER SAFE END, HEADER, INTER-CONNECTING PIPING AND TUBING PROPERTIES

	Surface Roughness (E/D)	Inside Diameter (inches)	Length (inches)	Shock Loss (K)
Safe Ends-Wing				
Inlet of Pass	.000237	.8440	24.0	.50
Outlet of Pass	.000237	.8440	24.0	1.0
Safe Ends-Back				
Inlet of Pass	.0003565	.5610	20.0	.737
Outlet of Pass	.0003565	.5610	20.0	1.23
Headers-Wing				
Top of Pass	.0003565	3.152	0.0	0.0
Bottom of Pass	.0003565	3.152	0.0	0.0
Headers-Back				
Top of Pass	.0003565	3.152	0.0	0.0
Bottom of Pass	.0003565	3.152	0.0	0.0
Inter-Connecting Pipe-Wing Panel				
Top of Pass	.00900	2.0	0.0	0.0
Bottom of Pass	.000237	.5610	0.0	0.0
Inter-Connecting Pipe-Back Panel				
Top of Pass	.00900	2.000	0.0	0.0
Bottom of Pass	.00871	2.067	104.0	3.0
Receiver Tubing				
Wing Panels	.000237	.8440	144.0	--
Back Panels	.000335	.6400	144.0	--

The surface roughness used for the receiver tubing is the normal roughness for cold drawn tubing. This value is significantly lower than that derived from the Martin Marrietta receiver testing [8] which used the total system pressure drop as a representative of the receiver pressure drop. This included the receiver tubing as well as the headers and inter-connecting pipe, however in calculating the roughness only the L/D for the tubing was used causing the roughness to be higher than that for book valves for cold drawn tubing. Based on this information, the commercially published value was used for calculating receiver pressure drop. The program then sums up the nodal pressure drops for a total pressure drop of 160.5 psi at 80624 lb/h of salt flow through the receiver. This resulting pressure drop includes frictional and gravitational losses. The pressure drop through the receiver for various loads is shown in Figure 3.5.2.

FIGURE 3.5.2
RECEIVER SUBSYSTEM PRESSURE LOSS

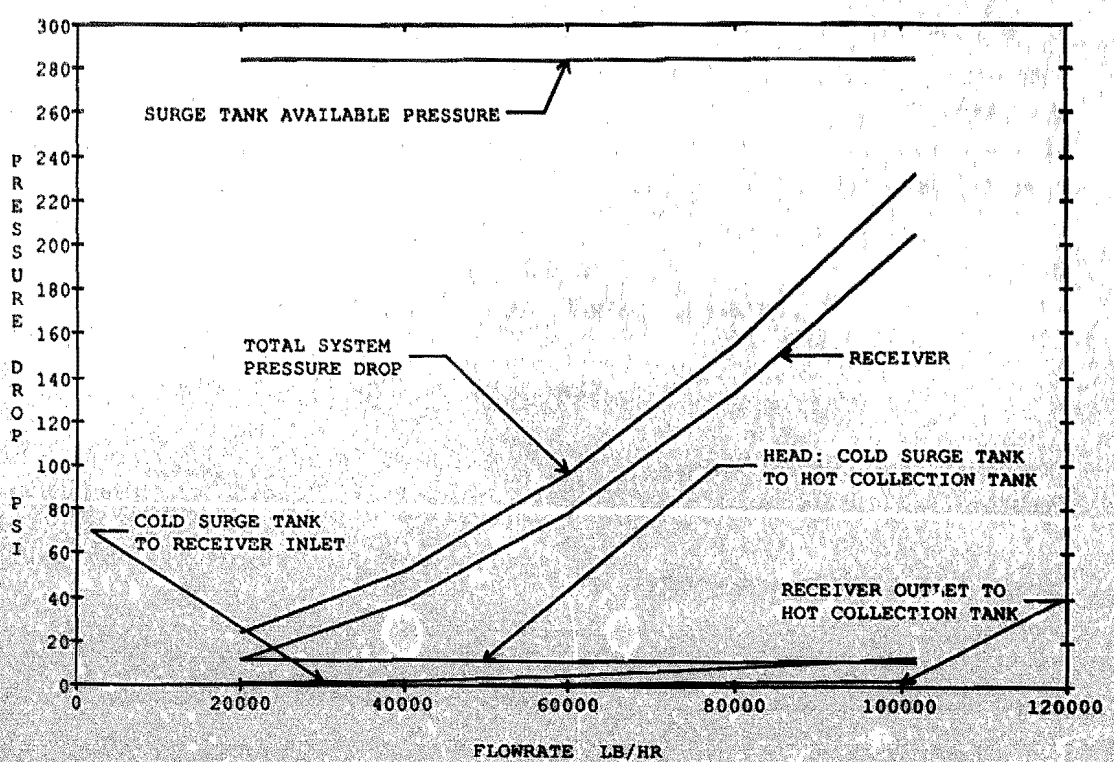

Control Valve Requirements

The receiver system control valves used in this test include four control valves (FCV101, 102, 103 & 104) used specifically for receiver flow control and setting the cold surge tank design pressure and one valve for controlling level in the cold surge tank (FCV151).

The four receiver flow-control valves are situated in two parallel piping runs. The valves are sized to operate with either one valve operating or two valves operating in parallel. Each valve is designed to handle full flow of 47,025 lb/h at an inlet pressure of 284 psig. The pressure drop through each valve at design point is about 70 psi at 70 percent of full stroke. Of the 70 psi, 40 psi is the pressure drop required at 100 percent, with 30 psi margin for control.

The cold surge tank level control valve FCV151 is a refurbished valve used during MSEE. Due to a change in the requirements for the cold boost pump upstream of the valve, it was necessary to modify the valve due to the increase in outlet pressure of the boost pump. The pressure drop thru the valve plus the loss and head in the riser piping sets the boost pump outlet pressure. The nominal operating conditions for the refurbished valve are a 50 psi pressure drop at 94,050 lb/h and a salt temperature of 550°F. All of the flow-control valves and the level-control valve are Mark One valves purchased from Valtek. Table 3-XII summarizes the valve characteristics.

TABLE 3-XII
RECEIVER CONTROL VALVE CHARACTERISTICS

	Size	Cv	Trim
Receiver Flow-Control Valves FCV101, 102, 103, & 104	1"	8.1	.72
Surge Tank Level-Control Valve FCV151	2"	19.3	1.25

Figures 3.5.3 and 3.5.4 summarize the valve position and pressure drop, respectively as a function of flow rate.

FIGURE 3.5.3
VALVE POSITION VS. FLOW

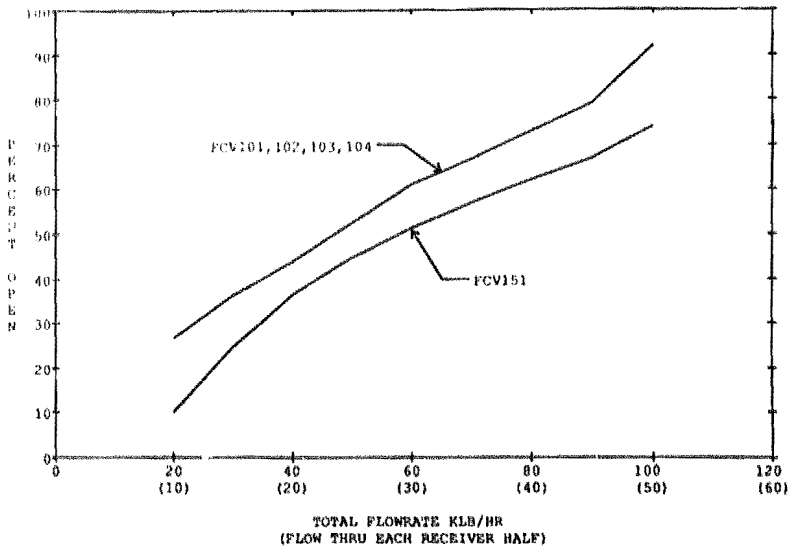

FIGURE 3.5.4
PRESSURE DROP VS. FLOW

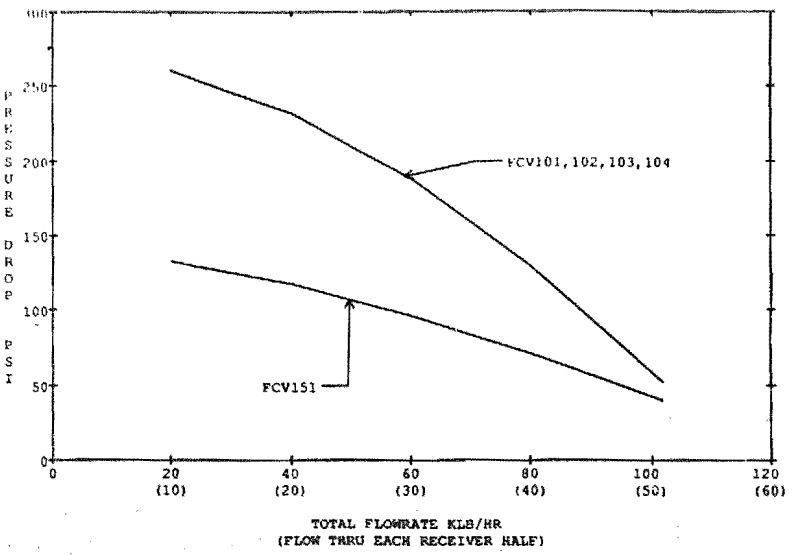

Balance of the System

The balance of the system includes the receiver riser and downcomer piping. The riser piping in the receiver subsystem consists of the piping from the top of the tower (elevation 300 ft) to the inlet of the cold surge tank (elevation 309-1/2 ft). There are 31 feet of 3-inch schedule 40, A106, grade B carbon steel. The frictional and shock losses account for 1.56 psi of unrecoverable pressure loss.

The new downcomer piping between the hot surge tank and the top of the tower consists of 37-1/2 ft or 3-inch schedule 40 type 304 stainless steel. This piping connects into the existing downcomer piping which begins at the top of the tower and runs to the hot storage tank.

3.5.2 Pump Requirements

The pumping requirements for the Category B receiver were determined based on the system pressure drops described in Section 3.5.1. The receiver system requires flow from two vertical cantilever pumps set up in series. These two pumps were used during MSEE and have been re-worked for use on MSS/CTE. Based on the required head for the Category B receiver and the flow and head from the cold pump, the boost pump was modified to meet the new receiver requirements. The first pump, the cold pump, receives flow from the steam generator subsystem then pumps it on to the boost pump which then supplies flow to the remainder of the receiver subsystem.

The cold pump was manufactured by Lawrence Pumps, Inc. and is designed to supply 120 gpm and 205 feet of head (185 psia). The minimum flow required by the pump manufacturer is 10 percent of design flow. This is set to prevent overheating and possible overloading of the pump shaft and bearings. The manufacturer's pump curve is shown in Figure 3.5.5.

FIGURE 3.5.5
AVAILABLE PUMP HEAD

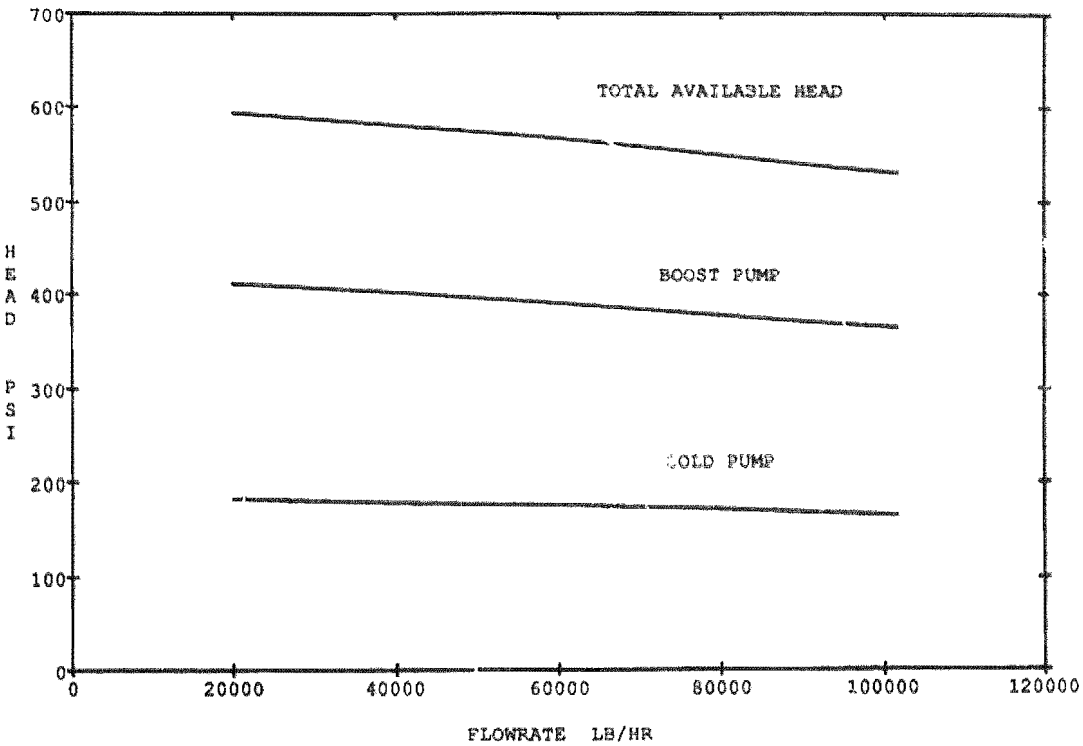

The boost pump requirements were established to meet the required receiver flow as well as flow recirculated from the boost pump to the cold pump sump. In addition to these requirements, an additional 15 percent margin was included. In order to establish the design point flow for the new boost pump, a design point inlet temperature of 550°F with a maximum absorbed heat load of 5.0 MW_t was used. Based on this, the boost pump was redesigned for 124 gpm and 450 feet of head (367 psia) at the design conditions. This includes 25 gpm recirculation flow to the cold pump sump and 15 percent margin. The old boost pump design as compared to the new boost pump is indicated in Table 3-XIII.

TABLE 3-XIII
BOOST PUMP

	Old Pump	New Pump
Design Flow, gpm	100	124
Design head, feet	185	450
Impellar Diameter, inches	12.5	12.5
Motor Horsepower, hp	40	125

The total available head curves for the boost pump and the cold pump are shown in Figure 3.5.5.

3.5.3 Subsystem Design Pressures

The receiver subsystem piping and components have been designed for maximum operating conditions. Design pressures have been established for two classes: 1) all ground level components and 2) all components above the top of the tower.

The ground level components are defined as all piping, and valves downstream of the boost pump. A maximum boost pump outlet pressure of 750 psig was established and the valves FCV151 and FCV199 refurbished to the new boost pump design. The riser piping is also included with the ground level components, and was checked to determine if the existing piping would handle the new design pressure. As a result, no changes to the existing piping were required.

The remaining components are included with the top of the tower components. These include the cold surge tank, receiver flow control valves, the receiver and all piping downstream of the cold surge tank. The surge tank, valves and receiver were designed for a maximum operating condition of 535 psig at 600°F. However normal operating conditions are 284 psig. The cold surge tank pressure relief valve was set to 535 psig and meets the requirements of ASME B31.1

3.5.4 Surge Tank Sizing

The receiver subsystem contains two surge/buffer tanks, one at the inlet of the receiver, the other at the receiver outlet. The cold surge tank (CST) is situated upstream of the receiver flow-control valves and serves as a buffer tank to control flow from the cold boost pump to the receiver. It also serves as a source of emergency flow to the receiver. The tank is pressurized with bottled air. The hot surge tank (or hot collection tank) is situated downstream of the receiver and serves as a buffer for flow to the thermal storage system (TSS). The hot tank is vented to atmosphere, and has the same volume as the cold surge tank.

The CST was sized for two purposes; first as a source of flow control from the cold boost pump to the receiver and second as a source of emergency flow to the receiver. The tank is 40 ft^3 and contains 30 ft^3 of salt with 10 ft^3 of cover gas. The size was determined in order to provide flow to the receiver in the case of an emergency condition. These conditions would either be loss of power to the system and heliostat field or loss of flow to the receiver from the cold boost pump due to loss of power or due to a pump trip. The tank has been sized to provide emergency flow for a period of 90 seconds. This is sufficient time to allow the back up power supply (as required by the Saguaro design) to come on line and the field to be defocused. The air supply to the CST is provided by bottled H_2 and is controlled through an air regulator and a check valve. The emergency flow system can be operated with or without an active bottled air supply. Without the bottled air supply, the pressure in the tank would maintain flow to the receiver for a longer period of time allowing the salt flow to decay naturally. The back up air supply would be used on a commercial plant however it is not necessary for the CRTF field which operates on a diesel power supply with commercial power for back up.

The emergency flow protection supplied by the CST was analyzed using a Babcock & Wilcox computer code LOP (Loss of Power). LOP analyzes the compressible flow through the piping from the air bottles and solves for the pressure and temperature of the air in the bottles and the CST and calculates a receiver

flow rate which will maintained for the 90 seconds. The design flow versus time is shown in Figure 3.5.6 for flow with and without bottled air.

FIGURE 3.5.6
COLD SURGE TANK BLOW DOWN

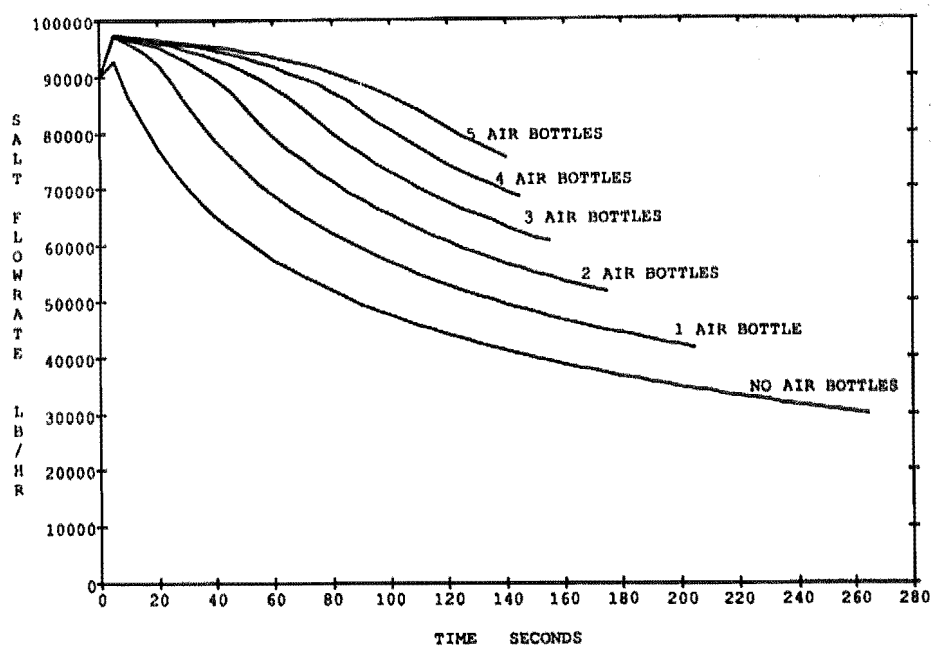

The hot surge tank (HST) was designed to the same volume as the cold surge tank. The HST serves as a buffer tank to the downcomer in case of blockage in the line. In the case of downcomer blockage the tank is sized to collect salt from the receiver for 90 seconds to allow for the field to be scrammed and flow through the receiver to be stopped. The tank is sized to hold 30 ft^3 of salt and 10 ft^3 of air, but is vented to atmosphere and is provided with an overflow drum should the salt volume exceed 40 ft^3.

Both the hot and cold surge tanks are designed to ASME Pressure Vessel and Boiler Code Section VIII, Div 1. The cold surge tank is designed for a pressure of 535 psig. The hot surge tank is designed for the static head of the salt only.

3.6 Design and Control of the Heat Trace

Because molten salt has a high melting point (420-460°F) all components and piping that will contain the salt must be preheated prior to filling. This prevents salt from freezing and blocking the lines. To accomplish this, electric heaters are applied to all molten-salt components. In past molten-salt experiments [9] great difficulty was experienced with the operation of the electrical heat trace. This experience was noted in the design of the system for the current test. The heat trace system employed a good quality product rated for the service, and a conservative thermal and electrical design approach in an effort to achieve a reliable system.

3.6.1 Types of Electric Heaters

Three types of heaters were used in the test receiver, depending upon the application: mineral insulated cable, strip heaters, and band heaters. On all piping, headers, and on safe ends of heat-absorption panels, mineral insulated cable was applied. Mineral insulated cable, (or MI cable) shown in Figure 3.6.1 consists of a metal sheath encasing a mineral insulation (usually magnesium oxide) with a resistance wire heater at its center. At the end of the heater, a cold lead is attached consisting of a similar metal sheathed cable with a larger conductor. The resistance heater wire is brazed to the cold lead conductor and the case is sealed with a steel fitting brazed to the case of both cables. This assembly is referred to as the "hot and cold junction." At the end of the cold lead, flexible electrical leads are attached with a crimped fitting. When powered, the cable heats with a uniform watt density along its length. Mineral insulated cable can be made in very long sections, thus easily installed on piping. The disadvantages of this type of installation are that to replace a failed cable, insulation must be removed from the entire line.

FIGURE 3.6.1
MINERAL INSULATED CABLE

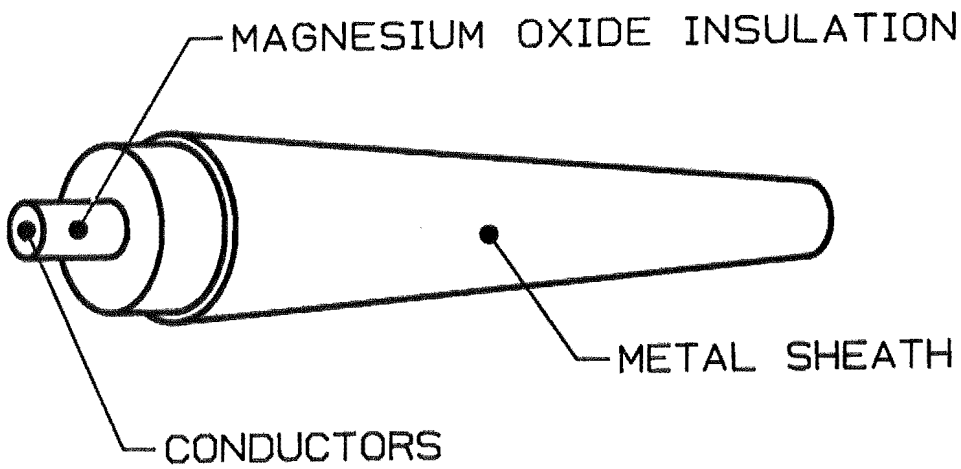

A) Heater Cable Construction

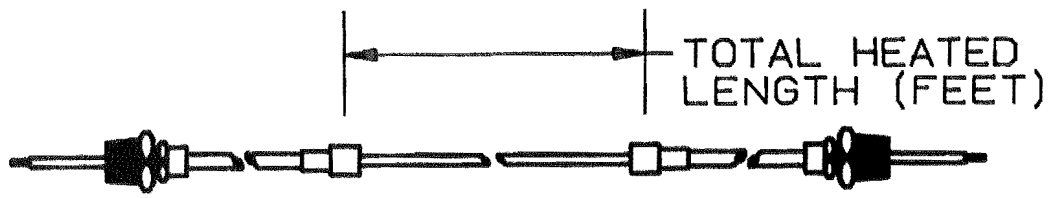

B) Assembled MI Cable

Several manufacturers produce MI cable. Although all types are similar in most respects, each type has aspects of its construction that make it unique. The approach used to select a cable manufacturer for this test was to ask several vendors for specific information about the materials, constructions, and rating of their cable. Based on this information (with some consideration of price) Pyrotenax cable was selected.

For heating valves and tanks, strip heaters were used. Strip heaters are made by embedding coiled resistor wire in a compressed mineral insulation block, then encasing it in a metal sheath. Terminal lugs are attached to the heater wire and penetrate the sheath, as shown in Figure 3.6.2.

FIGURE 3.6.2
STRIP HEATER

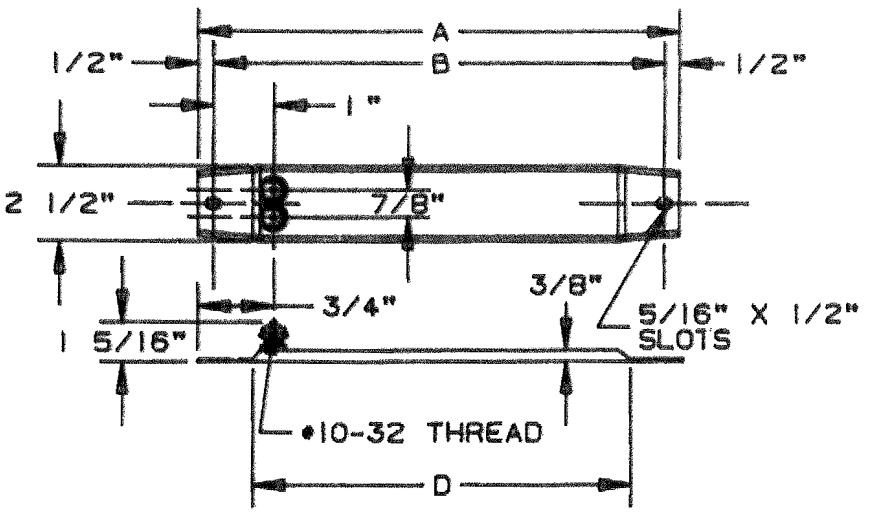

This type of heater is useful for providing a large amount of heat to a small area, such as a valve body. With a large component such as the surge tanks, the heaters can be placed on the surface of the tank in a pattern that allows conduction in the tank to uniformly distribute the heat. Because of their compact size, failed heaters are easy to replace through small penetrations cut into the insulation.

Band heaters, shown in Figure 3.6.3, are similar in construction to strip heaters, except they are formed in a circle ,which allows them to be applied to flanges. This type of heater is used on the isolation flanges of pressure transmitters in the system.

FIGURE 3.6.3
BAND HEATER

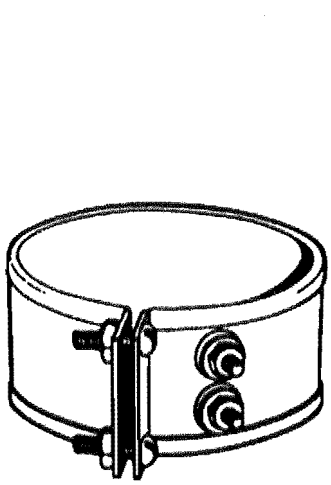

3.6.2 Thermal and Electric Design of Heat Trace

The controls for the receiver heat trace system are based on temperature feedback and on/off control of the heaters. In previous molten-salt systems, passive systems were used that allowed the heaters to run continuously. Problems developed when some heaters ran hotter than anticipated, and some components, particularly valves, could not be kept hot under all conditions. Modifications to the insulation were required to balance temperatures, and variable weather conditions caused wide swings in temperatures. With active control, a controller is required, along with relays to cycle power on and off, but the system is able to adapt to actual insulation, and to varying weather conditions. The system also allows for conservative design with respect to heater sizing and insulation. Heaters and insulation can be designed for severe conditions and design margins can be applied, assuring that the piping can be kept hot under a wide range of conditions.

The design of the heat trace system for the receiver involves thermal sizing, electrical design, zone selection, and installation methods. Thermal sizing of the heaters requires that insulation thickness and properties be known. To minimize the electrical parasitics of the receiver, 8 inches of insulation was specified for all heated surfaces. To simplify installation, blanket-type insulation was specified. Heat loss from the piping was predicted based on derating the "catalog conductivity" by a factor of 2. This was based on experience with field-installed insulation on other projects. Then heat losses were predicted for maximum wind conditions and an outside air temperature of 0°F. On top of this, a 15 percent margin was added to the heat loss calculation.

The electrical design of the heat trace involved selection of MI cables and heaters with the proper resistance to obtain the proper quantity of heat. The system was designed for 110-volt power in order to assure a long heater element life; a watt density limit of 50 watts per foot was set for the MI cable. This is significantly less than the limit set by the manufacturer, but reasonable in light of previous molten-salt experience with MI cable. Redundant (unpowered) cables were installed in all locations for use in the event that the primary cable failed.

The components requiring heat trace were divided into a number of "zones." Each zone was individually controlled. The system was divided so that each zone had 1) a common thermal boundary condition and 2) similar components. In addition, piping and components that contained flowing salt while in normal operation were separated from those containing stagnant salt. This allowed zones with flowing salt to be set to turn off when in operation. This resulted in a total of 62 zones for the receiver. Control of each zone was performed by the Accurex control system. One thermocouple was designated for control in each zone, with a set point of 525°F and a dead band of 10°F. Many other thermocouples were included in each zone for monitoring temperatures and detecting cold or hot spots.

The heat trace system was designed for installation in the field. The design called for MI cables to be strapped to the piping, then covered with stainless steel foil (shim stock). The foil was attached to the pipe with small

resistance spot welds. Insulation was then installed over this. The design also called for the cold leads to be installed in the field. Redundant cables that were accessible were sealed and not terminated. This reduced the number of cold leads required.

Detailed drawings of the heat trace system were prepared and are included in Appendix I of this report.

3.7 Door and Seal

The receiver door and seal arrangement is based on the features of the Saguaro design. The door is vertical and biparting, with an initial motion outward (away form the aperture) in the opening direction and a final motion inward to compress a high-temperature seal in the closing direction. The inner surface of the door is insulated, which thermally isolates the door structure from the high-temperature cavity. The lower door serves as a counterweight for the upper door, but the upper door is slightly larger using gravity to maintain a positive seal. The door is opened and closed through a drive mechanism consisting of a 1.5-HP motor, double shaft, sprockets, and chains located above the door. The door is guided by tracks positioned on either side of the door and behind the aperture insulation. In normal operation the door is automatically controlled; however, manual operation is possible using a handwheel. The receiver door is shown in Figure 3.7.1.

FIGURE 3.7.1
RECEIVER DOOR

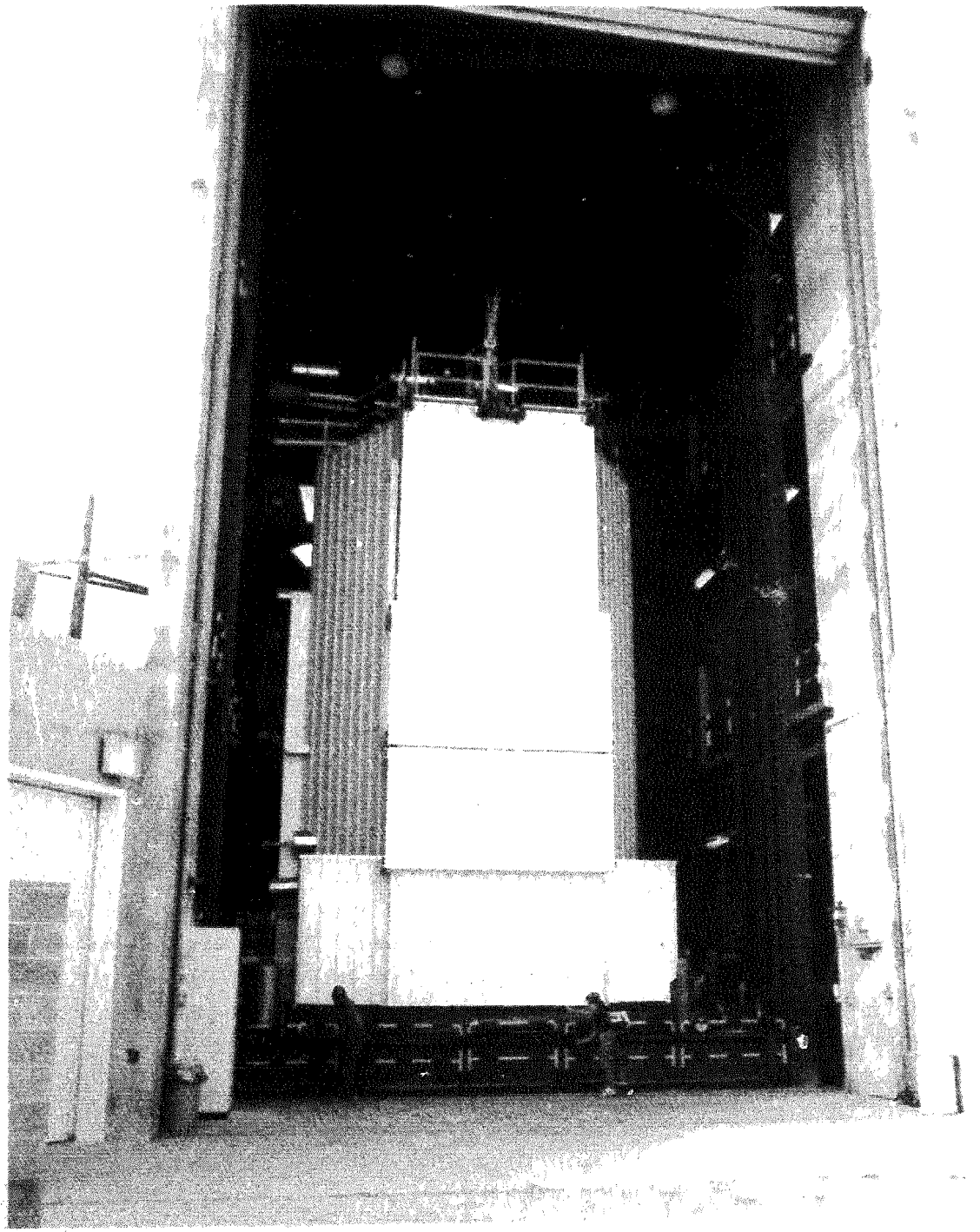

The receiver door minimizes heat loss from the cavity during non-operational periods; thereby, increasing energy collection to the receiver. The ability of the door system to effectively seal the cavity is an important design consideration.

The door system was designed and fabricated in accordance with AISC standards. Design loads considered include deadweight dynamic, wind and seismic. The door is constructed of A36 carbon steel plate and structural channel. Seal brackets are bolted to the perimeter of each door unit. Eight inches of Kaowool insulation is attached to the cavity side of the door structure using standard capacitance discharge welded pin stud connectors. The door seals border the insulation providing additional support and protecting the insulation from the environment. The weight of the door is carried by the chains and transferred to the main structure through the drive shafts and sprockets. A system of rollers and four steel tracks guide the door's travel. The original design employed sixteen 2.5-mm (1.0-inch) diameter flat tread bearing rollers; eight primary rollers would follow a machined slot of the door tracks and seal the door, and eight secondary rollers would track a surface normal to the aperture plane to ensure vertical alignment of the doors. Following installation of the receiver door and tracks, tracking problems were discovered. The tread width of the primary rollers was inadequate to account for the dimensional variations of the tracks, main structure, and door, which resulted in the door's inability to track properly. The primary rollers were replaced with eight flanged rollers having wider treads. To use the existing connections and tracks, the replacement rollers were sized accordingly and machined at a local fabricator. Oil-life bushings and washers were used to reduce roller friction. Standard flanged rollers are readily available for a future application.

The door tracks consist of four 1.9-cm (0.75-inch) thick structural angles with machined slots to guide the door's movement. The tracks were sized to accept a 2.5-cm (1-inch) diameter roller and 241 cm (95 inches) of door travel. The tracks are attached to the main steel columns located on either side of the aperture.

The door seal, shown in Figure 3.7.2, consists of a 10-cm (4-inch) diameter core of Kaowool blanket enclosed in a stainless steel, reinforced fiberglass fabric. The seal is commercially available under the trade name, Mesh Enclosed Round. The seals are attached and uniformly supported by brackets that bolt to the door.

FIGURE 3.7.2
RECEIVER DOOR SEAL

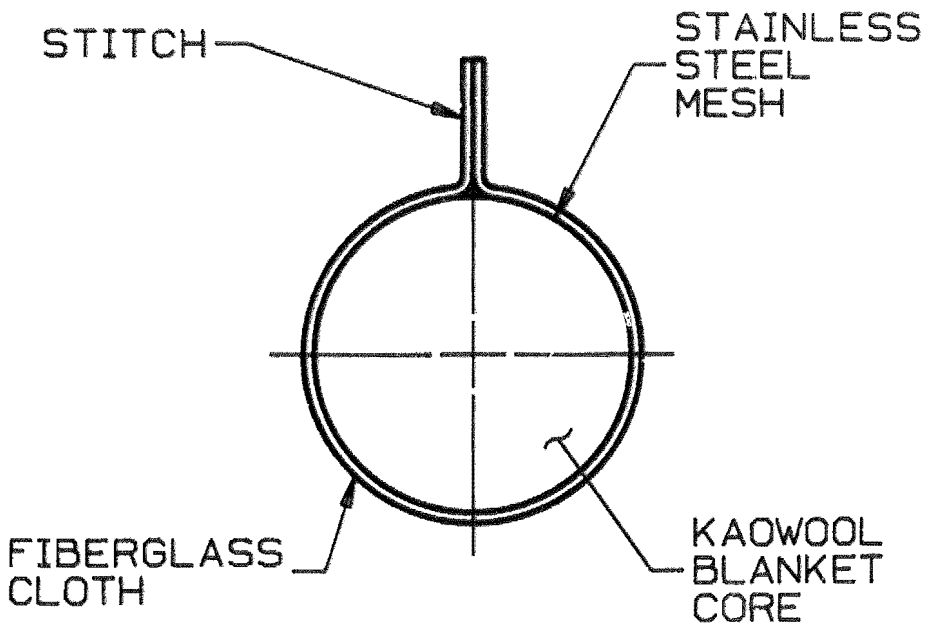

The clearance between the upper and lower door sections is sensitive to the door's position relative to the aperature. This is due to the angle of door closure. An additional seal was later installed at the interface of the upper and lower door sections to overcome an approximate 1.9-cm (0.75-inch) gap that remained following door closure. The gap apparently was the result of a dimensional stackup, including oversized door seals, between the door rollers and the cavity face. Because this seal experiences greater action than the door/cavity seals, future designs should employ a seal of high resilience and make provision for seal adjustment.

Each door is elevationally adjustable to obtain a uniform inward motion of the seals to optimally seal the cavity. Door track adjustment was not possible as the tracks were welded to the main structure.

A commercial receiver door would be much larger in size than the door of the test receiver and would require provisions for seal adjustment and replacement. Adjustable door tracks are also recommended, possibly offering an alternate approach to ajusting the door seals.

3.8 Receiver Control System

The design of the receiver control system was based on the need for automatic and operator control, equipment protection and safety, and operator monitoring of the receiver subsystem. Also, since this is an experiment, the control system is designed to monitor additional parameters for purposes of verifying the receiver design and performance. Accordingly, the design produced requirements and specifications relative to four main areas: control and instrumentation, equipment protection and safety, monitoring instrumentation, and operator control and monitoring.

Control of the receiver subsystem is divided into two areas: on-line and off-line. On-line control deals strictly with solar absorption activities, whereas off-line control deals with salt fill and drain, overnight conditioning, and other auxiliary activities. Control instrumentation deals with sensors (i.e., thermocouples, pressure transducers, flowmeters, etc.) and final control elements (i.e., valves, motors, etc.). The control and instrumentation design effort is concerned primarily with the on-line activities.

3.8.1 On-Line Control

On-line control is designed for automatic control of the receiver over its entire operating power range. The automatic control design entails stability, transient response, and instrument location and type analysis to provide a stable, responsive control-scheme. The receiver control scheme design consists of outlet salt temperature control and surge tank level control.

Feedback control, or closed-loop control, commonly uses a standard proportional-integral-derivative (PID) controller. This controller incorporates four tuning constants, or gains, as follows:

1) KSC - Overall Gain
2) KP - Proportional Gain
3) KI - Integral Gain
4) KD - Derivative Gain

These gains typically operate upon an error signal that is generated by the difference between the actual process variable and the desired value, or set point. The PID controller is functionally represented by the following equation:

$$\text{Output} = KSC\ [KP + KI \times \int dt + KD \times d/dt]\ \text{ERROR}.$$

Different combinations of the PID terms are used depending on the particular application.

Control of the Receiver Outlet Temperature

Control of the receiver-outlet salt temperature is designed to maintain the outlet salt temperature constant during incident power changes on the receiver panels caused by diurnal and weather conditions. The experience gained from operation of Solar One in Barstow and from the MSEE test is integrated into the design of the outlet temperature-control of the MSS/CTE receiver. Detailed design was accomplished by using a receiver subsystem computer simulation developed by McDonnell Douglas.

The receiver is divided into two control zones, east and west, so two control loops for the outlet's salt temperature are required. These two control loops operate independently but have identical configurations. This configuration is called the receiver control algorithm (RCA), which is illustrated in the block diagram of Figure 3.8.1. As illustrated, the RCA is composed of six components:

1) Flow-rate control,
2) Flux feed-forward control,

3) Average back tube temperature control,

4) Outlet temperature control,

5) Outlet temperature set-point generator, and

6) Back tube temperature set-point generator.

FIGURE 3.8.1

RECEIVER OUTLET TEMPERATURE CONTROL ALGORITHM

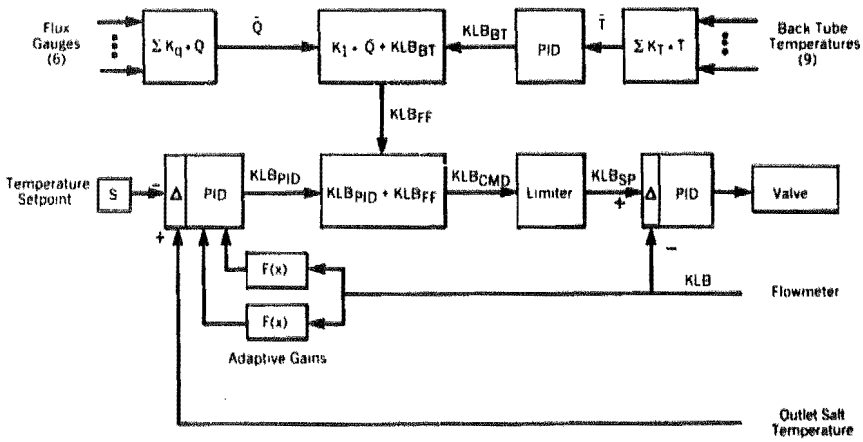

This composition results in a multiloop control structure containing three closed loops (components 1,3,4) and one open loop (component 2) that provides optimum temperature control performance in terms of cloud reaction and response time. The set-point generators automatically derate the receiver (component 5) when required and improve the outlet temperature set-point response time (component 6). The function and capability of each of these control components are described below.

Salt Flow Control

Flow control is required to minimize hydraulic coupling between the two control zones and to reduce flow loop calibration drift and component aging effects. The flow controller uses flowmeter feedback to maintain the desired salt flow rate by regulating the valve stroke through a 0-100

percent stroke command. Each of the remaining three control components computes a flow rate. These three flow rates are summed to generate a flow-rate set point for the flow controller. Therefore, the receiver temperature is controlled by regulating the flow rate through each control zone.

Anticipatory Control

The back tube thermocouples and flux gages provide information on changes much more quickly than the outlet salt thermocouple because they measure receiver panel information, not just outlet conditions. Therefore, their use for control is considered "anticipatory," which is typically associated with open-loop, feed-forward type of control. However, the use of back tube temperatures is actually a feedback (closed-loop) control loop while remaining anticipatory, since the temperatures are a result of internal, as well as external, processes (i.e., heat-transfer coefficient and area, salt, and metal properties, etc.). The use of flux gages is the only true open-loop, feed-forward control mechanism, because the incident flux on the receiver is a result of external processes only (i.e., sun position, clouds, number of heliostats in track, etc.).

Flux Feed-Forward Control

Anticipatory control improves temperature control significantly since transient information is known and utilized more quickly. Flux gages are particularly fast and have time constants of 0.25 seconds. These gages provide knowledge of the incident flux density or the relative amount of power to be absorbed.

Based on this, a flow rate for salt can be computed for the measured power. Since a flux gage measurement is localized and subject to calibration drift, the use of flux measurement is not exact.

Back-Tube Temperature Control

The average temperature back tube controller (PID) is employed to anticipate changes in temperature along the serpentine flow path and improve outlet

temperature set-point response. Nine thermocouples are utilized, located on the back of a tube in every other pass. Since the tube wall is relatively small and the thermocouple is placed on the back of the tube (away from incident flux), the temperature measurement should represent the bulk salt temperature within the tube at that point. The nine back-tube temperatures are averaged, or equally weighted, even though the simulation showed a little advantage to selective weighting. Average weighting was selected because of the risk associated with the highest weighted thermocouple failing and causing a high-temperature excursion. There was some concern that the change in average temperature with changes in flux distribution within the cavity, would adversely affect control. This could only be resolved with actual operation.

The back tube controller uses only the proportional and derivative (PD) terms for control. In this configuration, the controller responds to rapid temperature variations or transients. Consequently, this controller improves control by anticipating potential changes in the outlet temperature using temperatures along the flow path before the salt actually reaches the outlet.

Back Tube Temperature Set-Point Generator

The back tube controller's set point is a function of the outlet salt temperature's set point. It is known that the average back tube temperature will change when the outlet temperature changes during steady-state operation. However, even with a constant outlet temperature, the average tube temperature will vary with different flux distributions. The actual relationship between outlet temperature and average tube temperature, and sensitivity to flux distributions, is not thoroughly understood at this point. Consequently, the design of the back-tube temperature set-point generator is simply conceived as making the back tube temperature's set point proportional to the outlet temperature's set point.

Outlet Temperature Control

The outlet salt temperature controller (PID) is employed to negate the temperature error that results from the inexact anticipatory control. The controller ensures that an outlet temperature is produced equal to its set point. All three terms of the PID are used: proportional-plus-integral-plus-derivative. Since the process dynamics of the receiver change with respect to flow rate, the controller gains are automatically adjusted as a function of actual flow rate. These adaptive gain functions are illustrated by Figure 3.8.2. The overall gain (KSC) function is strictly linear, whereas the integral gain (KI) function is not. The function is linear at high flow rates but rapidly decreases near minimum design flow rate (12,000 lbs/h). This discontinuity represents the "anti-windup" feature that prevents the controller from continuing to integrate up in an uncontrollable situation; the receiver cannot be temperature controlled when very little or no flux is present. These adaptive gains provide optimum performance of the temperature controller over the full range of receiver operation.

FIGURE 3.8.2

ADAPTIVE GAIN FUNCTIONS

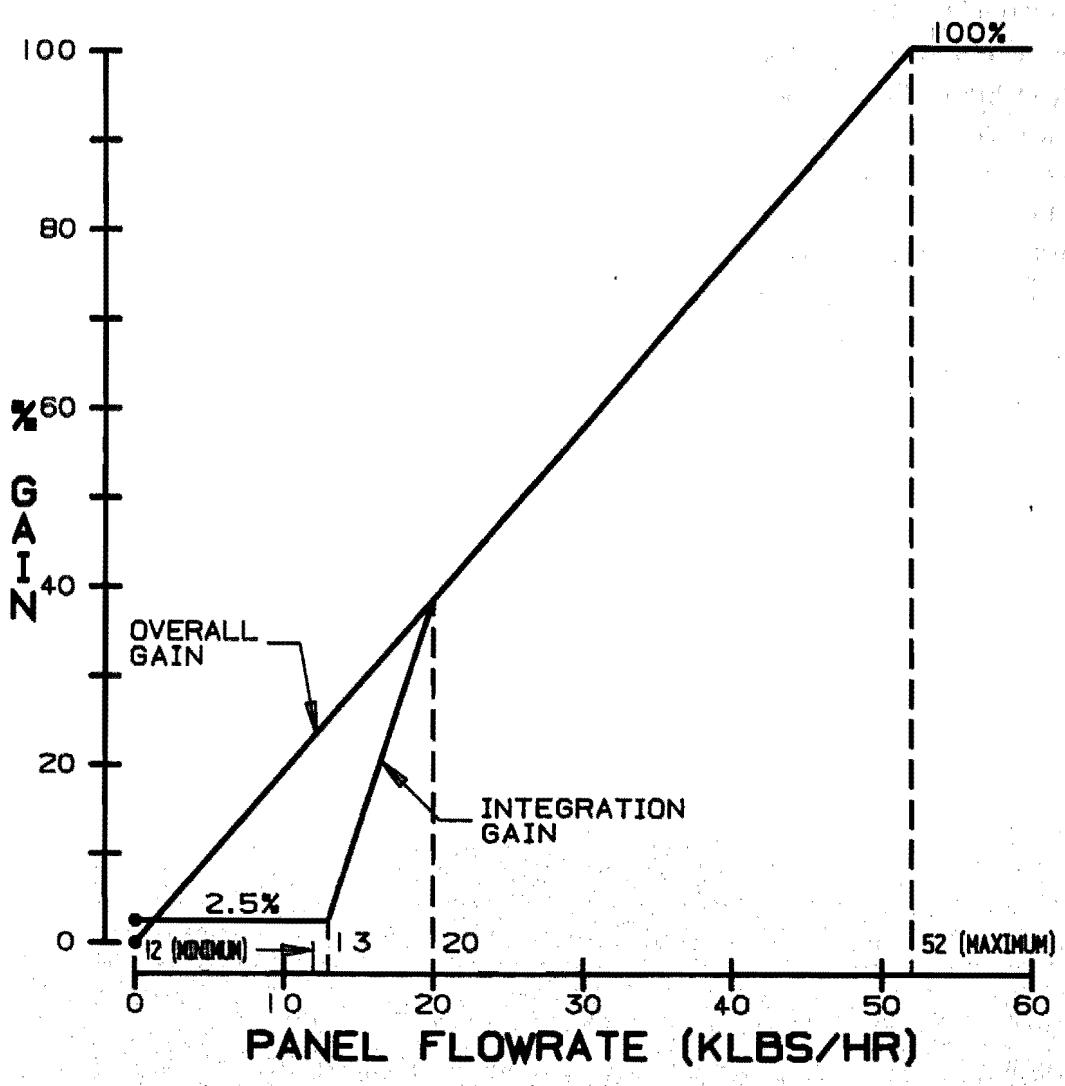

Outlet Temperature Set Point Generator

The outlet-temperature set-point generator, which is more commonly known as the sliding set-point mechanism, is designed to automatically vary the receiver's outlet-temperature under some conditions. This helps to prevent high outlet temperature excursions, which cause the receiver to trip off-line. This automatic set-point generator consists of four parts:

1) Bias (Error Limit)
2) Up-Ramp Rate Limit
3) Down-Ramp Rate Limit
4) Minimum Limit

These parts produce a set-point generator, which operates as follows. The bias determines when the set point will begin to decrease and how much error the controller will integrate upon (integrator windup). A bias of 50°F is added to the actual outlet salt temperature, then passed through a high/low limiter. The high set-point limit is, of course, the rated temperature of 1050°F, and the low limit is the minimum derated set point of 850°F. When the outlet temperature goes below 1000°F, the set point will begin to decrease. After the high/low absolute value limiter, the signal is passed through a high/low rate limiter, which limits the rate (°F/s) at which the set point can decrease and increase. This determines how rapidly the set point will derate and return to rated conditions. These rate limits are determined by temperature ramp rates, which keep stresses within design. The design established the rate limits to be ± 0.75°F/s.

Control of the Surge Tank Level

Control of the surge tank level is designed to maintain the level of both the cold and hot surge tanks at a set point during receiver operation. A detailed design was accomplished by using a computer simulation developed by McDonnell Douglas for the receiver subsystem.

The receiver has both a cold and a hot surge tank so that two level-control loops are required. These two control loops operate independently and have different loop configurations.

The level control of the cold surge tank is configured to maintain the desired (set-point) level by regulating the riser line valve stroke via a 0-100 percent stroke command and using level feedback. Level control is achieved using a simple, single-element control configuration, which uses proportional-plus-integral control.

The level control for the hot surge tank is configured the same as for the cold tank, but two controllers are required. Salt flow from the hot surge tank is regulated by two control valves; one valve allows flow to the cold storage tank and the other to the hot storage tank. Each valve has level control capability, and the controller with the lower set point is in control. The set point for the other controller is automatically biased 15 inches higher. The controller at the lower set point and control is automatically determined by the salt temperature at the bottom of the downcomer. The level set points are automatically switched to salt flow to the hot storage tank when the salt temperature exceeds 750°F and flow to the cold storage tank drops below 700°F. This control structure has the additional benefit of helping to prevent overflow of the hot surge tank, since one controller backs up the other with a 15-inch higher set point. In case of a problem with one valve, the other will take control at the expense of putting hot salt in the cold tank or vice versa.

Control Instrumentation

Control instrumentation is required to provide process data for the control configuration. The control scheme of the receiver requires thermocouples, flux gages, flowmeters, level transducers, and control valves for on-line automatic control capability.

Each of the two temperature control loops requires nine back-tube thermocouples, one outlet salt in-stream thermocouple, six flux gages, one flowmeter, and two control valves. The required location of this control instrumentation within each control zone is illustrated by Figure 3.8.3. Each of the two surge-tank level-control loops requires one level transducer and one control valve, except for the hot surge tank, which requires two control valves.

FIGURE 3.8.3

INSTRUMENTATION LOCATION REQUIREMENTS

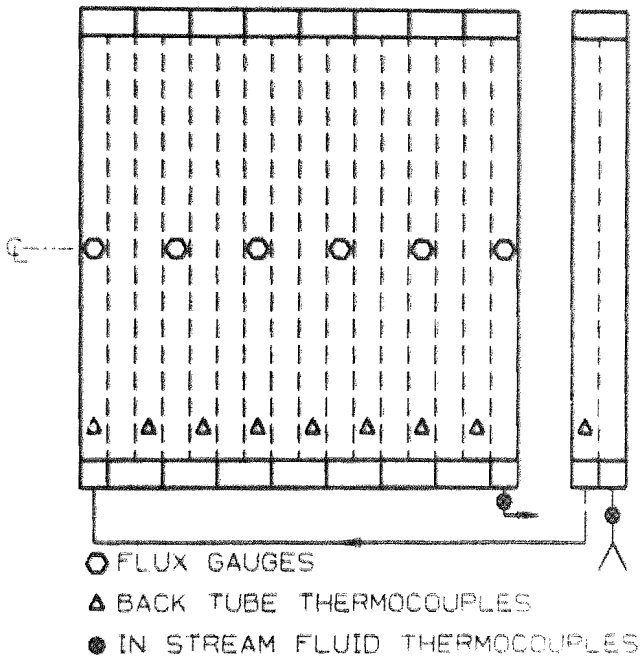

The control instrumentation must be capable of responding as rapidly as the process changes in order to effectively monitor and control any process. Therefore, the time response of control instrumentation is critical for achieving stable and fast transient response. Response time is commonly stated in terms of a time constant, which is the time required for an instrument to reach 63 percent of the final value of a step change. The back tube thermocouples require a time constant of 1 second or less, whereas the outlet salt (instream) thermocouples require a time constant of 10 seconds or less. These thermocouples have grounded tips and small sheath diameters to achieve these rapid response times. The level, flowmeter and flux instruments require a time constant of 2 seconds or less.

The sizing and characteristics of the control valve relate to the physical size and the plug and seat, or trim. The valve characteristics are

associated with the trim and are standardized by the use of C_V (valve coefficient) versus stroke. The C_V and the pressure drop across the valve for a particular stroke determine the flow rate. Each valve is designed for an equal percentage type of trim characteristic.

The valves for temperature control are sized to provide one-half of the rated total flow rate (because there are two control zones) with a 70 psi drop across the valve at 70 percent stroke. This produces a valve trip capacity design of 8.1 C_V at 70 percent stroke.

The valves for level control are not designed items, since they existed for previous experiments. However, they were verified to be adequate for this experiment. These valves have equal-percentage type trims.

Computer Simulation of the Receiver Subsystem

The computer simulation of the receiver subsystem was a valuable tool for formulating the control requirements, since it provided insight into the natural dynamics (behavior) of the receiver. The RCA was developed using this simulation. For design purposes, a nominal cloud was selected so that direct comparisons of control performances could be made as changes were made. The nominal cloud for this design was 1776 feet in length (twice the width of the heliostat field), travelled at 22 feet per second, had a west-to-east direction and zero transmittance. This "design cloud" in effect produced a transient in which the incident power went from 100 to 0 percent in 20 seconds, remained at 0 percent for 60 seconds, then went from 0 to 100 percent in 20 seconds for each control zone.

The simulation was run numerous times with various control gains for each control component (with all components operational) until the best response was achieved. "Best response" in this case was considered to be a small temperature overshoot (less than 2 percent) and the point at which the outlet temperature remained closest to the set point. This simulation effort produced the control gains for each component as listed in Table 3-XIV.

TABLE 3-XIV

RECEIVER CONTROL ALGORITHM GAINS

SIMULATION RESULTS

		East Zone	West Zone
Outlet Temp Controller	KSC =	.09	0.10
	KP =	1.0	1.0
	KI =	2.0	2.0
	KD =	0.06	0.06
Back Tube Temp Controller	KSC =	1.0	1.0
	KP =	0.32	0.35
	KI =	0	0
	KD =	.0115	.0125
Flow-rate Controller	KSC =	0.5	0.5
	KP =	0.9	0.9
	KI =	40.0	40.0
	KD =	0	0

The simulation was also used to compare control performance of various control schemes. Controller gain changes became necessary to maintain control stability in these cases. A control performance index was postulated for comparative analysis purposes. The index is based on the amount of off-specification salt produced. Specifically, the index is the time integral of the outlet temperature error and salt flow-rate multiple.

Table 3-XV represents the results of using different control configurations relative to the design cloud transient. The best performance is produced with the use of all three control components and weighted back-tube temperatures. This is the base to which all others are compared. The use of average back tube temperatures is only marginally worse (5 percent). Elimination of flux gages reduces performance by 57 percent, and not using back tube temperatures reduces performance by 92 percent. Using flux gages by themselves produced the worst control performance, with a 152 percent

reduction. The time response of each case is provided by Figures 3.8.4 through 3.8.17, where both temperatures and flow rates are shown.

TABLE 3-XV

PERFORMANCE COMPARISON TABLE

	Control Mechanism Used			Performance	
Case	Outlet	Back	Flux	#-°F (±2.5°F)	% Degradation
1	Normal	Wght	Normal	90,181 (base)	0
2	Normal	Avg	Normal	94,935	5
3	Normal	Avg		164,714	83
4	2 x Gain	Avg		141,570	57
5	2 x Gain	Wght		136,122	51
6	Normal		Normal	151,258 (bad overshoot)	68
7	1/2 Gain		Normal	172,726	92
8			Normal	172,726	152

FIGURE 3.8.4

MSSCTE RECEIVER CONTROL OUTLET TEMPERATURES

CASE 1

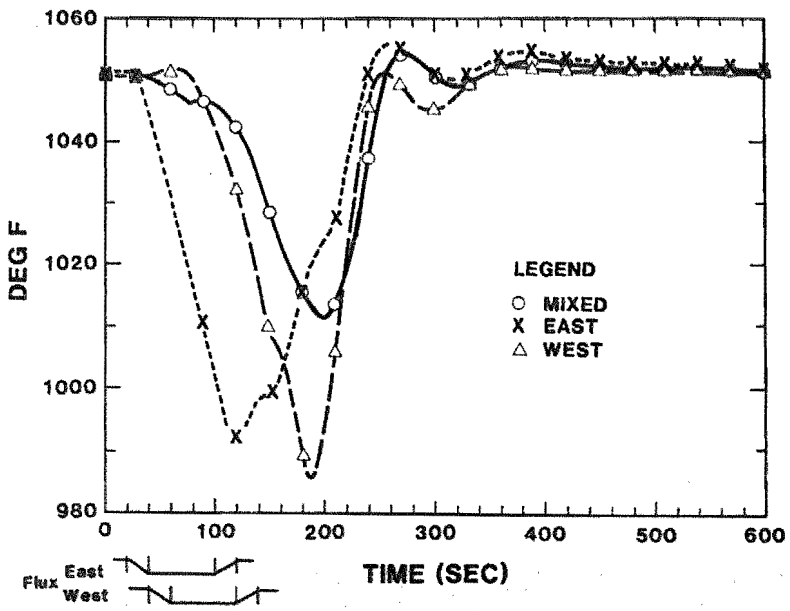

FIGURE 3.8.5
MSSCTE RECEIVER CONTROL FLOW RATES
CASE 1

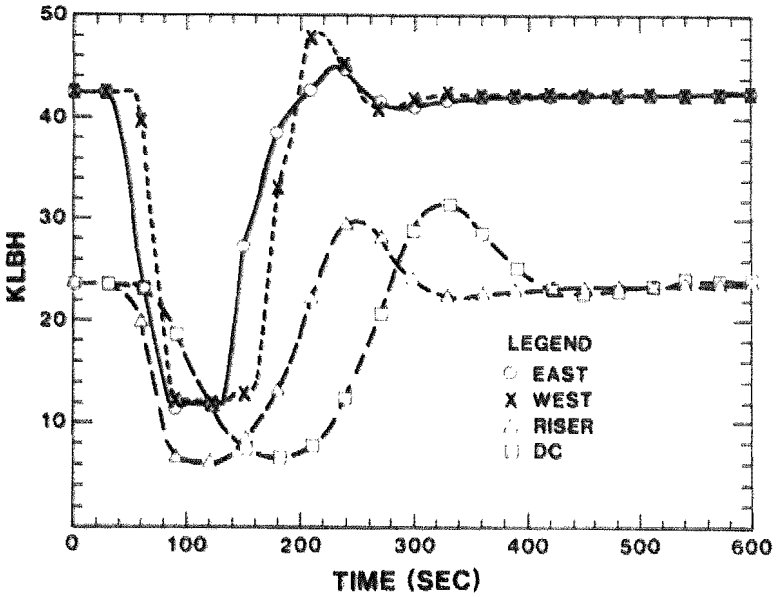

FIGURE 3.8.6
MSSCTE RECEIVER CONTROL OUTLET TEMPERATURES
AVERAGE BACK TUBE TEMPS CLOUD @ 20SEC, 1776FT @ 22FPS
CASE 2

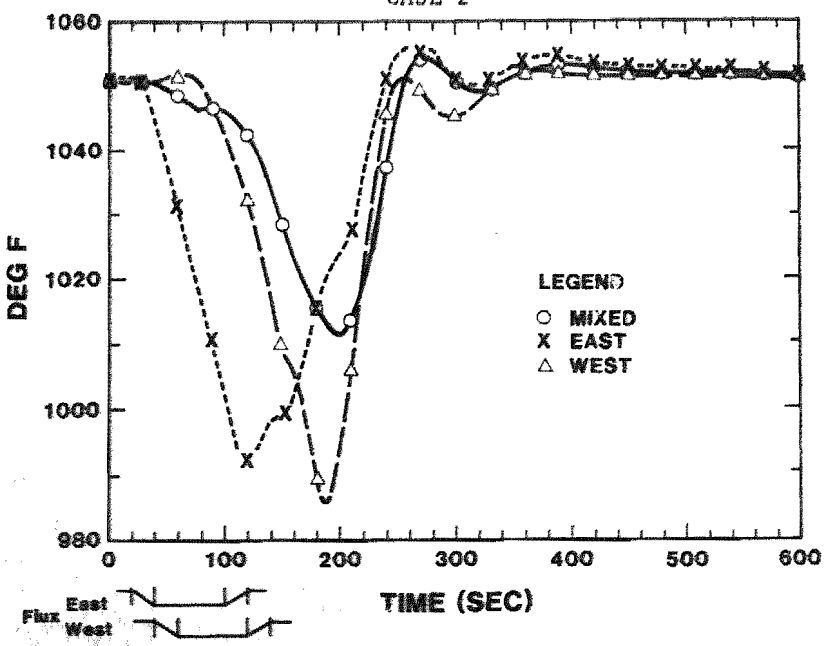

FIGURE 3.8.7
MSSCTE RECEIVER CONTROL FLOW RATES
AVERAGE BACK TUBE TEMPS CLOUD @ 20SEC, 1776FT @ 22FPS
CASE 2

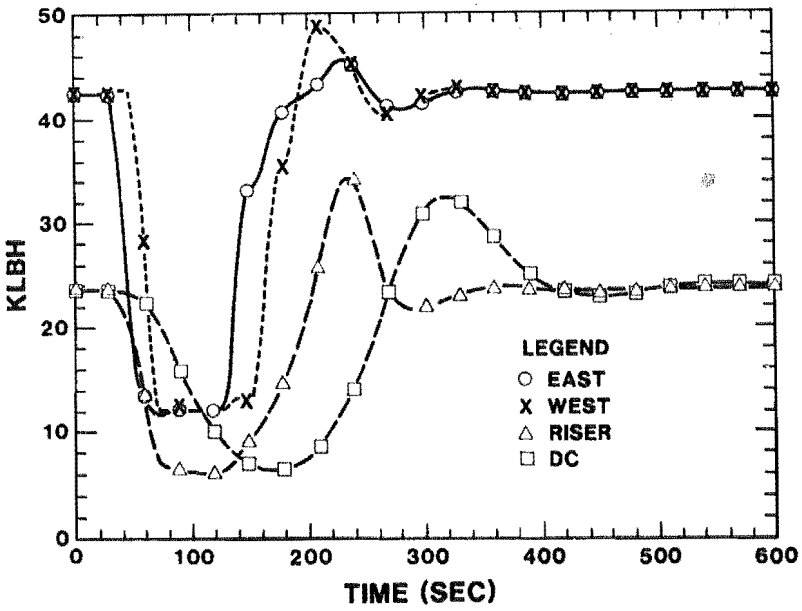

FIGURE 3.8.8
MSSCTE RECEIVER CONTROL OUTLET TEMPERATURES
NO FLUX FEED-FORWARD CLOUD @ 20 SEC, 1776FT @ 22FPS
CASE 3

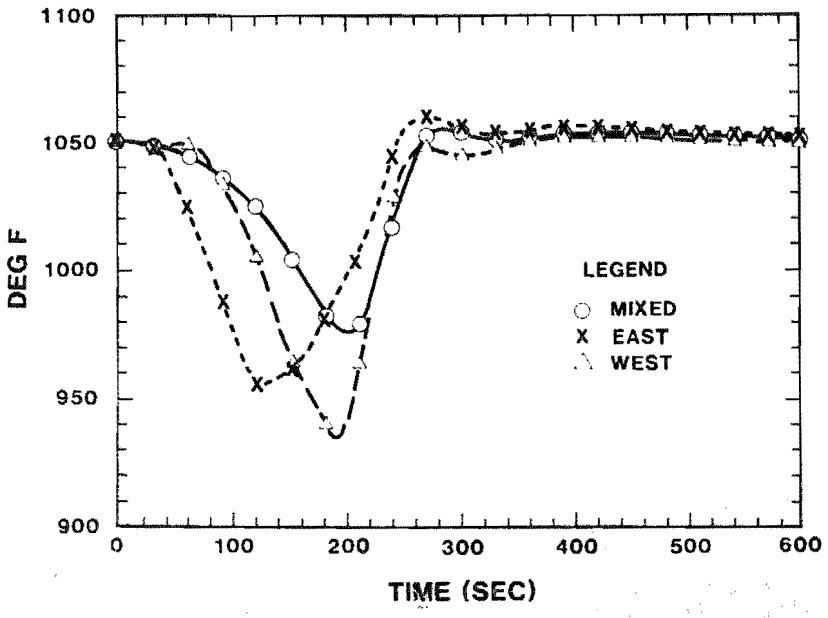

FIGURE 3.8.9
MSSCTE RECEIVER CONTROL FLOW RATES
NO FLUX FEED-FORWARD CLOUD @ 20SEC, 1776FT @ 22FPS
CASE 3

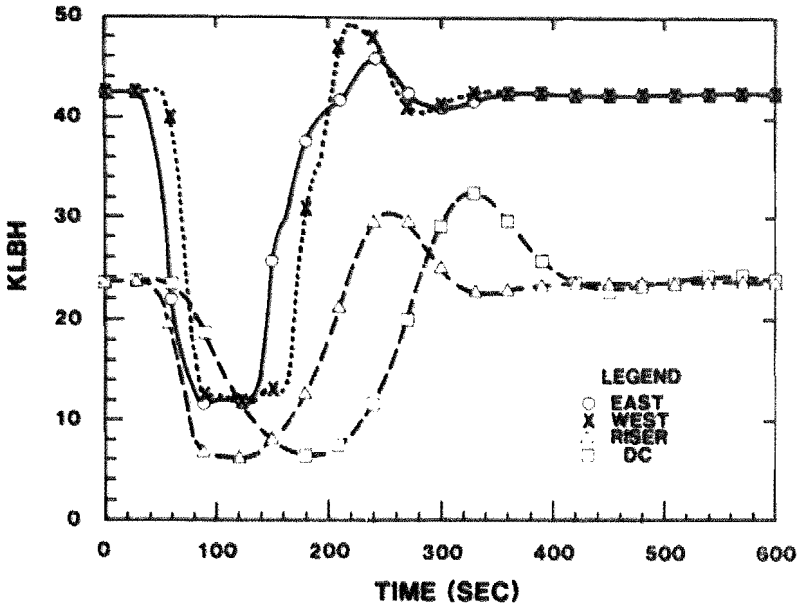

FIGURE 3.8.10
MSSCTE RECEIVER CONTROL OUTLET TEMPERATURES
NO FLUX FEED-FORWARD CLOUD @ 20SEC, 1776FT @ 22FPS
CASE 4

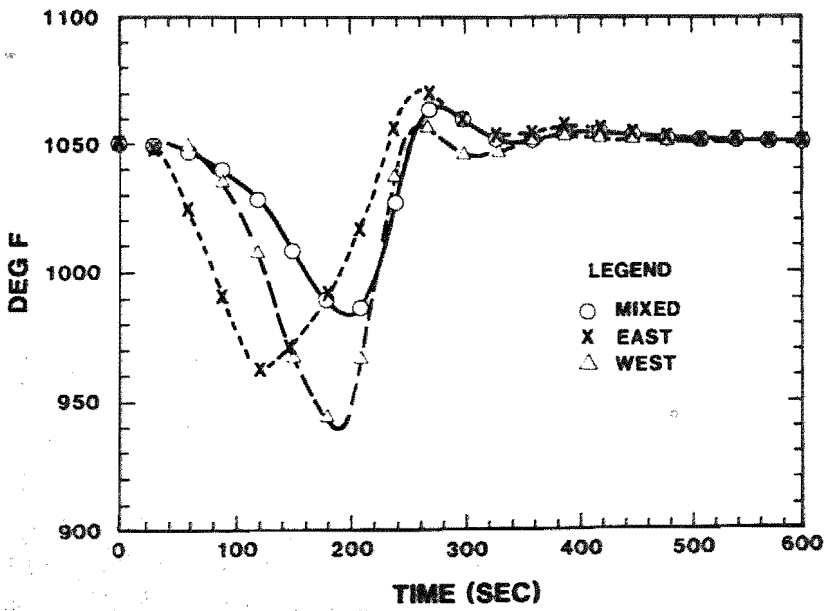

FIGURE 3.8.11
MSSCTE RECEIVER CONTROL FLOW RATES
NO FLUX FEED-FORWARD CLOUD @ 20SEC, 1776FT @ 22FPS
CASE 4

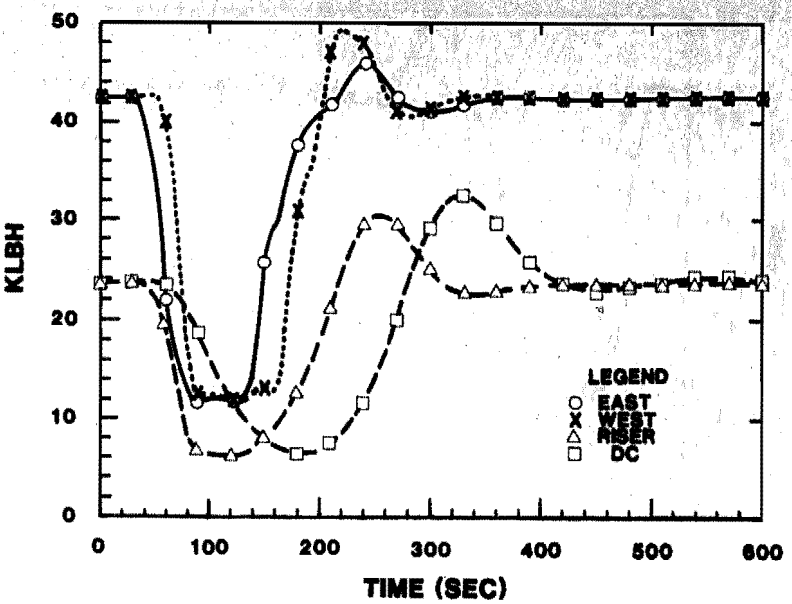

FIGURE 3.8.12
MSSCTE RECEIVER CONTROL OUTLET TEMPERATURES
NO BACK-TUBE CONTROL
CASE 5

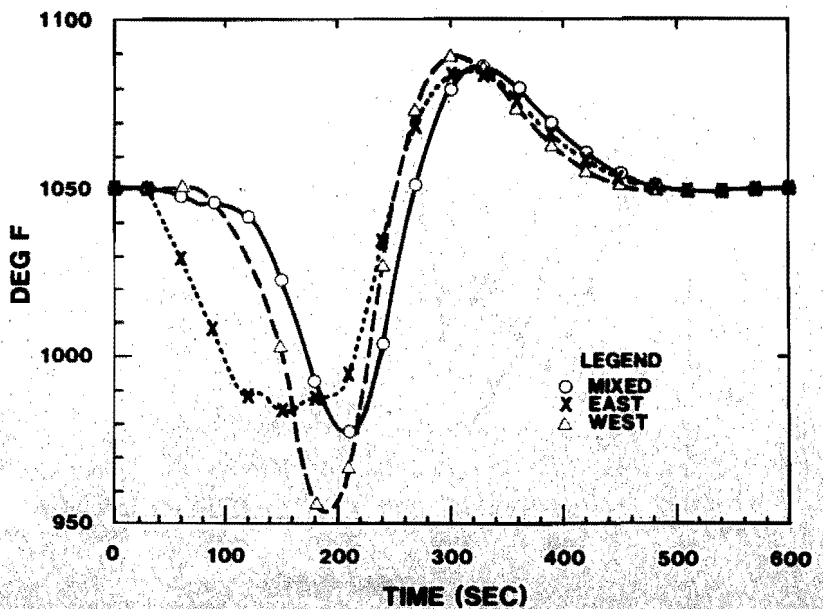

FIGURE 3.8.13
MSSCTE RECEIVER CONTROL FLOW RATES
NO BACK TUBE CONTROL
CASE 5

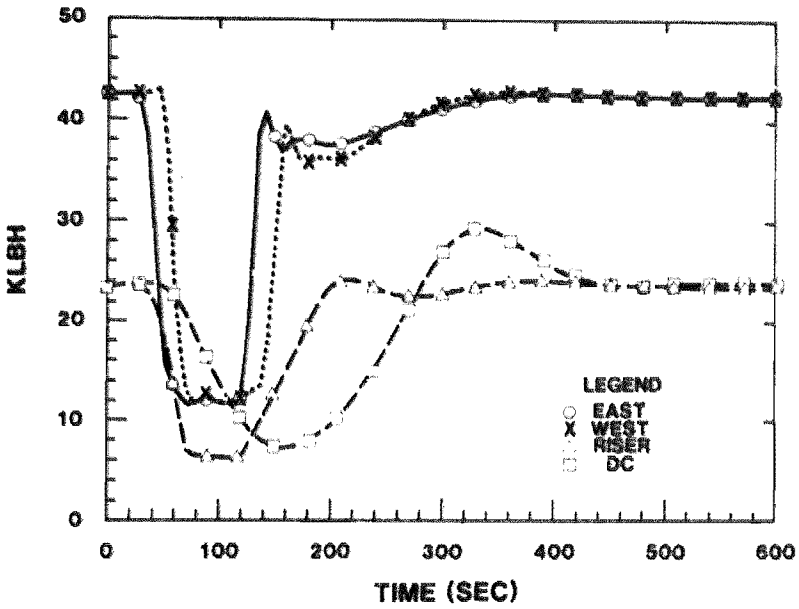

FIGURE 3.8.14
MSSCTE RECEIVER CONTROL OUTLET TEMPERATURES
NO BACK TUBE CONTROL
CLOUD 1776 FT, 22FPS @ 20SEC

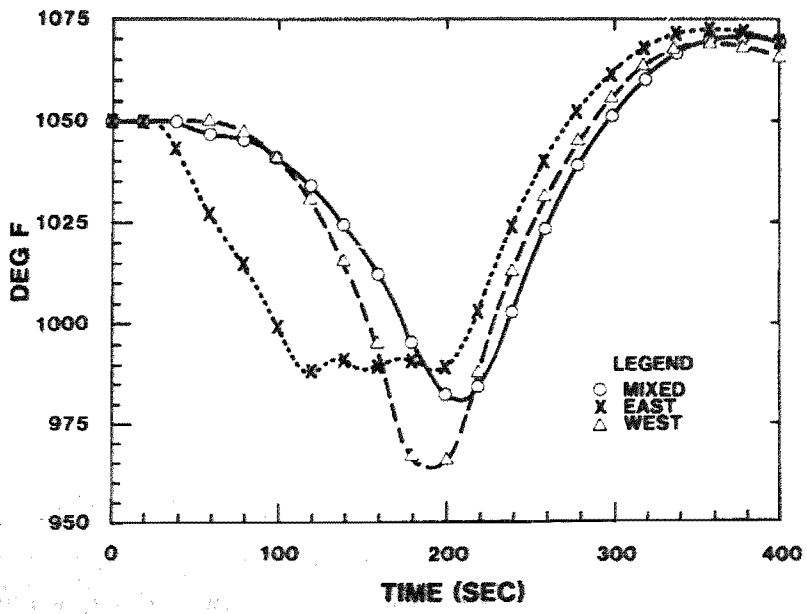

FIGURE 3.8.15
MSSCTE RECEIVER CONTROL FLOW RATES
NO BACK TUBE CONTROL
CLOUD 1776 FT, 22FPS @ 20SEC
CASE 6

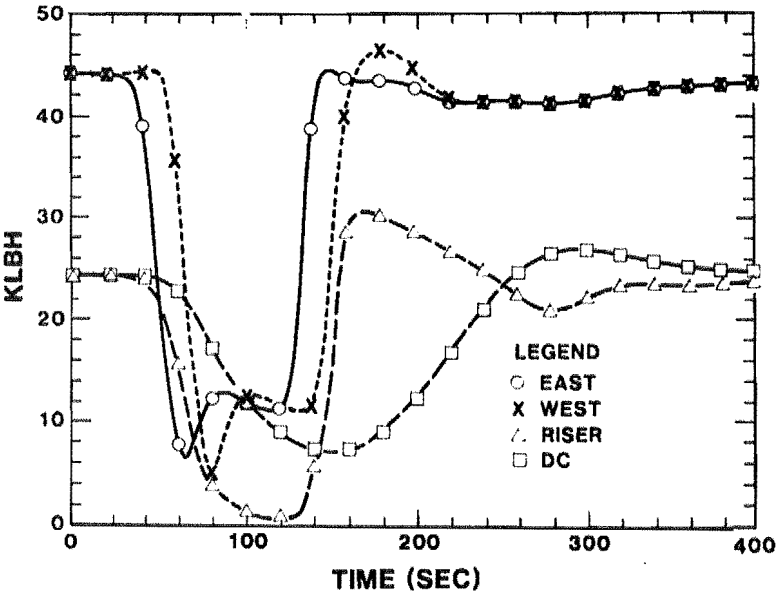

FIGURE 3.8.16
MSSCTE RECEIVER CONTROL FLOW RATES
FLUX FEED-FORWARD ONLY
CLOUD @ 20SEC, 1776FT @ 22FPS
CASE 7

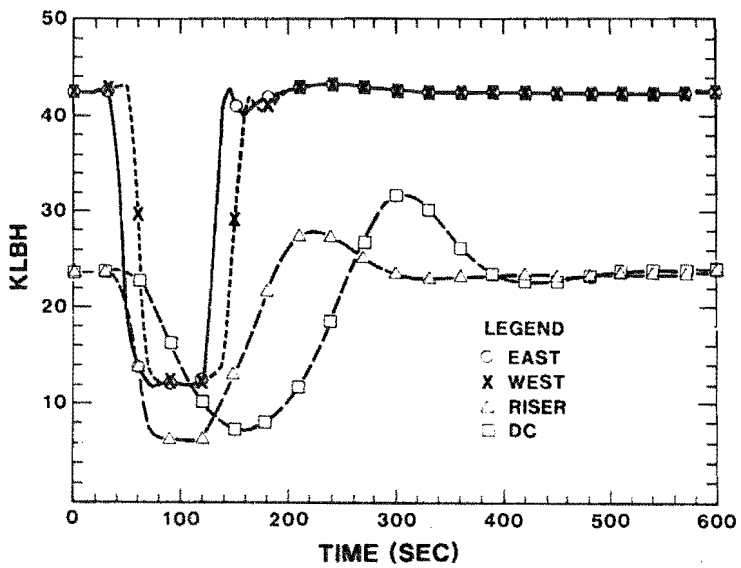

FIGURE 3.8.17
MSSCTE RECEIVER CONTROL OUTLET TEMPERATURES
FLUX FEED-FORWARD ONLY
CLOUD @ 20SEC, 1776FT @ 22FPS
CASE 7

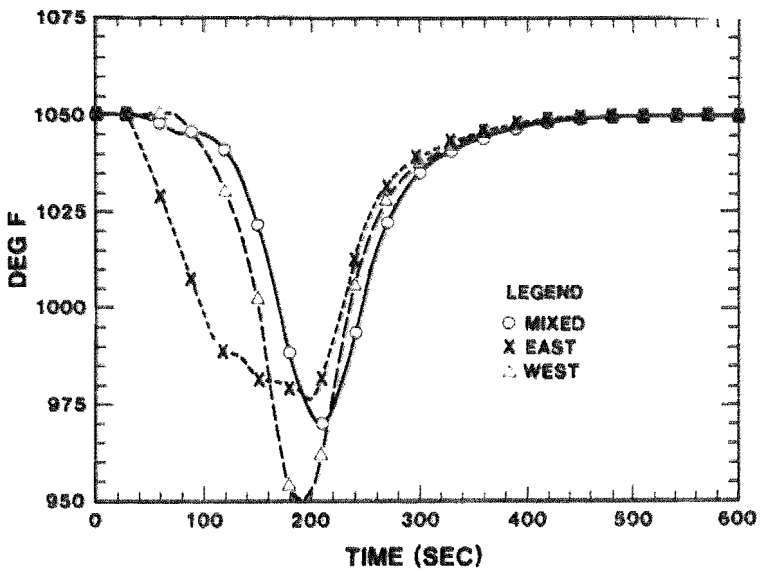

3.8.2 Off-Line Control

Off-line control is designed to support the receiver's on-line capability. It includes overnight conditioning, salt fill for start-up, and salt drain for shutdown. These support functions are operator controlled and could potentially be automated according to operating procedures. Off-line control provides the capability to control receiver hardware temperatures in all salt contact locations and the operational requirements of the salt fill, drain, and circulation. Several methods are designed into the receiver hardware to accomplish this task for economic evaluation.

The heat trace and its control play an important role in regulating receiver temperatures, but they are operated independently by the Acurex control system. The NET-90 provides additional monitoring and control of the temperature mainly for the receiver cavity's exposed panel tubes. Also, the

NET-90 provides remote control of the salt flow paths using open/close isolation-type valves with limit switch feedback.

Control instrumentation is required to provide process data for operations personnel and to provide process manipulation for controllability. The support functions require thermocouples, pressure gauges, level transducers, and control valves for off-line control capability.

The additional temperature monitoring and control capability requires 24 thermocouples distributed on the back of the receiver tubes and a relay contact for control of the cavity heater.

Remote control of the salt flow paths requires approximately 40 open/close isolation-type control valves. Each of these valves requires two limit switches to verify valve closure and full opening, resulting in 120 pieces of control instrumentation to be connected to the NET-90.

3.8.3 Equipment Protection and Safety

The equipment protection and safety (EPS) capability is designed to automatically prevent or terminate (trip) the receiver's operation or its specific equipment when adverse or unsafe conditions are detected. Unsafe conditions arise because of hardware mechanical limits, working fluid (molten-salt) limits, equipment overloads and failures, and control system failures. Therefore, safety relief valves, burst discs, circuit breakers, etc., are mechanically installed for absolute protection and safety.

Alarms are configured within the NET-90 to inform operations personnel when a limit is being approached and/or a failure has occurred. This information may or may not provide operations personnel with enough time either to correct the problem or to shut down the subsystem in an orderly fashion before the automatic EPS system takes action; it is dependent upon the particular mode of operation of the plant at the time and the specific alarm condition.

The automatic EPS capability is performed by the NET-90, where EPS functional logic is integrated with the control functions. This EPS logic is configured to take specific actions according to the specific failure or unsafe conditions specified in Table 3-XVI. Since the cold-salt side of the thermal storage subsystem is an integral part of the receiver salt loop, its EPS functions are included in Table 3-XVI. The table also includes actions to be taken by the operations personnel.

Loss of commercial power, even momentarily, is an important consideration. Uninterruptible power supplies are designed into the control system of the receiver to provide uninterrupted control for up to 15 minutes. This should allow enough time for operations personnel to shut down the receiver safely. Also, in the unlikely event that NET-90 control fails, a local valve control station is designed between the NET-90 and all valve actuators for local manual control capability.

TABLE 3-XVI
EQUIPMENT PROTECTION & SAFETY FUNCTIONS
RECEIVER SUBSYSTEM TRIPS

TRIP IDENTIFIER	TRIP CONDITION	INSTRUMENT IDENTIFIER	TRIP LEVEL	ACTION REQUIRED
RS-TED	ENABLE/DISABLE Switch for RS-EPS Functions	--	--	EPS - AUTO ENABLEs when either outlet salt temp exceeds 650°F for 30 seconds - AUTO DISABLEs when both outlet salt temps fall below 550°F for 10 min. OPERATOR - Set to ENABLE or DISABLE or RESET as required
RS-RESET	RESET Switch to CLEAR all RS-EPS Trips	--	--	
TR181W	West Control Zone Salt Outlet Temp High	TE126	>1080°F	EPS - Defocus heliostats - OPEN east & west control valves; overridden by TR185 & TR187 (LT161 bad quality only) to CLOSE OPERATOR - Control receiver as required from NET-90 consoles
TR181E	East Control Zone Salt Outlet Temp High	TE152	>1080°F	
TR184W	West Control Zone Tube Temp High for 30 S	TE122 TE119 TE116 TE114	>1070°F >1050°F >1030°F >1010°F	
TR184E	East Control Zone Tube Temp High for 30 S	TE148 TE146 TE144 TE142	>1070°F >1050°F >1030°F >1010°F	
TR183W	West Control Zone Loss of Salt Flow for 10 S	FCV101 PV	<8 KLBH	EPS - Defocus heliostats OPERATOR - Determine whether salt freeze or bad PT - Control receiver as required
TR183E	East Control Zone Loss of Salt Flow for 10 S	FCV103 PV	<8 KLBH	

EQUIPMENT PROTECTION & SAFETY FUNCTIONS
RECEIVER SUBSYSTEM TRIPS
(Continued)

TRIP IDENTIFIER	TRIP CONDITION	INSTRUMENT IDENTIFIER	TRIP LEVEL	ACTION REQUIRED
TR182	TSS Cold-Side Trip OR PCU-10 Failure OR Failure of RS surge tanks level controls	DI from PCU-10 Over Plant Loop	Open Contact	EPS (RS) - Defocus heliostats
	See TSS Trips: TR271 TR272 TR273 TR275 TR276			EPS (TSS) - STOP boost pump - CLOSE FCV151 OPERATOR - Shut down receiver and TSS cold-side as required from NET-90 console
TR185 (Doesn't require RS-TED ENABLE)	Hot Surge Tank Level High	LT161A	>55 In.	EPS - Defocus heliostats
		LT161A	>85 In.	EPS - CLOSE both east & west control valve
				OPERATOR - Shut down receiver from NET-90 console
TR186	Receiver Door Not Open	ZSH.DR	Open Contact	EPS - Defocus heliostats OPERATOR - Shut down receiver from NET-90 console

EQUIPMENT PROTECTION & SAFETY FUNCTIONS
RECEIVER SUBSYSTEM TRIPS
(Continued)

TRIP IDENTIFIER	TRIP CONDITION	INSTRUMENT IDENTIFIER	TRIP LEVEL	ACTION REQUIRED
TR187	Bad Control Input Quality for 5 S	TE126 TE152 PT130 PT140 DI/L(PCU10)	BQ BQ BQ BQ BQ	EPS - Defocus heliostats - OPEN east & west control valves; overridden by TR185 & TR187 (LT161A bad quality only) to CLOSE
		LT161A	BQ	EPS - Defocus heliostats - CLOSE east & west control valves after eight seconds
		ZSH.DR	BQ	EPS - Defocus heliostats
	BQ = Bad Quality			OPERATOR - Shut down receiver from NET-90 console - Employ instrument technician
TR188	Bad Control Output Quality for 5 S	FCV101 and FCV102 or VTC101 and VTC102 or FCV101 and VTC102 or FCV102 and VTC101 same for 103/104	BQ BQ <450°F <450°F BQ <450°F BQ <450°F	EPS - Defocus heliostats OPERATOR - Shut down receiver from local valve station and NET-90 consoles - Employ instrument technician
	BQ = Bad Quality			

EQUIPMENT PROTECTION & SAFETY FUNCTIONS
RECEIVER SUBSYSTEM TRIPS
(Continued)

TRIP IDENTIFIER	TRIP CONDITION	INSTRUMENT IDENTIFIER	TRIP LEVEL	ACTION REQUIRED
TR189	Bad Control Module Quality for 5 S	CIS-28 and CIS-29	BQ BQ	EPS - Defocus heliostats OPERATOR - Shut down receiver from local valve station and NET-90 consoles - Employ instrument technician
CIS-28 = Module Type - Slot # BQ = Bad Quality		AMM-12 ASM-13 ASM-14 ASM-15 ASM-16	BQ BQ BQ BQ BQ	EPS - Defocus heliostats - OPEN east & west control valves; overridden by TR185 & TR187 (LT161A bad quality only) to CLOSE OPERATOR - Shut down receiver as required from NET-90 consoles - Employ instrument technician
Loss of PCU12 - Power Supply Failure - Double MFC Failure		All DO go to off state such that valves go to fail position: All digital valves fail closed (FC) Except FCV171 (FO) All AO go to 4 mA so that valves go fully open (FCV101-104)		EPS (Failure Configuration) RS - Defocus heliostats EPS TSS - STOP boost pump - CLOSE FCV151 OPERATOR Shut down receiver local valve station - CLOSE FCV171

EQUIPMENT PROTECTION & SAFETY FUNCTIONS
THERMAL STORAGE SUBSYSTEM TRIPS (COLD SIDE TRIPS ONLY)

TRIP IDENTIFIER	TRIP CONDITION	INSTRUMENT IDENTIFIER	TRIP LEVEL	ACTION REQUIRED
TR271	Outlet Boost Pump Pressure Low	PT180 AND BP	<400 PSIG ON	EPS (TSS) - STOP boost pump - CLOSE FCV151 - TSS cold-side trip signal to RS EPS (RS) - Defocus heliostats
TR272	Cold Sump Level Low	LT201	<12 In.	
TR273	Loss of Boost Pump Hardwired: High Vibration Low/High Current Low Oil Level or Air Pressure CP OFF Loss of Power/Breaker	BP AND BP.ZSH	ON Open Contract	
TR276	Bad Control Output Quality for 5 S	FCV201 FCV151 FCV161	BQ BQ BQ	OPERATOR - Shutdown TSS cold-side and receiver as required from NET-90 consoles and local valve stations - Employ instrument technician
TR275	Bad Control Input Quality for 5 S	LT161 LT180 PT182	BQ BQ BQ	
	BQ = Bad Quality	LT201	BQ	Same as above plus: EPS (TSS) - CLOSE FCV201 and FCV211 - STOP cold sump pump
TR274	Cold Sump Level High	LT201	>55 In.	EPS (TSS) - CLOSE FCV201 and FCV211
		LT201	<49 In.	EPS (TSS) - OPEN FCV211 - FCV201 to AUTO - Reset TR274 to CLEAR
				OPERATOR - Acknowledge alarm and monitor

3.8.4 Monitoring Instrumentation

Monitoring instrumentation is designed into the control system to provide information for verification of the receiver's design and performance. Some of this information is beneficial for the operator to use in control and monitoring as well, but the design does not attempt to separate the two uses.

The different types of instrumentation integrated into the control system are

1) Thermocouples,
2) Pressure Gauges,
3) Flux Gauges,
4) Flowmeters,
5) Linear Displacement Gauges, and
6) Strain Gauges.

This instrumentation represents approximately 100 additional instruments that provide information, compared to 150 for controlling the receiver.

3.8.5 Operator Control & Monitoring

The operator control and monitoring design is based on the operator interface unit (OIU) of the NET-90. This unit is connected to the plant communication loop for operator access to the receiver subsystem, as well as to all the other thermal subsystems, from the central control room. The design pertains to the required configuration of an OIU to provide complete control and monitoring capability by the operator.

The NET-90 handles all of its communication, control, and monitoring capabilities by the use of tag identifiers, or tag IDs. Specific data and control points are associated with a tag ID, which is nothing more than an alpha-numeric name. These tag IDs are configured into a master tag list from which areas and groups of tag IDs, trends, and custom graphic pages are configurable for control and monitoring. Groups of tag IDs are designed for

both engineering and operational concerns. Area 1 is designed to contain the engineering-related groups, whereas Area 5 is designed for operational groups. Some operational groups are preconfigured trends so that the operator can easily and quickly observe process operation over time.

Custom graphics are designed to mimic the layout, geometry (2-D only), and interrelationships of the equipment to improve the operator's familiarity with the process and decision making when operational problems occur. Generally, three types of graphics are designed to focus in on a particular operational aspect. They are receiver start-up, on-line operation, and shut down.

Alarm conditions are announced at an OIU through flashing alarm indicators in areas, groups, and custom graphic pages. These alarms are designed to print out as they occur, and operator commands are also printed to aid in cause-and-effect analysis.

3.9 Instrumentation

Instrumentation of the receiver was installed to allow verification of aspects of the receiver design, and measure it's performance. Instrumentation included

- Thermocouples
- Pressure Gages
- Flux Gages
- Flowmeters
- Displacement Gages
- Strain Gages

The location of the instrumentation is presented in Figure 3.9.1 which is a schematic of the receiver piping. The instrumentation was selected to be compatible with the molten-salt and high flux solar environment, as well as with the Network 90 control system and the practices of the CRTF.

FIGURE 3.9.1

RECEIVER PIPING INSTRUMENTATION SCHEMATIC

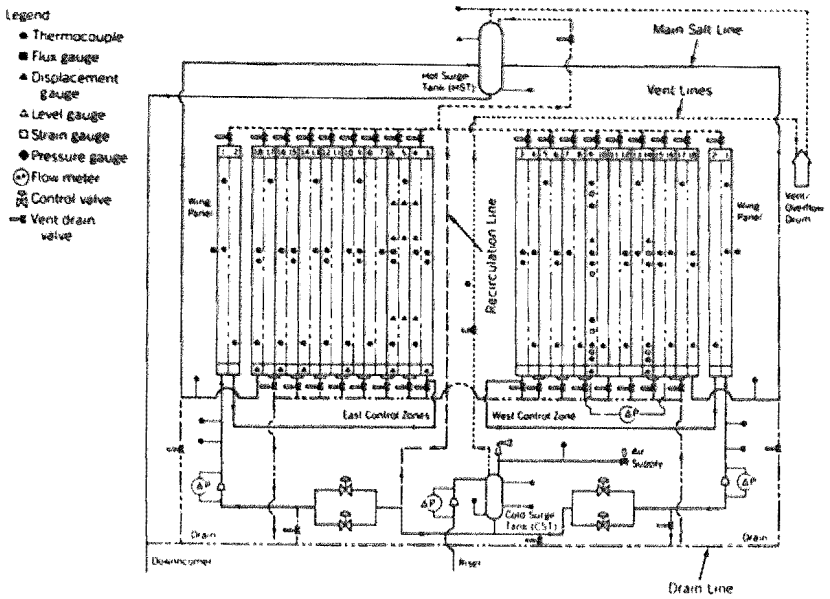

3.9.1 Thermocouples

All thermocouples installed in the receiver were type K (chromel-alumel), sheathed thermocouples. Most of the thermocouples were the ungrounded type, however grounded thermocouples were used to achieve quicker response for measuring inlet and outlet salt temperatures of each control zone. The ungrounded thermocouples employed weld pads which were attached to the outside of the piping or back side of the receiver panel by spot welding. Those were used for monitoring panel temperatures and control of heat trace. The grounded thermocouples were installed in the salt flow, passing through a compression fitting in the pipe wall.

3.9.2 Pressure Gages

Three absolute pressure transmitters and six differential pressure transmitters are used in the receiver. The transmitters sense pressure and generate a 4-20 milliamp (mA) electrical signal proportional to the pressure range for which the transmitter is calibrated for the Network 90 control system.

Twenty-four-volt dc power is supplied by the control system. One of the differential transmitters is used to measure the pressure drop in the Foster Wheeler panel. The others are used as level and flow sensors, which will be discussed later. Absolute pressure transmitters are located at the inlet of each flow control zone (downstream from the control valves) and at the top of the cold surge tank.

To sense salt pressure, all of the transmitters except the surge tank pressure transmitter employ remote seals consisting of a thin stainless steel diaphragm. Salt pressure is transferred to a high temperature silicone oil (syltherm) across this diaphragm. The transmitter senses the oil pressure at the end of a capillary tube connecting it to the oil side of the diaphragm. Figure 3.9.2 illustrates a typical differential pressure transmitter. The cold surge tank pressure transmitter is connected to the air space in the tank, and thus no isolation diaphragm is used.

FIGURE 3.9.2
PRESSURE TRANSMITTER WITH REMOTE SEALS

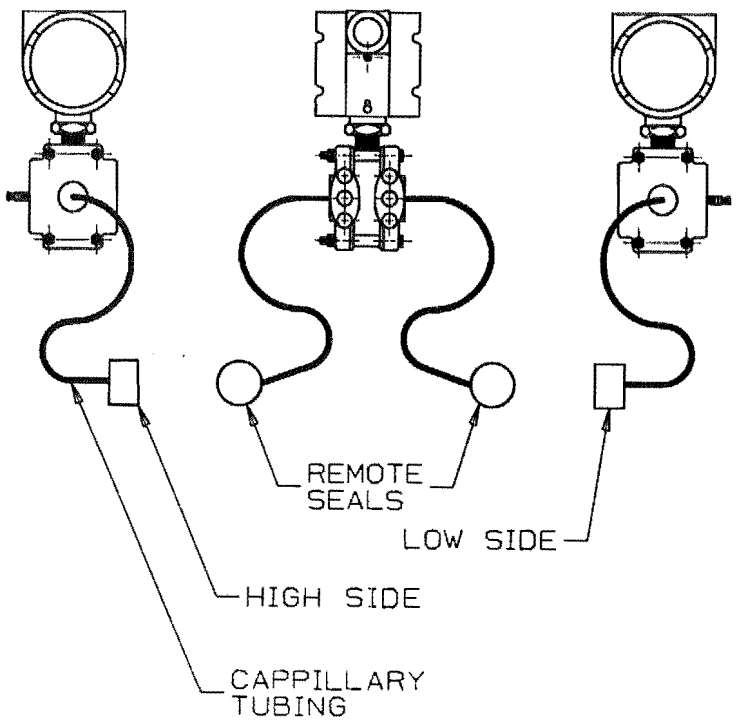

3.9.3 Flux Gages

Two types of flux gages were used in the receiver; air cooled and water cooled. These are illustrated in Figure 3.9.3. The gages generate a millivolt signal proportional to the flux incident on their sensing tip. The gage factor for each gage was determined individually by calibrating each one in the solar furnace at the CRTF. The small diameter extended tip of each gage is designed to extend through the receiver panel between tubes.

FIGURE 3.9.3
SOLAR FLUX GAGES

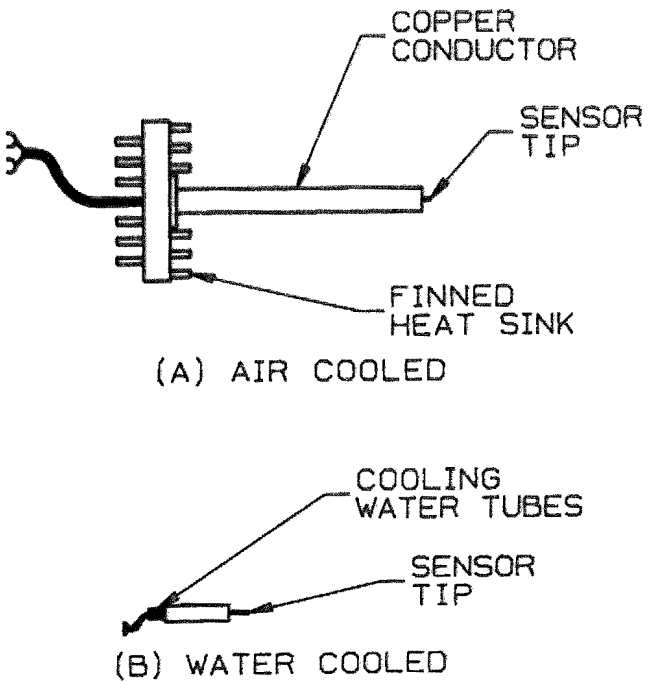

3.9.4 Flowmeters

Venturi type flow meters were installed in the riser line upstream of the cold surge tank and in each flow control zone inlet. The venturis, shown in Figure 3.9.4, were installed in vertical piping runs to allow for drainage.

They were fabricated of stainless steel, and sized to produce a nominal differential pressure of 200 inches of water at full flow. Transmitters such as those shown in Figure 3.9.2 were used to sense the differential pressure signal, and produce a 4-20 mA signal for the Network 90. A software zero offset calibration as configured into the Net-90 to allow correction for the static head of salt in the gage (since it was oriented vertically), and for drift.

FIGURE 3.9.4
SALT FLOW METER VENTURI

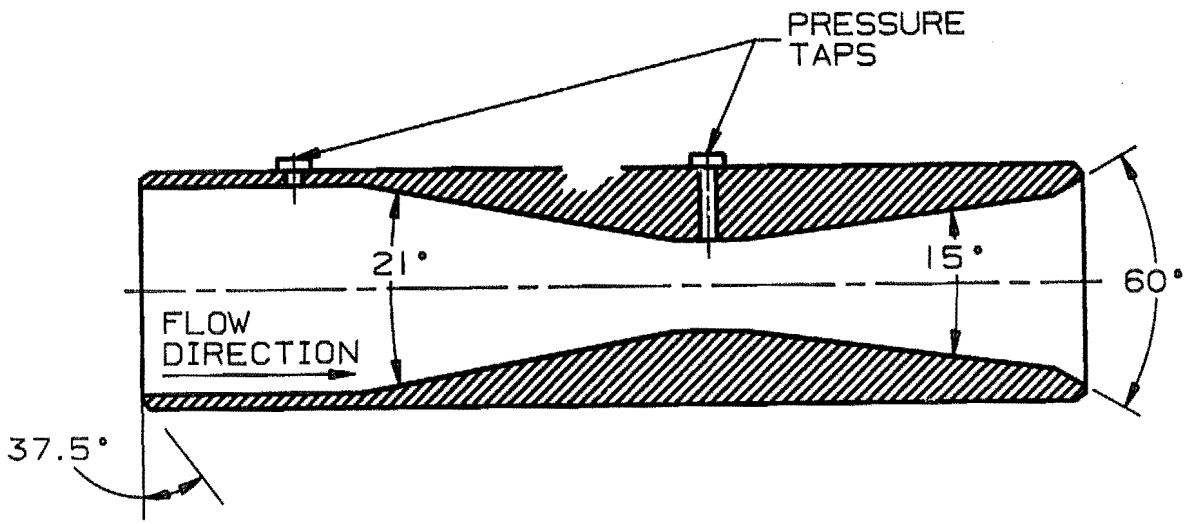

3.9.5 Displacement Gages

The displacement gages employed a fine cable wrapped around a spring loaded drum. As the cable moved in and out of the gage, the drum turned a precision potentiameter. The gage included the appropriate circuitry to generate a 4 to 20 mA signal for the Net-90 proportional to the extension of the cable. These gages were connected to several panel lower headers to measure the thermal growth of the panels, and to several tubes to measure their horizontal movement.

3.9.6 Strain Gages

Two types of strain gages, resistance and capacitance, were used in various locations on panel 3-west (the Foster Wheeler panel). The resistance gages were connected to a bridge circuit and generated a signal in the millivolt range. The capacitance gages were connected to an amplifying device that created a signal in the 0 to 10 volt dc range. Neither signal was compatible with standard Network 90 inputs in the control system, so they were recorded on a digital strip chart recorder.

3.10 Receiver Structure

The receiver structure was largely shop fabricated to facilitate field erection of the receiver hardware.

The major substructure serves as a shopping fixture for the receiver module containing the panels, cavity structure, vent and drain piping, and valves. The receiver module is shown in Figure 4.1.5. Two smaller structures consisting of columns and bracing were also fabricated and eventually supported field-installed hardware such as the tanks, piping, roof and grating. The welded structures were erected on a steel foundation of the lifting module in the CRTF tower. Interconnecting members and bolted connections, field installed, complete the structure. A sheet metal enclosure and roof were installed to protect the receiver components from the environment.

The various levels of the receiver are accessible using a caged ladder. The structure is constructed of A36 carbon steel using standard rolled shapes. Design and fabrication are in accordance with AISC Code, eighth edition. Design loads are discussed in Section 3.2.

SECTION 4

RECEIVER FABRICATION AND ERECTION

P. Reed - Babcock & Wilcox Corp.
G. Riley - McDonnell Douglas Astronautics Corp.

4.1 Shop Fabrication

Receiver components requiring shop fabrication include the panels, surge tanks, and door. The majority of piping and structural steel was also shop fabricated to facilitate receiver erection. The largest single component to be shop fabricated is the receiver module which contained the panels, cavity structure, and panel vent and drain piping and valves. The B&W panels and the receiver module were fabricated at Hydro Dyne in Massilon, Ohio. The surge tanks, door, and the balance of structural steel were fabricated at Bi-Con Services in Cambridge, Ohio.

4.1.1 Fabrication of the Babcock & Wilcox Panels

The receiver panels were fabricated in accordance with the ASME Pressure Vessel Code Section I, (Power Boilers). Non-destructive examination of the panel welds was in accordance with ASME Section V with additional requirements identified by the B&W drawings.

The receiver panels were fabricated in 2-pass units (subpanels) consisting of one common header at the top and two headers at the lower end. The subpanels were then assembled into either 4-pass or 6-pass panel assemblies. With the buckstays positioned on the subpanels, the tube clips and instrumentation attachments were welded to the panel back surface. Welding was manual using tungsten inert gas.

Panel welding was considered a critical process at panel fabrication. Because of the large number of panel welds and concern over welding to thin-wall tubing, additional requirements were implemented (exceeding the normal requirements of ASME Section V) to ensure weld quality. These requirements included the submittal of sample tube butt welds and tube attachment welds to B&W for detailed examination and a 100-percent liquid dye penetrant test of all panel welds. The completed receiver panels were shop hydrotested to 510 psig (1.5 times the design operating pressure) using demineralized water. Pressure was held for a sufficient amount of time to inspect all pressure boundary and panel attachment welds for leaks. Three leaks were detected at tube to header connections, repaired and re-hydrotested.

During field erection of the receiver, the system was hydrotested revealing six pinhole leaks occurring at various tube attachment welds. These leaks were not discovered earlier because the leaks were extremely small, not immediately passing water, and the hydrotest time was insufficient to detect this size of a leak. The field hydrotest was more thorough and offered better conditions for inspection.

Additional pinhole leaks were discovered through an air test. A helium leak check was also performed although no new leaks were detected. A total of twenty four leaks were discovered involving the B&W and FW cavity panels. The leaks were repaired by grinding the defects and replacing the weld filler metal. The repairs were checked with an air test and a final hydrotest.

The leaks were the direct result of burn through caused by premature withdrawal of a weld torch. The nature of the tube leak is illustrated in Figure 4.1.1. Proper welding technique requires a downslope of current before removing the weld torch to prevent a build-up of heat that impairs weld quality.

FIGURE 4.1.1

PINHOLE LEAK RESULTING FROM BURN-THROUGH

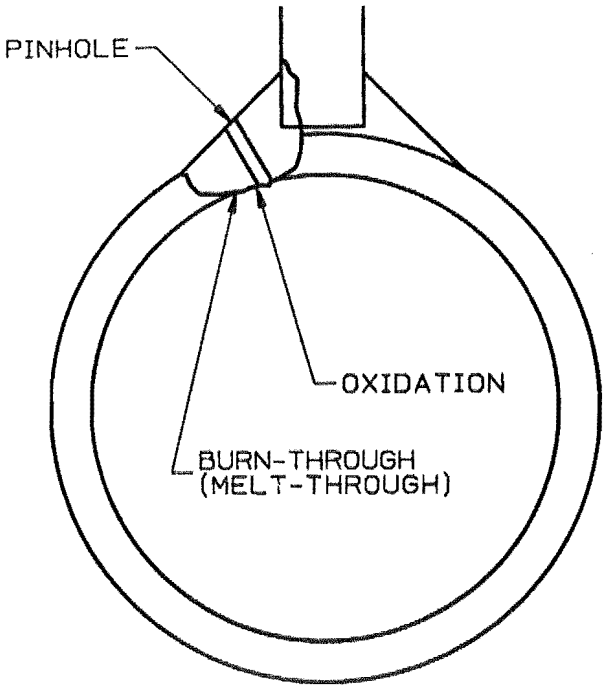

An automated welding process is recommended for a commercial size panel. Automated welding offers better control over heat input to the welds, repeatability, and potential cost savings.

The gas leak test was effective in identifying all defects and their precise locations. Also known as the "soap bubble test," the gas leak test is easy and inexpensive to perform. This test is recommended for commercial receiver designs to ensure weld integrity.

Excessive heat generated from the tube to header connection welds created unacceptable panel distortion particularly in the safe-end region. To minimize heat build-up, these welds were constructed incrementally with the headers and receiver tubes clamped in position. Weld distortion is a fabrication concern to a commercial size panel, although a larger panel would be less susceptable to this type of distortion.

The size and position of the tube indentations are critical to operation of the flux gages. A pair of indentations in adjacent tubes provides an opening in the panel wall for the flux gage sensor. The receiver tubes were indented prior to subpanel welding and fit-up was based on alignment of the indentations. Upon completion of the panel welds, many of the tube indentations were discovered to be out of tolerance. A recommended approach, assuring optimal alignment of tube indentations, is to construct the tube indentations subsequent to panel-header welding simply by springing the tubes away from the panel and indenting the second tube relative to the indentation of the first tube. The position of the gage support is then based on the actual indented opening.

4.1.2 Fabrication of the Foster Wheeler Panels

Foster Wheeler fabricated two wing panels and one rear panel for the solar central receiver. These three panels were completely shop fabricated and tested in individual modules to facilitate handling, shipping and installation. Figure 4.1.2 shows the panel configurations for the wing panel and rear panel supplied by Foster Wheeler from the plant at Dansville, New York.

FIGURE 4.1.2
PANEL CONFIGURATIONS

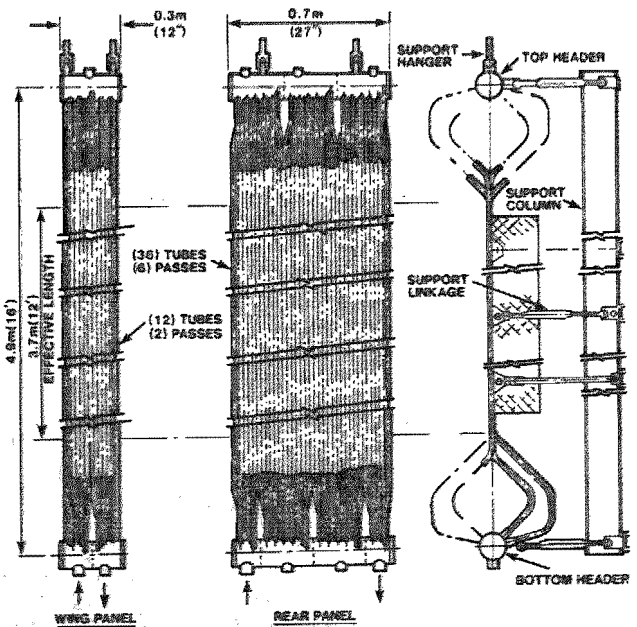

The panels were made of individual tubes welded to the top and bottom headers at each end of the panels. The tubes were supported from the back by a series of tube clips attached to independent tube support assemblies. Panels were hung in place of support lugs welded to the top header.

The wing panels were made using 304 stainless steel material for the tubes, headers, tube end stubs, sockolet couplings and tube clips. The rear panel tubes were Incoloy 800 material, and the headers, tube end stubs, sockolet couplings and tube clips were made from 304 stainless steel material. Instrumentation attachment parts for all panels were made from 304 stainless steel material. Tube support assemblies, support beam and shipping frames were made from carbon steel material.

The tubes were bent to the various configurations required for each panel tube. In parallel with the tube bending operation, the top and bottom headers' subassemblies were made.

The header subassemblies included standard-wall thickness stainless steel pipe, flat end covers, support lugs and hold back lugs. The pipe was cut to length; the ends were beveled, holes drilled for tube and sockolet coupling attachment and the thick walled tube stubs were attached and drilled. The flat end covers and divider baffles were machined from round stainless steel bar.

Each header was assembled with divider baffles and sockolet couplings manually welded in place. The bent tubes were fit up tangent to tangent and welded to the headers. After all tubes were welded, the flat end covers were installed and welded to the headers. Support lugs and hold back lugs were attached after all welding of the pressure parts had been completed. All pressure welds were dye-penetrant inspected at the root pass and final weld pass. A typical detail for a rear panel header is shown in Figure 4.1.3.

FIGURE 4.1.3

REAR PANEL HEADER

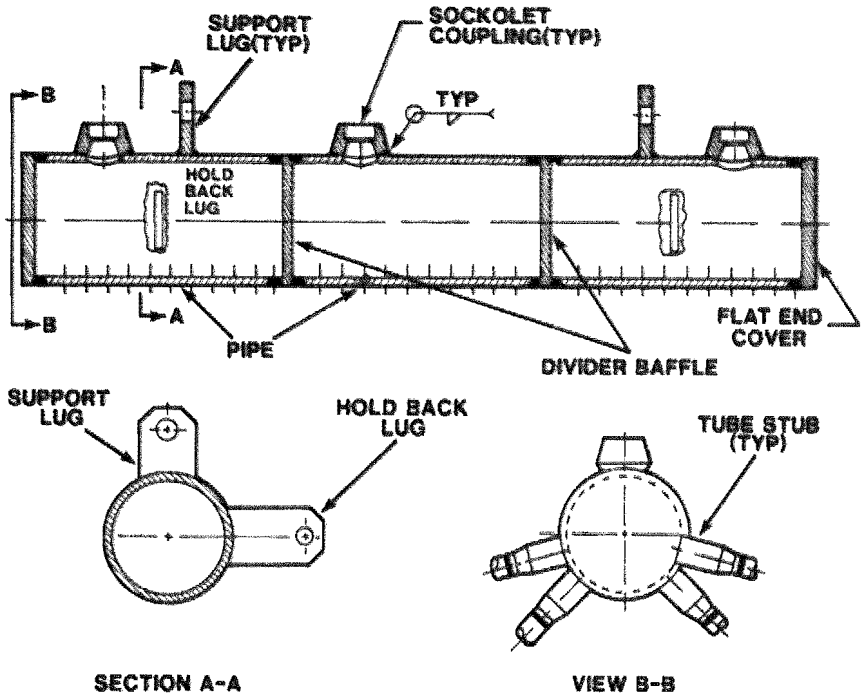

The tube clips were then welded to each of the tubes at the designated locations. After installation of all tube clips, the independent tube support assembly was installed and adjusted. A typical tube clip and rear panel support are shown in detail Figure 4.1.4. At this point, the parts for the displacement gauge attachment and flux gauge attachment were welded to the back of the tube panels. The completed panels were hydrostatically shop tested, drained and shipped to Babcock & Wilcox in Ohio for installation in the receiver module.

FIGURE 4.1.4

TUBE CLIP & REAR PANEL SUPPORT

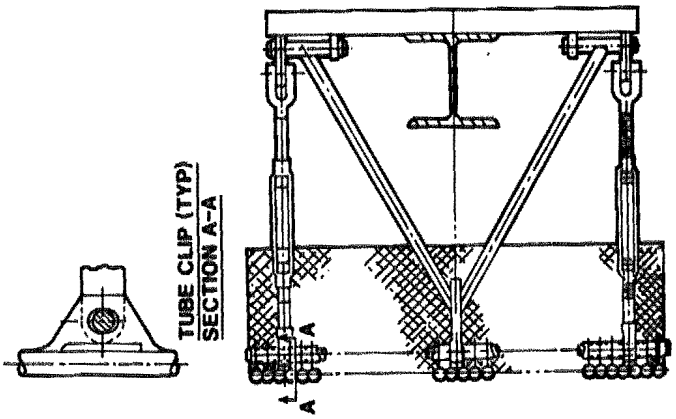

4.1.3 Receiver Module Fabrication

The receiver panels and immediate piping and valves were shop assembled into a single shippable component called the Receiver Module. The Receiver Module would facilitate field installation of the receiver system and permit a shop hydrotest of the receiver panels. A welded steel frame was constructed to house the receiver panels, header inter-connecting piping, panel vent and drain piping and valves, cavity enclosure, panel hangers, and the door drive mechanism. The shipping frame would later serve as part of the main support structure. The Receiver Module is shown in Figure 4.1.5.

FIGURE 4.1.5
RECEIVER MODULE

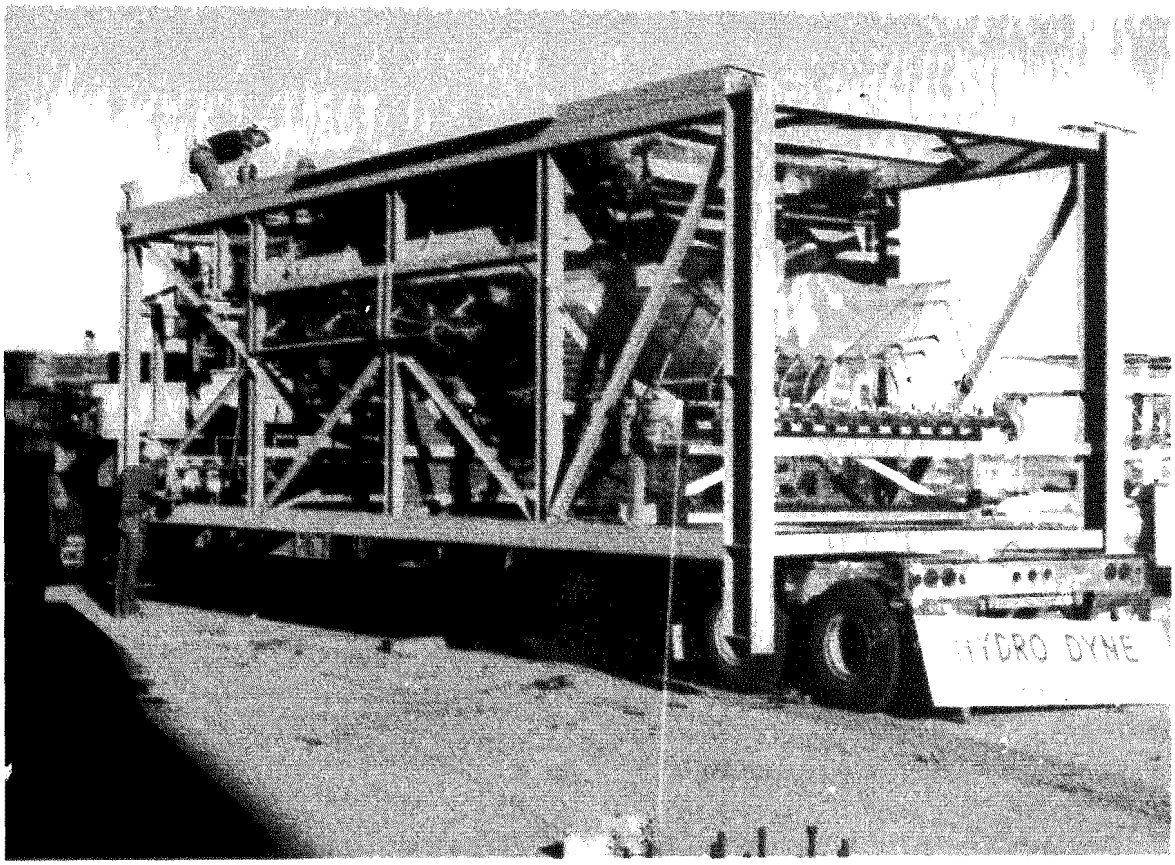

The Receiver Module was fabricated in accordance to the following codes: ASME Power Boiler Code Section I (pressure boundary), AISC Code (structural steel), AWS D1.1 (welding), and ASME Section V (inspection). The Receiver Module was hydrotested at 510 psig and Code stamped to ASME Section I.

The structure and pressure components were fabricated in parallel. Due to its size, the structure was constructed on its backside (the approximate size being 3.7 m (12 ft) width by 3.4 m (11 ft) depth by 11.6 m (38 ft) height. The cavity enclosure was constructed within the framework of steel and prior to panel installation thereby reducing potential for damaging the receiver tubes. The wing panels (supplied by Foster Wheeler) were installed from the top (aperture side), and lateral support pads welded to the structure. The cavity panels were installed horizontally and entering the cavity through the open cavity floor. The panels were then aligned using the bolted connections of the roller guide plates (B&W panels). With the vent and drain headers and valves positioned within the receiver module, inter-connection piping was installed completing Receiver Module fabricating. Temporary supports were installed to protect the receiver components during shipping including adjustable nylon straps that supported the panels and inter-connecting piping. Shipment to the CRTF was by truck.

Other shop assembly at the receiver panels did not succeed in satisfying the specified 0.32 cm (0.13 inch) maximum clearance between panels. Because of the horizontal position of the Receiver Module, the process of aligning the panels was cumbersome. Realizing that field adjustment of the panels would probably be necessary following erection, panel gaps exceeding the specified limit were accepted. Panel adjustment is discussed in Section 4.2.

4.1.4 Tanks, Door & Structure Fabrication

Shop fabricated receiver components included the surge tanks, receiver door and tracks, and two structural steel assemblies. In support of the receiver erection schedule, these components were fabricated in parallel to the receiver module.

The surge tanks were fabricated in accordance to ASME Section VIII Division I, Pressure Vessel Code, and inspected in accordance to ASME Section V. Pressure boundary welding included a seam weld in the shell, head to shell circumferential welds, and nozzle connection welds. All pressure boundary welds are full penetration. Welds were inspected using spot radiographic examination and visual examination. The cold tank was shop hydrotested to 5537 kPa (803 psig). The hot tank was hydrotested to 827 kPa (120 psig).

The receiver door and tanks were fabricated in accordance to American Institute of Steel Construction (AISC) Code. Each door section was constructed on large tables that served as a reference plane. A surveyors transit was used to level the tables and assure that the dimensional requirements of the door had been met. The dimensions between door roller connections are critical to door operation. Because of the welded construction of the doors, a tolerance was imposed on this dimension. The door of a commercial-scale receiver would be considerably larger and require some means of adjusting roller or track position.

Receiver door accessories include tracks and seal support brackets. Door tracks were fabricated from four A36 structural angles. 2.86 cm (1.13 inch) slots were machined into one leg outlining the path of door travel. Seal brackets were constructed of 0.32 cm (0.125 inch) carbon steel plate. A bolted connection between the bracket and door was necessary for attaching the seal. The brackets were shipped loose and installed at the site.

In addition to the structure of the receiver module, two structural steel assemblies were shop fabricated to form the suports for the working levels behind the receiver panels. Structural steel was fabricated in accordance to AISC Code. Each assembly consisted of three columns joined by diagonal bracing and platform support members. A caged ladder was constructed and attached to the steel framework of the one assembly. Pre-fabricated structural steel also included surge tank support steel and inter-connecting support members with bolted end connections. These members were for field installation to connect the support assemblies and module.

4.2 Field Erection

Field erection of the MSS/CTE test receiver was accomplished as an integrated effort between Babcock & Wilcox and Sandia National Laboratories. Two Babcock & Wilcox resident engineers managed the receiver construction and directed site work of contractors. CRTF provided the personnel to erect the receiver and provided overall coordination of site activity. Contractors involved with the receiver erection include electrical, mechanical, and insulation.

The erection phase began late in September 1985, with the placement of the receiver module in the CRTF tower. Long lead materials were ordered early in support of the erection schedule and included valves, a refurbished boost pump, and a Network 90 control system. The majority of construction activity was performed at ground level. The installed receiver was moved to the tower top in July 1986. At this time, final connections were made and a checkout of heat trace and Network 90 controls performed. In parallel to receiver installation, the supporting subsystems were prepared for operation. These subsystems are thermal storage system (TSS), steam generator system (SGS), heat rejection and feedwater system (HRFS), collector field system (CFS), and master control system (MCS). Operational checkout of the receiver began with cold salt flow in September 1986.

Schedule

An erection plan was developed as a joint effort between Babcock & Wilcox and Sandia National Laboratories to identify critical construction activities and predict overall installation time. The plan was refined using computer scheduling software based on the critical path method (CPM). Activities were identified and span times estimated relying heavily on input from CRTF. Material delivery dates were obtained from vendors. As construction progressed, the schedule was updated to reflect completed work. The critical construction activities were piping installation, heat tracing, insulation, and pre-operational checkout of heat trace and controls.

The use of a computer generated schedule offered an effective means of updating the schedule to implement changes, identify critical activities, and determine manpower requirements. Frequent schedule updates became necessary near the end of the construction period when the combined tasks of receiver checkout and subsystem start up tended to overlap, making the process manpower limited.

Quality Control

Measures taken to ensure quality during MSS/CTE construction include daily status meetings, design reviews, material inventory, early equipment checkout, and written procedures.

Daily status meetings, conducted at CRTF, were effective in resolving construction problems and schedule conflicts, and, in general, aided the day-to-day planning. The meetings were attended by everyone involved with the receiver construction including site project engineers, CRTF technicians, and contractors. In commercial construction, daily status meetings are recommended between the responsible construction personnel and contractors.

Design reviews were conducted prior to receiver erection to identify potential problem areas. The reviews were internal to Babcock and Wilcox and were attended by the design and project engineers, management, and a review team of selected experience and expertise.

Receiver hardware was inspected upon delivery to verify that the correct materials and quantities were sent and free of damage. A complete file of hardware specification documents, and copies of the purchase orders were maintained at the site for this purpose. Special attention was given to the purchase of stainless steel piping regarding carbon content. Low carbon stainless steel is commonly used by industry and therefore easy to obtain. Because the high operating temperature of the receiver exceeds 1000°F, the ASME Code requires the use of high carbon stainless steel. To avoid accidental substitution of the low carbon stainless steel, this requirement

was emphasized to the piping vendor. Upon delivery, material certifications were reviewed.

Equipment failures often occur during initial operation and result in schedule delays. To thwart these delays, early checkout of equipment was emphasized. A water test of the boost pump was performed at the vendors shop and was witnessed by engineers from Babcock & Wilcox and Sandia National Laboratories. The pump was also operated following installation at CRTF to verify pump performance in its operating environment. Although the pump water test was accepted, problems surfaced later during the initial operation at CRTF which involved an undersized keyway on the pump shaft and pump impeller vibration. Vendor involvement was necessary to diagnose the problems. The problems necessitated pump removal, disassembly, re-machining the keyway and replacement of the pump impeller. The early checkout of the pump permitted timely repair of the pump.

Vendor presence is recommended during installation of equipment, where fit-up or assembly is critical, and initial operation to verify performance. Additionally, a warranty should be obtained that covers initial operation of critical equipment such as pumps, valves and instrumentation. During MSS/CTE construction, many warranties had expired before the equipment was operated.

Procedures were prepared to control the installation of many receiver components. Written procedures are recommended for the installation of hardware such as heat trace, insulation, receiver paint, door, and instrumentation, where receiver performance depends on the method to which the hardware was installed. The procedures should be reviewed prior to equipment installation.

4.2.1 Module Placement and Structural Assembly

The receiver module placement is shown in Figure 4.2.1. The receiver module was placed on a foundation of steel beams bolted to the tower's lifting module. The backend structural frames and connecting members were erected using the hoist cranes located within the tower. Selected structural

members were not immediately erected allowing the surge tanks to be lowered into position. Access grating and handrail were installed making the receiver safe. A 10-ton capacity articulating crane was welded to the roof steel. Because the structure was not designed for full crane, capacity of the crane was derated to a two-ton capacity. Although the crane was installed primarily for use on top of the tower, the crane was used extensively during construction. To protect the receiver components, a steel plate roof was laid and seal welded to the top of the receiver. To avoid the possibility of damaging heat trace cable all structural welding was completed prior to heat trace installation.

FIGURE 4.2.1
RECEIVER MODULE ERECTION

Panel Alignment

The receiver panels were aligned following erection of the receiver module while the panels were easily accessible. Panel alignment was accomplished by adjustment of the panel lateral supports to obtain a uniform absorber surface geometry and provide adequate clearances for thermal expansion. Several gaps remained in the receiver following adjustment that exceeded the specified limit of 0.125 inch.

The largest gaps existed between panel assemblies and were the result of shop welded header piping which restrained adjacent passes. Because the gap size was not great enough to impact receiver operation or performance, the tube clearance requirement was relaxed to accept the as-built condition of the receiver. A similar procedure would be used to align the panels of a commercial receiver. The panels would be aligned following erection and prior to installation of inter-connecting piping.

Receiver Paint

The receiver panels were painted at CRTF with Pyromark 2500 which is a flat black paint designed to improve the absorptivity of the receiver. Because the receiver tubes were in the as-drawn condition, the surface was roughened by sandblasting using a 60 mesh garnet abrasive and wiped with trichlorethane to prepare the surface for painting. Three coats of Pyromark paint were applied by spraying and cured according to the manufacturers recommended procedure. The curing process involved initial air drying at ambient temperature for a minimum of 18 hours. Using the electric heaters in the cavity, the panels were then heated to 250°F for a two hour period. The temperature was increased to 480°F at a rate not exceeding 3.8°F/min. and held for a period of one hour. Final paint vitrification was accomplished by heating the receiver to 1000°F and holding for a minimum of 10 minutes.

An inspection of the paint following the low temperature cure revealed that the paint surface was extensively crazed-cracked and exhibited poor adhesion in many areas. Evaluation of the painted surface indicated that the crazing

was the result of excessive paint thickness. Three coats of paint were applied in the original painting. The damaged paint was removed using a wire wheel brush and hand-sanded using #36 paper. The receiver was re-painted with one coat of paint applied with a target thickness of 0.0007 inches. Thickness measurements of painted sample plates indicated that the dry film paint thickness of the receiver surface was between 0.003 and 0.006 inches. Additionally, the paint coverage appeared adequate on the receiver with no thin areas obvious. Based on these results, the single coat of paint was accepted.

A paint procedure should be developed for a commercial receiver which controls application of paint. The procedure should be tested to determine the shrinkage ratio of the paint and resulting dry film thickness. Commercial size panels would be shop painted and cured in a controlled environment such as a furnace.

4.2.2 Piping and Valves

Field installed receiver piping included inter-connecting piping between the receiver module, surge tanks, and tower piping. Connections to the receiver module consist of inlet, outlet vent and drain header nozzles. The existing tower riser, downcomer, and drain piping was modified above the top of the tower to accept the MSS/CTE receiver piping configuration. Bolted flanged connections were used at the receiver/tower interface to facilitate final connection of the receiver to the system.

Piping was fabricated and installed by a local contractor, Gardner-Zemke. The piping was specified on the drawings of Babcock & Wilcox. Material procurement was conducted at CRTF by Babcock & Wilcox resident engineers. Pipe material included A106 carbon steel used in the low temperature line (650°F) and 316 stainless steel used in the high temperature lines (1075°F). Pipe welding and inspection was in accordance to ANSI B31.1 Code. Inspection was performed by a local independent test lab and consisted of 100 percent radiographic examination of all stainless steel pipe welds equal to or greater than two inches in diameter.

The majority of piping which included valve bodies, flow venturis, and instrumentation connections was shop fabricated and delivered to the site in spool pieces. The spool pieces were then welded into place and temporarily supported with wooden blocks. Rigid calcium silicate pipe supports were later installed by CRTF personnel subsequent to heat tracing.

The receiver system was hydrotested at 1-1/2 times operating pressure. The receiver is vented in operation; therefore, to hydrotest the piping, the receiver discharge lines were temporarily capped isolating the hot surge tank from the system. Because of the higher design pressure of the receiver, cold surge tank, and supply piping, a second hydrotest was required upstream of the receiver control valves. The entire pressure boundary was thoroughly inspected during the field hydrotest. Numerous pinhole leaks were discovered on the backside of the receiver panels involving tube attachment welds.

A detailed inspection of the receiver panels followed to determine the extent of the tube leaks. The weld defects were field repaired and the system re-hydrotested. The receiver tube leaks are discussed further in Section 4.1.1.

4.2.3 Instrumentation

All receiver instrumentation was field installed to minimize the potential for accidental damage. The majority of instrumentation was procured by Babcock & Wilcox and installed by CRTF technicians. This instrumentation includes receiver and heat trace control thermocouples, heat flux gages, displacement gages, valve and door limit switches, and flow/level/pressure transmitters. Foster Wheeler procured and installed the thermocouples and strain gages on the panels they supplied (refer to subsection 2.1.2). Wireways and signal cabinets were installed by an electrical contractor under the direction of Babcock & Wilcox engineers and CRTF technicians.

Signal wiring was routed behind the receiver and to the junction boxes in the module gallery. Electrical schematics were developed at CRTF to define the routing of signal wiring and identify terminations. The schematics were

also useful later in checkout of the Network 90 controls to troubleshoot the system. Pressure measuring transmitters and heat flux gages were calibrated at CRTF prior to installation.

A Network 90 distributed process control system was installed during the receiver construction phase which replaced the Emcon controls used in previous tests. The controls hardware included three Process Control Units (PCU), a Computer Interface Unit (CIU), and three Operator Interface Units (OIU) and was sized to control and monitor the five subsystems at CRTF. Installation of the receiver control system is described in Section 4.3.

A pre-operational checkout of receiver controls and instrumentation was performed after the receiver was moved to the top of the tower and final connection made. The specific checks performed are described in subsection 4.3.4.

4.2.4 Heat Trace and Control

The heaters installed in the receiver include mineral insulated cable, strip heaters, and band heaters. The mineral insulated cable (MI cable) was applied to all piping, receiver headers, and safe ends. Strip or cartridge type heaters were applied to the flanges of the pressure transmitter connections. Radiant heaters were later installed in the cavity floor during operational testing consisting of oven heater elements.

The heaters were installed by the CRTF technicians and in accordance to Babcock & Wilcox drawings. Power wiring and the power relay cabinets were installed by the electrical contractor.

The MI cable was supplied by Pyrotenax (Pyrotenax USA inc., 35 Washington St., Perth Amboy, NJ 08861) and purchased in bulk. The cable arrived at the site in coils with the total length and power density specified. Upon installation, Pyrotenax was contacted to terminate the cable.

The strip and band heaters were supplied by Chromalox. The heaters were readily available and installation was straightforward. The Chromalox strip

heaters were easily adaptable to the small flat surfaces of the Nupro valve body (Nupro Company, 4800 E. 345th St., Willoughby, OH 44094). Considering the large number of valves employed by the receiver, the strip heater greatly simplified the task of "heat tracing" the valves. Band heaters were specified for all transmitter connections to provide a uniform heating of the transmitter diaphragm.

The power relay cabinets were fabricated at a local electrical supply shop. Four cabinets were required by the many heat trace zones of the receiver. Each cabinet was located within the receiver structure at an elevation consistent with the heat trace zones which it serviced.

Heat trace control was accomplished by the existing Acurex control system. Due to the limited number of control zones available within the Acurex, and the need to heat the transmitters individually, temperature controllers were used for each transmitter.

The task of heat tracing the receiver demanded three months of heater installation and checkout. The receiver system, with its extensive network of piping and valves, required 67 heater control zones (35 with MI cable and 32 with strip heaters), exceeding the requirements of any previous experiment. The original design used 57 heater zones. The additional zones were applied to the riser, downcomer, overflow piping, Foster Wheeler panel, lower header and safe end, and the pressure transmitters. Drawings were developed by Babock & Wilcox which specified heater size and configuration. Each MI cable was custom bent using a 1/4-inch tube bender and attached to the piping with metal banding straps. All structural and piping was completed prior to heat trace installation to avoid the possibility of damaging the sensitive MI cable with weld splatter.

Strip heaters were attached to either side of the Nupro valve bodies using bolted connections. Uniformly spaced on the tank surfaces, these strip heaters were attached using stainless steel shim stock. Shim stock, 3 mils thick, was capacitance-discharge welded to all components heat traced isolating the heaters from the insulation. The heaters would otherwise overheat as the insulation would impede heat transfer to the salt containing

component. Tubes, constructed from shim stock, were used at the cable ends where the heat trace cable penetrated the insulation. Typical head trace installations are presented in Figure 4.2.2 through 4.2.4.

FIGURE 4.2.2
RECEIVER HEAT TRACE

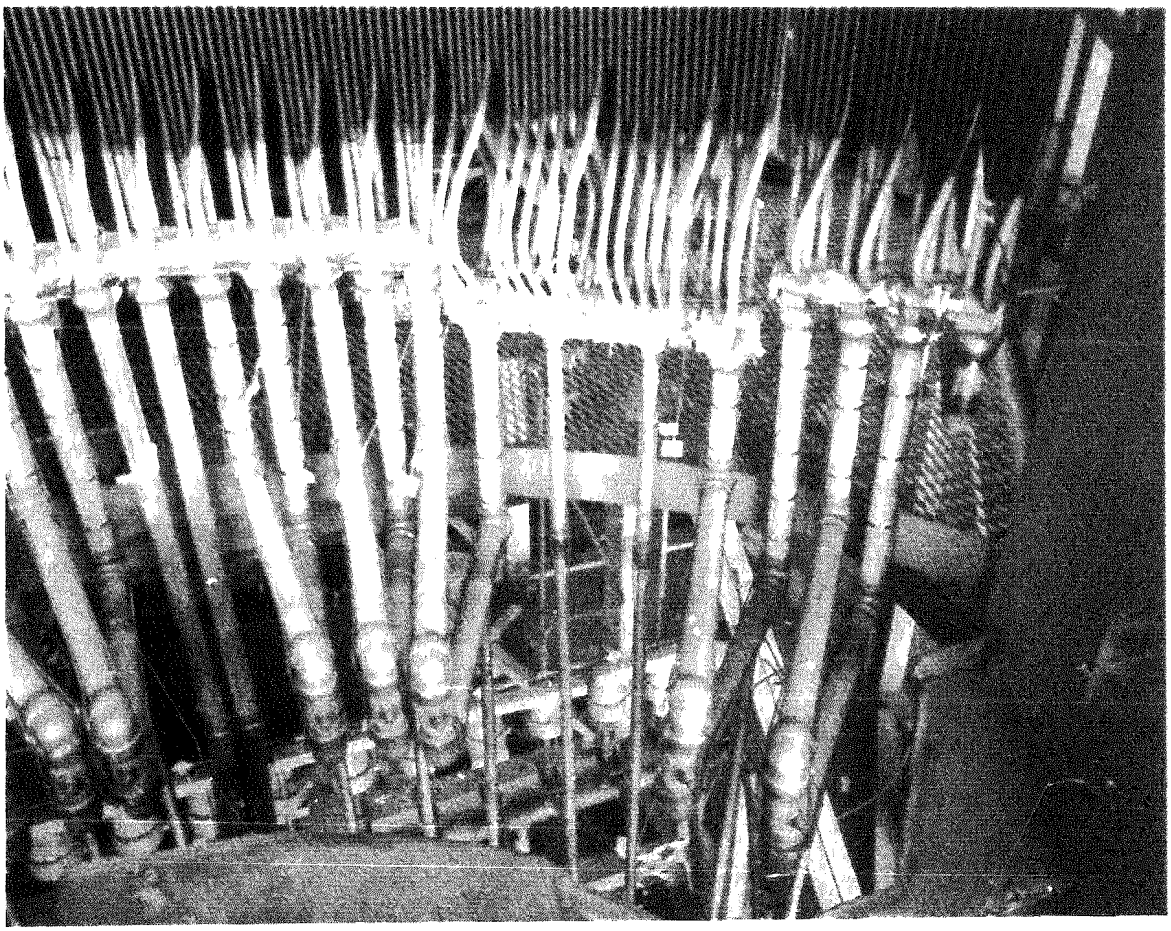

FIGURE 4.2.3
HEADER HEAT TRACE

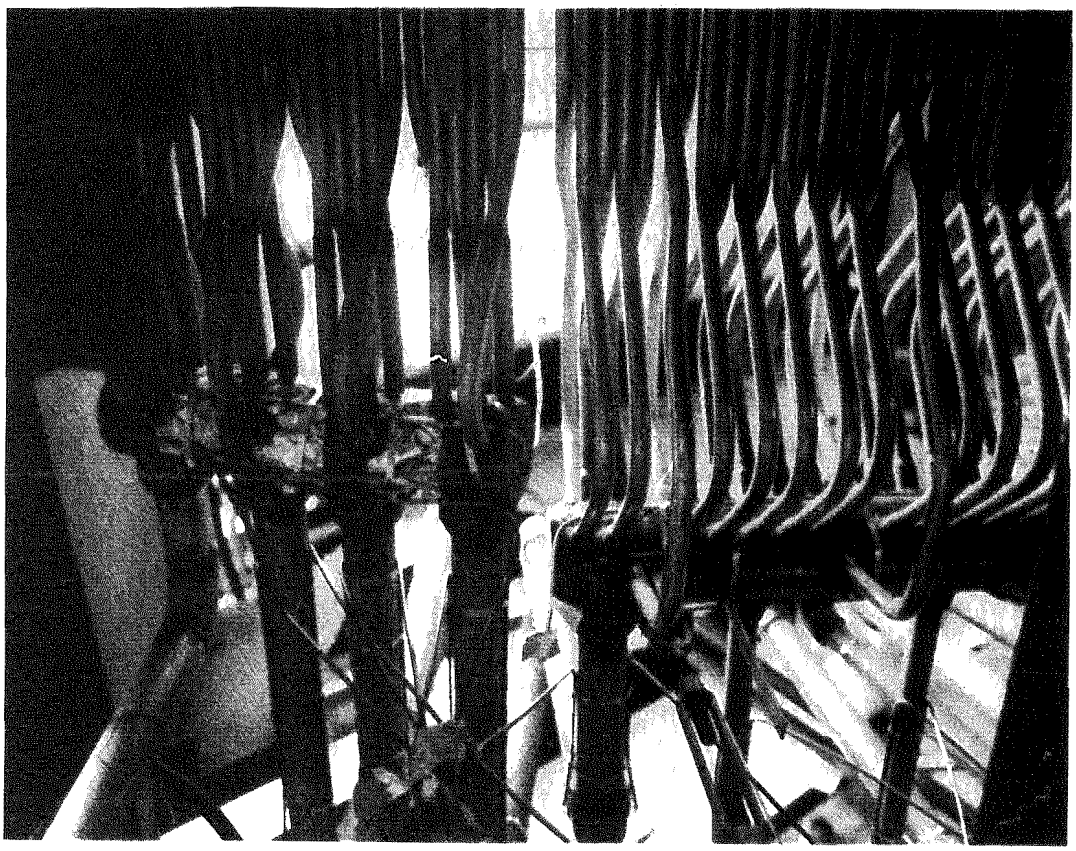

FIGURE 4.2.4
PANEL SAFE END HEAT TRACE

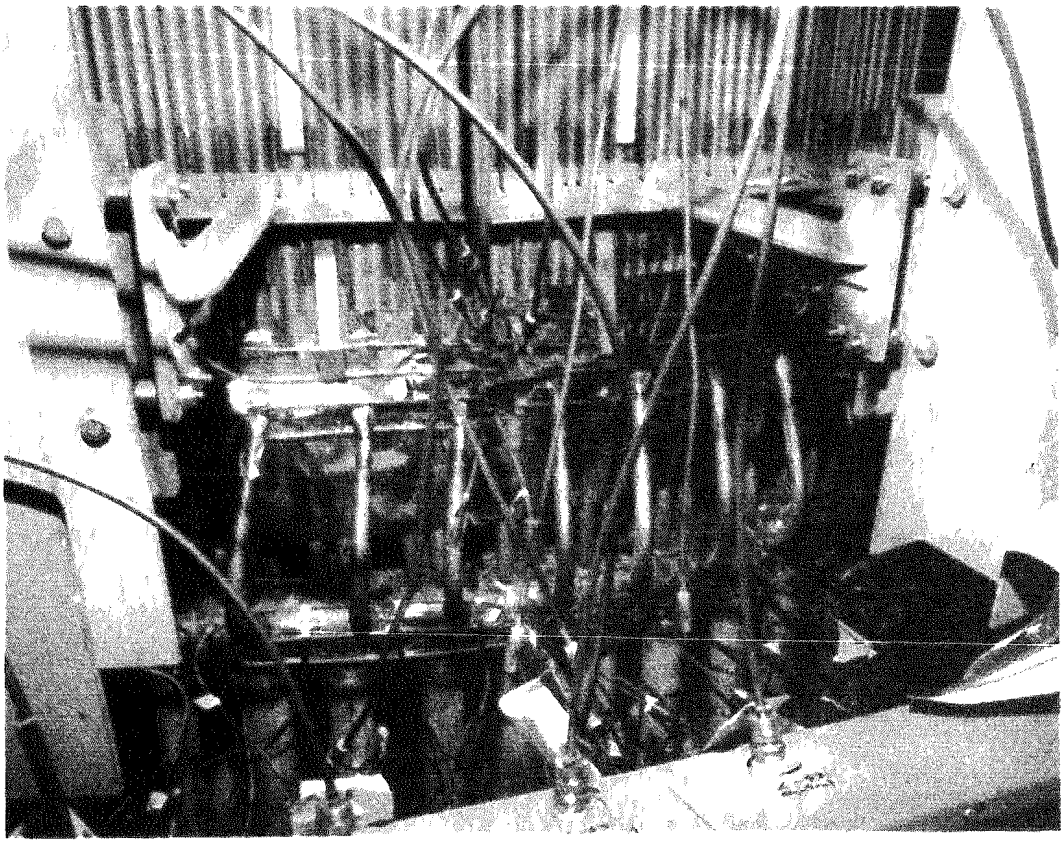

MI cable was field terminated by two Pyrotenax technicians. The task involved the fabrication of a hot-to-cold junction which joined a five foot length of cold lead cable to each end of the heater cable. The hot-to-cold junction consists of brazed connections joining the cable wires and sheathing of the two cables. The brazed connection joining the cable sheathing required a stainless steel fitting. Strip heaters were terminated using mechanical connections, and ceramic insulator beads were installed on the nichrome wire leads.

Each MI cable installed was tested and actual power density documented. Checks included megger and continuity to verify that the cable had not been damaged during installation. Cable ends were then sealed with silicon to prevent the entry of moisture. Hot-to-cold junctions were also checked at the time of installation. All defective junctions were replaced and retested. Before any of the receiver components were insulated, each cable was powered and amperage recorded. Heat trace zones were checked under power for controllability as they were insulated. Checkout continued until all zones were operating properly and were capable of maintaining temperature.

Various heat trace failures occurred during checkout of the heat trace system. Although three hot-to-cold junctions failed during initial operation, only one had failed after several months of operation. Many junctions, however, were rejected during installation which was attributed to the difficulty in field terminating the cable. Shop terminations are recommended to improve the quality of the connection and reduce the potential for failure.

Chromalox strip heaters originally had brazed terminations. Extensive failures occurred during initial checkout resulting from poor connections. Replacement heaters were installed using mechanical connections.

Four Chromalox strip heaters failed due to salt leakage at the control valves. The leakage was corrected and new heaters were positioned on the valve bodies to avoid contact with salt, should any future leak develop.

The original heaters specified for the transmitters were Cal Rod heaters. These heater were replaced with band heaters to provide a more uniform heating of the transmitter diaphragm.

Numerous pressure transmitters were damaged from overheating of the Syltherm oil in the capillaries of the transmitters. An attempt to maintain temperature using available variacs (passive control) was unsuccessful. Individual temperature controllers were then added to each transmitter heater zone controlling diaphragm temperature between 510°F and 520°F. The transmitter supplier, Rosemont, recommended that the temperature not exceed 600°F. Consideration should be given to the use of transmitters with higher temperature capillary fluids such as "NAK."

Many of the safe end heaters were incapable of maintaining temperature. Heaters were installed on the headers and the receiver tubes where the tube bends converge into the plane of the panel. Tube bends received heat via conduction. Insulation was modified as necessary to improve the condition. In the case of the Foster Wheeler lower header, insulation was removed and strip heaters were installed to create an oven effect, the large tube bends heated radiatively. The oven heater arrangement was effective in heating the safe end tubes and is recommended in future designs.

Heater replacement was a major effort requiring the removal of insulation and shim stock, and in the case of MI cable, new terminations. Heat trace failure usually results in operational delays. Redundant heaters provide some relief but are costly to the heat trace system. Because of the variety of heater sizes used, an inventory of spare heaters and parts was not practical to maintain. Additionally, terminating the MI cable requires special skill. Future heat trace systems should include some provision for heater replacement. Heater elements with mechanical connections are recommended for difficult areas such as the header-safe end region of the receiver. Compact heater elements using mechanical connections should be used to the maximum extent in future electrical heat heat trace systems to promote uniformity of hardware and improve serviceability.

Heat trace drawings should contain all necessary information to install and test the heat trace. The location of junction boxes, wireways, and control cabinets should be noted on the drawings. In difficult applications, a description of the cable routing would be helpful to minimize the potential for damaging the cable.

Redundant protection of individual heaters should be considered to prevent overheating in the event of a failure of a primary controller.

4.2.5 Insulation

An insulation contractor installed the majority of the receiver insulation. Kaowool blanket insulation was used extensively throughout the receiver and was applied in two-inch thick layers, with exception to small pipe sizes using one-inch blanket. Insulation was attached to the door, cavity, and panels using standard stainless steel pin studs and washers. Piping was wrapped and the insulation secured with wire ties. The insulation was protected from the environment by the ribbed metal siding that enclosed the receiver structure. Exposed piping was encased with aluminum jacketing.

The face of the receiver cavity (surrounding the aperture) was covered with two-inch insulation board. Super-rigidized HS board, supplied by Babcock & Wilcox was selected for the test receiver. Bolted connections were countersunk and covered with refractory cement. For additional protection, the surface was covered with an insulation coating. The receiver cavity and aperture is shown in Figure 4.2.5.

FIGURE 4.2.5
RECEIVER CAVITY

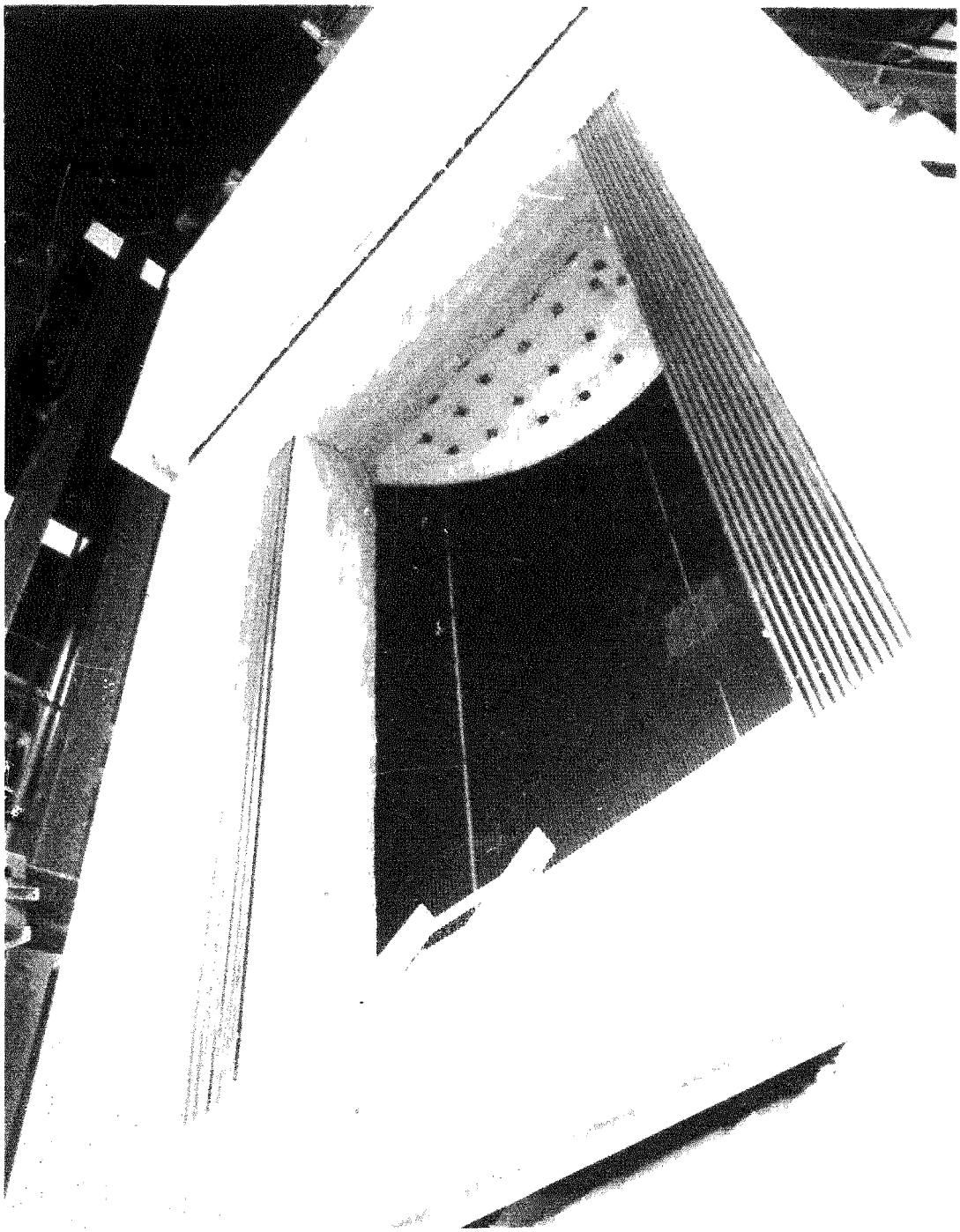

Calcium Silicate molded pipe insulation was used at pipe supports. In many of the supports, insulation and pipe clamps required some modification to improve fit-up. Pre-fabricated pipe supports are recommended for future designs offering simple installation.

Insulation details were provided on Babcock & Wilcox construction drawings. The drawings were revised as necessary to show the actual construction.

4.2.6 Electrical

Electrical construction consists of installation of power wiring and control/instrumentation or signed wiring. An electrical contractor was responsible for the installation of electric power wiring and assisted CRTF technicians with the installation of signal wiring. The electricians were licensed and certified per the latest National Electrical Code.

Power wiring was required for receiver heat trace, door motor, flux gage cooling system, ventilation fan and interior lighting. Electrical hardware installed by the electricians include conduit, wireways, power relay cabinet, junction boxes and the motor control center for the boost pump. Conduit and wireways were field routed and supported from the receiver structure. Heat trace lead cables were terminated into junction boxes located behind the receiver panels, above and below the receiver cavity. The heat trace cable and the wireways in these areas reduced accessibility to the receiver considerably.

Signal wiring was required for control of heat trace, receiver valve and door, and instrumentation. Network 90 control wiring was routed to the process control module (PCM) located in the gallery below the receiver. Heat trace control wiring was routed to the Acurex scanner also in the gallery. Electrical schematics were developed and maintained at CRTF for the purpose of routing and terminating control wiring. Checkout of the electrical hardware was performed by CRTF technicians and in conjunction with checkout of the receiver heat trace and control systems. Modifications to the control wiring were documented in the receiver control electrical drawing.

4.2.7 Door

The receiver door was installed early in the construction phase allowing sufficient time for checkout and adjustment. The tower cranes were used to erect the door and tracks. Insulation and seals were installed prior to erection. A surveyors transit was employed to level and align each track. Door level and elevational adjustment was accomplished using turnbuckles located at each door support and attached to the drive chain. This adjustment was critical to door sealability. Initial operation of the door was performed using a large handwheel attached to the gear reducer. Power wiring and automatic control was installed following mechanical checkout of the door.

Problems encountered during erection that required modification include the door seal and the door rollers. The modifications consisted of adding a second door joint seal and replacing the original rollers with flanged rollers. Design modifications are described in Section 3.7.

A final checkout of door operation was performed during initial receiver paint cure using the cavity radiant heaters. The cavity was heated to approximately 500°F and the seals inspected for signs of leakage. The seals appeared to be effective in maintaining cavity temperatures during the paint cure.

4.3 Installation of the Receiver Control System

Installation of the receiver control system involved hardware, software, and control graphics. Also, functional check-out was part of the installation to ensure proper operation of the control system. The hardware, software, and control graphics relate specifically to the NET-90. This installation included not only control but all other required functions to operate and monitor the receiver.

4.3.1 Hardware Installation

The hardware for the receiver control system is the process control unit (PCU) of the NET-90. A PCU consists of control and process I/O modules, card cage, power supplies, and termination units. The hardware installation for the receiver PCU required only integration of the module and termination unit, since the other hardware was already installed in the cabinet at the factory. Also, installation of the hardware required setting the cabinet in place within the receiver control module and supplying 120-volt power.

Power is provided by an uninterruptible power supply. The control and process I/O modules are housed by a card cage called the module mounting unit (MMU), which provides power and communication for the module. To achieve proper data communication, each module is assigned and installed with a unique address. The address is established by setting dipswitches located on the module. Some modules have additional dipswitches to establish desired options.

The termination units provide the interface between the modules and field wiring and perform process I/O filtering and isolation. Dipshunts are used to establish the required I/O type (i.e., 4-20 milliamps, 1-5 Vdc, 24 Vdc, 220 Vac, etc.) for each I/O point. Each termination unit has terminal strips for attachment of the field wiring and a cable lug for interconnection to the corresponding I/O module.

The initial hardware installation consisted of setting the module's dipswitches, placing the modules in the MMU, setting termination dipshunts, terminating field wiring, and connecting intercomponent cables. Once this was complete, the PCU was powered up and functional check-out was performed.

4.3.2 Software

The software of the control system was installed in the receiver's PCU hardware control modules. These are "smart" modules, which interpret and command I/O modules, execute control schemes, and communicate data and

commands for the operator interface units (OIUs) and between modules. These tasks are performed according to their software configuration.

The software configuration was installed by the use of menus, prompts, and fill-in-the-blanks. Firmware like this is common in modern control systems to install custom software. This method enables standard, preformatted load sheets to be used for ease of programming.

Installing the software for the I/O modules is straightforward, since they perform a known task for any installation. Consequently, their configuration is prestructured so that only filling in the blanks is necessary for the most part. However, the control modules are more flexible, since control schemes vary from one installation to another.

The software that implements the receiver control scheme is installed in the multi-function controller (MFC) module. This software performs the control scheme in the form of basic mathematical, logical, and algorithmic functions. These functions, or Bailey functions, are preformatted and operate according to the MFC's firmware structure and programming defined by the control engineer.

There are about 90 Bailey functions available to configure the control scheme, and each function is identified and configured by a unique function code number. Each individual function configured within an MFC is uniquely represented by a block number. The MFC has 2048 blocks, of which the first 30 (0-29) are fixed blocks (system defined) and the remainder (2018) are user configurable. The MFC executes these blocks in sequential order from 0 to 2047 over and over again as fast as possible.

The methodology of software configuration for a digital controller, such as an MFC, is important for proper and effective closed-loop control. Since the MFC executes the blocks sequentially, it is imperative that the input to each block be defined by a previous block so that cycle-time time delays are eliminated. This establishes the basic control structure of first sampling the inputs, executing the control functions in order of solution, then driving the outputs.

The MFC performs more than closed-loop control. It performs functions such as engineering calculations, equipment protection functions, and on/off controls, which are termed 'non-closed-loop functions.' It was necessary to establish a general block structure by functionally grouping blocks so that additions, modifications, and trouble-shooting could be done easily and in a logical manner. An important consideration for block grouping, or configuration grouping, was that blocks 1025 thru 2047 could not be configured to perform external input or output functions because of firmware restrictions. Consequently, the non-closed-loop functions are located in blocks 1025 and higher, and their corresponding I/O functions are located in the lower blocks, since a cycle-time time delay (0.25 seconds) was deemed inconsequential.

The basic block structure that follows was initially developed according to the configuration methodology when the amount of I/O and closed-loop control was first established.

BLOCKS	DESCRIPTION
0 - 29	System Fixed
30 - 249	Inputs
250 - 799	Closed-Loop Control
800 - 1024	Outputs
1025 - 2047	Other Functions

This basic block structure was further subdivided during detailed development of the configuration. The effort culminated in a more inclusive but still general block structure, shown in Table 4-I. This table represents the configuration structure used to install the required detailed software in the MFC of the receiver.

4.3.3 Control Graphics

The control graphics for the receiver were installed in the OIUs to provide the operator with customized control and monitoring capability. These custom control graphics mimic the receiver's equipment layout, geometry (2-D

only), and interrelationships for three general modes of operation - start-up, on-line, and shutdown.

A control graphics page, displayed on the CRT, consists of static and dynamic items. The static items are fixed descriptions, diagrams, and component symbols, whereas the dynamic items change according to the process, control scheme, and inputs from the operator. These items are displayed in one of eight selectable colors. Any one graphic may contain up to 100 dynamic items. All static items on a graphic are considered "background," whereas all dynamic items are considered "foreground."

Each of the nine control graphics installed for the receiver were initiated on sectioned paper. Using these paper graphics, the background was entered first, then the foreground. Several modifications were required for each to achieve the desired configuration. Entering control graphics required a special detachable graphics keyboard, since the operator's keyboard does not have the special graphics keys required.

TABLE 4-I

GENERAL BLOCK STRUCTURE OF SOFTWARE CONFIGURATION

BLOCK NUMBERS	DESCRIPTION
0 - 29	Controller Fixed Blocks
30 - 59	I/O for Control Interface Slaves
60 - 156	Digital Input Groups
157 - 188	Analog Input Lists
189 - 199	Module Bus Inputs
200 - 249	Operator Inputs
250 - 349	CONTROL - Analog West Zone
350 - 449	CONTROL - Analog East Zone
450 - 549	CONTROL - Digital West Zone
550 - 649	CONTROL - Digital East Zone
650 - 795	CONTROL - Spare Blocks
800 - 824	EPL I/O
825 - 849	Trending
850 - 1024	Exception Reports
1025 - 1099	Digital Valves (Open/Close) Logic
1100 - 1499	Calculations
1500 - 1799	Automation Logic
1800 - 2047	Equipment Protection Logic (EPL)

4.3.4 Functional Check-Out

Once the control system was installed, functional check-out was performed to ensure proper operation of the control system before the receiver was tested. The functional check-out of the hardware installation consisted of verifying that the I/O modules were operating correctly and the input values and output signals were proper. This check-out was very involved, because it is time consuming to achieve the goal of ensuring complete functional operation of the hardware.

The functional check-out of the software consisted of verifying that the conversion to engineering units was proper and that the control and equipment protection logic functioned properly. This was performed by simulating inputs, then verifying outputs and actions that are taken automatically. In particular, the functionality of the temperature control algorithm was verified by configuring a simple thermodynamic model of the receiver within the controller module, then interfacing the model to the algorithm. This particular check-out was instrumental in discovering and resolving functional problems before the receiver actually operated.

As in any installation, several problems were encountered and resolved. Many of these problems were a result of inadequate documentation by the manufacturer, which is not uncommon, so that trial-and-error, experience, and common sense prevailed to resolve them. Some of these solutions resulted in modifying hardware and software installation, and others required computer chip upgrades by the manufacturer for certain modules. During operational check-out of the system, the operators requested changes in the control graphics to improve the operator's control and monitoring capability.

SECTION 5

RECEIVER TESTING

S. Saloff, M. Lanning & G. Riley
McDonnell Douglas
Astronautics Corp.

The testing of the receiver was divided into two phases: 1) pre-operational check-out; and 2) operational testing. Pre-operational check-out was done to confirm the proper operation of the receiver, and perform initial tuning of the controls. Operational testing was divided into seven specific tests designed to collect data on the performance and capabilities of the receiver.

5.1 Pre-Operational Check-Out Tests

Operational check-out tests were performed on the receiver. These tests were performed to "shake down" the system, develop and verify heliostat warm-up patterns, familiarize the test crew with the receiver fill and drain sequence and modify these sequences as required. The check-out tests were also used to verify emergency flow response of the receiver system and perform cold and hot flow tuning of the receiver control valves. These check-out tests were essential and were made before performing any of the operational tests.

5.1.1 Heliostat Patterns

Operational check-out of aiming strategies for the heliostats, developed in Section 3.3, was required before beginning to evaluate the performance of the receiver. Check-out testing was performed for three heliostat patterns: (1) normal operation, (2) sunrise warm-up, and (3) late morning/midday warm-up.

Normal Operation

The baseline heliostat configuration and aim strategy described in Section 3.3 for normal operation was based on four main design requirements: (1) total incident power of 4.84 MW, (2) predicted absorbed power of 4.5 MWth, (3) design flux levels of 600 kW/m^2, and (4) minimization of spillage losses.

Several check-out tests were conducted to verify that the aiming strategies generated symmetrical flux distributions at solar noon. In addition, peak flux levels were monitored to assure the maximum design flux of 770 kW/m^2 was not exceeded. The technique for determining the flux distribution was based on data obtained from back-tube thermocouples, convective-cooled flux gages, flow-rate measurements, and finally, a visual examination of the beam projection on the receiver cavity.

To verify that the aiming strategy produced a symmetrical flux distribution, the base-line configuration was tested within 30 minutes of solar noon, when the incident power on each half of the receiver was theoretically balanced (based on a symmetrical heliostat field).

Preliminary operational test results obtained in December 1986 indicated that the absorbed power was biased toward the west-half of the receiver requiring an aim-point bias of 0.27 m east of centerline to balance the absorbed power on the receiver at solar noon. This configuration was retested in March of 1987 after a 2-month schedule delay. A quick-look data evaluation then indicated that the absorbed power was then biased toward the east half of the receiver at solar noon. Further testing is required to determine the cause of this apparent shift between December 1986 and March 1987.

A new vertical aim-point location was selected, this time only 0.17 m east of centerline. Here again, the absorbed power was still slightly biased toward the east half. As a result, a decision was made to relocate the aim points on the receiver centerline for the remainder of the test program. This shift back to the centerline was large enough to bias the

Normal Operation

The baseline heliostat configuration and aim strategy described in Section 3.3 for normal operation was based on four main design requirements: (1) total incident power of 4.84 MW, (2) predicted absorbed power of 4.5 MWth, (3) design flux levels of 600 kW/m^2, and (4) minimization of spillage losses.

Several check-out tests were conducted to verify that the aiming strategies generated symmetrical flux distributions at solar noon. In addition, peak flux levels were monitored to assure the maximum design flux of 770 kW/m^2 was not exceeded. The technique for determining the flux distribution was based on data obtained from back-tube thermocouples, convective-cooled flux gages, flow-rate measurements, and finally, a visual examination of the beam projection on the receiver cavity.

To verify that the aiming strategy produced a symmetrical flux distribution, the base-line configuration was tested within 30 minutes of solar noon, when the incident power on each half of the receiver was theoretically balanced (based on a symmetrical heliostat field).

Preliminary operational test results obtained in December 1986 indicated that the absorbed power was biased toward the west-half of the receiver requiring an aim-point bias of 0.27 m east of centerline to balance the absorbed power on the receiver at solar noon. This configuration was retested in March of 1987 after a 2-month schedule delay. A quick-look data evaluation then indicated that the absorbed power was then biased toward the east half of the receiver at solar noon. Further testing is required to determine the cause of this apparent shift between December 1986 and March 1987.

A new vertical aim-point location was selected, this time only 0.17 m east of centerline. Here again, the absorbed power was still slightly biased toward the east half. As a result, a decision was made to relocate the aim points on the receiver centerline for the remainder of the test program. This shift back to the centerline was large enough to bias the

absorbed power from the east to the west half of the receiver. Although the aim-point locations did not balance the power distribution at solar noon, time constraints prevented further refinement to the normal operational heliostat pattern before the start of testing.[1]

Finally, a visual examination of the beam projection on the upper and lower surfaces of the aperture frame indicated a satisfactory vertical distribution of the beam.

The collector field configuration used on the final day of operational check-out is shown in Figure 5.1.1. From the base-line configuration described in Section 3.3, 189 heliostats, 2 nonoperational, were used.

FIGURE 5.1.1
NORMAL OPERATION
ACTUAL FIELD CONFIGURATION

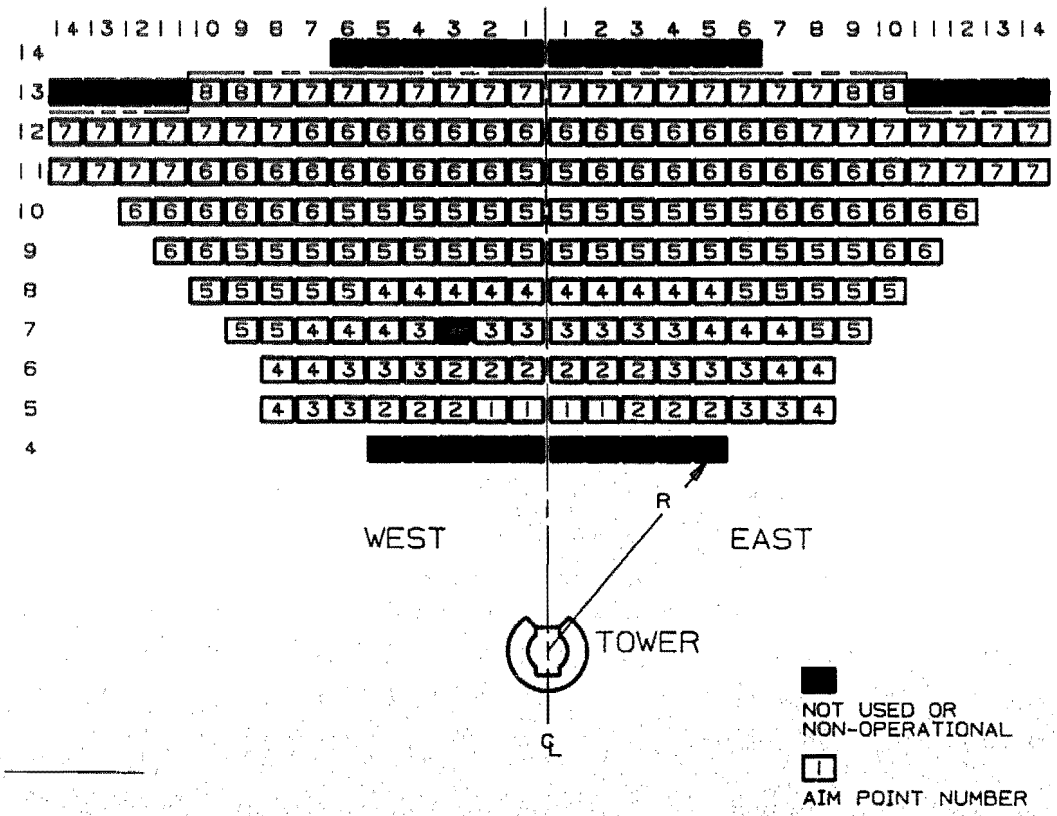

1. A more detailed evaluation of the power sensitivity to aim-point locations is discussed in Section 6.1.2.

Figure 5.1.2 depicts the flux distribution obtained from the air-cooled flux gages from the collector field configuration shown in Figure 5.1.1.

FIGURE 5.1.2
PANEL FLUX DISTRIBUTIONS

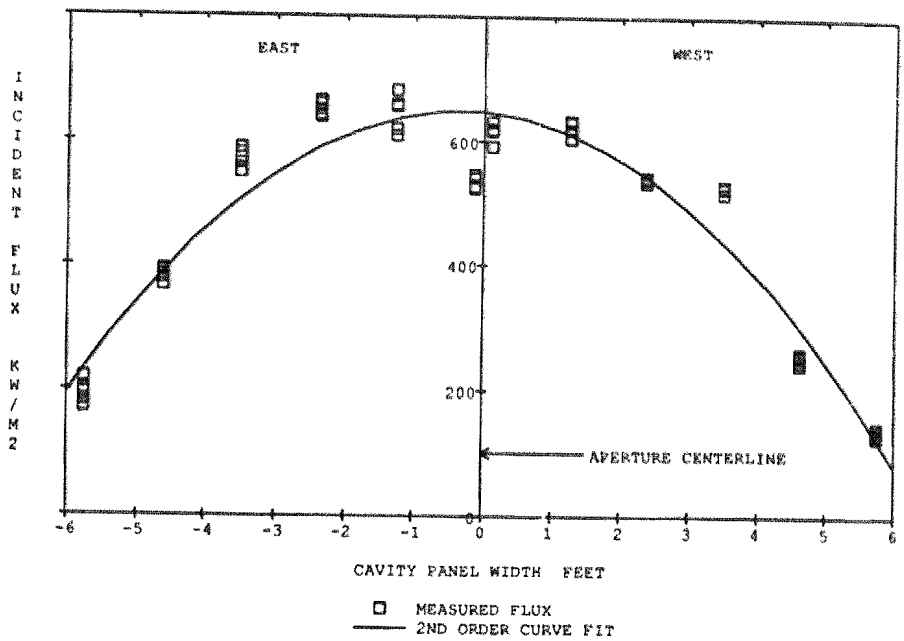

Sunrise Warm-Up

The sunrise warm-up pattern was developed to warm the receiver panels above the freezing point of salt within approximately 15 minutes and at the same time to distribute the incident flux evenly over 100 percent of the receiver surface. As discussed in Section 3.3, preliminary work was completed by McDonnell Douglas using its CONCEN computer code. Predictions made by CONCEN indicated only 33 heliostats were required to warm the receiver panels from ambient to 1000°F. However, after discussions with Sandia and on-site McDonnell Douglas personnel, it was felt that 33 heliostats were insufficient to warm the receiver panels immediately following sunrise. It

should be noted that approximately 75 percent of the heliostat field was targeted on the MSEE receiver for the early morning warm-up pattern. Also, experience gained during heliostat pattern development during the MSEE program indicated the aim-point locations selected by CONCEN, all located on the centerline of the cavity, were not capable of evenly distributing the flux to all areas of the receiver panels. Therefore, a new sunrise warm-up pattern, described in Section 3.3, was developed and tested on the receiver. Preliminary test results indicated the aim points were correctly located, although a few modifications were made to the collector field. The final configuration was shown in Figure 3.3.4.

Pre-operational check-out of the sunrise warm-up pattern indicated the panels could be brought up to temperature within approximately 10 minutes following sunrise. The actual temperature distributions, before and after warm-up, are shown in Figure 5.1.3.

FIGURE 5.1.3
SUNRISE WARM-UP--TEMPERATURE DISTRIBUTION ON THE RECEIVER PANEL

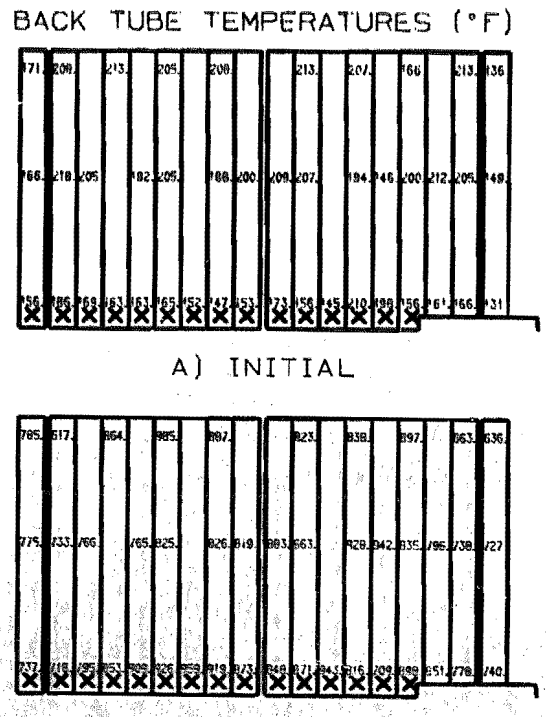

The average temperature ramp rate on the receiver tubes was approximately 100°F/min. (1.6°F/s).

Midday Warm-up

Development of the midday warm-up pattern was also based exclusively on test data. Several trial-and-error iterations were required to obtain the warm-up pattern configuration shown in Figures 3.3.3, 3.3.6, and 3.3.7.

Initially, when the midday warm-up was completed in October of 1986, panel temperatures ranged between 500° and 1000°F. However, when this warm-up pattern was retested in January of 1987, back-tube temperatures and flux gage data indicated the aim points were biased toward the west. Currently, there is no answer for this apparent shift in the aim-point locations, except for possible drift in the alignment and biasing of individual heliostats.

The old aim-point locations were biased toward the east until the panel temperatures and flux distributions were approximately symmetric. Test results indicated the panels could be warmed up within approximately 10 minutes at solar noon with 22 heliostats on target. The temperature distributions across the receiver panels, shown after warm-up in Figure 5.1.4, ranged between 500° and 1000°F. Average temperature ramp rates were approximately 100°F/min. (1.6°F/s) with an insolation level of 950 W/m^2.

FIGURE 5.1.4
MIDDAY WARM-UP--RECEIVER PANEL TEMPERATURE DISTRIBUTIONS

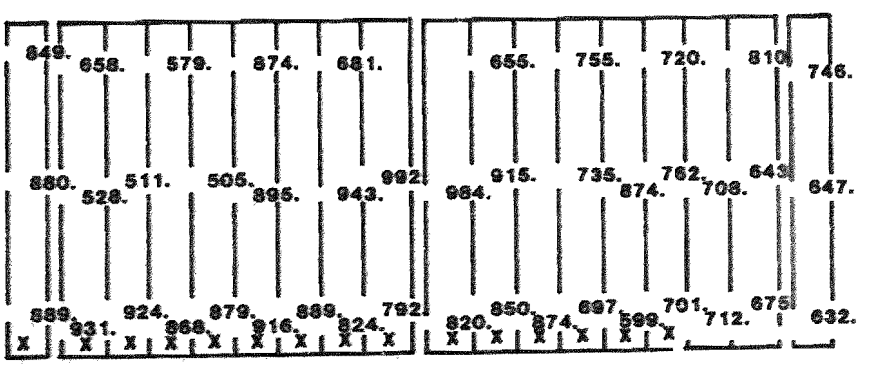

5.1.2 Receiver Salt Fill and Drain Sequences

One of the objectives during the pre-operational check-out tests was to develop fill and drain sequences for the receiver. To expedite this process, the base-line fill and drain sequences developed in the MSEE were used. In the MSEE program, both manual and automatic sequences were developed and used. Due to the time involved to configure the NET-90 computer for automatic sequences, only the manual sequences were used from the MSEE program. These sequences were then specifically modified to accommodate this receiver, which is comprised of two separate control zones. In the section on fill, the trace heaters that were used to preheat the critical components in the salt system are discussed, followed by the warm-up techniques for the receiver panel. In this receiver experiment, unlike the MSEE receiver, the cold surge tank was pressurized during the fill sequence. In the section on drain, the critical component temperatures are again discussed. During the drain sequence, the cold surge tank can be vented; the benefits are discussed. Finally, the drain times involved in draining the receiver are noted. For a detailed sequence of the receiver's fill and drain, refer to the receiver start-up and shut-down procedures (ROP#2 and #3) in Appendix D.

Receiver Salt Fill Sequence

In any receiver fill operation involving molten-salt (which freezes at approximately 450°F) the first critical sequence is to verify that the components are above the freezing temperatures of salt. These temperatures are controlled by an active computer system; however, the control room operator has to verify them before starting the fill sequence. The computer does not lock out control of critical components if temperatures are not above freezing for salt. This verification begins with the salt valves, particularly the bellows region in the valves which is their most fragile part. Keeping the salt lines, particularly the downcomer, above salt freezing temperatures is critical, because if the receiver is filled and the downcomer becomes plugged with frozen salt, it would not be possible to drain the receiver. The headers in the receiver, the cold and hot surge tanks, and the vent lines from the surge tanks must also be above salt's

freezing temperature. Once the piping temperatures are confirmed to be above freezing for salt, the next step is to verify that the temperature of the receiver panel is acceptable. The panel can be preheated several ways. On clear days the heliostats are primarily used to warm up the panel to above the freezing temperature for salt. On cloudy days or partly clear days, cavity heaters that are located in the floor of the receiver can be used to preheat the receiver panel with the door closed. Both of these techniques were thoroughly evaluated to determine the most efficient way to preheat the receiver panel.

Once the hardware temperatures are verified to be above freezing for salt, the actual receiver salt-fill sequence begins. The receiver is flood filled through both the riser and downcomer and vertically through all the tubes in the panel. It is very important to monitor the various temperatures during this fill operation to verify that critical events are occurring. The first temperature to monitor is TE161 just above the hot tank on the downcomer. This thermocouple is inside the piping and reacts instantly when the salt passes across it, assuring the operator that the salt is now proceeding in the riser and downcomer toward the tower. Thermocouples in the tower on the riser and downcomer are then monitored as the salt progresses up the tower toward the cold surge tank. Once the salt reaches the cold surge tank, the level indicator in the tank (LT151) reacts, indicating that the salt is at that level. At this stage, if the sun were to disappear, the door could be closed, and the panel would still remain above the freezing temperature of salt during the remainder of the receiver salt-fill process.

Next the salt panel temperatures are monitored in the receiver, these temperatures indicate when salt has completely filled the receiver and enters the hot surge tank. Once the level indicator for the hot surge tank, LT161, indicates a 56-inch salt level, the receiver is completely filled and the remainder of the receiver salt-fill process places the receiver in serpentine flow. Upon obtaining the 56-inch level in the hot surge tank, the drain valves are closed and the purge valves are sequenced closed to establish the serpentine flow through the receiver. The path of the salt flow is now from the riser, through the receiver panels, returning to the storage tanks through the downcomer. Subsequent to establishing serpentine

flow through the receiver, operating conditions in the surge tanks are established.

First, the level in the hot surge tank is reduced to 30 inches and the hot tank level control is activated. This allows plenty of volume in the hot surge tank to allow surges in level.

After this, pressure control in the cold surge tank is activated, causing the riser throttling valve (FCV 151) to come open and raise the cold surge tank pressure to 300 psi. Then air is charged from air cylinders into the cold surge tank to establish a normal operating level of 80 inches. This provides enough pressurized air in the system to maintain flow in the receiver for approximately 90 seconds, in the event of a pump trip, and allows time to remove the heliostats from the receiver.

Receiver Salt Drain

Before beginning the salt drain sequence in the receiver, it was extremely critical that all the hardware temperatures be verified to be above the freezing temperature of salt. The stagnant drain lines, in which salt does not flow during the actual operation of the receiver, must be checked to be above salt freezing temperatures.

The actual drain sequence was a modified version of the manual drain sequence used in the MSEE program, with one major difference. The cold surge tank in this experiment was vented, allowing the pressure to be reduced before it was drained. This simplified the drain process and avoided a potentially damaging two-phase flow that could have occurred through the control valves when the system was under higher pressure. Also, it shortened the drain time, because the control valves and all the drain and purge valves could be fully opened, allowing a faster drain of the receiver. The final drain time was approximately 20 minutes. This salt-drain duration ensured all of the receiver's residual salt was completely drained.

An important point noted during the operation of the fill and drain sequences was the importance of having large volume hot and cold surge tanks to avoid spilling salt, and to provide for venting the cold surge tanks during draining to avoid a potentially damaging two-phase flow.

5.1.3 Emergency Flow Response

The receiver was designed to provide emergency salt flow through the panels in case of a failure of a salt pump or the riser flow control valve (FCV 151). This capability was important so the panels would continue to be cooled in case the heliostats did not defocus quickly enough. Verification of the emergency flow response was done without the heliostats being focused on the panels and with the receiver in cold-salt serpentine flow. The test was performed by intentionally inducing a salt pump trip (by pulling the electrical breaker to the pump motor). The resulting emergency flow response was as expected and fulfilled the design requirement. The time response of the emergency salt flow from the cold surge tank is shown in Figure 5.1.5.

FIGURE 5.1.5
EMERGENCY FLOW RESPONSE

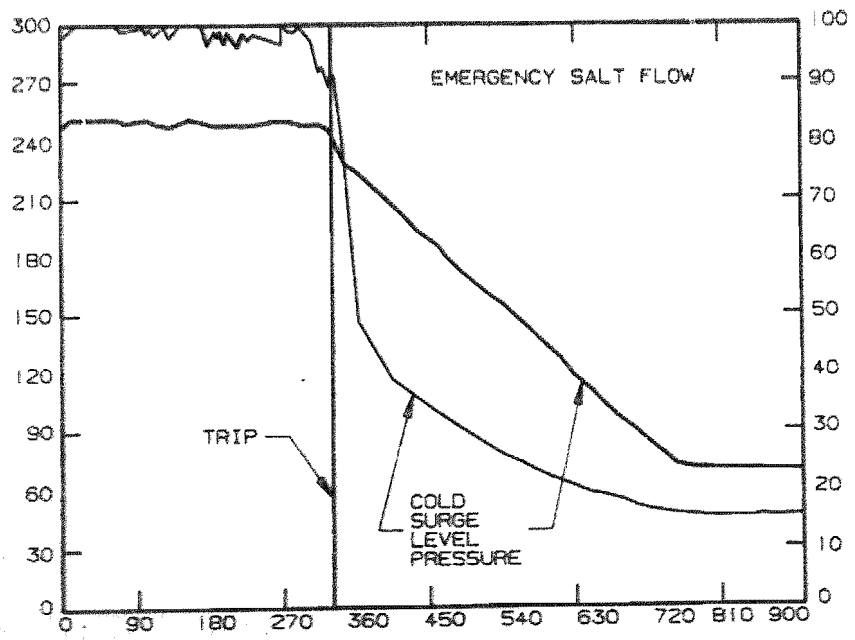

The emergency flow time for the cold tank response illustrates the initial immediate drop in cold surge tank pressure due to the tripped pump and the time required for the flow-control valve in the riser to be commanded and actually to close. Closure of this valve is critical and is an important design issue. It must preserve enough pressure in the cold surge tank to achieve the time required for emergency flow. After this initial immediate pressure decrease, the pressure and level in the cold surge tank and the salt flow through the panels naturally decay until terminated by an operator.

5.1.4 Cold Flow Tuning of the Receiver Controller

Cold flow tuning of the receiver controls was performed to achieve stable operation and fast response of the receiver's molten-salt levels, flow-rates, and pressures. The receiver's salt flow path and relative control valve locations are illustrated in Figure 5.1.6. Cold flow "tuning" consisted of establishing five control loops in three specific areas:

1) Cold Surge Tank Pressure Control (FCV151),
2) Panel Salt Flow Control
   a) West Zone Flow Control (FCV101)
   b) East Zone Flow Control (FCV103),
3) Hot Surge Tank Level Control
   a) Flow to Hot Storage Tank (FCV161)
   b) Flow to Cold Storage Tank (FCV162).

These loops were tuned to provide fast response time yet stable control over the entire operating range of the receiver.

FIGURE 5.1.6

RECEIVER COLD FLOW LOOP

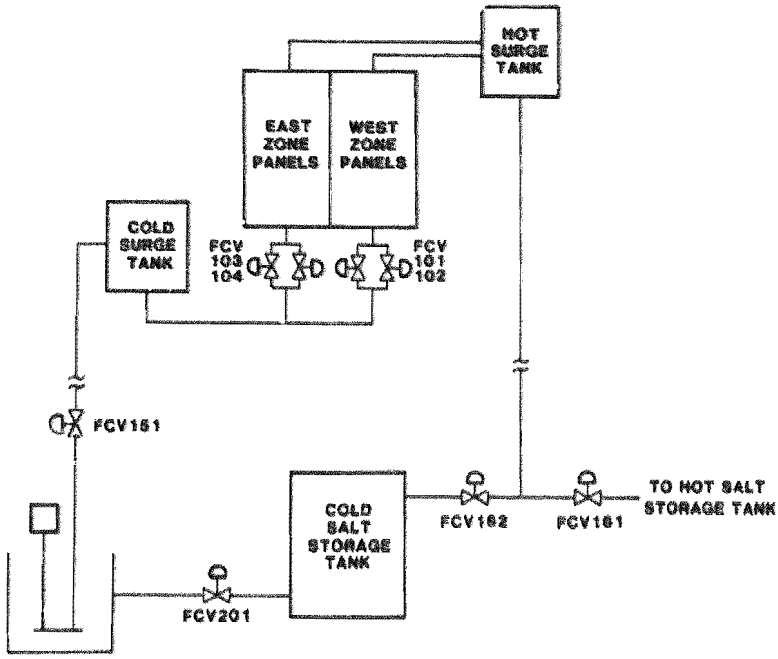

Pressure Control of the Cold Surge Tank

Originally the cold surge tank controls were designed to control on the level; however, initial operation proved the level transmitters to be unreliable. Therefore, the cold surge tank was changed to pressure control. This was acceptable since pressure and level control are essentially the same for a closed volume and an incompressible fluid (salt) with a cover gas. To prevent salt from being forced into the top of the tank or from being drained empty in an attempt to maintain pressure, the level signal was used to override the valve command open (low level) or closed (high level). The functional block diagram of this pressure control loop is illustrated in Figure 5.1.7.

FIGURE 5.1.7

BLOCK DIAGRAM OF THE PRESSURE CONTROL LOOP

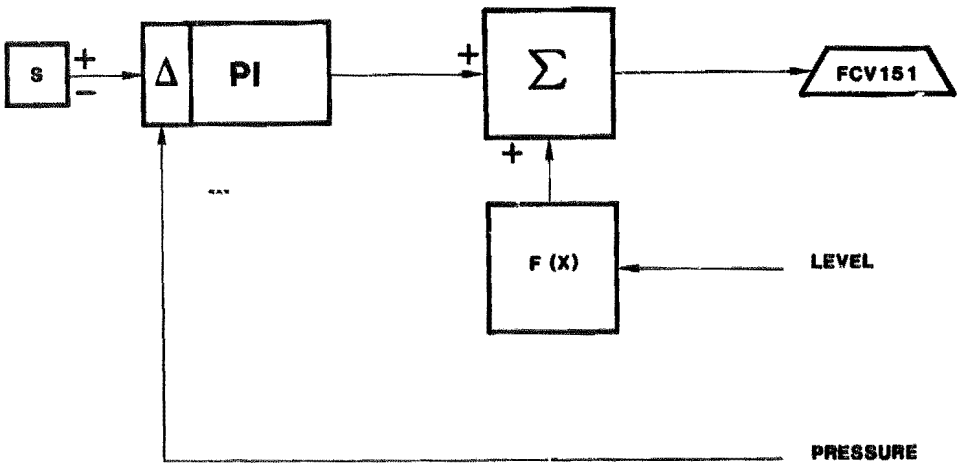

Control of the Receiver's Salt Flow Rate

Controlling the flow rate of the salt through each control zone was critical to achieving control of the outlet salt temperature. The flow rate of salt is physically manipulated by modulating control valves to achieve control of the flow. Each control zone had two fail-open, modulating control valves plumbed in parallel for redundancy. Each parallel valve was designed to accommodate flow rates over the entire operational range plus 10-15 percent over design point. However, during initial receiver operation the redundant control valves were damaged, (temperature problems resulted in bellows damage), so that tuning and operation were performed with only one valve for each zone.

The "tuning" procedure to control the flow rate of salt and its results are presented as a whole, since the tuning process for each control zone is identical. Because the control valve is the physical interface between the controls and the process, valve characterization is important. "Tuning" a zone consists of calibrating and characterizing the valve, then of

linearizing the control software for optimum capability to control flow over the entire flow range.

The following is the procedure used to establish optimum flow control for each control valve:

1) Calibrate Valve (Stroke Command vs Actual Command),
2) Characterize Valve (Flow Rate vs Stroke Command),
3) Linearize Valve Characteristics, and
4) Tune Flow Controller.

Valve calibration was done by adjusting the zero and span of the valve actuator so that the 0-100 percent stroke command from the control system generates a corresponding 0-100 percent actual valve stroke. To provide full-closure and full-opening of the valve, calibration is actually done so that a 5 percent open command results in 0 percent actual, and a 95 percent open command results in 100 percent actual. Calibration in this way assures that the valve can be commanded fully closed and open. Figure 5.1.8 illustrates this valve calibration, where percent valve command (% CO) is the control output from the control system, and percent valve position (ZT) is the actual measured stroke.

FIGURE 5.1.8
CONTROL VALVE STROKE COMMAND VS. ACTUAL

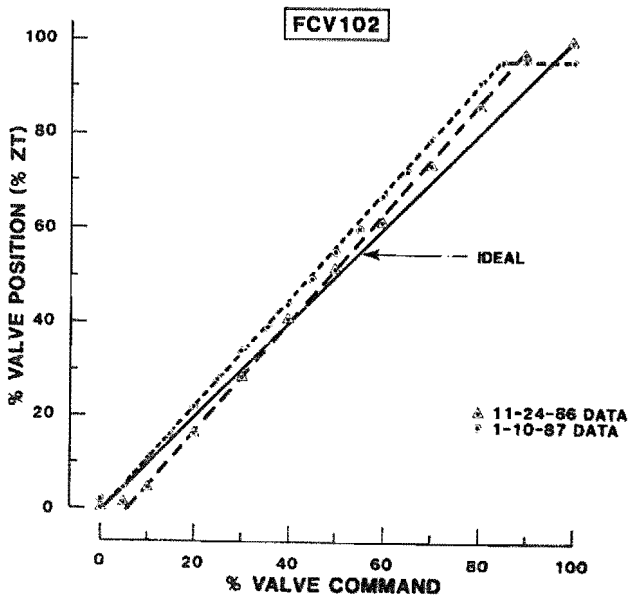

Actual valve calibration was not as easy because the total valve stroke was physically only 3/8 inch. During the course of testing, the calibration would drift significantly (for no apparent reason), making numerous recalibrations necessary. Also, the valve actuator would limit cycle (chatter) ±5 percent stroke about the stroke command. Although the chattering was intermittent, it caused significant flow-rate pertubations (±3,000 lb/h). For the most part, this did not cause a control problem since the chatter was high frequency at approximately 1 Hz, although data evaluation was somewhat complicated by these flow pertubations.

Valve characterization is important to verify how well the vendor met the specifications and to determine whether or not software linearization of the output signal is necessary. Valve characterization is done by commanding the stroke in 5 percent increments from 0 to 100 percent so that a flow versus stroke command curve can be generated. Also, pressures are recorded to generate a flow coefficient (C_v) curve.

The C_v curve is used to verify the valve design specification. Figure 5.1.9 shows both the specification and actual curves for the current experiment. As can be seen, the actual curve is less than that specified and does not have the same relative shape or contour, known as the C_v characteristic. The C_v characteristic is the standard method of specifying control valves. This particular valve was specified with an equal percentage C_v characteristic.

FIGURE 5.1.9

CONTROL VALVE ACTUAL C_v CURVE VS. SPECIFICATION

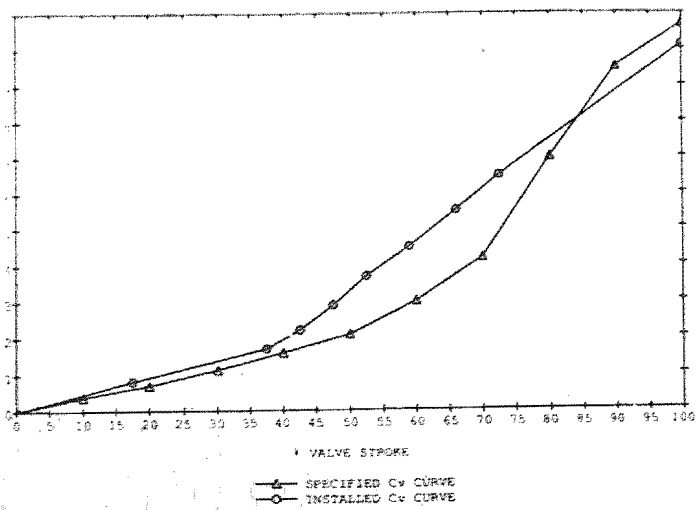

The flow curve has more practical implications relative to controls. Since the valve is regulated from 0 to 100 percent to control the flow rate, it is desirable to have a linear relationship between the control system command and the flow rate. This would provide an equal change in flow rate with an equal change in valve command over the entire flow range, important to achieve the optimum capability to control flow and ultimately the outlet's salt temperature.

Figure 5.1.10 illustrates the flow curve in which % CO is the control output command from the control system. The valve calibration is an integral part of this flow curve since the curve is a function of the control system command and not actual valve position. Linearization of the valve flow characteristics became necessary because the curve was highly nonlinear. A one-to five slope (delta flow/delta % CO) change over the flow range existed for the valve. This caused a control problem, because the flow controller was tuned for the higher gain region, causing poor response in the low-gain regions. If the controller had been tuned in the low-gain region, control instability would have occurred in the high-gain region.

FIGURE 5.1.10
STROKE COMMAND VS. FLOW-RATE

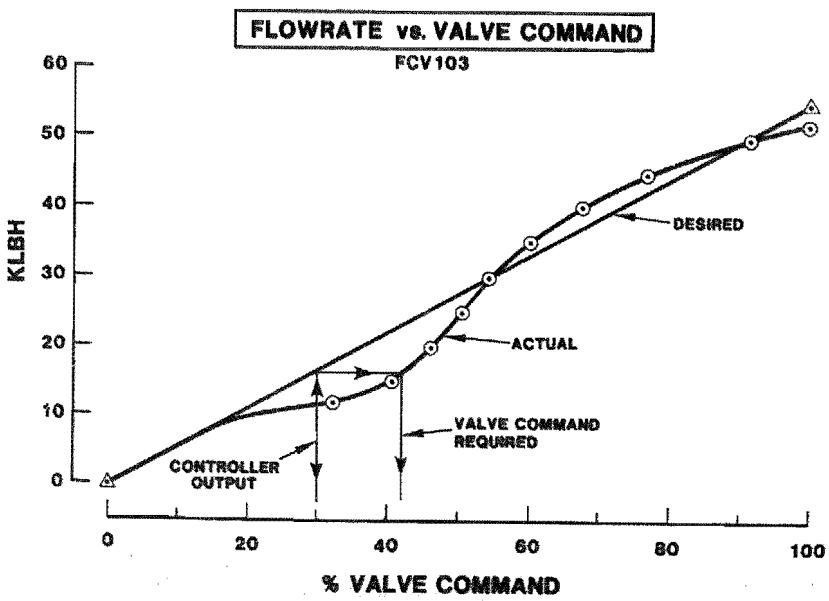

Valve linearization was accomplished by forcing the flow curve to be linear. This was done by generating a linearization curve that manipulated the stroke command sent to the valve in the control software. The linearization curve was produced using the flow curve in Figure 5.1.10. First, a desired linear flow curve was chosen so that the desired flow rate at 100 percent stroke is a little higher than the actual rate achievable. Then the linearization curve can be generated as illustrated in Figure 5.1.11. A point on this curve was determined by selecting a control command (% CO), then moving vertically until the desired flow curve is intersected, then moving horizontally until the actual flow curve is intersected, then finally moving vertically back down to the percent CO scale and reading the actual control command required. This procedure is used for numerous points and it generates table-of-controller output (% CO) versus valve-command (% VC) values. These points are plotted to generate the linearization curve.

FIGURE 5.1.11
LINEARIZATION CURVE

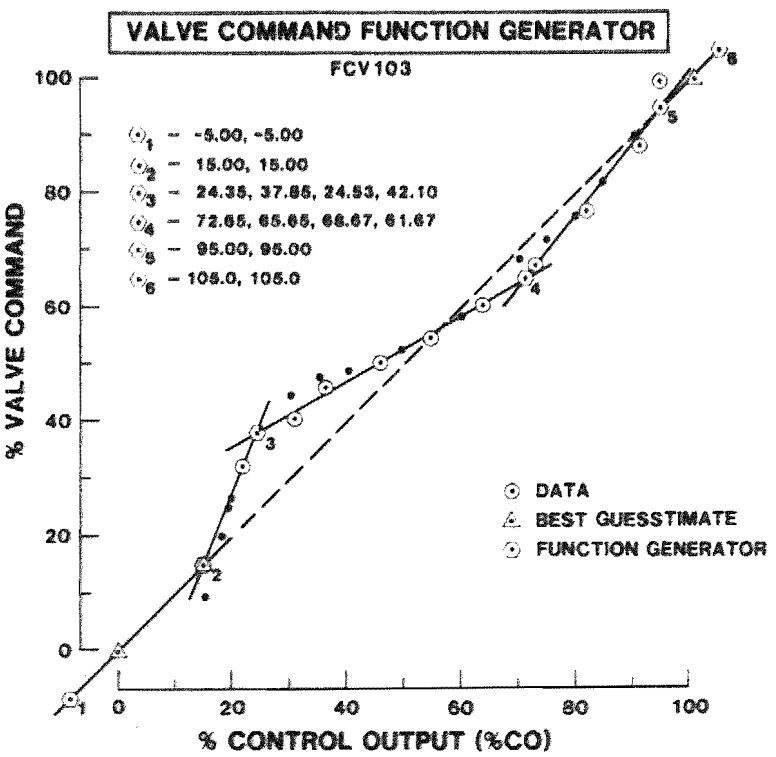

The linearization curve is implemented in the control software by a function generator, which may contain up to six coordinates to produce a piecewise linear approximation. Figure 5.1.11 illustrates the actual linearization curve and that used for control, approximated by the function generator. The actual linearization-curve points could have been run through a curve-fit program to generate a polynomial function that could be used in place of the function generator. However, since the valve calibration is an integral part of the linearization curve and the calibration tends to drift regularly, the linearization curve must be updated often. Modifications to the function generator are much easier to make than those to a polynomial, simply because the polynomial requires the generation of a curve-fit, and the error produced by the function generator is insignificant. Figure 5.1.12 is a block diagram illustrating the resulting control loop configuration. The function generator is inserted between the flow controller (PID) and the valve command signal to provide control loop linearization resulting in optimum control of the salt flow rate.

FIGURE 5.1.12
FLOW-RATE CONTROL LOOP

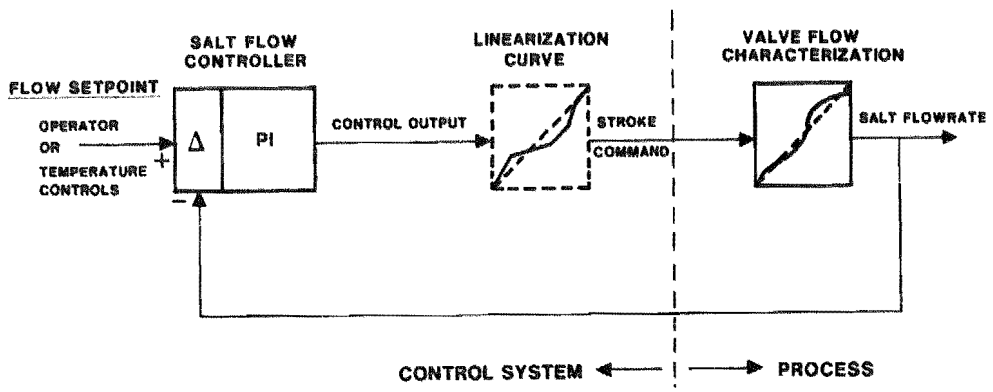

Flow control tuning was performed to produce a fast-as-possible response time, yet a stable flow control loop. The flow controller (PID), as illustrated in Figure 5.1.12, used proportional-plus-integral (PI) control. The derivative (D) term was not used because of noise amplification of the flow measurement. The use of a PI controller for flow control is typical for most industrial applications.

Control response tuning was accomplished by making flow step changes over the flow range. Since the response time of the flow loop was faster than the data acquisition system could record, response analysis and tuning was done solely from the control system console.

The tuning effort found that the predicted proportional gain (KP=0.9) from the simulation nearly matched the actual (KP=0.8). The integral gain however was much higher than predicted, a factor of 7 (KI=20). Having such a high integral gain was indicative of a valve with too high a gain (high process gain), caused by the valve's mere 3/8-inch stroke. Even though the actual flow response was not quite as good as predicted, the flow control performance was adequate to achieve control of the outlet's salt temperature, which was the goal of this tuning.

Controlling the Level of the Hot Surge Tank

Salt level control in the hot surge tank was accomplished by one of two control valves at the bottom of the downcomer. When the salt temperature at the bottom of the downcomer exceeded 750°F, automatic logic switched the level control to FCV161 for salt flow to the hot storage tank. When the temperature fell below 700°F, the automatic logic switched the level control to FCV162 for flow to the cold storage tank. This level control switching was accomplished by changing the level set points of the controllers for each valve. The valve that is to control level operates with a controller set-point for the desired hot surge tank level. The other valve controller receives a set-point 15 in. higher. As long as level is controlled at the lower level, the second valve remains closed. If the primary valve fails to control, however, the second valve provides protection from overflowing the

hot surge tank. This automatic level-control set-point switch over operated as designed and the level was maintained within 2 inches during the transition.

FCV162 level control tuning for salt flow to the cold storage tank from the hot surge tank was accomplished with the receiver in serpentine flow. The valve characteristic of flow rate versus valve stroke command was determined. Even though the characteristic curve was nonlinear, it was adequately linear for control purposes. This level control was a simple, single-element control loop. The level controller (PID) used proportional-plus-integral (PI) terms for control. The derivative (D) term was not necessary, since response was adequate without it. Level set-point step changes were made to confirm fast response yet stable control without oscillation.

FCV161 level control tuning for salt flow to the hot storage tank was done with cold salt, then verified when hot salt was first produced. The tuning constants for cold salt were found to be the same for hot salt.

This level control was a simple, single-element control loop and used the same controller terms (PI) as FCV162. Level set-point changes were also made to achieve a fast time response that was stable and nonoscillatory. The valve characteristics were not determined, since level response was excellent over the entire flow range of the receiver.

Transient Test for Maximum Flow

Once each individual control loop had been tuned, it was important to check that all the loops worked together properly. The receiver temperature was controlled by the salt flow rate so that the appropriate amount of cooling was provided for the exposed solar tubes. Thus, the flow rate through the receiver was regulated to maintain the outlet's salt temperature as incident solar energy varied. As the flow rate changed, the cold surge tank pressure and hot surge tank level controllers were capable of maintaining set-point to achieve complete control of the receiver's flow.

A maximum flow transient test was devised to verify the controllability of the receiver temperature. The flow controllers for each control zone (FCV101 & FCV103) were used to induce the transient. The flow controllers were initially set at design flow rate (half for each zone) and the controls were allowed to stabilize at design set-point (FCV151 = 300 PSIG, FCV162 = 30 inches, FCV101 = FCV103 = 48,000 lb/h). Once stable, the flow controllers (FCV101 & 103) were set to minimum flow (12,000 lb/h) for 60 seconds then to maximum flow (52,000 lb/h) for 10 seconds, finally they were set back to design flow. The ability to control the flow transient was considered acceptable, since limit cycling or instability did not occur and set-points were adequately maintained.

5.1.5 Hot Flow Tuning of the Receiver Controller

Hot flow tuning (using hot salt) the receiver's subsystem controls was performed to achieve stable control and fast response for the receiver's two salt outlet temperatures. Hot flow tuning consisted of characterizing the receiver's natural temperature response behavior and establishing the Receiver's Control Algorithm (RCA). This was done with clear-sky conditions, so that all operational parameters were known and steady insolation was available. The primary goal of hot flow tuning was to establish adequate temperature control in order to proceed to cloud transient testing where final control tuning would be performed.

Characterization of Natural Response to Temperature

Characterization of the receiver's natural response to temperature was important to verify the receiver's temperature control tuning and thermodynamic model (simulation). It was performed by making flow set-point step changes at two constant incident solar power levels of 50 and 100 percent. These power levels were relative to the percentage of the design heliostats tracking the receiver. This characterization is known as the open-loop response.

Since a percentage of the field was used, actual incident power on the panels varied from test to test. This resulted in test data at various

absorbed powers. Only one case is discussed, because all cases indicated the same result.

A natural outlet salt temperature response for one control zone at 100 percent field was performed as follows: The salt's flow rate was step-decreased in steps from 4,300 to 3,800 lbs/h and the outlet's temperature was allowed to stabilize at its final value. The temperature response curve was evaluated to determine the time delay and the time constant values. A straight line was drawn through the inflection point (maximum slope) of the response curve and through the initial (994°F) and final (1054°F) values. The 20 seconds from the time the flow set-point was stepped and the initial and inflection lines intersect represents the time delay. The 65 seconds from this same intersection to 63 percent of the final value (1032°F) is considered the time constant.

Under the same conditions, the simulation produced a 40-second time delay and a 74-second time constant. Comparatively, the actual natural response has 50 percent smaller time delay and a 12 percent smaller time constant. The time constants compare favorably, however, a factor of 2 in time delay existed. This in turn indicated the ability to increase the simulation control gains by a factor of 2.

Preliminary Receiver Control Algorithm Tuning

The Receiver Control Algorithm is comprised of three basic components (see Figure 3.8.1) for temperature control: flux feed-forward, outlet salt temperature controller (outlet controller), and back-tube temperature controller. These components were activated and tuned in a specific manner so that all three would ultimately be activated and work together properly.

Initially, only the flux feed-forward and outlet salt-temperature controller were activated. Since the flux on the panels was relatively constant, the flux feed-forward was producing a constant (bias) desired flow rate. In this configuration, the flux feed-forward component produced a desired flow rate proportional to the average panel flux, and the outlet controller corrected this flow rate with a plus-or-minus value. The corrected desired

flow rate was the required salt flow rate to produce an outlet salt temperature equal to the outlet salt temperature set-point.

The tuning constants of the outlet controller were initially set according to simulation results. The receiver was brought to steady-state at 100-percent power, then the outlet controller set-points were changed in steps for fine tuning. The ultimate outlet temperature response to a set-point change is illustrated in Figure 5.1.13, where a 27-percent overshoot, rise time of 1.6 minutes, and 4.75-minute settling time were achieved. This was done, again, at 50-percent power, where a 20-percent overshoot, rise time of 2.8 minutes, and 6.5-minute settling time were achieved. The difference in the responses was attributable to the different power levels, since the dynamics of the process change with power, or actually with flow rate.

FIGURE 5.1.13
SET-POINT RESPONSE WITHOUT BACK-TUBE CONTROL @ 100%

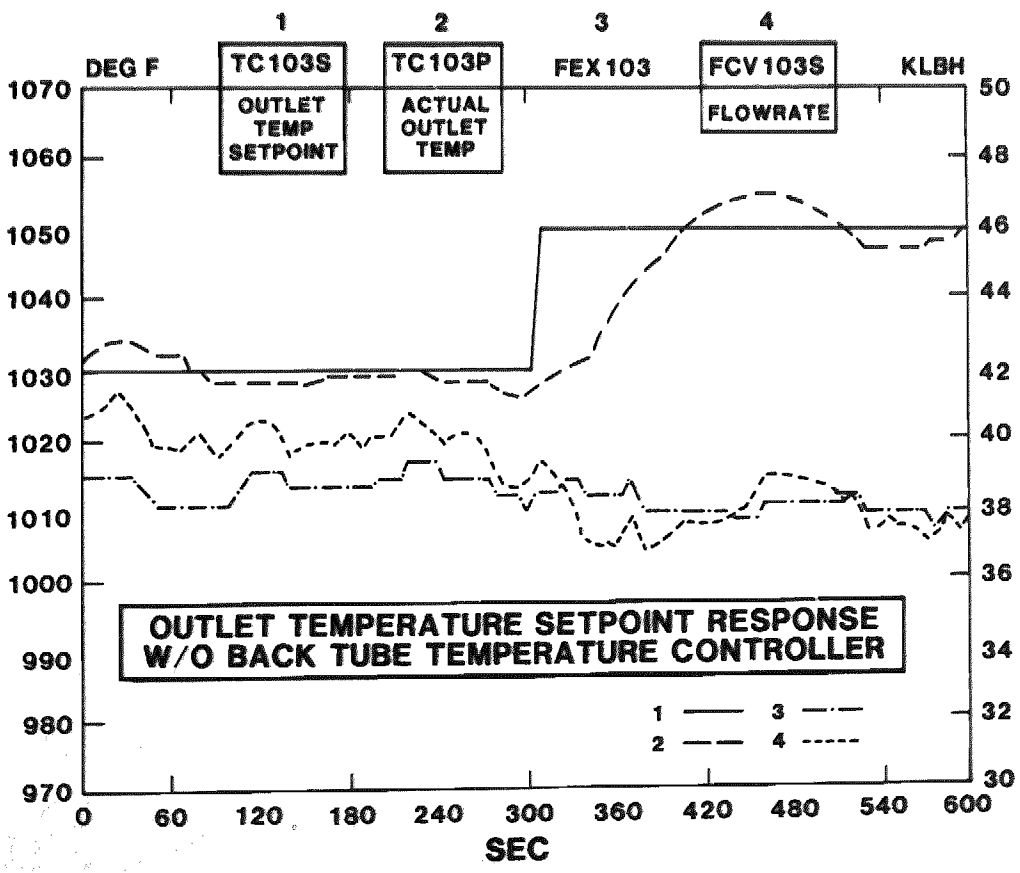

Then power was ramped off and on the receiver to simulate a cloud passing over the field. The outlet controller was set with a constant set-point and the heliostat field was symmetrically reduced from 100 to 50 percent tracking, then returned to 100 percent once the outlet temperatures stabilized. The time response achieved was a 20-percent overshoot and 6.0-minute response time.

Next, the controller for the back tube was activated so that the receiver's control algorithm was fully enabled. The tuning constants for the back tube's controller were set according to the simulation results. The tuning constants for the outlet controller were increased by a factor of 2 from the gains found when the back-tube controller was disabled. The ability to double these gains was because the back-tube controller added considerable damping and corresponding stability, as found from the simulation effort (see Section 3.9).

Set-point changes to the outlet temperature were made to tune the complete RCA. The tuning constants were changed to achieve the best possible response. The resulting set-point step response at 100-percent power is illustrated in Figure 5.1.14, where a 6-percent overshoot, rise time of 1.67 minutes and 2.33-minute settling time were achieved. The corresponding response by the simulation is shown in Figure 5.1.15, where a 15-percent overshoot, rise time of 1.67 minutes, and 4.0-minute settling time were achieved. The actual response was better than that simulated, since the natural response was found to be better and the control gains were higher.

A complete evaluation of the receiver's "controllability" is provided in section 6.5 on MSS/CTE receiver performance evaluation. Hot flow tuning primarily provided confidence in our ability to control the receiver so that testing could progress into operational tests without uncontrolled temperatures.

FIGURE 5.1.14

SET-POINT RESPONSE OF FULLY ENABLED RCA @ 100%

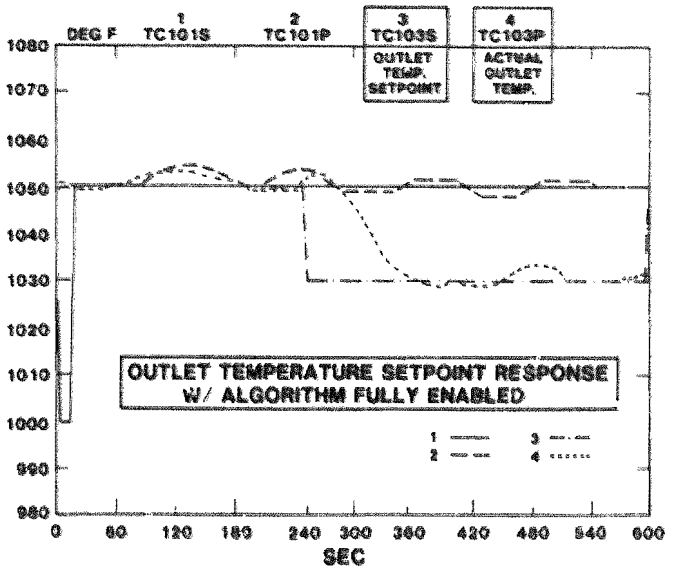

FIGURE 5.1.15

SIMULATION SET-POINT RESPONSE @ 100%

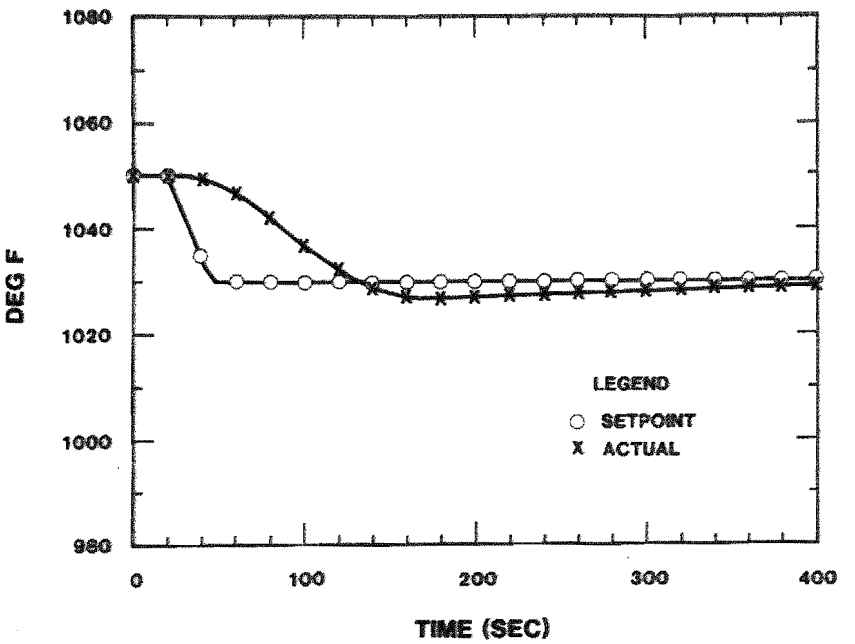

5.2 Operational Tests

Seven specific operational tests were developed in the MSS/CTE test plan to accomplish the program objectives of this experiment:

1) Steady-State Performance,
2) Simulated Clouds,
3) Flux-On and Flux-Off Thermal Losses,
4) Maximum Transients,
5) Optimum start-up,
6) Overnight Conditioning, and
7) Optimum Operation.

Six of the seven tests were completed. Number 7 was deferred to the continued testing portion of the program to be performed by Sandia National Laboratories. Each of these tests is described in the following subsections.

5.2.1 Steady-State Performance

Characterizing the steady-state performance of the receiver is essential for determining the overall efficiency of a cavity-type receiver. Steady-state performance consists of (1) steady-state absorbed power and (2) steady-state thermal losses. This section deals exclusively with the operational testing associated with item (1). Specialized tests determining "flux-on" thermal losses, item (2) is covered entirely in Section 5.2.3.

To determine steady-state absorbed power, the receiver was operated using the normal operational heliostat pattern described in Section 3.2. Testing was accomplished over a 10-day period in order to determine the receiver's performance from early morning through late afternoon. There were three requirements necessary to establish the receiver in a steady-state condition: (1) east and west half outlet temperatures controlling at the design set-point of 1050°F, (2) clear-sky conditions present throughout the test and (3) the maximum number of operational heliostats on target. The duration of each test depended on weather conditions and/or the amount of

cold salt remaining in thermal storage. Absorbed power measured in this test was compared to incident power calculated with the HELIOS computer code [26] to estimate thermal losses, more details are presented in Section 5.2.3.

5.2.2 Cloud Transient Controllability

The ability to maintain temperature control of the receiver in spite of cloud passages is an important factor relative to the overall performance of the receiver and to annual energy predictions. Therefore, specific testing was planned and performed to address the controllability of the receiver's outlet salt temperatures. In particular, this testing addressed the receiver control algorithm (RCA).

The original test plan was modified significantly to accommodate a compressed test schedule. This was possible since the tuning results of the hot flow compared favorably with the simulation results. The plan was further modified because of limitations on heliostat control; the heliostat control system was incapable of executing commands and processing updates rapidly enough to perform the original test definitions. These modifications did not however, compromise the objectives of this test.

The issue of receiver temperature ramp rate limitations arose during initial testing of the receiver. This issue is important because of thermal stress effects causing tube-to-header fatigue, which ultimately impacts the receiver's lifetime. A temperature ramp rate limit of $\pm 0.75°F/s$ was imposed to bring stress within design limits. However, in order to test and demonstrate receiver controllability in cloud transients, the receiver temperature ramp rate limit was not adhered to. The salt outlet temperature's set-point ramp rate limits remained intact. It is anticipated that the receiver temperature ramp rate limitation could be reduced in a commercial receiver by improved header design.

Another important issue during transient testing was thermal stress on tubes, which also impacts the receiver's lifetime. This issue was not new, and its magnitude was of concern from the beginning. High stresses in

the tubes are generated when the salt flow rate is disproportionate to the incident flux on the tubes. This problem manifests itself during heavy cloud transients, when the outlet temperature degrades significantly from set-point. When this occurs and the cloud clears, the temperature controls suppress the flow rate for some time even though high fluxes are present. Controlling in this fashion provides rapid temperature recovery from clouds and maximizes the receiver's output at the expense of tube fatigue. To significantly lessen tube fatigue, a new control strategy was developed in which the integrity of the original RCA was maintained.

The whole issue of a receiver's lifetime and stresses is thoroughly addressed in the thermal/structural evaluation Section (7.1.1).

To accommodate the compressed test schedule, stress requirements, and heliostat control limitations, the transient testing was performed in three categories:

1) Partial Power Transient, (100 --> 50 --> 100 percent of heliostat field),
2) Simulated West-to-East Cloud Transients with Heliostat Field, and
3) Natural Cloud Transient.

These three test categories provided the required test data for control performance evaluation.

The following paragraphs describe these testing categories and their methodology and concerns. The controllability evaluation section (6.5) presents the test results and their evaluation.

Partial Power Transients

Partial power transients were initially done to perform final control tuning of the RCA. The partial power transients were performed to determine the controllability of the receiver at different power levels and transitioning from one level to another. In general, this testing provided information

on low power operation of the receiver. Technically, this testing determined the linear response of the receiver at different power levels.

To provide data for this testing and others, the heliostat field was symmetrically divided into four groups of 25 percent. Maintaining symmetry was important so that panel flux distributions were reasonably preserved, as would be the case under low power conditions. Other percentages are possible, but loss of symmetry occurs to some degree.

Two heliostat groups of 25 percent were used to provide data relative to one condition: 50 percent power. These two groups were removed from and then aimed back on the receiver around solar noon, when insolation is nearly constant. Since a percentage of the heliostat field was used, the actual incident power on the receiver was also a function of insolation for any particular test day. The variability of insolation from day to day did not impair these tests.

Two sets of data were acquired. One set was acquired for power transient controllability, in which the two groups were removed then placed back on with a constant outlet temperature set point. The other set was acquired for temperature set-point response in which the two groups were removed, temperatures were allowed to settle, then changes to the outlet's temperature set-point were made. These data provided information relative to the linear response of the receiver for both incident power transients and outlet temperature set-point changes under rated and derated conditions.

Simulated West-to-East Cloud Transients

A simulation of a west-to-east cloud passage was performed to verify the temperature controllability of the receiver under a known and controlled transient. A west-to-east cloud transient was chosen because the prevailing winds are in the west-to-east direction and because this transient can produce the worst case situation for control. Also, the McDonnell Douglas receiver simulation effort used a west-to-east cloud passage to design and develop the RCA.

Originally, the heliostat field was to simulate the west-to-east cloud used in the design. However, the through-put limitations of the heliostat control system (HCS) prevented the simulation of the design cloud. Consequently, the simulated cloud was slowed down so the HCS was able to perform the transient. The simulated cloud used for this test had the following characteristics:

1) West-to-east direction,
2) Speed of 8 ft/s (5.5 MPH),
3) Width of 1100 feet, and
4) Transmittance of 0 percent.

Even though this simulated cloud differed from the design, it produced a worst case transient for control performance evaluation.

The heliostat field is comprised of 28 north-south columns of heliostats, 32 feet apart. Each column starting from the west was commanded off the receiver every four seconds. Once all heliostat beams were off, they were commanded back on the same way. Because of randomness within the HCS, this test procedure, in and of itself, produced some variations in the test results from one test to the next. Therefore, each new control configuration to be tested was usually subjected to three simulated clouds in order to establish a true trend.

The advantage of using a simulated cloud transient was the ability to compare different control strategies on the same basis, since the same transient was used. Several different control strategies were tested and all are relative to the design RCA. The following is a list of strategies tested with a simulated cloud:

1) Design configuration,
2) Design configuration without sliding set-point,
3) Design less back-tube control, and
4) Design less flux control.

The design configuration is the only one found to control temperatures without exceeding the high temperature trip of 1060°F.

Three tests with simulated cloud transients were run without the sliding set-point (#2 on previous page) in the design configuration so that a constant set-point of 1050°F was input. All three tests resulted in a high temperature trip (the heliostats being pulled off). Obviously, the sliding set-point mechanism is required in order to prevent high-temperature trips.

The design configuration was modified temporarily to determine whether temperature control could be achieved without the use of flux gauges or back tube temperature instrumentation (#3 & #4 on previous page). In both cases the outlet temperature controller was active. The controller tuning constants were changed though in order to maintain stability. These changes were made according to simulation results for which the overall gain was twice as high when the back-tube control was active and half as much when the flux feed-forward control was active. These two modified configurations were tested and both resulted in high- temperature trips. This testing was very limited (one transient each) and warrants further investigation. Because of the tube stress problem, the outlet temperature plus flux feed-forward control configuration is a best.

The RCA design configuration was tested with the sliding set-point mechanism containing different parameter values. These parameters determine the speed with which the outlet temperature is returned to rated temperature (1050°F) as well as how much derated salt (<1050°F) is produced. Since temperature ramp rates became a problem during testing, the set-point ramp rates were limited in order to bring actual ramp rates within allowable limits. Even though these design ramp limits were violated somewhat.

Natural Cloud Transients

The actual performance capability of the RCA was determined by its ability to control receiver temperatures in natural cloud transient conditions. Many days of testing were performed with natural cloud transients.

5.2.3 Thermal Losses

Steady-state thermal losses, mentioned in Section 5.2.1, were important for determining the overall efficiency and design effectiveness of the receiver. Measurement of thermal losses from the reciever, however, was difficult and required specialized testing techniques.

Losses can be measured or estimated two ways. First, by comparing measured absorbed power with a calculation of incident power. The other method, described in this section, does not rely as heavily upon predictions.

Flux-On

This section describes two methods for determining the operational "flux-on" thermal losses, neither of which requires the absolute total incident power to be known. Both methods, however, require testing to be conducted within 1 hour of solar noon in order to minimize changes in the performance of the collector field and in insolation. Steady wind conditions and a constant insolation above 950 W/m^2 are essential for successfully completing each test.

Barron Method (Method of Complimentary Partitions)

This method [35] maintained the design outlet temperature of 1050°F throughout the entire test and thermal losses are relatively constant for different power levels.

The normal operational heliostat pattern described in Section 3.2 was divided into two alternately spaced, symmetrical groups, each representing 50 percent of the total incident power available to the receiver. Each 50-percent group was individually targeted on the receiver at opposite sides of solar noon to average cosine and shadowing losses. Both groups were simultaneously targeted on the receiver at solar noon. In each case, the receiver was allowed to achieve and maintain steady state for approximately 20 minutes before adding or deleting a group. The test matrix, shown in

Table 5-I, depicts the time table for establishing the receiver in steady state for each test condition.

TABLE 5-I

METHOD OF BARRON TIME TABLE

TEST	Group	Incident Power (%)	Time from Solar Noon (H:Min:Sec)
1	1	50	-0:40:00 to -0:20:00
2	1 & 2	100	-0:10:00 to +0:10:00
3	2	50	+0:20:00 to +0:40:00

Constant Flow Method

Thermal losses calculated from the method of "Complementary Partitions" lacked consistency and were much lower than expected. Flow-rate uncertainty was attributed to be the most likely cause, and as a result, a second method was developed.

In the constant flow method, the flow rate was held constant by manually fixing the valve positions for a given incident power level. The receiver was operated at steady-state conditions at incident power levels of 100, 50, 25 and 0 percent.

Figure 5.2.1 depicts the technique used for determining thermal losses by maintaining constant flow. First, steady-state absorbed power was calculated and curve fit as a function of incident power. Next, a line tangent to the curve was determined at the flux-off loss point and extrapolated out to the 100 percent incident power level. The difference between this tangent line and the 100 percent field absorbed power is the

'flux on' loss. The total thermal losses were then calculated by summing the "flux-off" and "flux-on" components.

FIGURE 5.2.1
CONSTANT FLOW METHOD

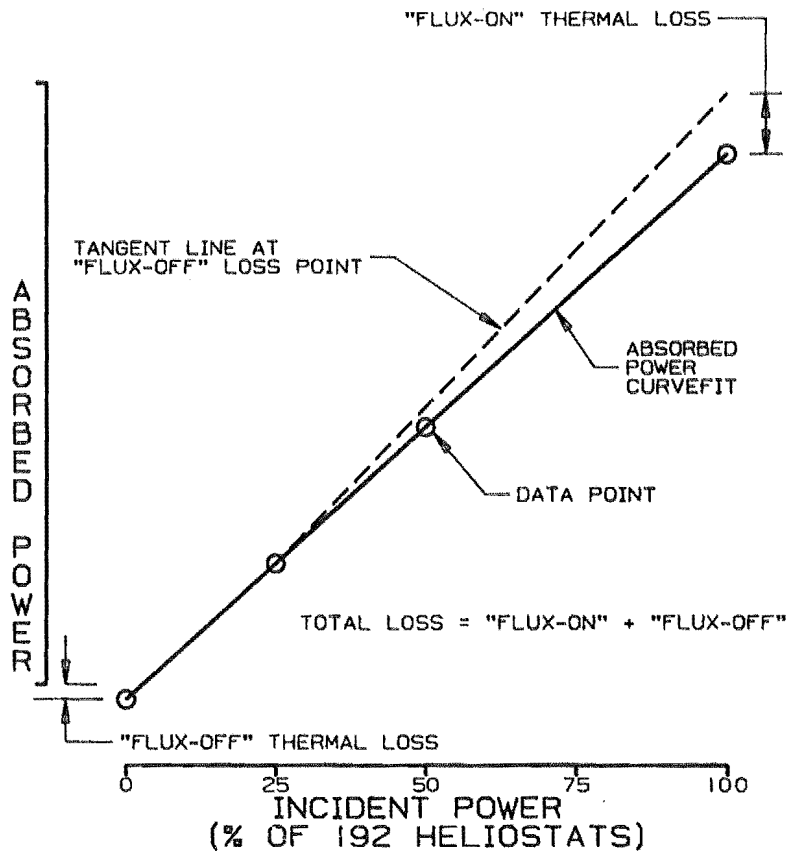

Although this method initially showed promise, further testing revealed a flaw in this technique. First, as the average salt temperature increased, the pressure drop through the receiver decreased. This decrease in internal resistance increased the pressure drop across the flow-control valves and therefore slightly raised the actual flow rate through each half of the receiver. Since the flow rate did not truly remain constant, this method was dropped in favor of the Method of Complimentary Partitions.

Flux-Off

Measuring flux-off thermal losses provides additional information for determining the overall efficiency of the receiver. This method is relatively accurate and simple compared to the methods used for measuring "flux-on" thermal losses. Although "flux-off" loss measurements do not take into account increases in radiation, convection, and conduction losses that occur at higher operational temperatures, it provides a base-line for calculating the "flux-on" thermal losses. In addition, this method was also useful for determining the effectiveness of the cavity door in reducing the thermal losses when the receiver is operating in stand-by conditions.

Seven days of "flux-off" loss data were collected at several flow rates, covering a variety of wind conditions with the cavity doors closed, cracked, and fully open. Each test was run with the receiver in a steady-state "cold flow" condition. The duration of each test was approximately 5 to 10 minutes, beginning when the temperature drop across each half of the receiver became constant.

5.2.4 Overnight Conditioning

Description

In this test the receiver was kept above the freezing temperature of salt by keeping the door closed and circulating cold (570°F) salt in the receiver from the thermal storage subsystem located on the ground. Hot salt (>750°F) from the hot storage tank was made available to be blended with the cold salt as required to maintain the temperature in the receiver panel above salt freezing temperature.

Objective of the Test

The objective of this test was to determine the most efficient method to maintain the receiver in a warm condition overnight to permit rapid morning start-up.

Test Sequence

Before starting this test, the trace heat of the receiver and all the piping were turned on and verified to be operational. Also, the inventory of salt in both the hot and cold storage tanks was verified to provide the energy required for overnight conditioning. Since this test was performed on a cloudy day, the cavity heater for the receiver was turned on the night before and verified to be on.

In this test, a normal fill sequence was used to flood fill the receiver through both the riser and downcomer completely through the purge valves. However, there was one exception; FCV159, the valve that allows salt to enter the hot surge tank from the top of the receiver was closed, requiring the salt to flow downward through the receiver in a parallel manner, thus keeping the receiver panels warm. During this test, if the inventory in the cold storage tank were not adequate to provide the required energy to keep the receiver warm, hot salt from the hot storage tank would be blended in the cold sump and pumped through the receiver.

Subsequent to filling the receiver and starting the downward parallel flow, all trace heaters in the salt loop were turned off except those on the valves and the stagnant lines. This minimized the electrical parasitics in the salt loop. Following the overnight hold condition, all control circuits for the trace heaters were turned on and a normal drain sequence was performed.

Results

During this test, continuous weather data were recorded; ambient air temperature, barometric pressure, relative humidity, and wind speeds and direction. The primary data recorded were salt inlet and outlet temperatures from the receiver, back tube temperatures on the receiver panels, salt inlet pressures, flow rates, pump currents, currents of the active trace heaters, and cycling of the trace heaters. The final output in evaluating the data was to determine the energy required to maintain the receiver in a warm condition, ready to be started immediately in the

morning. This energy was to be compared with the alternate methods of rapid start-up, including cavity heaters and early morning sunrise heliostats, to determine the most efficient way to maintain the receiver in a warm standby condition overnight.

This test was performed using both the cold-salt pump and boost pump located at ground level. This resulted in excessive parasitics and added energy to the cold salt. Because of the additional energy, the temperature of the cold salt actually increased throughout the test, and blending hot salt to the cold salt to maintain temperature was not required.

Small Nupro valves were used in this receiver. During this test, the valve bonnet temperatures decreased to below the freezing point for salt. Before terminating the test and draining the receiver, the salt flow was stagnated, and this allowed the temperatures of the valve bonnets to increase sufficiently above the freezing point of salt to allow draining. Normally 500°F is considered hot enough to safely operate the valves. The reason for the low temperature valve bonnets is discussed in Section 6.4.

5.2.5 Optimization

Optimizing performance is essential for determining the maximum amount of energy the receiver is capable of collecting on a daily, monthly and yearly basis. This requires the optimum use of the daylight hours for start-up, shutdown, normal operation and cloud transients.

Since only a few test days were devoted to optimization, the procedures presented in this section, which cover only optimum start-up and normal operation, should be considered preliminary. It is currently planned to cover optimization in more detail during the "Continued Testing" phase schedule for the summer and fall of 1987.

Start-up

The objective of optimum receiver start-up is to efficiently use the (solar) insolation available immediately after sunrise. This could be accomplished using two different approaches.

In the first approach, it is essential to warm the receiver panels above the freezing point of salt before beginning start-up. This can be accomplished by developing the sunrise warm-up pattern described in Section 3.2. This pattern is targeted on the receiver at sunrise, warming the panels from ambient to minimum of 475°F and maximum of 1050°F. At this time, the receiver is established in serpentine flow and the normal operational heliostat pattern is brought on target.

In the second approach, if electric cavity heaters are used, the receiver can be established in serpentine flow anytime before sunrise, but preferably only a few minutes before in order to minimize parasitics. This approach enables the normal operational heliostat pattern to be targeted on the receiver at sunrise, allowing the working fluid to absorb the solar energy that would normally be used to warm the panels. Although this approach is attractive because of its simplicity, the energy gained from establishing the receiver in serpentine flow before sunrise must be weighed against the energy consumed by the cavity heaters. Both approaches were evaluated on a preliminary basis during testing. Further discussion on these approaches can be found in Section 6.4.

In addition to optimizing start-up with cavity heaters or heliostats, modifications to the normal operational pattern are required to efficiently distribute the flux on each half of the receiver. During early morning, the east half of the receiver is subjected to higher incident fluxes due to the "cosine" effect. This causes an absorbed power imbalance, requiring extra time for the west half of the receiver to stabilize. Therefore, in order to optimize the incident power distribution, heliostat aim points were biased 0.25 m west. Although this increased the fluxes on the west half of the receiver, spillage became a factor since the heliostat field was no longer aimed along the vertical centerline of the aperture. As a result,

future work in this area will require the individual targeting of heliostats in order to balance incident power while minimizing spillage.

Daily Operation

Lack of testing time prevented a detailed evaluation of optimized receiver performance from sunrise to sunset. Here again, only preliminary testing was accomplished.

Operating the receiver efficiently throughout the day may possibly require modifying the heliostat aim points to compensate for the "drift" in absorbed power. As mentioned in the previous section, the east half of the receiver is subjected to higher incident fluxes during early morning; however, as the day progresses, this flux distribution shifts from the east to west half of the receiver, theoretically balancing at solar noon. Therefore, to balance the incident power on both halves of the receiver throughout the entire day, heliostat aim points were biased approximately 0.10 m/hr from west to east.

To minimize spillage that occurs from changing the bias of the entire collector field throughout the day, heliostats need to be targeted individually. Although this may provide improvements in receiver performance, the disadvantages of a complicated aiming strategy may outweigh the gains in performance, if any exist. Further testing is needed to determine if daily optimization of heliostat aiming strategies provides a reasonable increase in annual performance.

5.3 Operability, Procedures, and Lessons Learned

Many concerns about the operability of solar thermal central receivers during start-up, normal operations, shutdown and emergencies have been resolved during past experiments, particularly the most recent Molten-Salt Electric Experiment. The previous procedures and lessons learned were evaluated, and applicable portions were incorporated into this experiment. The primary focus here will be on the operability of the receiver with regard to the dual panel receiver in this experiment.

5.3.1 Start-up

Operability during early morning or sunrise and midday start-up is discussed in this section. Start-up of the receiver occurs subsequent to warm-up of the receiver panels. The warm-up can be accomplished using heliostats, cavity heaters, or overnight conditioning with cold-salt flow.

Sunrise Start-up

Start-up of the receiver at sunrise or shortly after sunrise can be accomplished one of three ways; using the early morning heliostat pattern discussed in Section 5.1.1, using cavity heaters, or overnight conditioning with cold-salt flow discussed in Section 5.2.4. From an operational standpoint, the overnight salt flow conditioning would be the quickest way to start up the receiver, because the receiver would already be in cold-salt flow and would only require establishing serpentine flow and sequencing the heliostats with operational aim points onto the empty receiver panel. The second fastest method would be to use the cavity heaters, which would allow preheating the receiver panels before sunrise. With both of these methods, serpentine flow could be established prior to sunrise allowing energy collection to start at sunrise. If the heliostats were used to warm up the receiver panels, the early morning warm-up pattern would be used as described in Section 5.1.1. This method requires an additional 15 minutes before the fill sequence, and delays start-up past sunrise until both warmup and fill sequence are complete. In addition, two different heliostat aiming strategies must be used which complicates the start-up procedure.

Midday Start-up

Operationally, the midday start-up of the receiver is essentially the same as for early morning, except that when using the heliostats to warm up the panel, a different heliostat pattern would be used. However, about 20 percent of the early morning warm-up pattern would be used during the midday warm-up of the panels. The cavity-heater panel preheat technique and the overnight salt flow method would remain the same for midday start-up of the receiver.

5.3.2 Shutdown

Normal shutdown, emergency shutdown due to power outage and equipment failures, and lessons learned from these operations are discussed in this section.

Normal Shutdown

Normal shutdown included verifying component temperatures, completing a normal drain sequence of the receiver, and securing the receiver following the draining. Before removing the heliostats from the receiver, the outlet temperature set point was ramped down to control the temperature ramp rate of the receiver tubes during shutdown. In addition, component temperatures were verified to assure they were above the freezing point of salt. Subsequently, a normal drain sequence was initiated by opening all the drain and purge valves, venting the cold surge tank, and allowing the receiver and the piping to drain completely to the ground level storage tank.

After completely draining the receiver, a posttest visual inspection was performed. This involved inspecting the receiver panel for potential salt leaks, buckled tubes or any other unusual condition that may have occurred during testing. When severe conditions were noted, a posttest meeting was held to discuss these conditions and determine the corrective action required.

Emergency Shutdowns

When an emergency condition, such as a power outage, occurred during normal operation of the receiver, emergency procedures were used to shut the system down. Uninterruptible power supplies were employed throughout the digital control system, such that system monitoring was preserved. Thus during a power outage, although the salt pumps stopped operating and other pieces of equipment ceased operation or went to their failed position the actual shutdown and draining of the receiver progressed normally because the control system remained powered, and sufficient residual compressed air was available to operate valves.

Lessons Learned

The use of uninterruptible power supplies throughout the digital control system was a major improvement. They eliminated many panic conditions generated by power outages and equipment failures and allowed for a virtually normal shutdown of the receiver.

A second important improvement relative to MSEE concerned the cold surge tank vent. During the draining sequence in the receiver, the cold surge tank is vented from 300 psig to atmospheric pressure, eliminating the potentially damaging two phase flow through the control valves.

5.3.3 Control and Monitoring by the Operator

In this section the primary discussion focuses upon the digital control system and its use and operation in controlling and monitoring the processes of this experiment. Also discussed are the various computers used in system monitoring temperatures and their interaction with the process control system. Finally, the discussion centers upon operators in the control room and on computers monitoring the overall process of this experiment.

Digital Control

The process digital control system was a major piece of equipment in this experiment and it provided control and visibility of the processes in the control room. It allowed the operators to both control the process and monitor all the critical parameters and take appropriate action as required to control the experiment.

Even for a novice who had never operated a digital control system, the system was very easy to use and master. In our particular experiment, the operator used only manual sequences. Auto sequences were not used either in the fill or the drain sequences, primarily because of the time required to input the sequences into the process control computer and perform the required check-out.

The primary lesson learned concerning the digital control system was its ease of use, its short learning curve, and the fact that it can be programmed by individuals without a strong programming background. Second, auto sequences can be integrated into this system readily, easing the workload of the operator. And finally, certain changes to the software can be made while the process is in operation.

Multiple Computer Systems

In our particular experiment, control was divided among three separate and independent computers. These computer systems were the digital process control system (NET-90), the Acurex heat-trace control system, and the heliostat control system. The main lesson learned was that these individual computer systems should be integrated into one master system. This would allow operators to monitor and control the entire plant using a single system as well as facilitate plant automation and improve system operation.

Monitoring

The control room operators monitored the plant processing using three OIU's. Having three units allowed the operator flexibility in monitoring several different subsystems simultaneously or in monitoring a trip page on one of the OIUs, with an overall system on another and a subsystem on the third. This flexibility is invaluable in effective and rapid operator control. Additional flexibility was obtained throughout the use of dynamic color graphics on an OIU which allowed direct operator interaction such as opening and closing valves and changing set-point valves.

The primary lesson learned was that at least one OIU per subsystem with dynamic color graphics is required for secure and effective operator control and monitoring. In addition, the need for an integrated master control system became readily apparent because of verbal chaos in emergency situations and awkwardness in normal situations.

5.3.4 Final Procedures

In this section the iterative process employed in developing the final procedures used in this experiment is described. In addition, the applicability of these procedures to a commercial scale central receiver power plant is discussed. Finally, several lessons learned in procedure development are addressed.

Molten-Salt Electric Experiment

During the later phase of the MSEE Project, an integrated systems operations program was conducted for approximately 1 month. The experiment was operated 7 days a week for a minimum of 12 hours a day. The operations were designed to simulate as closely as possible those of a commercial utility power plant, and also to develop operating procedures and control strategies similar to those that would be employed by an electric utility. The development of these new procedures for the integrated systems operations testing occurred in five areas:

1) Heliostat early morning warm-up pattern,
2) Receiver early morning rapid start-up,
3) Heat-rejection feed-water subsystem early morning rapid start-up,
4) Steam generation subsystem early morning rapid start-up, and
5) Simulated turbine generator start-up.

For this project, only the receiver's early morning warm-up pattern and its start-up operating and shutdown procedures were developed and refined.

Each of the subsystem procedures was divided into four basic sections: pretest check list, operations, posttest check list, and emergency procedures. For the pretest check list, both control room and field check lists were developed, with the control room operator and field technicians coordinating their activities by radio. The control room pretest check list activities consisted of verifying that the temperatures of salt systems were acceptable and the control system and components were configured for start-up. As each of the field technicians in the various subsystems proceeded

through the field check list, the control room personnel verified the equipment configuration was as required.

The operations portion of each procedure was controlled from the control room by the console operators. However, during these operations the field technicians were kept aware of critical operations.

Subsequent to testing, posttest check lists were completed for each of the subsystems by the field technicians and the control room to secure the equipment. The control room operator then secured the master control system and the remaining control room equipment.

Tests Required to Finalize Procedures

The tests required to finalize the operating procedures were obtained primarily from three conditions: start-up, operations, and shutdown. Procedures used in the start-up included the sunrise heliostat pattern, a normal start-up heliostat pattern, and the cavity heaters. In the operations portions of the operating procedures both steady-state and transient conditions were used in finalizing the procedures, as well as emergency conditions during fill sequences, normal operations, and drain sequences. The shutdown portion included the normal drain of the receiver and securing the receiver subsequent to the final drain.

Commercial-Scale Applicability

The final operating procedures developed from this experiment can be applied to commercial solar central receiver power plants because the configuration of the receiver would be similar. In a commercial solar receiver, heaters would be used to preheat the piping, valves, headers, etc. Even if bellows-sealed valves were replaced with packing-sealed stems, trace heaters would be required and the procedures would be similar.

The procedures involved in filling sumps before operating the pumps can also be applied to a commercial-scale plant. Procedures in pressurizing the receiver's cold-salt surge tanks would apply directly to commercial-scale

plants. Finally, the procedures in operating cavity or radiant heaters in the receiver would also apply.

The primary lesson learned from the finalized procedures used in this experiment is that they can be applied to commercial scale power plants with a central receiver design. Therefore, if large scale test facilities or demonstration plants are designed and operated, these procedures could be applied to those facilities and refined to its particulars with minimal foreseen effort.

SECTION 6

EVALUATION OF THE RECEIVER'S PERFORMANCE

D. Smith -Babcock & Wilcox Corp.
M. Lanning - McDonnell Douglas Astronautics Corp.
R. Skocypec - Sandia National Laboratories
R. Boehm - University of Utah
G. Riley - McDonnell Douglas Astronautics Corp.

The primary function of a solar receiver is to absorb the solar energy made available to it from the collector field. In this section of the report, the capability of the test receiver to collect energy is examined based on the data from the tests. The primary measure of this receiver's ability to absorb the solar energy from the collector field was its efficiency, defined as its thermal output divided by the power available at its aperture plane. The receiver's thermal output was calculated from the measurements of salt flow rate, and inlet and outlet temperature. The power available at the aperture plane was not measured, however, so the receiver's efficiency had to be calculated by indirect means. Two methods were used to calculate the efficiency: 1) measured output divided by calculated thermal input, and 2) thermal loss measurement by the "Baker modification to the method of Barron." The "Barron" method infers losses from measured thermal output at two different power levels and employs an analytical characterization of the receiver. The method of calculated input power was used to predict the receiver's efficiency as a function of time of day, whereas the "Baker modification" is limited to application at solar noon. Sections 6.1 and 6.3 present these measures of efficiency. The performance of the receiver is also evaluated analytically in Section 6.2 by using a computer model. This work supported the "Baker modification" loss evaluation, but also stood alone as a measure of the receiver's expected efficiency.

Important to a receiver's ability to collect energy are its characteristics when started. The test receiver was operated in three modes for start-up.

These three modes are discussed in Section 6.4, and comparisons are drawn based on energy collected, energy consumed, and start-up times.

Another aspect of a receiver's performance is its control. Section 6.5 discusses the receiver's controls and their ability to function and collect energy during clear and cloudy conditions. Section 6.6 summarizes all aspects of the receiver's performance and discusses its capability to collect energy on an annual basis. Chapter 6 concludes with a discussion of the uncertainties of measuring the receiver's power.

6.1 Steady-State Evaluation

This section reports the results of the test receiver's steady-state performance evaluation. Its performance at solar noon is presented first, followed by a discussion of the receiver's performance as a function of time of day for the 9 hours during which a 1050°F outlet temperature could be maintained. Steady-state evaluation of the receiver at solar noon is important because (1) it establishes the maximum performance characteristics for the receiver and, (2) it provides a comparison between the actual test data and the design predictions for the receiver.

Steady-state test data were collected on 14 days between March 30 and April 29 (of 1987). Solar noon data were collected on 7 of these days. Figure 6.1.1 presents the times when data were taken for steady-state evaluations. The period of the test was within the 40 days after the spring solstice of 1987. During this time, 12 to 13 hours of sunlight are usually available between sunrise and sunset. To account for variations in daily insolation, all the test data were normalized to the insolation curve obtained on March 31, 1987. This curve, shown in Figure 6.1.2, depicts the insolation history from 4 hours before to 4 hours after solar noon. This was the best full-day insolation data obtained during testing. To account for daily changes in the heliostat field, all the test data were also normalized to 192 heliostats, representing the number of heliostats used in the design predictions for the receiver.

Receiver efficiencies are predicted in this section using the method of predicted energy input vs. measured receiver power both at solar noon and as a

function of time of day. Also included a discussion of the east-west bias of the CRTF collector field. The data collected showed evidence that the receiver power was biased slightly to the west.

FIGURE 6.1.1
STEADY-STATE DATA POINTS

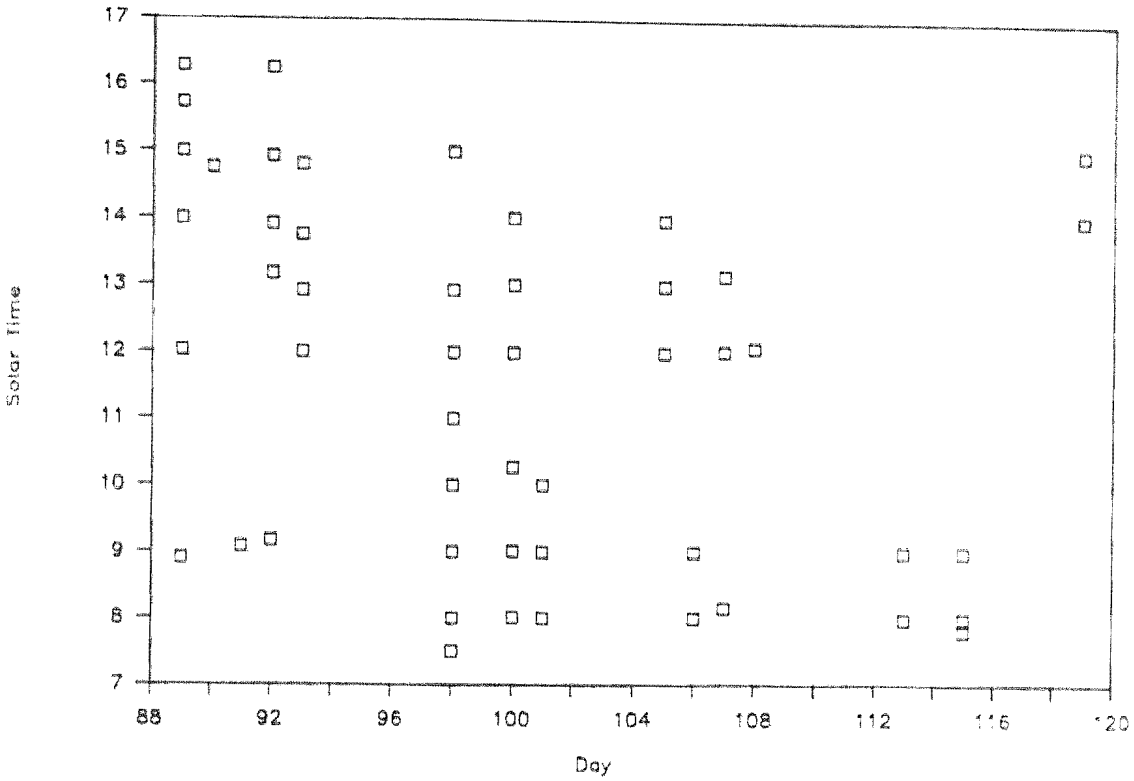

6.1.1 Steady-State Absorbed Power at Solar Noon

To determine the steady-state absorbed power at solar noon, the receiver was operated with a salt outlet temperature of 1050°F with the maximum number of base-line heliostats on target (see Section 3.2). The absorbed power was measured during a 10-minute window centered around solar noon. The data obtained during each test were averaged and corrected for hot-salt flow calibration (see discussion in Section 6.7) and then normalized to 192 heliostats and to a solar noon insolation of 1065 W/m^2 taken from the insolation curve shown in Figure 6.1.2. These results are presented in Table 6-I.

FIGURE 6.1.2

IDEAL DAY SOLAR INSOLATION

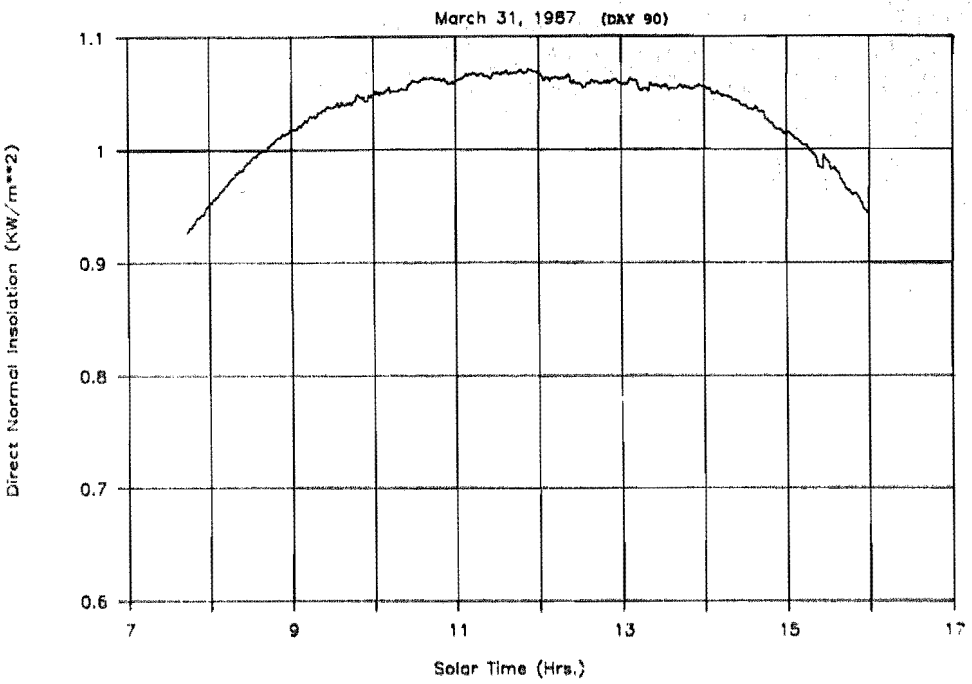

TABLE 6-I

MEASURED AND NORMALIZED RECEIVER SOLAR NOON POWER

DAY	HELIOSTATS ON TARGET	INSOLATION W/m^2	MEASURED RECEIVER POWER (MW) EAST	WEST	TOTAL	NORMALIZED* RECEIVER POWER (MW) EAST	WEST	TOTAL
03/30/87	189	1067	2.16	2.46	4.62	2.19	2.50	4.69
04/03/87	187	1047	2.14	2.40	4.54	2.23	2.51	4.74
04/08/87	189	1029	2.21	2.42	4.63	2.32	2.55	4.87
04/10/87	190	1048	2.19	2.38	4.57	2.25	2.44	4.69
04/15/87	187	1055	2.18	2.39	4.57	2.26	2.48	4.73
04/17/87	187	1034	2.17	2.34	4.51	2.26	2.48	4.77
04/18/87	186	1040	2.16	2.37	4.53	2.28	2.51	4.79
	AVERAGE POWER		2.17	2.40	4.57	2.26	2.49	4.76

*192 Heliostats, 1065 W/m^2

The average measured power from the receiver was 4.57 MW and the normalized average is 4.76 MW. Of note is the fact that there was a slight imbalance in absorbed power favoring the west receiver zone. This anomaly is discussed further in Section 6.1.3.

The efficiency of a receiver is defined as the energy collected, divided by the energy available to the receiver. The energy available to the receiver is the energy reflected by the collector field arriving at the aperture plane. For the receiver, two measures of efficiency were significant. The first was the "receiver efficiency" defined as the absorbed power divided by the power falling within the receiver aperture (including the wing panels), this is a standard definition of receiver efficiency. The second measure was the "total receiver efficiency," which is the absorbed power divided by the total power arriving at the aperture plane. This number will be lower because it treats the external spillage as a loss, but it indicates how well the receiver is matched to the heliostat field.

Steady solar-noon data were taken on 7 days between March 30 (day 89) and April 18 (day 108). Gross field power was calculated each day as the direct normal insolation times the mirror area for the active CRTF heliostats for the given day. This number was then reduced first by shading, blocking, and cosine losses as determined by the HELIOS [26] program. The power was then reduced by the mirror reflectivity and by the atmospheric transmission, which were taken to be .807 (based on a measurement taken on April 6) and a value of .995 (provided by HELIOS respectively). Figure 6.1.3 presents a stair-step diagram for the average conditions.

The efficiency calculated for the receiver was 88.7 percent, while the total receiver efficiency was calculated to be 83 percent. The uncertainty in these numbers is relatively high. This results from uncertainties in the HELIOS predictions of incident power, and uncertainties in the measurement of absorbed power. (Uncertainties in power measurement are discussed in Section 6.7.) Uncertainties in calculation of receiver efficiency are discussed in Section 6.6.

FIGURE 6.1.3

SOLAR NOON POWER STAIR STEP

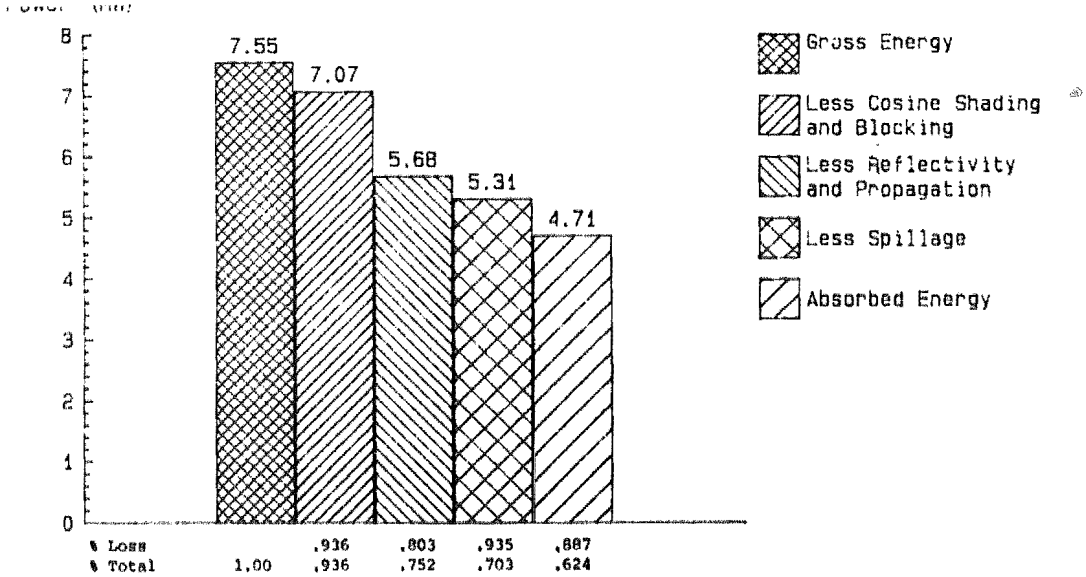

6.1.2 Clear-Day Energy Collection

During the test period of March 30 to April 29, the steady-state absorbed power for a full day's operation was measured over a range of 9 hours, beginning 4 1/2 hours before, and continuing to 4 1/2 hours after solar noon. During this period, the incident power on both halves of the receiver was sufficient to maintain an outlet temperature of 1050°F at the minimum flow rate of 12,000 lb/h. Table 6-II presents the normalized total absorbed power for the test receiver as a function of time of day, based on correlation of all of the data.

TABLE 6-II
DAILY POWER

Solar Time	East Power (MW)	West Power (MW)	Total Power (MW)
07:30	1.22	0.83	2.05
08:00	1.54	1.21	2.74
09:00	1.97	1.76	3.73
10:00	2.19	2.13	4.32
11:00	2.27	2.36	4.63
12:00	2.25	2.48	4.73
13:00	2.14	2.51	4.65
14:00	1.93	2.44	4.37
15:00	1.60	2.22	3.82
16:00	1.09	1.80	2.89
16:30	0.75	1.49	2.24

Theoretically, the absorbed power for each half of the receiver should have balanced at solar noon. However, test results indicated the actual absorbed power balanced approximately 90 minutes before solar noon. This is further illustrated in Figure 6.1.4, which presents the absorbed power for each half of the receiver as a function of time of day.

FIGURE 6.1.4
RECEIVER POWER AS A FUNCTION OF TIME OF DAY

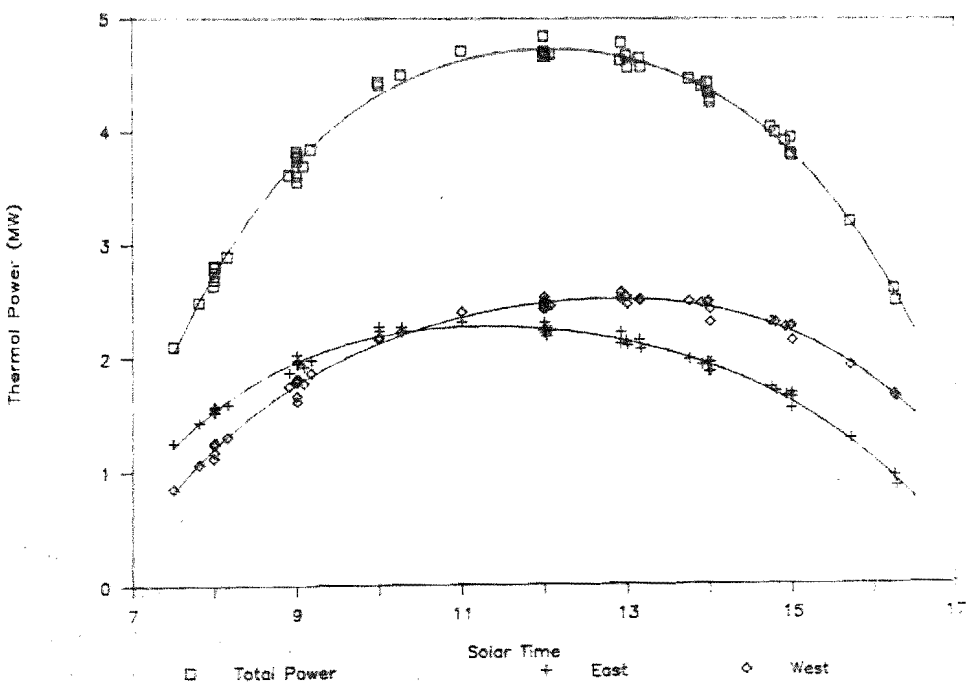

Section 6.1.3 discusses the sensitivity of the power distribution to aim-point location in more detail and explains the reasons the absorbed power was not balanced for each half of the receiver at solar noon.

To calculate the receiver's efficiency as a function of time of day, steady-state data points were analyzed at even-hour increments both before and after solar noon. Data readings recorded every minute were averaged over 10-minute intervals to establish each steady-state point. To eliminate daily variations from the data, all data were normalized, as described in Section 6.1. The measured power was based on the measured temperatures and flow. The input power of the receiver was calculated from a table of CRTF collector field performance parameters provided by the HELIOS program. This table (Table 6-III) provides cosine, shadowing, blocking, and spillage loss as a function of day and time of day for the test period.

TABLE 6-III
HELIOS COLLECTOR FIELD PERFORMANCE PARAMETERS

Day	Hours from Noon	Cosine	Shading & Blocking	Spillage & Propagation	Total
89	0	0.946	1.000	0.930	0.710
89	1	0.938	1.000	0.926	0.701
89	2	0.915	0.999	0.911	0.672
89	3	0.876	0.970	0.884	0.607
89	4	0.823	0.849	0.840	0.474
89	4.5	0.792	0.724	0.813	0.376
119	0	0.921	1.000	0.931	0.692
119	1	0.913	1.000	0.926	0.682
119	2	0.890	0.998	0.911	0.653
119	3	0.851	0.975	0.881	0.590
119	4	0.798	0.873	0.833	0.469
119	4.5	0.767	0.768	0.804	0.382

Based on these data, the performance of the CRTF collector field was predicted for each of the steady-state data points. Gross power of the collector field was defined as the mirror area of the collector field times the direct normal insolation. This represented the maximum power that could have been intercepted by the field if all mirrors were directed normal to the sun's rays. This value was first reduced by predicted shading of the

mirrors by adjacent heliostats, blocking of reflected sunlight by other heliostats, and by the cosine effect due to each heliostat being positioned to bisect the angle between the sun and the receiver. These effects were most pronounced in the early morning and late evening hours.

A reduction was made for mirror reflectivity and atmospheric transmission. The mirrors at the CRTF had a reflectivity of 88 percent when clean. During the period of the test, the reflectivity of the mirrors was measured at 80.6 percent, indicating mild soiling. Atmospheric transmission losses of 5 percent were estimated and taken into account. Of the solar energy that reached the plane of the receiver aperture, some fell on non-absorbing surfaces outside the cavity. This is called external spillage. The remaining power fell either on the wing panels or entered the receiver aperture, where a portion of it was absorbed.

Figure 6.1.5 presents the performance of the collector field and the receiver based on all of the steady-state data points. Based upon these results, the receiver's efficiency could be calculated. Figure 6.1.6 presents the receiver's efficiency as a function of the time of day. Both the basic "receiver efficiency," (the ratio of absorbed power to the power falling on the wing panels and into the aperture, exclusive of external spillage) and the "total receiver efficiency" (the ratio of receiver power to the power arriving at the aperture plane) are presented. There is a fair amount of scatter in the data in this plot. It may be the result of several factors, including variation in losses due to daily weather conditions of wind, insolation, etc., and random errors in the measurements. The receiver efficiency also shows very little variation as a function of time of day, but the total efficiency (including spillage) showed significant variation. To understand this trend, it is useful to look at Figures 6.1.7 and 6.1.8. Figure 6.1.7 presents efficiency as a function of absorbed power. From this plot, it is apparent that receiver power is the significant independent variable. Figure 6.1.8 shows thermal loss (including reflected loss) as a function of absorbed power. Apparently, losses from the cavity are lower at lower power levels, almost in proportion to power level. This could be the result of lower surface temperatures within the receiver when operating at lower powers. For total receiver loss (including spillage) the spillage

loss must increase as a function of time of day, with higher spillage when the sun is lower in the morning and evening. This trend is seen in Figure 6.1.9 which shows losses plotted as a function of time of day. Figure 6.1.10 presents a stair-step diagram for the energy collected during the 9 hours from 7:30 to 4:30 solar time. The energy collected during the 9 hours of steady-state operation was 35.7 MW_{th} based on the normalized data. This number was based on an outlet temperature of 1050°F for 9 continuous hours. Early morning and late afternoon energy collection is discussed in Section 6.4. The average total efficiency and the average receiver efficiency (excluding spillage) for the 9 hours was calculated as 79.7 and 88.1 percent, respectively. These are lower than the solar noon efficiencies because the efficiency varied with the time of day, as shown in Figure 6.1.6.

FIGURE 6.1.5
DAILY COLLECTOR FIELD AND RECEIVER PERFORMANCE

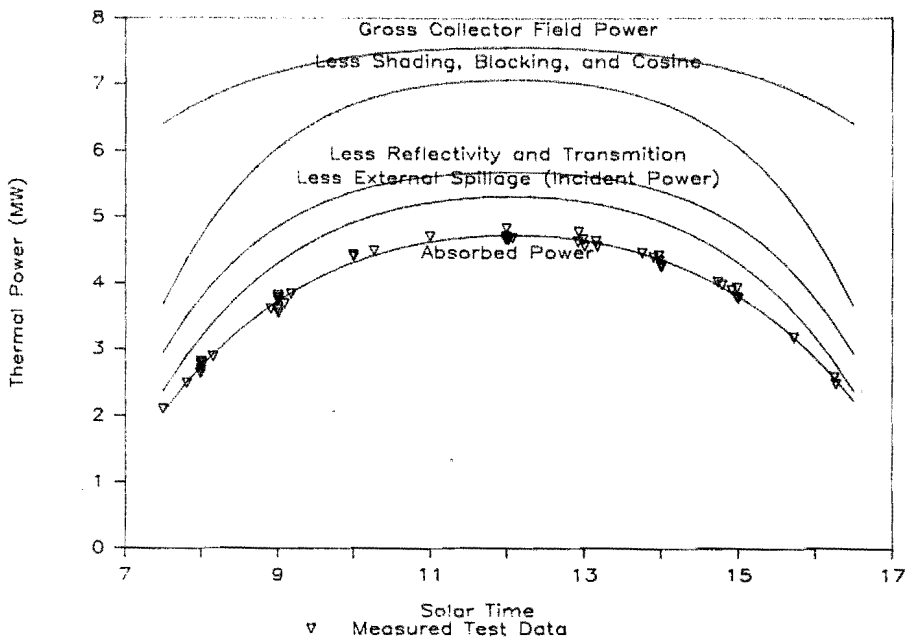

FIGURE 6.1.6

RECEIVER EFFICIENCY VS. TIME OF DAY

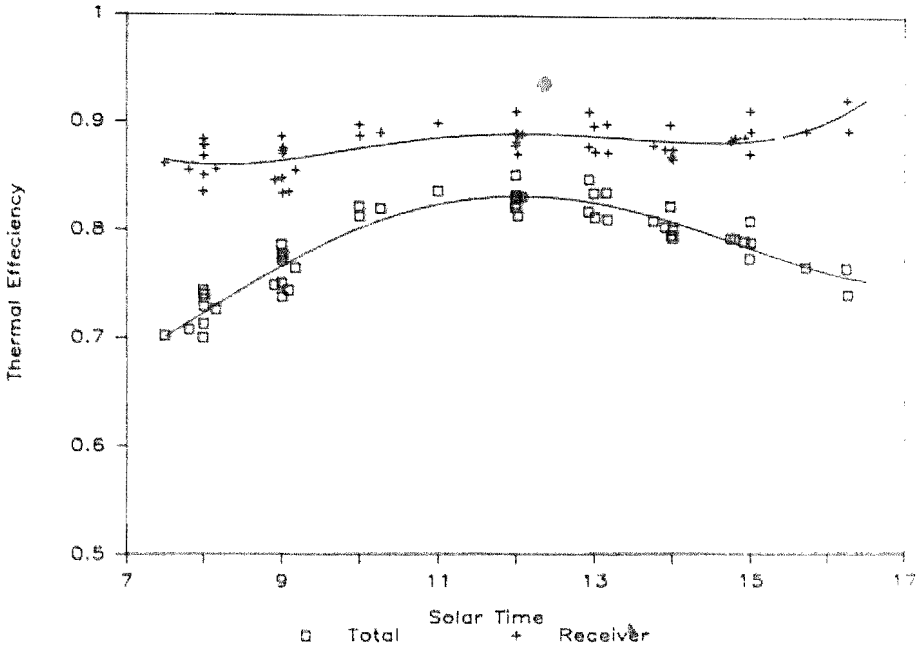

FIGURE 6.1.7

RECEIVER EFFICIENCY ABSORBED POWER

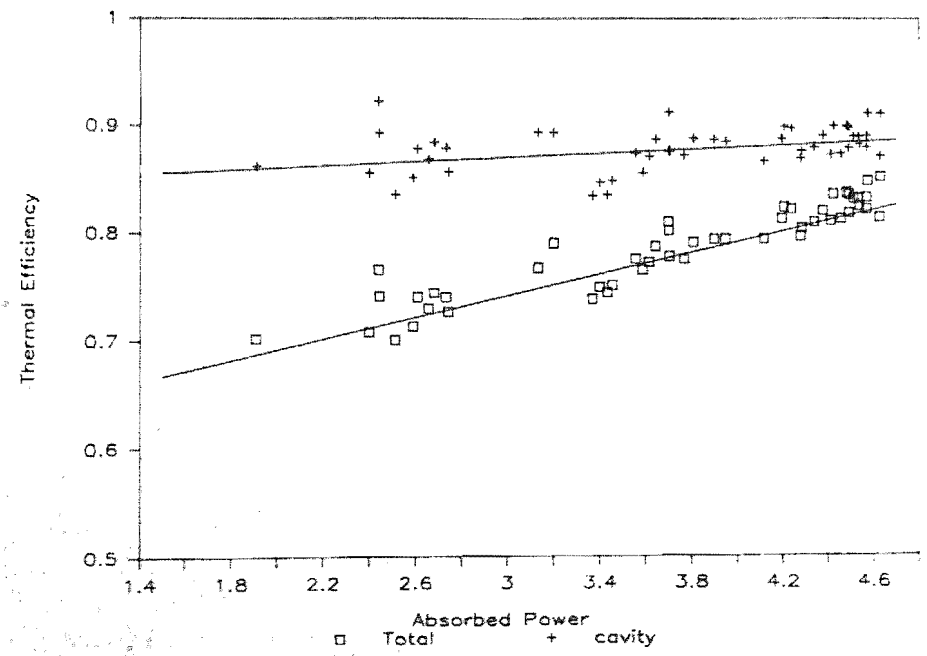

FIGURE 6.1.8

RECEIVER LOSS VS. POWER

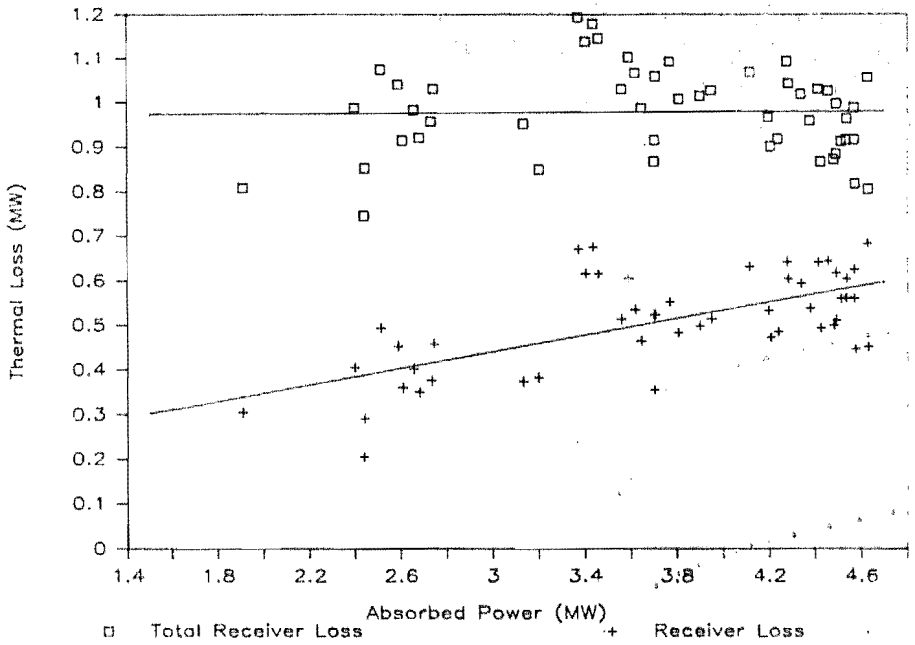

FIGURE 6.1.9

RECEIVER LOSS VS. TIME OF DAY

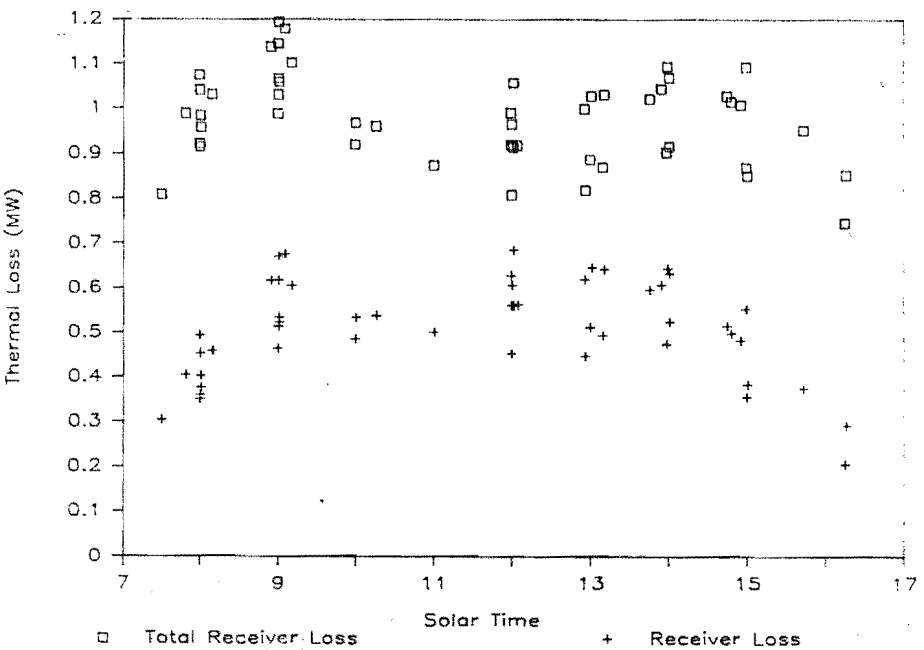

FIGURE 6.1.10
THERMAL ENERGY STAIR STEP

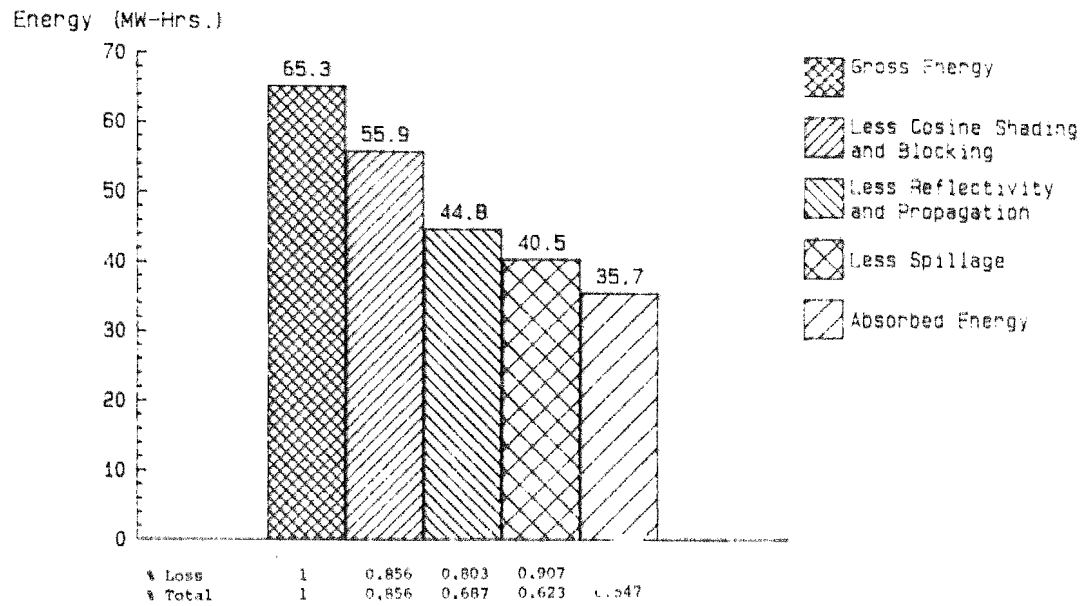

9 hrs., 7:30 to 4:30 Solar Time

6.1.3 Sensitivity of the Power Distribution to Aim-Point Locations

Because both the receiver and the CRTF collector field were symmetric, it would be expected that the east and west zones of the receiver would have collected the same power at solar noon and would have behaved the same on either side of solar noon. During the initial check-out of the receiver, however, this was found not to be the case. With the heliostats aimed at the vertical center line of the receiver aperture, the apparent measured power from the receiver's west zone was higher than that of the east zone. No reason for this exists in the receiver's geometry, but it was suspected that errors in flow measurement and small errors in the field alignment might be responsible. An investigation was conducted to determine the sensitivity of the receiver's power to aim-point locations.

The heliostat's aim points for this receiver were distributed along the vertical centerline of the aperture, as discussed in Section 3.2. During the receiver's check-out, the aim points were shifted in an attempt to balance power between the two flow control zones. The receiver was operated at solar noon with aim points on the vertical centerline, and with aim points displaced 6.7 inches to the east. The results of these tests are shown in Figure 6.1.11. With aim points on the vertical centerline, power was biased 230 kW to the west. With the aim points moved 6.7 inches to the east, power was biased 240 kW to the east. Based on linear interpolation, power would balance with an aim point 3.3 inches to the east. Clearly, the power balance was quite sensitive to aim-point location. Because this offset was small, and because the accuracy of the flow measurement was limited (therefore limiting the accuracy of power measurement, see Section 6.7), it was decided to conduct testing with the aim points at the aperture centerline and accept the anomaly in the data.

FIGURE 6.1.11
ABSORBED POWER SENSITIVITY TO AIM-POINT LOCATION

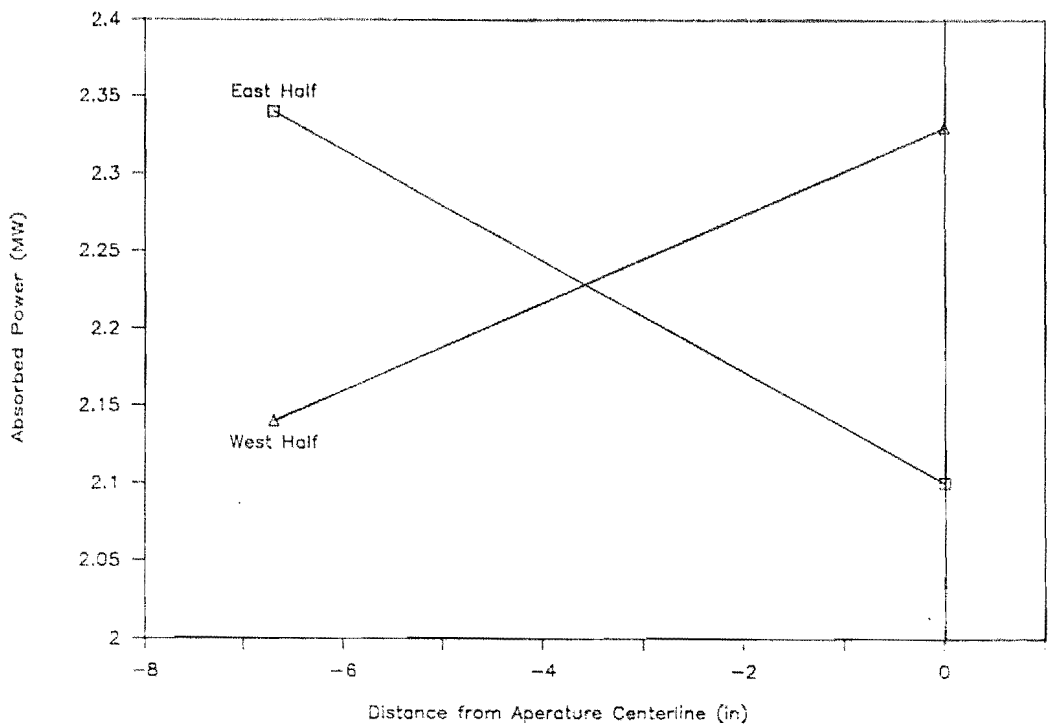

6.2 Thermal Modeling of the Receiver's Cavity

Numerical models of the thermal characteristics of the receiver's cavity are tools to evaluate and interpret test data and provide predictive capabilities for future design analyses. In particular, the impact of current design details or future design changes on the receiver's thermal performance can be evaluated. Accurate predictions of the thermal performance for a solar central receiver require realistic models of the energy transfer that occurs within the receiver. The energy transfer involves multiple mechanisms. One goal of numerically modeling the receiver is to identify and include the dominant mechanisms in the simplest acceptable manner. Section 6.2.1 presents a brief overview of this numerical model (CAVITY2), including assumptions inherent in the model, and finally a more detailed discussion of the code methodology. Section 6.2.2 presents both local (spatially resolved) and global (entire cavity) results. Calculated local variables include: salt temperature, front surface temperature, inner wall temperature of the tube, convective flux, absorbed flux, and absorption efficiency for a number of different conditions. Global results from the model include: radiative losses, convective losses, absorbed power, receiver thermal efficiency, area-averaged surface temperature, and the salt-mass flow rate in the east and west zones required to maintain a 1050°F salt outlet temperature.

6.2.1 Description of the Model

Given the solar flux distribution on the surface of the receiver's cavity (as calculated, for example, by the HELIOS code [26]) and the desired inlet and outlet salt temperatures, the code performs steady-state energy balances on local elements of the receiver in an iterative technique. The model presented here includes molten-salt energy absorption (radial tube conduction and axial salt advection), gray (one-band) radiative transfer between surfaces and the aperture of the receiver (with no atmospheric participation), and convective energy transfer to the atmosphere at a local level. The model is based on an earlier code, CAVITY, developed at SNL, Livermore [27]. To achieve numerical stability, underrelaxation is

required. Some material properties are temperature dependent, although the radiative properties are not, and furthermore are taken to be gray values.

Assumptions inherent in this model include: (1) the cavity is at steady-state; (2) only the receiver cavity is modeled (the wing panels were not included); (3) all cavity surfaces are homogeneous, gray and diffuse, and the air within the cavity is radiatively non-participating. (No attempt has been made to include "microscale" effects, such as the scalloped nature of the absorbing tube elements. The elements are modeled as flat planes, although corrections have been made for non-planar flux surface areas when determining the energy absorbed by the salt.); (4) non-absorbing surface elements transfer energy convectively with the atmosphere and radiatively with other surfaces; (5) absorbing surface elements transfer energy convectively with the atmosphere, radiatively with other surfaces, and advectively with the flowing salt; (6) each surface element is characterized by a uniform temperature and uniform net heat flux; (7) conduction through the tube wall is radially one-dimensional (no axial or circumferential conduction) and therefore conduction between tube elements is neglected; (8) fluid flow in the tubes is fully developed, with no phase change; axial conduction in the fluid is neglected.

A more detailed discussion of the model methodology follows. The receiver cavity is configured using 292 discrete elements. The program SHAPEFACTOR [28] was used to generate the shape factors necessary to quantify the radiative transfer between each element. Once the receiver cavity geometry is defined, the inlet and outlet salt temperatures and solar incident flux on each element are specified (from HELIOS), an initial estimate of the absorbing panel front surface temperatures is made, and the convective flux for the nonabsorbing elements are initially assumed to be zero. The primary calculation loop consists of the following steps:

1) Radiative Analysis: A single-band (gray) radiative exchange analysis using the net-radiation method (as discussed in [29]) predicts the net non-radiative energy transfer for the absorbing elements and the surface temperature for the nonabsorbing elements. To achieve numerical stability, all radiosities in the radiative calculation are

"relaxed" prior to using them in the current iteration by a relaxation factor (approximately 0.7).

2) Convective Analysis: Using the current surface temperature estimates, convective transfer for each element is calculated using one of three submodels: 1) globally derived convection: a spatially uniform heat-transfer coefficient is calculated using the global Siebers and Kraabel correlation [30]. This method prorates the convective flux over the receiver surface using element temperature and ensures global energy conservation. It must be noted that although this submodel is termed a "global" submodel, the convective energy transfer is applied at each local energy balance. It is termed a global convective submodel only because it is based on a global correlation. 2) Local convection: a locally varying convective heat-transfer coefficient is based on the relationship $Nu = 0.052Gr^{0.36}$ [31], for which the length scales are taken to cancel (identically if the exponent is 1/3). Nu is the Nusselt number and Gr is the Grashof number. Properties are evaluated at ambient temperatures. This method produces a heat transfer coefficient and convective flux that is more sensitive to local surface temperature conditions than the global convective estimates. Both the global and local convection submodels use a constant ambient temperature as the convective sink temperature. 3) No convection: due to the complications and uncertainties associated in specifying the local convective coefficients, the receiver's thermal characteristics had been previously evaluated with no convective transfer. This option can be used for comparative purposes.

3) Local Energy Balance: The net non-radiative flux estimates for the absorbing elements are updated to account for the convective loss. The energy available to radially conduct through each tube and into the salt is determined by an energy balance on each absorbing element panel.

4) Convergence Check: These net non-radiative flux values are checked for convergence with the estimates from the previous iteration.

5) Match-Specified Conditions: If convergence has not been achieved, the following iterative loop is initiated to determine the flow rate of the salt mass (based on average salt temperatures) necessary to produce outlet salt temperatures that match the specified values: 1) A local convective heat-transfer coefficient (for the energy transfer from the tube's inner surface to the salt) is calculated, based on the current salt-mass flow rate estimate and local temperature-dependent properties. The correlation used is $Nu = \max(4.364, 0.023Re^{0.8}Pr^{0.4})$, where Re is the Reynolds number and Pr is the Prandtl number [27]. 2) Next, local fluid temperatures are updated based on the current mass flow rate and energy conduction through the tube into the salt, Q_{cond}. 3) The inner wall temperature is updated based on Q_{cond}, the fluid heat-transfer coefficient and fluid temperatures, accounting for the tube perimeter surface area. (Note that since the elements are radiatively modeled as planar surfaces, the cross-sectional area is used for all radiative transfer.) Steps 1-3 are repeated to give the salt's convective heat-transfer coefficient, inner tube wall temperatures and fluid temperatures that are consistent with Q_{cond} and the salt-mass flow rate. 4) The salt-mass flow rate is updated if the calculated outlet temperature is not equivalent to the desired salt outlet temperature. Steps 1-4 are repeated until the desired salt outlet temperature is achieved.

6) Update and Iteration: The outer tube's surface temperatures are updated and iterated to be consistent with Q_{cond} and the tube inner wall temperatures. Repeat steps 1-6 until the tube's conductive energy converges.

6.2.2 Results

Global results are presented in Table 6-IV for a number of different conditions. All results apply to day 120 with solar insolation of 1.05 kW/m^2. Solar incident flux levels for 100 percent field conditions are predicted by HELIOS with 191 heliostats on-line, providing 4836 kW of power

at the receiver aperture. Field incident flux levels of 50 percent are taken to be half of the full-field values. Unless otherwise specified, parameter values used in generating the Figures include the spectrally weighted absorptivity (taken equivalent to the emmissivity) of Pyromark (0.948) and Kaowool ceramic fiber insulation (0.3). The global values presented in Table 6-IV are solar power incident on the cavity surfaces, which include Q_s, (the power includes internal spillage on the nonabsorbing walls of the receiver, i.e., it is the power through the aperture); power absorbed by the salt, Q_{abs}; power lost by convective transfer to the atmosphere, Q_{conv}; power lost by radiative transfer through the aperture (including both the reflected solar and emitted infrared energies), Q_{rad}; receiver's thermal efficiency, η, defined as the ratio of the absorbed power to solar incident power; area-averaged front surface temperature $\bar{T}$ (averaged over all cavity surfaces); and the east and west salt mass flow rates, $\dot{m}_e$ and $\dot{m}_w$, respectively, that will provide 1050°F outlet salt under the conditions specified. It must be stressed that these predictions are based on a single-band radiative analysis, which is less representative than a multiple-band analysis, although the distributions, parameter effects and global values should not vary significantly.

TABLE 6-IV

GLOBAL RESULTS

	Q_s (kW)	Q_{abs} (kW)	Q_{conv} (kW)	Q_{rad} (kW)	η (%)	$\bar{T}$ (°F)	$\dot{m}_e$ (klb/h)	$\dot{m}_w$ (klb/h)
Noon, 100% Field Global Convection	4836	4426	149.0	260.8	91.52	909.1	45.39	45.43
Noon, 100% Field 1/2 x Global Convection	4836	4479	84.08	272.8	92.62	983.6	45.93	45.97
Noon, 100% Field 2 x Global Convection	4836	4331	268.0	237.3	89.55	849.0	44.41	44.45
Noon, 100% Field No Convection	4836	4544	0	291.6	93.97*	1070	46.6	46.64
Noon, 100% Field Local Convection	4836	4416	160.6	259.7	91.31	903.9	45.28	45.32
Noon, 100% Field Global Conv, $\epsilon_{kaowool}$=0.1	4836	4425	152.3	257.9	91.51	922.3	45.39	45.42
Noon, 100% Field Global Conv, $\epsilon_{kaowool}$=0.7	4836	4415	165.1	255.4	91.31	971.7	45.28	45.32
Noon, 100% Field Global Conv/No Internal Spillage	4836	4309	123.9	220.0	89.11**	802.9	44.23	44.23
Noon, 100% Field Global Conv, Pyromark Conductivity Included	4836	4414	152.7	269.0	91.28	923.9	45.27	45.30
11:00 a.m., 100% Field Global Convection	4702	4303	145.6	253.0	91.52	895.8	44.35	43.94
Noon, 50% Field Global Convection	2421	2119	121.9	180.0	87.53	799.2	21.73	21.75

*If global convection losses are included based on $\bar{T}$ = 1072.°F(191.9kW), η = 89.9%.

**Predicted internal spillage is 187kW.

The base-line case is taken to be solar noon, 100 percent field with the global convection submodel (spatially uniform heat transfer coefficient as determined by the Siebers and Kraabel correlation). A thermal efficiency of just over 91 percent with absorbed power of 4.426 MW is predicted. The largest thermal loss mechanism is radiative transfer, although convective transfer is of the same order of magnitude. The slight difference in salt-mass flow rates between the east and west zones is due to very small asymmetric effects in the calculated internal spillage values. Absorbed power and salt mass flow rates compare well with experimental data (for example, the measured maximum absorbed power at solar noon was 4.76 MW normalized for insolation of 1.065 kW/m^2 and 192 heliostats on-line). To determine the sensitivity of the receiver's thermal performance to convective losses, two additional cases were run: a case in which the convective heat-transfer coefficient (still assumed uniform and applied locally) was taken to be half of that predicted by the Siebers and Kraabel correlation; and a case in which the heat-transfer coefficient was taken to be twice that of the Siebers and Kraabel prediction. Since the surface temperatures equilibrate to different values in each case, the predicted Q_{conv} values in Table 6-IV are not exactly half or double those of the base case. $\bar{T}$ varies by about 70°F, with a corresponding change in efficiency of a few percent. If no convective transfer is allowed, $\bar{T}$ increases by more than 150°F, with some surfaces as hot as 1500°F. The efficiency artificially increases in this case since the increased radiative loss does not fully compensate for the lack of convective loss. As noted in the footnote to the Table, if global convection losses are included based on the predicted $\bar{T}$ for no convection, η decreases by ~1.5 percent from the global convection case. The local convective submodel, as described in the previous section, predicts slightly higher Q_{conv} and slightly lower $\bar{T}$, with essentially no change in η from the global convection prediction.

The base value of the Kaowool insulation emissivity, $\epsilon_{kaowool}$ is 0.3. Two cases were run to determine the impact of the radiative properties of the material of the nonabsorbing walls (the material constitutes a significant

portion of the cavity's surface area). The Kaowool emissivity was changed to 0.1 and 0.7. These values were applied to all cavity surfaces other than the Pyromark-coated absorbing salt panels. Interestingly, both cases produced higher $\bar{T}$ (and therefore higher Q_{conv} and slightly lower η) than the base case. When $\varepsilon_{kaowool} = 0.1$, the walls are more reflective and the nonabsorbing elements are at more uniform temperatures, producing a net increase in $\bar{T}$. When $\varepsilon_{kaowool} = 0.7$, the nonabsorbing elements have a greater temperature range, also giving an increase in $\bar{T}$. Similar results are obtained when the local convection submodel is used.

If internal spillage is not accounted for, Q_{abs} drops and η decreases since, although $\bar{T}$, Q_{conv} and Q_{rad} are lower, the spillage energy (approximately 183 kW) cannot be absorbed. Comparing Q_{abs} between this case and the base case indicates that an appreciable amount of internally spilled energy is eventually absorbed by the salt. An exact value cannot be obtained from this comparison because the temperatures of the nonabsorbing surfaces vary considerably, reflected in the $\bar{T}$ values in Table 6-IV.

Since the thermal conductivity of Pyromark is not well known, most runs did not include the effects of its conductivity (i.e., the temperature difference between the absorbing surface and the tube's outer wall is neglected). The effect of the current conductivity estimate of 0.4 W/mK on the thermal performance of the receiver was determined using a coating thickness of 0.025 mm (0.001 inches). As indicated in Table 6-IV, $\bar{T}$ increases slightly (approximately 15°F) with a very small change in η (0.24 percent). The temperature drop from the absorbing surface to the salt approximately doubles because, although the Pyromark is ~65 times less thick than the alloy 800 tubes, it is ~50 times less conductive. The smaller-than-expected effect of Pyromark's conductivity on the global values is, in part, due to the fact that approximately 62 percent of the cavity surface area is nonabsorbing surfaces, much of which is typically at higher surface temperatures than the absorbing panels.

Conditions at 1 hour before solar noon, designated as 11:00 a.m., were virtually identical to those at solar noon. The solar incident flux was slightly lower, with a corresponding decrease in the temperature of the nonabsorbing surfaces, which is reflected in the $\bar{T}$ values in Table 6-IV.

Results for 50 percent incident flux levels (representative of conditions during flux-on loss testing) indicate that losses decrease, but do not decrease in proportion to the incident power level. This is because the absorbing panel's front surface temperatures remain at levels near those for 100 percent field power (assuming the outlet salt temperature remains constant), whereas the nonabsorbing surface temperatures drop significantly. This suggests that correction for non-constant losses in the Barron flux-on loss technique is necessary. For example, a 50 percent reduction in incident flux produces a 26.3 percent decrease in heat loss, maintaining the same outlet temperature (see Table 6-IV).

Comparing these global predictions to the results of other global loss estimate techniques used in MSS/CTE, it appears that these loss values are above those estimated from flux-on loss testing, but are similar to those estimated from a measured output technique, in which the solar incident flux is calculated from HELIOS predictions and the absorbed power is measured, producing the loss figures. The loss estimates in Table 6-IV appear reasonable when compared to the design efficiency, recognizing the uncertainty in the measured data from the experiment.

Figures 6.2.1 thru 6.2.23 show local distributions of data that correspond to the global results in Table 6-IV.

FIGURE 6.2.1
SOLAR INCIDENT FLUX (kW/m^2)
SOLAR NOON, 100% FIELD

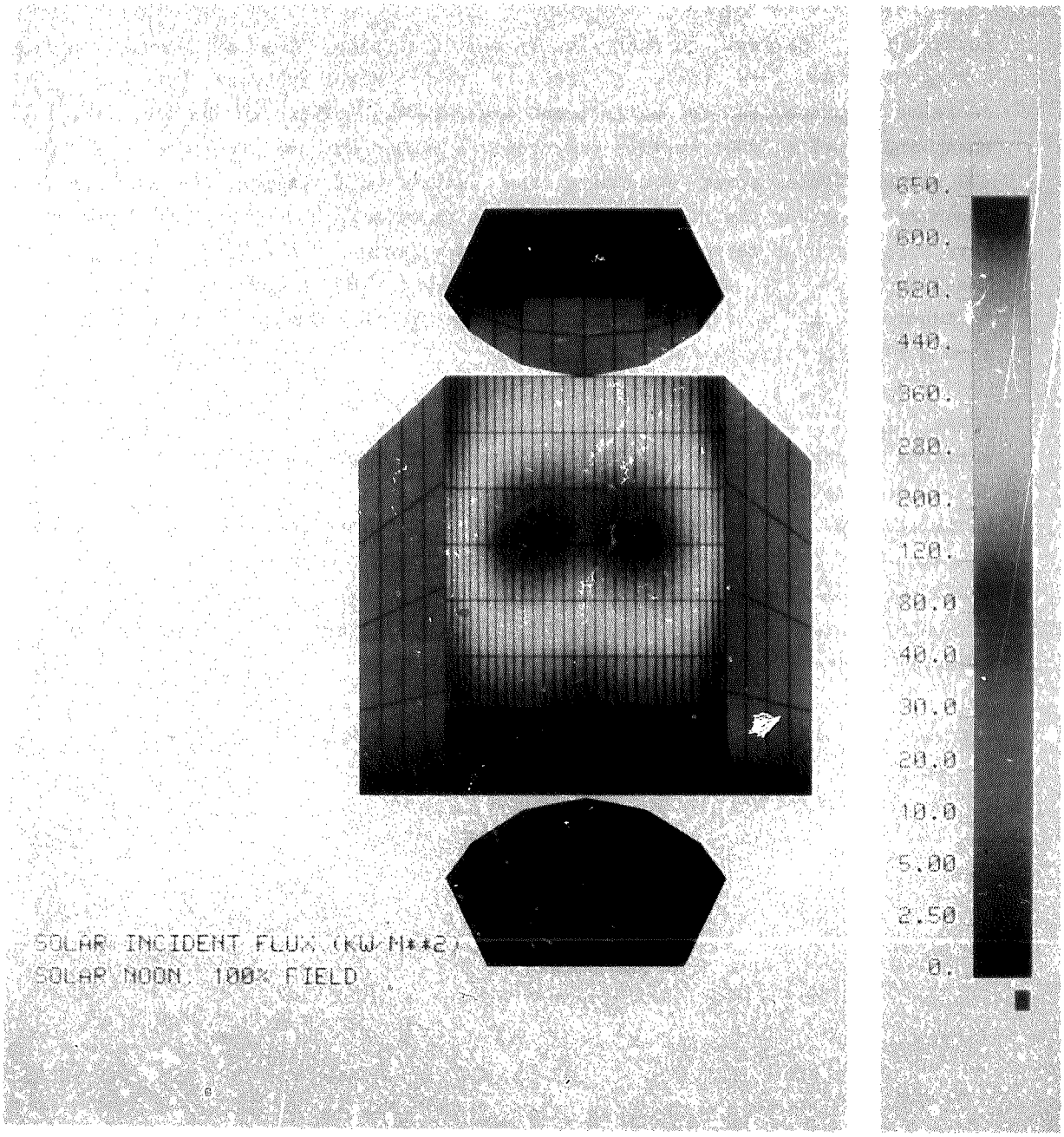

FIGURE 6.2.2
SOLAR INCIDENT FLUX (kW/m^2)
11 a.m., 100% FIELD

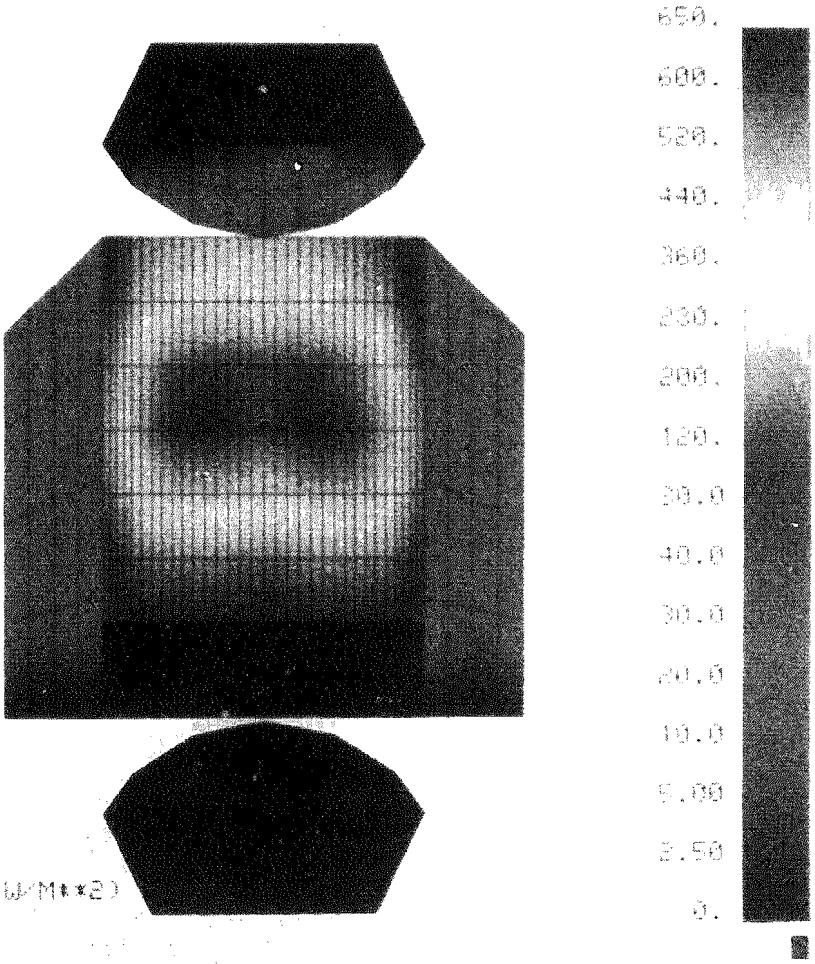

FIGURE 6.2.3

SALT TEMPERATURE (°F)

SOLAR NOON, 100% FIELD GLOBAL CONVECTION

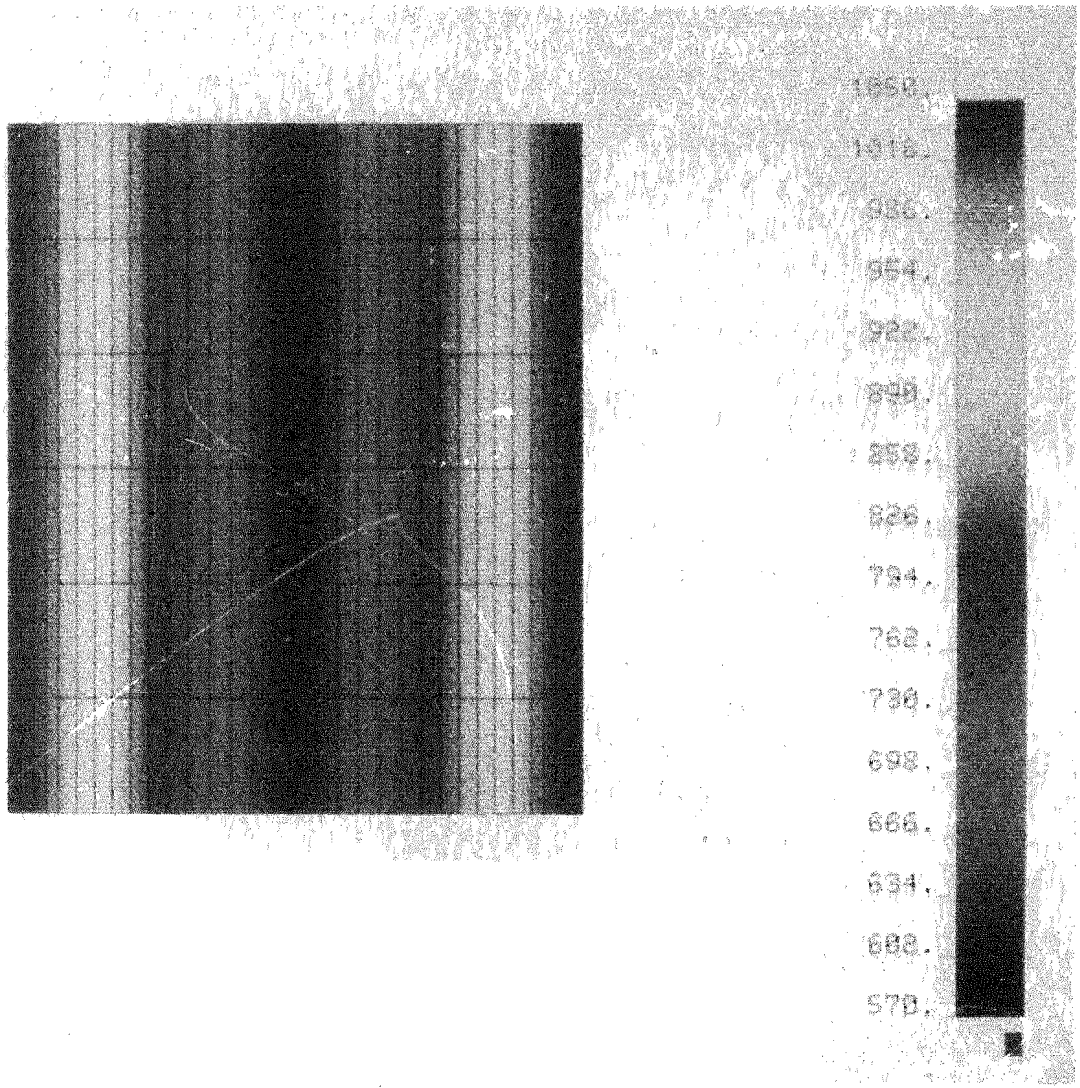

6.2.4

FRONT SURFACE TEMPERATURE (°F)

SOLAR NOON, 100% FIELD GLOBAL CONVECTION

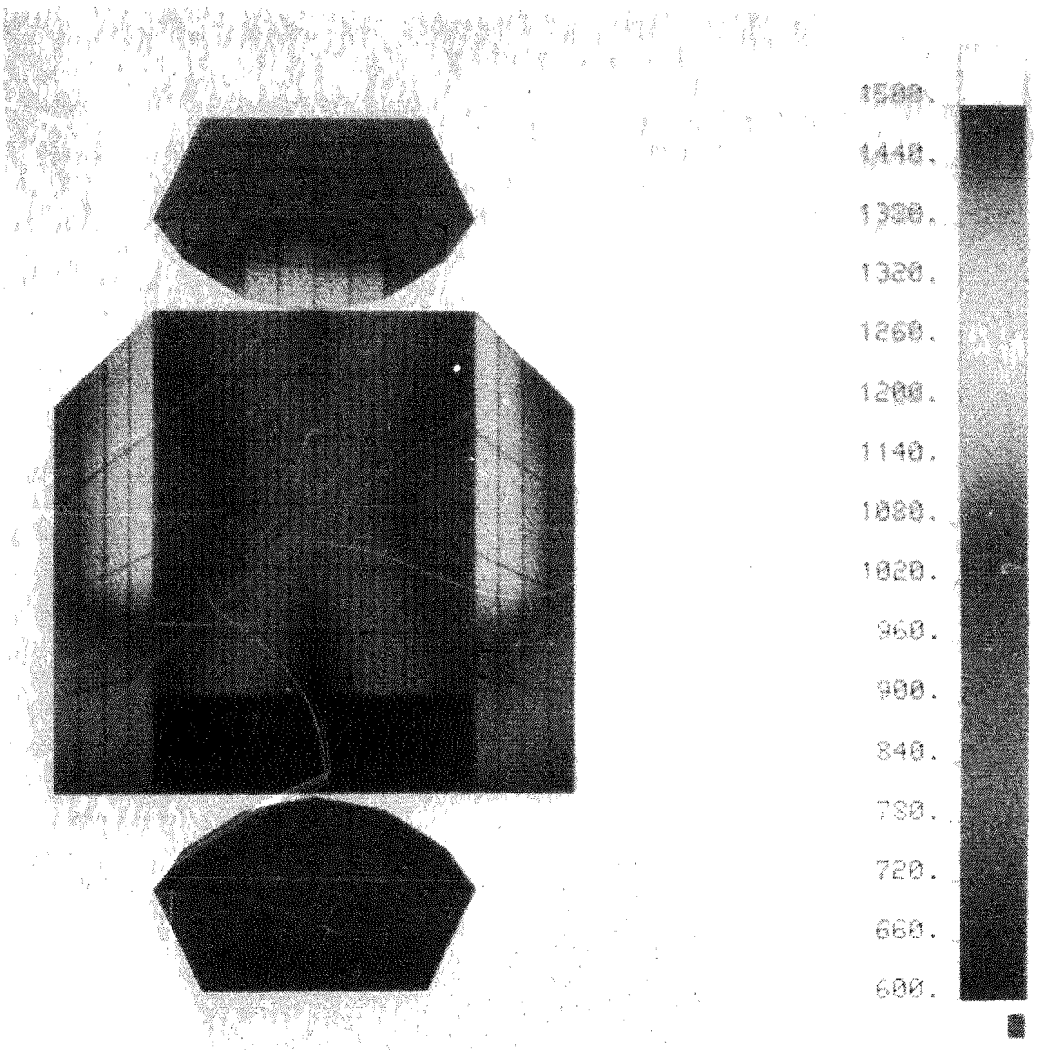

FIGURE 6.2.5

FRONT SURFACE TEMPERATURE (°F)

SOLAR NOON, 100% FIELD (2X) GLOBAL CONVECTION

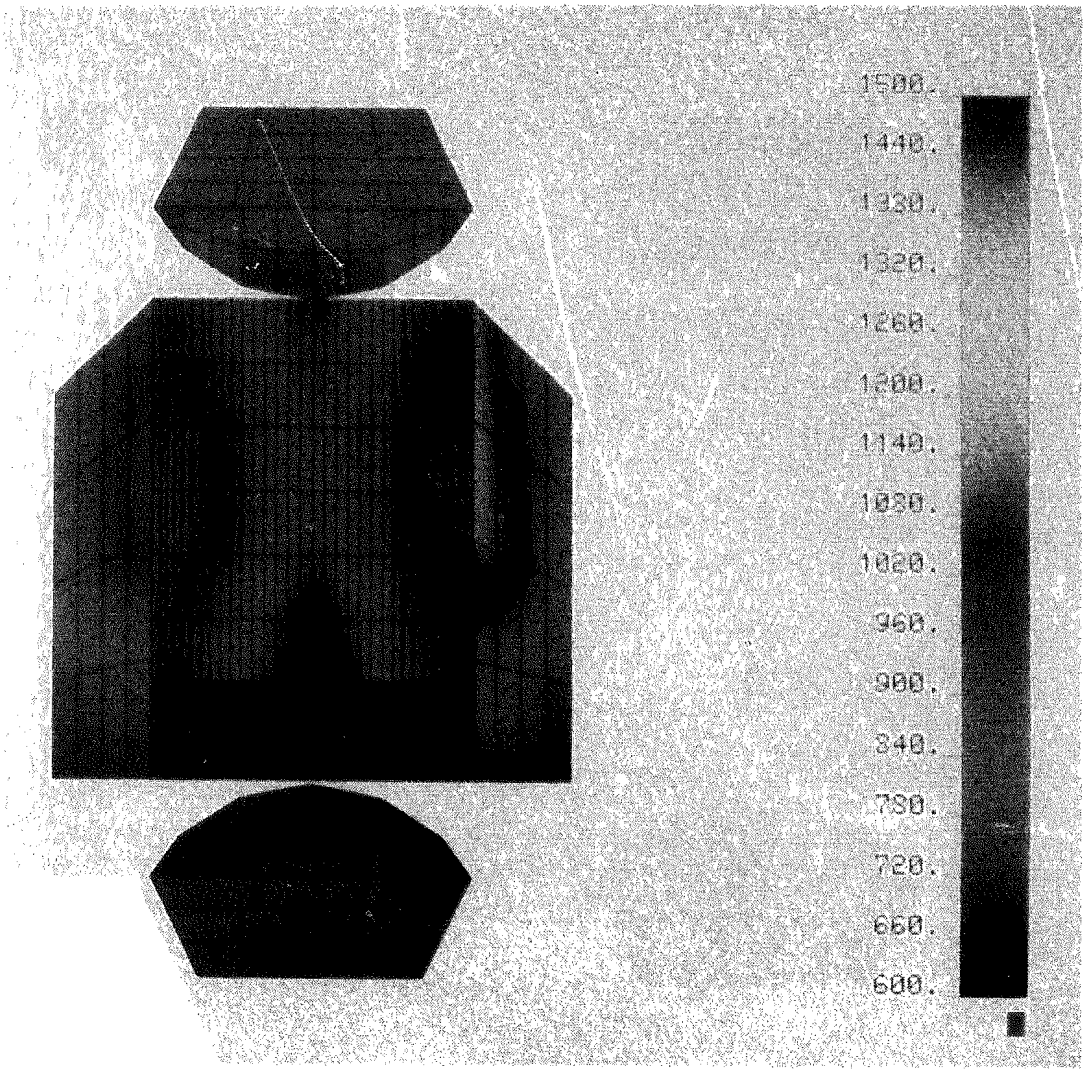

FIGURE 6.2.6

FRONT SURFACE TEMPERATURE (°F)

SOLAR NOON, 100% FIELD (1/2) GLOBAL CONVECTION

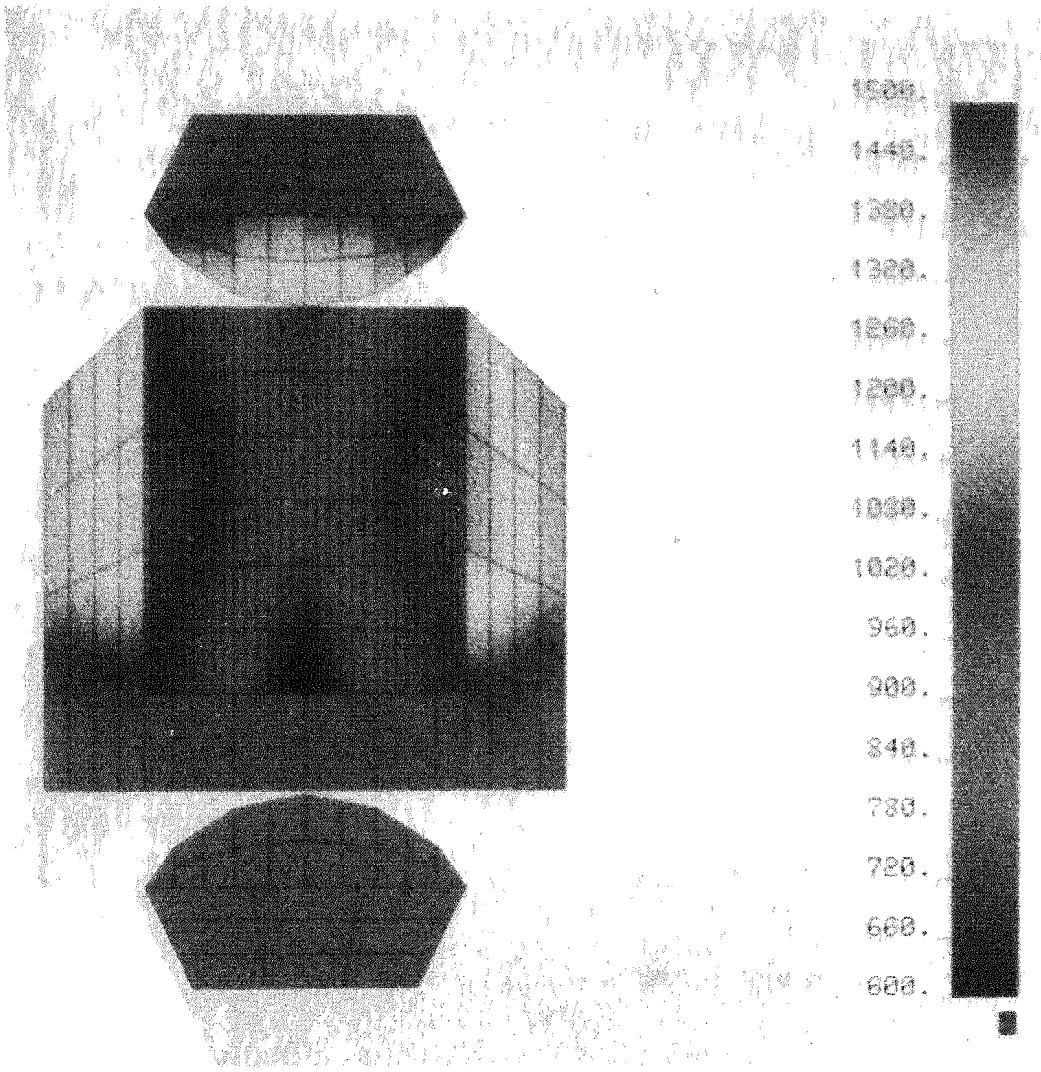

FIGURE 6.2.7
FRONT SURFACE TEMPERATURE (°F)
SOLAR NOON, 100% FIELD NO CONVECTION

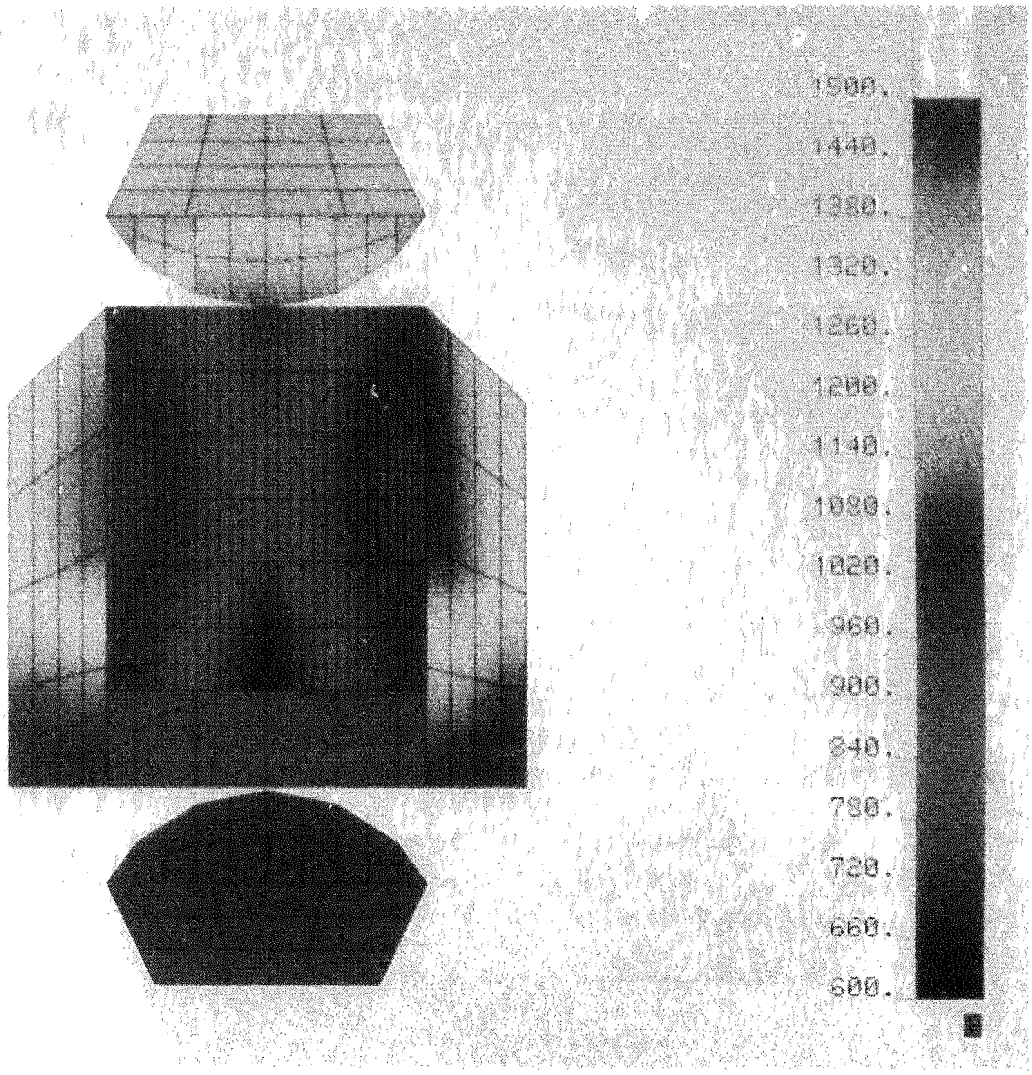

FIGURE 6.2.8

FRONT SURFACE TEMPERATURE (°F)

SOLAR NOON, 100% FIELD LOCAL CONVECTION

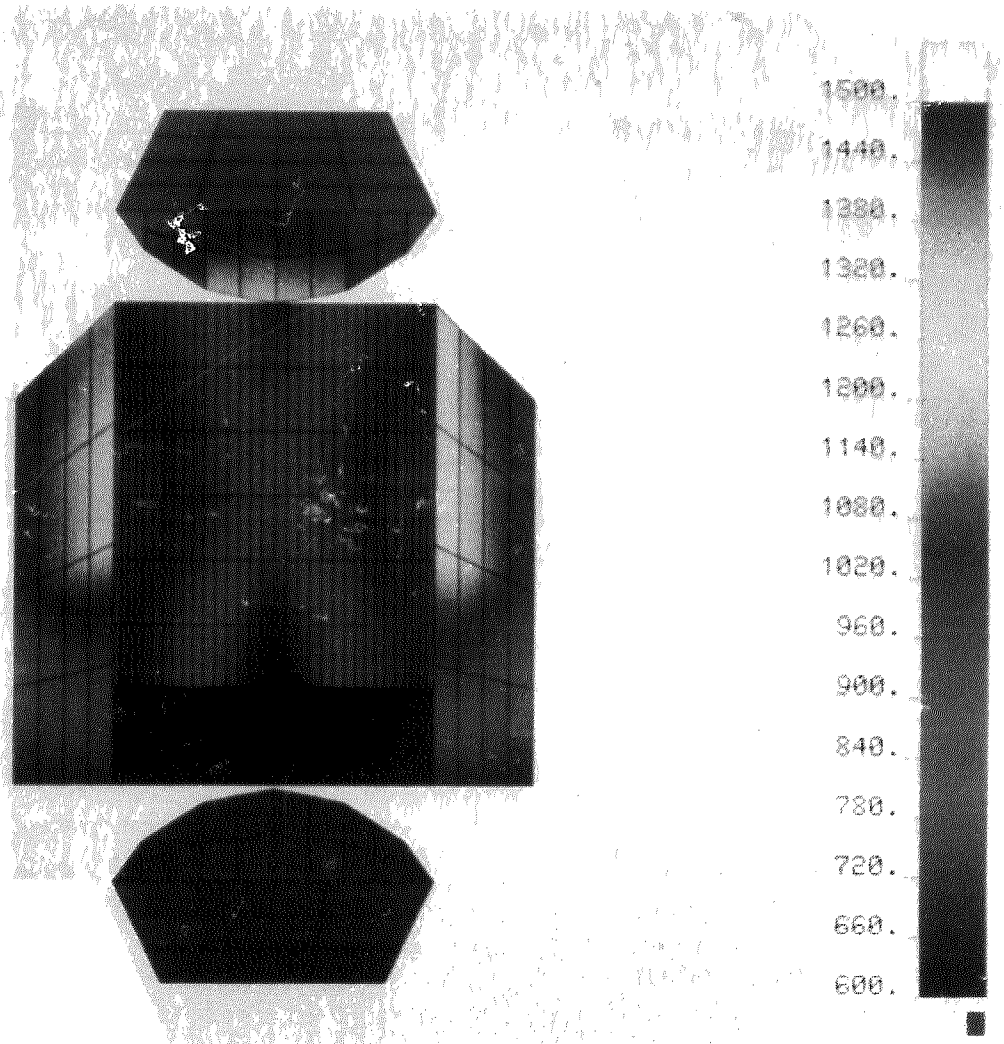

FIGURE 6.2.9

FRONT SURFACE TEMPERATURE (°F)

SOLAR NOON, 100% FIELD GLOBAL CONVECTION KAOWOOL ABSORPT=0.1

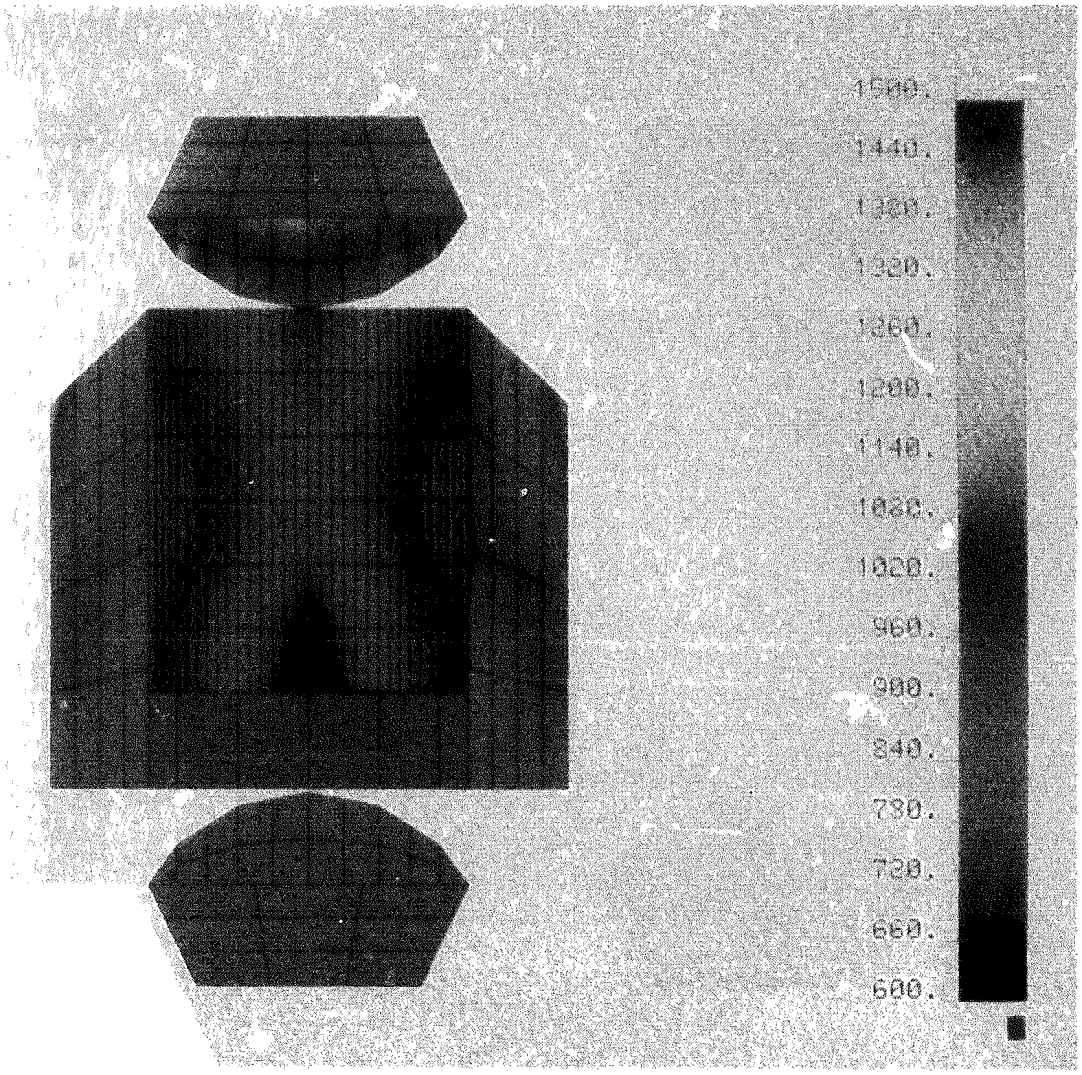

FIGURE 6.2.10

FRONT SURFACE TEMPERATURE (°F)

SOLAR NOON, 100% FIELD GLOBAL CONVECTION KAOWOOL ABSORPT=0.7

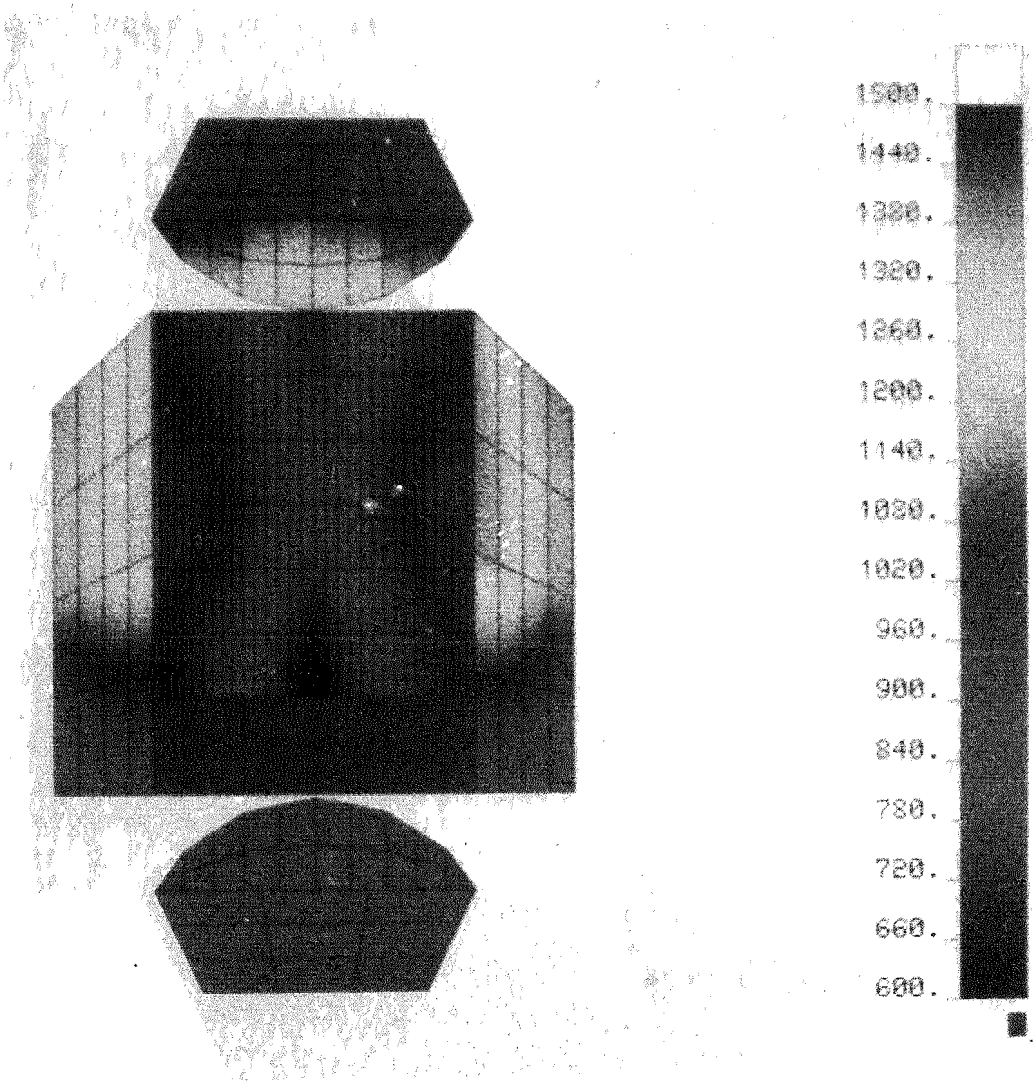

FIGURE 6.2.11

FRONT SURFACE TEMPERATURE (°F)

SOLAR NOON, 100% FIELD NO INTERNAL SPILLAGE GLOBAL CONVECTION

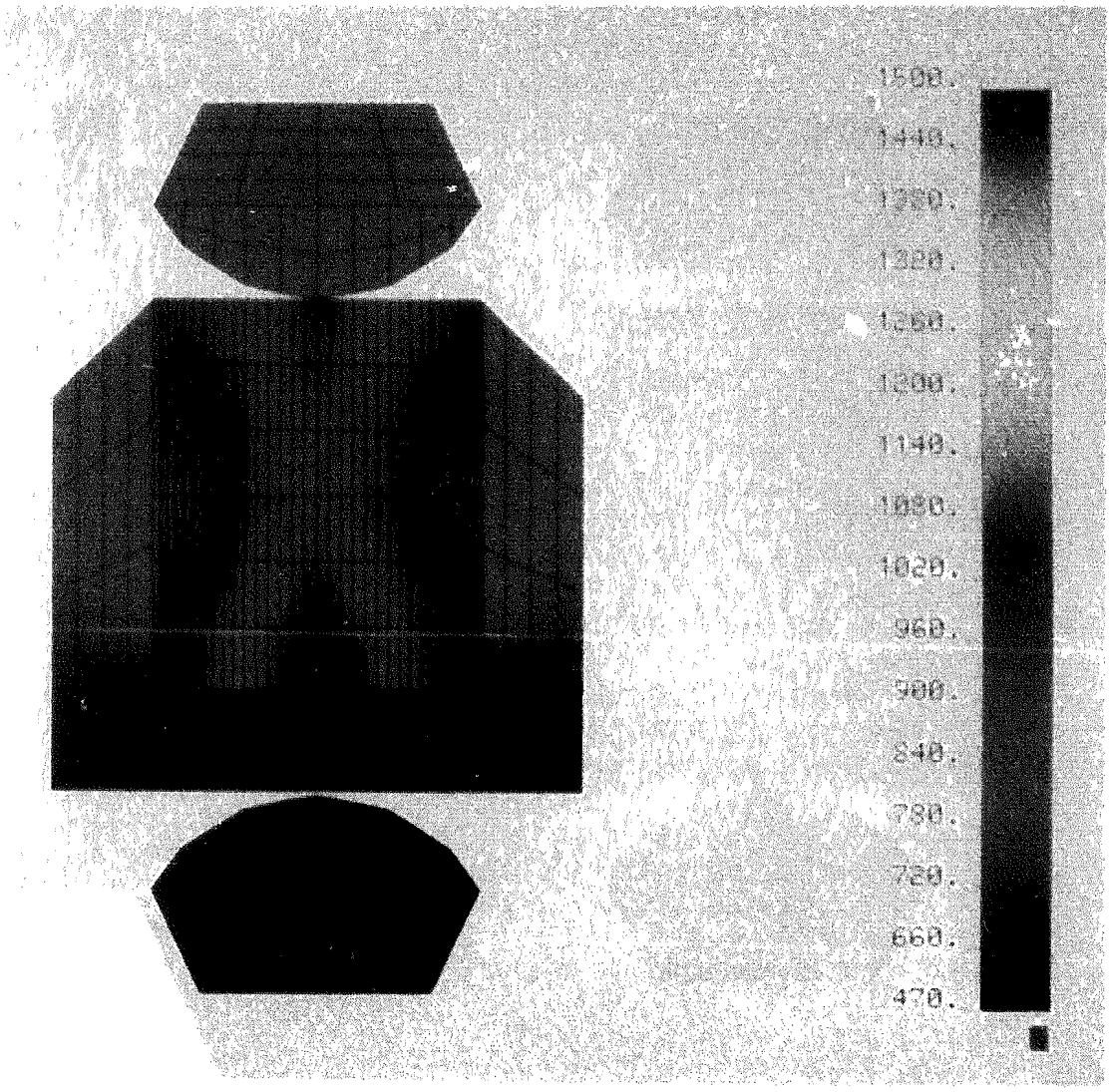

FIGURE 6.2.12

FRONT SURFACE TEMPERATURE (°F)

SOLAR NOON, 100% FIELD GLOBAL CONVECTION PYROMARK COND. INCL.

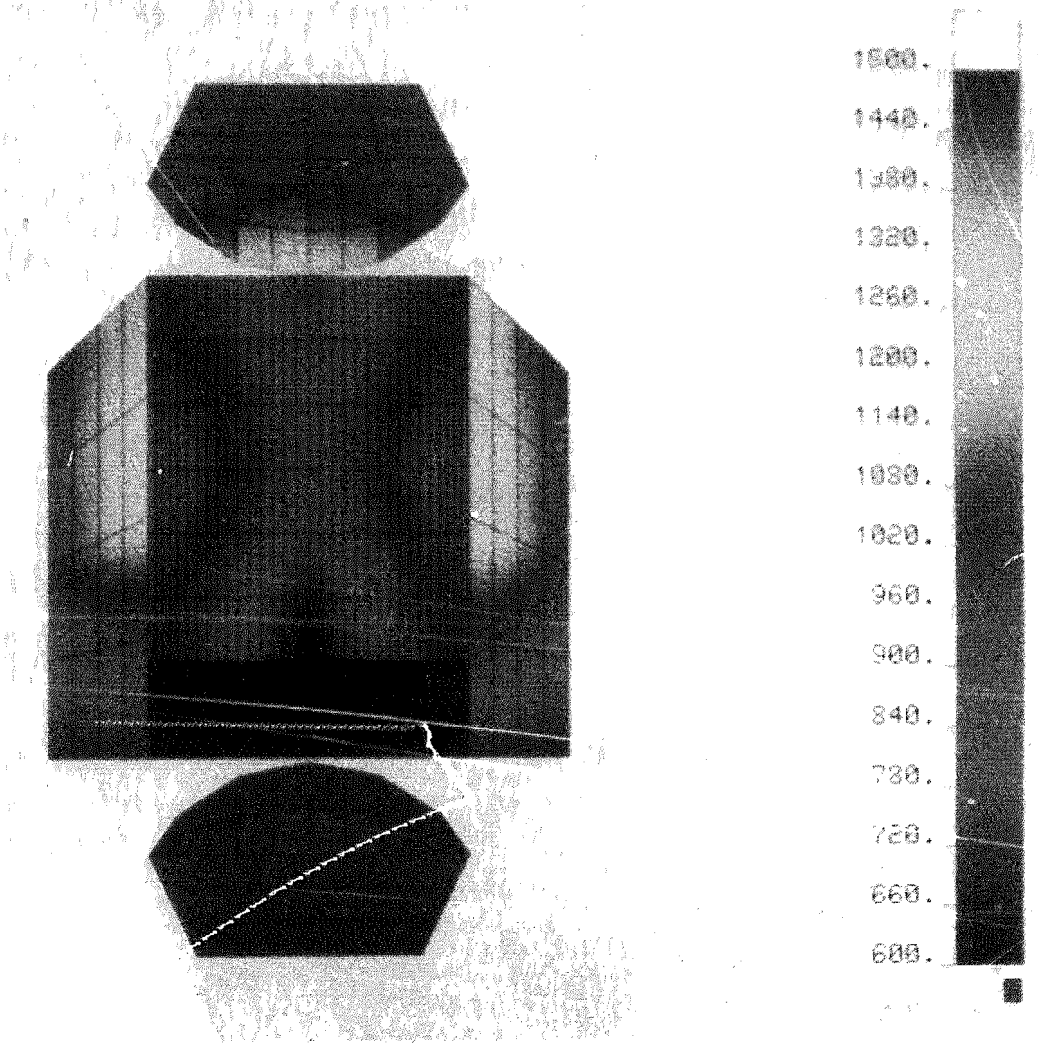

FIGURE 6.2.13

FRONT SURFACE TEMPERATURE (°F)

11 a.m., 100% FIELD GLOBAL CONVECTION

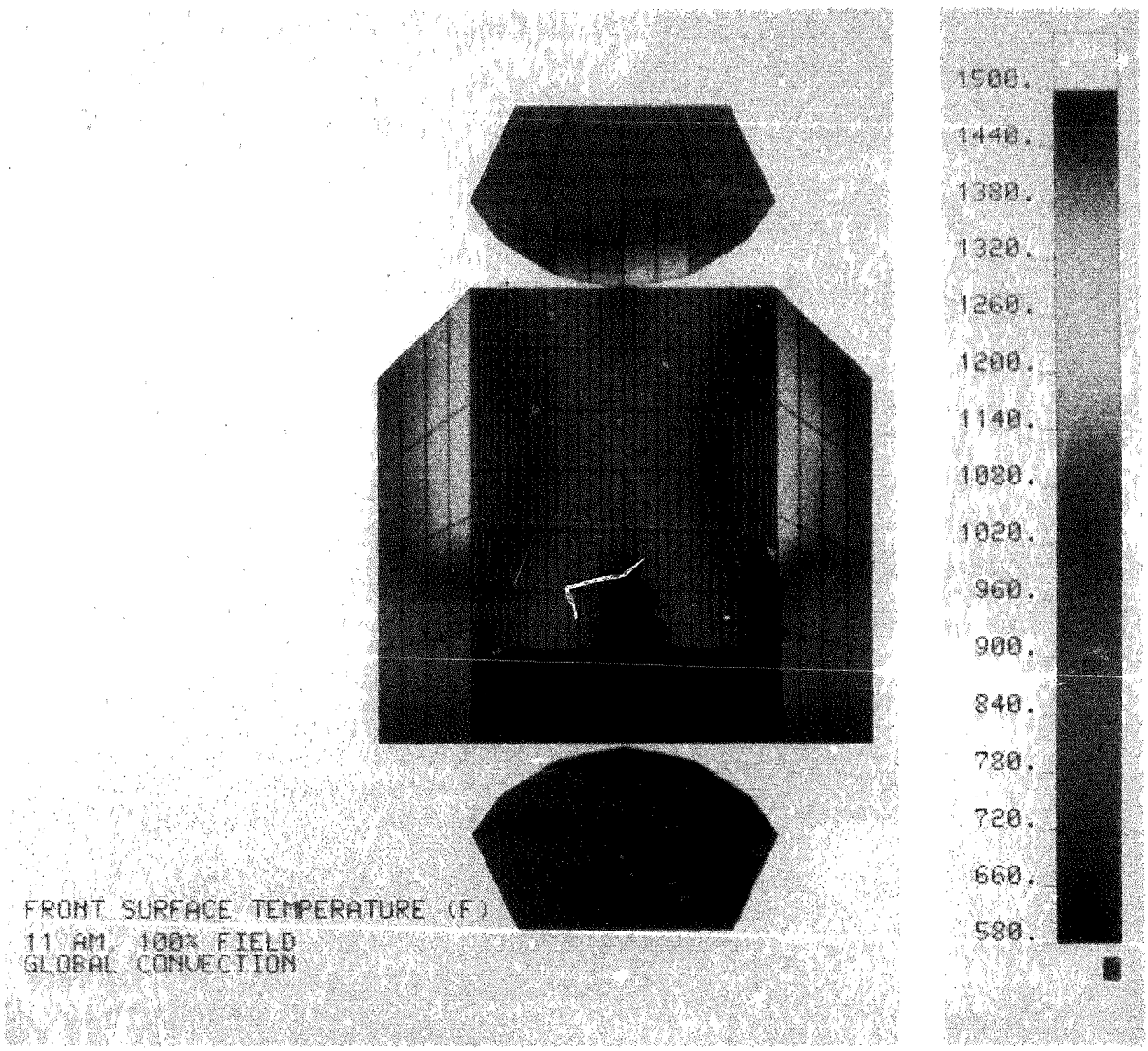

FIGURE 6.2.14

FRONT SURFACE TEMPERATURE (°F)

SOLAR NOON, 50% FIELD GLOBAL CONVECTION

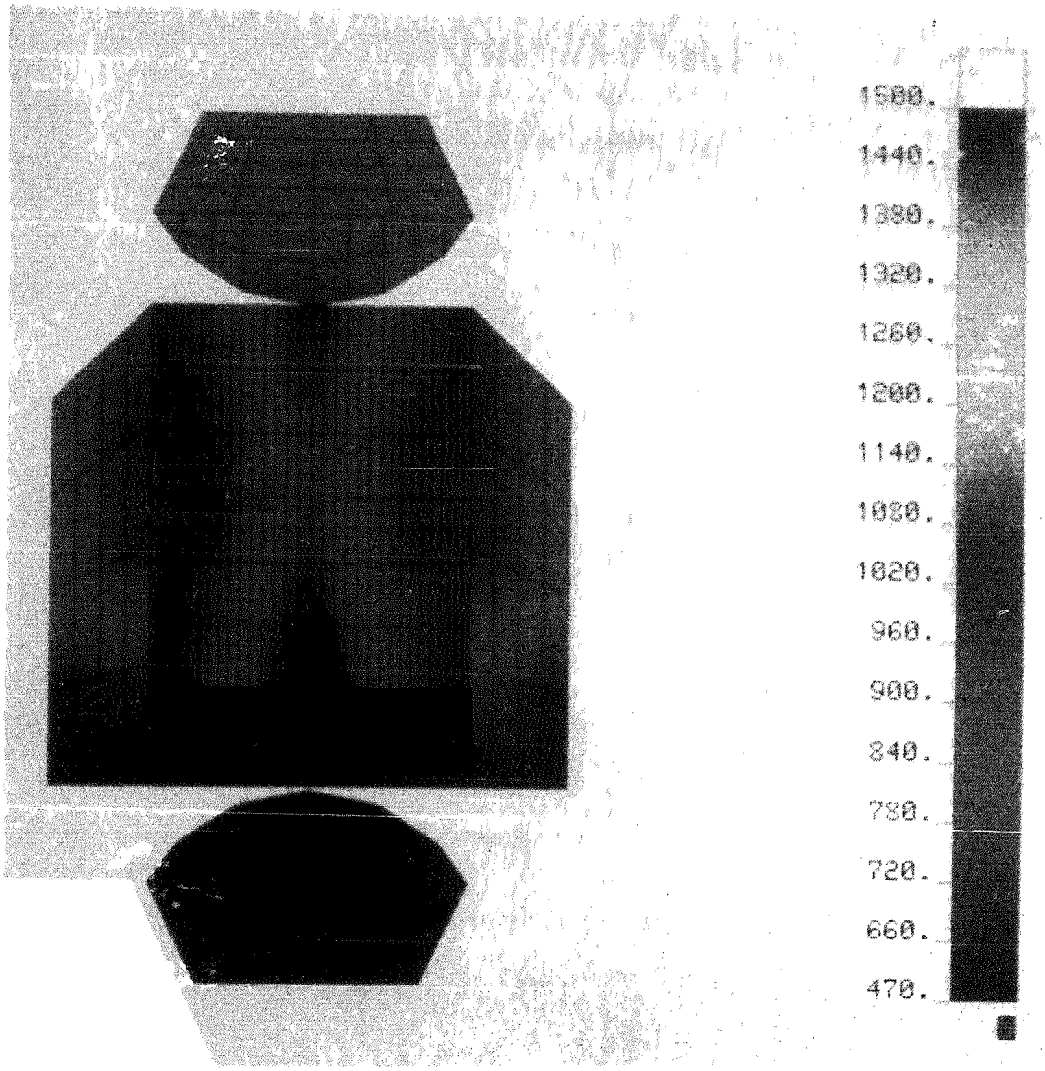

FIGURE 6.2.15

TUBE INNER WALL TEMPERATURE (°F)

SOLAR NOON, 100% FIELD GLOBAL CONVECTION

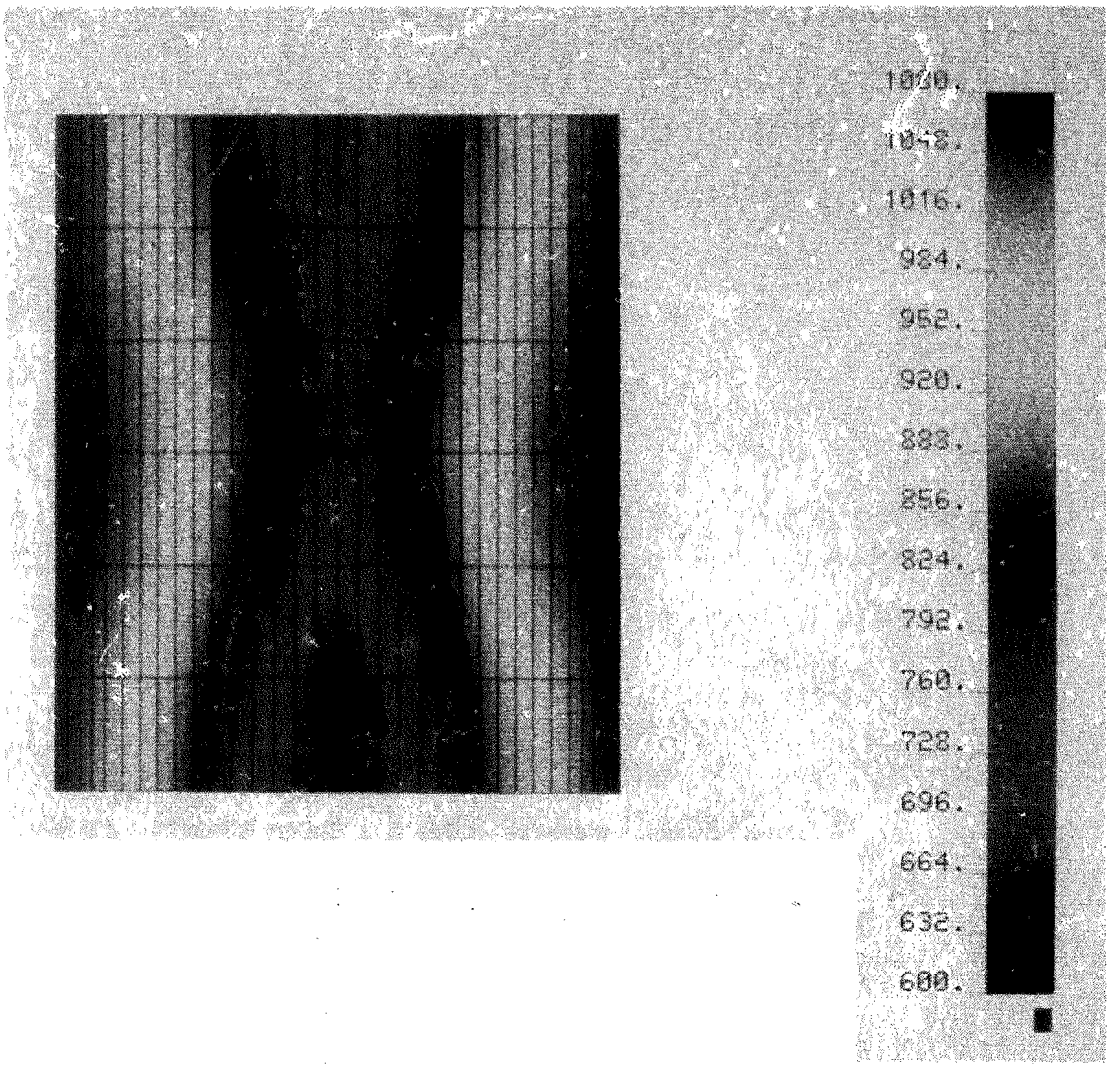

FIGURE 6.2.16

CONVECTION FLUX (kW/m^2)

SOLAR NOON, 100% FIELD GLOBAL CONVECTION

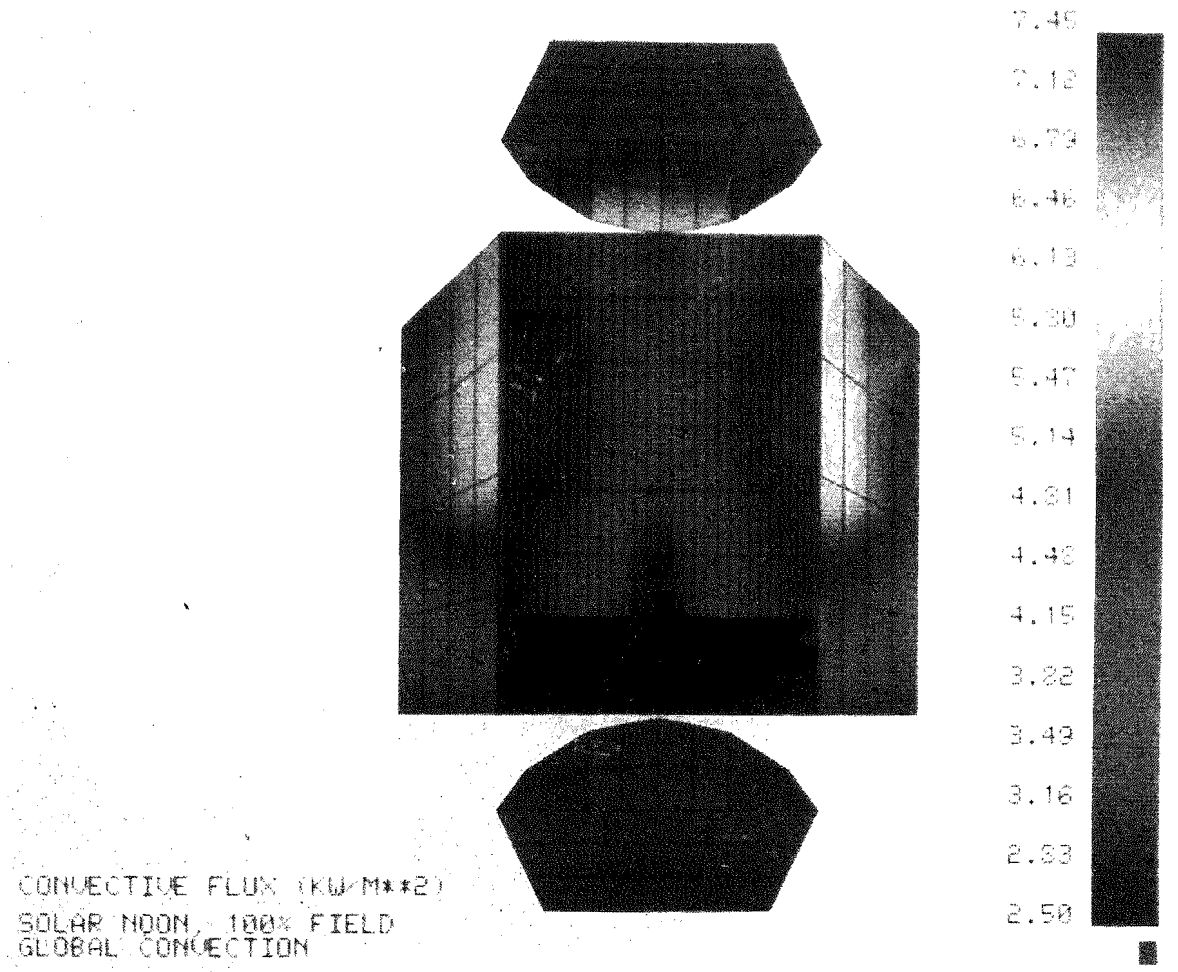

FIGURE 6.2.17
CONVECTIVE FLUX (kW/m^2)
SOLAR NOON, 100% FIELD LOCAL CONVECTION

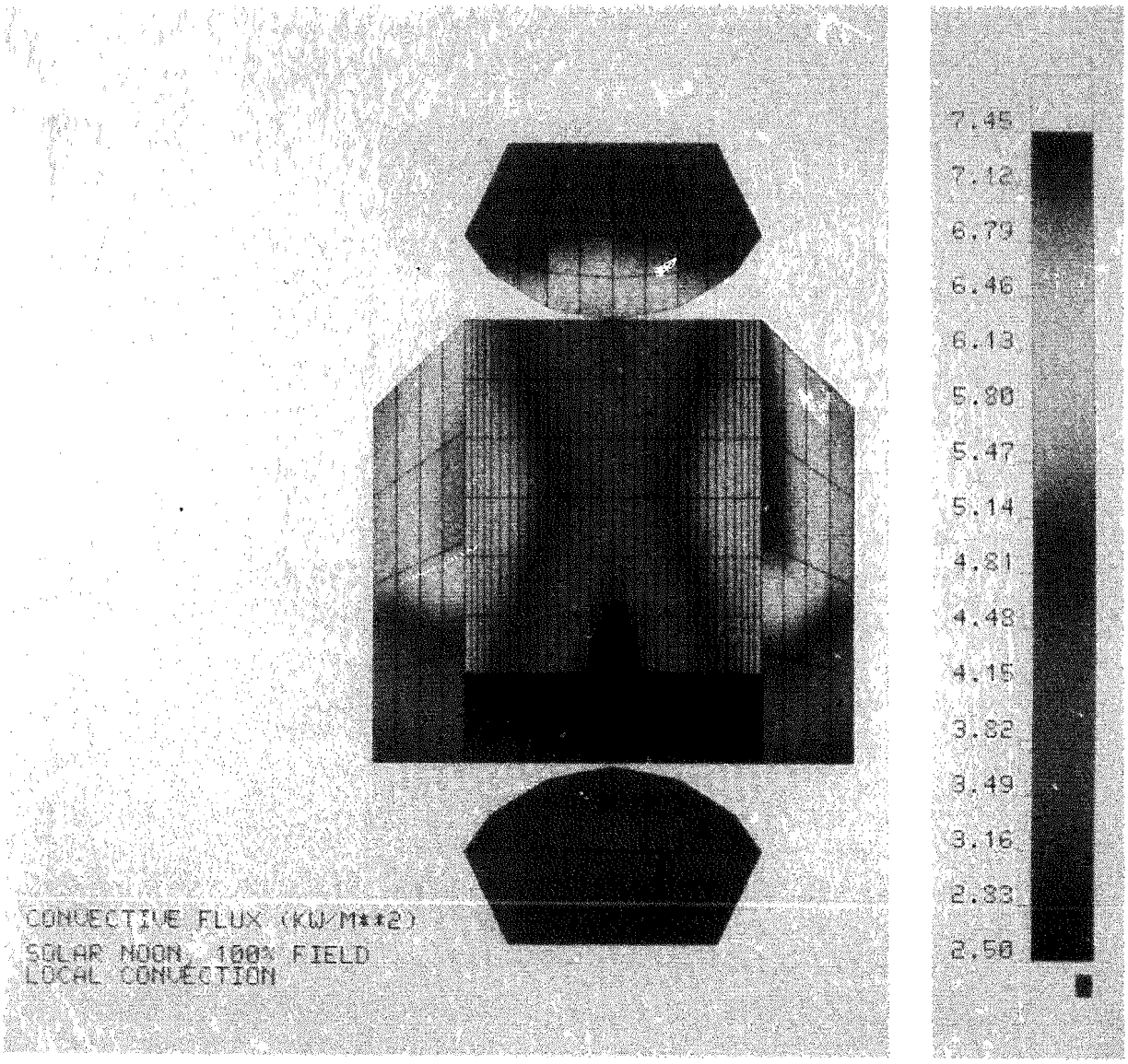

FIGURE 6.2.18
ABSORBED FLUX (kW/m^2)
SOLAR NOON, 100% FIELD GLOBAL CONVECTION

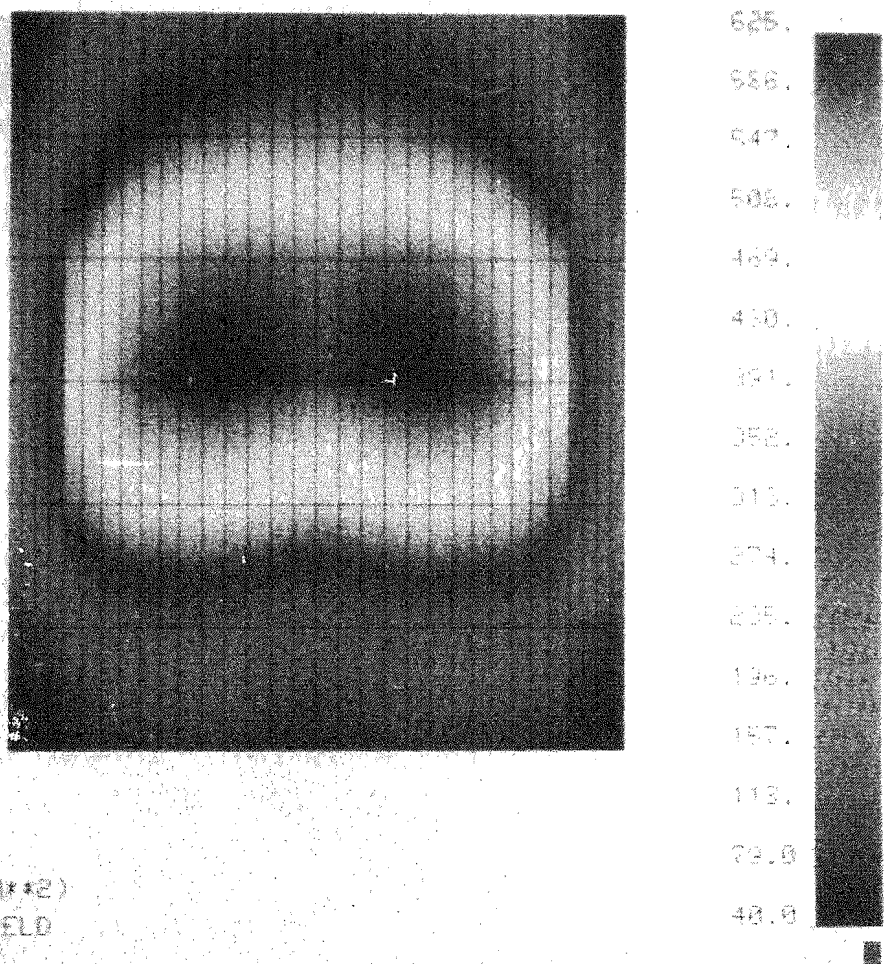

FIGURE 6.2.19
ABSORBED FLUX (kW/m^2)
11 a.m., 100% FIELD GLOBAL CONVECTION

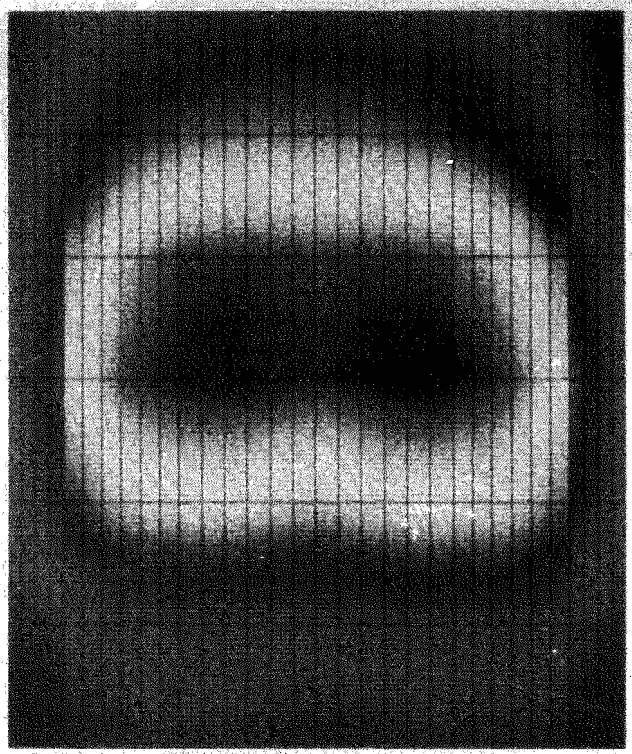

FIGURE 6.2.20
ABSORBED FLUX (kW/m^2)
SOLAR NOON, 50% FIELD GLOBAL CONVECTION

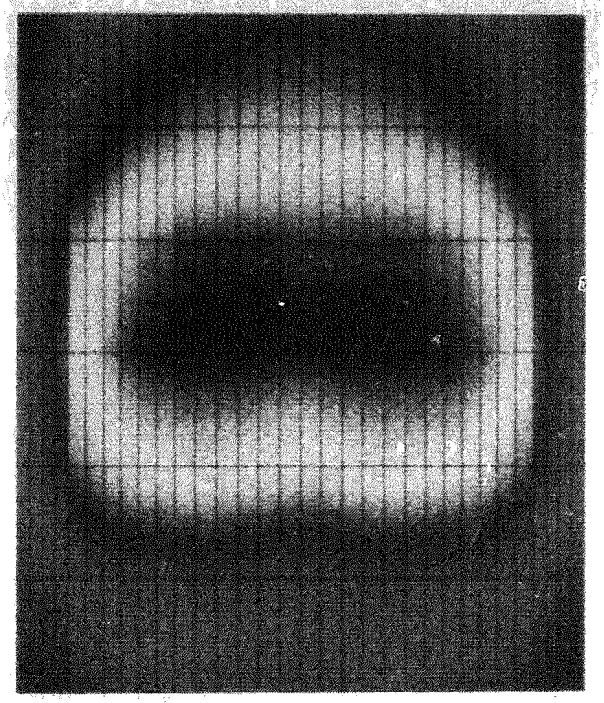

FIGURE 6.2.21

ABSORPTION EFFICIENCY

SOLAR NOON, 100% FIELD GLOBAL CONVECTION

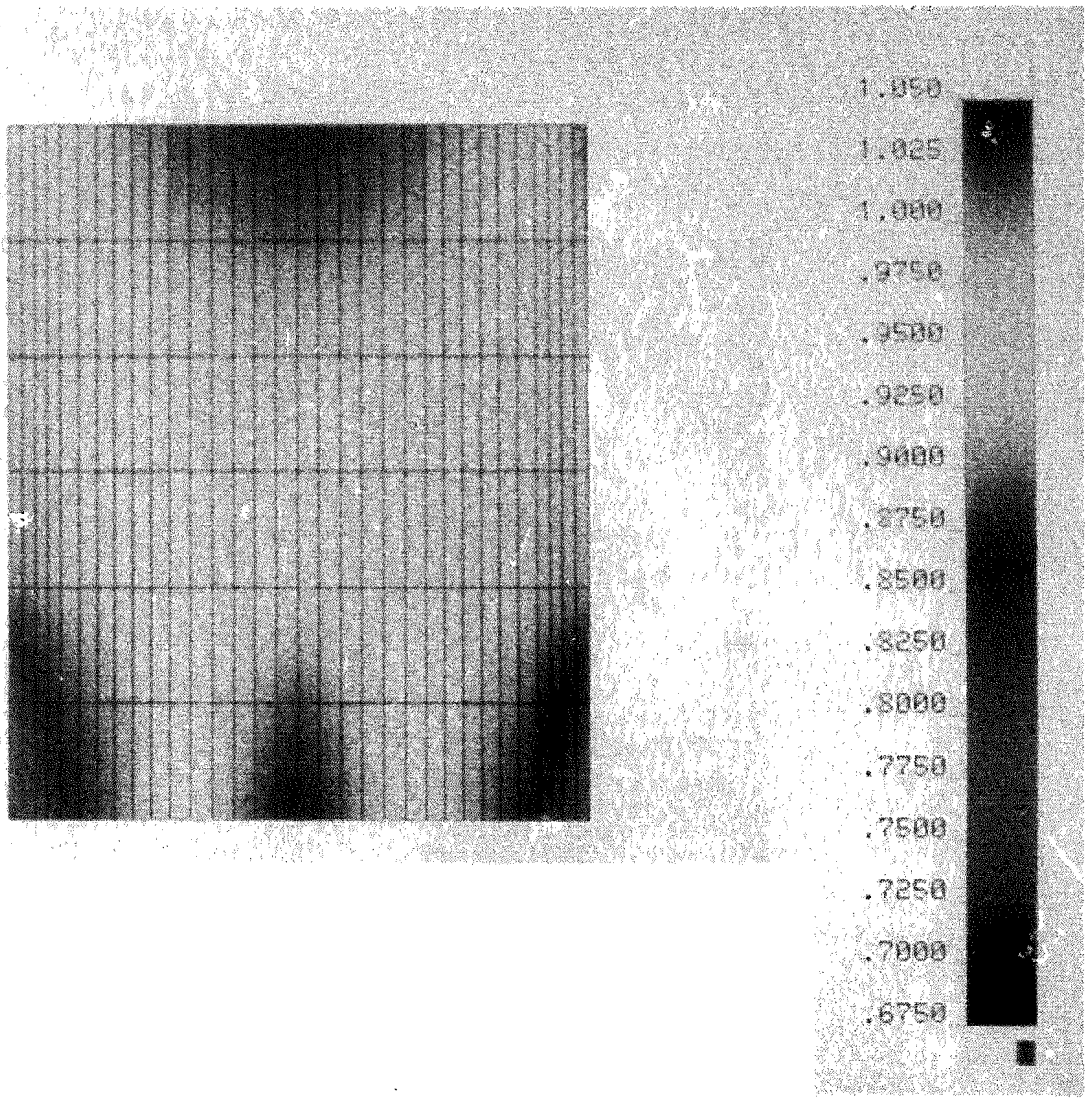

FIGURE 6.2.22

ABSORPTION EFFICIENCY

11 a.m., 100% FIELD GLOBAL CONVECTION

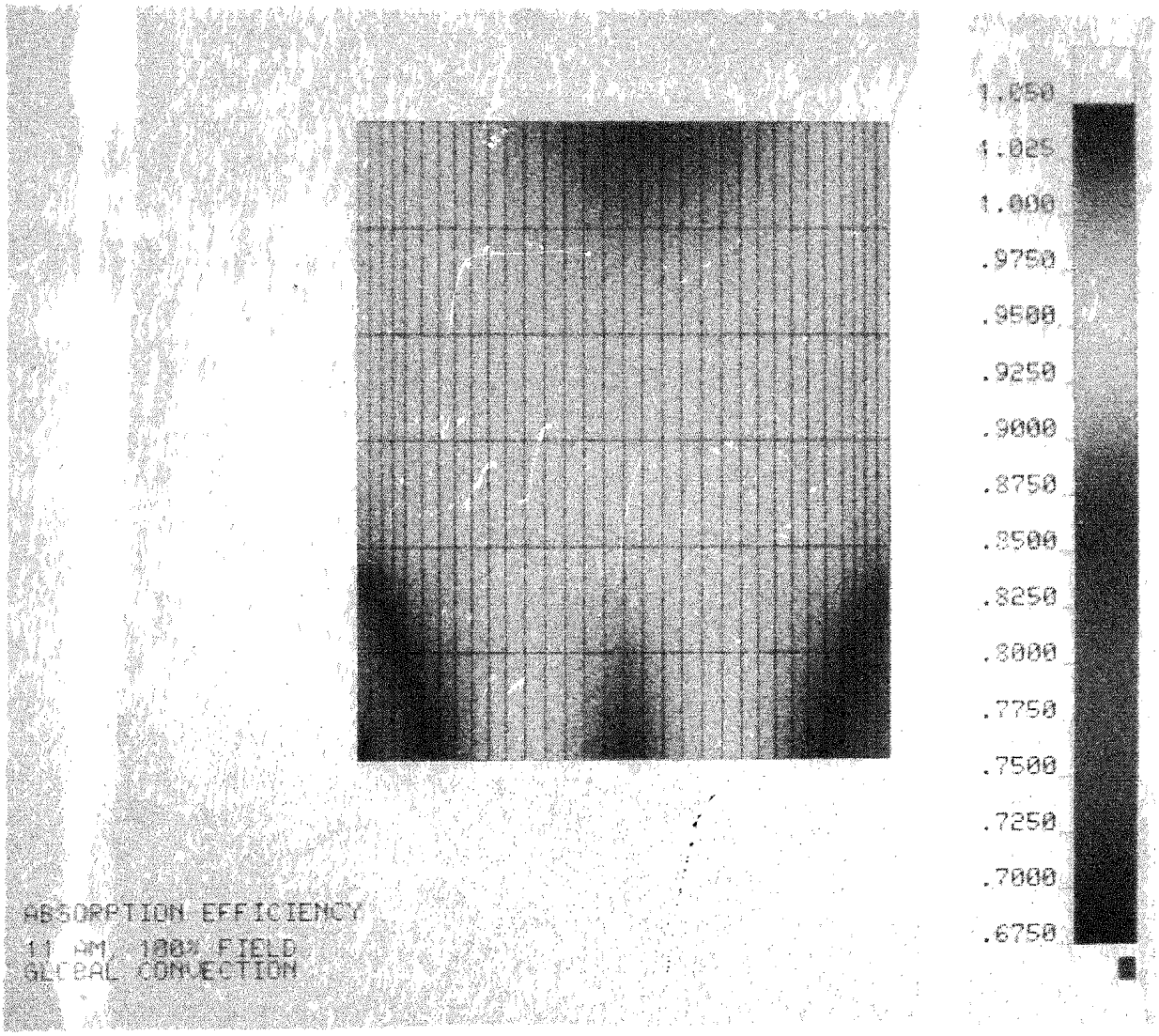

FIGURE 6.2.23
ABSORPTION EFFICIENCY
SOLAR NOON, 50% FIELD GLOBAL CONVECTION

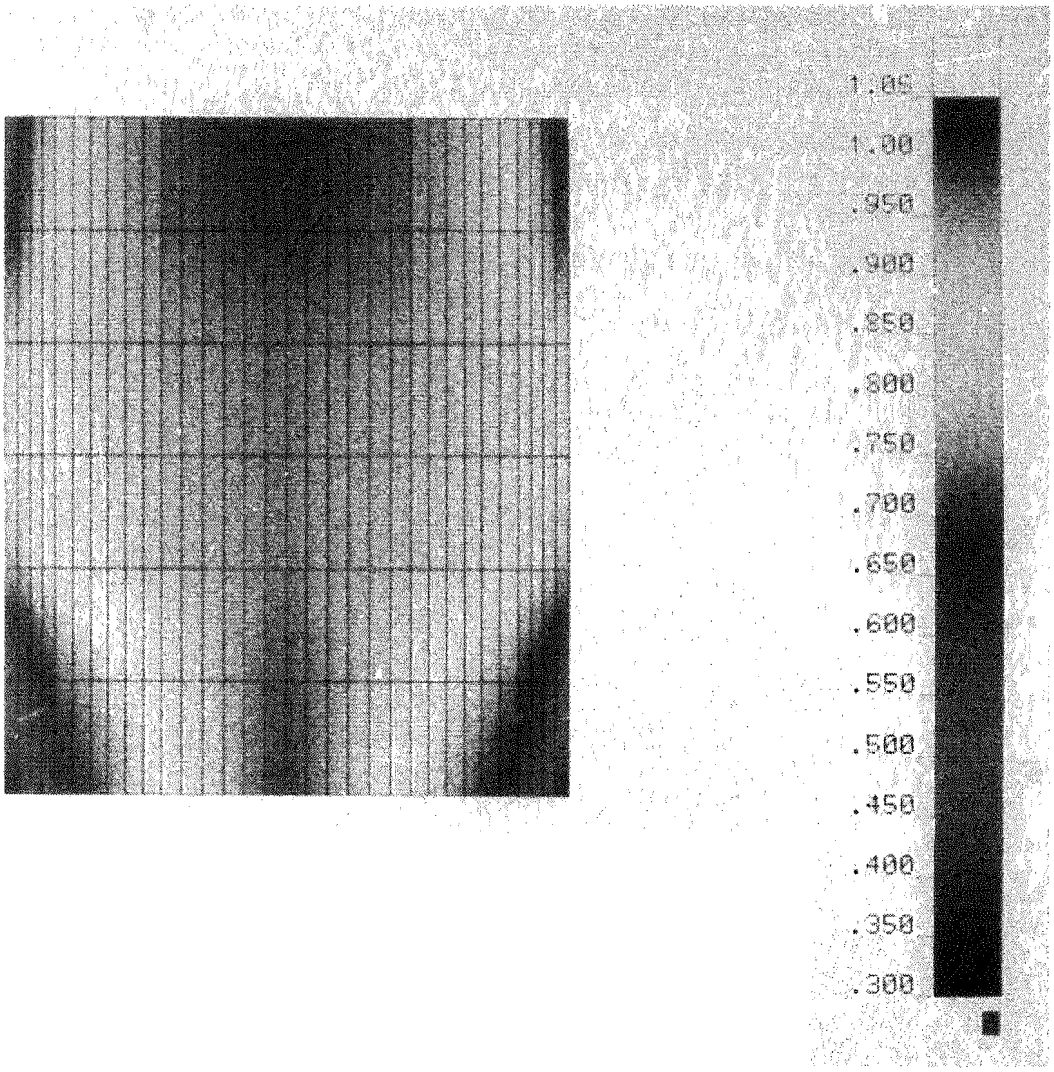

Before discussing these figures, some items must first be addressed. First, the figures show distributions on views of either the receiver's cavity surfaces unfolded (side panels out, floor down, ceiling up), or the absorbing panels only. Note that the cylindrical aspect of the absorbing panels is maintained so that the panels near the sides appear "narrower" due to the viewing angle. Second, the distributions are meant to be primarily informative in terms of trends, while being as quantitative as possible. Efforts were made to maintain a consistent scale when feasible, although the highest and lowest values were changed to reflect the maxima and minima for each figure. An interpolation routine is used to generate the distributions, and care must be used when interpreting the distributions, because there is only a single data value at each element. Finally, it must again be mentioned that these results are produced by a single-band radiative model, and the spectrally varying radiative properties were approximated by gray values. This is particularly important when considering the fibrous Kaowool insulation, which constitutes all surfaces other than the absorbing panels. For example, preliminary results from a current 2-band analysis of the base-line case indicates $\bar{T}$ drops by ~50°F and η increases by ~1 percent (due to the higher reflectivity of the Kaowool insulation in the solar spectrum). The only effective changes in the analysis are the radiative properties of the surface materials--the 2-band analysis used both solar-weighted and infrared-weighted values and the single-band analysis used a single gray estimate.

Seven different parameters were investigated:

1) Solar Incident Flux: Figure 6.2.1 presents the solar incident flux as predicted by HELIOS for solar noon and includes internal spillage (energy passing through the aperture but incident on surfaces other than the absorbing panels). The distributions are essentially symmetric as expected, with the west (right, as pictured) side having a slightly greater incident flux. Conditions at 1 hour before solar noon were comparable (see Figure 6.2.2).

2) Salt Temperature: The salt temperature plotted in Figure 6.2.3 is seen to monotonically increase in temperature as it flows in the east and west serpentine patterns from the prescribed inlet temperature of 573°F to the prescribed outlet temperature of 1050°F. The salt-mass flow rate and salt temperature predictions are quantities that should most closely compare with directly measured data. The agreement between flow-rate data and predictions has already been discussed. The salt temperatures correlate well with measured data for the back-tube temperatures. For example, data from April 15, 1987, for Barron flux-on loss tests (half-power, full-power, half-power) indicate reasonably constant back-tube temperatures for the center panels between 600-750°F and the side panels between 1030-1050°F, comparing well with those indicated in Figure 6.2.3. Of course, since the salt outlet temperature of 1050°F is maintained, this is not the most severe test of the numerical model, but does indicate the integrated absorbed power levels are appropriate.

3) Front Surface Temperature: Figures 6.2.4 thru 6.2.14 indicate the temperature distributions of the absorbing panel's front surface are a function of the salt's temperature distribution and the incident flux distribution. That is, the surface temperature increases with Q_s, but remains above the salt temperature at that point. The nonabsorbing element's temperatures are affected by convective heat transfer and radiative properties. As discussed above, these surface temperatures decrease when the global convection is doubled (Figure 6.2.5) and increase when it is halved (Figure 6.2.6); they significantly increase when no convection is allowed (compare Figures 6.2.4, 6.2.9 and 6.2.10). The local convection submodel (Figure 6.2.8) produces a greater temperature gradient across the nonabsorbing elements due to the greater temperature-dependency inherent in this analysis. The absorbing panel's temperatures remain relatively constant across these cases because their temperature is dominated by non-convective energy transfer. The effect of changing the Kaowool absorptivity/emissivity on the uniformity of the nonabsorbing wall temperatures is indicated in Figures 6.2.9 and 6.2.10 as discussed earlier (compare Figures 6.2.4

and 6.2.6). The effects of other parameters on the local front surface temperature distributions were also investigated. If no internal spillage occurred, the nonabsorbing wall temperatures dropped significantly (as much as 440°F, Figure 6.2.11). Including the Pyromark conductivity in the analysis produced a relatively uniform increase in the temperatures of the absorbing panel's surface (Figure 6.2.12). Conditions at 1 hour before solar noon were very similar to those at solar noon, with a very slight decrease in surface temperatures ($\bar{T}$ decreased by 13°F, see Figure 6.2.13). Power conditions of 50 percent (Figure 6.2.14) decrease the nonabsorbing wall temperatures, although the absorbing panel temperatures remain relatively constant.

4) Temperature of the Tube's Inner Wall: The distributions are generally similar to the temperature distributions of the front surface, with values between the temperature of the local front surface and of the local salt (see Figure 6.2.15). The maximum allowable inner wall temperature of the tube is 1112°F, above which the nitrate salt becomes chemically unstable and very corrosive. For all conditions investigated, the inner wall temperatures of the tube were less than 1080°F. The effect of including the thermal conductivity of the Pyromark coating on the tube's inner wall temperatures was small, because the salt temperature was constrained. Therefore, the front surface temperature increased.

5) Convective Flux: The distributions (Figures 6.2.16 and 6.2.17) generally followed the temperature distributions of the front surface with the local convective submodel values having a greater dependence on the surface temperature than the global convective submodel values.

6) Absorbed Flux: The distributions (Figures 6.2.18 thru 6.2.20) were similar to the incident flux distributions and were symmetric. The distribution shapes were the same within 1 hour of solar noon.

7) Absorption Efficiency: In general, the absorption efficiencies (see Figures 6.2.21 and 6.2.23) were greater than 90 percent. The absorption efficiency, as defined earlier, reflects all methods of energy transfer, so that when the efficiency is greater than 1 percent it is due to modes of energy transfer to that element other than direct solar incident flux. That is, when the efficiency is greater than 1 percent, the contributions are due to the cavity environment (external environment efficiencies cannot be greater than one). The efficiencies at 1 hour before solar noon (Figure 6.2.22) are very slightly lower than those at solar noon. There is no discernible effect of altering the nonabsorbing element absorptivities from 0.3 to either 0.1 or 0.7. There is a significant difference between the 100 percent field and 50 percent field incident power efficiency values. The 50 percent field efficiency values (Figure 6.2.23) are markedly lower, since solar incident energy is halved whereas the radiative and convective losses remain relatively constant, constrained by the desired salt temperature. The energy available to be absorbed is much lower, resulting in low efficiency values.

Flux-off radiative losses out of the cavity were calculated as a function of assumed isothermal absorbing panel temperatures and are plotted in Figure 6.2.24. The nonabsorbing walls are taken to be adiabatic. The area-averaged temperatures for the cavity and for the nonabsorbing element are listed in Table 6-V for these conditions. These data and those in Table 6-IV were used as radiative loss estimates in independent global convection loss modeling.

7) Absorption Efficiency: In general, the absorption efficiencies (see Figures 6.2.21 and 6.2.23) were greater than 90 percent. The absorption efficiency, as defined earlier, reflects all methods of energy transfer, so that when the efficiency is greater than 1 percent it is due to modes of energy transfer to that element other than direct solar incident flux. That is, when the efficiency is greater than 1 percent, the contributions are due to the cavity environment (external environment efficiencies cannot be greater than one). The efficiencies at 1 hour before solar noon (Figure 6.2.22) are very slightly lower than those at solar noon. There is no discernible effect of altering the nonabsorbing element absorptivities from 0.3 to either 0.1 or 0.7. There is a significant difference between the 100 percent field and 50 percent field incident power efficiency values. The 50 percent field efficiency values (Figure 6.2.23) are markedly lower, since solar incident energy is halved whereas the radiative and convective losses remain relatively constant, constrained by the desired salt temperature. The energy available to be absorbed is much lower, resulting in low efficiency values.

Flux-off radiative losses out of the cavity were calculated as a function of assumed isothermal absorbing panel temperatures and are plotted in Figure 6.2.24. The nonabsorbing walls are taken to be adiabatic. The area-averaged temperatures for the cavity and for the nonabsorbing element are listed in Table 6-V for these conditions. These data and those in Table 6-IV were used as radiative loss estimates in independent global convection loss modeling.

FIGURE 6.2.24

CAVITY RESULTS FLUX-OFF RADIATIVE LOSS

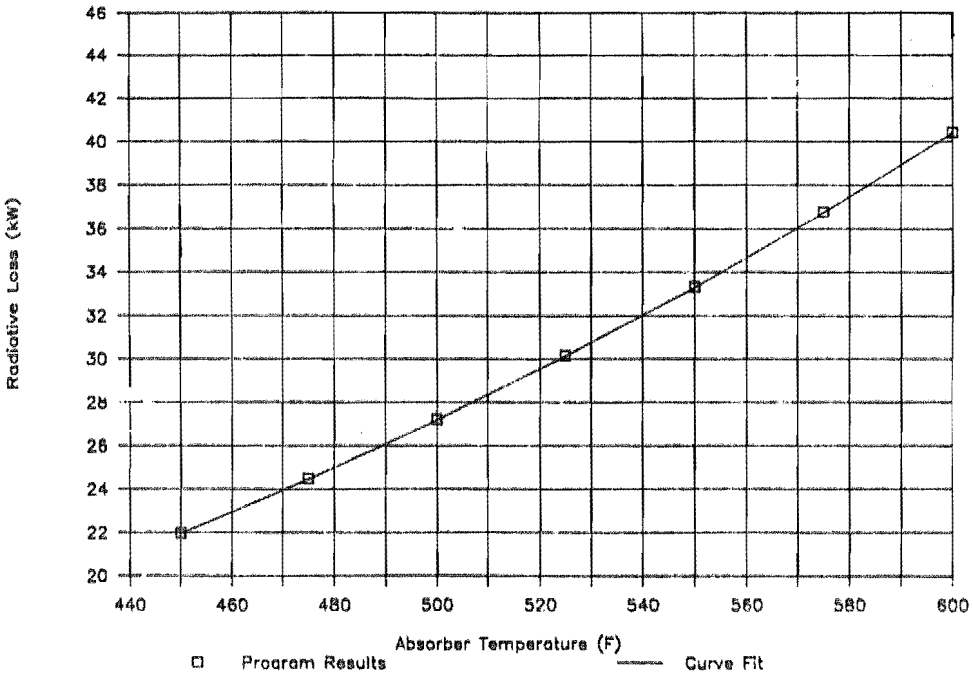

TABLE 6-V

FLUX-OFF RADIATIVE LOSS

T_{abs*}(°F)	Q_{rad}(kW)	T_{cavity}(°F)	$T_{nonabs**}$(°F)
450	21.97	382.9	341.2
475	24.49	406.1	363.2
500	27.21	429.3	385.2
525	30.16	452.4	407.2
550	33.34	475.6	429.2
575	36.77	498.7	451.2
600	40.45	521.9	473.2

*abs = Absorbing Panels

**nonabs = Nonabsorbing Elements

6.2.3 Conclusions and Recommendations

The current modeling effort for the MSS/CTE receiver experiment indicates the global receiver's thermal efficiency is invariant within a few percent to most parameters investigated, although front surface temperatures of the nonabsorbing surfaces vary considerably, particularly with the type of convective submodel used. Absorption efficiencies indicate the effects of the environment of the cavity enclosure. Temperatures of the tube's inner wall remained under 1080°F, ensuring the nitrate salt remained chemically stable. Parameter variations affect local distributions more than the global results. Results for 50 percent field conditions indicate a correction for non-constant losses in the Barron flux-on loss method is required.

The required modeling detail is shown to be dependent on the data desired. That is, if strictly estimates of global efficiency are required, significant convective modeling efforts may not be necessary. Since radiative transfer is the dominant loss mechanism and the absorbing panel's temperature is controlled by the desired outlet salt temperature, a simplified radiative analysis may suffice. If additional information is desired, such as local temperature distributions, a desired model is warranted. Optimizing the receiver design or understanding the effects of design or material changes on the receiver's thermal conditions both require models that realistically portray the cavity energy transfer, as demonstrated by these results.

These conclusions were based on a single-bank radiative analysis. It indicated that radiative losses are the dominant loss mechanism in this cavity receiver. Work is currently underway on a semi-gray two-band analysis to account for the spectrally varying radiative properties of the cavity materials. Also, infrared camera measurements of the front surface temperatures are currently in progress and may provide experimental data to compare directly to model predictions. This will be a more severe test of the numerical model.

6.3 Evaluation of Thermal Loss

This section presents the results of thermal loss evaluations performed on the test receiver. Losses from the receiver were measured in two modes: (1) with the heat flux off the receiver ("flux off") both with the receiver door closed ("door closed") and with the door open, and (2) with the door open with operating heat flux ("flux on"). The overall goal of this portion of the testing was twofold. First, we wanted to measure the receiver's thermal losses at the design point. Second, we planned to infer convection losses from the receiver so that these losses could be compared with empirical correlations.

Information about heat loss is very important to the designer and operator of a solar central receiver. Understanding thermal losses allows configuration of a more cost-effective receiver and heliostat field. Insight into the losses also allows better understanding of critical choices, such as whether to select a cavity configuration or an external receiver. The losses also affect the day-to-day operation of receivers, including development of realistic procedures for dealing with cloud transients, overnight conditioning, and other aspects.

There has been interest in understanding heat losses from central receivers since the current thrust of work on central receivers was initiated in the 1970s. Convection, radiation (both reflection and re-radiation), and conduction modes are present. As indicated by Boehm [32], the understanding that has emerged is that (1) radiation losses can be (but perhaps not easily) analyzed in a straightforward manner with existing theory and calculations, (2) conduction losses should normally be small enough to be ignored, and (3) convection losses are not well understood. Existing understanding of convection losses in experiments has been summarized by Boehm [32] and appropriate design correlations are presented by Siebers and Kraabel [30].

Although many attempts have been made to measure the thermal losses in central receivers, they have been hampered by a number of issues. For one,

the desire to infer losses from the difference between incident and useful power has been thwarted because the incident power has not normally been measured. Instead, the incident power has been predicted using computer codes. This approach results in high uncertainties in the thermal loss data. Thermal losses can also be measured when salt circulates in the receiver, but with no heat flux on the receiver. Experimental uncertainties in the use of a flux-off loss testing (more is given on this method of evaluation below) are found to be considerably lower, which is another issue. Losses measured in this way, however, may not be representative of losses at normal operating conditions, since temperature gradients are in the opposite direction from those found in normal operation, and the temperature levels at which the data are taken are normally lower than design operation.

Descriptions of the tests performed are given below. In addition, the reduced data for heat losses are summarized. An accounting of many modes of heat transfer from the cavity, back panels, and wing panels is necessary (see Figure 6.3.1). Two approaches to the heat-loss evaluations are reported. One is the traditional flux-off method. The other is a more recently conceived flux-on approach called the Baker Modification to the Barron Method. The latter allows flux-on losses to be evaluated without requiring the incident power on the receiver to be measured or estimated.

FIGURE 6.3.1

DIAGRAM INDICATING THE VARIOUS HEAT LOSS MODES

INCLUDED IN THE PRESENT ANALYSES

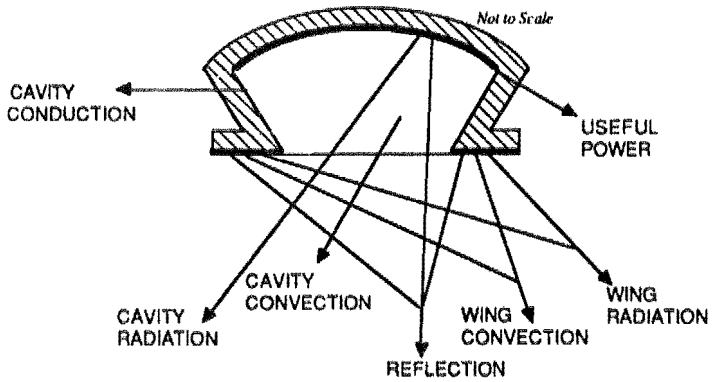

CAVITY CONDUCTION Empirical determination from flux-off data, ratioed for temperature effects.

CAVITY RADIATION From Sandia calculation.*

CAVITY CONVECTION Determined from our calculation.*

WING CONVECTION From our calculation.

WING RADIATION From our calculation.

USEFUL POWER From our calculation.

REFLECTED POWER Implicitly accounted for. Not in flux-off tests.

*Uses Sandia estimate of tube surface temperature for flux-on data evaluation.

Where possible, comparisons of experimentally inferred data to predictions are given. This experiment involves a combined external (due to the wing panels) and cavity receiver. Accurate, simplified prediction methods for this complicated configuration are lacking. However, Siebers and Kraabel [30] have given some guidelines for design correlations for convective losses separately for external and cavity configurations. Comparisons between the experimental data and the recommended design correlations are given.

The combined nature of the receiver's external wing panels and cavity had implications throughout the loss evaluations. Because the fundamental nature of the receiver is a cavity form, attempts are made throughout to isolate the loss aspects of the cavity from those of the wings. Because of where temperature sensors were located and the general nature of various tests, this aspect was handled differently in some situations. This point is discussed where it is pertinent in each section.

Critical to the inference of convective losses by any method is the use of an estimate of the radiative losses. For the present work, estimates of cavity radiation have been made by Sandia National Laboratories-Albuquerque personnel. Documentation of this work is given in Section 6.2. Estimates of radiation loss for the wings are described later.

6.3.1 Flux-Off Data Analysis

The Form of the Data

A series of experimental evaluations was made with no flux on the receiver. In this mode, hot salt enters the receiver at approximately 525°F, flows through the receiver, and exits the receiver at a lower temperature than it entered. This is due to the various modes of heat loss present. Boehm, Nakhaie, and Bergan [32] showed that this type of test can be quite effective in estimating the thermal losses from central receivers.

Since these types of tests are performed with no flux on the receiver, operation in this mode can occur during a wide range of weather conditions.

It is therefore possible to gather a great deal of data from flux-off conditions, allowing correlation of losses with a wide range of environmental situations.

Typical flux-off data are shown in Figure 6.3.2 for one limited time period. The pertinent temperatures are given for two salt flow rates. These particular data were taken for cases in which the receiver doors were open. Other cases were taken with the doors closed and with the doors opened slightly (doors "cracked"). In addition, some data in each of the cases are for high-mass flow rates and others are for low-mass flow rates. The magnitude of the mass flow rate is important in flux-off because this variable will, in turn, affect the resulting value of the salt temperature difference in flowing through the receiver.

FIGURE 6.3.2
TEMPERATURE VS. TIME TRACES FROM A TYPICAL DOOR-OPEN FLUX-OFF LOSS TEST

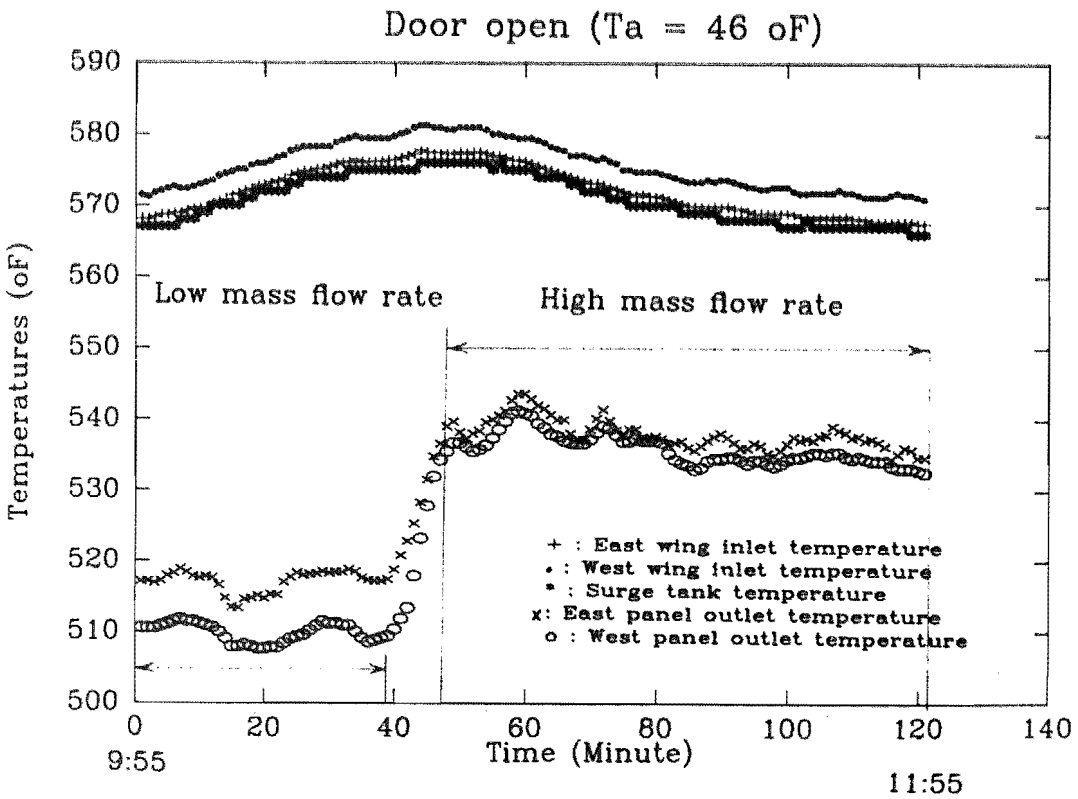

Here there was an attempt to isolate the cavity losses from the overall losses. This was possible because there were approximate ways to estimate the temperatures of the salt flows into the cavity regions.

Problems with Temperature Measurement

Problems arose with temperature measurement. These data have a profound effect on the overall results because the overall temperature difference (between the inlet to the receiver and the outlet from the receiver) was quite small. There was a desire to isolate the wing panel losses from the cavity losses for analysis purposes. However, for much of the testing, the salt temperatures between the outlet from the wing panels and the inlet to the cavity panels were not recorded on the main data acquisition system. This required that estimates of the main panel's inlet temperatures be made by examining the back-tube temperatures. Since the overall temperature change of the salt in its traverse through the receiver was small during flux-off conditions, a linear interpolation between appropriate back-surface temperatures was thought to be an accurate estimate of the salt temperature between the exit from the wing and the entrance to the cavity.

Another problem with temperature measurement was accuracy. Offset errors were found to exist by comparing the temperature in the cold surge tank with the temperatures at the inlet to both the wing panels. Theoretically these three temperature measurements should not differ significantly at any one time, but it was found that they did not agree (by between 5 and 10°F). These offset errors resulted in uncertainties in the calculation of losses from the data. When flux-off losses are determined with high flow rates, uncertainties due to the temperature offsets will be exaggerated. A combination of the inlet and cold surge tank temperature values was used to infer the inlet temperature to the receiver, where needed.

Conduction Losses

The present receiver had an insulated enclosure (doors) that could be positioned to cover ambient exposure of the active surfaces. This allowed an estimate of "conduction" losses through the shroud to be made. The approach

used in estimating conductive losses was to measure the heat loss from the salt when the doors were closed. By calculating the loss through the doors and subtracting that amount from the total loss with the doors closed, the "conduction" heat loss could be inferred. In this calculation, the thermal performance of the door was assumed to be dictated by its insulation. The appropriate temperature difference was assumed to be a value between the average temperature of salt and the ambient temperature.

The term "conductive" is placed in quotations because it is a simplification to call the resulting quantity "conduction"; there may be infiltration both through the shroud assembly as well as around the doors, in addition to what would commonly be called conduction through the shroud. Final loss evaluations made with the door "cracked" compared to "closed" showed a great increase in thermal loss. However, there still could be door-gap infiltration with the door "closed."

To determine a correlation between the "conduction" losses and wind velocity, the door-closed heat losses were plotted against wind velocity. When this plot was done, a strange relationship was demonstrated, in that some of the "conduction" losses at high wind speed were actually considerably lower than those found at low speed. Further study indicated that the data at the higher wind speeds were taken with the salt-mass flow rates set at very high values. Although this fact should not make much difference with ideal instrumentation, in real systems the high flows will make errors in the temperature readings even more important when the heat losses are calculated. Hence, the data taken when the flow rates were very high were judged to be less precise and were eliminated. The resulting data are shown in Figure 6.3.3.

FIGURE 6.3.3

RECEIVER CONDUCTION LOSS

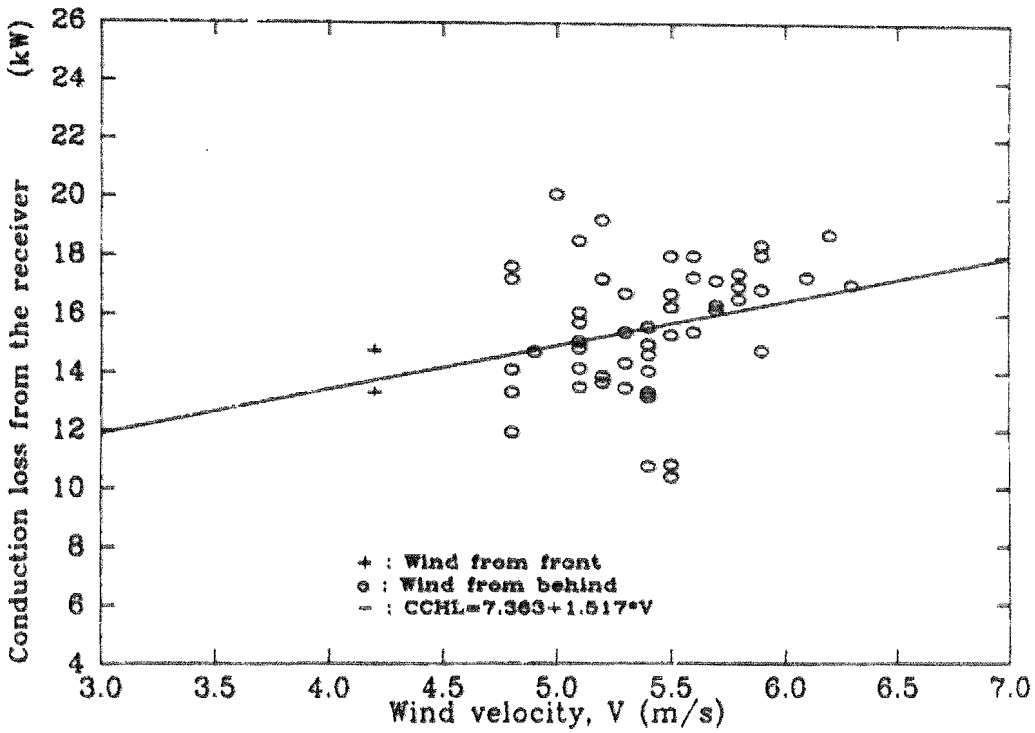

General Data Reduction

We wanted to evaluate the thermal loss from the cavity and to isolate this portion of the receiver from the wing panels for the flux-off conditions. To do this, the temperature of the salt between the wings and the cavity had to be inferred. The inlet temperatures to each side were estimated from the wall temperatures in the wing panels and the panel itself as shown below.

For the west panel: $T_{iw} = TE_{103} - (TE_{103} - TE_{104})/3.$

For example, $T_{iw} = 590 - 1/3(590 - 581) = 587°F,$

and on the east panel, $T_{ie} = TE_{133} - 1/3(TE_{133} - TE_{134}),$

where TE_{103} and TE_{133} are tube back-wall temperatures at the wing panel outlets, and TE_{104} and TE_{134} are back-wall temperatures midway up the first cavity passes.

With the temperatures determined, the total heat loss (Q_t) from the cavity panels could be estimated.

Q_t = heat loss from west panel + heat loss from east panel; and

$$Q_t = \dot{m}_w C_p (T_{iw} - T_{ow}) + \dot{m}_e C_p (T_{ie} - T_{oe}).$$

The subscripts i and o refer to inlet and outlet conditions, and the subscripts e and w refer to east and west.

The radiation heat loss (Q_{rad}) was calculated from the following correlation, which was the best fit of data furnished from Sandia calculations (see Table 6-V in Section 6.2):

$$Q_{rad} = -8.912 + 0.089\bar{T} - 0.179 \times 10^{-3}\bar{T}^2 + 0.328 \times 10^{-6}\bar{T}^3 - 0.9697 \times 10^{-10}\bar{T}^4.$$

Here Q_{rad} is in Btu/s and $\bar{T}$ (the average receiver absorber temperature) is in °F.

Conduction loss from the cavity shroud (Q_{cond}) is defined as the energy lost to the environment through the shroud walls, ceiling, and floor. In other words, this is all heat loss except for the useful energy and the loss through the aperture. This loss was estimated from tests of the loss with the doors closed. From these cases, a door-closed heat loss given by the Q_t

equation above is denoted as $(Q_t)_{door\ closed}$. Thermal conduction loss through the door for these cases was then estimated as

$$Q_{door} = k_{door} A_{door} (T_r - T_\infty)/\Delta.$$

Here k_{door} is the thermal conductivity of the door insulation ($k_{door} = 0.3$ Btu/h ft^2°F/in.), A is the area of the door (A = 108 ft^2), Δ is the thickness of the insulation on the door (8 in.) T_r is the average temperature of the receiver, and T_∞ is the ambient temperature. The conduction loss was then estimated for the door-closed conditions from:

$$Q_{cond} = (Q_t)_{door\ closed} - Q_{door}.$$

Q_{cond} was calculated from the available door-closed data. A curve fit was generated to represent the calculated values for use in general data reduction. The following was found:

$$Q_{cond} = 7.36 + 1.52\ V.$$

Here Q_{cond} is in kW and V is the wind speed in m/s. For the small temperature variations typical of the flux-off cases, temperature difference effects were not obvious in the data.

The convection heat loss from the cavity (Q_{conv}) is found from the total loss, decreased by the quantities already discussed;

$$Q_{conv} = Q_t - Q_r - Q_{cond}.$$

One question that arises is whether the conduction-loss term should be adjusted to account for door losses when applied to the cavity only (as is the case here) compared to when it is applied to the whole receiver (which is the basis of its derivation). One could argue for or against that approach with equal validity. From the scatter of the data (see Figure 6.3.3) it is clear that concern for precision in this very imprecise term is not warranted.

6.3.2 Flux-On Evaluations

Before giving a detailed description of the method used to evaluate data for the flux-on cases, it should be noted that a large number of results of analytical calculations using the CAVITY2 code were furnished by Sandia. They included tabulations of estimates of the average surface temperature, radiative loss from the cavity, convective loss from the cavity, and total loss from the cavity aperture. These quantities were given as a function of the time of day (solar noon) and ±1 hour from solar noon, 50 percent and 100 percent incident power, for 191 heliostats on target and for either 950 or 1050 W/m^2 direct normal insolation. A discussion of these calculations is in Section 6.2. It should only be noted that estimates of these quantities were available for any experimental conditions pertinent to this test from a linear interpolation or extrapolation of calculated data.

Another important point is that for the flux-on situations evaluated, it was less apparent that the salt temperatures between the wing panels and the cavity panels could be inferred from the panel's back-surface temperatures, as was done in the flux-off data analysis. Hence, we used the approach here to evaluate the total thermal losses from the complete receiver and then inferred the convective losses from the cavity by calculation. This is described further below.

As a bit of background about the experimental method used, the first step was developed during the testing of the MSEE [10] receiver. Because there

is a large uncertainty in the determination of the receiver's incident power during normal flux-on conditions, Dan Barron of McDonnell Douglas suggested a method of evaluating losses, referred to as the "Barron Method." A discussion of this method is given in Boehm, et al. [34]. In simple terms, two cases are considered. One is with the full heliostat field focused on the receiver, and the other is with 50 percent of the heliostats on the receiver. If it is assumed that both cases can be operated with the same average receiver surface temperature, the total heat loss (which should be the same for both cases, because the losses are driven by the difference in temperature between the receiver surface and ambient temperature) will be the same for both cases and will be given by:

$$Q_{loss} = Q_{u,high} - 2\,Q_{u,low},$$

where Q_{loss} is the total heat loss, and Q_u is the useful power absorbed by the receiver fluid.

Baker, of SNL, Livermore, noted that the assumption of a constant receiver surface temperature with variations in incident flux is not an easy condition to meet in normal situations. In fact, the operational scheme used with many receivers (and that normally used here) attempts to keep the outlet salt temperature constant. Because the flux varies widely, this will result in considerable variation of surface temperature. Baker [35] proposed a method to incorporate surface temperature variation indirectly by accounting for losses that varied with the incident flux. His contribution is called the Baker Modification to the Barron Method (or simply the Baker Modification) in the following discussion.

In the Baker Modification, it is assumed that three separate cases are evaluated for each loss test. The first and third use complementary numbers of heliostats and the second uses the complete field. For the test performed in the present program, the number of heliostats used was always 50 percent in the first and third cases, and all were used in the second

case. Hence, a subscript of 2 denotes the full incident power case, whereas 1 and 3 denote the 50 percent incident power cases.

Total thermal loss at the full-power case is then found from

$$Q_{loss,2} = \frac{Q_{u,2} - (Q_{u,1} * IR1 + Q_{u,3} * IR3)}{IR1 * LR1 + IR3 * LR3 - 1}.$$

In this relationship, the $Q_{u,1}$ quantities are the useful powers absorbed by the salt in each of the three cases. IR1 is the ratio of the individual heliostat flux parameters in case 2 divided by the quantities in case 1, and IR3 is the corresponding ratio between cases 2 and 3. The quantities in the top and bottom of the IR ratios are determined by the product beam radiation incident upon the heliostat field and the heliostat performance value. The latter was assumed to be the same for all cases in a given run. LR1 is the ratio of the total thermal losses in cases 1 and 2, and LR3 is the ratio of the case 3 losses to the case 2 losses. These quantities are found from calculated estimates of the thermal losses. A critical assumption of the method is that, although the absolute values of the losses may not be known with better accuracy simply from calculation, the ratio of the losses between cases may be known with better accuracy. Thus the two ratios are then used to find a better estimate of the thermal losses at the full power condition via the equation given above. If LR1 = LR3 = 1 and IR1 = IR = 1, the Baker Modification reduces to the Barron Method, as it should.

The equation given before the previous paragraph is the starting point for the evaluation of the thermal losses. As noted there, the key experimental quantities needed for the evaluation are the mass flows for the two sides and the corresponding temperatures entering and leaving the receiver. From this, the useful power can be determined for each minute of the test. A typical plot of these data is shown in Figure 6.3.4. It is interesting to

note the significant fluctuations of the useful power with time. This is due in large degree to the fluctuations in the mass flow rates.

Once the total thermal loss is found, the convection loss from the receiver (wings plus cavity) can be inferred from the following relationship:

$$Q_{conv,cav} + Q_{conv.wings} = Q_{loss,2} - Q_{rad,cav} - Q_{rad,wing} - Q_{cond}.$$

The radiation from the cavity was estimated from a table of SNLA data (see discussion of the cavity heat-transfer calculations in Section 6.2). The other quantities, including the wing panel convection, were calculated from methods incorporated in the data reduction routines and are described below.

FIGURE 6.3.4
USEFUL POWER VS. TIME DURING FLUX-ON TESTING

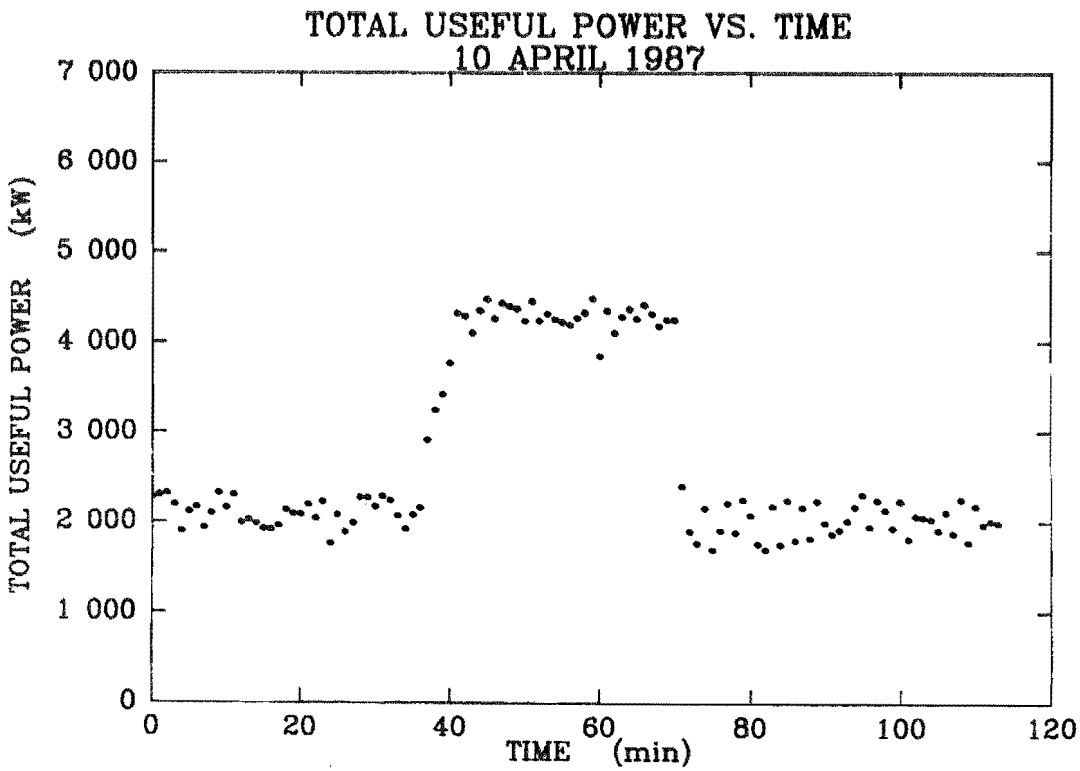

Typical plot of useful power vs. time during the flux-on testing. Note the half-power, full-power and half-power sequences required for Baker Modification of the Barron Method.

The convection of the wing panel was estimated from recommended correlations given by Siebers and Kraabel [30]. Estimates of both natural and forced convection heat-transfer coefficients (h_{nc} and h_{cc}) were made and combined in the nonlinear fashion, as per Siebers and Kraabel's [30] recommendation, as follows:

$$h_{nc,wing} = 0.81\ (T_{wing} - T_{\infty})0.426;$$

$$h_{fc,wing} = (k/w_{wing})0.664\ Re_{w}^{1/2} Pr^{1/3};$$

$$h_{wing} = (\ h_{nc,wing}^{3.2} + h_{fc,wing}^{3.2})^{1/3.2},$$

$$Q_{conv,wing} = H_{wing}\ A_{wing}(\ T_{wing} - T_{\infty}\ ).$$

In these equations T_{wing} denotes the temperature of the wing and Re_{w} represents the Reynolds number of the flow over the wing, based upon the wing width, and k is the conductivity of air.

Radiation of the wing was estimated assuming half the interaction is with the ambient temperature and the other half is with the temperature of the sky. The latter quantity, related to the ambient temperature is shown below:

$$Q_{rad,wing} = \sigma\ \epsilon\ A_{wing}[\ 2\ T_{wing}^{4} - T_{sky} - T_{\infty}^{4}]/2$$

where the temperature of the sky is given by [36]:

$$T_{sky} = 0.0552, T_{\infty}^{1.5}$$

and $\varepsilon = 0.97$, and $A_{wing} = 24\ ft^2$.

Conduction loss from the receiver was estimated from the correlation described earlier, except the amount of loss was linearly scaled upward to account for temperature effects. Thus the conduction loss could be found as a function of wind velocity and the difference between the average salt temperature in the receiver and the ambient temperature.

6.3.3 Cavity Convective Loss Estimates (from Predictions)

One of the main reasons to determine heat losses during a test of a central receiver is to be able to evaluate existing data correlations and possibly to improve on them for use in future designs. The approach and the correlation used here are given below.

There are several components to the total heat loss, as is discussed above. Wing and cavity panel radiation, conduction, and wing panel convection are calculated as discussed earlier. Here the method used to predict the cavity convection is described. Some elements of the general approach that are not applicable to this configuration are not given here. See the full description in Siebers and Kraabel [30].

First consider the contribution of natural convection. A heat-transfer coefficient for natural convection is found from the following correlation recommended by Siebers and Kraabel, which results in the equation:

$$h_{nc,o} = 0.81\ (\bar{T}_r - T_{\infty})^{0.426}.$$

$\bar{T}$ is the area-averaged surface temperature inside the cavity. For the flux-off experiments, this temperature was assumed to be well represented by the average salt temperature in the cavity. When comparing it to the flux-on experiments, it was inferred from Sandia calculations. This result must then be corrected for its effect on cavity lips, as Siebers and Kraabel also note:

$$h_{nc} = h_{nc,o}(A_3/A_1)^{0.63}.$$

Here temperatures are in °C and heat-transfer coefficients are in $W/m^2°C$. The area ratio relates the inside cavity area below a plane containing the top of the aperture to the total inside cavity area. For this cavity the ratio is about 0.73. The natural convection loss is found from this value and from the total heated area. This latter quantity is the total inside area of the cavity.

To find the contribution of forced convection, we again use the correlation recommended by Siebers and Kraabel for the Nusselt number and the heat-transfer coefficient.

$$Nu_w = 0.0287Re_w^{0.8}Pr^{1/3},$$

and

$$h_{fc} = k\ Nu_w/W_a.$$

The Nusselt and Reynolds numbers are based on the width of the aperture, W_a, and properties are evaluated at the film temperature, $T_f = (T_r + T_\infty)/2$. The correlation is assumed to hold independent of the wind direction relative to the receiver.

Finally, the combined convection heat transfer is found from the general form suggested by Siebers and Kraabel [30]:

$$Q_{conv,cav} = [h_{fc} A_{aperture} + h_{nc} A_{cavity}](\bar{T}-T_{\infty}).$$

Again, note that $\bar{T}$ is the representative temperature of the cavity surface, estimated as was described earlier. This convective loss is used with estimates of the other heat flows to compare it to the experimentally determined values.

6.3.4 Results and Discussion

Results found during the testing are shown in reduced form in figures in this section. In all cases, the data for a period of time have been averaged, and these averaged data have been used in processing the results shown. This point should be kept in mind during the discussion that follows.

First consider the flux-off results (see Figure 6.3.5). Here total heat loss from the cavity is plotted against wind speed. The data are divided into two sets, for wind directions from the front of the receiver and wind directions from the back. Although the data are limited, the losses when the wind is from the back appear to be somewhat less than the corresponding wind-from-the-front cases.

FIGURE 6.3.5

TOTAL HEAT LOSS FROM FLUX-OFF TESTING

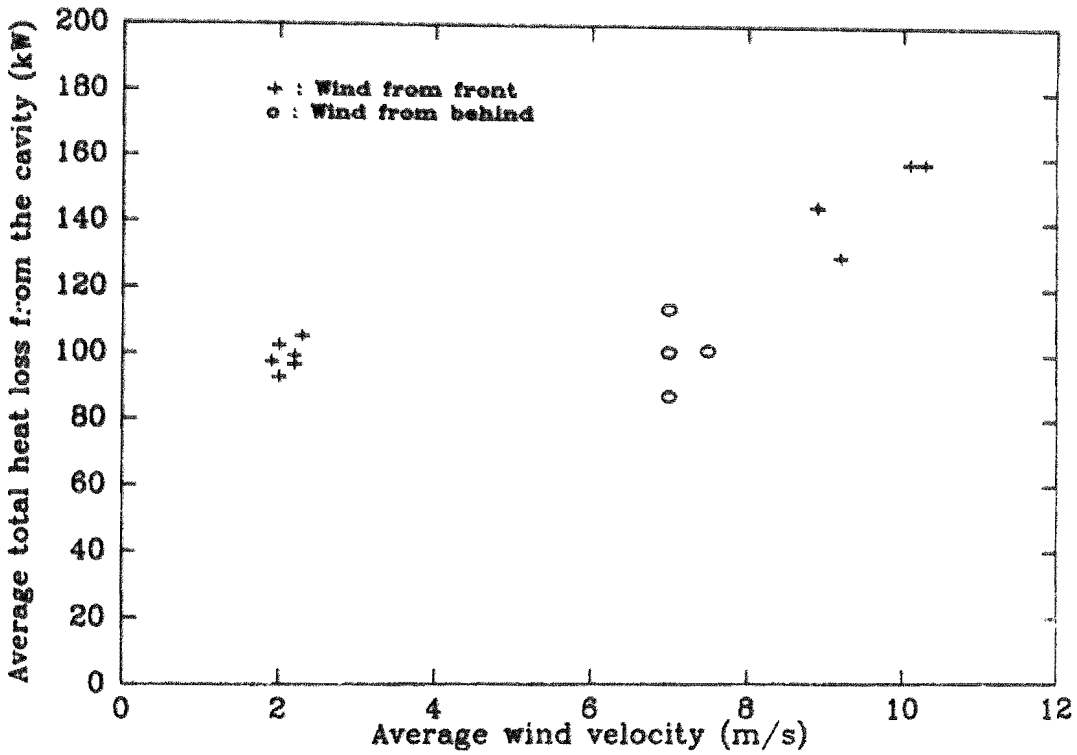

It is also of interest to examine the inferred convective losses from the cavity with regard to wind speed and to comparisons with predictions. These two aspects are illustrated in Figures 6.3.6 and 6.3.7.

FIGURE 6.3.6

ESTIMATED CAVITY CONVECTIVE LOSSES FOR ALL FLUX-OFF CASES

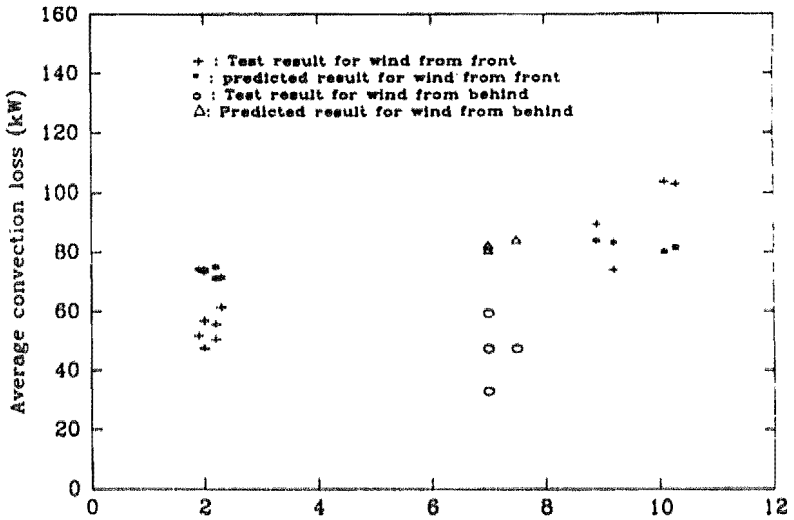

Time-averaged data have been used in reducing these data. Results of experiments and use of predictive correlations are shown.

FIGURE 6.3.7

CAVITY CONVECTIVE LOSSES FROM TESTING AND THE PREDICTED LOSS

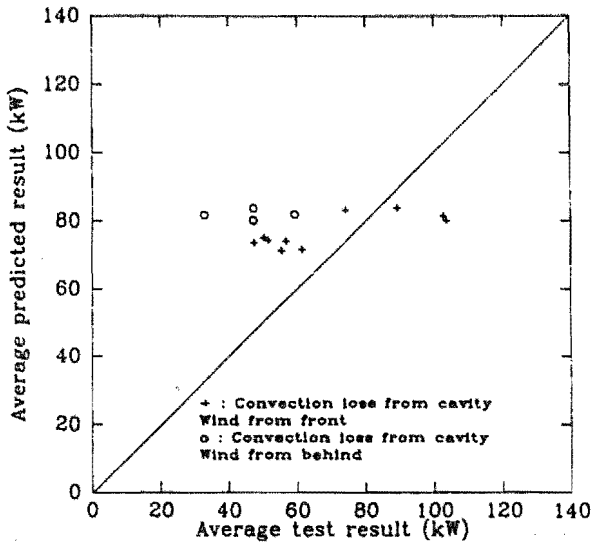

Consider the effects of wind speed on cavity convective losses; see Figure 6.3.6. A plot similar to one in Figure 6.3.5, is presented here, but now only the convective losses are shown. Since the calculated radiation is independent of wind speed, the small variations in total heat loss shown in Figure 6.3.5 are now translated to larger variations in convective heat losses. There is now a greater distinction between the "wind-from-front" and "wind-from-behind" cases.

To see how well the design correlations would predict the actual data, note Figures 6.3.6, and 7. In Figure 6.3.6, the predicted convective loss is shown for each experimental data point, in addition to the experimental data already discussed. In Figure 6.3.7, the cavity convective heat loss from the test is plotted against the predicted cavity convective heat loss. If there were completely accurate experimental data, and a completely accurate set of correlations were used by which to compare them, the data would fall on a line through the origin with a unit slope. It can be seen from the plot that some of the experimental data are overpredicted and some underpredicted. However, all the data for cases in which the wind is coming from behind the receiver are overpredicted.

Figure 6.3.8 completes the presentation of the flux-off data. In this figure, a comparison is given between the convective loss, conductive loss, and radiative loss from the cavity only for flux-off testing. It is clear that the convective loss is dominant, in contrast to what is found for the flux-on tests discussed below. Results for the total configuration (wings plus cavity) would be similar, but with the radiation being decreased slightly and the convection being increased slightly compared with the cavity results shown here.

FIGURE 6.3.8
FLUX-OFF DISTRIBUTION OF THERMAL LOSSES FOR THE
CAVITY PORTION OF THE RECEIVER

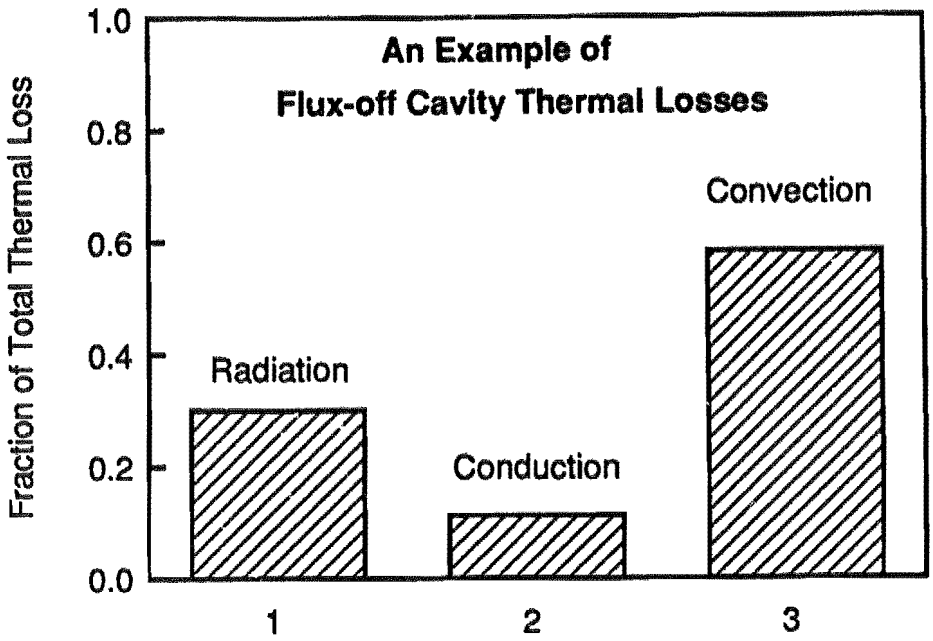

Next consider the flux-on data shown in Figures 6.3.9 and 6.3.10. The first of these plots gives the total thermal loss (radiation, convection, and conduction) for the wings and the cavity, whereas the second of these plots shows the cavity convection loss only. All five experimental data points are shown as a function of wind speed, indicating both the experimentally determined value as well as the calculated value in each case. In all cases, the predicted loss is greater than the measured value. The scatter in the data is a result of the basically large value of uncertainty (more discussion of this point is given below) associated with the experimental technique. If the half power case shows too high a power, or the full-power

case shows too low a power, but either is within the uncertainty range, this kind of scatter will result. Wind direction is shown listed near each experimental data point.

FIGURE 6.3.9
TOTAL RECEIVER HEAT LOSS FOR THE BARRON METHOD

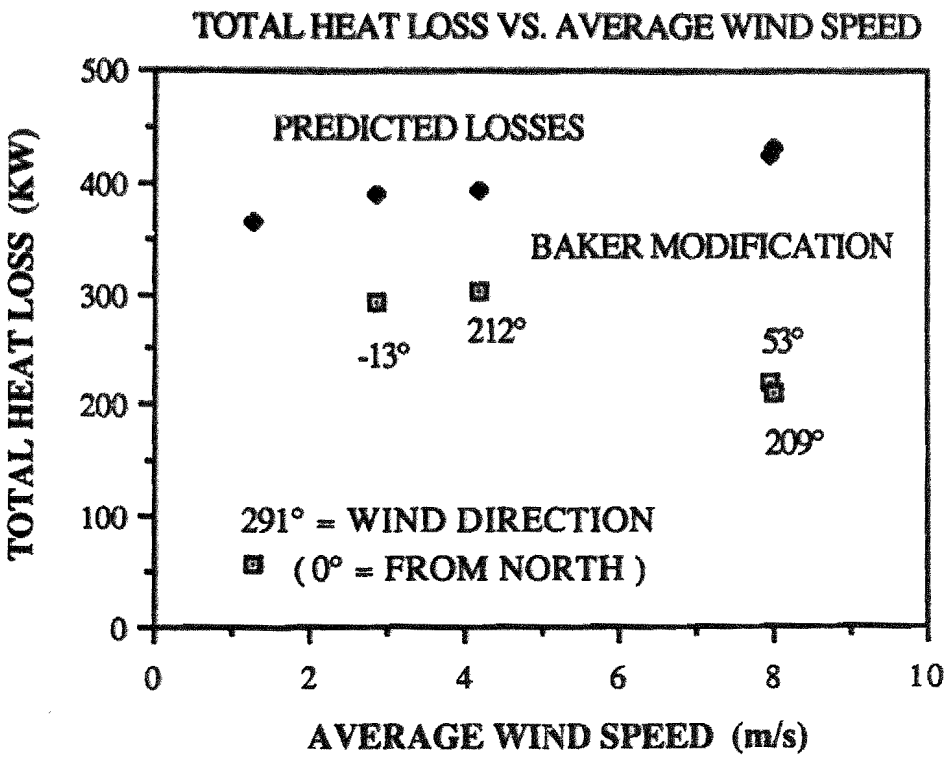

FIGURE 6.3.10
FLUX-ON CAVITY CONVECTIVE LOSSES

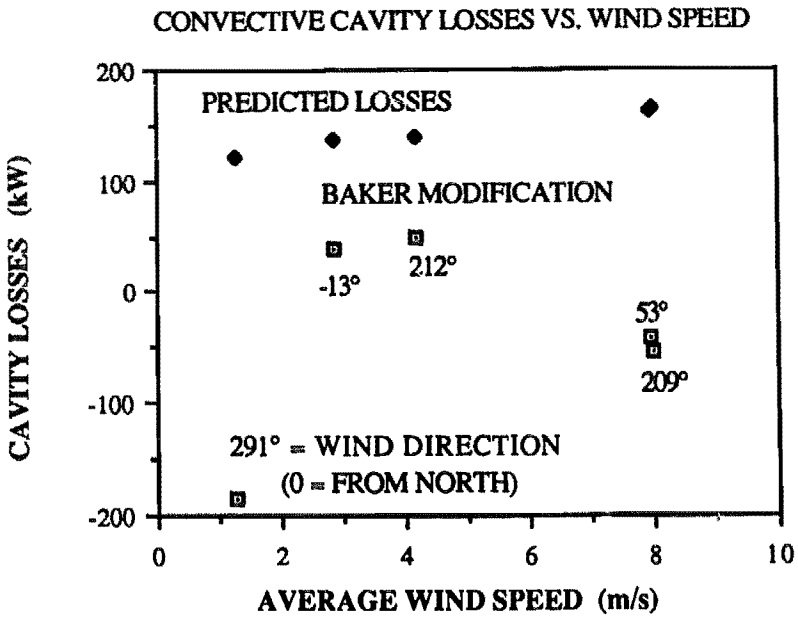

Results of possible errors in the technique are readily apparent when the cavity convective losses are examined (see Figure 6.3.10). Here estimates of all of the other contributions are subtracted from the total loss to find the cavity convective contribution only. Although estimates of the cavity convective losses are obviously positive, three of the five experimental points indicate a negative loss (thus really a gain). In general this kind of unreasonable result is due to overestimation of some or all of the other heat loss modes. To see one reason why this unrealistic result might occur, examine Figure 6.3.11. Here all of the component estimates for one data point are shown. Note the dominance of the cavity radiation in the thermal losses. Since the convection is relatively small and is inferred by subtracting all other losses from the total thermal loss, any overestimation of any of the flows, but particularly the radiation, might cause the

convective loss to appear negative. This negative value underlines the very high uncertainty associated with convective loss estimates for flux-on cases. As was done in Figure 6.3.10, wind direction (in degrees) is shown for each experimental point. Attempts to correlate the convective loss with wind direction (distinguishing between wind from the front and wind from behind) met with no success.

FIGURE 6.3.11
DISTRIBUTION OF HEAT-LOSS CONTRIBUTIONS

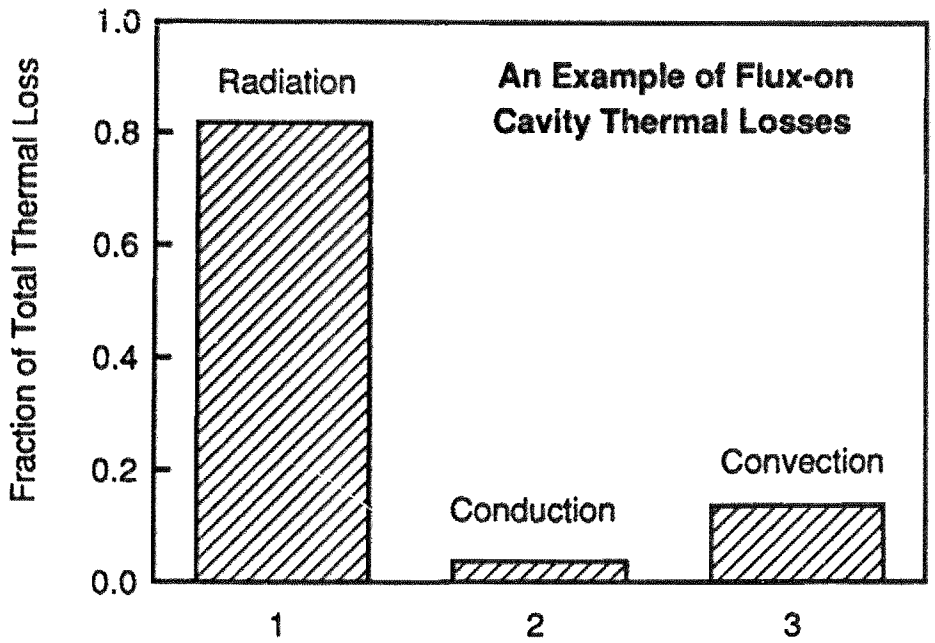

Estimates were made about uncertainties in the convective losses calculated from the experimental data. They yielded estimates of approximately 50 percent for the flux-off cases and approximately 80 percent for the flux-on data. Previous flux-off data have had similar uncertainties [32]. However, the data presented here for flux-on testing have lower uncertainties than those presented for the MSEE receiver [30]. The reason for the improvement in the latter situation is the use of the Baker Modification.

6.3.5 Discussion of the Data

One of the most common problems associated with experimental efforts on solar central receivers before the Category B program was that the data were too limited both in the numbers of the various parameters monitored (incident flux, flow rate of the coolant, wind speed, temperatures at appropriate locations, etc.) as well as the amount of separate data cases evaluated. There was an attempt in the present program both to enlarge the numbers of sensors used and to perform tests over longer elapsed time. Although this was generally accomplished, there are still limitations in the data. Some of the limitations resulted from an unanticipated shortened period of testing due to surface coating of the receiver, the pump, and other problems. Other limitations resulted from the lack of ability to log all data on the NET-90 system. Other specific problems are noted below.

Accuracy of all data was hampered by not having recorded the temperatures between the wings and the main panels. A differential thermocouple between the inlet and outlet of each half of the main panel would have been quite valuable in reducing errors in the data.

Variations in controlling the flow rate affected the scatter in the data. Had the flow rates been steadier, errors in the final results would have been decreased.

The efforts to evaluate loss would have benefitted from the ability to measure (rather than calculate) the temperatures of the heated surface. It was hoped that an infrared camera could be used on this test to infer the temperature distribution on the surface. Since most of the losses are affected by the front surface temperature, this is a particularly important variable.

Insufficient data were taken to allow better convective correlations to be developed. Future tests should be designed so that considerable amounts of

data might be taken to allow empirical treatment of many of the loss parameters to be evaluated.

6.3.6 Conclusions and Recommendations

A series of flux-off and flux-on thermal loss tests were performed in a variety of conditions. An attempt was made to infer the conductive losses from the receiver by performing loss evaluations with the receiver doors closed and subtracting from the total an estimated loss from the doors. The resulting data may be biased to be larger than they actually are due to door-infiltration from the doors. Even with possible overestimation, the conductive losses appear to be small. This is in agreement with earlier ideas about these losses. It is found that the flux-off data are both under- and overpredicted by the existing convective correlations. When the wind direction is from behind the receiver, the experimental data are overpredicted by the existing correlations. Existing correlations typically overpredict the heat loss for flux-on situations. Effects of wind direction are difficult to ascertain. Experimental uncertainties in the flux-off convective loss data appeared to be about 50 percent.

The Baker Modification to the Barron Method of flux-on testing has been used to perform thermal loss evaluations from the test data. It appears that the Baker Modification decreases experimental uncertainties typical of the Barron Method (well over 100 percent) to approximately 80 percent. Flux-on testing, however, is not without its problems. Estimates of the convective loss from the cavity based on flux-on loss data showed that only two out of four points yielded a positive loss. Part of the explanation of the higher number of inconsistencies in the latter category is that the other thermal losses from the cavity may have been overestimated.

Some improvements in the experimental techniques could allow evaluation of the effects of the important variables. Included should be a salt-temperature-sensing differential thermocouple across the active panels in the receiver. Surface temperatures should be measured, and steadier control of the mass flow is recommended.

6.4 Evaluation of Overnight Conditioning and Start-Up

The receiver's piping and panel must be heated to a temperature above the freezing point of salt before the salt flow may be started, otherwise the salt may freeze and block the pipes. The receiver's piping is generally insulated and heated with electric heat-trace cable to keep it hot, but the receiver's panel presents a special problem. The methods investigated to heat the panel were:

1) Panel warm-up using heliostats,
2) Panel warm-up using electric cavity heaters, and
3) Continuous molten-salt circulation.

In this section, the three methods will be described and compared based on the energy they consume, the solar energy collected, and the ease of operation. Start-up energy requirements are summarized in Section 6.4.4.

6.4.1 Start-up with Heliostats

Early morning start-up using heliostats to warm the receiver's panel was accomplished at sunrise on May 21. Figure 6.4.1 shows the receiver's absorbed power as a function of time and notes significant points in time during the start-up. (Note that at approximately 8:00 a.m. a communication problem within the collector's field controls caused a heliostat scram. Recovery from this took 10 minutes. Where necessary, data have been interpolated through this time period.) Heliostats of the early morning warm-up pattern were tracking the receiver at sunrise (6:32 MDT). Fifteen

minutes was required to heat the panel so that all locations were above 450°F. The factors that limit start-up time are the available field power and a maximum limit of 33 kW/m^2 for acceptable tube thermal stress and tube temperature during heat up. Figure 6.4.2 shows representative panel temperatures for the solar start-up as a function of time. Figure 6.4.3 shows the location of panel thermocouples and flux gages available to monitor the heat up process. Data from several thermocouples are shown. representative of the range of panel temperatures that occur during start-up. When the panel was hot, the warm-up heliostats were removed, the door was closed, and salt flow was started from the pumps. Then the receiver was filled and normal flow initiated. Once this was accomplished, the door was opened, the full collector field was brought on target, and energy collection began. This occurred approximately 36 minutes after sunrise for the May 21 test. At this point, the power of the heliostat field was not high enough to allow rated outlet temperature for the minimum flow rate of 12,000 lbs/h per zone. This salt is either returned to the cold tank, or sent to the hot tank, depending upon its temperature, retaining the energy in the storage system.

The rated outlet temperature was achieved 86 minutes after sunrise on the east zone, and 95 minutes after sunrise on the west zone. This is shown in Figure 6.4.4.

FIGURE 6.4.1

EARLY MORNING START-UP RECEIVER POWER

SOLAR START-UP

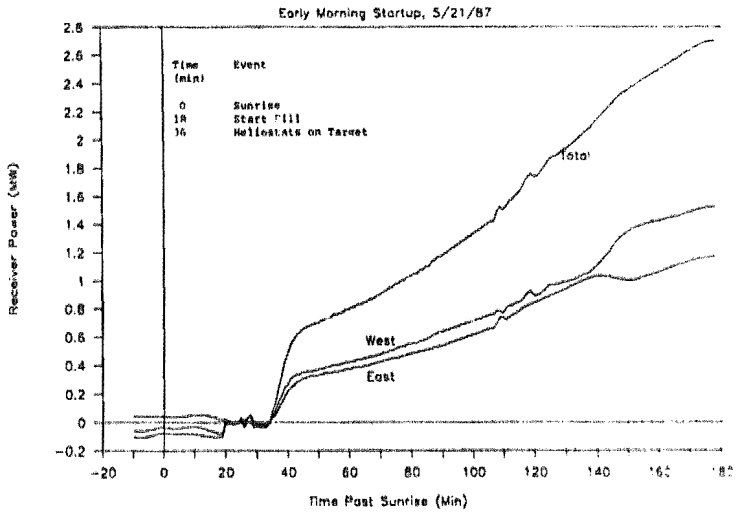

FIGURE 6.4.2

PANEL WARM-UP TEMPERATURES

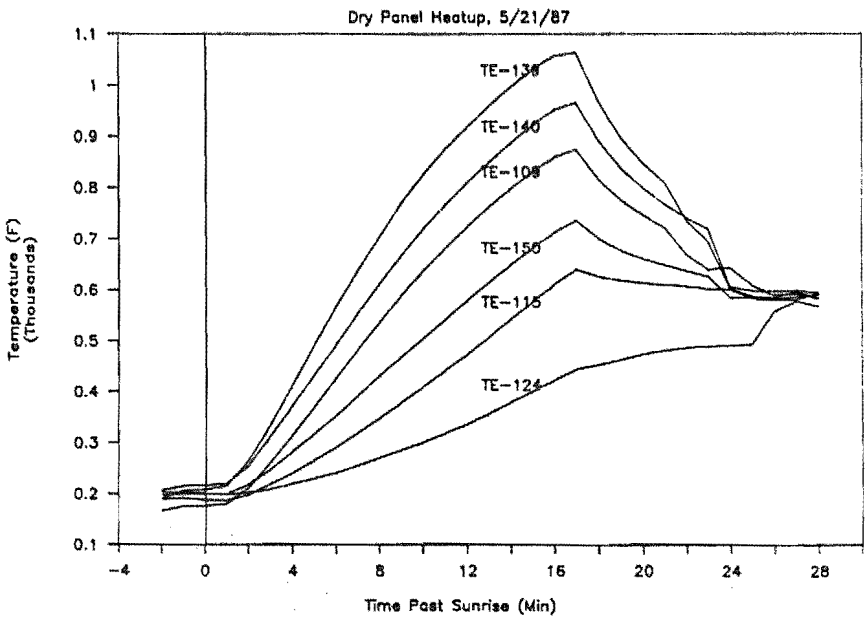

FIGURE 6.4.3

RECEIVER PANEL INSTRUMENTATION

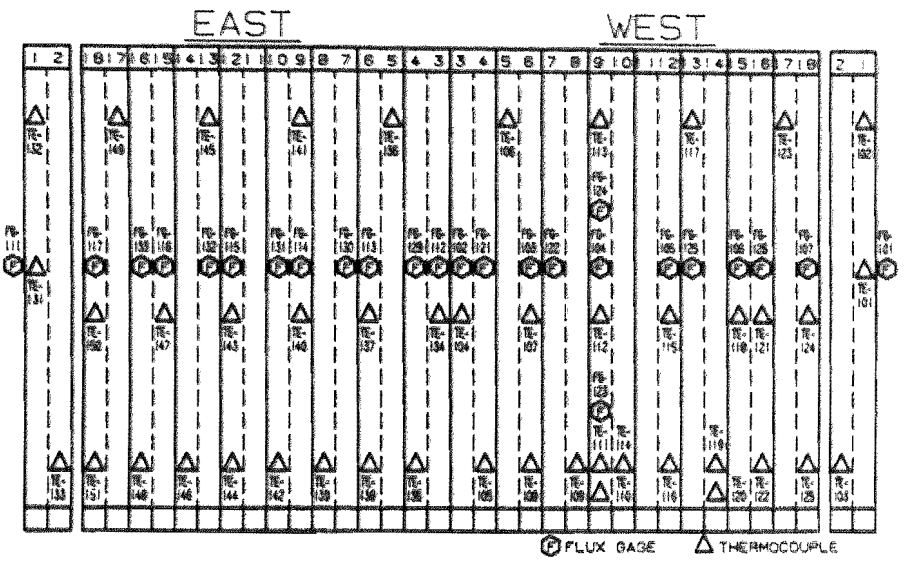

FIGURE 6.4.4

EARLY MORNING START-UP RECEIVER OUTLET TEMPERATURE

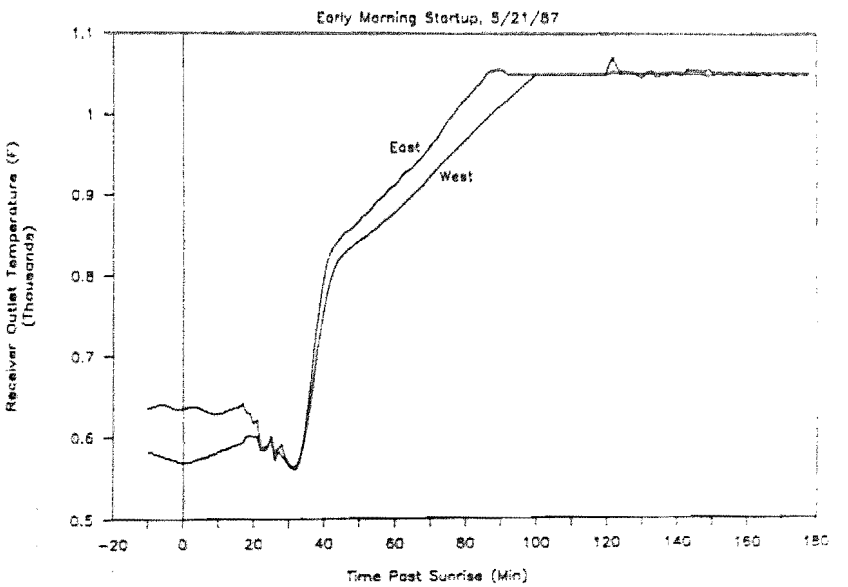

The result was that in the first 95 minutes of operation, 18 kWh was collected at a salt temperature less than 750°F, and 944 kWh was collected at temperatures between 750°F and 1050°F. The salt with a temperature less than 750°F is sent to the cold storage tank, warming it, and the salt above 750°F is sent to the hot storage tank. This degrades the temperature in the hot storage tank somewhat, depending on current inventories. At 95 minutes past sunrise, the receiver operated in normal sun-following mode, controlled by the receiver's control algorithm.

Operationally, start-up with heliostats was found to be a fairly complex operation. Two heliostat warm-up patterns were developed to accomplish such a start-up; an early morning pattern and a midday pattern. Each pattern consisted of a select group of heliostats and appropriate aim points as described in Section 3.3. The early morning warm-up pattern employed 68 percent of the heliostats in the field to achieve warm-up in the 15 minutes after sunrise. To use this pattern, warm-up had to be started within approximately 15 minutes of sunrise in order to limit the flux on the receiver to 33 kW/m^2 and thus limit the stress on the receiver's tube to an acceptable value. The midday warm-up pattern was designed for use within 2 hours of solar noon and employed 22 heliostats, or 12 percent of the field. During this time, the field power was relatively constant. No warm-up patterns were developed for the approximately 2.5 hour period between sunrise and mid-day. These patterns would need to be developed for operational flexibility in a plant that required solar start-up.

Receiver warm-up was a manual operation requiring a great deal of attention to the temperatures of the panel and interaction between the receiver operator and heliostat field operator. Often, real-time adjustments in the collector field configuration had to be made to prevent a portion of the receiver's panel from exceeding 1000°F, while waiting for other regions to reach 500°F. If partially cloudy conditions existed, the problem became more difficult, and there existed a risk of over-heating or over-stressing the receiver unless close attention was paid to solar conditions and to the

receiver's temperatures. The cavity door was found to be useful during solar start-ups. If nonuniform panel temperatures developed, the heliostats could be taken to stand-by and the door closed to allow temperatures to equalize without much loss of total energy in the panel.

The method of heating the receiver panel was developed to the point of being a fairly routine operation that could generally be accomplished without any major difficulties. It did, however, place some limitations on operation, affect the amount of energy collected, and carry with it some operational risks.

6.4.2 Start-up with Electric Cavity Heaters

In order to facilitate checking out the salt flow of the receiver early in the test program before the start of solar operation, a set of tubular heaters was mounted in the floor of the receiver cavity. Six commercial oven-type heating elements were used, mounted beneath a steel grid to facilitate standing on the cavity floor. The elements consumed 11.8 kW of electric power, and with the cavity door closed were capable of maintaining a cavity temperature of 550°F. By leaving them powered overnight, it was possible to start salt flow before sunrise and have the full collector field track the receiver starting at sunrise. A start-up like this was performed on April 8. Figure 6.4.5 shows the receiver's absorbed power vs. solar time. During this start-up, sufficient field power was not available to achieve rated salt outlet temperature from both zones until 78 minutes after sunrise. (The reason that this start-up time is different from that for solar start-up of May 21 is discussed in Section 3.2) Figure 6.4.6 shows receiver outlet temperature plotted as a function of time during the start-up.

FIGURE 6.4.5
EARLY MORNING START-UP RECEIVER POWER
CAVITY HEATER START-UP

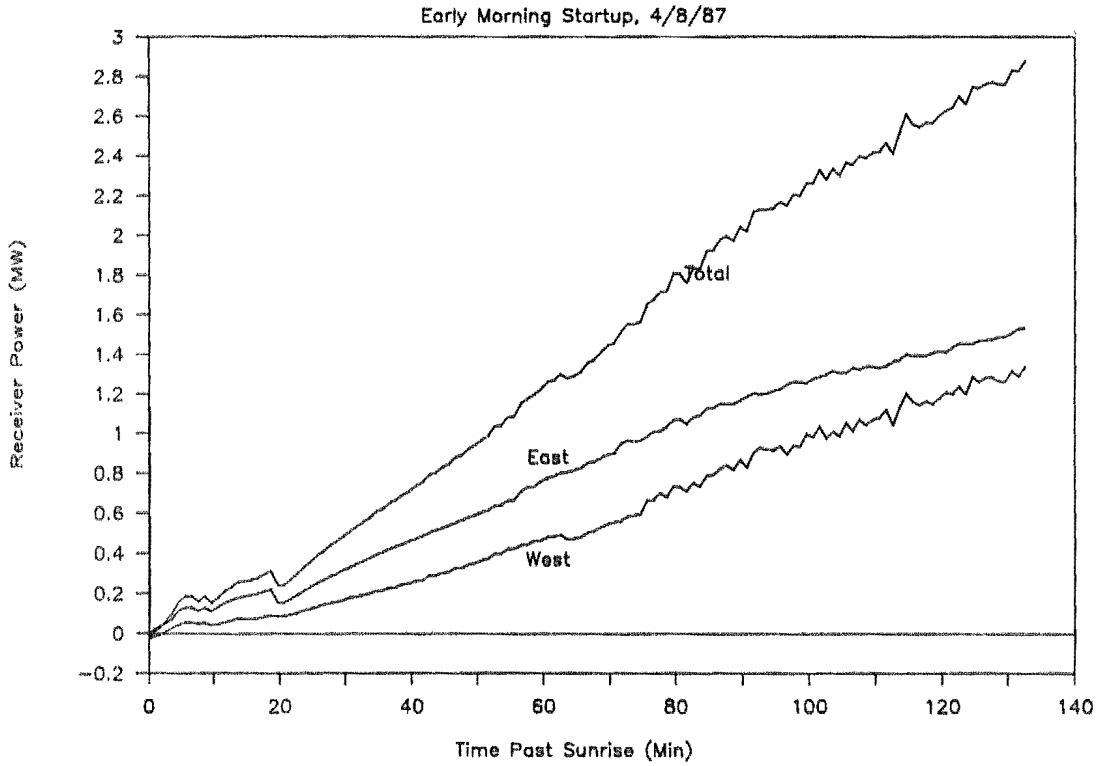

FIGURE 6.4.6
EARLY MORNING START-UP RECEIVER OUTLET TEMPERATURE
CAVITY HEATER START-UP

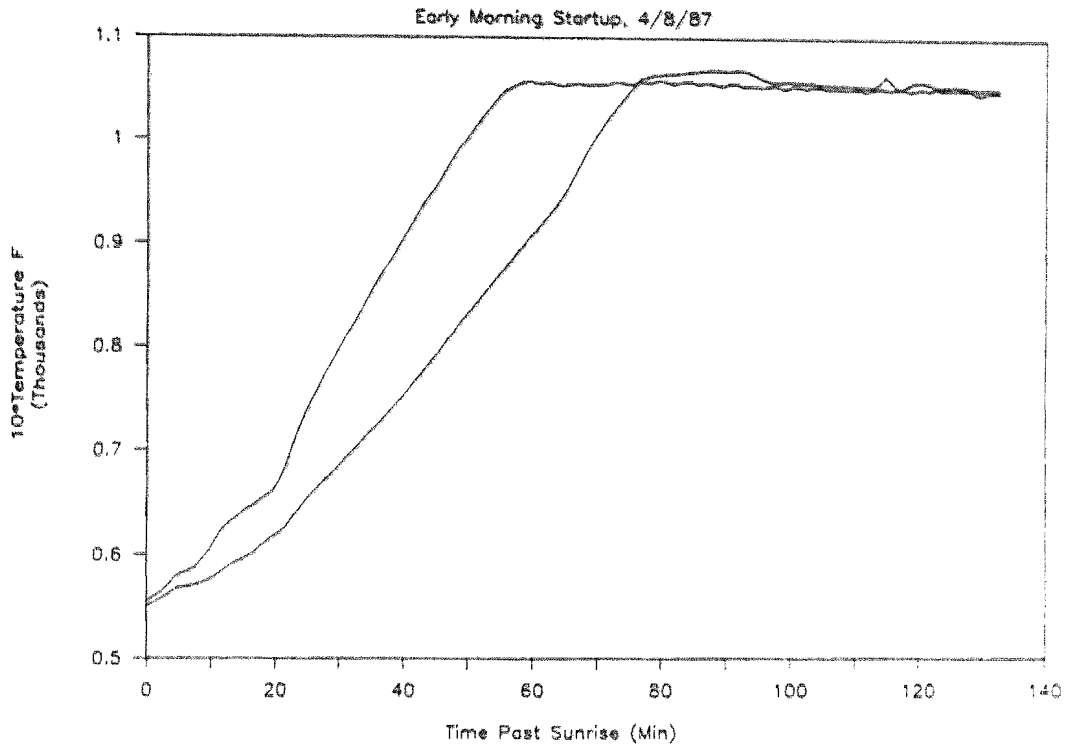

During this start-up 926 kWh was collected in the first 78 minutes. Of this, 132 kWh was collected in salt with a temperature below 750°F which was sent to the cold-salt storage tank, and 812 kWh was collected at a salt temperature between 750°F and 1050°F which was sent to the hot-salt storage tank.

The cavity heater made receiver start-up a simple operation, and salt flow could be established with the cavity door closed under any weather conditions. This would allow collection of solar energy under partially cloudy conditions, when it would be difficult to start the receiver

with a solar warm-up. As a side benefit to the test program, it also allowed start-up on fully cloudy days so that flux-off loss tests and simulated overnight circulation tests could be performed on cloudy days without impacting the time available for solar operation. The disadvantage of the heater was that it was a significant parasitic electrical load.

6.4.3 Overnight Circulation

As discussed previously, both the panel and the piping must be above the freezing temperature of salt. In the previous sections, two methods to heat the receiver panel were discussed. Both of these methods required that the receiver's piping be heated by the electrical heat-trace system. The test program investigated a third method to allow receiver start-up; by maintaining salt in circulation in the receiver from one day to the next. This method offers the advantage that the receiver's piping, along with the riser and downcomer, are kept warm with minimum use of electrical heat trace.

The flow path for overnight circulation differed from normal operational flow, as salt flowed downward in each of the receiver panels. There are two advantages to this method of circulation. First, salt enters and leaves the receiver passes through the vent and drain piping, allowing salt flow to keep this piping warm and thus eliminating the need to power its heat trace. This leaves a minimum of receiver piping left with stagnant salt. The second advantage is that all panels are in downflow which prevents buoyancy-induced circulation in the panels.

During overnight circulation, total flow in the receiver is controlled with the riser throttling valve. The hot surge tank is kept in level control, and the downcomer valves regulate flow out of the receiver as in normal operation.

Simulated overnight conditioning by salt circulation was performed first on May 6, then again on May 22. On May 6, circulation was initiated with full receiver flow (approximately 90,000 lbs/h). After steady conditions were reached, flow was reduced in increments until it was insufficient to keep the receivers piping hot.

When this occurred, the piping temperatures dropped below the 525°F heat-trace set point, and the heat-trace system activated itself to maintain piping temperatures. For this test, salt was circulated from the ground using the main salt pumps, which generate much more pressure than required for downflow circulation. The excess head was throttled by the riser flow-control valve. As a result of the excess energy put into the salt by the pumps, the salt inventory temperature rose during the test. Figure 6.4.7 shows the temperature of one of the receiver's vent lines during the test.

FIGURE 6.4.7
OVERNIGHT CIRCULATION HEAT TRACE TEMPERATURES

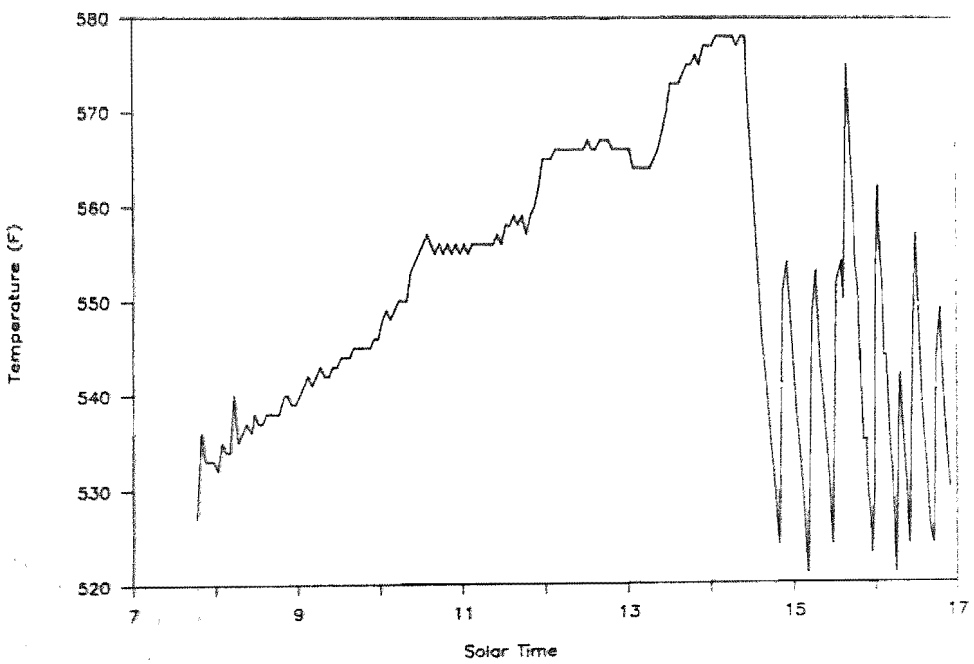

When flow was reduced to 12,000 lbs/h, one of the receiver vent lines was starved for flow. When this happened, the line cooled and the heat trace began cycling to maintain temperature. Based on this event, it was estimated that a flow of approximately 20,000 lbs/h was required to maintain good flow distribution in the receiver.

With a total flow of 20,000 lbs/h, all lines with flowing salt were kept at salt temperature, and heat trace did not operate on these lines. A problem was encountered, however, with the Nupro vent and drain valves. This type of valve is shown in Figure 6.4.8. When salt was circulating in these valves, the valve bonnet region, where the bellows seal is located, cooled to approximately 150°F below salt temperature. This occurred because the bonnet region could not be fully insulated, since the valve actuator was located close to the top of the valve bonnet. The valve is heated by small strip heaters mounted on the valve bodies. Normally, with stagnant salt in the valve, or with the receiver drained, the body temperature was maintained high enough to keep the bonnet at 550°F. With salt flowing through the valve, however, the body temperature was maintained at salt temperature and the bonnet temperature fell due to heat loss to the actuator. In a future installation, care must be taken to insulate and heat trace all valves so that salt flow keeps the valve bonnet hot, or heaters must be applied directly to the valve bonnet to maintain its temperature. For this test, the valve heat trace was turned off manually by reducing its set point, allowing the valve bonnet to get cold. Care was taken not to move the valve while in this condition. This was not required since the valves were open, allowing eventual draining of the receiver. After the receiver was drained, the valve temperatures recovered.

FIGURE 6.4.8
VENT/DRAIN VALVE

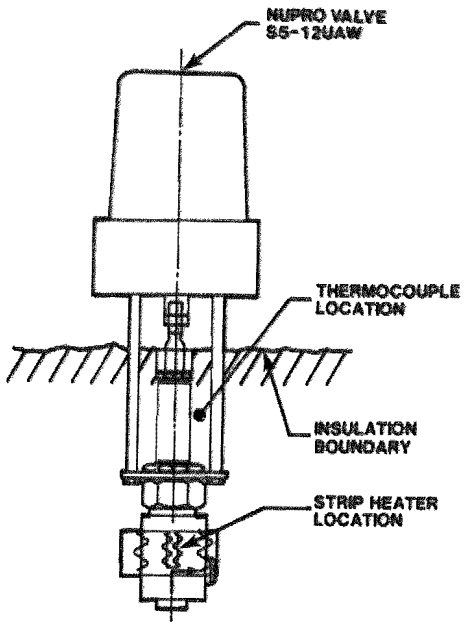

With the drain and vent-valve heat trace turned off, the heat-trace power requirement was reduced to 3.3 kW. The receiver was operated in this condition for approximately 2 hours on May 22. During this time, heat trace operated only on the stagnant drain lines for the cold surge tank and panel outlet lines, the cold and hot surge tank vents, and on the pressure transmitter isolation diaphragms. A small amount of flow was maintained through the receiver flow-control valves by opening them slightly, eliminating the need to operate the heat trace on these lines. Because the control valves employed a nested bellows arrangement near the flow stream,

as shown in Figure 6.4.9, the bellows temperature stayed at the temperature of the flowing salt and no heating of the valve was required.

FIGURE 6.4.9
VALTEK RECEIVER FLOW-CONTROL VALVE

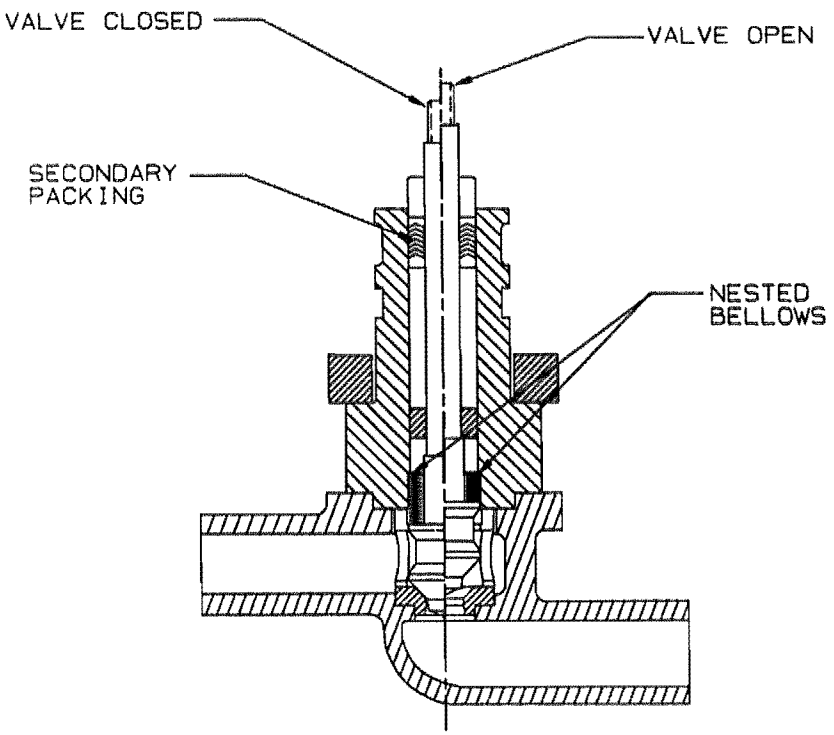

The salt pumps consumed 130 kW of power to maintain circulation. (This calculation is based on current measurements and assumes a 100 percent power factor.) Because the main salt pumps were employed, they used more power than would be required if a small pump sized for the job were employed. The vertical cantilever pumps are very inefficient when operated at low flow. At full flow, the pumps consume 144 kW of electric power, maintaining 95,000 lbs/h flow at a pressure of approximately 500 psi. To maintain overnight circulation at 20,000 lbs/h requires a head of only 200 psi, largely due to

static heads. This represents only 8.5 percent of the pumping power of full-load operation. Assuming the same pumping efficiency, a small pump sized for circulation would only consume 12 kW. (8.5 percent of 144 kW). Table 6-VI presents an energy balance for salt circulation compared to normal heat-trace load. The normal heat-trace load for the receiver is 33 kW for the piping, 12 kW for cavity heaters, and 39 kW for riser and downcomer piping. By comparison, circulation with a small pump would require only 15 kW of electric power. An additional 69 kW of thermal power would be extracted from the thermal storage subsystem to make up thermal losses. This could be extracted by cooling the cold-salt inventory or by blending a small amount of hot salt into the cold pump sump during recirculation.

TABLE 6-VI
OVERNIGHT CIRCULATION ENERGY BALANCE

	Normal Heat Trace	Salt Circulation
Electrical Riser/Downcomer	39 kW	0 kW
Heat Trace Load Receiver	35 kW	3 kW
Receiver Cavity Heater	12 kW	0 kW
Salt Pumping Power	0 kW	12 kW
Salt Storage Thermal Loss	0 kW	69 kW
Total Electrical	86 kW	84 kW
Total Thermal	0 kW	71 kW

Although the total energy to keep the receiver warm is the same, the use of stored thermal energy is preferable to the use of electric heat.

Operationally, circulation in the receiver is only moderately complex. The transition from normal operation to circulation requires only repositioning the vent and drain valves and venting excess air from the cold surge tank. Returning to normal operating mode is simply the reverse. An operator is

required to monitor the system and handle any upsets. For this reason, this test was only performed on cloudy days when the control room was being manned. A higher degree of automation, with provisions to shut down the salt pump and drain the receiver in the event of a problem, could potentially eliminate the requirement for an operator.

Overnight circulation does not eliminate the need for either heat trace or a method of starting the receiver from a cold condition; however, it does minimize dependence on them, and combines the advantages of being constantly ready to collect solar energy while requiring minimal parasitic electric consumption.

6.4.4 Comparison of Start-Up Methods

The differences in the three overnight receiver operations and their associated methods for morning start-up fall into three categories: energy consumed, energy collected, and ease of operation. With respect to energy, each method has different parasitic power requirements and collects different amounts of thermal energy at start-up. Solar start-ups require no electricity to heat the cavity, but miss some solar energy collection. Start-ups using the cavity heater collect extra solar energy, but at the cost of operating an additional electric heater. Overnight circulation from the ground minimizes electrical consumption by substituting stored thermal energy for electricity powering heat trace. This requires pumping power but the bulk of this power goes into heating the salt, again substituting for heat trace power. Overnight circulation also places the receiver in position for maximum energy collection. Operationally the methods differ greatly, affecting the amount of operator interaction required and the procedures needed for start-up. Solar start-ups are relatively complex, requiring special collector field configurations. Cavity heaters require fill and drain sequences, and continuous circulation requires that transitions be made between serpentine flow and down-flow circulation.

Table 6-VII compares the power consumption of the three methods. The energy consumption based on a 12-hour overnight hold is also shown.

TABLE 6-VII
COMPARISON OF POWER & ENERGY CONSUMPTION
POWER/ENERGY

	Solar Start-Up (kW/kWh)	Cavity Heater (kW/kWh)	Overnight Circulation (kW/kWh)
Receiver heat trace electric consumption	35/420	35/420	3.3/39
Cavity heater electric consumption	0	12/144	0
Pump electric consumption	0	0	12/144*
Riser/Downcomer heat trace electric consumption	39/468	39/468	0
Stored thermal energy consumption	0	0	71/852
Totals:			
Electric	74/888	87/1032	15/180
Stored Thermal	0	0	71/852

*Projected values

Relative to a solar start-up, operation of the cavity heater consumes 144 kWh more electricity overnight due to the losses from the cavity itself. When operated, the cavity heater increases the power consumption of the receiver by one third. Overnight circulation, since it also heats the cavity, will consume the additional power as well, but this power will come from stored thermal energy.

The energy collection capabilities of the methods are less straightforward to compare. The overnight circulation method and the cavity-heater methods are equivalent with regard to energy collection, because they both allow the receiver to be ready to collect power at sunrise or whenever sun is available. Solar start-ups normally just delay start-up in the morning for

approximately 36 minutes while the receiver is heated, filled with salt, and normal serpentine flow is established.

Direct comparison of energy collected from the April 8 early start-up using cavity heaters and the May 21 start-up using heliostats is misleading. On May 21, an attempt was made to balance the power from the east and west receiver zones by offsetting the aim points to the west (see the discussion of section 5.2). Additionally the CRTF collector field varies somewhat with time of year, and the two tests were performed 1 1/2 months apart at a time of year when changes are fairly pronounced. (Sunrise on April 8 occurred at 6:07 solar time, and on May 21 it occurred at 5:30.) As a result, the total power of the receiver for the two cases was different after the full field had been brought onto the receiver. Rather than making a direct comparison of the energy collected for the two cases, the data of May 21 will be normalized to conditions of the April 8th start-up. Figure 6.4.10 shows total power from the start-up using the cavity heaters, and the projected total power based on a solar start-up. For the solar start-up, heliostats are assumed to come on target 34 minutes after sunrise, and power to ramp up over the following 6 minutes. Once all heliostats are on target and receiver power ramps up, the two cases are assumed to be the same.

FIGURE 6.4.10
START-UP POWER COMPARISON

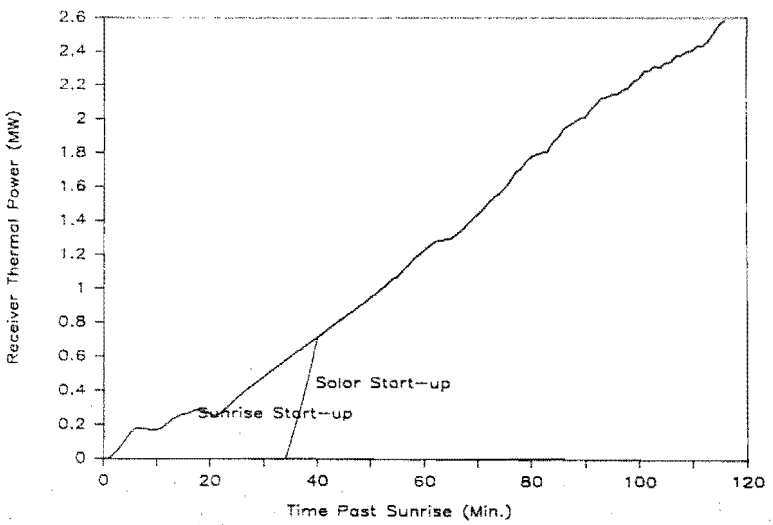

The energy collected and the receiver outlet temperatures are shown in Figures 6.4.11 & 12. Based on these data and the assumption that a start-up from overnight circulation would be equivalent to a start-up using the cavity heater, Table 6-VIII presents energy collection for the three methods.

FIGURE 6.4.11
START-UP ENERGY COMPARISON

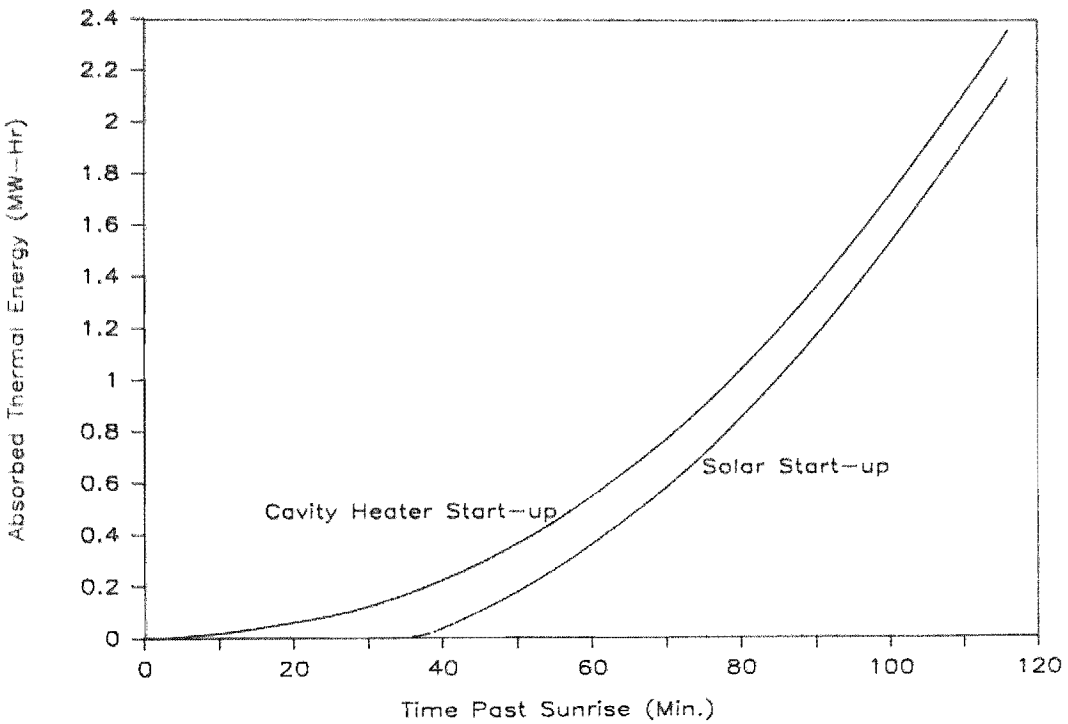

FIGURE 6.4.12
START-UP OUTLET TEMPERATURE

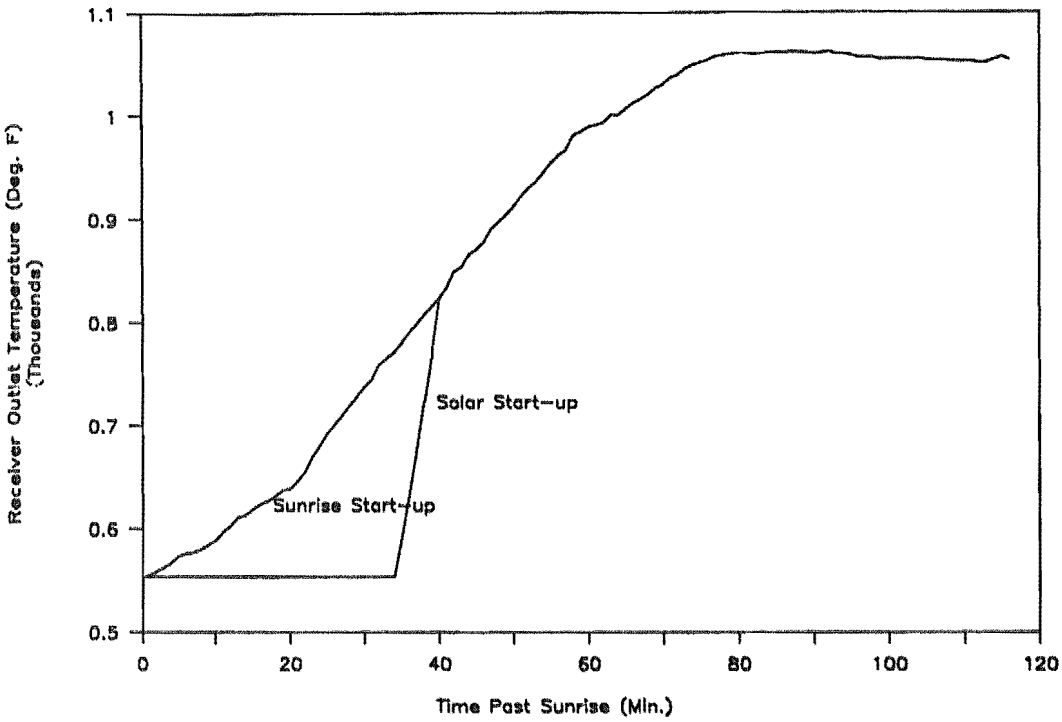

TABLE 6-VIII
THERMAL ENERGY COLLECTION COMPARISON

	Energy collected below 750° (kWh)	Energy collected between 750° and 1050° (kWh)	Total start-up energy (kWh)
Solar start-up	23	663	686
Cavity Heater start-up	132	741	873
Overnight Circulation	132	741	873

Relative to a solar start-up, starting with the cavity already hot at sunrise collected an additional 187 kWh. Of this energy, 109 kW was collected in the form of extra salt at temperatures below 750°F and 78 kW of

salt above 750°F but less than 1050°F. Salt with a temperature less than 750°F was returned to the cold tank, raising its temperature slightly. The energy was not lost, however. Heat added to the cold tank reduces the energy required to later heat the salt to 1050°F. Salt above 750°F was sent to the hot tank, which degraded its temperature by an amount that depended upon its salt inventory, but adding to its total energy.

Using the solar start-up as a base-line, a comparison of the total energy collected and consumed by starting at sunrise with cavity heaters and by overnight circulation is shown in Table 6-IX.

A negative value indicates more energy consumed, or less produced, than for a solar start-up.

TABLE 6-IX
TOTAL ENERGY DIFFERENCE RELATIVE TO
SOLAR START-UP

	Electric Energy	Thermal Energy
Cavity Heater	-144 kWh	+187 kWh
Overnight Circulation	+708 kWh	-665 kWh

Use of the cavity heater allows additional collection of thermal energy in the mornings, but not sufficiently to offset the electric consumption of the heater, given that no more than 30 percent of the thermal energy can be converted to electricity. Overnight circulation, however, makes substantial savings in electric consumption by substituting thermal energy. Some of this thermal energy is made up by extra energy collection, and the balance reduces the useful power that can be extracted from storage during the day. Since electricity is more valuable than thermal energy, this should represent a major savings for a commercial plant. The amount of savings would depend upon the value of electricity consumed in the evening compared to the value of electric power produced during the day.

To conclude the energy comparison, several qualitative points should be made. First, the heat-trace operating strategy employed in this receiver may not be optimal with regard to energy consumption. The system operated continuously, cycling heaters on and off to maintain piping temperatures overnight and also on days when the plant was not operating. It should be possible to turn off portions of the heat trace in the evening, after sufficient time to allow the receiver to drain. Then it could be turned on again early in the morning, allowing sufficient time for the piping to heat up and to melt away residual salt in the system. This would require more sophisticated control than that available with the Acurex heat-trace controller, but could save substantial amounts of electricity. Second, the extra energy that can be collected at sunrise by using the cavity heater, or by continuously circulating salt, may represent only a portion of the extra energy that could be collected. Often because of weather or other operational conditions, start-up does not occur at sunrise. For a midday start-up, for instance after clouds burn off, continuous circulation or the use of a cavity heater would allow more rapid start-up than if a solar warm-up of the panel were required to start flow. At sunrise, only a small amount of energy is missed in the approximately 30 minutes required for a solar start-up. At midday much more energy would be lost (as much as 2.25 MW-h). This leads to the conclusion that the method of thermally conditioning the receiver will affect the amount of energy that can be collected in various weather conditions and therefore on an annual basis.

Operationally, the cavity heater offers the simplest process for starting the receiver. Because the tubes are always hot, the receiver's fill sequence can be initiated at any time, and because the receiver is drained at night, no monitoring of the process is required. Continuous circulation simplifies the actual start-up operation even further, since no filling of the receiver is required. Overnight, however, the presence of salt in the system, and the operation of the circulation pump would require an operator to monitor the system and initiate a drain if a failure occurred. This operator might not be required, however, if the system were further automated. Solar start-ups are relatively the most complex. The warm-up pattern of heliostats and aim points must be developed as a function of time of day and time of year. In addition to this, some operator action is

required to 'fine tune' the pattern and achieve a uniform heat-up. Start-up in partially cloudy conditions is more difficult, but can be achieved by use of the cavity door to allow the panel's temperature to equalize and retain the cavity's heat while clouds pass.

6.5 Evaluation of Controllability

Evaluation of the receiver's controllability is discussed for automatic and operator control. Control and monitoring by an operator are necessary for performing receiver start-up, shutdown, and recovery from trip conditions or emergency situations. The ability to automatically control cloud transients is crucial to maximizing receiver output and annual energy production. This evaluation is relative to the receiver's control system design of Section 3.9, the operational check-out tests of Section 5.1.5, and operational tests of Section 5.2.2. Reading those sections is necessary to understand fully the evaluation below.

Assessing the ability of operators to control and monitor the receiver was based on observations made of operators as well as their comments during the course of testing. No specific testing was performed to address this issue technically. Therefore, this evaluation was based on perceived operator effectiveness in using the man/machine interface supplied with the computer-based process control system (Bailey NET-90).

Again, this section presents the test data and an evaluation of receiver controllability. In addition, the modifications to improve this controllability and their evaluation are presented, as well as the comparison of actual results against those predicted by the McDonnell Douglas receiver simulation.

The controls were initially evaluated relative to an analysis of linear controls to determine closed-loop stability at different power levels. From this, the ability to operate (under control) at derated conditions was determined. Then the ability to automatically control cloud transients was evaluated relative to simulated and natural clouds. Finally, the ability of operators to control and monitor the receiver is presented.

Since there were two control zones (east & west), two independent Receiver Control Algorithms (RCAs) were used for control. These control zones were physically identical, so both RCAs were structurally and functionally identical. Therefore, the RCA is referred to herein as a single entity.

6.5.1 Tuning & Derated Operation of the Control Algorithm

The hot flow tuning given in Section 5.1.5 provided improvements in the ability to control the RCA over the original tuning constants used in simulation. The operational tests described in Section 5.2.2 further refined the tuning of the RCA. The modifications and the evaluation of the results are presented here.

The RCA was tuned using partial power transients and outlet temperature set-point changes. Modifications were made to the design configuration of the RCA in order to improve its temperature response to both power transients and set point changes.

Outlet Temperature Response to Set Point

The improvement in outlet temperature response to set-point consisted of modifying three of the components within the RCA (RCA components are discussed in Section 3.8.1):

1) Adaptive gain functions of the outlet temperature controller,
2) Adaptive gain functions of the controller using back-tube temperatures, and
3) Set-point generator for the controller of the back-tube temperatures.

These modifications became necessary because of stand-off errors and the inability to the outlet temperature controller to integrate out errors in derated conditions. These errors were the difference between set point and actual outlet temperatures.

The stand-off error was caused by the use of the set-point generator for the controller of the back-tube temperatures. The original design was simple, and the generator set the back- tube temperature set point proportional to the outlet temperature set point as follows:

$$TSET_{BT} = K\ (TSET_{OT}).$$

This was inadequate, since the actual back-tube temperature went beyond its set point once the actual outlet temperature achieved its set-point. This indicated that the proportionality factor (K) was not large enough at the new set point, which meant the relationship was not strictly proportional.

Since the receiver has a minimum temperature equivalent to inlet temperature (550°F), the set-point generator was changed to account for the operational temperature range as follows:

$$TSET_{BT} = K\ (TSET_{OT} - 550) + 550.$$

This method resulted in a larger K, which produced the required larger change in the back-tube temperature set point and improved the match between set point and actual back-tube temperature. More important, the larger set-point change produced a larger controller output, or flow-rate change. Consequently, the stand-off error was reduced significantly (±10°F).

The stand-off error was practically impossible to eliminate totally since the average back-tube temperature was dependent upon the flux distribution. Different flux distributions with the same total energy content produce different average back-tube temperatures. The magnitude of this problem is unknown, due to a limited amount of operational experience; it was perceived to be quite small.

The second modification was required to correct the inability of the outlet temperature controller to integrate out errors in derated conditions. This problem manifested itself early in the morning and late in the afternoon, or whenever low flow rates (12,000-18,000 lb/h) occurred. It was observed that the back-tube controller was counteracting practically every attempt by the

outlet controller to integrate out its temperature error; this was similar to a tug-of-war game in which neither side wins.

The outlet temperature controller had to dominate control in order to force the outlet temperature to its set point. Initially, the outlet temperature controller's integrator adaptive gain function was modified to an anti-windup only configuration rather than a linear plus anti-windup configuration as illustrated by Figure 6.5.1. This increased the integrator's gain at low flow rates as required, and stability was still maintained. However, this improved the situation only slightly; it simply increased the intensity of the tug-of-war game. It then became necessary to adapt the back-tube temperature controller's overall gain in order to reduce its effect at low flows. This adaptive gain function was equivalent to that used for the outlet temperature controller's overall adaptive gain function. The combination of these two modifications produced the desired result of providing the ability to integrate out errors in derated conditions.

FIGURE 6.5.1
OUTLET TEMPERATURE CONTROLLER ADAPTIVE INTEGRATION GAIN FUNCTION

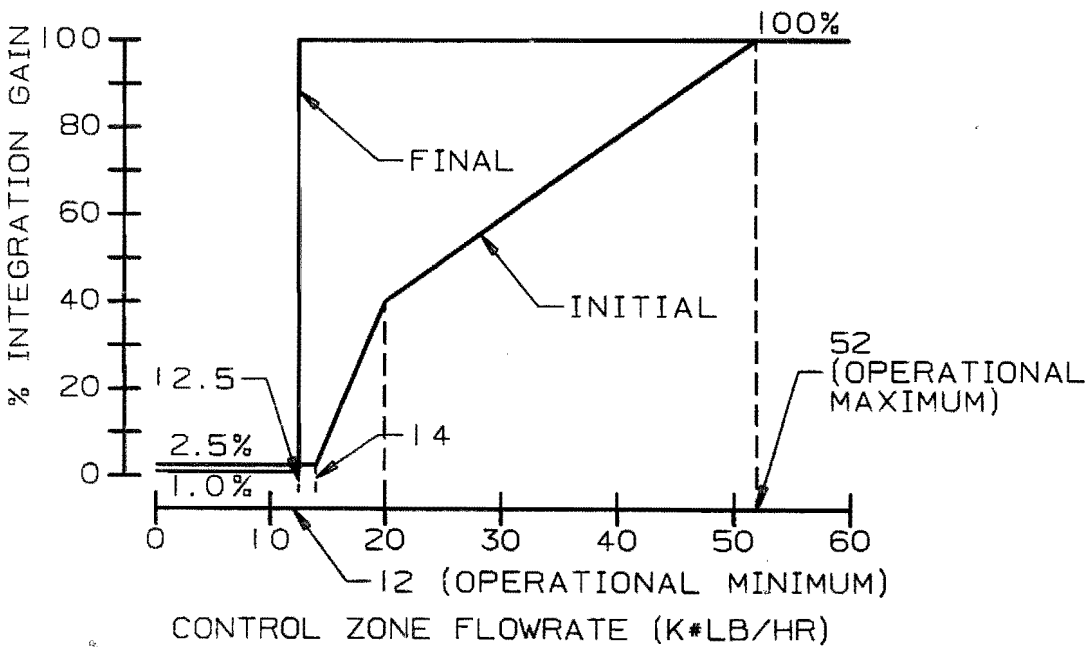

Outlet Temperature Response to Power Transients

The improvement in outlet temperature response to power transients consisted of modifying two items within the RCA:

1) Outlet controller tuning constants, and
2) Back-tube controller tuning constants.

These tuning constants were changed relative to the constants predicted by the receiver simulation. The thrust was to increase the constants until marginal stability (oscillations) occurred. In the case of the back-tube controller, which uses derivative control, the constants were increased until noise amplification became a problem. Once these conditions were found, the overall gain for each controller was reduced by 3dB, or 29 percent, to provide adequate stability margins.

The final tuning constants for the outlet temperature controller were:

KSC = ADAPTIVE (0.20 @ 100 percent)
KP = 1.0
KI = ADAPTIVE (Anti-Windup Only with 1.5 @ 100 percent)
KD = 0.

The final values were different from the simulation results. The overall gain (KSC) was twice as high, even though the linear adaptive function was unchanged. The proportional gain (KP) was unchanged. The integral gain (KI) was less by 25 percent, and the adaptive function was changed from linear plus anti-windup to anti-windup only, as depicted by Figure 6.5.1. The derivative gain (KD) was changed to zero, or simply not used because there was essentially no value added by using it. During design its use was thought to be beneficial during large transients. However, testing showed this was not the case.

The final tuning constants for the average back-tube temperature controller were:

KSC = ADAPTIVE (2.0 @ 100 percent)
KP = 0.32
KI = 0
KD = 0.046.

The overall gain was changed to an adaptive function and was twice as high. The adaptive function was linear and identical to that used for the overall gain of the outlet temperature controller. The proportional and integral gains were unchanged. The derivative gain was four times as high as predicted.

The difference between the actual tuning constants obtained and those predicted by the simulation was relatively small, yet significant from a performance point of view. The generally higher values of the tuning constant indicated that the actual response of the receiver was better than predicted, which was the case demonstrated by the natural response given in Section 5.1.5. This actual natural response of the receiver indicated a general ability to increase gains by a factor of 2, which was indeed the general case.

Also, this response indicated that conservatism existed in the simulation. The time delay used was over-estimated by a factor of 2, which resulted from a judgmental error; apparently water/steam simulations require this additional time delay, and molten-salt simulations do not. The 12 percent discrepancy in the time constant was relatively small and apparently was a result of over-estimating the amount of thermal mass actually present.

Derated Operation

Testing demonstrated the ability to operate the receiver in derated power conditions. The RCA was able to control the outlet temperature even though response time was considerably longer (10-15 minutes) in derated conditions. This time is deceptive for operators, since they tend to expect a similar

response under all conditions. This will never be the case, so operators need to be trained for the variable nature of the receiver's response. Only a limited amount of testing was performed in derated conditions, however the results obtained were considered representative and very positive.

6.5.2 Automatic Control During Cloud Transients

The operational data obtained according to the operational tests performed, described in Section 5.2.2, are evaluated here relative to the ability to automatically control cloud transients. The concern about thermal stresses, which were caused by temperature ramp rates and flow mismatching flux, significantly impactsd the testing performed. The modifications, test results, and the evaluat´ ı are presented.

The ability to automatically control cloud transients dealt primarily with the receiver control algorithm (RCA). The functional objectives of the RCA were to maintain the outlet salt temperature at set point (desired value) and prevent tripping the receiver off-line because of high temperature so that the receiver output was maximized. Because of stress-related problems, an additional objective of minimizing fatigue stress became necessary.

Minimizing stress was counter to the original objective of maximizing output. Consequently, a trade-off existed between maximizing output and lifetime. An in-depth evaluation of this issue is presented in the thermal/structural evaluation section (7.1). The modifications made to reasonably reduce stresses without seriously impacting the receiver's output are presented here along with a discussion of the condition with which a commercial system that maximizes output will have to deal.

Automatic control of cloud transient is addressed relative to simulated and natural cloud transients. Simulated transients were used to evaluate the outlet temperature set-point generator, or sliding set-point mechanism. Natural cloud transients were used to introduce and evaluate a new "dual control strategy."

Simulated Cloud Transients

Simulated cloud transient tests demonstrated the requirement for the sliding set-point mechanism, since high-temperature trips occurred when it was not used. This mechanism was originally designed to automatically derate the receiver output to prevent high-temperature trips when clouds clear. To address the temperature ramp-rate problem, the up and down set-point ramps generated by the mechanism were adjusted in order to control ramps within allowable limits ($\pm$ 0.75°F/s).

The parameters of the sliding set-point mechanism consist of the following:

1) Bias (error limit),
2) Down-ramp rate limit,
3) Up-ramp rate limit, and
4) Minimum limit.

These four parameters determine the nature and speed of the outlet temperature recovery to a cloud transient as explained in the design section (3.12).

Even though a complete parametric study was not accomplished, three tests were performed as shown in Table 6-X.

TABLE 6-X
SLIDING SET-POINT TEST PARAMETERS

PARAMETER	TEST 1	TEST 2	TEST 3
BIAS (°F)	50	25	25
UP RAMP (°F/S)	0.50	0.50	0.75
DOWN RAMP (°F/S)	0.75	0.75	1.50
MIN LIMIT (°F)	850	850	850

Test 1 was the base-line configuration, and it took 7.4 minutes for the outlet temperature to return to rated conditions as illustrated by Figure 6.5.2. The large 50°F bias made it difficult for the controller to maintain set-point.

FIGURE 6.5.2
OUTLET TEMPERATURE RESPONSE TO TEST #1

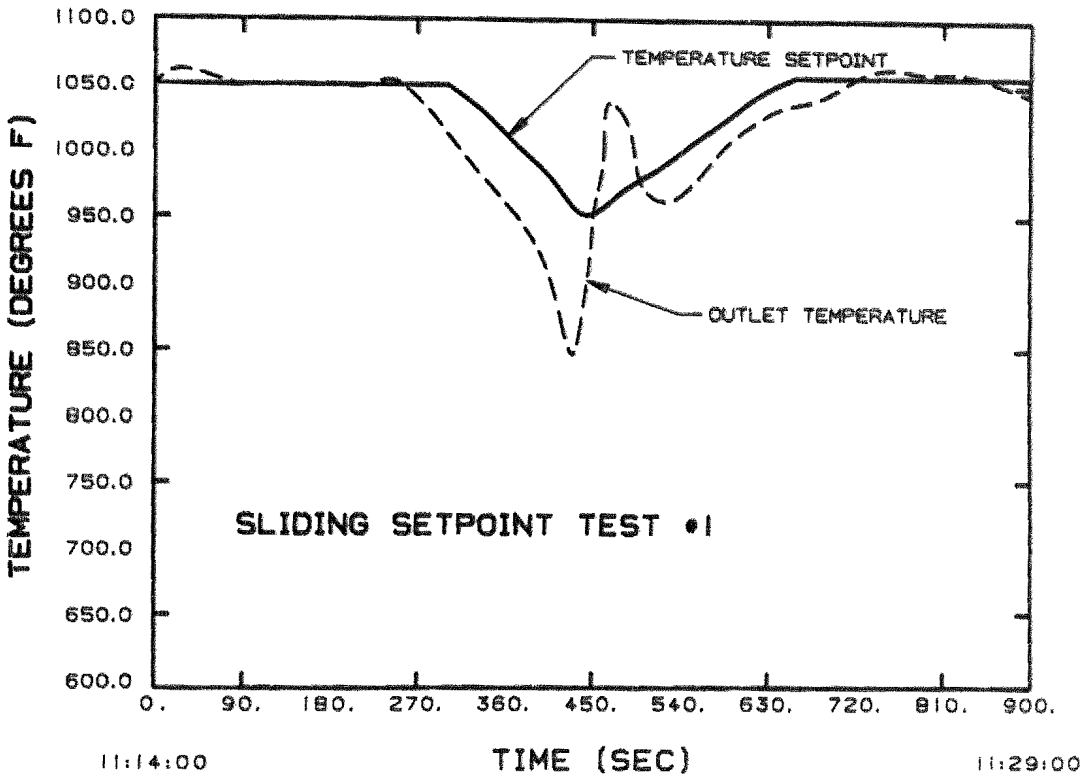

Test 2 was the same as Test 1, except the bias was changed to 25°F. This improved the controllers ability to follow the set point but derated the temperature longer, as illustrated in Figure 6.5.3. It took 8.9 minutes for the outlet temperature to recover, or an additional 20 percent compared with Test 1. This resulted in better control at the expense of receiver output.

FIGURE 6.5.3
OUTLET TEMPERATURE RESPONSE TO TEST #2

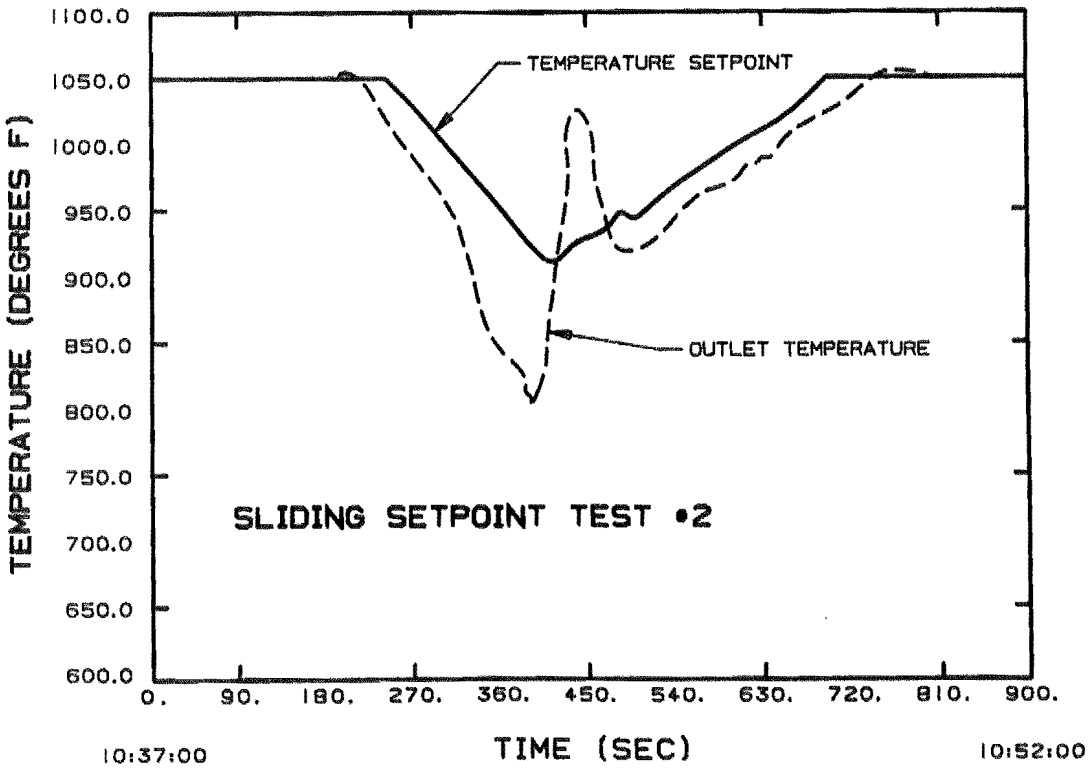

Test 3 was the same as Test 2, except that the down ramp was increased by 200 percent and the up ramp was increased by 50 percent. This increase resulted in a deeper derated set-point, but it also recovered more quickly, as illustrated in Figure 6.5.4. However, the actual temperature was unable to track this set point. The recovery time was acceptable at 8.2 minutes, or an additional 11 percent compared with Test 1.

FIGURE 6.5.4

OUTLET TEMPERATURE RESPONSE TO TEST #3

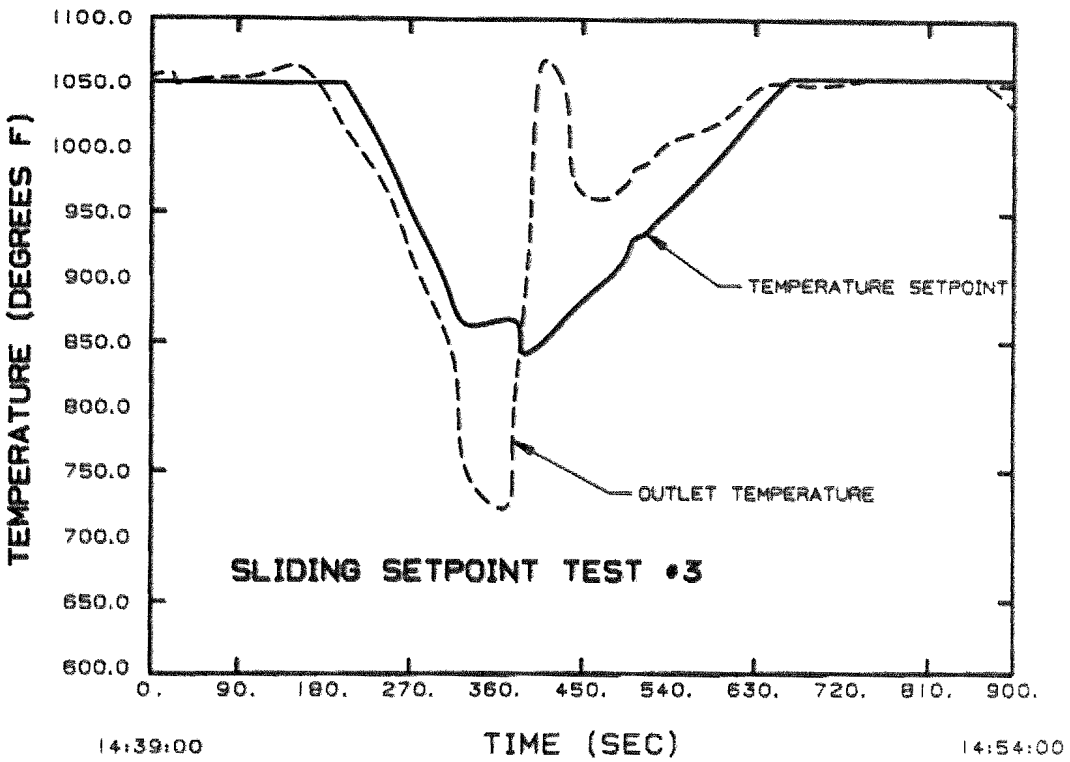

Parameters of Test 2 were used through the remainder of testing because of good set-point tracking. However, these parameters were not optimum.

In all three tests the outlet temperature went high when the cloud cleared This spike was due to the flux-feed forward gain being set to achieve 1050°F, which it did very nicely. However, the set point was not 1050°F. An improvement could be made here by adjusting this gain according to set point; however, this modification was not tested.

Preliminary results indicated that all three components of the RCA were required. Limited testing (one test each) was performed when the flux control and/or where the back-tube temperature control was not used. Both tests resulted in high-temperature trips of the outlet.

Natural Cloud Transients

Initial testing was done with the RCA in the design configuration. However, this configuration commonly produced temperature ramp rates of 11°F/s as well as mismatched flow with incident flux for a significant period of time. This situation resulted in high stresses in tube-to-header connections and in the tubes themselves.

To help alleviate the stress problems, the RCA was modified into a dual strategy configuration. The design configuration stayed intact but became switchable from one strategy to another. During normal operation the RCA was in the design configuration, or normal temperature control. When extended cloud coverage occurred, the RCA was automatically switched to flux feed-forward control only. This control method essentially eliminated the tube stress problem since the flow was forced to match the flux independent of temperature. However, the tube-to-header stress problem still existed even though the temperature ramp rate was reduced by one-half (6°F/s). The response of the system to a natural cloud with the entire receiver at inlet temperature is illustrated in Figure 6.5.4. Figures 6.5.5 and 6.5.6 show the corresponding average flux and flow rate.

FIGURE 6.5.5
OUTLET TEMPERATURE RESPONSE TO A NATURAL CLOUD

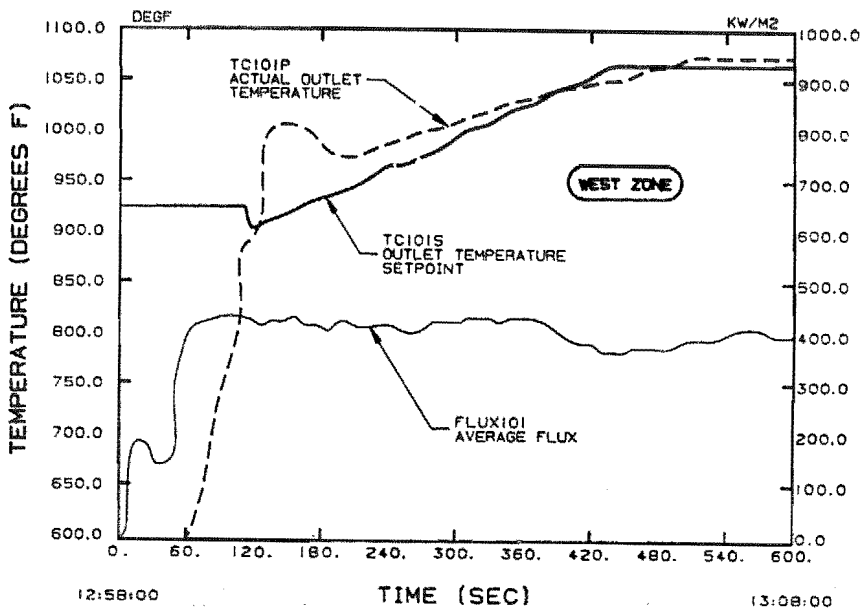

FIGURE 6.5.6

CORRESPONDING FLUXES & FLOW RATE TO FIGURE 6.5.5

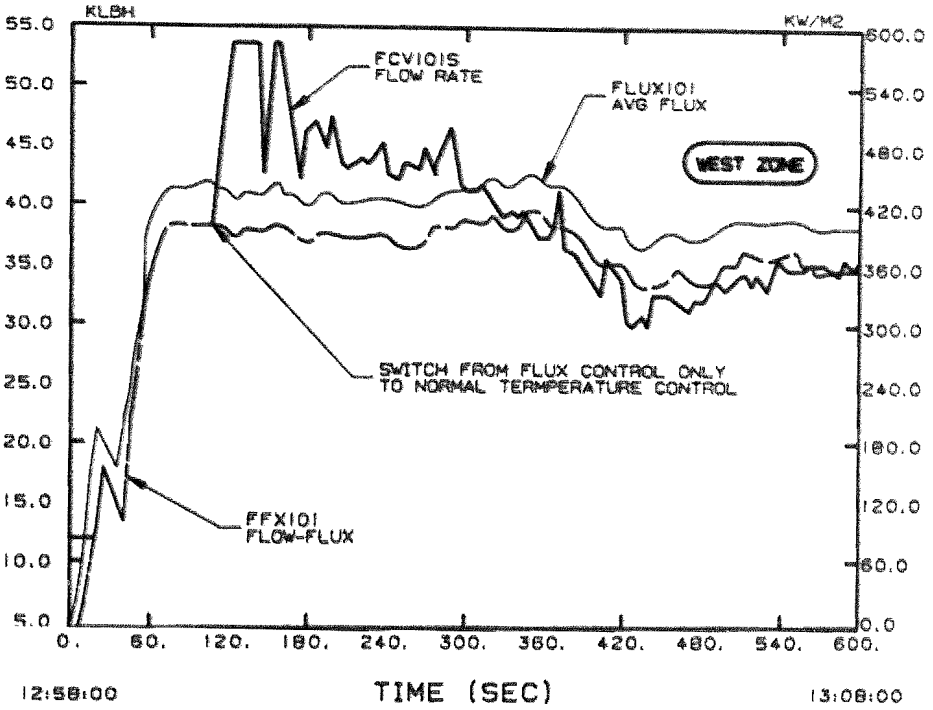

Since there were two methods of control, automatic switching logic was developed to switch from one method to another. The logic used outlet temperatures and timers to determine when to switch from one to the other. When the outlet temperature went below 850°F for 30 seconds, control was switched to flow-flux control. When the outlet temperature went above 850°F for 30 seconds, control was switched to normal temperature control. The 850°F breakpoint was chosen because temperature control was possible at and above this outlet temperature and because 850°F was the minimum set point. This logic has not been optimized.

This testing demonstrated the ability to control cloud transients and the fact that ± 6°F/s ramp rates have to be tolerated. If the ± 0.75°F/s ramp rate had been a strict operational limit, the receiver would not have been allowed to operate in cloudy conditions. Because clouds are always

prevalent, this limitation would seriously degrade annual energy production and make this technology uneconomical in future applications of the technology.

6.5.3 Control & Monitoring by an Operator

This evaluation focuses upon the control-room operators who monitored and controlled the overall process of the experiment. Two primary operators were required; one for the process control and one for heliostat field control. Since no specific tests were performed to evaluate the operators' effectiveness, real-time observations and comments were noted and an informal discussion was held with the operators. The evaluation concentrates on four specific areas:

1) Procedures,
2) Digital process computer,
3) Supporting computers, and
4) Improvements.

Procedures

Final procedures from the MSEE Experiment were used after adapting them to this receiver and the new process computer. Control of the process was very effective using these procedures. However, in a commercial power plant two sets of procedures should be utilized. One should be for training purposes, with detail such as the procedures used on this experiment, and a second set should use one-line instructions for operators familiar with the equipment. These procedures could be easily installed into the process computer and called up on the CRT as required by the operator.

Digital Process Computer

All of the operators agreed that the state-of-the-art digital process computer is very effective in controlling a solar power plant. Ease of operation of the process computer was the most favored aspect. They also liked the basic arrangement of the keyboard and the flush keys. The active

graphics and the alarm page provided easy response to emergencies. However, all agreed that more experience in the process is required for immediate response to emergency situations. Finally, the ease of reconfiguring the graphics was favorable in the digital process computer.

Supporting Computers

Several other computers were used to support the digital process computer; the heliostat computer, the heat-trace computer and the data-processing computer. The operators agreed that using these multiple computers made it more difficult to operate and control the process of the experiment. It also required an additional operator to control the heliostats separately. As experience was gained however, computers did not present any problems with the operators monitoring and controlling the experiment.

Improvements

The operators agreed that the main improvement in control would be to integrate all the supporting computers into one control system that would control all aspects of plant operation. This would apply especially to a commercial solar power plant. Second, all of the start-up, operations, and shutdown sequences should be programmed for automatic sequencing by the master-control system computer. However, manual overrides should be provided for the operator. Finally, the master-control system computer should be programmed to automatically respond and save the system in emergencies. These emergencies could be displayed on the CRT with specific one-line procedures to save the system, allowing operator intervention and a quick recall of what should be implemented in a given emergency situation.

6.6 Overall Performance Predictions

Prediction of energy collection on an annual basis is of great importance to system designers. The receiver's capability to collect energy is a function of its thermal efficiency, which is a function of absorbed power and also its operating characteristics, especially with respect to start-up and operation in cloudy and other off-design conditions. As a result, annual

efficiency depends upon the annual weather in which the receiver operates. This section summarizes the test results for receiver efficiency and then discusses the ability to start and operate the receiver under various conditions. The description is based on capabilities demonstrated in the tests and attempts to provide a system designer with sufficient information to predict annual energy collection, given weather conditions for a specific site.

6.6.1 Average Steady-State Performance

Receiver losses were measured by two different methods: 1) subtraction of the measured output power from input power calculated with the HELIOS program as discussed in Section 6.1, and 2) by flux-on loss testing as described in Section 6.3. Receiver efficiency can be calculated based on losses derived from both methods, and these can be compared to efficiency predictions made with the CAVITY-2 computer code as discussed in Section 6.2. Receiver efficiency is plotted in Figure 6.6.1 and thermal loss is plotted in Figure 6.6.2 as a function of receiver absorbed power. Data points are shown for the measured input method and the flux-on test method, as well as predictions made by the CAVITY-2 program for the nominal case at 100 and 50 percent power. The results of the CAVITY-2 program are in general agreement with the test results. Thermal loss predicted by CAVITY-2 does not include the effects of the wing panels; however, this does not greatly affect the losses or efficiency predicted by the code. The power incident on the wing panels was only 4 percent of the total incident power or 210 kW at solar noon. Losses from the wing panels are estimated to have been less than 25 kW.

FIGURE 6.6.1

RECEIVER EFFICIENCY BY ALL METHODS

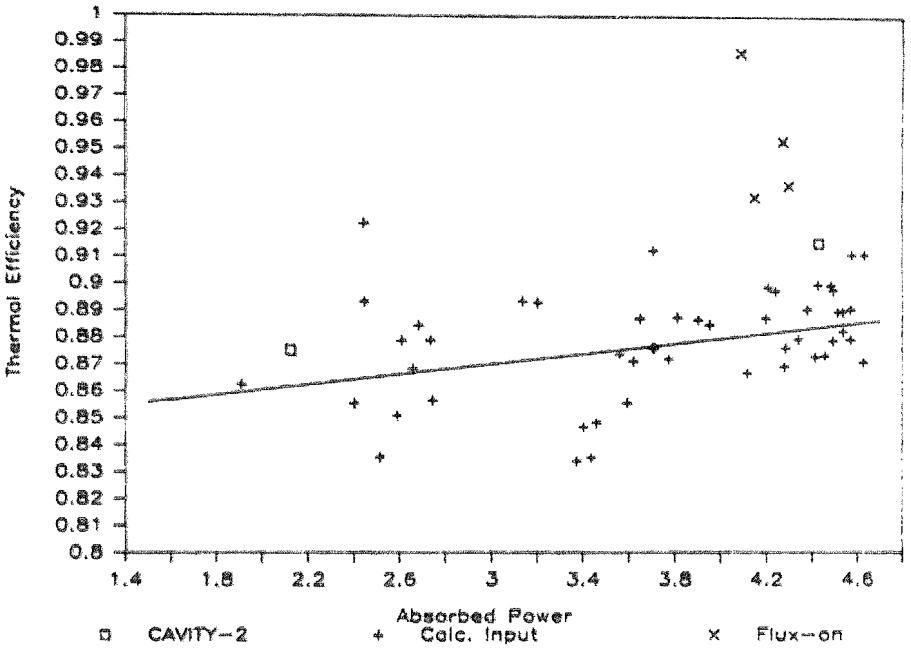

FIGURE 6.6.2

THERMAL LOSS BY ALL METHODS

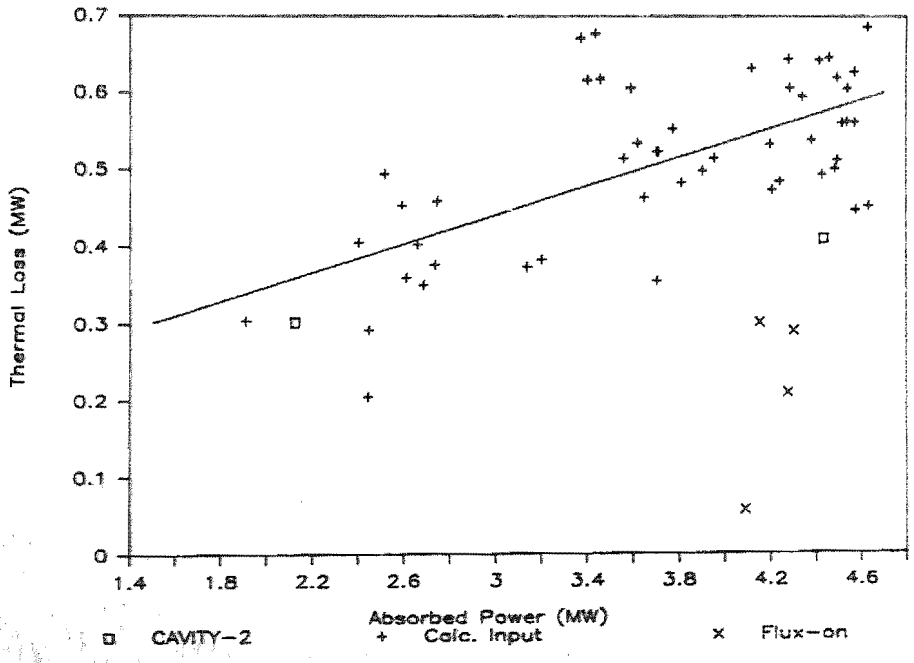

The results of the CAVITY-2 code indicate that the thermal loss is a function of absorbed power. The calculated input-loss data did not show this trend, but the variation shown by CAVITY was within the scatter of the calculated input data.

The flux-on loss test results show generally lower losses and therefore higher efficiencies than the CAVITY predictions or calculated input measurements. The flux-on loss test results, however, appear to be unrealistically low. This is because for three of the five measurements, the measured losses were less than just the radiative loss predicted by the CAVITY-2 code. The reason for this discrepancy is not clear; however, the flux-on loss test results are very sensitive to the flow measurement. The estimated flow measurement uncertainty is large enough to account for the poor results (see Section 6.7)

6.6.2 Annual Energy Considerations

This section describes the conditions under which direct normal solar insolation is available for collection by the receiver, based on the test results.

In addition to the receiver's steady-state efficiency, other aspects of receiver performance that impact its ability to collect energy on an annual basis are the ability to operate at low power and the ability to start up and operate under partly cloudy conditions. An analysis of power production for the Solar 1 plant in Barstow [37] identified two related factors that reduce annual energy production. They were the "operating days availability" and "useful insolation availability." "Operating days insolation availability" refers to the fraction of the horizon-to-horizon direct normal insolation available on days when neither winds nor cloudy conditions prevent operation of the plant. "Useful insolation availability" refers to the fraction of the direct normal insolation on operating days that allows collection of useful energy. For 1984, these two factors reduced the output of Solar 1 by 26 percent. Obviously these factors must be included when estimating the annual energy production from a solar receiver.

The Solar 1 analysis does not set criteria for "operating days insolation availability" but, of the two factors contributing to it, cloudy conditions or low insolation is a receiver limitation and high winds are a collector field limitation. The criterion used for "useful insolation availability" is the fraction of insolation above 500 w/m^2. Although a single number limit is convenient, it is an over-simplification of a complex set of receiver start-up and operating limitations.

A discussion of insolation availability must address the following issues:

- Receiver turndown ratio.
- Ability of the receiver to operate at low power, and disposition of the energy collected.
- Ability of the receiver to operate in intermittent clouds.
- Ability of the receiver to start up in partly cloudy conditions.

Turndown Ratio

The turndown ratio of the test receiver was 3.5 to 1 based on a full load flow of 42.3 thousand lbs/h at an absorbed power of 4.5 MW_{th} and a minimum controllable flow rate of 12.0 thousand lbs/h. Rated outlet temperature (1050°F) could be achieved with absorbed thermal power as low as 1.3 MW. This would correspond to an operation with an insolation of roughly 275 W/m^2 at solar noon, or operation 70 minutes after sunrise (as discussed in Section 6.4) when the insolation would be approximately 800 W/m^2, but cosine, shading and blocking effects in the collector field are large.

Low Power Operation

At power levels below 1.3 MW_{th}, (a limitation of the 12 klb/hr flow rate) the test receiver did operate and collect energy. This energy was returned to the molten-salt storage subsystem as salt with a temperature below the rated 1050°F outlet temperature, which is called "warm" salt. This energy, however, was retained within the storage system. The CRTF molten-salt storage subsystem generally accepts salt at temperatures less than 750°F (corresponding to .65 MW absorbed power) into the cold tank, and sends salt

above 750°F into the hot tank. Warm salt returning to the cold tank preheats the cold salt used to feed the receiver. When adequate sun returns, higher receiver flow rates are achieved while maintaining the rated outlet temperature. The increase in flow is proportional to the amount of preheating of the cold salt, and thus the energy collected at salt temperatures below 750°F contributes to useful energy at rated outlet conditions. In order to allow this contribution, however, two limitations of the receiver and the storage system must be met. First the receiver must be capable of the higher flow rate. The test receiver is designed to collect 4.62 MW with an inlet temperature of 590°F (see Section 3.5), and test results confirm that these flow rates can be achieved. The second is a limitation imposed by the thermal storage subsystem. The maximum cold storage tank temperature is 600°F at the CRTF. If operation below .65 MW occurs for a long enough period, this temperature will be reached, and the receiver will have to be shut down.

Operation at power levels between .65 MW and 1.3 MW (minimum flow constraints) results in receiver salt outlet temperatures between 750°F and 1050°F. This salt is returned to the hot tank. Mixing warm salt into the hot tank reduces the temperature of the hot salt stored in it. In a steam Rankine electric power plant, this would affect the steam generation subsystem and the eventual production of electricity. Normally, the steam generator's outlet temperature would be reduced. The net result depends upon the minimum allowable turbine steam inlet temperature and the turbine efficiency as a function of inlet temperature and steam flow rate.

At some minimum power level, the energy collected will not be sufficient to balance the additional power consumed by the receiver's operation relative to stand-by conditions. This power level depends on the system's electric conversion efficiencies, which are beyond the scope of this study. Some insight is gained based on the operating conditions of the test. The test receiver consumes approximately 170 kW more electricity when operating than in a standby mode (see Table 6-XI). Assuming a 30 percent power conversion efficiency, operating the receiver with thermal power below 565 kW is not justified.

TABLE 6-XI
RECEIVER PARASITICS

	Operating	Stand-by
Molten-Salt Pumps	144 kW	--
Trace Heat		
Riser/Downcomer	17 kW	30 kW
Receiver	15 kW	35 kW
Collector Field and Controls	52 kW	--
Totals	228 kW	65 kW

Operation with Intermittent Clouds

Operation with intermittent clouds has all the issues and difficulties of low-power operation, plus a number of new issues relating to the receiver's response to transient conditions. Transient conditions require the control system to act, attempting to maintain outlet temperature without overshoot, and to some extent minimize thermal/structural concerns. The receiver demonstrated a good ability to collect energy while operating on several days with actual clouds. A typical day is presented in Figures 6.6.3 thru 6.6.9.

FIGURE 6.6.3

DIRECT NORMAL SOLAR INSOLATION

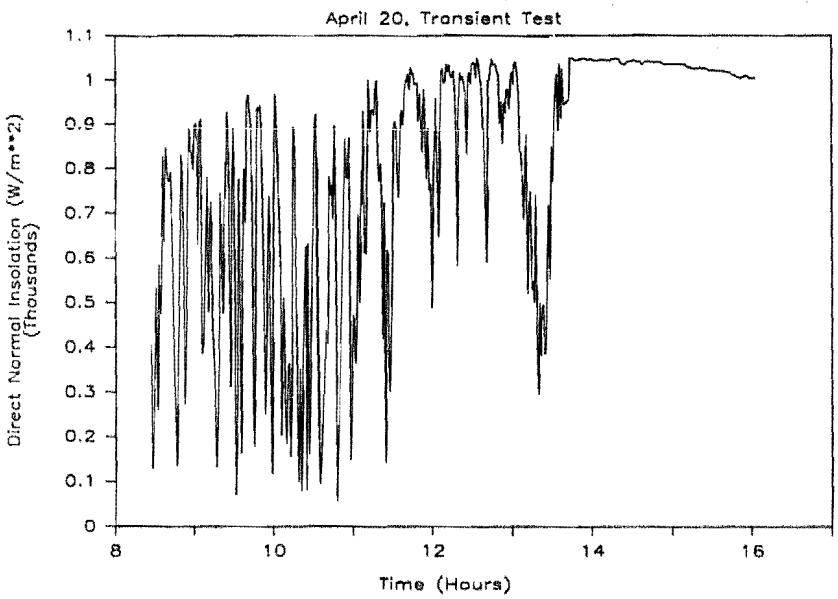

FIGURE 6.6.4

20-MINUTE AVERAGE DIRECT NORMAL INSOLATION

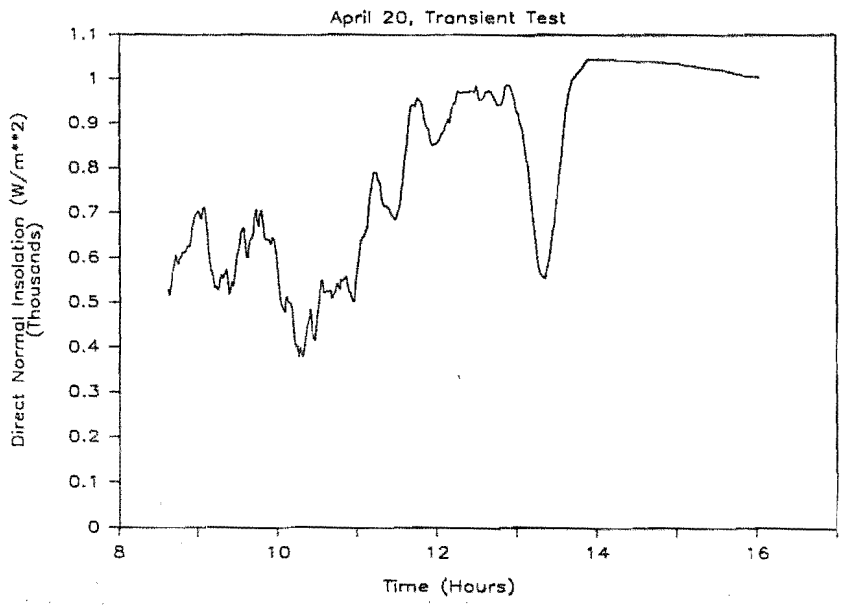

FIGURE 6.6.5
RECEIVER POWER

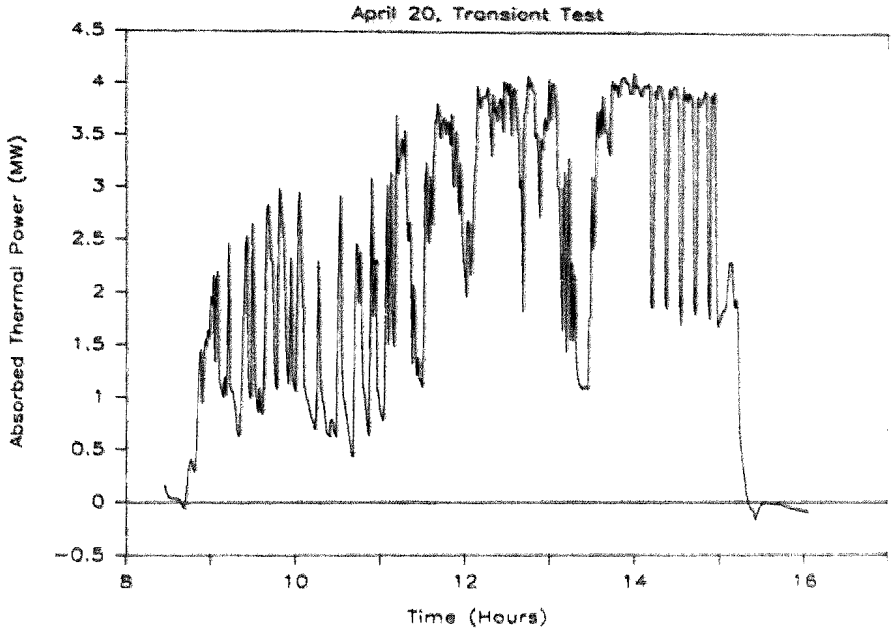

FIGURE 6.6.6
20-MINUTE AVERAGE RECEIVER POWER

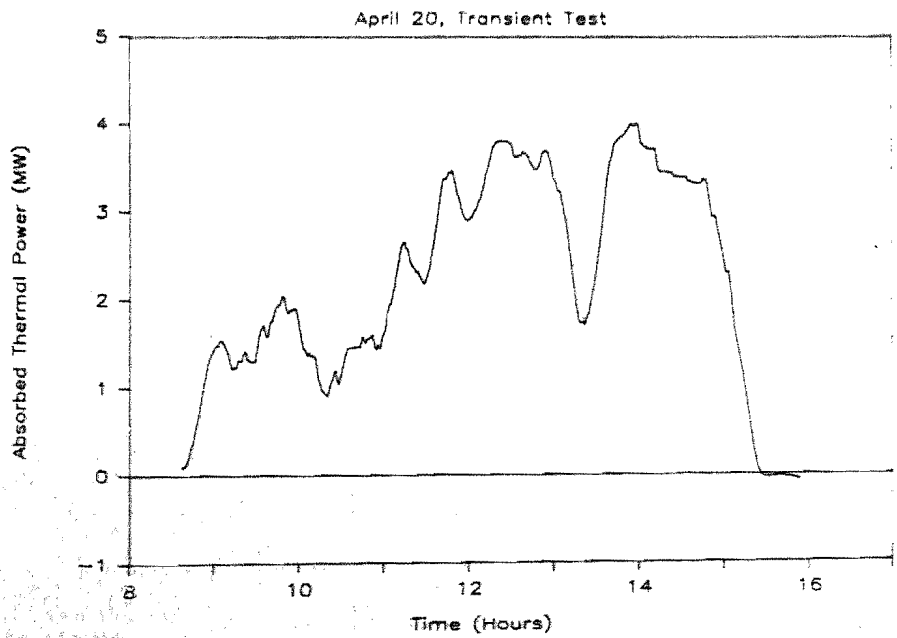

FIGURE 6.6.7

RECEIVER INLET AND OUTLET TEMPERATURES

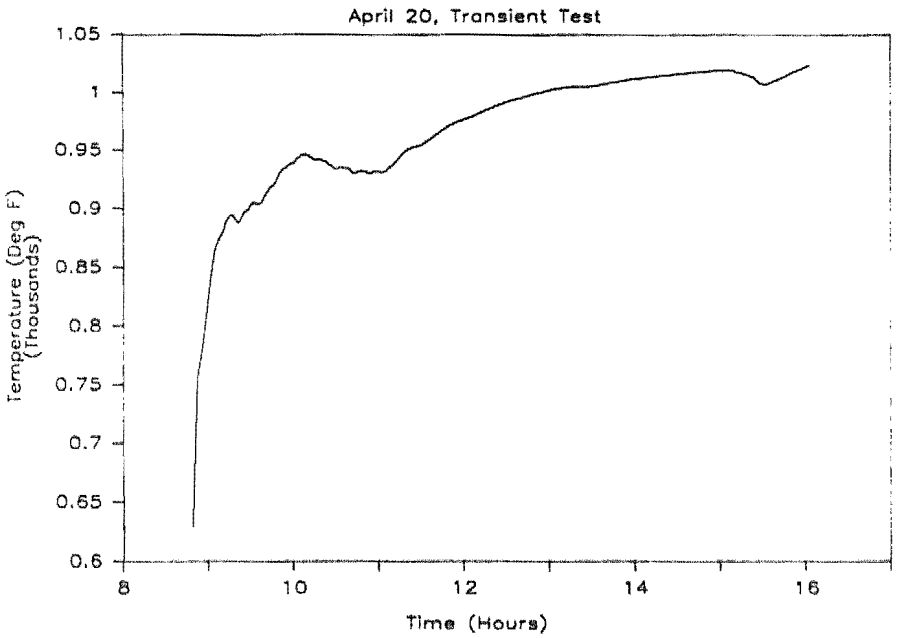

FIGURE 6.6.8

BULK AVERAGE SALT TEMPERATURE FOR THE HOT TANK

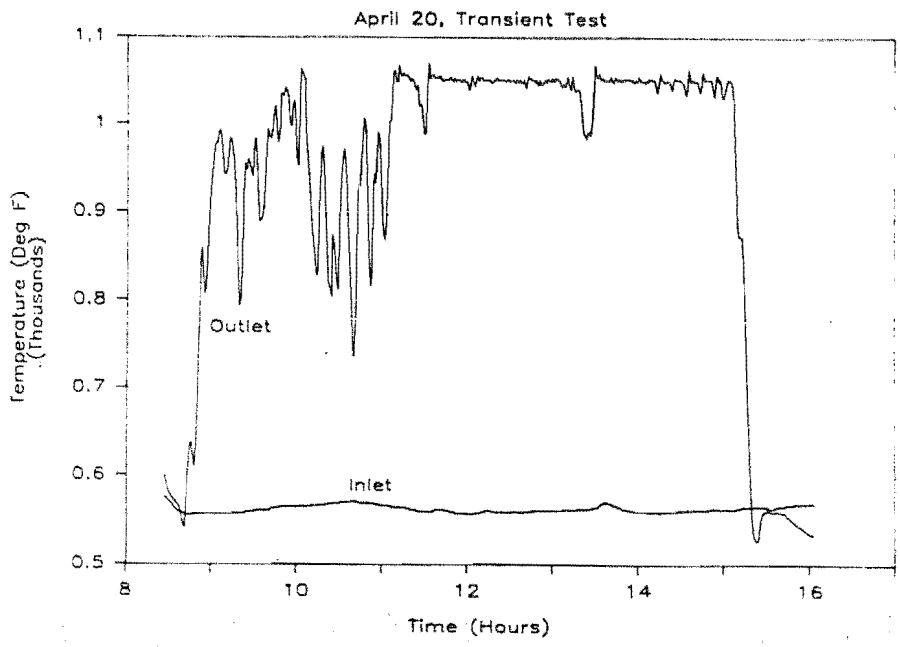

FIGURE 6.6.9

TOTAL ENERGY COLLECTION

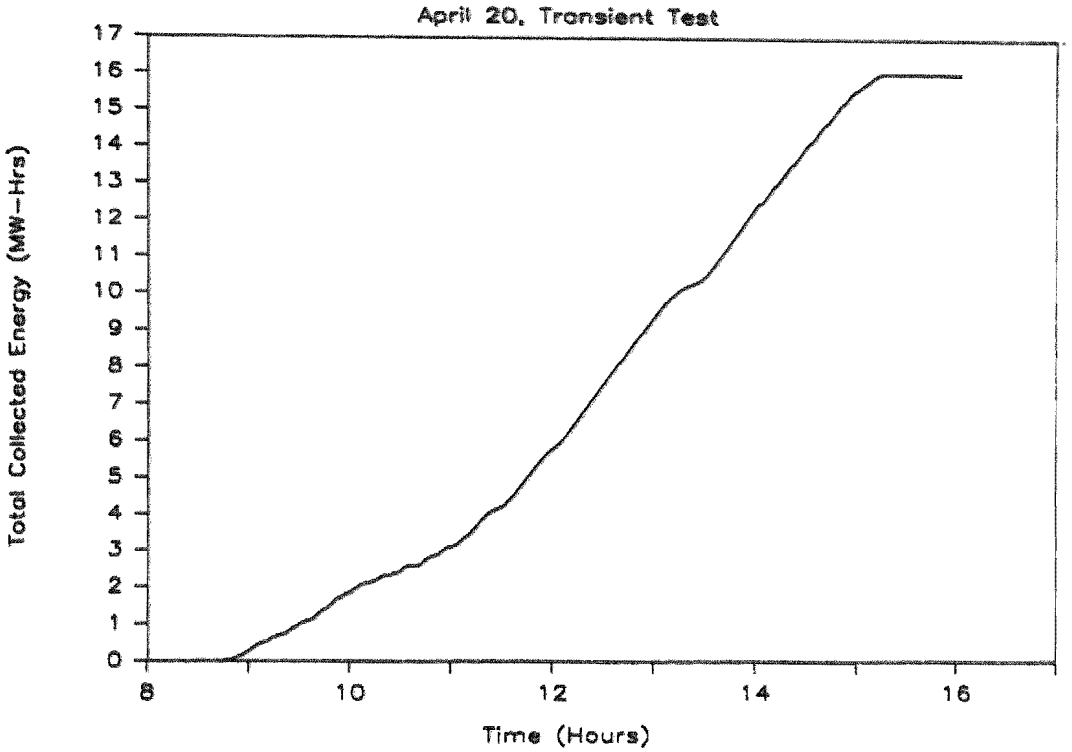

Figure 6.6.3 shows solar insolation for April 20, 1987. Intermittent cloudy conditions prevailed until approximately 2 p.m. when the clouds cleared. The 20-minute average insolation is illustrated in Figure 6.6.4. Until noon, the average insolation was approximately 500 W/m^2. At noon, clouds became less frequent, and the 20-minute average insolation rose to about 900 W/m^2. Around 1 p.m., a large, thin cloud passed over, and after that, conditions cleared. Receiver power is shown in Figure 6.6.5, and 20-minute average power is shown in Figure 6.6.6. The receiver achieved an average power of about 1.5 MW until noon, then exceeded 3.5 MW when conditions improved. After 2 p.m., when clear conditions prevailed, simulated cloud transients were performed, resulting in the power spikes illustrated in Figure 6.6.5.

The receiver outlet temperatures are shown in Figure 6.6.7. During the worst of the clouds, the outlet temperature varied quite a bit, but after 10 a.m., the temperature was approximately 950°F, and by 1 p.m., it was above 1000°F, as shown in Figure 6.6.8. The total energy collected until 3 p.m. was approximately 11 MW_{th}, as shown in Figure 6.6.9.

The ability to operate in such poor solar conditions and collect useful energy is a major advantage of molten-salt receivers. Although the outlet temperature was degraded somewhat, 1000°F salt should be sufficient to operate a normal power plant with only slightly reduced efficiency.

Receiver Start-up

Rapid, early morning start-up is important to take full advantage of available solar energy. The receiver demonstrated two modes of start-up; one, used solar energy from the collector field to heat the panels, the other used either the electric cavity heaters or overnight circulation to keep the cavity warm for immediate sunrise start-up. Both capabilities are discussed in Section 6.4.4. Solar heating of the panel delayed start-up by approximately 40 minutes while the panel was heated, salt flow initiated, and the full field brought on target. The additional energy collected, however, was small (187 kW-h) because the power availability near sunrise is small. When the additional parasitics of operating the pumps and collector field are factored in start-up earlier than 40 minutes past sunrise is not justified. In cloudy conditions, however, the cavity heaters (or alternatively overnight circulation) demonstrated a significant advantage.

The test receiver was capable of starting under any conditions by using the cavity heaters with the cavity doors closed. This allowed the panel to be heated to 550°F and then filled and salt flow initiated. In addition to allowing the receiver to start at sunrise, it allowed start-up during partly cloudy conditions. If start-up were restricted to solar warm-up of the panel, 15 minutes of clear conditions would be required to heat the panel before filling it. On a cloudy day such as the one that occurred for the

April 20 transient test, start-up would likely have been delayed until 11 a.m. at the earliest, with a resulting loss of approximately 3 MW_{th} of solar energy.

Summary of Annual Energy Prediction

The properties of the receiver that must be defined to allow prediction of its capability to collect solar energy on an annual basis are:

1) Thermal efficiency as a function of absorbed power;
2) Definition of its start-up limitations; and
3) Definition of specific limitations regarding low power or cloudy condition operation.

The test receiver demonstrated an average daily efficiency of 88.1 percent for 9 hours of operation. Start-up using cavity heaters (or overnight circulation) was not limited at all by weather conditions. When the collector field was used for start-up, at least 15 minutes of cloud-free conditions was required to allow heat-up of the panel prior to start-up. Low power operation was limited only by the fact that below an absorbed power of 1.3 MW_{th}, the outlet temperature is degraded because of salt flow limitations. Generally, operation below about 600 kW did not provide sufficient energy to offset the additional parasitics consumed by operation for the test receiver. For most applications, however, the energy collected at degraded salt temperatures would still be usable. The receiver demonstrated the capability to operate in most cloudy conditions, making use of the solar energy between clouds.

No attempt is made here to give an actual annual energy estimate. A system designer should base such an estimate on typical weather data for a given site, making certain that cloudy conditions are well characterized so they can be compared to specific receiver limitations. This is necessary to develop accurate predictions. For the molten-salt cavity receiver, these limitations are fairly small, especially if the cavity is heated which eliminates weather effects upon start-up. The limitations imposed by solar start-up, however, can be quite significant, as shown by the April 21

transient test data. For an unheated receiver (including exposed molten-salt receivers) weather data must be evaluated carefully to segregate the "available" direct normal insolation from the total integrated annual energy. This available insolation would be the portion occurring only after conditions for start-up are met.

6.7 Uncertainty of Measurements

With any measurement, there is some degree of uncertainty associated with the actual measured numerical value. The quantification of uncertainty for certain measurements is useful in evaluating and determining the relative confidence in performance calculations. It is this confidence that determines how well we know actual performance.

The term "measurement uncertainty" implies a statistical approach to quantification. Quantifying measurement uncertainty requires a method of characterizing measurement errors that is not overly restrictive and less arbitrary than simply stating some plus-and-minus number. Characterizing measurement errors statistically is a rigorous approach and leads to a defendable result. In general, measurement uncertainty deals with quantifying the different errors into biases and deviations (precision index), properly combining these errors, and establishing the total uncertainty of the measurement. Accordingly, this approach requires an understanding of both statistics and the specific measurement process.

The primary performance calculation used for the receiver is the basic heat balance equation:

$$Q = C_p \text{ (Delta T) (Mass Flow Rate)}$$

POWER = (Heat Capacity Coef.) (Temp. Difference) (Salt Flow Rate).

The measurements of salt flow rate through the receiver and the temperature difference (Delta T) across the receiver are two very important parameters for calculations of the receiver's performance. Therefore, the uncertainty

of these measurements was determined for each of the two receiver control zones.

6.7.1 Salt Flow Rate

A detailed analysis of the uncertainty in measuring the salt flow rate was performed. The measurement process for flow rate was complicated by unreliable flowmeters. Consequently, the flow rate through the receiver was correlated to the inlet pressure measurement of the panels as a means of providing a reliable measure. All errors for this measurement process were quantified, and a total uncertainty was established. This uncertainty was determined to be approximately ± 3,000 lbs/h.

The detailed analysis that produced this result is provided in Appendix I.

The correlation of receiver flow rate with inlet pressure was accomplished in two steps. First, a "sump depletion" experiment was conducted to measure receiver flow rate in a single zone by closing the inlet valve to the other zone, closing the inlet valve to the cold-salt pump sump and observing the sump level as a function of time. Since all salt leaving the cold pump sump passed through the receiver, and the diameter of the sump was known, salt flow for each zone could be calculated. Figure 6.7.1 illustrates the correlation of sump level with time for a single test. During the test, inlet pressure for the zone was also recorded. This experiment was repeated for several flow rates for each receiver zone. Using these data points, a fifth order curve was derived using a least square method to correlate flow rate with inlet pressure. These curve fits are shown in Figures 6.7.2 and 6.7.3 for the east and west receiver control zones respectively.

FIGURE 6.7.1

COLD-SALT PUMP "SUMP DEPLETION" DATA

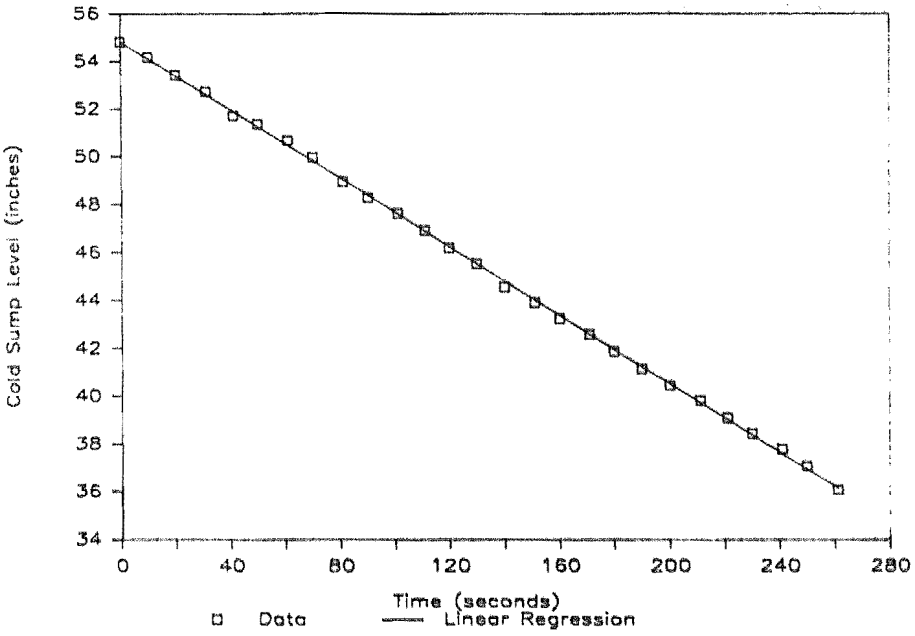

FIGURE 6.7.2

FLOW CORRELATION WITH PRESSURE -- EAST ZONE

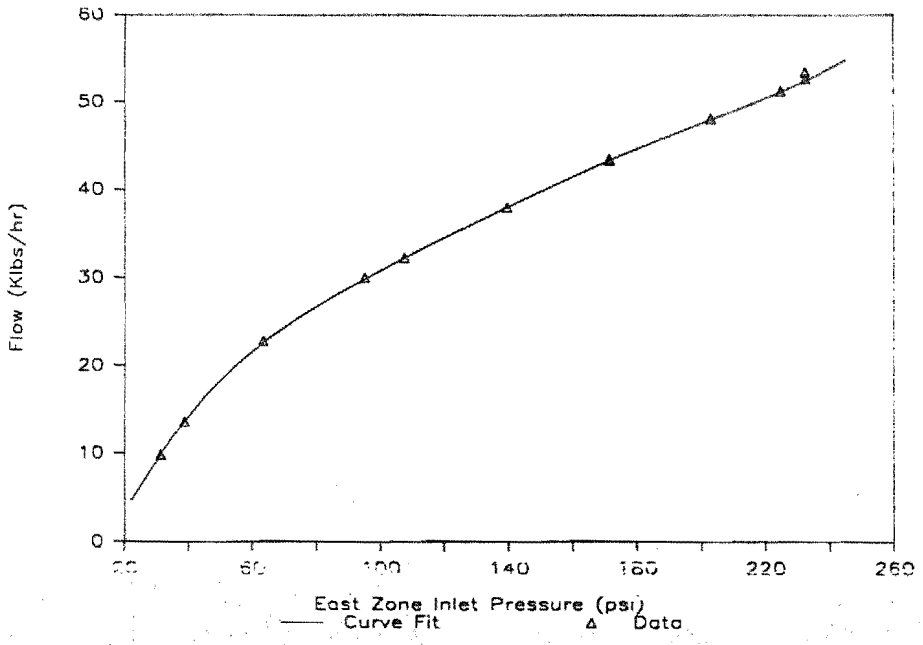

FIGURE 6.7.3

FLOW CORRELATION WITH PRESSURE -- WEST ZONE

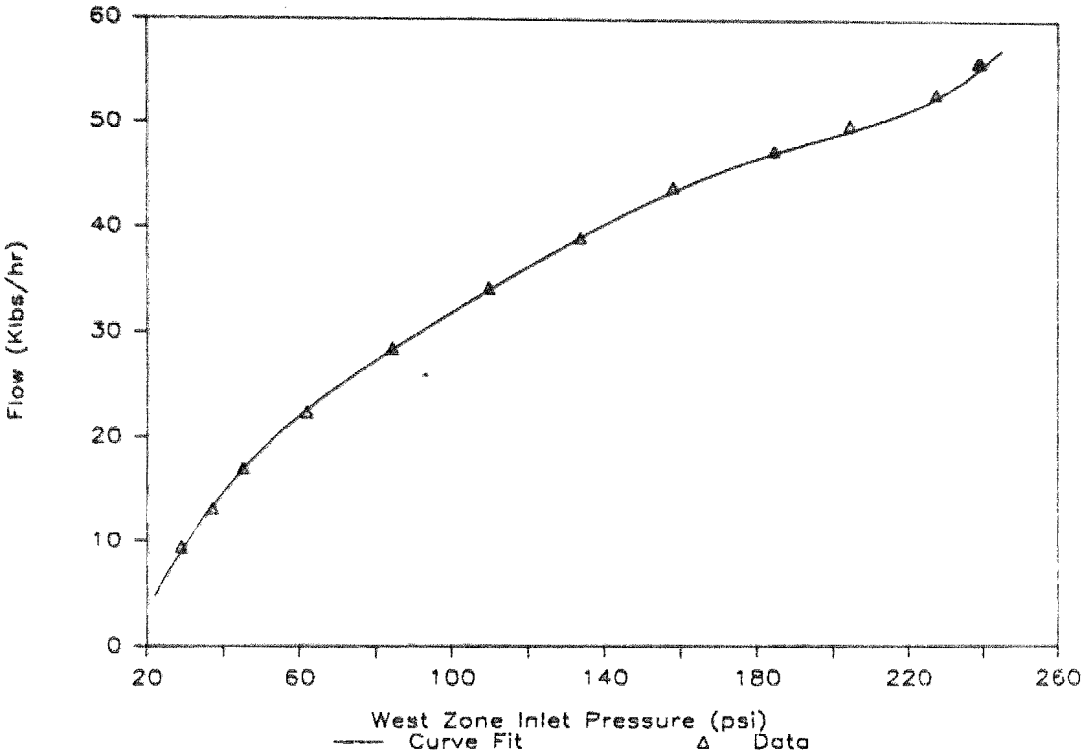

Second, because flow to one zone had to be stopped to allow flow in the other zone to be measured, the experiments to establish flow in individual zones were conducted with no heat flux on the receiver. It was known, however, that salt properties change with temperature. This affects the receiver pressure drop for a given flow rate. To correct for this, a second set of "sump depletion" tests was conducted with the receiver outlet temperature at rated conditions. For these tests, a portion of the collector field was focused on the receiver and the controls were allowed to establish the proper flow rate to achieve a 1050°F outlet temperature.

These tests were conducted near solar noon and with symmetric collector field arrangements so that nearly equal flow was established in each control zone. Then the inlet valve to the cold-salt pump sump was closed and the level change was observed to allow calculation of actual receiver flow.

This test was conducted several times for a 50 percent, 75 percent and 100 percent collector field. For each test, total "indicated" receiver flow was calculated based on the fifth order curve fit of the cold flow data. The ratio of true hot salt flow to "indicated" flow was then calculated for each point. These values are presented in Figure 6.7.4, along with a theoretical ratio derived from analytical calculations of receiver pressure drop for cold and hot flow conditions.

Several things can be noted from this presentation. First, measured flow rates when in hot flow are significantly greater than those indicated by the cold flow correlations. This is true both for the actual data and in theory. Also, there is a fair amount of scatter in the measured data, and generally no trend, as a function of flow rate, can be discerned to the scatter. The average ratio of true hot flow to indicated flow for all data points was 1.06. For the purposes of data reduction, indicated flow rates were corrected by this ratio.

FIGURE 6.7.4
HOT FLOW CORRECTION FACTOR

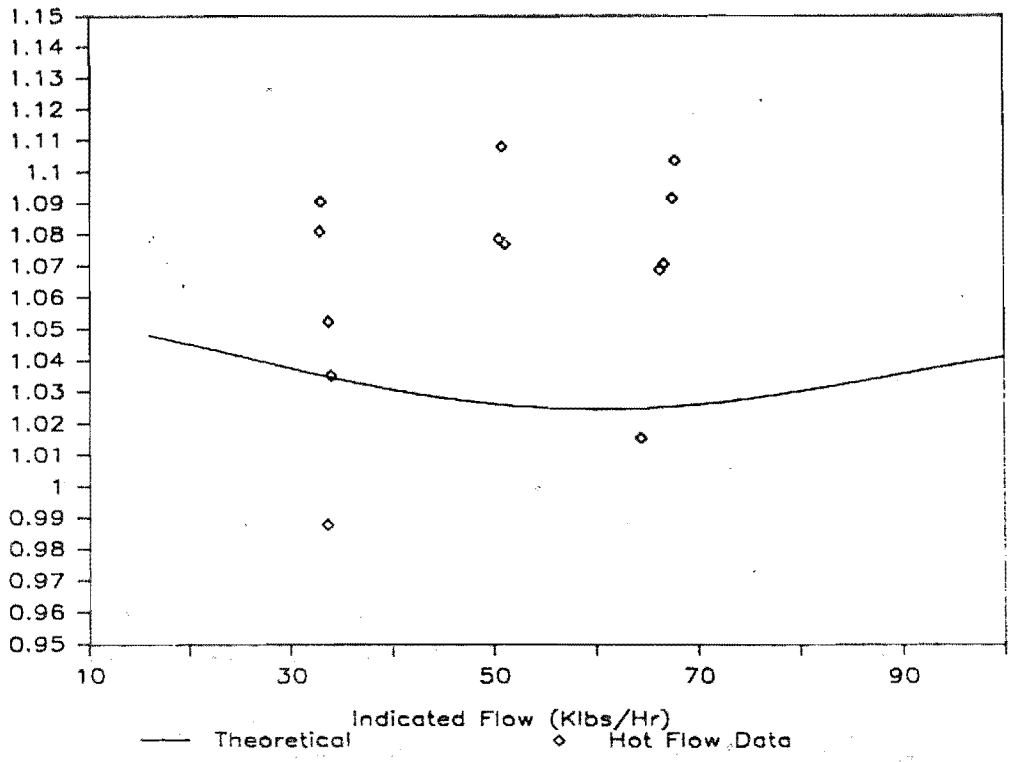

6.7.2 Temperature Measurement

A substantial effort was made to try to determine the uncertainties in measuring temperatures during the receiver testing. Four temperature measurements were critical to its performance evaluation and they were obtained from four Type-K thermocouples located at the salt inlet and outlet positions for each half of the receiver. Even small errors are important particularly during the flux-off loss testing.

Uncertainties in temperature measurement were not limited only to thermocouple errors. Errors were also induced by the NET-90 process control and data acquisition systems. Therefore, total uncertainties in measurement included errors associated with these two systems as well. The exact method used to determine the uncertainty in temperature measurement is provided in Appendix I2.

The results of determining uncertainty in temperature measurement were unable totally to account for errors in measurement obtained during operational check-out. For instance, both inlet thermocouples were located at equal distances downstream from the cold surge tank. The salt flow path was identical for each half, and as a result, the temperature drop between the cold surge tank and the two inlet thermocouples should have been equal. However, biases determined for each inlet thermocouple did not decrease the temperature difference to within its range of random uncertainty.

For example, Table 6-XII shows the indicated temperatures obtained from each inlet thermocouple on March 25, 1987. Also shown are the resultant actual temperatures determined from the biases established for each thermocouple (see Appendix I, Table 1.).

TABLE 6-XII

THERMOCOUPLE BIAS VALVE

Thermocouple	Indicated Temp (°F)	Bias (°F)	Actual Temp (°F)
TE100	587.8	-3.0	590.8
TE130	584.6	-3.7	588.3

Remember, these biases took into account errors produced by all parts of the system (thermocouples, NET-90 and data acquisition systems). Although the bias-correction decreased the temperature-spread, there remained a 2.5°F difference between each thermocouple. Next, the random uncertainties established for each thermocouple are shown in Table 6-XIII.

TABLE 6-XIII

THERMOCOUPLE UNCERTAINTY

Thermocouple	Actual Temp. (°F)	Random Error (°F)	Uncertainty Range (°F)
TE100	590.8	±0.82	|590.0| - 591.6
TE130	588.3	±0.80	587.5 - |589.1|

Problems also existed with the outlet thermocouples. For example, with the cavity doors closed, thermal losses should have balanced for each side of the receiver. Therefore, if the salt flow rates through each side had been equal, the difference in outlet temperatures should have been small (less than 1°F at flow rates of 52,000 lb/h per side). More important, the temperature drop across each half of the receiver should have been equal in order to balance the thermal losses. Here again, the difference in temperature drop between the two sides exceeded the range of uncertainties established for each thermocouple.

Due to a compressed test schedule, additional time could not be allocated to resolve uncertainties in temperature measurement. Therefore, indicated temperature data were used to generate the performance characteristics for the receiver. Reasonable measurement uncertainties of ±5°F (includes bias and random errors) could be assumed from previous experience; however, this number is not analytically defendable.

We have two recommendations to possibly alleviate the problems described in this section. First, verify that each thermocouple is correctly calibrated and installed in its proper position. This is extremely important for establishing thermocouple biases. Second, for accurate temperature measurement, directly install all thermocouples critical to evaluating receiver performance to a separate data acquisition system. The intent is to eliminate errors associated with the NET-90 process control system.

SECTION 7

RECEIVER DESIGN EVALUATION

D. Smith - Babcock & Wilcox Corp.
G. Carli - Foster Wheeler Corp.
P. Bator - Babcock & Wilcox Corp.

Proper design methods for the receiver will allow larger, scaled up receivers to be built with confidence that they will perform as intended. In this section, the design of the receiver will be evaluated relative to the results of the test. The intent of the design was to address the entire spectrum of conditions that the receiver would be subject to. The objective of testing a small-scale subsystem is not only to confirm the design methods used, but to reveal unanticipated aspects, or combinations of events that were not addressed. By performing such evaluation, design deficiencies can be addressed before larger units are built. As a result, the risk of scaling up to large units can be dramatically reduced.

7.1 Receiver Panel Design

The most critical component of the test receiver is the heat absorption panel. The design of the panel is very solar unique and, as such, it is one of the main subjects of the test. The panels were designed for efficient receiver operation, and for long life. The test results are examined in this section and compared to design conditions to assess how well these objectives were met. The receiver employed two types of panels, one fabricated by the Babcock & Wilcox Company and the other made by Foster Wheeler. The evaluation of each type of panel is addressed in each of the following two subsections.

7.1.1 Evaluation of the B&W Panels

The receiver panel has been evaluated relative to its design in several ways. In some cases, it is possible to determine if the design was proper from the

short term testing that was done. For example, pressure drop is measured and compared to predictions. For other issues, such as fatigue, only indirect evaluation is possible. The test program could not be long enough to assess if the panel met its fatigue life objectives (30 year life), but comparisons of measured flux and predicted flux, and of stresses derived from measurements, and fatigue limits were made to judge indirectly if design objectives were met. The following subsections each address an aspect of the panels performance relative to the design.

Thermal/Hydraulics

The pressure drop through the Foster Wheeler wing panel and the Babcock & Wilcox receiver panels, was computed using the computer program SRPAN4A (Solar Receiver Parameter Analysis, Version 4A). This code calculates the pressure drop through the heated and unheated portions of the receiver tubing as well as the safe ends, headers and inter-connecting pipe as the salt flows from pass to pass. The code takes into account the changes in fluid properties as the salt is heated then sums up the pressure drop from each pass, safe end, header, and inter-connecting pipe. Each pass is divided into nodes of equal length, 1 foot per node for the receiver, and the pressure drop calculated using local salt conditions and tube properties. The properties for the tubing, safe ends, headers, and inter-connecting pipe are listed in Table 3-XI.

The predicted pressure drop is indicated by the solid line in Figure 7.1.1. The actual data for flow and pressure drop was taken using sump depleations during cold flow. The data was taken over a complete range of flows and the resulting pressure drops compared to those predicted by SRPAN4A. The data taken compares favorably with that predicted over the range of flows with the predicted being about 7 percent higher than the actual at flows greater than the design point flow.

FIGURE 7.1.1
RECEIVER PRESSURE LOSS

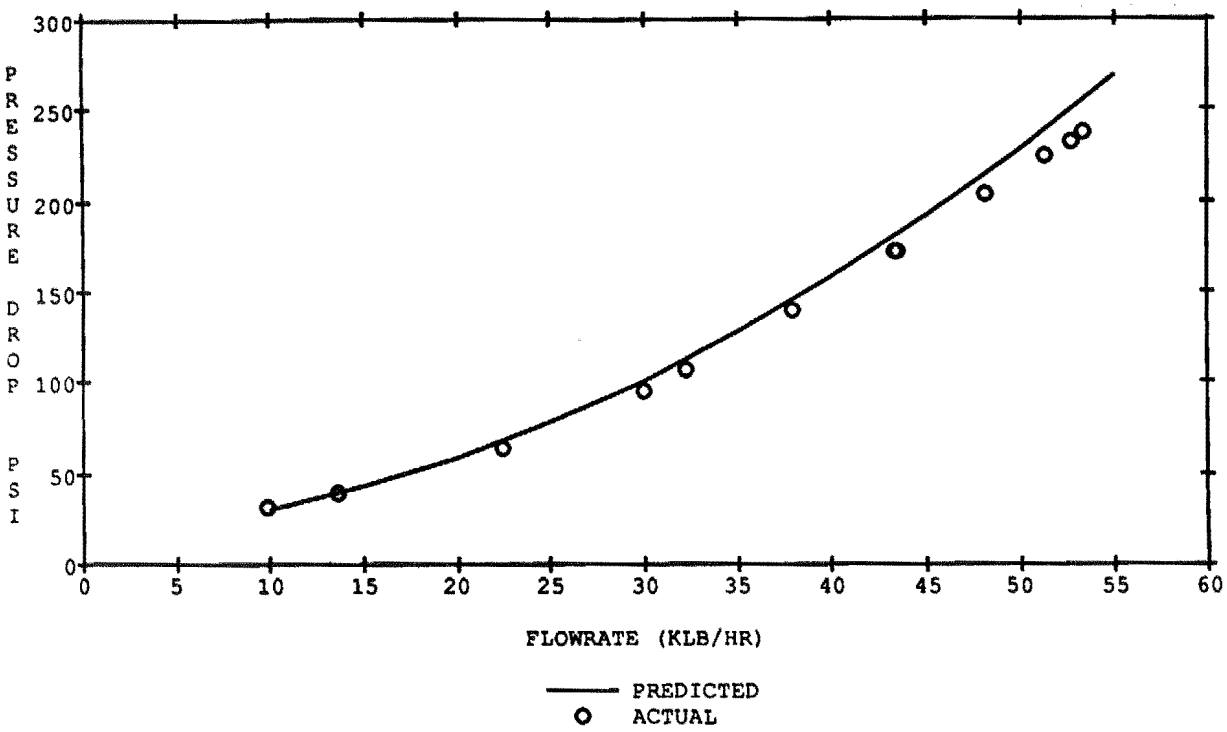

Steady-State Full Load Flux Limits

The sizing of the test receiver is based on the capability of the pane to absorb flux. Section 3.2 of this report discussed the development of these limits based on the fatigue properties of the tube material. During the test, the heat flux on the panel was measured using heat flux gages mounted in the panel. The measured flux is presented in Figure 7.1.2, along with the design flux limit, and the predicted flux limits. The measured values are taken from the solar noon steady-state data points. The values have been normalized to design power conditions by adjusting them by the ratio of design power to measured absorbed power.

FIGURE 7.1.2

HEAT FLUX DATA AND LIMITS

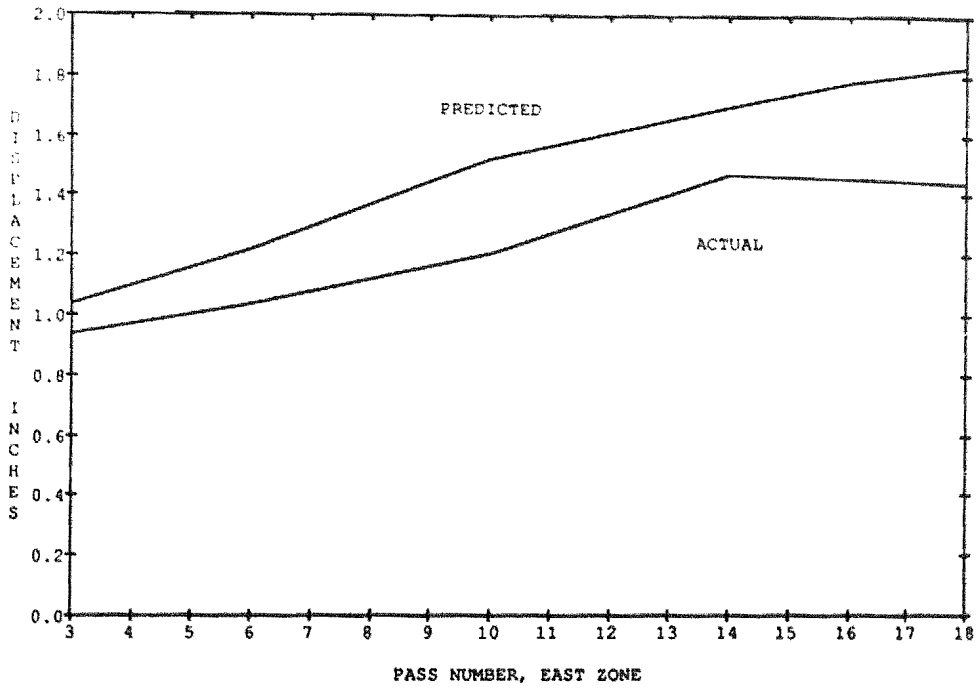

Several things should be noted from this figure. The measured heat flux is in general agreement with predictions but, when examined closely, measured fluxes tend to be higher than predictions in the middle of the receiver and lower toward the edge. Also, several of the measurements exceed the allowable curve. The range of accuracy for the flux gages is estimated to be 15 percent based on drift observed between subsequent gage calibrations. This error band in the measurement allows only the conclusion that the cavity layout generally yields the desired flux levels. The possibility exists that the limits are being exceeded due to the level of uncertainty. Designers of future receivers should bear in mind that programs that predict receiver flux, while generally correct, cannot be confirmed with a high degree of accuracy. For conservative design, some margin must be included between the predicted flux and the limits.

Part Load Thermal Stress

The flux limits introduced in Section 3.2 and discussed in the previous paragraph are based on full load steady-state operation. When operating at lower loads heat flux is lower, but limits are also reduced. This is because salt flow rate is reduced in proportion to the load and the resulting heat transfer coefficient inside the tube is lowered. The tube thermal stress results from both the temperature difference through the tube wall, and the average front wall to back tube wall temperature difference. If the thermal resistances were constant, tube temperature and thermal stress would be proportional to heat flux. Since the heat transfer coefficient is a function of salt flow, tube stress is not reduced in direct proportion to heat flux. The relationship between tube stress and salt flow rate for the particular thermal/hydraulics of the test receiver is illustrated in Figure 7.1.3. For this receiver, tube thermal stress is found to be proportional to flow rate raised to the -.47 power times heat flux. This is of little importance for quasi-steady operation since tube thermal stress nonetheless drops with heat flux, even if it is not directly proportional. The effect becomes important during rapid transients, however, when salt flow varies independently of heat flux.

FIGURE 7.1.3
APPROXIMATE TUBE STRESS CORRELATION

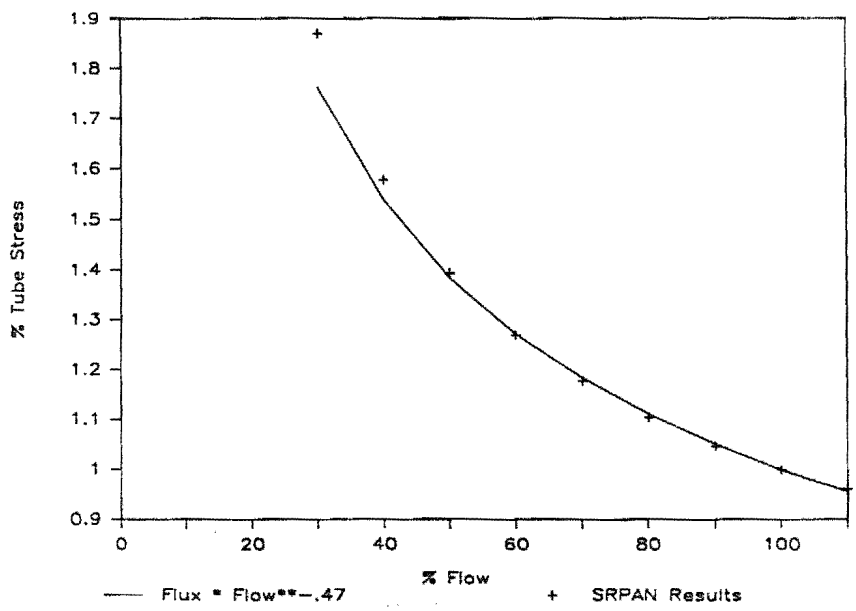

Panel Tube Transient Thermal Stress

During rapid transients, such as those caused by cloud passage, salt flow is controlled in an attempt to maintain the outlet temperature. Often, when outlet temperature has dropped below the set point, salt flow is reduced in a proportion greater than the reduction in heat flux as the control system tries to increase the outlet temperature. If this mis-match between flow and heat flux is large, severe tube stress can occur.

Figure 7.1.4 and 7.1.5 present heat flux, salt flow, and tube stress as a percent of design values for simulated cloud transient tests performed on two occasions. In both cases, the simulated cloud blocked the entire collector field long enough to allow outlet temperature to drop. When the heat flux returned, salt flow remained low for a period, giving outlet temperature a chance to respond. During this period, the tube thermal stress peaked as much as 50 percent above the design value. The impact of this on fatigue life can be serious. For typical conditions, a 50 percent increase in stress (or actually mechanical strain) results in an order of magnitude reduction in fatigue life. A similar situation was also demonstrated during natural cloud transients as shown by Figures 7.1.6 and 7.1.7.

FIGURE 7.1.4
SIMULATED CLOUD TRANSIENT (5/22/87)

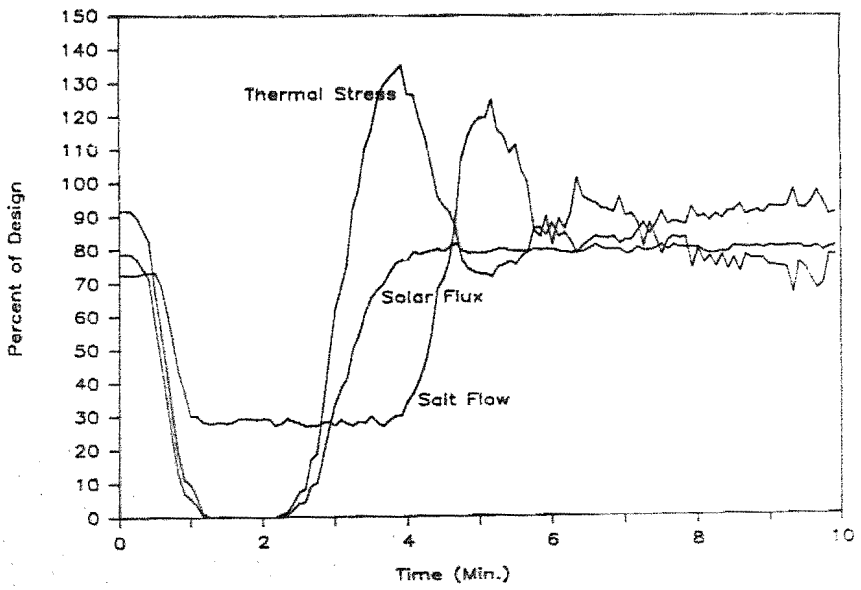

FIGURE 7.1.5

SIMULATED CLOUD TRANSIENT (5/4/87)

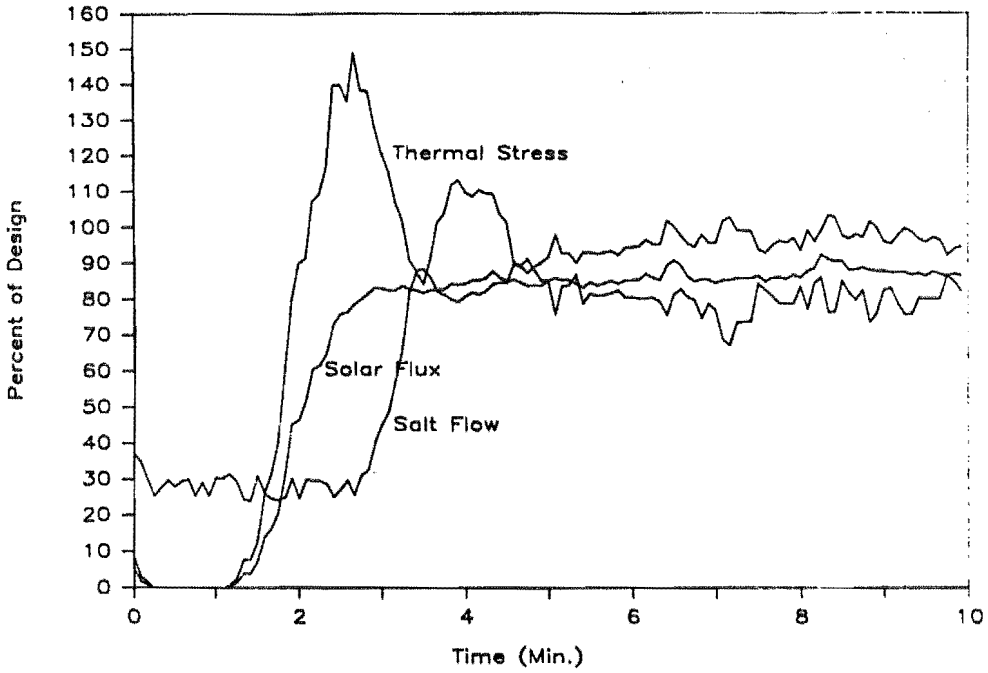

FIGURE 7.1.6

NATURAL CLOUD TRANSIENT (5/14/87)

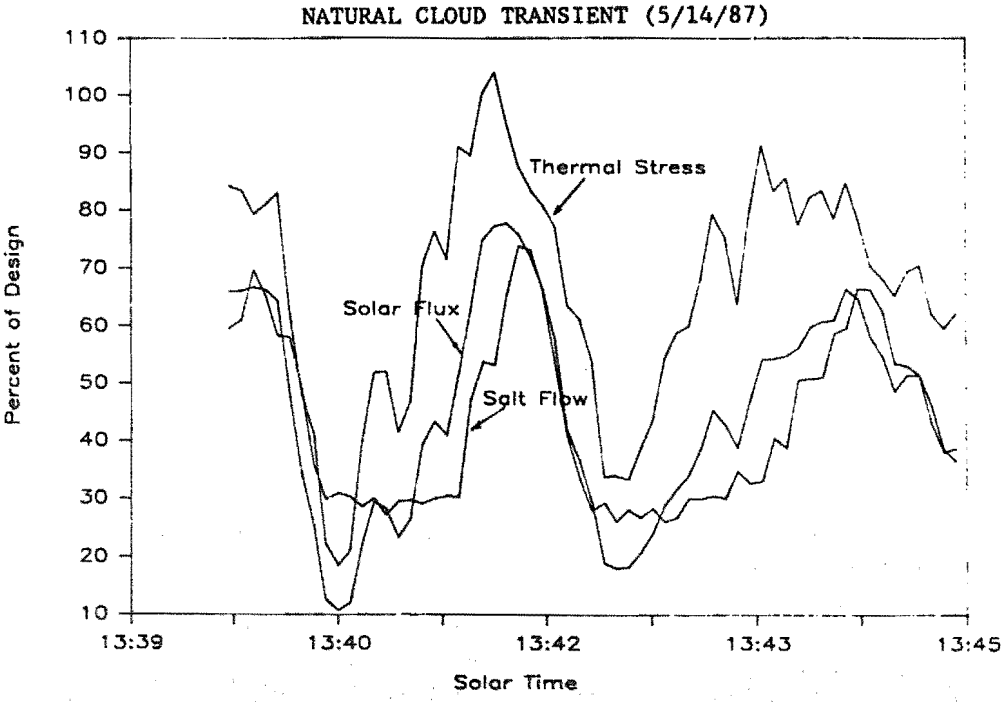

FIGURE 7.1.7
NATURAL CLOUD TRANSIENT (5/14/87)

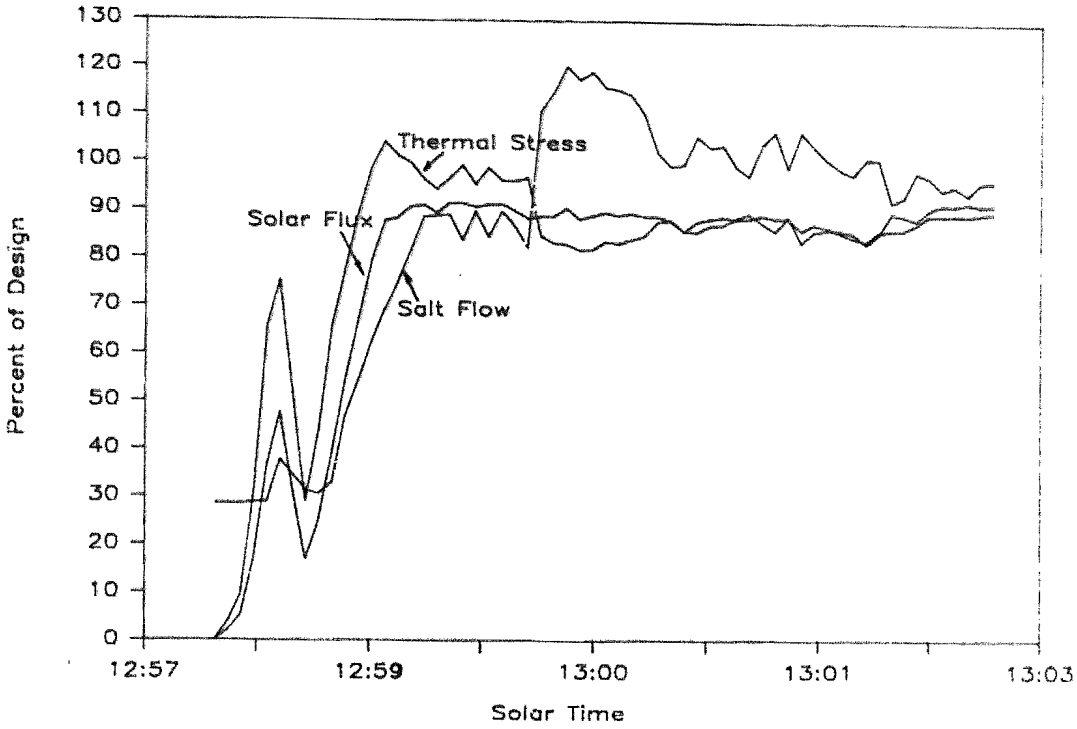

Although the control algorithm does an excellent job of maintaining outlet temperature, it allows large thermal stress cycles to occur. This is because the problem was not recognized during the control algorithm development, and no performance goals based on fatigue were established. For a commercial receiver design, this problem must be addressed by improvements in receiver control, and by including the transient effects when stress limits are set.

Panel Header Transient Thermal Stress

Another quite different thermal stress problem can occur during transients at the panel headers. At each end of the receiver panels, the receiver tubes are welded to thicker walled "safe end" tubes which are in turn welded into the panel headers. This configuration is shown in Figure 7.1.8. A typical safe

end tube to header weld is shown in Figure 7.1.9. This type of weld is called a "J" groove weld. Thermal stresses develop at this location whenever the salt temperature changes significantly, because the tube responds more quickly to changes in temperature than the header. The temperature difference that occurs results in a thermal stress. The magnitude of the stress depends primarily on the temperature ramp rate. Because the largest temperature changes occur at the outlet of the last receiver pass, this is the location of the worst stresses, and because the stress is cyclic, fatigue will eventually occur.

FIGURE 7.1.8
BABCOCK & WILCOX HEADER ARRANGEMENT

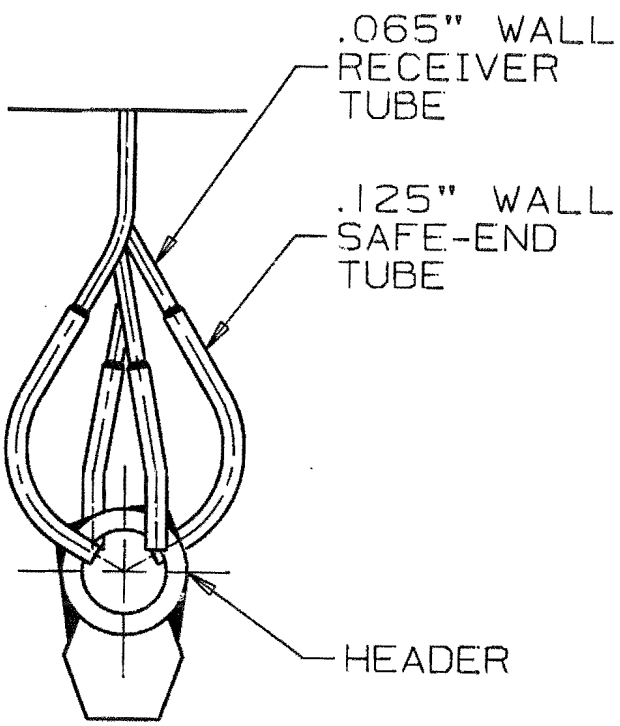

FIGURE 7.1.9

BABCOCK & WILCOX HEADER-TO-SAFE-END TUBE WELD

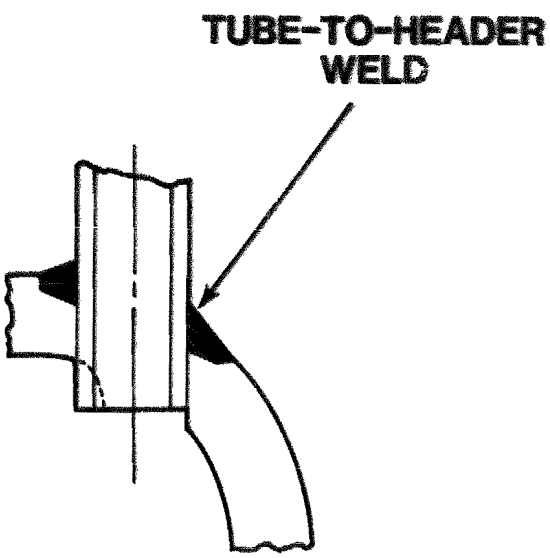

Temperature ramp rate limits were set for this connection based on a simplified stress analysis performed during the design of the receiver. These limits are presented in Table 7-I.

TABLE 7-I

TEMPERATURE RAMP RATE LIMITS

FOR THE BABCOCK & WILCOX PANELS

Normal Operation	0.8°F/sec
Emergency (Few Cycles)	8.0°F/sec

Receiver outlet temperature ramps occur whenever the receiver is started up, shut down, or during clouds if outlet temperature cannot be maintained. During receiver testing, it was found that the normal operation limit was very restrictive and could not be met under some conditions. For start-up, the condition was met by applying power to the receiver gradually. This was accomplished by sequencing the heliostats of the collector field onto target two at a time every six seconds with maximum receiver flow. Once the full

field was on target, the temperature control algorithm was activated and set for 1050°F outlet temperature. The algorithm was modified to limit the outlet temperature set-point ramp rate to 0.75°F/sec to meet this limit. The outlet temperature for a typical start-up is shown in Figure 7.1.10.

FIGURE 7.1.10
START-UP OUTLET TEMPERATURE RAMP (MAY 26)

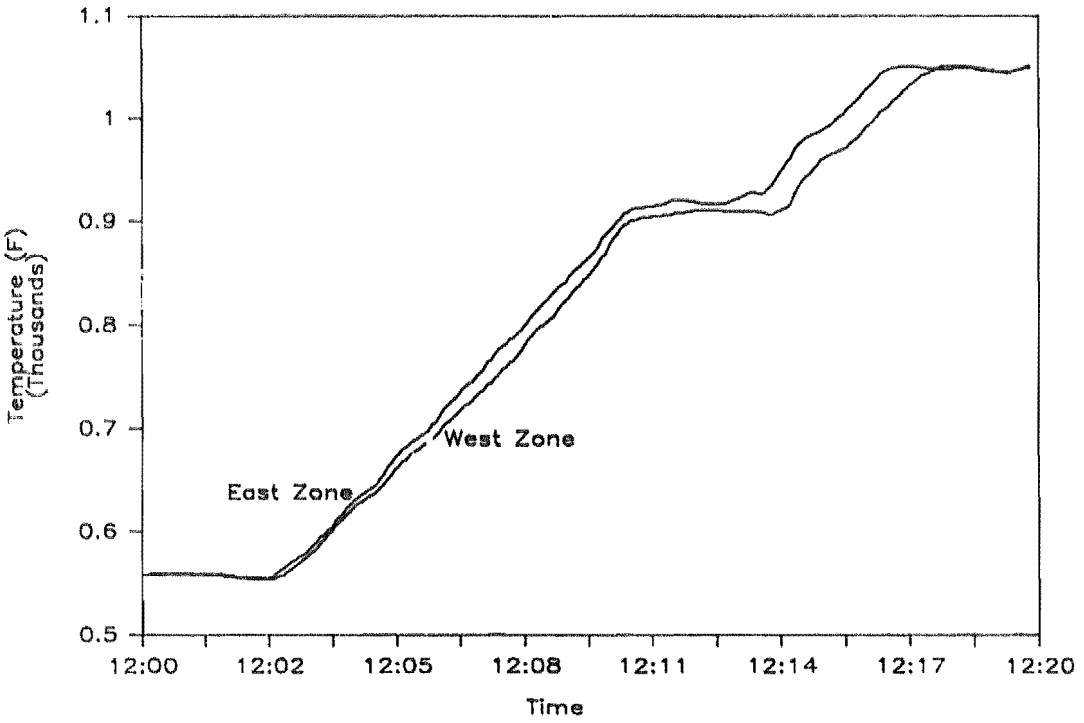

To shut down the receiver, the outlet temperature set-point was first reduced to 750°F. The control algorithm would reduce the outlet temperature to this value, if possible, according to its temperature ramp limit. It was not always possible to achieve this outlet temperature because of the maximum flow limitations of the system. The controls drive the receiver control valves open to increase receiver flow and thus reduce outlet temperature. Once fully open, maximum flow is achieved, resulting in minimum outlet temperature for the given receiver power. Once minimum outlet temperature was achieved (or

750°F), the collector field could be defocused. When receiver power was gone, the controls established minimum flow which resulted in acceptable outlet temperature ramp rates.

Although problems with start-up and shutdown were solved, cloud transients presented another problem. In order to collect maximum solar energy, it was desirable to operate the receiver in automatic mode in all cloud conditions. Large, rapidly moving clouds presented problems. If a cloud covered the collector field for approximately five minutes, the outlet temperature of the receiver would decay to match the inlet with the receiver at minimum receiver flow. This would present a ramp rate larger than desirable. When the sun returned, however, the situation was worse. With full flux, the receiver controls demand full flow, but the temperature ramp up is severe. The outlet temperature goes from inlet temperature to the minimum set-point temperature (as provided by the sliding set-point) in the time it takes for flow to traverse the receiver panel. This results in ramp rates as high as 6°F per second. Figure 7.1.11 illustrates such cloud induced temperature ramps.

FIGURE 7.1.11
OUTLET TEMPERATURE RAMP (MAY 14)

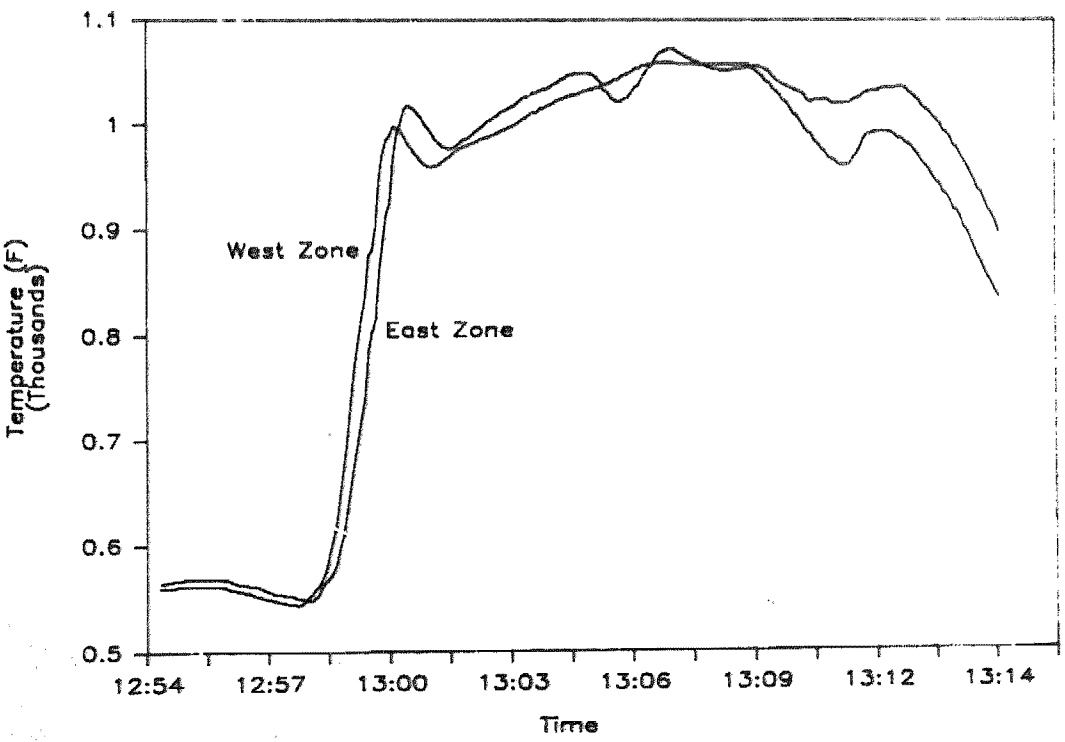

The power ramp up when a cloud cover clears the collector field is simply too large to accommodate mild temperature ramps. Significant solar energy is available in clouds, however, as discussed in Section 6.7. Fortunately, better alternatives to the "J" groove weld exist. These alternatives can significantly improve the thermal fatigue resistance of the tube-to-header joint. In the next generation of receiver designs, this issue should be addressed up-front in the design stage, and more transient tolerant designs used.

Panel Thermal Expansion

The Babcock & Wilcox receiver panels were instrumented with linear displacement transducers to monitor panel thermal expansion throughout the test. The six transducers were connected between the receiver structure and the bottom of the receiver pass to measure thermal expansion of the receiver panel.

The average tube temperatures were used to predict the panel expansion. The maximum predicted thermal expansion for any given panel is 46 mm (1 13/16 in.) at 1050°F. Figure 7.1.12 shows the thermal expansion of passes 3 through 18 with the receiver operating at an outlet temperature of 1050°F. The displacement of each pass is less than that predicted during the design of the receiver thermal expansion system.

FIGURE 7.1.12
EAST ZONE THERMAL EXPANSION

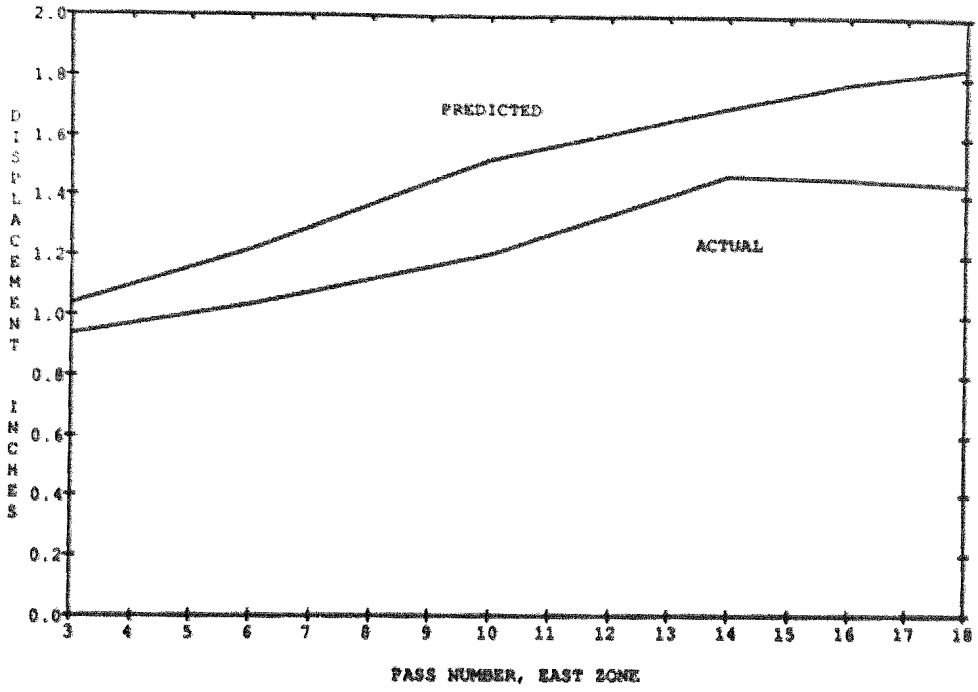

7.1.2 Evaluation of the Foster Wheeler Panel

Instrumentation

Figure 7.1.13 shows the approximate location of the main instruments of FW Panel 3W. Since passes 9 and 14 were the most critical (see Section 3.2), they were heavily instrumented with thermocouples (TE), flux gages (FG), strain gages (SG), and displacement transducers (ZPD). Instruments that have their symbols "filled" (Figure 7.1.13) were connected to the Bailey NET-90 control system, and their data were available on tape or diskettes through the data acquisition system (DAS). The others were connected to a strip-chart recorder. Not shown are thermocouples connected to the Acurex System, which were only available through computer print-outs and were not recorded because of problems with the DAS.

FIGURE 7.1.13

PANEL 3W INSTRUMENTATION

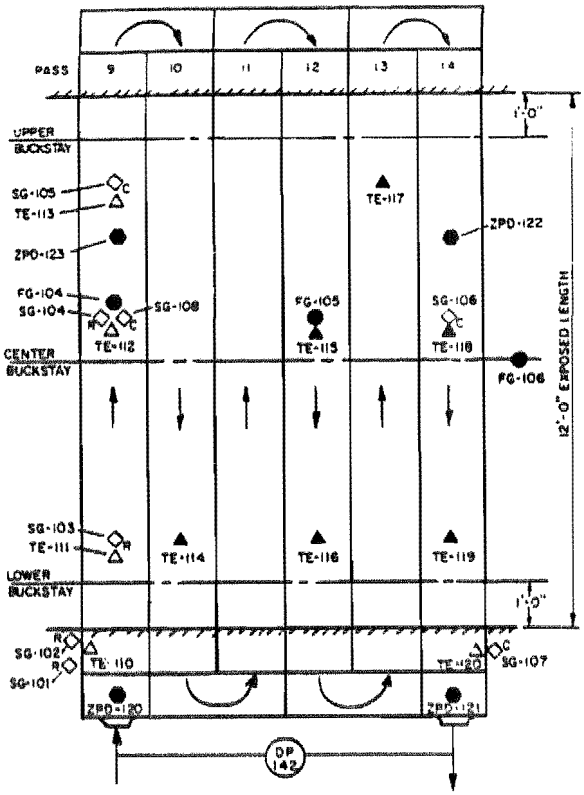

Pressure Drop

The pressure drop through the FW panels (including tube entrance and exit losses and the unheated inlet and outlet jumper tubes--the bent portion of the tubes used to connect the panel tubes with the headers) was computed by the computer program SOLAR.TH, using the Darcy-Weisbach formula with friction factors from the Colebrook equation [38].

Because of the temperature dependence of salt properties, SOLAR.TH computed the pressure drop through the panel in 0.3-m (1-ft) elements along the flow path, using local salt conditions. The sum of the individual pressure drops gave the total pressure drop for the pass. Inlet and outlet header losses were calculated according to FW design standards.

The predicted pressure drop is shown as a solid line in Figures 7.1.14 and 7.1.15. The plots span the entire range of tested salt flow-rates--from 10 to 125 percent of design flow-rate. In both cases the agreement between predicted and measured pressure drop is excellent.

FIGURE 7.1.14
PANEL 3W PRESSURE DROP (3/23)

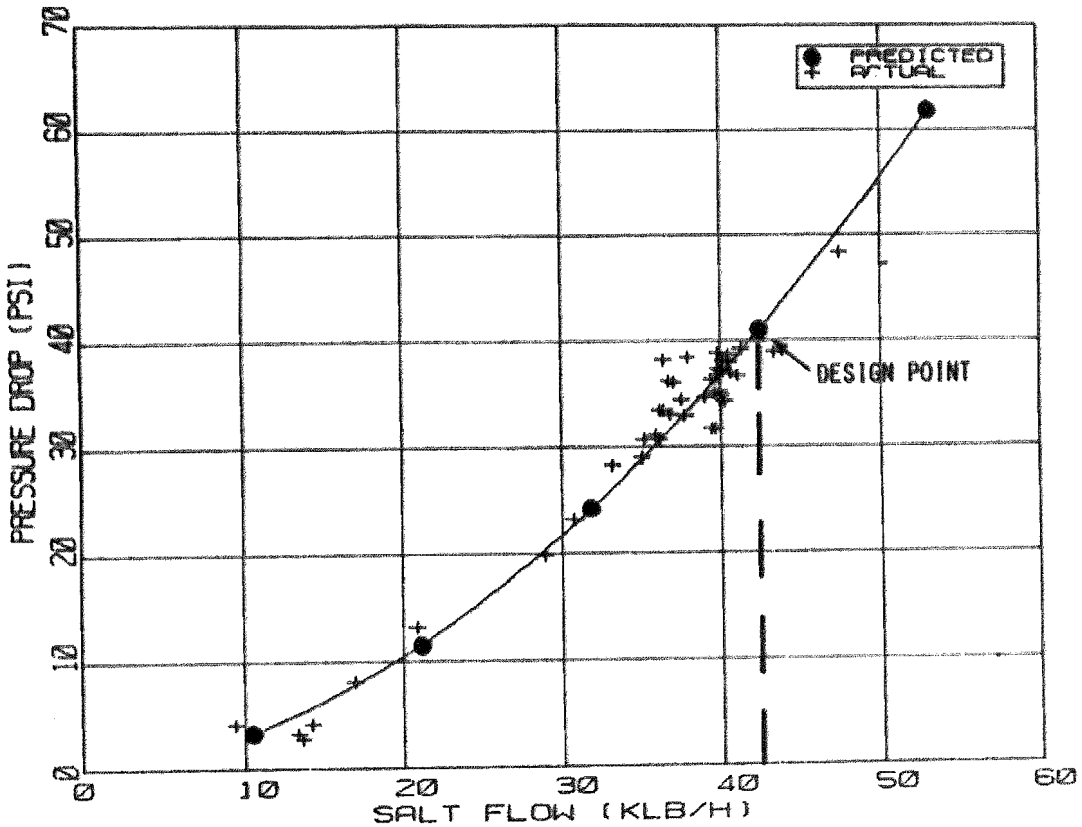

FIGURE 7.1.15
PANEL 3W PRESSURE DROP (4/28)

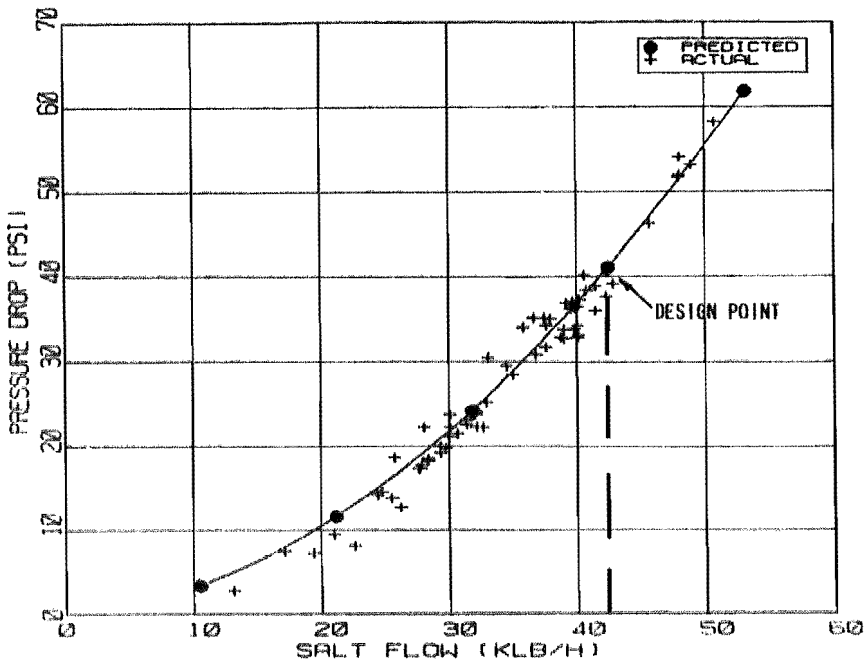

Thermal Expansion

Foster Wheeler cavity Panel 3W was equipped with four linear motion transducers. Two (ZPD120 and ZPD121) were connected between the receiver structure (fixed end) and the bottom header to measure the panel's thermal expansion (growth) in the vertical direction. The other two (ZPD122 and ZPD123) were connected between the receiver structure (fixed end) and Tubes 3 and 33 (at a mid-point between the upper and middle support linkages) to measure the movement of those tubes in the forward or backward (north/south) direction.

SOLAR.TH calculated the average tube-wall temperature at each nodal point, using an equation that takes into account the nonuniform heat flux distribution [4]. The average tube-wall temperatures were used in the program to predict the vertical thermal expansion of the panel. At design point

conditions, panel expansion ranges from 31 mm (1.21 inches) in pass 9 to 33 mm (1.32 inches) in pass 14. The vertical thermal expansion when the receiver was in hot standby (no flux) at 288°C (550°F) was predicted to be 15 mm (0.60 inches).

Figure 7.1.16 compares the predicted and measured vertical thermal expansion of the panel. The two upper lines in this Figure represent the vertical expansion of the panel when the receiver was operating at 299°C (570°F) in a recirculation mode with no incident solar flux (before 9:00 a.m. on April 28). As expected, the lines are horizontal, since both ends of the header moved the same amount (the panel was at a uniform 299°C [570°F]), thus thermal expansion was equal on both sides of the panel. The two lower lines in Figure 7.1.16 represent the thermal expansion of the panel (movement of the lower header) between 9:45 and 10:30 a.m. on April 28 when the receiver was operating under steady-state conditions with the outlet salt temperature at about 556°C (1050°F). As expected, the lines are tilted, since the right (outlet) side of the panel (pass 14) was hotter and expanded more. Predicted thermal expansion was slightly higher than that measured (somewhat conservative).

FIGURE 7.1.16
PANEL 3W STEADY-STATE THERMAL EXPANSION (4/28)

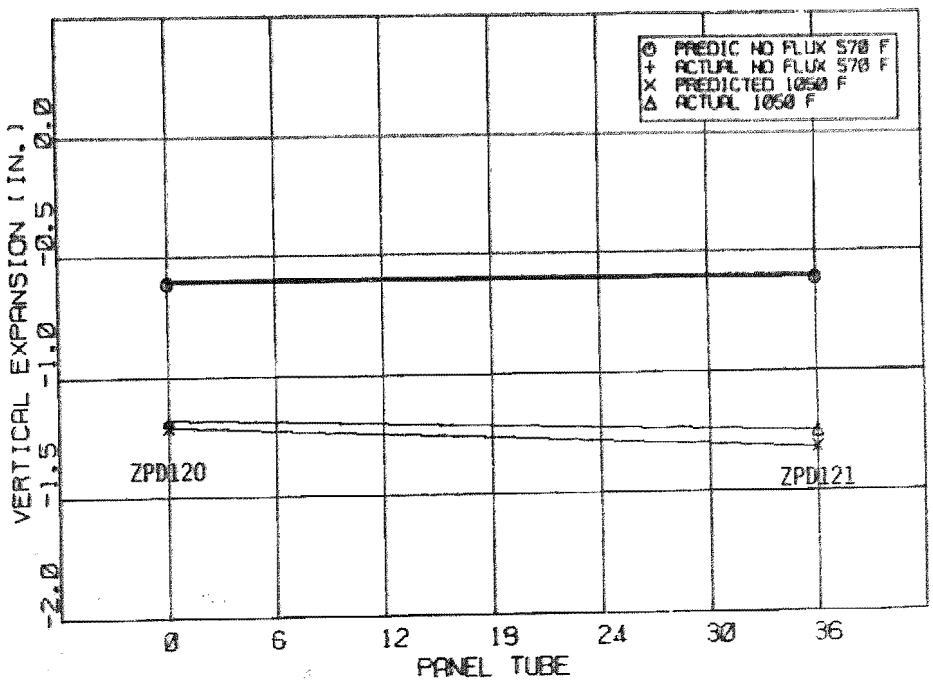

Figure 7.1.17 represents the thermal expansion of the panel (movement of the lower header) during the test conducted on the morning of April 28, when the receiver was operating during a heating period, followed by steady-state operation and by a cloud transient operation. Vertical thermal expansion of the panel followed closely the incident solar flux and outlet salt temperature. A comparison between the salt outlet temperature data and the thermal expansion data indicates that there is about a 2-minute lag between the two (i.e., it took about 2 minutes after the panel reached a steady-state temperature for it to stop growing).

FIGURE 7.1.17
PANEL 3W THERMAL EXPANSION

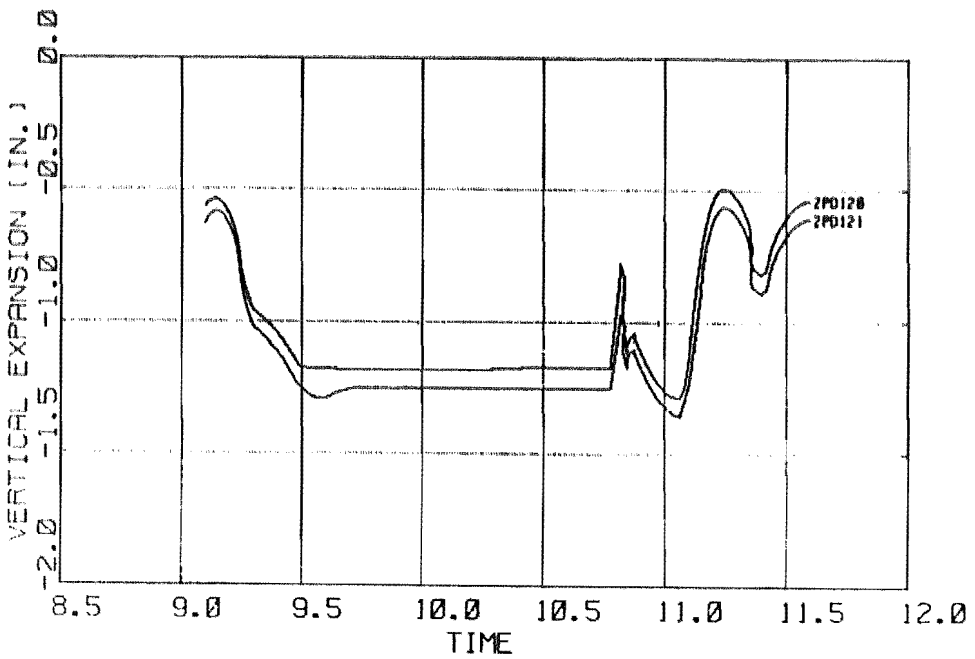

Figure 7.1.18 represents the horizontal deflection (front-to-back) of the mid-point between upper and middle supports for tubes 3 (pass 9) and 33 (pass 14) as measured by displacement transducers ZPD122 and ZPD123 (Figure 7.1.19). They indicate that the tubes essentially did not move (bow out) during

receiver operation. (The time period is the same as for the previous figure.) This confirms the generalized plane-strain assumption for the panel made during the stress analysis and design task.

FIGURE 7.1.18
PANEL 3W HORIZONTAL DEFLECTION (4/28)

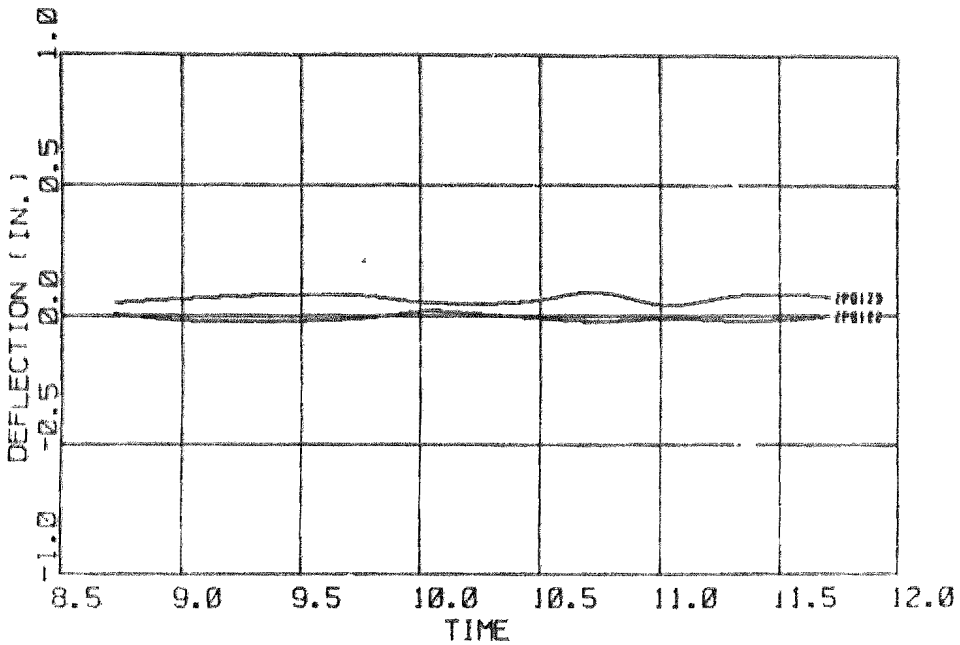

Support Linkage Temperatures

To check assumed design temperature vs. actual (measured) temperatures on support linkages, FW installed five thermocouples in the middle support linkage at the locations shown in Figure 7.1.19.

FIGURE 7.1.19

PANEL 3W SUPPORT LINKAGE

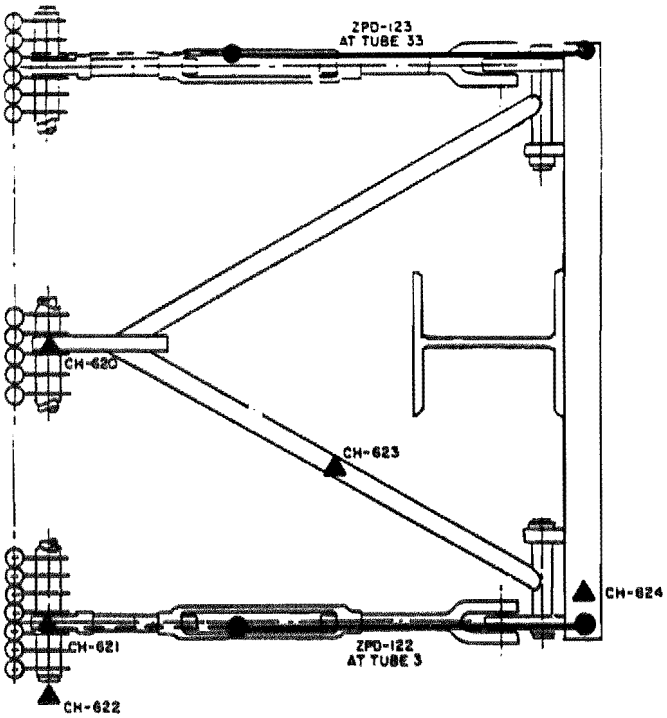

Figure 7.1.20 shows support linkage temperatures as measured by thermocouples CH620 through CH624 during the test conducted the morning of April 28. The data from CH620 through CH622 confirm the assumption is conservative that the design temperature for the support rod and clips is approximately equal to the outlet salt temperature of the panel. The data from CH624 confirm the design assumption that the temperature of the vertical support beam is approximately equal to the ambient temperature.

FIGURE 7.1.20

PANEL 3W LINKAGE TEMPERATURES (4/28)

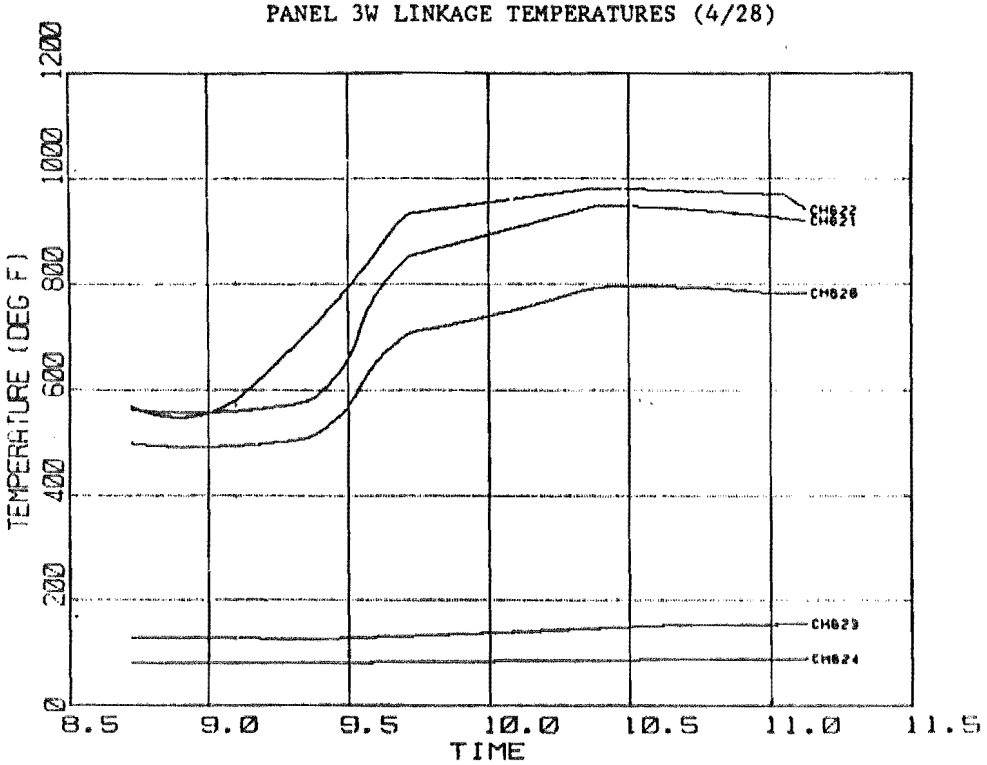

During some tests, some very high temperatures (above 593°C [1100°F]) were measured by thermocouples CH620 and CH621. We believe they were the result of gaps that opened between the tubes, allowing the solar flux to impinge directly on the collars and support rod, causing the high temperature readings.

The problem was solved by adding extra insulation between the support linkage and the tubes. This was a temporary fix; it is imperative that some way be found in future receiver designs to prevent the solar flux from impinging on the support linkage.

Flow Distribution

One major uncertainty in receiver design has been the possibility of uneven flow distribution in the panels and flow recirculation in a downflow pass [4]. Uneven flow distribution and flow recirculation can lead to excessive tube-wall temperatures and tube failures. Thus the FW panels were provided with special instrumentation to ascertain whether either of these conditions was present in the panels. Thermocouples were installed in the back of each tube outlet of pass 2 (wing panel) and pass 14 (cavity panel 3W) [about 0.3 m (1 ft) below the exposed portion of the tubes]. These passes were selected because they had the greatest potential for those conditions to develop. Both were downflow passes and had the largest variation in heat flux.

Figure 7.1.21 shows the temperatures measured by thermocouples CH561 through CH566 at the exit of pass 14 during the test conducted on the morning of April 28. Analysis of the data showed that the outlet temperature in the six tubes was very similar. With the exception of CH561, all outlet temperatures fell within the predicted temperature variation, an indication that there was a good flow distribution within the pass at flows close to the design conditions.

FIGURE 7.1.21
PANEL 3W PASS 14 OUTLET TEMPERATURES (4/28)

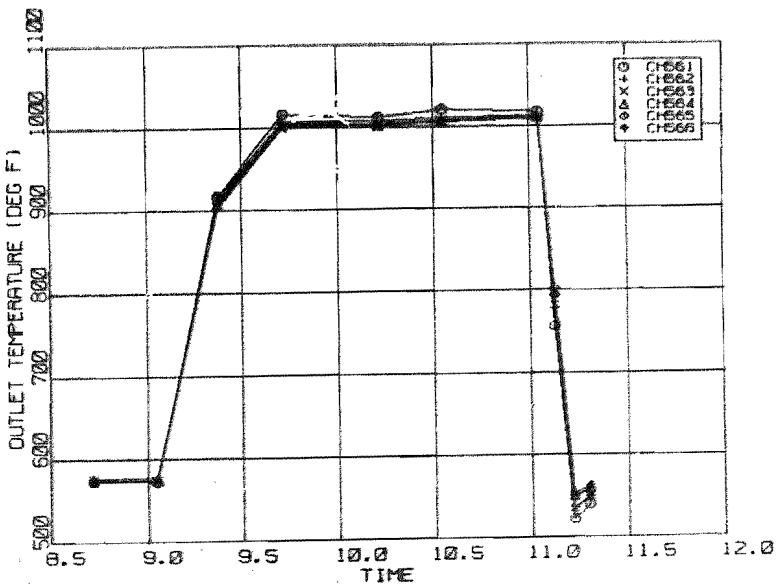

CH561 is the outlet temperature thermocouple of the edge tube of the panel in pass 14. The higher measured temperatures indicate that the edge tube experienced a higher heatup than the others while operating with heat flux, and it cooled faster than the others when the solar flux was removed from the receiver. The explanation is that, since this is the edge tube, more tube surface was exposed, allowing it either to absorb more heat during heat flux operation or lose heat faster during cool-down periods.

The flow distribution analysis--made during the design of the panels--indicated that the wing panel operating at low flow had the greatest potential for uneven flow distribution and flow recirculation. Unfortunately, the temperatures of the six thermocouples, installed by FW with the specific purpose of checking the flow condition in the wing panel pass 2, were not recorded because of incompatibility between the Acurex system and the DAS.

Incident Heat Flux

Since peak tube-wall and salt temperatures are closely related to distribution of incident fluxes, five heat flux gages (three water cooled and two passively cooled) were installed in Panel 3W to measure actual solar flux at critical locations and compare it with predictions. Locations of heat flux gages are shown in Figure 7.1.13. The water-cooled gages ceased to function (plugged) very early in the test program and were never replaced. Thus data were recorded only from flux gages FG104 and FG105.

Figure 7.1.22 presents the predicted design-point incident solar flux across Panel 3W at two levels: at the centerline and at 0.4 m (16 in.) above the centerline. The measured values at 1 p.m. on April 10 are plotted in the figure. This particular time was selected for detailed analysis because the receiver was operating under steady-state, near design-point conditions.

Figure 7.1.23 shows the predicted design-point incident heat flux in passes 9 and 14. For comparison, the heat flux measured by FG104 (pass 9) at 1 p.m. on April 10 is plotted.

FIGURE 7.1.22

PANEL 3W INCIDENT SOLAR FLUX (4/10)

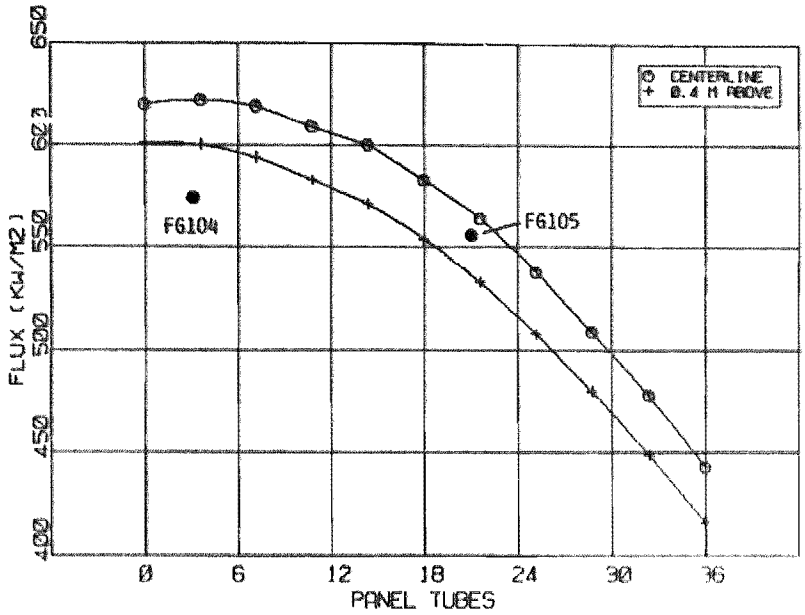

FIGURE 7.1.23

PANEL 3W INCIDENT SOLAR FLUX TO PASSES 9 AND 14 (4/10)

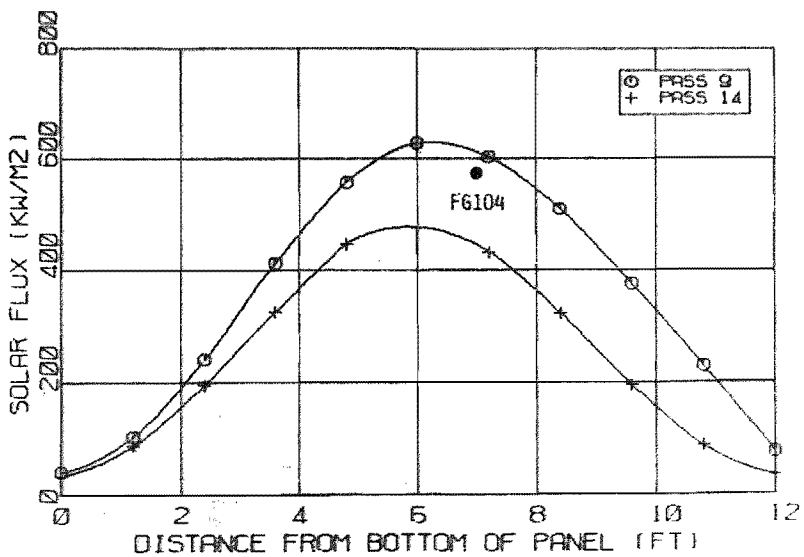

Temperature Profile

Metal temperatures were predicted for the design conditions by the computer program SOLAR.TH described in Section 3.2. Three temperatures were predicted at each location: peak tube-wall (O.D.), film salt (I.D.), and salt bulk.

Figure 7.1.24 presents the predicted tube-wall and temperatures for pass 9 under conditions during the 1 p.m. test on April 10. Superimposed on the predictions of salt bulk temperature are the data obtained by thermocouples TE110 thru TE113. Excellent agreement was obtained.

FIGURE 7.1.24

PANEL 3W/PASS 9/TUBE 3 TEMPERATURES (4/10)

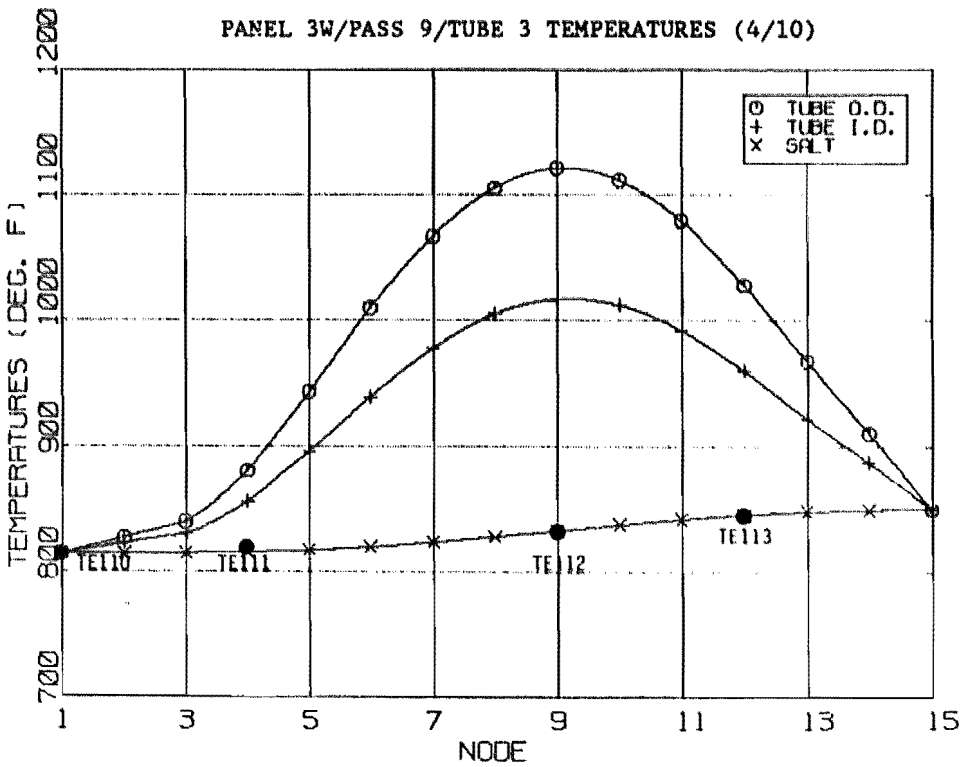

Figure 7.1.25 presents the predicted tube-wall and salt temperatures for pass 14 under the same conditions at 1 p.m. on April 10. Superimposed on the predictions of salt bulk temperature are data obtained by thermocouples TE118

through TE120. Excellent agreement was obtained between predicted and measured values. A close examination of this Figure indicates that the predicted salt film temperature exceeded the salt temperature limit between Nodes 7 and 9. [The salt temperature limit is 593°C (1100°F), where decomposition of salt begins [4]]. Although the incident heat flux did not exceed the design-point values, the inlet salt temperature to Panel 3W was about 17°C (30°F) higher than the design-point inlet salt temperature, enough to push the film temperatures over the limit. The temperature given by thermocouple TE120 was consistently lower than predicted values. TE120 was located in the jumper tubes, halfway between the end of the exposed part of the panel and the headers. Examination of other test data indicated that there was about a 3°C (5°F) temperature drop between TE119 and TE120. The temperature data given by TE120 were checked using data from nearby thermocouples and all showed similar drops in temperature.

FIGURE 7.1.25
PANEL 3W/PASS 14/TUBE 3 TEMPERATURES (4/20)

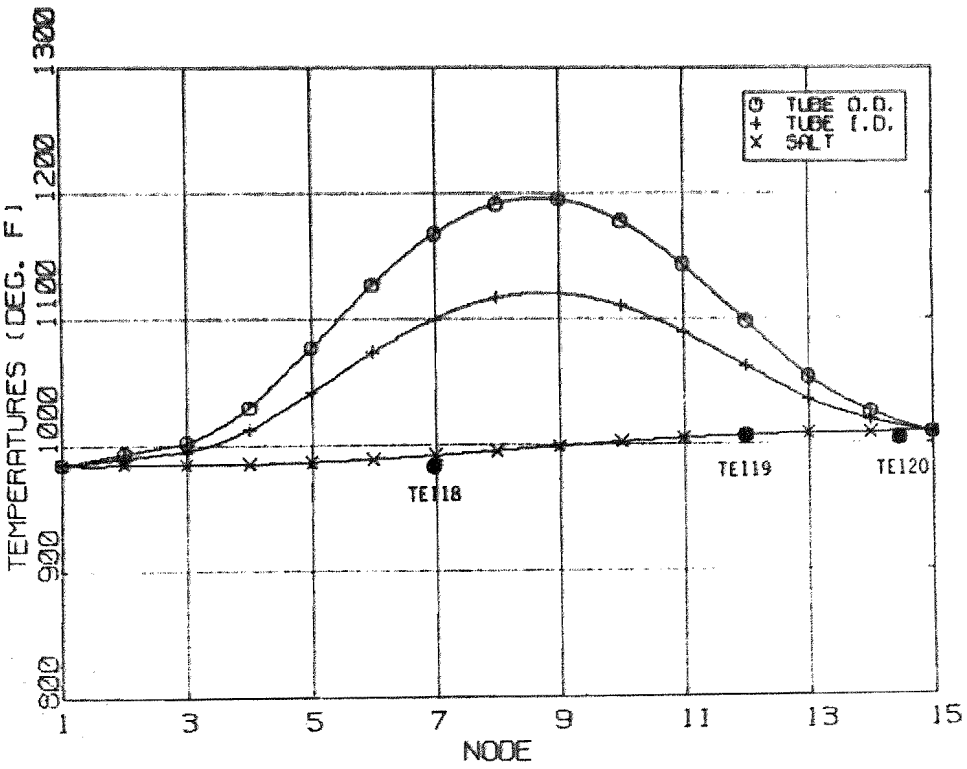

The dip in the data is not fully understood. A probable explanation is that the jumper tubes were poorly insulated and a significant amount of heat was lost between the end of the exposed (active) panel area and the headers.

Figure 7.1.26 presents the loci of predicted peak tube wall (O.D.), peak film salt (I.D.), and salt bulk temperatures under the conditions existing at 1 p.m. on April 10. Superimposed on the predictions of salt bulk temperature are the temperature data given by thermocouples TE110 through TE120. Excellent agreement was obtained between predicted and measured values.

FIGURE 7.1.26
PANEL 3W PEAK TEMPERATURES (4/10)

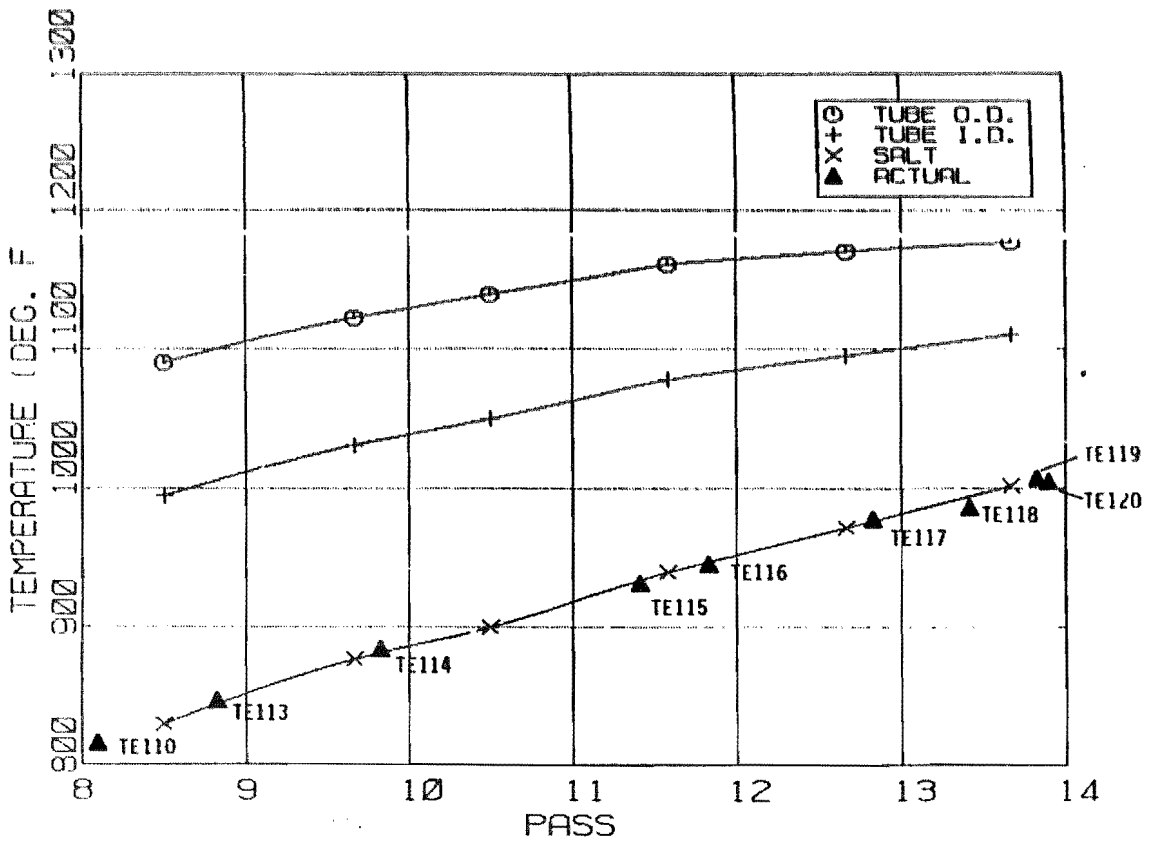

Strain Gages

The solar receiver panel was instrumented by eight strain gages; four of them were of the resistance type (SG-101 to SG-104) and the other four were of the capacitance type (SG-105 to SG-108). Both types of gages were calibrated by using the data provided by the manufacturer as well as additional data from testing in Foster Wheeler's laboratories. After their calibration, the strain gages were mounted on the panel in locations specified in Figure 7.1.13. Initially, they were connected to the computerized data acquisition system. However, because of difficulties with the data acquisition system, the gages were later disconnected.

The data from the gages were recorded on charts (using a strip-chart recorder) as continuous plots with printed data at 1-hour intervals. The strain gage data were read manually from the printed charts and entered into Foster Wheeler's computer system for postprocessing and evaluation. All other supporting data for strain evaluation, such as flux and temperature distributions, were available at 1-minute intervals from the tapes created by the data acquisition system.

Post-processors were written on the FWDC computer system to interpret the data received from the strain gages. The post-processors use the strain gage calibration procedures to convert the voltage readings to strains. To account for the temperature sensitivity of the strain gages, data from FWDC calibration tests and the manufacturer's specifications were built into the post-processor.

To determine the adequacy of the theoretical calculations, we made a set of analyses to predict the strains at the given conditions. As will be seen later, the data for the capacitance gages showed excellent agreement with theoretical calculations. The data from the resistance gages were unsatisfactory; a detailed study is needed to clearly understand the performance of the resistance gages.

Theoretical Analysis

The tubes in the panel consisted of a straight section and a small loop. The tubes were supported by three intermediate supports with the tube ends welded to the headers. The tube-to-header joints were only partial restraints, as the headers were allowed to rotate. To determine the effect of the partial restraint at the tube ends, we considered two sets in the analysis: a first with hinged ends and a second with fixed (rotating) ends.

The loading on the tube was the thermal loading induced by the variable heat flux, both around the circumference and along the length, and the internal pressure. The problem clearly was three-dimensional. However, by using the following simplifying assumptions, the problem was reduced to a combination of local (2-D) and global (1-D) analyses:

- Heat transfer in the axial direction of the tube is negligible.
- In the stress analysis, the tube cross section remains plane after deformation (no warping).

Using these assumptions, the tube was analyzed in the following steps:

- A local analysis of the tube cross section was performed to determine the detailed temperature distribution for a peak flux of 1 MW/m^2.
- Assuming that the film coefficient does not vary along the tube length, the temperatures along the entire tube were determined by scaling them.
- A global analysis of the entire tube under a linear diametral thermal gradient, varying along the length, was performed to determine the bending strains.
- The change in strain at each strain gage location, as a result of the unit change in peak heat flux on the tube, was determined.

Local Analysis

To determine the detailed temperature distribution in the tube cross section, we made a local analysis of the tube. By using the computer program NONAX, the steady-state temperature distribution was determined. NONAX is a special-purpose program developed by FW to perform thermal and stress analysis on thick-walled cylinders made of homogeneous and isotropic materials. The loading may be axisymmetric or nonaxisymmetric. It may consist of an arbitrary combination of internal and external tractions, axial load, axial bending, and an arbitrary temperature distribution. Elastic, elastic-plastic, and creep analyses under varying load cycles and hold times can be done using this program. NONAX is considerably less expensive to run than multipurpose finite-element programs.

The model used in the analysis is shown in Figure 7.1.27. The thermal boundary conditions and properties were as follows:

	Pass 14	Pass 9
Peak Flux (MW/m^2)	1	1
Film Coefficient [W/m^2-°C(Btu/h·ft^2-°F)]	8490 (1500)	7640 (1350)
Thermal Conductivity-- [W/m^2-°C(Btu/h·ft^2-°F)]	74.7 (13.2)	74.7 (13.2)

The linearized front-to-back temperature variation (Delta T) was then determined by integration. The value of Delta T was 180°C (325°F) for tubes in pass 14, and 195°C (352°F) for the tubes in pass 9.

FIGURE 7.1.27
TUBE MODEL USED FOR LOCAL ANALYSIS

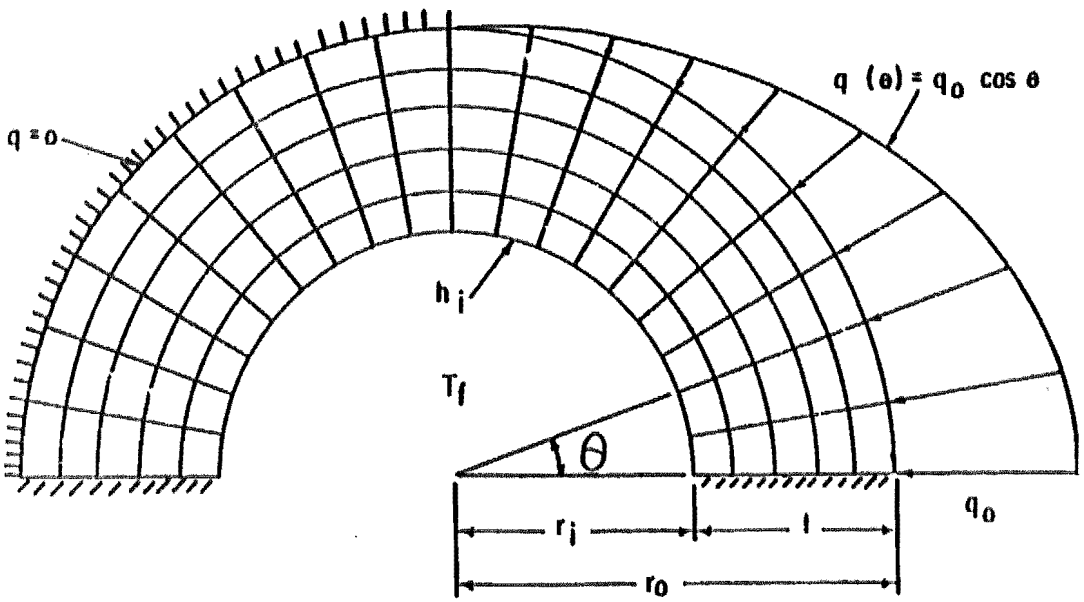

Global Analysis

The entire tube was modeled as a beam by using finite-element analysis. Two shapes were considered in the analysis: a large loop at the ends and a small loop at the ends. Typical finite-element mesh is shown in Figure 7.1.28. The tube was supported by three intermediate supports. Two types of boundary conditions were considered at the ends of the tubes--one fixed against rotation and the other free rotation. Axial expansion was allowed along the entire tube. The loading consisted of a linear diametral thermal gradient along the length in the exposed area. The magnitude of the gradient was varied in the ratio of the expected flux distribution. The peak thermal gradient in each case was as determined in the local analysis [i.e., 180°C

(325°F) for tubes in pass 14, and 195°C (352°F) for tubes in pass 9]. The following four sets of analyses were made:

Large bend in Pass 14 - Tube 1	Small bend in Pass 14 - Tube 3
Large bend in Pass 9 - Tube 36	Small bend in Pass 9 - Tube 33

FIGURE 7.1.28
PANEL MODEL USED FOR GLOBAL ANALYSIS

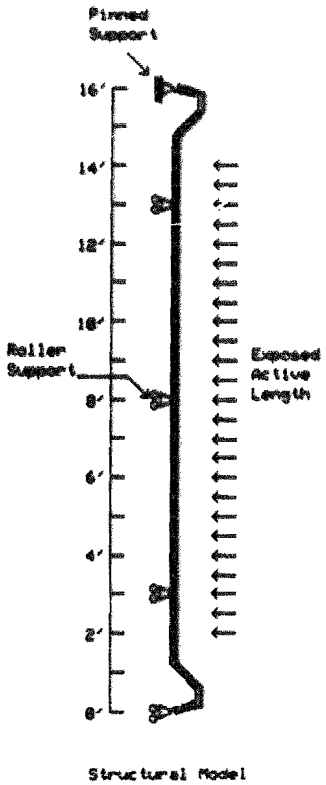

Expected Strains at Gage Locations

The strain change for a unit change in peak flux (MJ/m^2) was obtained from the bending moments determined in global analysis by the simple beam formula:

$$MD/2EI,$$

where M = Bending moment

D = Tube O.D. (1 in.)

E = Young's Modulus (21 x 10^6psi)

I = Moment of inertia of tube cross section about its diameter (0.02097 $in.^4$).

The variation of bending strain at the back of the tube is shown in Figures 7.1.29 and 7.1.30. Figure 7.1.31 shows the bending strain for the tubes in pass 14 for the large and small bends with both pinned and fixed-end conditions. Figure 7.1.30 shows the same for tubes in pass 9. As these figures show, neither the boundary conditions at the ends of tubes (fixed or pinned) nor the bend geometry (large or small) had significant influence on the strains. An interesting point to be noted in these figures is that the strains in the tube near the headers were extremely small for all conditions, indicating that these areas of the tube were of little concern from a stress point of view. However, the results did not address the stress concentrations near the tube-to-header joints and transients.

FIGURE 7.1.29
STRAIN IN TUBES (PASS 14)

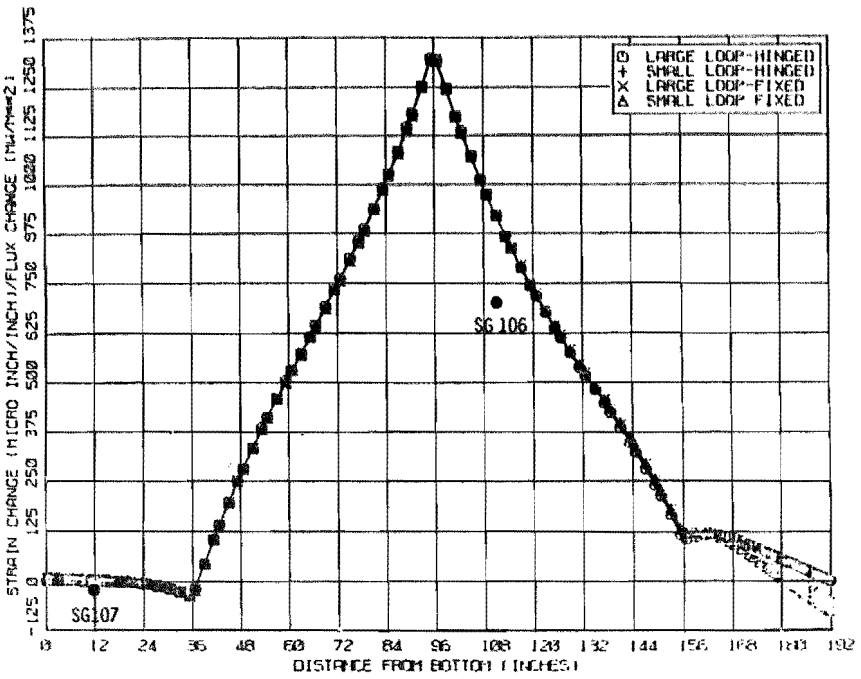

FIGURE 7.1.30
STRAIN IN TUBES (PASS 9)

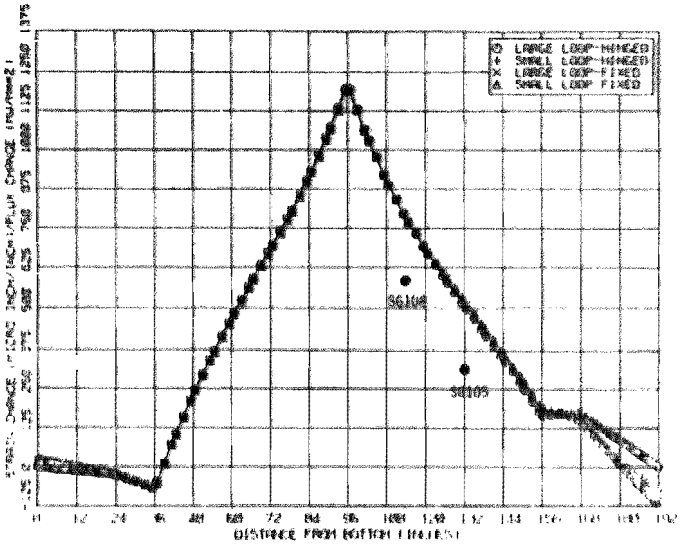

FIGURE 7.1.31
STRAIN DATA FROM RESISTANCE GAGES

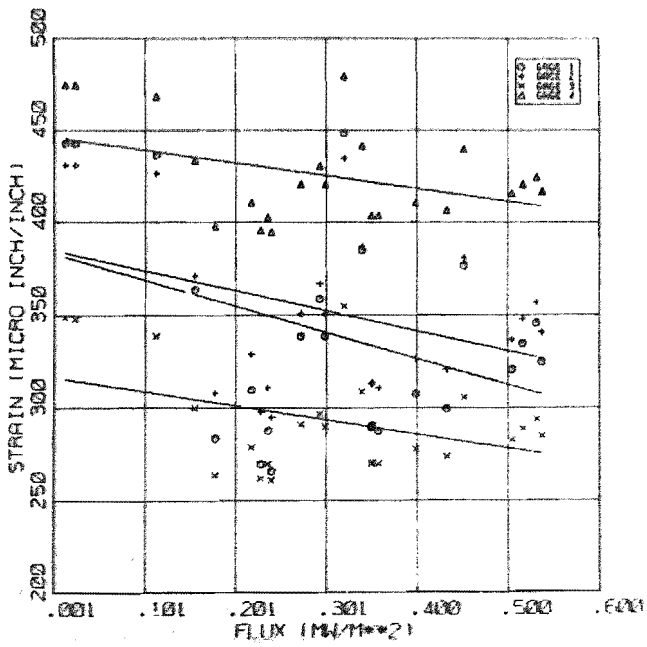

Processing Strain Gage Readings

The data from the gages were recorded on charts as continuous plots with printed data generated at 1-hour intervals. The strain gage data were read manually from the printed charts and entered into Foster Wheeler's computer system for postprocessing and evaluation. Other supporting data needed for strain evaluation were the flux and temperature variations at the gage locations. The supporting data were obtained from the tapes created by the data acquisition system at the site. The data were processed by the computer program developed at FWDC. This program took the readings from the strain gages, flux gages, and thermocouples, and evaluated the strains according to calibration rules developed by FWDC. The output from the program contained two files:

A file containing flux vs. strains; and
A file containing change in flux and change in strain between two sequential time increments.

The output files were used for plotting the results. Plotting was done by using FWDC in-house software. Figures 7.1.31 and 7.1.32 show the variation of strains with peak flux data obtained experimentally. Figure 7.1.31 presents the results from resistance gages and Figure 7.1.32, capacitance gages. Both figures also show the least square fit line between the peak flux and strain for each gage. The slope of the least square line, which represents the change in strain for unit change in flux, was used for comparison with theoretical results. The slopes obtained from experimental data are plotted in Figures 7.1.29 and 7.1.30, which also show the theoretical results. Excellent agreement was observed between the data obtained from capacitance gages and theoretical predictions. Agreement between results obtained from resistance gages and theory was unsatisfactory. Noting that the resistance gage SG-104 and the capacitance gage SG-108 were at the same location in the panel, one would expect identical data from the two gages, but the measured values deviated considerably. We have concluded that the resistance gages need additional study before they can be used for the strain prediction on receiver panels.

FIGURE 7.1.32

STRAIN DATA FROM CAPACITANCE GAGES

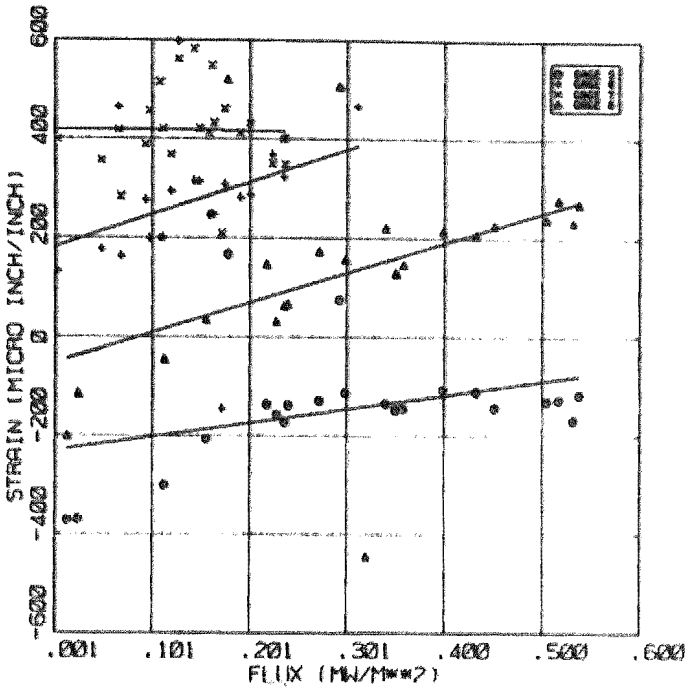

Summary of Foster Wheeler Panel Evaluation

The results of the data analysis of the FW panels indicate excellent agreement between the predictions and the actual data. The agreement was better than expected and confirms the validity of the FW computer model/programs as well as the design assumptions. This is particularly true regarding FW predictions of panel pressure drop, panel thermal expansion, flow distribution, heat absorption, tube-wall temperatures, and tube stress/strains.

The capacitor strain gages worked very well, but the resistor-type gages did not. It is difficult to determine what was wrong with the resistor-type capacitors, since the strain gage data were not recorded until mid-March; thus critical strain gage data for the first few months of panel cycling were lost.

The analysis as well as the experimental work showed that the stresses at the tube-to-header junction were small for a steady-state loading. As a result, the effect of stress concentration at this location was not studied. Transient conditions could, however, induce higher stresses.

Because of constraints imposed by the project's cost and time, a detailed analysis of the transients was not made; we highly recommend including this task in future studies on the subject.

7.1.3 Receiver Paint Evaluation

The receiver panels were painted with Pyromark series 2500 black paint. This paint as applied in the field after the receiver assembly at the CRTF was completed. The paint was cured according to the manufacturer's specifications by operating electric heaters inside the receiver cavity with the receiver door closed. This careful curing and vitrification of the paint resulted in a uniform coating with good optical and mechanical properties.

After the painting was completed the absorptivity of the paint was measured in the solar spectrum using a solar spectrum reflectometer. The reflectivity reading was corrected for the effect of the curved tube surface, then subtracted from 1 to yield absorptivity. The results of these measurements are presented in Table 7-II.

TABLE 7-II
RECEIVER PANEL INITIAL ABSORPTIVITY
EAST ZONE

Vertical Location (ft.)	Panel:	4-East		3-East			2-East		
	Tube:	6	18	10	20	30	10	20	30
9.5		0.972	0.972	0.973	0.973	0.973	0.973	0.975	0.973
5.75		0.972	0.972	0.973	0.973	0.973	0.973	0.975	0.973
2.5		0.972	0.972	0.973	0.973	0.973	0.975	0.972	0.972

WEST ZONE

Vertical Location (ft.)	Panel:	2-West		3-West			4-West		
	Tube:	10	20	30	10	20	30	10	20
9.5		0.973	0.973	0.972	0.976	0.972	0.976	0.973	0.972
5.75		0.972	0.971	0.973	0.971	0.978	0.972	0.972	0.971
2.5		0.972	0.972	0.971	0.972	0.973	0.972	0.972	0.972

WING PANELS

Vertical Location (ft.)	Panel:	1-East		1-West	
	Tube:	3	12	1	10
6		0.972	0.971	0.972	0.972
2		-	-	-	-
0		0.970	0.971	0.970	0.967

In Table 7-II, the vertical location is in feet from the bottom of the panel heated portion, and the tubes are counted from the east edge of each panel assembly. The average absorptivity of the back panel was .973 and of the wing

panels was .971. This is very close to the maximum absorptivity achievable with Pyromark paint, and is an indication that the paint is properly cured for comparison, the initial absorptivity of the Solar 1 receiver which was cured at operating temperature only (approximately 700°F average) was .93 [39].

In addition to the solar spectrum measurements, the emissivity for 100°C and 300°C black body spectra were also measured using an infrared reflectometer. These readings were taken at just a few locations, and are presented in Table 7-III and Table 7-IV.

TABLE 7-III
RECEIVER PANEL 100°C BLACK BODY EMITTANCE
EAST ZONE

Vertical	Panel:	4-East		3-East			2-East		
Location (ft.)	Tube:	6	18	10	20	30	10	20	30
9.5		0.865	0.834	0.854	-	0.844	0.871	-	0.857
5.75		-	-	-	-	-	-	-	-
2.5		-	-	-	-	0.854	0.865	-	0.842

WEST ZONE

Vertical	Panel:	2-West		3-West			4-West		
Location (ft.)	Tube:	10	20	30	10	20	30	10	20
9.5		0.843	-	0.862	0.877	-	0.883	0.859	-
5.75		-	-	-	-	-	-	-	-
2.5		0.889	-	-	0.848	-	0.862	0.871	-

TABLE 7-III (CON'T)

WING PANELS

Vertical Location (ft.)	Panel: Tube:	1-East 3	1-East 12	1-West 1	1-West 10
6		0.864	0.833	0.859	0.864
2		-	0.844	0.857	0.835
0		0.85	0.878	0.857	0.875

TABLE 7-IV
RECEIVER PANEL 300°C BLACK BODY EMITTANCE
EAST ZONE

Vertical Location (ft.)	Panel: Tube:	4-East 6	4-East 18	3-East 10	3-East 20	3-East 30	2-East 10	2-East 20	2-East 30
9.5		-	0.78	-	-	-	-	-	-
5.75		-	-	0.778	-	0.769	-	-	-
2.5		-	-	-	-	0.78	0.78	-	0.761

WEST ZONE

Vertical Location (ft.)	Panel: Tube:	2-West 10	2-West 20	2-West 30	3-West 10	3-West 20	3-West 30	2-West 10	2-West 20
9.5		-	-	-	-	-	-	-	-
5.75		0.806	-	-	0.806	-	0.83	0.807	-
2.5		-	-	0.807	0.784	-	0.802	0.802	-

TABLE 7-IV (CON'T)
WING PANELS

Vertical Location (ft.)	Panel:	1-East		1-West	
	Tube:	3	12	1	10
6		0.817	0.769	0.809	0.762
2		-	0.787	0.791	0.807
0		0.834	0.806	0.761	0.796

The average 100°C and 300°C emittance values are .860 and .792 respectively for the back panels and .856 and .794 for the wing panels. These also provide evidence that the paint was cured properly [39].

After approximately 240 hours of solar operation, on June 5, 1987, the solar absorptivity was measured again to see if any changes were occurring. Only the back panel was examined. The results are presented in Table 7-V.

TABLE 7-V
RECEIVER PANEL ABSORPTIVITY AFTER OPERATION
EAST ZONE

Vertical Location (ft.)	Panel:	4-East		3-East			2-East		
	Tube:	6	18	10	20	30	10	20	30
9.5		-	-	-	-	-	.976	-	0.978
5.75		0.978	0.979	0.978	-	0.978	0.977	-	0.979
2.5		0.977	0.978	0.977	-	0.978	0.978	0.978	0.977

TABLE 7-V (CON'T)

WEST ZONE

Vertical	Panel:	2-West		3-West			4-West		
Location (ft.)	Tube:	10	20	30	10	20	30	10	20
9.5		0.978	-	0.977	-	-	-	-	-
5.75		0.979	-	0.977	-	-	-	-	-
2.5		0.978	-	0.978	0.977	0.978	0.977	0.977	0.972

The average absorptivity after approximately 240 hours of operation was .977, a slight apparent increase, but within the ±1 percent accuracy of the reflectometer.

Insufficient service time has been accumulated to determine if the paint will degrade with time. At Solar 1, this became a problem, however it may have resulted from the initial improper cure. In any event, this receiver paint job has demonstrated that "laboratory" values for Pyromark absorptivity can be achieved on a solar receiver in the field. These are accomplished by proper application and proper curing of the paint, and result in system efficiency improvements of several percent.

The receiver paint was degraded in 13 local areas where molten-salt leaked from pin holes in tube attachment clip welds on the backs of tubes. The paint blemishes ranged in size from about 2 inches in diameter to the largest which was 18 inches long by 10 inches wide. Approximately 2% of the surface was affected. Figure 7.1.33 is a photograph of one of the large blemishes.

FIGURE 7.1.33
PAINT BLEMISH

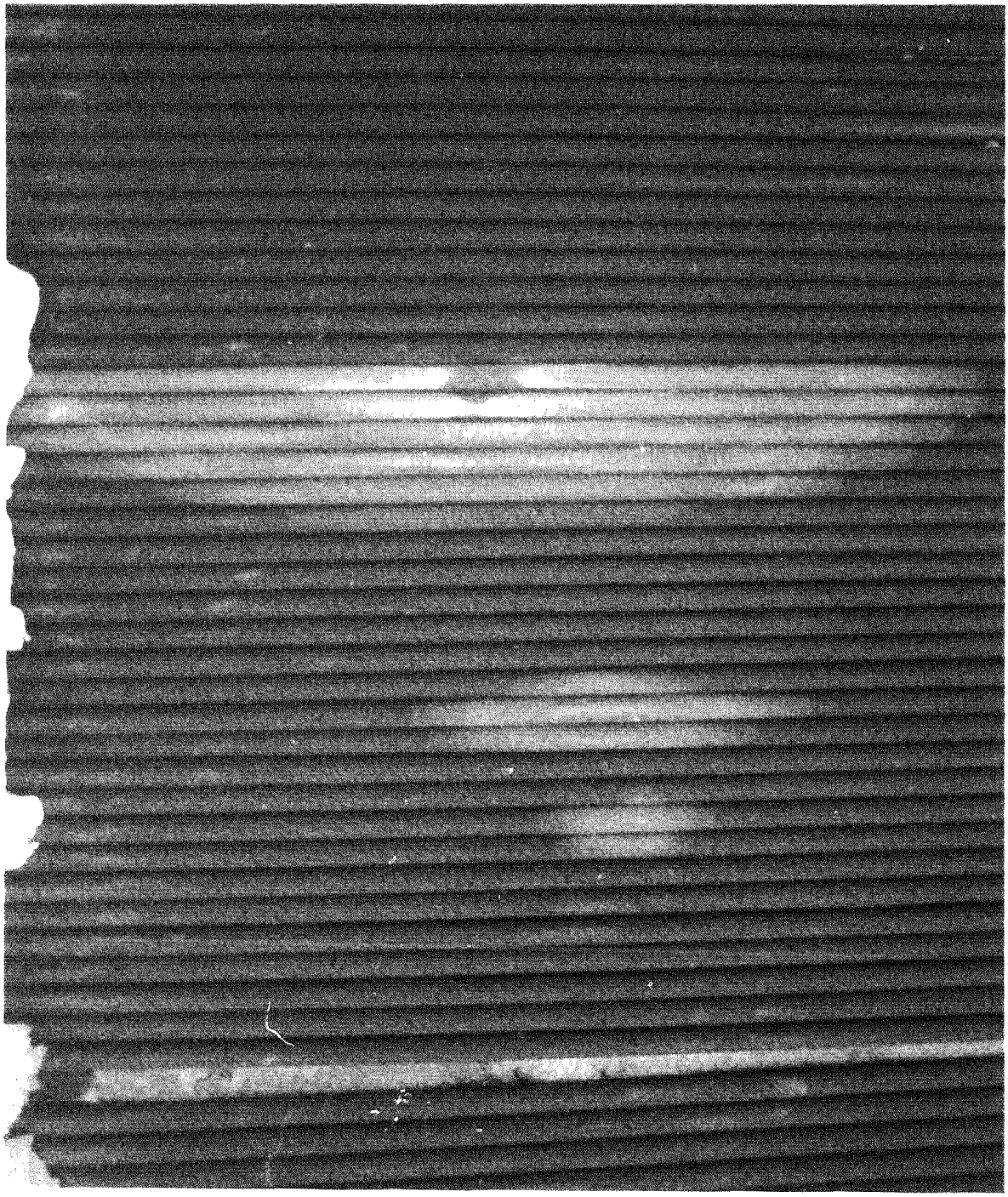

In addition to the absorptivity of the bulk of the paint, an attempt was made to characterize the absorptivity of the blemishes where salt had leaked onto the surface. Measurements were taken at 1-inch intervals down the vertical centerline of one of the larger blemishes. The readings are presented in Table 7-VI.

TABLE 7-VI
SOLAR ABSORPTIVITY OF THE PAINT BLEMISHES

	Top	1"	2"	3"	4"	5"	Bottom
Absorptivity	.972	.913	.972	.836	.865	.893	.955

The average measured absorptivity of the spot based on these measurements is .901.

7.2 Balance of Receiver Design

7.2.1 Instrumentation

Instrumentation employed in the receiver included thermocouples, flow meters, level sensors, pressure gages, displacement meters, flux sensors, and strain gages. A detailed list of instrumentation is provided in Appendix C. Locations of the instrumentation is illustrated in Figure 7.2.1. Overall, the instrumentation provided for good control of the receiver, but as a result of several problems with specific instruments, only fair measurement of performance. Problems with instrumentation were associated with either the high flux solar environment or the molten-salt environment.

FIGURE 7.2.1
RECEIVER SUBSYSTEM

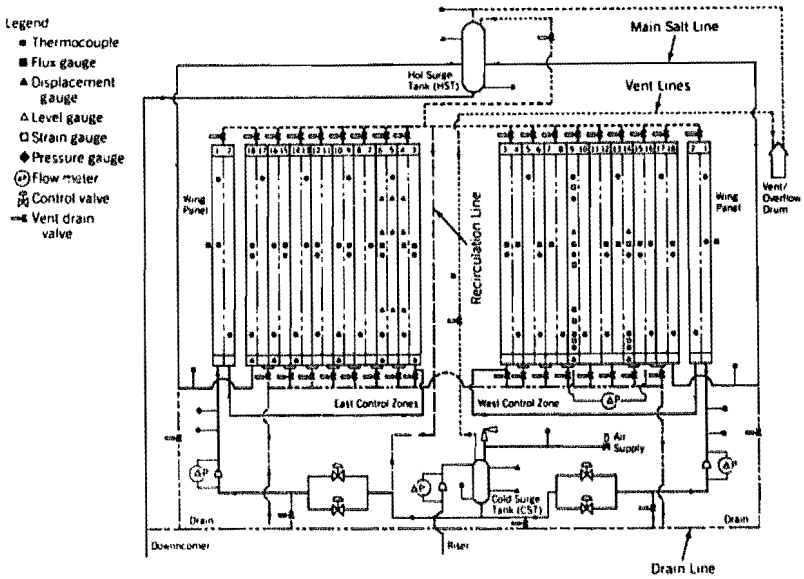

Thermocouples used were sheathed type K thermocouples. Critical inlet and outlet salt temperature thermocouples were calibrated to allow compensation with respect to the standard curve for type K. The thermocouples worked quite well, although there were some problems with digital conversation and the recording of the readings.

The salt flow meters did not perform well. The receiver employed three venturi-type flow meters in vertical piping runs. The pressure difference across the venturis was measured using oil filled double isolation type pressure transducers. The transducer calibration did not remain constant during testing due mainly to zero shifts. Apparently the problem was with the oil used to isolate the salt from the actual transducer since the type of transducer used is known to be reliable. The region of the diaphragm separating the oil must be heated to prevent freezing of the salt. The

diaphragms were maintained at 500°F by the use of electric band heaters. The oil used in the transmitters is sylthern. At 500°F, the possibility exists that zero shifts could be associated with the use of this oil since its vapor pressure becomes significant at this temperature. Since the transducers did not give good readings, flow measurement was derived from the inlet pressure reading for each zone. This pressure was measured with similar transducers, but the range of the measurement was zero to 300 psi as opposed to zero to 200 inches of water. Zero shifts that may have been the result of oil properties would be insufficient on this range. As discussed in Section 6.7, this method of flow measurement was adequate for control, but resulted in large uncertainty bands in performance measurements.

Two types of salt level sensors were used in the receiver--one for the vented hot surge tank, another for the pressurized cold surge tank. Both were pressure sensing devices. The hot surge tank level transmitter measured the pressure of the bottom of the tank by sensing the pressure in an air filled tube extending down to the bottom of the tank. The tube was kept full of air by passing a low volume rate flow of air down the tube letting it bubble up through the tank. The pressure transmitter sensed just ambient temperature air pressure, and the device worked very well. For the pressurized cold surge tank, two double isolation delta pressure transmitters similar to those used to measure venturi pressure difference were used. These experienced zero shifts similar to the flow meters. As a result, differences in the readings of the two sensors were commonly as high as 20 inches. These provided only a gross indication of tank level, but were adequate to support emergency trip indication. For control of tank level, pressure in the trapped air space in the tank was used.

Aside from their use in level and flow sensors, pressure was measured at the inlet of each flow zone, across the Foster Wheeler panel, and in the cold surge tank. All but the cold surge tank gage used an oil filled double isolation transmitter, and these performed well. For cold surge tank pressure, the ullage air pressure was sensed with an ordinary air pressure transmitter. This worked well, but if the tank was over-filled (as on two occasions) salt filled the air line and transmitter. Both times, the salt was washed out, and the transmitter, once re-calibrated, still worked.

Displacement meters were located on several lower headers to measure vertical growth, and one on the panel tubes to measure lateral deflection. These instruments worked well through the test.

Two types of flux sensors were used in the test. Both employed the same type of sensing element, but different methods of cooling. One gage was air cooled and had solid copper body extending through the insulation to a finned heat sink. The other employed water cooling. The air cooled gages worked well. Of 12 gages, only one failed completely. The accuracy of the gages, however, was estimated to be only ±15 percent based on occasional re-calibration of the gages.

Several water cooled gages failed as a result of plugging of the small (less than 1 mm square) flow channel in the gage. This type of gage has inadequate cooling for the service and a bad tendency for plugging. There appears to be no reason why larger cooling channels could not be employed in the gage to resolve the problem.

Strain gages were installed on the Foster Wheeler panel in several locations. Two types of gages were used--resistance type and capacitance type. Good data was measured by the capacitance gages, while the resistance gages did not yield good data (see Section 7.1.2).

Instrumentation was digitized and displayed by the Baily Network-90 process controller. Data was subsequently passed on to the Hewlett-Packard data acquisition system where it was recorded. This system worked well for most data. Two exceptions, however, were high resolution thermocouple measurements, and strain gage readings. High resolution thermocouple data was required for flux-off loss tests. The Network 90 did not have sufficient resolution in its standard thermocouple inputs to accurately measure temperature differences on the order of 10°F. For the strain gages, no standard input channels were of the required type. These are generally not drawbacks for process control. For specialized and detailed measurements of this type, an instrument dedicated to the device is required.

7.2.2 Heat Trace and Control

The function of the heat trace system was to heat the salt piping above the salt melting point and maintain that temperature. The goal of such a system is to do this with minimum maintenance and minimum control problems. The heat trace on the test receiver performed adequately and made improvements over some previous systems; however, problems were still encountered. The following sections discuss these main issues and the specific problems encountered with the system.

Heating and Maintaining Temperature

In general, the heat trace system implemented on the test receiver was able to heat the receiver salt components to operating temperature and maintain their temperature. The methods used for sizing the heat trace resulted in a system that could maintain sufficient pre-heat in all weather conditions for most of the system. Problems were encountered in a few areas, however, and these are discussed below.

Heat Trace on Long Lines

When a mineral insulated (MI) cable is applied to a long run of piping, it supplies a constant watt density along the length of the pipe. Any variation in the insulation applied to the line, or in the boundary conditions result in temperature variations. In most cases these variations are moderate (less than 200°F from the coldest to the hottest thermocouple), but in some cases the differences are worse. This condition can also occur when multiple components are included in a single control zone. Because of the imprecise nature of insulation and the variability of boundary conditions, it is virtually impossible to achieve good uniformity in heat loss. In each heat trace zone, a number of thermocouples were applied for monitoring and control. In general, once the system was installed and checked out, the thermocouple that generally had the lowest reading was selected for control with a minimum set point. The other parts of the zone would then generally run hotter than this. This method worked well, but it was found that 200°F variations from

cold spot to hot spot in heat trace zones were common, and some variations were greater. In most cases, this did not cause problems because the piping (all 304 stainless steel) and the heat trace could tolerate operation at the higher temperature.

The worst temperature difference of this type occurred on the lower drain header (heat trace zone 45). This line is illustrated in Figure 7.2.2.

FIGURE 7.2.2
POWER DRAIN HEADER

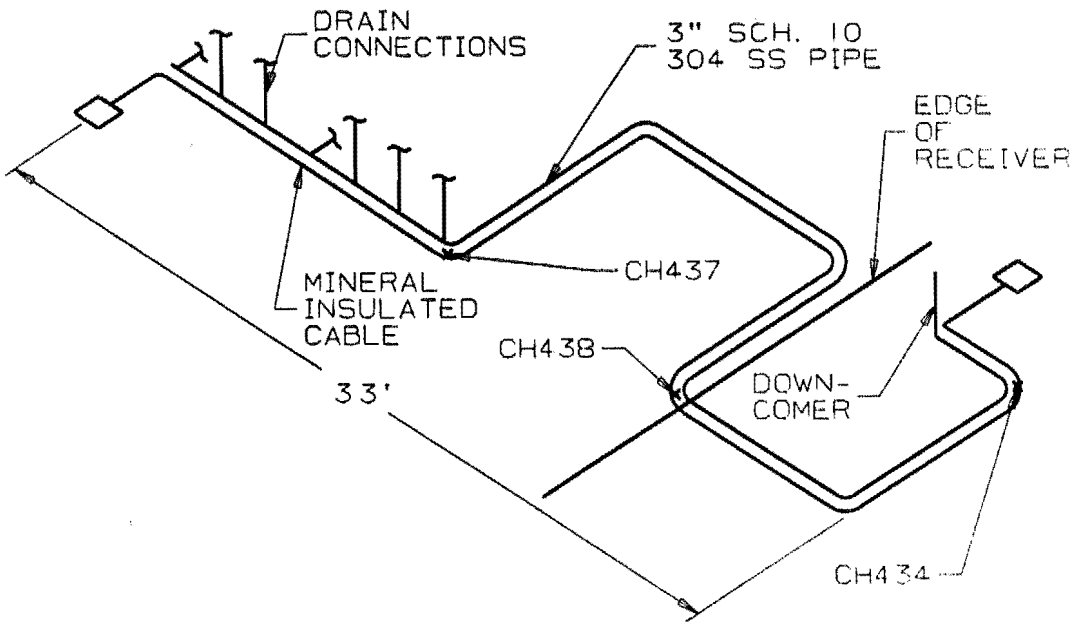

This line runs under the receiver flooring for most of its length, then exits for part of its length where the outside of its insulation and lagging is exposed to the weather. There are three thermocouples on this line, two are outside, and one under the floor. While the thermocouples outside operate near 500°F, the protected one operates at 940°F. While far from ideal, the circuit does operate and essentially must be accepted.

In other situations, however, this can lead to problems. The pressure transducers used on the receiver employ a silicone oil fill-fluid separated from the molten-salt by a thin stainless steel diaphragm. This diaphragm must be heated to prevent freezing of the molten-salt, but the oil cannot tolerate temperatures above 600°F. Originally, 14 transducers in various locations in the receiver were all heated by a common controller on a common zone. This lead to overheating and failure of most of the diaphragms. This problem was resolved by using separate temperature controllers for each diaphragm or set of diaphragms at a given location. Again, the reason is that heat loss rates can vary a great deal due to local variations in boundary conditions. A close tolerance on a component's temperature can only be maintained by using individual heaters and control to compensate for these variations.

In addition to loss balance problems, some components require uniform heating as well. The receiver flow control valves employ strip heaters on either side of the square bonnet flange to heat the bellows region of the valve. Originally the heater on one side was powered, and the other reserved as a redundant heater. It was found that this uneven heating caused thermal stresses in the valve flanges which lead to salt leaks. This was aggravate by the fact that the four valves were temperature controlled by a single controller, resulting in some valves running above their 600°F design temperature (the valve bodies are carbon steel). This problem was resolved by powering heaters on both sides of the flange in parallel, and using separate controllers for the east and west zone valves.

In addition to the balance problems, two situations developed where the heat trace could not maintain component temperature. The first of these occurred in the "safe end" tubes of the Foster Wheeler panel. In order to fill the panel, it must be heated above the salt freezing temperature. A particularly difficult area to heat was the receiver tubes between the header and the part of the panel exposed to the cavity. This region is illustrated in Figure 7.2.3 for both the Foster Wheeler panels and the Babcock & Wilcox panels. Heat trace is applied to the headers, and to the panel tubes at the point where they exit the insulation into the cavity. Between these points, the tubes bend out of plane, making them difficult to heat trace.

FIGURE 7.2.3

HEADER AND SAFE END HEAT TRACE

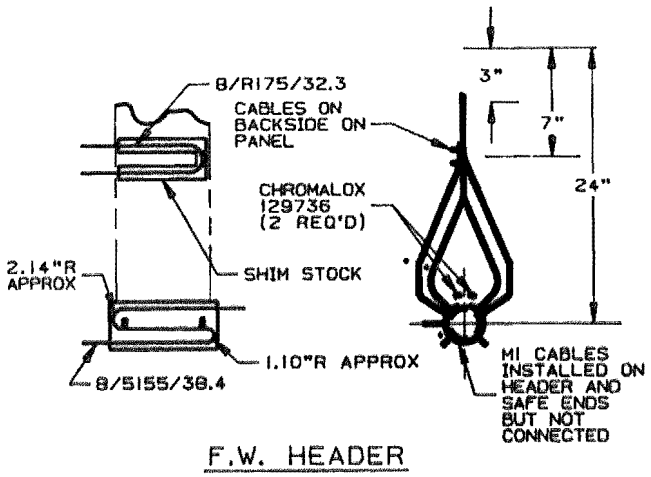

F.W. HEADER

• - THERMOCOUPLE LOCATION

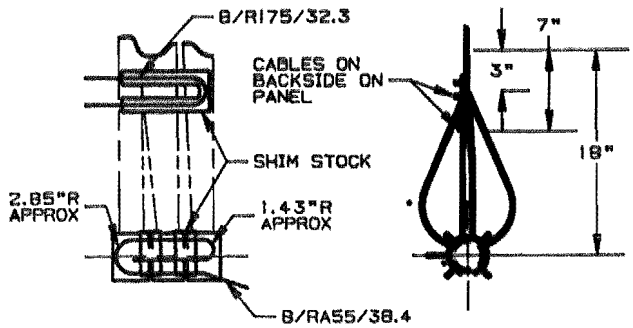

The original design called for insulating this area fully to prevent air circulation and anticipated that conduction into these tubes would heat them sufficiently. In the Babcock and Wilcox panels, this worked well. In the Foster Wheeler panels, however, the longer safe end tubes could not be maintained hot by conduction alone. Eventually, it became necessary to remove the insulation in a cavity between the out of plane safe end tubes and place strip heaters into this cavity. This resolved the problem at the expense of additional heat.

The second situation where heat trace failed to sufficiently heat a component was quite different. This was on the Nupro vent and drain valves. Here, strip heaters were attached to the valve body and a thermocouple was installed on the valve bonnet, above the top of the valve bellows as shown in Figure 7.2.4.

FIGURE 7.2.4
NUPRO VALVE BELLOWS SEAL ARRANGEMENT

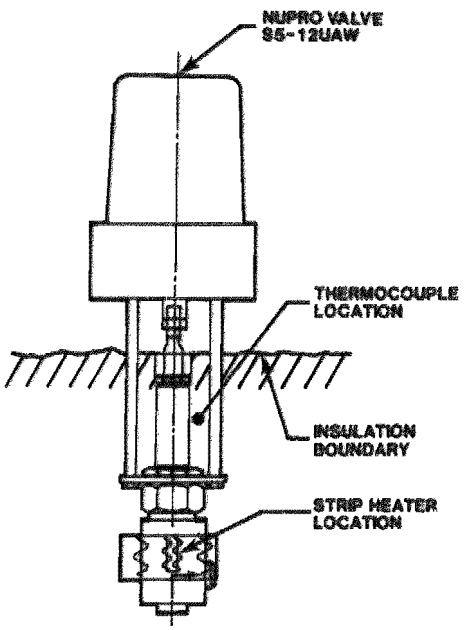

The heater was operated to keep the bellows above the salt freezing point. This worked well during standby mode with the receiver drained. However, when 550°F salt flowed through the valve, such as in standby circulation mode, or draining, the thermocouple reading dropped to around 400°F. The reason for this was that since the thermocouple was a distance away from the heater, a body temperature significantly greater than 550°F was required to get the bonnet temperature up to 550°F. With salt flow, however, the body was cooled to salt temperature, and the bonnet temperature decayed to a lower

temperature, indicating that the valve bellows was too cold to move the valve. To avoid this problem in future valve applications, care should be taken to place the heater and the thermocouple at the critical location--the bellows.

Heat Trace Controls

The active control methods employed in the test receiver's heat trace system was simple, but worked fairly well. The control logic was implemented on an Acurex data logger that was capable of opening and closing contacts in response to temperature alarms. For each heat trace zone, several thermocouples were installed to monitor temperature, but a single one was used for control. This normally worked well, as the temperature differences between thermocouples normally constant. Appendix L presents a listing of heat trace zones along with their corresponding thermocouples, and average, maximum and minimum temperature measurements for a shutdown period. This information was available through the Data Acquisition System (DAS). Informational and control channels are marked along with control set points. Normally the lowest temperature thermocouple in a zone was used for control with a set point of 525°F. This allowed the zone to shut off when salt was flowing in the system since the cold salt temperature was above this set point. In several zones, this convention could not be followed because of peculiar circumstances. This included zones where different thermocouples read lowest under different conditions, or where thermocouples were located too close to heating elements and thus responded too quickly to heater activation. In future applications, a more sophisticated heat trace controller could provide some advantages. Logical operations on temperatures such as "and" and "or" functions would be useful, along with fault checking logic to eliminate shorted or open thermocouples. significant benefits could be realized by incorporating the heat trace control into the master process controller, or providing communication with the process controller. This would allow actively turning off zones with flowing salt, and monitoring of valve bonnet temperature to prevent operation of cold valve bonnets.

Heat Trace Maintenance Issues

The heat trace system is one of the largest and most complex systems supporting the operation of the receiver. It required extensive maintenance often on a daily basis to keep the test in operation. Most of the maintenance items became fairly routine and the technicians became adept at troubleshooting and correcting the problems. This resulted in minimal impact on the test, but a significant expenditure of manpower for maintenance. Some of the most common items are discussed below.

MI Cable Maintenance

A common failure in the heat trace system was the shorting or open-circuiting of a MI cable hot to cold junction. This occurred on many occasions during the test program. To fix this required that the fault be found. This required cutting out the junction on one end of the cable, then if the fault remained, the junction at the other end. If one of the junctions was the fault, the ends would be re-brazed and the cable re-assembled and put back into service. On the first indication of the failure, it was impossible to tell if a hot-to-cold junction had failed or if the cable itself had failed. If the cable was bad, the redundant cable had to be put into service. During the test program, three cable failures occurred, one in zone 45 on the lower drain header (which had the worst temperature imbalance), one on a Foster Wheeler safe end region (which was eventually taken out of service in favor of strip heaters) and one on the hot surge tank vent line (which is discussed below). In all cases, the redundant cable operated adequately to complete the program (when a redundant cable existed).

The heat trace of zone 62, the hot surge tank vent, was added to the heat trace system fairly late in construction. Originally it was thought that this line would be left without heat trace, assuming that a single overflow would not plug the line. Because of safety concerns, this approach was dropped and MI cable was applied to the line. A single cable was applied without redundant. This cable failed part way through the test program. This failure emphasized one of the major drawbacks of MI cable. Because cable is applied

along the entire length of pipe that is being heated, when a cable must be replaced, the insulation has to be removed from the entire line. This makes the replacement of any MI cable a major task. Of course, both a primary and redundant cable were applied during the replacement, but the effort resulted in several days of down time for the test.

Strip and Band Heater Maintenance

The strip heaters and band heaters used on the valves, surge tanks, and transmitter isolation diaphragms experienced failures for a number of reasons. First, the electrical terminations are made on the heater itself, and they therefore operate at the temperature of the heater. Brazed connections to the terminals on all such heaters failed and many heaters were replaced as a result. Mechanically tying the lead wires to the terminal stud with the nut provided proved much more reliable than a brazed connection to the lug.

Another source of failure was salt leaks. Although these heaters are enclosed in sheaths, the sheaths are not tightly sealed. If even a small amount of salt leaked from a flange with this type of heater, the salt entered the heater and shorted it out. This occurred several times on transmitter isolation flanges and on the receiver control valve bonnet flanges.

Although many failures of these heaters occurred, they benefitted from their compact nature. This made the heaters relatively easy to replace by removal of only a small window in the insulation. Once installed properly, the heaters proved fairly rugged. This combined with their ability to be replaced with relative ease makes then a good choice for any component capable of distributing heat within itself by conduction from one or several of these heaters.

7.2.3 Emergency Flow System

The receiver subsystem design includes an emergency flow protection system in the event of loss of power to the heliostat field or a pump trip. In either event, the hot and cold surge tanks were sized to maintain flow to the receiver for a period of 90 seconds. The flow provides cooling for the

receiver while the heliostats are removed and, in the case of power loss, switch over to backup power. A complete description of the surge tank sizing and the emergency flow system is discussed in Section 3.5.4.

Simulations to test the emergency flow system were run in order to evaluate the capability of the cold surge tank (CST) to maintain flow for 90 seconds. On January 13, 1987, the system was tested when an unplanned pump trip occurred. High current signal, caused by an increased load, was the result of the boost pump impellar coming off the shaft, tripping the pump off. This forced the flow to the receiver to be maintained by the CST while the heliostats were removed. At 14:25:38 the pump tripped, within 5 seconds the CST level control valve FCV151 closed and the CST began supplying flow independently to the receiver. Within the first 30 seconds the flux was removed and the emergency cooling maintained. Beyond the initial 30 seconds, flow to the receiver was maintained for an additional 20 minutes as shown in Figure 7.2.5.

7.2.5
COLD SURGE TANK BLOW DOWN (1/13/87)
RECEIVER FLOW

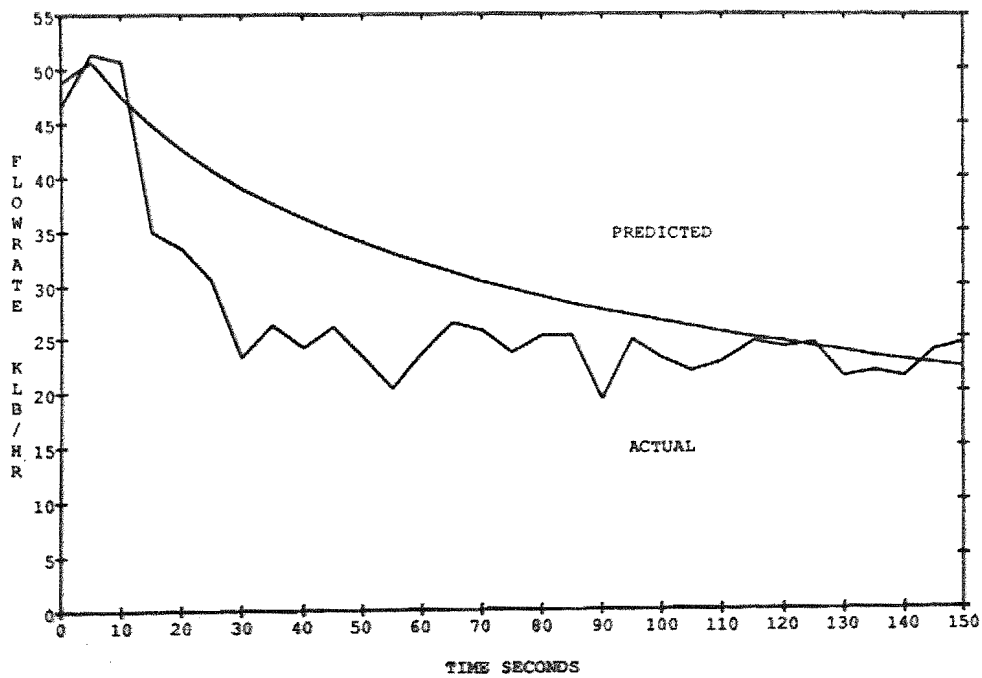

The actual flow was maintained without additional pressurization from air bottles and decayed naturally as the pressure decreased in the CST. The actual flow falls below that predicted due to the fact the code LOP, which predicted the flow, assumes a constant valve position during the event. Actually, the flow-control valves adjust to maintain flow while the pressure drops off. Figures 7.2.6 and 7.2.7 show the decaying tank pressure and level as compared to that predicted by LOP.

FIGURE 7.2.6
COLD SURGE TANK BLOW DOWN (1/13/87)
SURGE TANK PRESSURE

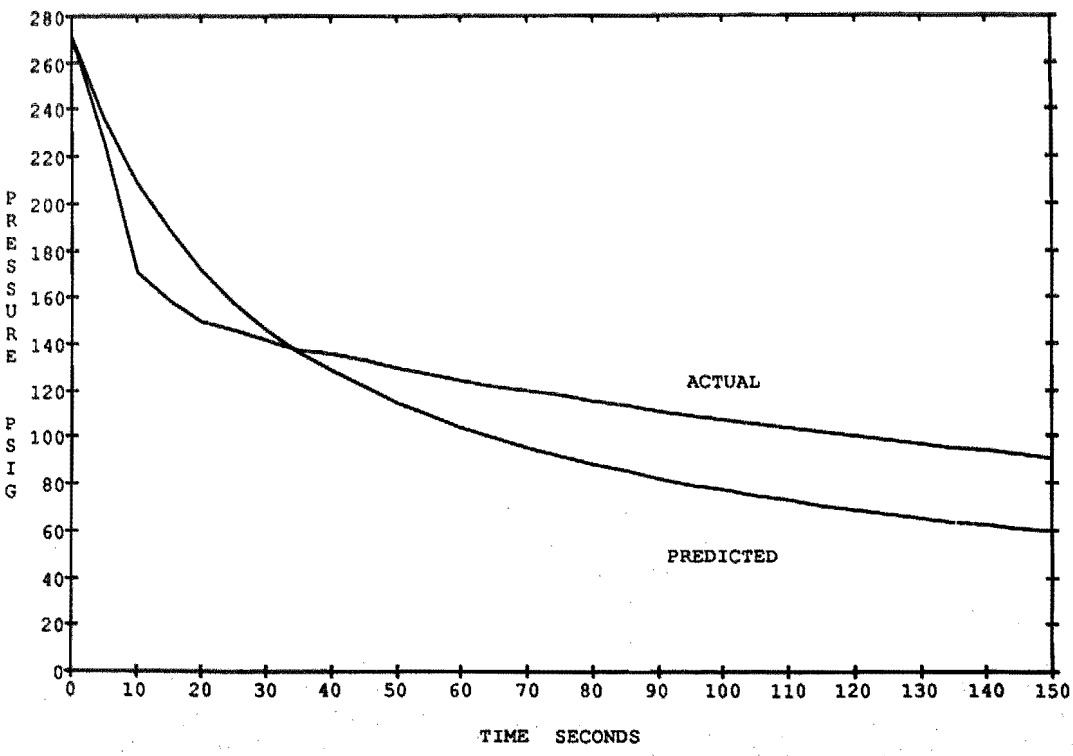

FIGURE 7.2.7
COLD SURGE TANK BLOW DOWN (1/13/87)
SURGE TANK LEVEL

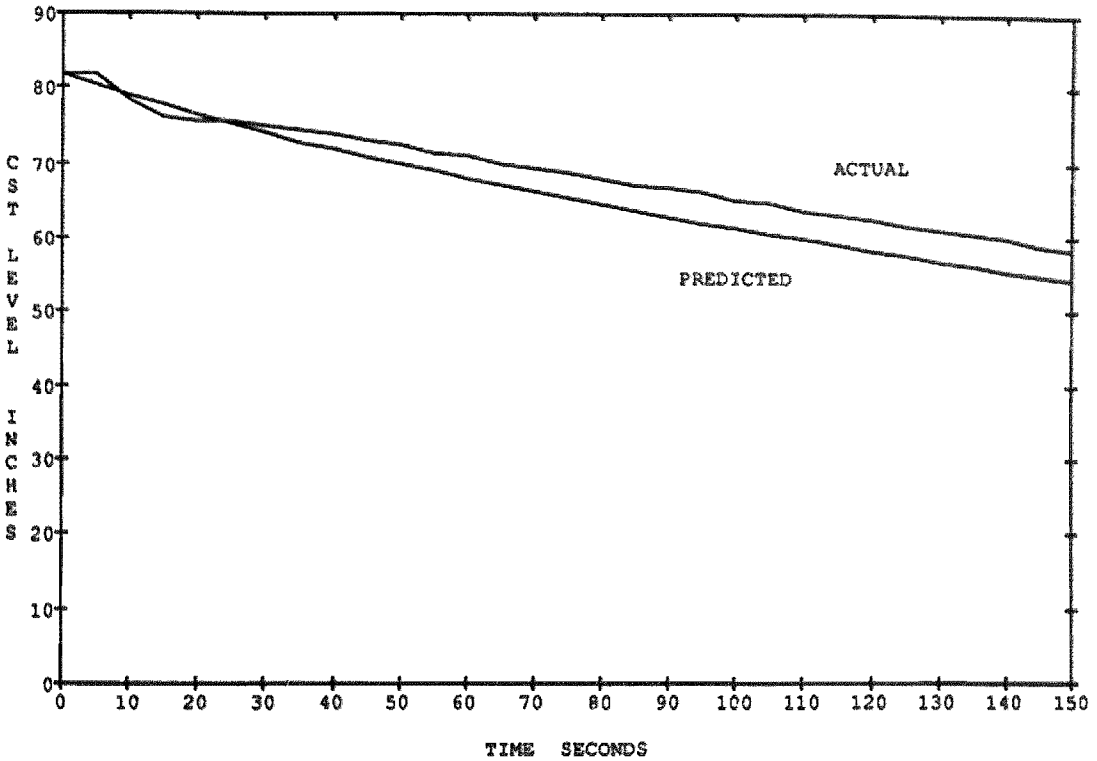

The flow-control valves for the predicted flow and pressure have been set to initial valve positions which occurred during the actual event. The initial pressure of the CST when the pump tripped was also programmed into LOP for comparison.

Overall, the emergency flow system performed as expected and was capable of maintaining flow to the receiver until the heliostat field was removed.

SECTION 8

CONCLUSIONS AND RECOMMENDATIONS

D. Smith & P. Reed -
Babcock & Wilcox Corp.
S. Saloff, G.Riley, and M. Lanning -
McDonnell Douglas Astronautics Corp.
J. Chavez and R. Skocypec - Sandia National Laboratories

The objectives of the test program were outlined in Section 1.3. These objectives were addressed by the test program. Many of the objectives were quite broad in nature and could not be fully met, but generally all the objectives were met, at least in part, by the test program. Table 8-I lists the specific objectives listed in the introduction to this report, and summarizes the results and accomplishments of the test program. The balance of this section presents a summary of the entire test program broken down by major tasks, and presents the significant conclusions drawn and recommendations offered for future designs. Recommendations are generally directed at a scale up of the test receiver to a larger intermediate demonstration plant, or commercial scale plant.

TABLE 8-I
TEST PROGRAM RESULTS AND ACCOMPLISHMENT SUMMARY

Specific Objectives	Results and Accomplishments
Demonstrate receiver performance and operation under steady-state, transient, and emergency conditions.	Receiver efficiencies determined from data in reasonable agreement with analytical predictions; error band on efficiency data identified. Panel Thermal Expansion as expected.

TABLE 8-I (CON'T)

Define the operating range, flexibility and limitations of the receiver design.	Identified salt temperature ramp rates during cloud transients for which header design is inadequate.
Obtain, evaluate and document receiver efficiency to verify design and identify uncertainties.	Identified a mis-match of salt flow and absorbed flux during cloud transients for which tube stresses are 50 percent over design.
Investigate the effectiveness of the emergency cooling system design.	With proper operation, significant energy collection during partly cloudy conditions transients is possible.
Verify the ability of the thermal expansion/contraction design to prevent excessive thermal stresses.	Salt leaks at tube clip welds did not impact receiver operation.
	Emergency cooling system operation/strategy works.
	The use of a software equipment protection system (EPS) was demonstrated.
Verify receiver thermal-hydraulic characteristics.	Receiver pressure drop agrees well with predictions.
	Turn down ratio of 4:1 was achieved.
Develop efficient operational methods and control systems to maximize receiver output.	On-line energy collection at sunrise demonstrated using cavity heaters for pre-sunrise warm-up.

TABLE 8-I (CON'T)

	Solar start-up at sunrise without cavity heaters demonstrated.
	Significant energy collection during partly cloudy conditions demonstrated.
	Algorithm was developed which controls receiver outlet temperature within reasonable limits, minimizing trips.
	Flux gages are a necessary and important part of receiver control.
Demonstrate the operation, performance and reliability of critical receiver components, overnight thermal conditioning operations, cavity doors, and door seals.	Receiver panels have performed well; however relatively low number of equivalent design thermal cycles to date.
	Bellows seal valves, for both control and isolation service, have performed satisfactorily; in particular the nested bellows design in the control valves shows promise.
	Incremental improvements in the design and operation of heat trace systems have been made.
	MI cable provides satisfactory heat trace capability with active control.
	Strip heaters are a viable alternative to MI cable in certain applications.

TABLE 8-I (CON'T)

	Insulating heat traced piping with a flexible inner layer of blanket is better than using rigid calcium silicate alone.
	Panel insulation performed well; no degradation due to shine through.
	Flux gages provided satisfactory signals and response for the receiver outlet temperature control.
	Salt side, low DP measurements (flow, level) continue to be less than satisfactory.
	Overnight thermal conditioning methods were demonstrated: --circulation --cavity heaters.
	Cavity doors and door seals operated and performed reliably.
Investigate panel absorber surface coating durability.	Proper coating application and curing are required for good coating absorptivity and long life.
	A laboratory measure of absorptivity (0.97) is achievable in field installations with proper curing.

TABLE 8-I (CON'T)

	Coating absorptivity has remained essentially unchanged throughout the test period.
	Salt leak sites (tube clip weld leaks) locally damage the coating and degrade the absorptivity.
Demonstrate panel tube-wall conditions compatible with 30-year life.	Heat flux was shown to be consistent with 30-year limits.
	Cloud transient flow/flux mismatch showed tube overstress not consistent with 30-year life.

8.1 Receiver Fabrication

The receiver was fabricated by conventional means employed commonly in the boiler industry. The most solar unique facit of the receiver, from the standpoint of fabrication was the use of thin (1/6 mm, .064 inch) walled alloy 800 tubes. Although alloy tubes are often used in boiler, thin-walled tubes are unique to this receiver design where pressures are relatively low, and heat fluxes are high. The following issues were found to be critical in receiver fabrication, primarily due to the thin-walled tubes employed.

8.1.1 Welds

Receiver panel welding remains a critical fabrication process. Proper control of heat input to the welds reduces the potential for burn through of the receiver tube. An automated welding process is recommended for the tube attachment welds and tube butt welds of a commercial panel offering control of heat input and repeatability.

8.1.2 Inspection

A gas "soap bubble" leak test effectively located the tube leaks of the receiver panels. Future inspection of receiver panel welds should include this test (in addition to a dye penetrant test) to assure weld quality.

8.2 Erection

Several conclusions were drawn from the experience gained through the erection of the test receiver. Recommendations regarding specific aspects of erection are presented to promote the success of future receiver installations.

8.2.1 Schedule

An erection schedule was developed using the critical path method (CPM) and computer scheduling software. Construction activities and span time estimates were determined as a joint effort between Babcock & Wilcox and Sandia; material deliveries were supplied by vendors. The use of a computer generated schedule offered an effective means of updating the schedule and identifying critical activities. Realistic span time estimates are essential to effective scheduling and should be obtained from the best source of experience.

8.2.2 Quality Control

Measures taken to ensure quality during construction are also applicable to commercial receiver construction.

8.2.3 Daily Status Meetings

Daily status meetings, conducted at the site, were effective in resolving problem areas and schedule conflicts, and aided day-to-day planning. In commercial construction, daily status meetings are recommended between the responsible construction personnel and contractors to review work in progress and plan near term activities, identifying potential problem areas and any conflicts.

8.2.4 Design Reviews

Potential problem areas can also be identified through design reviews avoiding lengthy and costly delays during construction.

8.2.5 Material Inventory

Careful handling of material inventory is necessary to maintain quality control. Material deliveries should be checked against the specifications, purchase order (quantity) and inspected for damage.

Material certificates for stainless steel piping were checked for minimum carbon content. Low carbon stainless steel is commonly used by industry and therefore easy to obtain. Because of the high operating temperature at the receiver, the Code requires the use of high carbon stainless steel. To prevent accidental substitution of the low carbon stainless steel, this requirement should be emphasized to the piping vendor.

8.2.6 Vendor Interface

Equipment failures often occur during initial operation. Both the customer and the vendor should be present to witness checkout of critical equipment for early detection of problems. Vendor involvement is recommended for installation of equipment such as pumps where fit-up is critical. Equipment warranties occasionally expire before equipment is installed and operated. Every attempt should be made by the purchaser to obtain a warranty that covers initial operation of critical equipment such as pumps, valves and instrumentation.

8.2.7 Heat Trace

Heat trace cable was purchased in bulk (coil) and field terminated. Numerous hot-to-cold junctions were rejected. Shop fabricated terminations are recommended to improve the quality of the connection and reduce the potential for failure.

Heat trace drawings should contain all necessary information to install and test the cable. In difficult applications, a description of the cable routing would be helpful to minimize the potential for damaging the cable as a result of the installation.

Chromalox strip heaters were replaced due to failure of brazed connections to heaters. Replacement heaters used mechanical connections. Band heaters were used on transmitter flanges to provide a uniform heating of the transmitter diaphragm.

However, numerous pressure transmitters were damaged from overheating of the Syltherm oil in the capillaries of the transmitters. An attempt to maintain temperature using available variacs (passive control) was unsuccessful. Individual temperature controllers were then added to each transmitter heater zone controlling diaphragm temperature between 510°F and 520°F. The transmitter supplier, Rosemont, recommended that the temperature not exceed 600°F. Consideration should be given to the use of transmitters with higher temperature capillary fluids such as "NAK."

Many of the safe-end heaters were incapable of maintaining temperature. Heaters were installed on the headers and the tubes were heated by conduction. Insulation was modified as necessary to improve the conduction. In the case of the Foster Wheeler lower header, insulation was removed and the heater was heated radiatively. The oven heater arrangement was effective in heating the safe end tubes and is recommended in future designs.

Future heat trace systems should include some provision for heater replacement. Heater elements with mechanical connections are recommended for difficult areas such as the header-safe end region of the receiver. Compact heater elements using mechanical connections should be used to the maximum extent in future electrical heat trace systems to promote uniformity of hardware and improve serviceability.

Redundant protection of individual heaters should be considered to prevent overheating in the event of a failure of a primary controller.

8.2.8 Paint

The Pyromark 2500 receiver paint was adequate for the test receiver, however, application is critical. The specifications described in Section 4.2 are recommended for a paint procedure developed for a commercial receiver.

8.3 Receiver Operation

The experiment was effectively controlled by one operator using the NET-90 digital control computer. The heliostats were controlled by an additional operator because the configuration in this experiment used a separate heliostat computer. The use of three monitors in the digital control system was very useful and allowed the operator flexibility in selecting various subsystems to be displayed and controlled. In addition, the active graphics were important in allowing the control room operator immediate access to critical information in cases of emergency. In future commercial scale facilities, a master control system should be integrated into the design of the overall system. This would allow a single control room operator not only to control the process but also the heliostat field. The master control system computer could then command the heliostats as required, on and off the receiver, which could lead into a completely automated system.

8.3.1 Basic Operation

The operations consisted basically of start-up, normal operation and shut-down, with an additional test: overnight conditioning. The start-up of the receiver was relatively easy because the cold and hot surge tanks were the same size and relatively large. This relieved the operator of concerns of spilling salt from the hot tank vent. The start-up sequence could easily be automated and should be in a commercial-scale facility. Early morning start-up using heliostats, cavity heaters, or overnight salt flow worked very effectively in collecting the energy during the early morning hours. From an operational standpoint, any of these methods could be used for early morning start-up.

Subsequent to the start-up during the normal operation of the receiver, steady-state operation was performed routinely and automatically by the digital control system. During transient conditions and actual cloud conditions, the receiver control algorithm automatically controlled the flow rate on each half to maintain the correct outlet temperature. Controlling the receiver was basically reduced to observing the alarm page on one CRT in order to react to any emergency condition. Emergencies involving loss of commercial power, were simplified greatly because uninterruptible power supplies were installed on the field control computer and control room monitors. In the event that a control computer failed, the automatic heliostat SCRAM would be initiated, removing the heliostats from the receiver. In a commercial-scale power plant uninterruptible power supplies should be installed on all critical control hardware. Automatic system trips should also be incorporated in the controls to protect plant equipment.

The shut-down phase of the operations was simplified greatly because the surge tanks were the same size and also because the cold surge tank could be vented. This allowed for an easy gravity drain with equalized pressures throughout the receiver. This sequence could also be automated and should be automated in a commercial-scale plant.

From an operational standpoint, the overnight conditioning, in which salt flowed through the receiver, was very effective in maintaining the receiver above the freezing temperature of salt. It also allowed the receiver's temperature to be increased as soon as insolation was acquired, because the receiver was already in salt flow. Useful energy was collected immediately upon acquiring insolation. This sequence could easily be automated in a commercial-scale power plant.

The use of radiant heaters to preheat the receiver panel could also be effectively used in a commercial plant, with the process computer controlling a timer to turn the heaters on at the appropriate time, ensuring proper panel temperatures are ready at sunrise.

8.3.2 Procedures

The procedures used to control the receiver's start-up, operations, and shutdown could very easily be adapted to a commercial-scale plant, assuming a similar receiver configuration. Two separate sets of procedures should be considered for a commercial plant; one to train the operators in the control room to operate the receiver (and the complete facility) and a second set as "one line" procedures for operators already familiar with the system. These "one line" procedures could be installed in the process control computer and displayed on the monitor in the control room for easy access. Even the automatic start-up, operational, and shutdown sequences could be displayed on the monitor.

8.3.3 Equipment Operation

From an operational standpoint, only four basic pieces of equipment are discussed here--trace heat, valves, pumps, and piping. The receiver's trace heat was actively controlled and was cycled on and off as required to maintain a proper temperature on the components. This system functioned very effectively, but could be refined for a commercial plant by integrating control into the overall control system. Each zone should be integrated in the process control computer, and critical components such as valves should be interlocked by temperatures in the process control computer. This integration would not allow the control room operator or the computer to move the position of the valve and possibly damage the bellows if its temperature were not acceptable.

The relatively small control valves used on this experiment operated effectively; however, the valves were constantly "hunting" throughout the experiment. As a result, maintaining constant flow was difficult.

In summary, from an operational standpoint, this receiver was very forgiving in start-up, normal operations and shutdown, and the procedures can easily be automated and adapted to commercial-scale plants of similar receiver configuration.

8.4 Control of the Receiver

The receiver's controls essentially performed as designed. Modifications were made, but none of them altered the basic control structure or methodology.

8.4.1 Simulation

The use of a computer simulation of the receiver subsystem during design simplified the basic control structure. Even though the simulation did not perfectly match the actual performance of the receiver, the similarity was quite good.

The real usefulness of a simulation is to provide an understanding of and insights into the phenomenons to be controlled. Also, different control strategies can be easily evaluated relative to one another, so that those strategies that hold promise can be tested on the real system. This reduces start-up and test time considerably, provided the simulation reasonably emulates the real system.

8.4.2 Controls/Fatigue Issues

It is highly recommended that controls and mechanical engineers coordinate their design efforts relative to receiver tube stress and fatigue in future designs. This issue has major implications for the operation, procedures, controls, annual performance and lifetime of the receiver.

During a cloud transient, the entire collector field remains focussed on the receiver. As a result, all of the available solar energy is absorbed by the salt. The control algorithm for this receiver was designed to maintain 1050°F outlet salt temperature to the maximum extent possible. Test results, however revealed that this can result in severe fatigue cycling of the receiver. In order to reduce the fatigue cycles, it will be necessary to make a compromise

between maintenance of maximum salt outlet temperature, and fatigue life, or ultimately flux limits and receiver sizing which also govern fatigue life. In order to make such a compromise, it will be necessary to look at a solar plant as a system and judge the importance of maintaining the 1050°F outlet temperature.

In a conventional molten-salt solar electric generation plant, the temperature of the salt collected by the receiver governs the temperature of the steam that can be produced by the steam generator. This temperature affects the efficiency of the turbine that drives the electric generator, and thus effects the overall thermal-to-electric conversion efficiency of the plant, or determines if the turbine can even operate. Given knowledge of these systems effects, the control algorithm could be designed for best plant performance, and the fatigue impact would be factored into the receiver design.

8.4.3 Automation

Further automation of solar power plants is possible, and it is recommended that this be pursued. Automation of solar power plants would provide:

1) Reduced operation and maintenance cost;
2) Remote observation & plant management; and
3) Maximum system performance.

However, initial costs and capitalization would be higher and the initial system design should consider providing the ability to achieve this goal. To do this, all control and monitoring of the process, heat trace, and ideally the collector field would need to be integrated into one control system.

8.4.4 Surge Tank Control

Future receiver designs should use cold surge tank pressure control as opposed to level control. The receiver controls were originally designed for level control, but were switched to pressure control early in the test program. Since the tank is closed, pressure and level are directly related so pressure control accomplishes the same effect as level control. Pressure

instrumentation in this application has much quicker response and is more reliable. In addition, cold surge tank pressure is more important to maintaining receiver flow control. Level is important, but it is adequate to just monitor level and issue an alarm to the operator if it goes out of range.

8.4.5 Receiver Salt Flow Control

Measurement of receiver salt flow is important to the control of the receiver's outlet temperature. This makes a reliable flow sensing element important in any receiver design. In addition, accurate flow measurement is required for evaluating receiver performance. In this receiver, the flow meters were found to be unreliable. Consequently, panel inlet pressure was calibrated with flow and used in the control algorithm. In addition, for more accurate measurements, cold salt pump "sump depletions" were used (this being a "bucket and stopwatch" type method). This proved adequate for the test, but direct flow measurement would be preferable, and further development of molten-salt flow sensors merits further investigation. An alternate flow measurement method, such as the sump depletion method should also be incorporated in future designs as a backup for "on line" recalibration of flow meters.

Flow-control valves are also a critical element in receiver control. In the receiver, valves with short strokes were used as a compromise to reduce the size of the bellows seal. This resulted in poor valve performance as the valve positioner was not accurate enough for this stroke. Care should be taken when specifying control valves to assure accurate control.

8.5 Receiver Performance

One of the most important characteristics of the receiver is its ability to collect energy. The most important aspect is the basic steady-state efficiency. Significant solar energy, however, may be available in less than ideal steady conditions. It is therefore also important to characterize the receiver's ability to start up under various conditions, and its ability to operate and collect energy in partially cloudy conditions.

Performance of the collector field is also important to the ability to collect energy. The collector field provides not only the operating flux, but also can serve the function of preheating the receiver. Proper aiming is required to serve these functions.

8.5.1 Steady-State Performance

The basic receiver efficiency was calculated by two methods. The first, and most straightforward is the "calculated input" method discussed in Section 6.1. The second method is the "method of complementary field partitions" (flux-on testing) discussed in Section 6.3. Both methods suffer from fairly large uncertainties in the resulting efficiency measurements. The steady state efficiency derived by both methods is presented in Figure 8.5.1.

FIGURE 8.5.1
RECEIVER EFFICIENCY

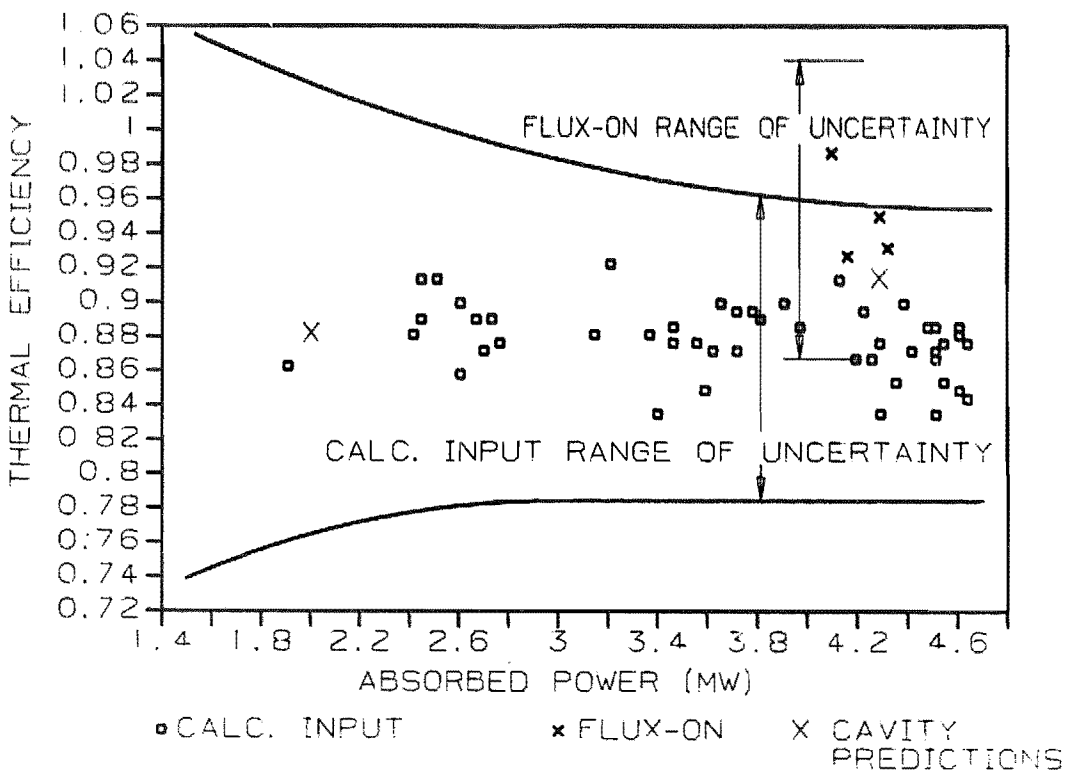

Overall, the data supports the conclusion that the receiver has an efficiency of about 89 percent, dropping a few points at lower powers. The complimentary field measurements support the calculated input method values at the higher power levels, although the efficiency values derived by this method are probably high based on comparison to predictions of radiative losses. The data also supports the analytical predictions of the CAVITY code also shown in Figure 8.5.1. This is very important as such codes can allow optimization of the design. A drawback in the data is the wide band of uncertainty, shown in the figure.

Accurately evaluating the performance characteristics for the receiver is essential for designing an efficient, large-scale commercial receiver. As was mentioned in Section 6.7, flow-rate and temperature measurements are critical in this evaluation. Unfortunately, current technology has not yet developed a flow measurement device capable of operating accurately in a molten-salt environment. Therefore, to accurately measure flow rates of salt, cold-salt sump depletions will have to be continued throughout future testing. Temperature measurements, however, can be accurate if care is taken in thermocouple application.

8.5.2 Receiver Start-up

Three methods of starting the receiver were demonstrated. On most days, the cavity heater was operated overnight, allowing the receiver to be filled with the receiver door closed, prior to focusing solar energy on the receiver. This was the most convenient method of start-up, but a penalty was paid to power the heater overnight. A cheaper alternative was start-up using solar energy to warm the panels. This method required more operator involvement in the start-up. If done at sunrise on a clear day, only a small amount of power is lost while the plant is started. Approximately 45 minutes are required to heat the panel, fill the receiver with salt, and bring the full collector field on to target. Partially cloudy conditions can make solar start-ups difficult, even though a significant amount of solar energy may be available.

The third start-up method is similar to the first in that the cavity is heated overnight. With this method stored, solar energy is substituted for the

electric cavity heat by circulating salt through the receiver. Not only is this a more economical way to heat the cavity, but it carries the additional benefit of substituting stored solar heat for most of the electrical heat trace on the receiver piping as well as that on the riser and downcomer. For the test, the main salt pumps were run and the flow was throttled back to perform the test. Because the main pumps were used, the pumping power for this was greater than all the heat trace saved, but the required pumping power was small. A small pump could have done the job for a fraction of the heat trace power saved.

All three start-up methods were demonstrated, and there is a high degree of confidence that any of them would work on a scaled-up plant. The most efficient method is salt circulation in the receiver. It makes a big cut in electrical parasitics, and gives the flexibility to operate any time there is sun. The other two methods are workable, but carry some limitations.

8.5.3 Partial Cloud Performance

Another aspect demonstrated by the test is that energy can be collected by this type of receiver in partially cloudy conditions. Analysis of the Solar 1 plant performance showed that on an annual basis, this can make a big difference in the "bottom-line" energy produced at a plant. At Solar 1, almost 25 percent of the integrated annual solar direct insolation is considered not "available" due to cloudy conditions or wind [37] (wind is a limitation on collector field operation and the two effects are not separated in the analysis). This is a big advantage for molten-salt plants with storage, allowing better annual efficiencies. Although energy collection was demonstrated, some mechanical challenges were discovered that must be addressed as discussed in Section 7.1.

8.5.4 Collector Field and Aiming Strategies

One of the most important methods for maximizing the receiver's performance is to optimize the collector field's aim-point locations. For example, to minimize spillage, it is best to locate the heliostat aim points at the center of the aperture. Although this aiming strategy would minimize spillage, flux

levels would exceed the allowable limits for the receiver panels. As a result, aim-point locations are spread along the vertical centerline of the receiver. Each aim point, however, remained in the aperture plane.

The normal operational aiming strategy used for the receiver was effective in reducing spillage and minimizing the incident power on the nonabsorbing panels. Flux gage data also indicated that flux levels did not exceed maximum allowable flux limits on the absorbing panels. Optimization of the normal operational aiming strategy is still required. Lack of test time prevented a detailed evaluation of daily absorbed energy as a function of aim-point locations.

The collector field aiming strategies developed for warming the receiver panels were successful in achieving start-up without the use of cavity heaters. Receiver warm-up was accomplished at both sunrise and midday using two separate warm-up patterns. Each pattern was developed by trial-and-error basis in order to obtain panel temperatures between 500°F and 1000°F. In addition, each pattern was capable of warming the receiver panels in approximately 15 minutes. Transitioning to receiver start-up was done by taking the heliostats off target, closing the cavity door, and beginning salt flow to the receiver. Future testing could refine this start-up procedure, minimizing the transition time from warm-up to normal operation.

8.5.5 Analytical Modeling

The current modeling effort for the test receiver using the CAVITY computer code indicates the global receiver thermal efficiency is invariant within a few percent with most parameters investigated, although front surface temperatures vary considerably, particularly with the type of convective submodel used. Parameter variations affected local distributions more than the global results. Therefore, the modeling detail required is dependent on the data desired. If strictly global efficiency estimates are required, significant convective modeling efforts may not be necessary. If additional

information is desired, such as local temperature distributions, a more detailed model is warranted. Optimizing the design of the receiver or understanding the effects of design or material changes on the receiver's thermal conditions both require models that realistically portray the cavity's energy transfer, as demonstrated by these results.

8.6 Design Evaluation

The receiver and its component equipment must be able to stand up to the intended service and provide the required life. Although the receiver was designed for the test conditions, not all situations can be anticipated. This is one of the main reasons for performing small-scale system tests, so that any short comings with design methods can be identified and addressed before larger plants are built.

8.6.1 Receiver Panel

The main solar-specific component of the receiver is the receiver panel. Sizing of the receiver panel is based on considerations of fatigue of the panel, and the panel must accommodate normal and transient operation to achieve the required life. Because the test is of short duration, relative to the panel's intended lifetime, failures alone cannot be used as an indication of inadequate design. The test conditions must be analyzed to determine if the panel would be expected to achieve the required life.

Steady State Panel Flux

The panel was designed to withstand a basic operating solar flux level (based on thermal stress fatigue limits). The receiver cavity geometry was laid out to achieve fluxes that approach, but do not exceed the limits. The test was not nearly long enough to confirm if these limits are truly valid, but long lifetime is likely, as long as the flux limits are not exceeded. The measurements of the flux gages confirm that the actual flux levels were close to those predicted for the design. This is discussed in Section 7.1. The accuracy of the gages, however, is not good enough to confirm the predicted solar flux with precision.

Transient Response

During transient operation, the thermally induced panel tube stresses that contribute to fatigue are no longer characterized by just the level of solar flux. This is because the salt flow rate is being controlled in an attempt to maintain a desired outlet temperature, not to maintain steady cooling of the tubes in proportion to the flux level. As shown in Section 7.1, this can lead to stresses that exceed the design level by as much as 50 percent. This can have large implications on fatigue life as a 50 percent increase in thermally induced stress (or more precisely: mechanical strain) can result in reduction of fatigue life by a factor of 10. This must be addressed from two points of view. For the mechanical engineer setting flux limits based on thermal fatigue, an allowance must be made for transient effects; that is during transients, the salt flow rate cooling the tube wall will not always be proportional to the flux. The controls engineer must recognize that temperature control is not the only objective of the controls. Flow control in transients will have a marked influence on the lifetime of the receiver. Another objective of the control algorithm must be to minimize the fatigue service of the receiver.

Panel Support System

When the panel is heated, it must be free to expand so large stresses and distortions do not result. The receiver panel support system is designed to control the position of the panel, while allowing for this growth. The receiver was built with panels of two different types: one by Babcock & Wilcox and the other by Foster Wheeler. Section 3.2 includes a description of the panel support systems of both types of panel. The Babcock & Wilcox design employs lateral supports, or "buckstays" that are attached to the structure using rollers which allow the panel to grow longitudinally. Individual tubes are each held to the buckstay with clips that allow the tubes to move relative to each other to account for individual expansion. The Foster Wheeler supports use a rotating link to attach panel buckstays to the structure. These links allow the panel to grow longitudinally similar to the rollers, but result in a small amount of horizontal motion of the panel as the link rotates. The tubes of the Foster Wheeler panel are attached to the buckstay

by a slotted clip. This slot allows for a tube-to-tube expansion. After several months of operation while conducting the test, recorded panel displacements, and observations indicate that both expansion systems work well. Longitudinal growth of the panels matches design predictions, and lateral deflections of the tubes are small. No permanent tube deformations were observed, however, tube deformations are time dependent and could potentially develop in continued operation. Regular visual inspection of the panels is recommended for future receiver testing. The lateral movement imposed by the rotation of the Foster Wheeler links has resulted in no ill effects. In several locations in the panel, the tangent tube construction has allowed gaps to develop between tubes, but these have been relatively small, and no damage to insulation or buckstays has been observed.

Tube Clip Welds

One deficiency in the panel support system has become apparent. The tube clips of both designs are welded to the back of the tubes. In both cases, a manual "TIG" (tungsten inert gas) welding process was used. Small leaks have developed in the welds in locations where "burn through" occurred. Burn through occurs when the tube-wall metal under the weld melts through the full wall thickness. When the metal solidifies, it shrinks, and can leave a small hole. Several holes were detected and repaired during fabrication and erection, and some appeared after the receiver was operated. Although the holes are very small, salt for the leaks migrated to the front of the tubes, where it reacted with the paint causing blemishes on the panel front surfaces. The leaks were small enough that they probably would have never been detected in a water system. Salt, however, does not evaporate and tends to creep along hot surfaces in a very thin film. The damage to the receiver paint occurred at 13 locations. Most of these were small (about an inch in diameter) and some of them appear to have stopped growing as if the leaks have become plugged. A few of the blemishes have grown quite large (18 inches long by 8 inches wide). At the end of (this phase) the testing, approximately 2 percent of the panel surface was affected.

The problem is one of fabrication procedures. It is expected that with additional development of weld procedures and quality control, no leaks would occur. For a large plant, automated welding equipment should be used to improve the quality of the welds.

Header Designs

One additional deficiency was found with the panel design. This was with the design of the headers, and the tube to header welds. Salt temperature ramps up or down each time the receiver is started up, shut down, or a large cloud passes. These temperature ramps set up thermal stresses in the headers as different parts respond to the temperature changes at different rates. The two different header designs employed in the receiver had deficiencies when dealing with the rapid temperature ramps that occurred. The problems were different in each header design.

In the Babcock & Wilcox headers, the critical location was the weld where the "safe end" tube was welded to the header. A "J" groove type weld was employed here. This type of weld is not a full penetration weld, and this results in a stress riser at the root of the weld. The temperature ramp rate limits allowable for this type of joint were often exceeded during normal testing. Although no failure has occurred, it is recognized that the design is deficient in this area.

In the Foster Wheeler header, heavy wall tube stubs were welded to the header, after which they were drilled through. This allowed a full penetration weld with no stress riser and little discontinuity in wall thickness between the stub and header. This configuration did not have the temperature ramp limit of the Babcock & Wilcox design. However, the Foster Wheeler header design did have a temperature ramp limit similar to the Babcock & Wilcox design as a result of combining several pass headers into a single assembly with divider plates separating the header chambers. These divider plates are subject to large thermal stresses during temperature ramps.

In a subsequent receiver design, this limitation should be eliminated by design. This would be possible by combining the best features of both headers employed by this receiver.

Paint

A final component of the panel to consider is its paint. The paint used was Pyromark series 2500 to blacken the panel surface for high absorptivity. The paint is applied by ordinary methods, then cured to achieve its final properties. The solar absorptivity of the paint was measured before and after testing. The solar weighted absorptivity of the paint after its initial cure was an average of .973 based on readings taken at 57 locations on the panel. Individual absorptivities ranged from .967 to .975. These measurements are indicative of fully cured paint. After testing, absorptivity measurements were taken again. No degradation was apparent.

The performance of the paint is apparently the result of the careful curing process used in the cavity receiver. By using electric heaters inside the closed cavity, paint curing procedures were followed exactly. Properly cured paint has high absorptivity, adheres well, and does not degrade rapidly in service. Care should be taken to insure a properly cured paint coat. When applied properly, Pyromark paint is an excellent receiver coating.

Balance of the Receiver

Aside from the receiver panel, there are many aspects of the receiver subsystem that are specific to molten-salt or solar applications. These include the cavity enclosure and aperture frame, the door, heat trace, molten-salt valves and piping, and instrumentation. Conclusions from the tests, and recommendations for future plants in these areas are presented here.

Cavity Enclosure and Aperture

The insulation board, framing the aperture, and the blanket insulation used in the cavity and attached to the backside of the panels remained intact throughout testing and showed no signs of degradation. The cavity enclosure,

receiver door, and aperture structure were effective in minimizing heat loss from the receiver panels. To attain maximum sealability in a commercial receiver design, field-installed cavity and panel insulation is recommended. This approach eliminates the need for costly panel-to-panel and panel-to-cavity joints that are likely to contribute to heat loss.

Receiver Door

The receiver test was successful in confirming the door design. Considering the design modifications to the door rollers and seal, the receiver door performance exceeded expectations. The door demonstrated reliable operation and excellent sealability. The larger door of a commercial receiver design however, would require greater adjustability of the seals and better provision for seal replacement. Flanged rollers are recommended for future door systems to assure reliable service.

Heat Trace

The new features of the heat trace system in this test receiver were active control, more extensive user of strip heaters, and a new vendor for the MI cable. Active control of the heat trace generally worked well. The molten-salt piping system could be maintained hot over a broad range of weather conditions. A key point, however, is that large variations in temperature within a zone are likely. This can result in overheating some regions since the coldest spots must be kept above the salt freezing temperature. For components that are sensitive to temperature, such as valves or instrumentation, separate control zones must be used. Although the data-logger used on this experiment was adequate for control, it would be a great improvement to integrate the heat trace into the main process controller. This would allow more flexible control by allowing such activities as shutting off heat trace on flowing lines, better control logic by checking for the lowest thermocouple measurement in a zone, and interlocking of valve movement based on acceptable bellows temperature. It also would reduce the number of separate computer systems needed to operate the system.

Regarding the heaters themselves, the key aspects are reliability and replaceability. The change in heat trace vendor to Pyrotenax made a significant improvement in reliability of the MI cable. Hot to cold junctions continue to be a maintenance problem, but this can be field repaired. The bigger problem with MI cable is still replaceability. Although the cable was more reliable, some cable failure still occurred. A redundant cable helps, and no cable replacements were required during the test (where a redundant was available), but in longer term service, replacement could eventually be necessary. This would be a big problem with the MI cable installed as it is on this receiver. The strip and band heaters, on the other hand, did not have high reliability. In particular, they were sensitive to salt leaks. They were, however, very easy to replace. For applications like the cold surge tank, where several are required, they tend to provide a certain amount of self-redundancy. That is, a few can fail, and the rest still keep the tank hot. Because of this, these heaters should be used wherever possible.

Overall, the heat trace methods used for this test were adequate, and could be employed on larger plants. There still is a great deal of room, however, for improvement before heat trace would loose its position as the most troublesome aspect of any molten-salt system.

Piping and Valves

The piping system presented no real problems for the test. Standard welded construction, with stainless steel used for hot salt lines and carbon steel for cold lines performed well. When setting design temperature, however, consideration should be given to heat trace conditions which may result in greater temperatures than expected, especially in stagnant salt lines. Flanged connections should be avoided because they can leak, but with adequate care, they can be made to work where piping must frequently be disconnected. Bellows seal valves did their jobs adequately, but the failure of two bellows in the redundant receiver control valves serves as a reminder of how delicate they are. It is imperative that control valves not be moved with frozen salt on the bellows. The nested bellows in the receiver control valves were a big improvement relative to convoluted bellows as they resulted in compact valves, and the bellows were kept hot by salt flow. This allowed valve heat trace to

be turned off when salt was flowing. The small Nupro valves worked well and provide good, relatively inexpensive, salt valves for small capacity applications.

8.6.2 Instrumentation

The instrumentation employed in the receiver is listed in Table 8-II. Overall, the instrumentation was adequate to operate and control the receiver. Several of the instruments did not work as anticipated, however, and alternatives had to be used.

TABLE 8-II
RECEIVER INSTRUMENTATION SUMMARY

Instrument & Location	Type	Experience
Thermocouple	Type K, sheathed	Worked well
Pressure Transmitters		
Salt flow riser and both control zones	Venturi, double isolated pressure differential transmitter (oil filled)	Large zero drift unreliable
Both flow control zones	Receiver inlet pressure vs. flow, double isolated absolute pressure gage (oil filled)	Adequate, but wide uncertainty band
Salt level cold surge tank (pressurized)	Pressurized tank double isolated pressure differential transmitter (oil filled)	Adequate, but large zero drift and uncertainty band
Hot surge tank (vented)	Vented tank, bubbler type	Worked well
Pressure inlet of both flow control zones	Double isolated absolute pressure transmitter (oil filled)	Worked well
Foster Wheeler Panel, Inlet to outlet	Double isolated differential pressure transmitter (oil filled)	Worked well
Displacement Gages		
Horizontal deflection panel 2-East and 3-West	Transmitter (4-20 mA output)	Worked well

TABLE 8-II (CON'T)

Vertical displacement panels 2,3,4-East and 3-West	Transmitter (4-20 mA output)	Worked well
Solar Flux Gages		
All panels	Air cooled	Worked well
All panels	Water cooled	Water cooling passage plugged
Strain Gages		
Panel 3-W	Resistance	Failed to produce useful data
Panel 3-W	Capacitance	Produced some useful data

The most serious of the problems occurred with the low range differential pressure transmitters employed with the Venturis (to indicate flow) and with cold surge tank to sense level. In both cases, large zero shifts occurred as a function of time making the gages unreliable. In the case of flow, an alternative indication was derived from the high range inlet pressure measurements. The problem with the low range transmitters was apparently related to the syltherm oil fill fluid. At the operating temperature of the gage, the vapor pressure of the oil is significant relative to the measurement range, and may have affected the readings. The transmitter itself is known to be reliable in this pressure range. Alternative flow measurement using either a different transmitter fill fluid (NAK for example) or other types of sensor should be developed.

The second important failure was that of the water cooled flux gages. Several of these failed from overheating when the cooling passages in the gages plugged. The balance were taken out of service due to the plugging problem, leaving the air cooled gages to serve for control and monitoring. The problem with the plugging of the water channels could probably be solved by working with the gage vendor and specifying larger flow the plenums. (Standard gages of this type are available.)

The failure of the resistance strain gages is not of great concern since this type of detailed instrumentation would not be required on a commercial design.

Overall, adequate instrumentation exists to support operation of the test receiver, or a scaled up plant. Improvements, if not absolutely necessary, would be desirable for flow measurement.

8.6.3 Post Exam Test

Various post-examinations (described below) are recommended for the test receiver at the end of the next phase of testing.

Panels

Non-Destructive Examination

A detailed inspection of the receiver panels should be performed. Documenting the magnitude and location of tube deformations will serve as a benchmark data for continued receiver testing. The condition of panel buckstays and insulation should be documented noting any signs of wear or overheat. This is particularly true where large panel gaps exist creating higher than normal temperatures. Flux gages and their supports should be inspected for damage resulting from receiver operation.

Destructive Examination

The salt-side surface of the receiver tube should be inspected for corrosion. Critical areas to check for corrosion include the welds and heat affected zone (HAZ) of the tube to safe end connection and the HAZ of the tube attachments. Corrosion inspection should be made near the receiver outlet where salt temperatures are highest.

Receiver Paint

Paint thickness should be measured and documented. Taking measurements at various locations on the surface of the receiver would show uniformity of thickness. Thickness is critical to heat absorption.

SECTION 9

9.0 REFERENCES

1. Battleson, K.W., "Solar Power Tower Design Guide," SAND81-8005, April 1981, Sandia National Laboratories, Albuquerque, New Mexico and Livermore, California.

2. Tracy, T., "Conceptual Design of Advanced Central Receiver Power Systems," DOE Contract EG-77-C-03-1724, September 1978, The Martin Marietta Corporation, Denver, Colorado.

3. Babcock & Wilcox Company, The, "Molten Salt Receiver Subsystem Research Experiment," SAND82-8178, November 1982, Sandia National Laboratories, Albuquerque, New Mexico and Livermore, California.

4. Foster Wheeler Company, "Molten Salt Receiver Subsystem Research Experiment," SAND82-8177, November 1982, Sandia National Laboratories, Albuquerque, New Mexico and Livermore, California.

5. Weber, E.R. (Arizona Public Service Company), "Saguaro Power Plant Solar Repowering Project," DOE/SF10739-2, July 1980, The Department of Energy, San Francisco, California.

6. Weber, E.R. (Arizona Public Service Company), "Preliminary Design of a Solar Central Receiver for a Site Specific Repowering Application," DE-FC03-82SF11675-1, August 1983, The Department of Energy, San Francisco, California.

7. Southern California Edison, Bechtel Power Corp., McDonnell Douglas Corp., California.

8. Martin Marietta Corporation, "Alternate Central Receiver Power System, Phase II," MCR-81-1707, March 1981, Martin Marietta Aerospace Corporation, Denver, Colorado.

9. Martin Marietta Corporation, "Molten Salt Electric Experiment, Phase I," SAND85-8175, August 1985, Sandia National Laboratories, Albuquerque, New Mexico and Livermore, California.

10. Holl, R.J., Barron, D.R., and Saloff, S.A. (McDonnell Douglas Astronautics Company), "Molten Salt Electric Experiment," EPRI Rsearch Project Contract RP 2302-2, Electric Power Research Institue. To be published.

11. Bergan, N.E., "Testing of the Molten Salt Electric Experiment (MSEE) Solar Central Receiver in an External Configuration," SAND86-8010, Sandia National Laboratories, Albuquerque, New Mexico and Livermore, California. To be published.

12. Martin Marietta Corporation, "Molten Salt Thermal Storage Subsystem Research Experiment," Sandia Contract Number 20-2988, September 1982, Sandia National Laboratories, Albuquerque, New Mexico and Livermore, California.

13. Babcock & Wilcox Company, The, "Molten Salt Electric Experiment Steam Generator Subsystem Final Report," SAND85-8181, April 1986, Sandia National Laboratories, Albuquerque, New Mexico and Livermore, California.

14. "Criteria for Design of Elevated Temperature Class 1 Components in Section III, Division 1 of the ASME Boiler and Pressure Vessel Code," May 1986.

15. Bradshaw, R.W., "Thermal Convection Loop Corrosion Tests of 316SS and IN800 in Molten Nitrate Salts, SAND81-8210, Sandia National Laboratories, Albuquerque, New Mexico and Livermore, California, February 1982.

16. Bradshaw, R.W., "A Thermal Convection Loop Study of Corrosion of Alloy 800 in Molten $NaNO_3$-KNO_3, SAND82-8911, Sandia National Laboratories, Albuquerque, New Mexico and Livermore, California, January 1983.

17. Kistler, B.L., "Fatigue Analysis of a Solar Central Receiver Design Using Measured Weather Data," SAND 86-8017, Sandia National Laboratories, Albuquerque, New Mexico and Livermore, California. To be published.

18. Jones, W.B., Bourcier, R.J., "Thermal Fatigue of Solar Receiver Candidate Alloys," Proceedings of the DOE Solar Central Receiver Technical Annual Meeting, SAND 85-8241, Sandia National Laboratories, Albuquerque, New Mexico and Livermore, California, December 1985.

19. Jones, W.B., Bourcier, R.J., Van Den Avyle, J.A., "Thermomechanical Fatigue of Solar Central Receiver Collector Tube Alloys," SAND87-1258, Sandia National Laboratories, Albuquerque, New Mexico and Livermore, California, August 1987.

20. Sieder E.N., and Tate, G.E., "Heat Transfer and Pressure Drop of Liquids in Tubes," Ind. Eng. Chem., Vol. 28, 1936, p. 1429.

21. Hausen, H., "Darstellung des Warmeuberganges in Rohren durch verllge-meinerte Potenzbeziehungen," VDI Zeit, No. 4, 1943, p. 91.

22. Dittus, F. W., and Boelter, L.M.K., University of California (Berkeley), Pub. Eng., Vol. 2, 1930.

23. ASME Boiler and Pressure Vessel Code, The American Society of Mechanical Engineers, New York, 1983.

24. Narayanan, T.V., Rao, M.S.M., and Carli, G., "Structural Design and Life Assessment of a Molten Salt Receiver," presented at the ASME 1984 PVP Conference, San Antonio, June 17-21, 1984.

25. Rao, S.M., "NONAX - A Computer Program for Thermoelastic-Plastic-Creep Analysis of Thick-Walled Cylinders Under General Nonaxial Symmetric Loading," Foster Wheeler Development Corporation, Report No. EST-78-5, 1979.

26. Biggs, F., and Vittitoe, C.N., "The Helios Model for the Optical Behavior of Reflecting Solar Concentrators," SAND76-0347, Sandia National Laboratories, Albuqerque, New Mexico and Livermore, California, 1979.

27. Sayers, D.D., "CAVITY - A Computer Code to Couple Radiative Exchange in a Cavity Type Receiver with the Conductive - Convective Exchange to the

Working Fluid," Sandia National Laboratories Internal Memorandum RS8245/20, Albuquerque, New Mexico and Livermore, California May 1985.

28. Emery, A.F., "Instruction Manual for the Program SHAPEFACTOR," SAND80-8027, Sandia National Laboratories, Albuquerque, New Mexico and Livermore, California, 1980.

29. Siegel, R., and Howell, J.R., Thermal Radiation Heat Transfer, 2nd Ed., McGraw-Hill, New York, 1981.

30. Siebers, D., and Kraabel, J., "Estimating Convective Energy Losses from Solar Central Receivers," Report SAND84-8717, Sandia National Laboratories, Albuquerque, New Mexico and Livermore, California, 1984.

31. Boehm, R.F., "A Review of Convective Loss Data from Solar Central Receivers," J. Solar Energy Engineering, 109, pp 101-107, May 1987.

32. Boehm, R., Nakahaie, H., and Bergan, N., "Flux-Off Convective Heat Loss Evaluation of the MSEE External Receiver," ASME Paper 86-WA/Sol-2, 1986.

33. Boehm, R., Nakahaie, H., and Bergan, N., "Evaluation of a Flux-On Method for Determining Thermal Losses from Solar Central Receivers," Proceedings of the ASME Solar Energy Conference, 1987.

34. Boehm, R. "A Review of Convective Loss Data From Solar Central Receivers," Journal of Solar Energy Engineering 109: 101-107, May, 1987.

35. Baker, A., "International Energy Agency (IEA) Small Solar Power Systems (SSPS) Loss Tests by Complementary Heliostat Field Configurations," report, to appear, 1987.

36. Duffie, J., and Becknam, W., Solar Engineering Of Thermal Processes, New York: J. Wiley and Sons, p. 122, 1980.

37. Radosevich, L.G., "An Analysis of Power Production Performance for Solar 1, the 10 MWe Solar Thermal Central Receiver Pilot Plant," SAND87-8008, Sandia

National Laboratories, Albuquerque, New Mexico and Livermore, California, June 1987.

38. Giles, R.V., "Theory and Problems of Fluid Mechanics and Hydraulics", 2 ed., Schaum Publishing Company, New York, 1956, p. 99.

39. Nelson, C. and Mahoney, A.R., "The Effect of Vitrification Temperature Upon the Solar Average Absorptance Properties of Pyromark Series 2500 Black Paint, SAND86-0675, Sandia National Laboratories, Albuquerque, New Mexico and Livermore, California.

12/04/91
UNLIMITED RELEASE
INITIAL DISTRIBUTION

U.S. Department of Energy (2)
Forrestal Building
Code CE-132
1000 Independence Avenue, SW
Washington, DC 20585
Attn: G. Burch
S. Gronich

Advanced Thermal Systems
7600 East Arapahoe
Suite 215
Englewood, CO 80112
Attn: D. Gorman

Arizona Electric Power Cooperative, Inc.
P.O. Box 670
Benson, AZ 85602
Attn: D.W. Kimball

Babcock and Wilcox (2)
91 Stirling Avenue
Barberton, OH 44203
Attn: P.A. Bator

Bechtel National, Inc. (3)
50 Beale Street
50/15 D8
P.O. Box 3965
San Francisco, CA 94106
Attn: P. DeLaquil
B. Kelly
R. Lessley

Black & Veatch Engineers
11401 Lamar
Overland Park, KS 66411
Attn: L. Stoddard

Bureau of Reclamation
Code D-3710
P.O. Box 205007
Denver, CO 80225
Attn: S. Hightower

Electric Power Research Institute
P.O. Box 10412
Palo Alto, CA 94303
Attn: E. DeMeo

Foster Wheeler Solar Development Corporation
12 Peach Tree Hill Road
Livingston, NJ 07039
Attn: S.F. Wu

HGH Enterprises, Inc.
23011 Moulton Parkway
Suite C-13
Laguna Hills, CA 92653
Attn: Dick Holl

McDonnell Douglas Space Systems
5301 Bolsa Avenue
Huntington Beach, CA 92647
Attn: J.B. Blackmon

National Renewable Energy Laboratory
1617 Cole Boulevard
Golden, CO 80401
Attn: T.A. Williams

Rocketdyne Division
Rockwell International Corp.
6633 Canoga Avenue
Canoga Park, CA 91303
Attn: E. Bauemister

Sacramento Municipal Utility District
6201 S. Street
P.O. Box 15830
Sacramento, CA 95852-1830
Attn: L. Wichert

San Diego Gas and Electric Company
P.O. Box 1831
San Diego, CA 92112
Attn: R. Figueroa

Science Applications International Corp. (2)
2109 Airpark Road, SE
Albuquerque, NM 87106
Attn: D. Smith

Solar Power Engineering Company
P.O. Box 91
Morrison, CO 80465
Attn: H.C. Wroton

Southern California Edison (3)
P.O. Box 800
2244 Walnut Grove Ave.
Rosemead, CA 91777
Attn: C. Lopez
M. Skowronski

Tom Tracey
6922 South Adams Way
Littleton, CO 80122

University of Houston
Solar Energy Laboratory
4800 Calhoun
Houston, TX 77704
Attn: L. Vant-Hull

University of Nevada Las Vegas
College of Engineering
4505 Maryland Parkway
Las Vegas, NV 89154-4027
Attn: B. Boehm

Distribution:

400	J.A. Leonard
1512	R.D. Skocypec
3141	S.A. Landenberger (3)
3145	Document Processing for DOE/OSTI (8)
3151	G.C. Claycomb (3)
6200	B.W. Marshall
6201	P.C. Klimas
6215	C.P. Cameron
6215	C.W. Matthews
6215	E.E. Rush
6215	Solar Tower Library (3)
6216	C.E. Tyner
6216	D.J. Alpert
6217	J.M. Chavez (10)
6217	G.J. Kolb
8523-2	Central Technical Files

☆ U.S. GOVERNMENT PRINTING OFFICE: 1992—673-122/6014